Nader Jalili

Piezoelectric-Based Vibration Control

From Macro to Micro/Nano Scale Systems

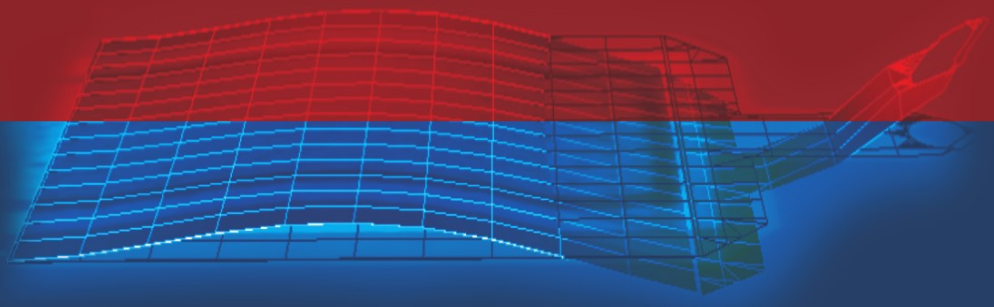

Piezoelectric-Based Vibration Control

Nader Jalili

Piezoelectric-Based Vibration Control

From Macro to Micro/Nano Scale Systems

Springer

Nader Jalili
Department of Mechanical and Industrial Engineering
373 Snell Engineering Center
Northeastern University
360 Huntington Avenue
Boston, MA 02115, USA
n.jalili@neu.edu

ISBN 978-1-4419-0069-2 e-ISBN 978-1-4419-0070-8
DOI 10.1007/978-1-4419-0070-8

Library of Congress Control Number: 2009933099

© Springer Science+Business Media, LLC 2010
All rights reserved. This work may not be translated or copied in whole or in part without the written permission of the publisher (Springer Science+Business Media, LLC, 233 Spring Street, New York, NY 10013, USA), except for brief excerpts in connection with reviews or scholarly analysis. Use in connection with any form of information storage and retrieval, electronic adaptation, computer software, or by similar or dissimilar methodology now known or hereafter developed is forbidden.
The use in this publication of trade names, trademarks, service marks, and similar terms, even if they are not identified as such, is not to be taken as an expression of opinion as to whether or not they are subject to proprietary rights.

Printed on acid-free paper

Springer is part of Springer Science+Business Media (www.springer.com)

To Jaleh, Paneed and Pouya,
the lights on my journey,
To my parents,
for their unconditional supports,
And to the one who reignited love and hope
in me, and made this possible.

Preface

Starting from an elementary level in mechanical vibrations, this self-contained book provides readers with a comprehensive understanding of physical principles, while also highlighting recent advances, in piezoelectric materials and structures used in a variety of vibration-control systems. The contents are cohesively divided into three major parts, each consisting of several chapters. The first part of the book itself can serve as a single-source book on an introduction to mechanical vibrations which starts with the required preliminaries, followed by a unified approach to vibrations of discrete and continuous systems. The second part presents the fundamentals of piezoelectric-based systems with an emphasis on their constitutive modeling as well as vibration absorption and control techniques using piezoelectric actuators and sensors. Building based upon Parts I and II, the last part of the book provides readers with an insight into advanced topics in piezoelectric-based micro/nano actuators and sensors with applications ranging from molecular manufacturing and precision mechatronics to molecular recognition and functional nanostructures.

With its self-contained and single-source style, this book can serve as the primary reference in a first course for senior undergraduate and graduate level students as well as reference for research scientists in the mechanical, electrical, civil, and aerospace engineering disciplines. Although a background in undergraduate vibrations and dynamics is preferred, most fundamental concepts and required mathematical tools are briefly reviewed for the readers' convenience. Such an easy-to-follow format makes this book particularly useful for engineers working in the areas of vibration-control and piezoelectric systems, undergraduate students and graduate students interested in the fundamentals of vibrations and control, and researchers working on advanced piezoelectric-based vibration-control systems.

The materials presented here are the results of over 10 years of intense study and research. Along this long journey, many individuals were instrumental in making this book a success and I would like to acknowledge their help and support. First and foremost, I would like to express my sincere gratitude to my former advisors, Professor Ebrahim Esmailzadeh (MS thesis advisor) who taught me fundamentals of vibrations without such foundations I would not be here today, as well as Professor Nejat Olgac (PhD major advisor) who not only taught me the essence of system dynamics and controls, but also taught me patiently and unselfishly many real-life lessons that have become the guiding principles of my professional and

personal life. I am also indebted to many of my former graduate students. Without their hardwork and dedication, this book would have not been even started. The most influential individuals who have directly contributed to this book include Dr. Saeid Bashash (MS 2005, PhD 2008) for his major contributions on hysteresis compensations and collective efforts in modeling and control of piezoelectric-based systems with applications to MEMS and NEMS presented in Chaps. 7–10; Dr. Mohsen Dadfarnia (MS 2003) for his contributions on piezoelectric-based vibration-control systems discussed mainly in Chap. 9; Dr. Amin Salehi-Khojin (PhD 2008) for his contributions on piezoelectric-based modeling of nanomechanical cantilever systems as well as nanoscopic properties of next-generation piezoelectric actuators and sensors given in Chaps. 8, 9, and 12; Dr. S. Nima Mahmoodi (PhD 2007) for his contributions on nonlinear modeling of nanomechanical cantilever systems presented in Chap. 11; Ms. Mana Afshari (MS 2007) for her contributions on nanomechanical cantilever systems with applications to biosensing discussed in Chap. 11; Dr. Reza Saeidpourazar (PhD 2009) for his contributions on modeling and control of microcantilever-based manipulation and imaging systems discussed in Chap. 10; and finally Dr. Mahmoud Reza Hosseini (PhD 2008) for his contributions in nanomaterials-based sensors modeling and fabrication given in Chap. 12. Special thanks also go to the staff at Springer, Mr. Steven Elliot and Mr. Andrew Leigh for their encouragement to start this enterprise and help throughout this interesting and fruitful experience.

Boston, MA *Nader Jalili*

Contents

Part I Introduction and Overview of Mechanical Vibrations

1 Introduction 3
1.1 A Brief Overview of Smart Structures 3
1.2 Concept of Vibration Control 5
1.2.1 Vibration Isolation vs. Vibration Absorption 6
1.2.2 Vibration Absorption vs. Vibration Control 7
1.2.3 Classifications of Vibration-Control Systems 8
1.3 Mathematical Models of Dynamical Systems 9
1.3.1 Linear vs. Nonlinear Models 9
1.3.2 Lumped-Parameters vs. Distributed-Parameters Models 11

2 An Introduction to Vibrations of Lumped-Parameters Systems 13
2.1 Vibration Characteristics of Linear Discrete Systems 13
2.2 Vibrations of Single-Degree-of-Freedom Systems 14
2.2.1 Time-domain Response Characteristics 15
2.2.2 Frequency Response Function 17
2.3 Vibrations of Multi-Degree-of-Freedom Systems 18
2.3.1 Eigenvalue Problem and Modal Matrix Representation 19
2.3.2 Classically Damped Systems 21
2.3.3 Non-proportional Damping 23
2.4 Illustrative Example from Vibration of Discrete Systems 25

3 A Brief Introduction to Variational Mechanics 35
3.1 An Overview of Calculus of Variations 35
3.1.1 Concept of Variation 36
3.1.2 Properties of Variational Operator δ 38
3.1.3 The Fundamental Theorem of Variation 39
3.1.4 Constrained Minimization of Functionals 43
3.2 A Brief Overview of Variational Mechanics 45

3.2.1 Work–Energy Theorem and Extended Hamilton's Principle 45
3.2.2 Application of Euler Equation in Analytical Dynamics 49
3.3 Steps in Deriving Equations of Motion via Analytical Method 51

4 A Unified Approach to Vibrations of Distributed-Parameters Systems 55
4.1 Equilibrium State and Kinematics of a Deformable Body 56
4.1.1 Differential Equations of Equilibrium 56
4.1.2 Strain–Displacement Relationships 58
4.1.3 Stress–Strain Constitutive Relationships 62
4.2 Virtual Work of a Deformable body 64
4.3 Illustrative Examples from Vibrations of Continuous Systems 69
4.3.1 Longitudinal Vibration of Bars 70
4.3.2 Transverse Vibration of Beams 74
4.3.3 Transverse Vibration of Plates 81
4.4 Eigenvalue Problem in Continuous Systems 86
4.4.1 Discretization of Equations and Separable Solution 87
4.4.2 Normal Modes Analysis 97
4.4.3 Method of Eigenfunctions Expansion 100

Part II Piezoelectric-Based Vibration-Control Systems

5 An Overview of Active Materials Utilized in Smart Structures 115
5.1 Piezoelectric Materials 116
5.1.1 Piezoelectricity Concept 116
5.1.2 Basic Behavior and Constitutive Models of Piezoelectric Materials 116
5.1.3 Practical Applications of Piezoelectric Materials 118
5.2 Pyroelectric Materials 119
5.2.1 Constitutive Model of Pyroelectric Materials 119
5.2.2 Common Pyroelectric Materials 120
5.3 Electrorheological and Magnetorheological Fluids 120
5.3.1 Electrorheological Fluids 120
5.3.2 Magnetorheological Fluids 121
5.4 Shape Memory Alloys (SMAs) 123
5.4.1 SMA Physical Principles and Properties 123
5.4.2 Commercial Applications of SMAs 124
5.5 Electrostrictive and Magnetostrictive Materials 125
5.5.1 Electrostrictive Materials 125
5.5.2 Magnetostrictive Materials 126

6 Physical Principles and Constitutive Models of Piezoelectric Materials 129
6.1 Fundamentals of Piezoelectricity 130
6.1.1 Polarization and Piezoelectric Effects 130

6.1.2 Crystallographic Structure of Piezoelectric Materials 132
6.2 Constitutive Models of Piezoelectric Materials 134
6.2.1 Preliminaries and Definitions 134
6.2.2 Constitutive Relations 135
6.2.3 Nonlinear Characteristics of Piezoelectric Materials 139
6.3 Piezoelectric Material Constitutive Constants 140
6.3.1 General Relationships 140
6.3.2 Piezoelectric Coefficients 142
6.4 Engineering Applications of Piezoelectric Materials and Structures .148
6.4.1 Application of Piezoceramics in Mechatronic Systems 149
6.4.2 Motion Magnification Strategies for Piezoceramic Actuation 149
6.4.3 Piezoceramic-Based High Precision Miniature Motors 150
6.5 Piezoelectric-Based Actuators and Sensors 151
6.5.1 Piezoelectric-Based Actuator/Sensor Configurations 151
6.5.2 Examples of Piezoelectric-Based Actuators/Sensors 154
6.6 Recent Advances in Piezoelectric-Based Systems 156
6.6.1 Piezoelectric-Based Micromanipulators 156
6.6.2 Piezoelectrically Actuated Microcantilevers 156
6.6.3 Piezoelectrically Driven Translational Nano-Positioners 158
6.6.4 Future Directions and Outlooks 158

7 Hysteretic Characteristics of Piezoelectric Materials 161
7.1 The Origin of Hysteresis 161
7.1.1 Rate-Independent and Rate-Dependent Hysteresis 162
7.1.2 Local versus Nonlocal Memories 163
7.2 Hysteresis Nonlinearities in Piezoelectric Materials 163
7.3 Hysteresis Modeling Frameworks for Piezoelectric Materials 164
7.3.1 Phenomenological Hysteresis Models 165
7.3.2 Constitutive-based Hysteresis Models 170
7.4 Hysteresis Compensation Techniques 179

8 Piezoelectric-Based Systems Modeling 183
8.1 Modeling Preliminaries and Assumptions 183
8.2 Modeling Piezoelectric Actuators in Axial (Stacked) Configuration .185
8.2.1 Piezoelectric Stacked Actuators under No External Load 186
8.2.2 Piezoelectric Stacked Actuators with External Load 189
8.2.3 Vibration Analysis of Piezoelectric Actuators in Axial Configuration – An Example Case Study 192
8.3 Modeling Piezoelectric Actuators in Transverse (Bender) Configuration 198
8.3.1 General Energy-based Modeling for Laminar Actuators 198
8.3.2 Vibration Analysis of a Piezoelectrically Actuated Active Probe® – An Example Case Study 205

8.3.3 Equivalent Bending Moment Actuation Generation 213
8.4 A Brief Introduction to Piezoelectric Actuation in 2D 219
8.4.1 General Energy-based Modeling for 2D Piezoelectric Actuation 219
8.4.2 Equivalent Bending Moment 2D Actuation Generation 224
8.5 Modeling Piezoelectric Sensors 226
8.5.1 Piezoelectric Stacked Sensors 227
8.5.2 Piezoelectric Laminar Sensors 229
8.5.3 Equivalent Circuit Models of Piezoelectric Sensors 230

9 Vibration Control Using Piezoelectric Actuators and Sensors 233
9.1 Notion of Vibration Control and Preliminaries 233
9.2 Active Vibration Absorption using Piezoelectric Inertial Actuators ..235
9.2.1 Active Resonator Absorber 237
9.2.2 Delayed-Resonator Vibration Absorber 242
9.3 Piezoelectric-Based Active Vibration-Control Systems 251
9.3.1 Control of Piezoceramic Actuators in Axial Configuration .252
9.3.2 Vibration Control Using Piezoelectric Laminar Actuators ..263
9.4 Piezoelectric-based Semi-active Vibration-Control Systems 284
9.4.1 A Brief Overview of Switched-Stiffness Vibration-Control Concept 286
9.4.2 Real-Time Implementation of Switched-Stiffness Concept 290
9.4.3 Switched-Stiffness Vibration Control using Piezoelectric Materials 293
9.4.4 Piezoelectric-Based Switched-Stiffness Experimentation ...298
9.5 Self-sensing Actuation using Piezoelectric Materials 302
9.5.1 Preliminaries and Background 302
9.5.2 Adaptation Strategy for Piezoelectric Capacitance 304
9.5.3 Application of Self-sensing Actuation for Mass Detection ..306

Part III Piezoelectric-Based Micro/Nano Sensors and Actuators

10 Piezoelectric-Based Micro- and Nano-Positioning Systems 313
10.1 Classification of Control and Manipulation at the Nanoscale 313
10.1.1 Scanning Probe Microscopy-Based Control and Manipulation 315
10.1.2 Nanorobotic Manipulation-Based Control and Manipulation 319
10.2 Piezoelectrically Driven Micro- and Nano-Positioning Systems 321
10.2.1 Piezoelectric Actuators Used in STM Systems 322
10.2.2 Modeling Piezoelectric Actuators Used in STM Systems ...322
10.3 Control of Single-Axis Piezoelectric Nano-positioning Systems 328
10.3.1 Feedforward Control Strategies 330

10.3.2 Feedback Control Strategies 332
10.4 Control of Multiple-Axis Piezoelectric Nano-positioning Systems 336
10.4.1 Modeling and Control of Coupled Parallel Piezo-Flexural Nano-Positioning Stages 336
10.4.2 Modeling and Control of Three-Dimensional Nano-Positioning Systems 351

11 Piezoelectric-Based Nanomechanical Cantilever Sensors 359
11.1 Preliminaries and Overview 360
11.1.1 Fundamental Operation of Nanomechanical Cantilever Sensors 360
11.1.2 Linear vs. Nonlinear and Small-scale vs. Large-scale Vibrations 363
11.1.3 Common Methods of Signal Transduction in NMCS 363
11.1.4 Engineering Applications and Recent Developments 366
11.2 Modeling Frameworks for Nanomechanical Cantilever Sensors 368
11.2.1 Linear and Nonlinear Vibration Analyses of Piezoelectrically-driven NMCS 368
11.2.2 Coupled Flexural-Torsional Vibration Analysis of NMCS 388
11.3 Ultrasmall Mass Sensing and Materials Characterization using NMCS 399
11.3.1 Biological Species Detection using NMCS 401
11.3.2 Ultrasmall Mass Detection using Active Probes 411

12 Nanomaterial-Based Piezoelectric Actuators and Sensors 419
12.1 Piezoelectric Properties of Nanotubes (CNT and BNNT) 420
12.1.1 A Brief Overview of Nanotubes 420
12.1.2 Piezoelectricity in Nanotubes and Nanotube-Based Materials 421
12.2 Nanotube-Based Piezoelectric Sensors and Actuators 423
12.2.1 Actuation and Sensing Mechanism in Multifunctional Nanomaterials 423
12.2.2 Fabrication of Nanotube-Based Piezoelectric Film Sensors 426
12.2.3 Piezoelectric Properties Measurement of Nanotube-Based Sensors 432
12.3 Structural Damping and Vibration Control Using Nanotubes-Based Composites 434
12.3.1 Fabrication of Nanotube-Based Composites for Vibration Damping and Control 434
12.3.2 Free Vibration Characterization of Nanotube-Based Composites 436

12.3.3 Forced Vibration Characterization of Nanotube-Based Composites 441
12.4 Piezoelectric Nanocomposites with Tunable Properties 446
12.4.1 A Brief Overview of Interphase Zone Control 446
12.4.2 Molecular Dynamic Simulations for Nanotube-Based Composites 448
12.4.3 Continuum Level Elasticity Model of Nanotube-Based Composites 451
12.4.4 Numerical Results and Discussions of Nanotube-Based Composites 451
12.5 Electronic Textiles Comprised of Functional Nanomaterials 455
12.5.1 The Concept of Electronic Textiles 455
12.5.2 Fabrication of Nonwoven CNT-based Composite Fabrics 455
12.5.3 Experimental Characterization of CNT-based Fabric Sensors 459

Mathematical Preliminaries 463
A.1 Preliminaries and Definitions 463
A.2 Indicial Notation and Summation Convention 466
A.2.1 Indicial Notation Convention 466
A.2.2 The Kronecker Delta 467
A.3 Equilibrium States and Stability 468
A.3.1 Equilibrium Points or States 468
A.3.2 Concept of Stability 469
A.4 A Brief Overview of Fundamental Stability Theorems 471
A.4.1 Lyapunov Local and Global Stability Theorems 471
A.4.2 Local and Global Invariant Set Theorems 474

Proofs of Selected Theorems 477
B.1 Proof of Theorem 9.1 (Dadfarnia et al. 2004a) 477
B.2 Proof of Theorem 9.2 (Dadfarnia et al. 2004b) 480
B.3 Proof of Theorem 9.3 (Ramaratnam and Jalili 2006a) 482
B.4 Proof of Theorem 10.1 (Bashash and Jalili 2009) 483
B.5 Proof of Theorem 10.2 (Bashash and Jalili 2009) 484

References 487

Index 505

About this Book

Piezoelectric-Based Vibration Control: From Macro to Micro/Nano Scale Systems covers a comprehensive understanding and physical principles in piezoelectric materials and structures used in a variety of vibration-control systems. With its self-contained and single-source style, this book provides a widespread spectrum of discussions ranging from fundamental concepts of mechanical vibration analysis and control to piezoelectric actuators and sensors. Starting from an elementary level in mechanical vibrations, this book

- Offers the reader a detailed discussion of vibration of continuous systems as a single-source book,
- Provides actual actuator and sensor configurations, along with illustrative hands-on problems and examples that can be applied by the reader, and
- Covers advanced topics in piezoelectric-based micro/nano actuators and sensors with applications ranging from precision mechatronics to molecular recognition and functional nanostructures.

Piezoelectric-Based Vibration Control: From Macro to Micro/Nano Scale Systems with its easy-to-follow format is a must-read for all engineers working in the areas of vibration control and piezoelectric systems, undergraduate students interested in fundamental of vibrations and control, up to graduate students and researchers working on advanced piezoelectric-based vibration-control systems.

Part I
Introduction and Overview of Mechanical Vibrations

This first part of the book presents a brief introduction to mechanical vibrations starting with an overview of smart structures and vibration-control systems followed by an overview of vibrations of discrete and continuous systems. The four chapters in this part are organized as follows. The first chapter provides an introduction to what is covered in this book, starting with the definition of smart structures and concept of vibration control and its classifications, and ending with an overview of different modeling and control strategies for both discrete and continuous dynamical systems. Chap. 2 provides readers with a brief overview of vibrations of lumped-parameters systems including modal matrix representation and decoupling strategies for the governing equations of motion. Some of the mathematical preliminaries including an introduction to calculus of variation and variational mechanics are reviewed in Chap. 3 to prepare the reader for the materials covered in Chap. 4. Finally, the last chapter in this part presents an overview of vibrations of distributed-parameters systems along with some illustrative examples from vibration of continuous systems (e.g., longitudinal vibration of bars, and transverse vibrations of beams and plates). The comprehensive treatment offered in this chapter follows a unified approach in which an energy-based modeling framework is adopted to describe the system behavior in an easy-to-follow manner. The materials presented in this part shall form the basis for the subsequent modeling and control developments for both piezoelectric-based actuators and sensors as well as vibration-control systems discussed in Parts II and III.

Chapter 1
Introduction

Contents

1.1 A Brief Overview of Smart Structures 3
1.2 Concept of Vibration Control 5
1.2.1 Vibration Isolation vs. Vibration Absorption 6
1.2.2 Vibration Absorption vs. Vibration Control 7
1.2.3 Classifications of Vibration-Control Systems 8
1.3 Mathematical Models of Dynamical Systems 9
1.3.1 Linear vs. Nonlinear Models 9
1.3.2 Lumped-Parameters vs. Distributed-Parameters Models 11
Summary

This chapter provides an introduction to what is covered in this book. A general definition of smart structures along with a list of few select active materials as the building blocks of smart structures is given first. The concept of vibration control and its classifications are presented next, followed by an overview of different modeling and control strategies for both discrete and continuous dynamical systems.

1.1 A Brief Overview of Smart Structures[1]

There are numerous definitions for smart or intelligent[2] structures in the literature that vary in almost every engineering or science discipline. Despite such varieties, it is widely accepted that a smart structure is a structure that possesses both *life features* and *artificial intelligence* (see Fig. 1.1). The life features concern with the notion that the structure has sensing and actuation functions, the attributes that exist

[1] The words "structures" and "systems" are used interchangeably for "smart structures" in the literature. We must, however, note that "structures" typically refer to particular elements or mechanical components, while "systems" are more general forms and include a collection of components that may be defined by real or imaginary boundaries. It is worthy to note that all structures are systems.

[2] There is an increasing interest within the smart structures community in replacing the traditionally used word "smart" with "intelligent".

N. Jalili, *Piezoelectric-Based Vibration Control*,
DOI 10.1007/978-1-4419-0070-8_1, © Springer Science+Business Media LLC 2010

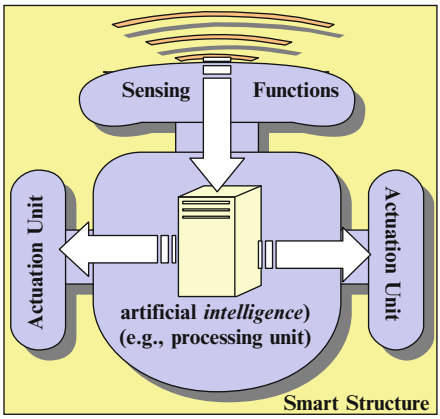

Fig. 1.1 Conceptual definition and attributes of smart structures

in almost every living thing. These life functions can either inherently exist in the structure (the property of the material) or be synthetically embedded in the structures. The artificial intelligence feature concerns with the fact that a smart structure has the unique capabilities, through computers, microprocessors, control logic and algorithms, to adapt to changes (e.g., environmental conditions) and external stimuli to meet the stated objectives and to provide adaptive functionality. This feature forms the processing function of a smart structure as shown in Fig. 1.1.

A smart structure typically comprises of one or more active (or functional) materials. These active materials act in a unique way in which couple at least two of the following fields to provide the required functionality: mechanical, electrical, magnetic, thermal, chemical and optical. Through this coupling, these materials have the ability to change their shape, respond to external stimuli and vary their physical, geometrical and rheological properties. Some of the typical active materials along with their milestone years and coupling fields are listed here (Tzou et al. 2004 and references therein).

- pyroelectrics (315 B.C., couple thermal and mechanical fields),
- electrorheological fluids (1784, couple electrical and mechanical fields),
- magnetostrictive materials (1840, couple magnetic and mechanical fields),
- piezoelectrics (1880, couple mechanical and electrical fields),
- shape memory alloys (1932, couple thermal and mechanical fields),
- magnetorheological fluids (1947, couple magnetic and mechanical fields),
- electroactive polymers and polyelectrolyte gels (1949, couple electrical and mechanical fields),
- electrostrictive materials (1954, couple electrical and mechanical fields), and
- photostrictive materials (1974, couple optical and mechanical fields).

We will present a more detailed description along with potential applications of a few selected active materials from the above list later in Chap. 5. These descriptions include their working principles, physical properties and brief overview of their constitutive equations. While studying these and other active materials, piezoelectric materials stand above the most common active materials for use in many

mechatronic and vibration-control systems. Hence, a dedicated chapter (Chap. 6) is devoted to provide an extensive discussion on piezoelectricity and piezoelectric materials along with their practical applications in sensing and actuation for use in vibration-control systems. In order to keep the book focused on piezoelectric-based systems, we prefer not to provide more details on the other smart structures and systems other than those briefly presented in Chap. 5, and refer interested reader to cited references (Gandhi and Thompson 1992; Banks et al. 1996; Culshaw 1996; Clark et al. 1998; Srinivasan and McFarland 2001; Smith 2005; Leo 2007).

1.2 Concept of Vibration Control[3]

While dealing with mechanical vibrations, two important and related components must be considered; namely, uncertainties and control for the analysis to be complete (Benaroya 1998). In modeling a dynamic system, two scenarios may be encountered. If the system parameters can be made known under ideal conditions, the developed model is called "direct" or "forward", see Fig. 1.2a. For the cases where there are unmodeled dynamics, complex behavior or ever-present parametric uncertainties, an "inverse" approach is used as shown in Fig. 1.2b. It must be noted that both of these frameworks can be "deterministic" or "probabilistic", depending on the level of knowledge of system parameters and/or modeling uncertainties. The latter modeling approach is a more general approach that takes into account all possible conditions, external stimuli and physical and geometrical properties. For example, when modeling an engine valve, the stiffness of the valve or its

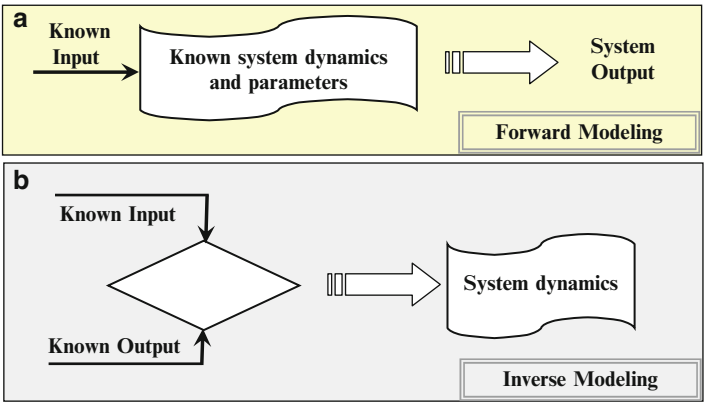

Fig. 1.2 Forward (**a**) vs. inverse (**b**) modeling approaches

[3] Most parts of this section may have come directly from our book chapter on the subject matter (Jalili and Esmailzadeh 2005).

damping characteristics may vary with engine operating and environmental conditions, hence, they can become uncertain. Although this modeling approach is more general and useful for many practical cases, dealing with uncertainties and unmodeled dynamics is not a trivial task. As a remedy to this, vibration control could be used to overcome these uncertainties and modeling shortfalls. This forms our main motivation for developing this book in vibration-control systems. Coupled with attractive features of piezoelectric materials, these vibration-control systems can be practically implemented for many engineering and natural systems as discussed extensively in Part II (Chaps. 8 and 9).

Vibration control, vibration isolation and vibration absorption are often used interchangeably in the literature as their ultimate objective is to eliminate, alter or otherwise limit the vibration response characteristics of a dynamic system. In order to better understand and realize the unique features of each of these systems, we outline, next, their definitions, applications and distinctions.

1.2.1 Vibration Isolation vs. Vibration Absorption

In vibration isolation, either the source of vibration is isolated from the system of concern (also called "force transmissibility", see Fig. 1.3a), or the device is protected from vibration of its point of attachment (also called "displacement transmissibility", see Fig. 1.3b). Unlike the isolator, a vibration absorber consists of a secondary

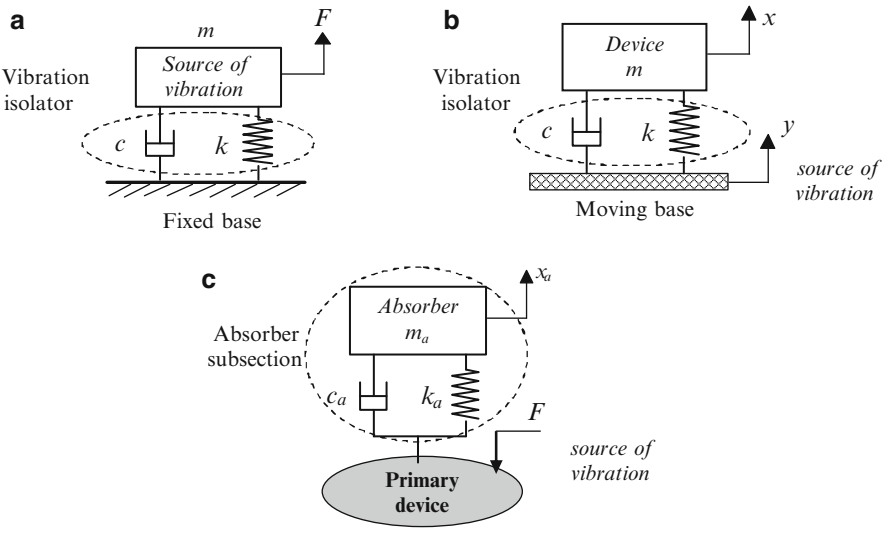

Fig. 1.3 Schematic of; (**a**) force transmissibility for foundation isolation, (**b**) displacement transmissibility for protecting device from vibration of the base, and (**c**) application of vibration absorber for suppressing primary system vibration
Source: Jalili and Esmailzadeh 2005, with permission

system (usually mass-spring-damper trio) added to the primary device to protect it from vibrating (see Fig. 1.3c). By properly selecting absorber mass, stiffness, and damping, the vibration of the primary system can be minimized (Inman 2007).

1.2.2 Vibration Absorption vs. Vibration Control

In vibration control schemes, the driving forces or torques applied to the system are altered in order to regulate or track a desired trajectory while simultaneously suppressing the vibrational transients in the system. This control problem is rather challenging since it must achieve the motion tracking objectives while stabilizing the transient vibrations in the system. Several control methods have been developed for such applications; optimal control (Sinha 1998), finite element approach (Bayo 1987), model reference adaptive control (Ge et al. 1997), adaptive nonlinear boundary control (Yuh 1987), and several other techniques including variable structure control (VSC) methods (de Querioz et al. 2000; Jalili 2001a; Jalili and Esmailzadeh 2005).

In vibration absorber systems, a secondary system is added in order to mimic the vibratory energy from the point of interest (attachment) and transfer it into other components or dissipate it into heat. Figure 1.4 demonstrates a comparative schematic of vibration control (both single-input control and multi-input configurations) on translating and rotating the flexible beams which could represent many industrial robot manipulators as well as vibration absorber applications for automotive suspension systems (Jalili 2001a,b; Jalili and Esmailzadeh 2001; Dadfarnia et al. 2004a, b).

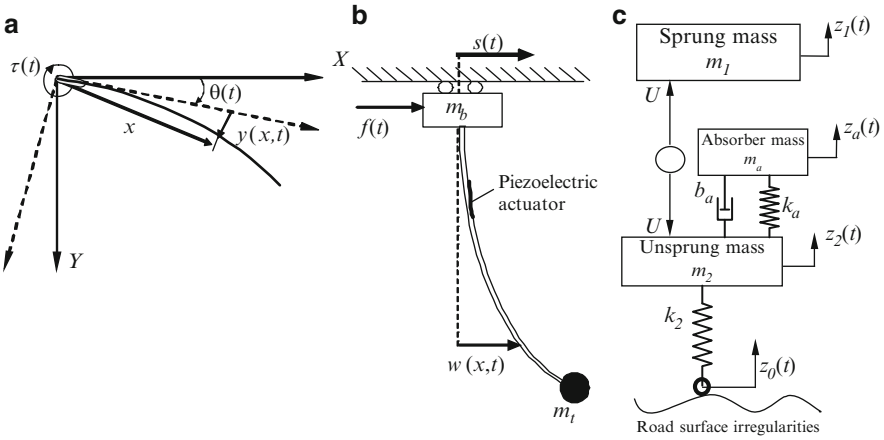

Fig. 1.4 A comparative schematic of vibration-control systems; (**a**) single-input simultaneous tracking and vibration control, (**b**) multiinput tracking and vibration control and (**c**) a 2DOF vehicle model with dynamic vibration absorber
Source: Jalili and Esmailzadeh 2005, with permission

1.2.3 Classifications of Vibration-Control Systems

Passive, active, and semi active are referred, in the literature, as the three most commonly used classifications of vibration control systems (either as isolators or absorbers), see Fig. 1.5 (Sun et al. 1995). A vibration control system is said to be active, passive, or semi active depending on the amount of external power required for the vibration control system to perform its function. A *passive* vibration control consists of a resilient member (stiffness) and an energy dissipator (damper) to either absorb the vibratory energy or to load the transmission path of the disturbing vibration (Korenev et al. 1993), Fig. 1.5a. This type of vibration control system performs best within the frequency region of its highest sensitivity. For wide band excitation frequency, its performance can be improved considerably by optimizing the system parameters (Puksand 1975; Warburton et al. 1980; Esmailzadeh and Jalili 1998a; Jalili and Esmailzadeh 2003). However, this improvement is achieved at the cost of lowering the narrow band suppression characteristics.

The passive vibration control has significant limitations in structural applications where broadband disturbances of highly uncertain nature are encountered. In order to compensate for these limitations, *active* vibration-control systems are utilized. With an additional active force introduced as a part of absorber subsection, $u(t)$ in Fig. 1.5b, the system is then controlled using different algorithms to make it more responsive to the source of disturbances (Sun et al. 1995; Soong and Constantinou 1994; Olgac and Jalili 1998; Jalili and Olgac 2000a,b; Margolis 1998). *Semi active* vibration control system, a combination of active/passive treatment, is intended to reduce the amount of external power that is necessary to achieve the desired performance characteristics (Lee-Glauser et al. 1997; Jalili and Esmailzadeh 2002; Jalili 2000, 2001b; Ramaratnam and Jalili 2006), see Fig. 1.5c.

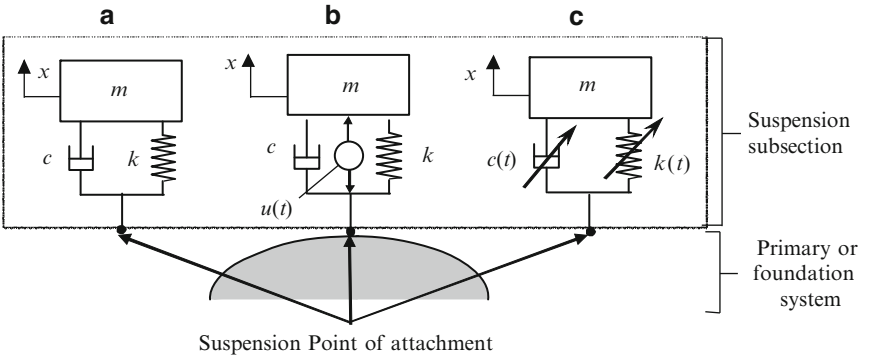

Fig. 1.5 A typical primary structure equipped with three versions of suspension systems; (**a**) passive, (**b**) active, and (**c**) semiactive configurations
Source: Jalili and Esmailzadeh 2005, with permission

1.3 Mathematical Models of Dynamical Systems

Mathematical modeling of a dynamic system refers to the process of describing the system in terms of governing (differential) equations. These equations are typically obtained from either a direct approach or numerical methods (e.g., finite element method). Concerning the direct approaches, there are two different modeling strategies; (1) Newtonian and (2) Analytical methods. The former method is based on deriving the equations of motion using the free-body-diagram of the system and taking into account the effects of external forces applied on the boundary of the system. This typically requires a "system decomposition" exercise, where the dynamic system is considered to have been built based upon its components. A nontrivial task in this process is handling the forces and moments in the interface zones, where different system components intersect.

To avoid such complication and in order to present a unified approach for modeling the vibration-control systems considered in this book, we adopt the second modeling approach, i.e., the analytical approach. This is an energy-based modeling framework in which interactions between different fields (e.g., electrical, mechanical and magnetic) can be conveniently established and presented. This is especially important as the piezoelectric-based vibration-control systems considered in this book fall into this category of interacting different fields systems. Along this line, a unified energy-based approach especially applied to continuous systems is presented and detailed in Chap. 4. This approach will form the basis for the subsequent modeling and control developments for both piezoelectric-based systems as well as vibration-control systems discussed in Chaps. 8 and 9, respectively.

1.3.1 Linear vs. Nonlinear Models

It is clear that most natural and practical systems are nonlinear in nature. Examples include gearboxes with inherent backlash, machine components with dry frictions and linear systems possessing dead zones (due to manufacturing deficiencies, for instance) or undergoing large amplitude vibrations. Figure 1.6 depicts some demonstrable examples of these naturally nonlinear systems.

The linearized models developed for these nonlinear systems are our own idealization which may not be justifiable. However, linear assumptions can be made for the small-amplitude vibrations considered in this book. In order to exemplify the breakdown of such assumptions, however, we will discuss, in Chaps. 10 and 11, some of the nonlinear modeling aspects of the vibration-control systems used for micro/nano actuators and sensors. More specifically and through extensive experimental testing and verification on piezoelectric-based nanomechanical cantilever sensors, it is shown that a nonlinear-comprehensive modeling is essential in capturing the minute vibrational responses at these scales (see Chap. 11). We refer interested readers in nonlinear modeling to Nayfeh et al. for a comprehensive

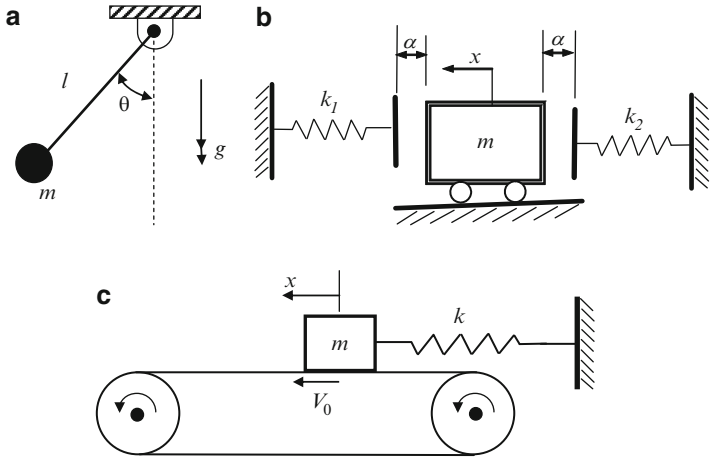

Fig. 1.6 Schematic representation of nonlinear systems; (**a**) nonlinear pendulum due to large-amplitude vibration, (**b**) linear mass-spring with dead-zone representing backlash in geared systems, and (**c**) simple model of friction-limited mass-spring system with inherent dry friction

modeling and control of nonlinear discrete (Nayfeh and Mook 1979) and continuous (Nayfeh and Pai 2004) systems.

Nevertheless, even when linear assumptions are made for many vibration problems in this book, it must be emphasized that the ultimate vibration-control system (i.e., combined plant and controller) could be very well nonlinear. This is typically due to the utilization of nonlinear controllers to improve system performance for these linear systems. For instance, if the plant dynamics for a linear vibration problem can be represented in the following form

$$\dot{\mathbf{x}} = \mathbf{A}\mathbf{x} \tag{1.1}$$

where $\mathbf{A}$ represents the system parameters coefficient matrix and $\mathbf{x} \in \mathbb{R}^n$ is the states vector representing displacements, for instance. When system (1.1) is augmented with some controllers (this is a common scenario for most active vibration-control systems), the combined plant/controller dynamics could take the following general form

$$\dot{\mathbf{x}}(t) = \mathbf{f}\left(\mathbf{x}(t), \mathbf{u}\left(\mathbf{x}(t)\right)\right), \tag{1.2}$$

in which the general (nonlinear) controller $\mathbf{u}\left(\mathbf{x}(t)\right) \in \mathbb{R}^m$ is utilized. As clearly seen, the combined closed-loop system can be nonlinear. For this, a relatively complete treatment of stability analysis and theories for nonlinear systems is given in Appendix A to ease the active vibration-control systems developments in Part II.

1.3.2 Lumped-Parameters vs. Distributed-Parameters Models

Similar to the linear and nonlinear modeling viewpoints, physical systems can be mathematically modeled as either discrete or continuous systems. All real systems are made of physical parameters that cannot be assumed isolated, and hence, are continuous by their nature. An idealization of these naturally continuous systems is the discretization of these systems into many isolated components that can be described by independent degrees-of-freedom (DOFs). Figure 1.7 demonstrates this idealization process on a flexible beam where only one mode (fundamental) of vibration is considered when discretizing this continuous system.

$$k_{\text{eq}} = 3EI/L^3 \tag{1.3}$$

$$m_{\text{eq}} = \frac{1}{3}\rho AL \tag{1.4}$$

Discrete or Lumped-parameters Modeling: Discrete or "lumped-parameters" systems are governed by ordinary differential equations (ODEs) since the modeling can be performed for each of the independent DOF and isolated parameter. A linear multiDOF (MDOF) system is typically characterized by its natural frequencies, damping ration and "mode shapes". Later in Chap. 8, we will demonstrate how some of the piezoelectric-based systems can be modeled as lumped-parameters systems. It is obvious that the design and development of the active vibration controllers based on such simplified models of naturally continuous systems can be very convenient. It must be, however, cautioned that the real-time implementation of such simplified controllers may lead to system instability, spillover and divergence since the continuity and nonisolated nature of the system parameters are ignored. Hence, there is a trade-off between the level of model reduction and simplification and ease of control design and development. These issues will be discussed and addressed in more detail using extensive example case studies given in Chaps. 8 and 9.

Continuous or Distributed-parameters Modeling: If physical parameters of a dynamic system (e.g., mass, stiffness) cannot be assumed isolated, then the system is distributed-parameters in nature. Hence, a continuous system consists of infinitely many number of particles or DOFs. To mathematically describe the motion of such

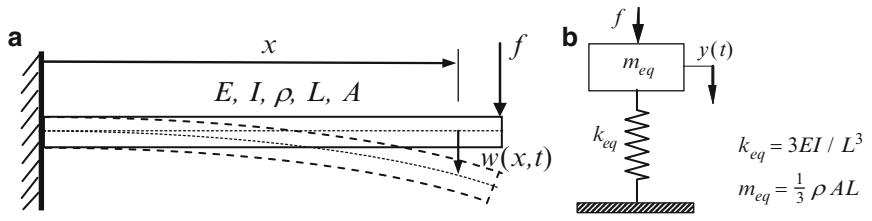

Fig. 1.7 Schematic representation of idealistic discretization (**b**) of a naturally continuous system (**a**)

system, one shall need an infinite number of ODEs. However, since the distance between the two adjacent particles is very small in such continuous system and displacements must be continuous, the motion of a continuous system can be conveniently described by a finite number of *displacement* variables. These displacements are functions of both spatial coordinates as well as time, and hence, the resulting governing equations are partial differential equations (PDEs) instead of infinite number of ODEs. These PDEs need to be associated with some boundary conditions (due to the dependency of displacement variables to spatial coordinates) in addition to the typical initial conditions in ODEs. Instead of "mode shapes" that serve as one of the attributes of lumped-parameters systems, a set of "eigenfunctions" is utilized in distributed-parameters systems to help in discretization the governing equations of motion. Once this discretization is accomplished, the same procedure used for decoupling the equations of motion in MDOF systems can be followed. We will defer more detailed discussions and example case studies for such discretization steps to Chaps. 2 and 4.

Summary

This chapter presented a general definition of smart structures along with a list of few selected active materials as the building blocks of smart structures. The concept of vibration control and its classifications including vibration absorption and isolation were briefly reviewed. The chapter ended with the notion of mathematical modeling of physical systems including the description of different modeling strategies for both discrete and continuous dynamical systems. The preliminaries introduced in this chapter will be used extensively in the subsequent chapters.

Chapter 2
An Introduction to Vibrations of Lumped-Parameters Systems

Contents

2.1 Vibration Characteristics of Linear Discrete Systems 13
2.2 Vibrations of Single-Degree-of-Freedom Systems 14
2.2.1 Time-domain Response Characteristics 15
2.2.2 Frequency Response Function 17
2.3 Vibrations of Multi-Degree-of-Freedom Systems 18
2.3.1 Eigenvalue Problem and Modal Matrix Representation 19
2.3.2 Classically Damped Systems 21
2.3.3 Non-proportional Damping 23
2.4 Illustrative Example from Vibration of Discrete Systems 25
Summary
Exercises

This chapter provides a brief overview of vibrations of lumped-parameter systems, also referred to as discrete systems. A generalized treatment of these systems using modal matrix representation is presented first, followed by decoupling strategies for the governing equations of motion. Although brief, the outcomes of this chapter are used in the subsequent chapters when the equations of motion governing the vibrations of continuous systems or vibration-control systems reduce to their respective discrete representations. We leave the more detailed discussions and treatment of these systems to standard vibration books cited in this chapter (Tse et al. 1978; Thomson and Dahleh 1998; Rao 1995; Inman 2007; Meirovitch 1986; Balachandran and Magrab 2009).

2.1 Vibration Characteristics of Linear Discrete Systems

As mentioned in Chap. 1, most systems considered here are assumed to be linear, and hence, the principle of superposition holds. They are governed by a set of ordinary differential equations (ODEs) as opposed to partial differential equations (PDEs) in continuous systems.

N. Jalili, *Piezoelectric-Based Vibration Control*,
DOI 10.1007/978-1-4419-0070-8_2, © Springer Science+Business Media LLC 2010

A single-degree-of-freedom (SDOF) linear system can be characterized by two independent quantities, that is, natural frequency and damping ratio. These will be briefly defined in the next section. Similarly, a linear multi-degree-of-freedom (MDOF) system can be characterized by its natural frequencies and damping ratios, as well as a third set of quantities referred to as "mode shapes." The latter quantity will form the basis for representing the vibrations of MDOF systems in terms of many SDOF systems and in a compact and decoupled arrangement as discussed later in this chapter.

2.2 Vibrations of Single-Degree-of-Freedom Systems

Consider the SDOF system shown in Fig. 2.1 where a sinusoidal force $f(t) = F_0 \sin(\omega t)$ is applied to mass m, with F_0 being the magnitude of the applied force and ω being its frequency. The differential equation of motion for mass m can be easily obtained as

$$m\ddot{x}(t) + c\dot{x}(t) + kx(t) = F_0 \sin(\omega t) \tag{2.1}$$

where $x(t)$ is the displacement of mass m and measured from the equilibrium state of the system (*see* Sect. A.3).

Utilizing the principle of superposition in system (2.1), one can assume the following solution for displacement $x(t)$

$$x(t) = x_c(t) + x_p(t) \tag{2.2}$$

where $x_c(t)$, referred to as the *complimentary solution* or zero-input response, is the solution to the initial conditions [while the right-hand side of (2.1) is set to zero], and $x_p(t)$, referred to as the *particular solution* or zero-state response, is the solution to the input excitation (here, f).

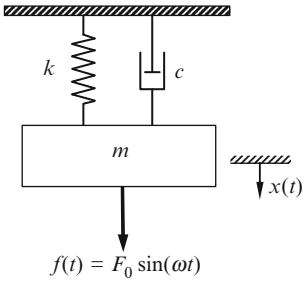

Fig. 2.1 A simple SDOF system

2.2.1 Time-domain Response Characteristics

Considering the general solution (2.2), we first concentrate on the complimentary response $x_c(t)$ and assume the following solution

$$x_c(t) = e^{st} \tag{2.3}$$

where s is a constant (in general, a complex quantity). Substituting solution (2.3) into the equation of motion (2.1), while also noting that input is set to zero for this solution yields

$$ms^2 + cs + k \triangleq CE(s) = 0 \tag{2.4}$$

where we have utilized the fact that $e^{st} \neq 0$. Equation (2.4), or $CE(s) = 0$, is referred to as the *characteristic equation* of the system.

The roots of the characteristic equation $CE(s) = 0$ are obviously functions of the system parameters, m, c and k. Depending on the values of these parameters, three cases are encountered; (1) two distinct real roots (overdamped), (2) two repeated real roots (critically damped) and (3) two complex conjugate roots (underdamped). The type of the characteristic roots also determines system behavior and many of the response characteristics without the need to solve the equation of motion. For instance, in the case of two real roots, the second-order dynamic system (2.1) is decomposed of two first-order systems, thereby obeying the response characteristics of a first-order system such as absence of overshoot or oscillatory behavior.

Taking into account the most frequently experienced case in many vibratory systems and to avoid repeating standard materials from the vibrations of SDOF systems, we only consider the underdamped case where the system is really a second-order system. For this, we divide both sides of (2.4) by m to arrive at the following so-called *standard* form of the characteristic equation of second-order systems

$$s^2 + 2\zeta\omega_n s + \omega_n^2 = 0 \tag{2.5}$$

where system natural frequency ω_n and damping ratio ζ are defined as

$$\omega_n = \sqrt{k/m}, \quad \zeta = \frac{c}{c_r} = \frac{c}{2\sqrt{km}} \tag{2.6}$$

The roots of quadratic (2.5) can be easily obtained as

$$s_{1,2} = -\zeta\omega_n \pm \omega_n\sqrt{\zeta^2 - 1} \tag{2.7}$$

As mentioned earlier, restricting the discussion only to underdamped cases, we assume $\zeta < 1$ in order for (2.7) to result in complex conjugate roots. In this case, the roots of (2.7) can be recast in the more suitable form,

$$s_{1,2} = -\zeta\omega_n \pm j\omega_d, \quad j = \sqrt{-1} \tag{2.8}$$

where $\omega_\mathrm{d} = \omega_\mathrm{n}\sqrt{1-\zeta^2}$ and is referred to as the *damped* natural frequency of the system.

Hence, the general form of the complimentary solution (2.3) can be written as

$$x_\mathrm{c}(t) = C_1 \mathrm{e}^{s_1 t} + C_2 \mathrm{e}^{s_2 t} = C_1 \mathrm{e}^{(-\zeta\omega_\mathrm{n} + j\omega_\mathrm{d})t} + C_2 \mathrm{e}^{(-\zeta\omega_\mathrm{n} - j\omega_\mathrm{d})t} \tag{2.9}$$

where C_1 and C_2 are constants and can be determined using the initial conditions. After some manipulations and using Euler identity,[1] solution (2.9) can be expressed in the following more compact form,

$$x_\mathrm{c}(t) = \alpha \mathrm{e}^{-\zeta\omega_\mathrm{n} t}\left(\sin\left(\omega_\mathrm{d} t + \beta\right)\right) \tag{2.10}$$

where α and β are constants and can be determined using the available initial conditions.

Now that the complimentary solution has been determined, we focus our attention to the particular solution x_p (or response to input excitation). From our elementary differential equations background, one can assume the following general solution for x_p to comply with the type of input (or right-hand side) given in (2.1).

$$x_\mathrm{p}(t) = X\left(\sin(\omega t - \phi)\right) \tag{2.11}$$

Substituting solution (2.11) into the equation of motion (2.1) and after some manipulations and comparing the coefficients of sine and cosine terms on both sides of the resulting equation, the unknowns X and ϕ can be obtained as

$$X = \frac{F_0}{k\sqrt{((1-r^2)^2 + (2\zeta r)^2)}}, \quad \phi = \tan^{-1}\left(\frac{2\zeta r}{1-r^2}\right) \tag{2.12}$$

where $r = \omega/\omega_\mathrm{n}$ is the frequency ratio. The complete solution can now be obtained by superimposing the solutions (2.10) and (2.11) as

$$\begin{aligned} x(t) = x_\mathrm{c}(t) + x_\mathrm{p}(t) &= \alpha \mathrm{e}^{-\zeta\omega_\mathrm{n} t}\left(\sin\omega_\mathrm{d} t + \beta\right) \\ &+ \frac{F_0}{k\sqrt{((1-r^2)^2 + (2\zeta r)^2)}} \sin\left(\omega t - \tan^{-1}\left(\frac{2\zeta r}{1-r^r}\right)\right) \end{aligned} \tag{2.13}$$

Equation (2.13) represents the complete solution $x(t)$ for the general SDOF system (2.1).

[1] $e^{j\theta} = \cos\theta + j\sin\theta$, $j = \sqrt{-1}$.

2.2.2 Frequency Response Function

Most vibration systems can be better characterized in frequency-domain since a non-dimensional relationship between vibrational characteristics and system physical parameters can be obtained. For this, the equations of motion are transferred into Laplace domain and analyzed in response to either tonal or broadband excitations as discussed next.

Transfer Function: The transfer function of a linear system is defined as the ratio of output to input variables in Laplace domain with zero initial conditions (ICs). That is,

$$T(s) = \left.\frac{\Im(\text{output})}{\Im(\text{input})}\right|_{\text{when all ICs are set to zero}} \tag{2.14}$$

Implementing this definition to system dynamic (2.1) results in the system transfer function

$$T(s) = \frac{X(s)}{F(s)} = \frac{1}{ms^2 + cs + k} \tag{2.15}$$

where $X(s) \triangleq \Im\{x(t)\}$ and $F(s) \triangleq \Im\{f(t)\}$. For a multiple-input-multiple-output (MIMO) system, this definition is extended to

$$T_{ij}(s) = \left.\frac{X_i(s)}{F_j(s)}\right|_{\substack{\text{when all ICs are set to zero} \\ \text{and all inputs except } F_j \text{ are zero}}} \tag{2.16}$$

where $T_{ij}(s)$ is the transfer function between output $X_i(s)$ and input $F_j(s)$.

Frequency Response Function (FRF): The so-called frequency response function (FRF) or frequency transfer function (FTF) can be simply obtained by replacing "s" with "$j\omega$" in the expression for transfer function, that is,

$$\text{FRF}(\omega) \triangleq T(s)|_{s=j\omega} \tag{2.17}$$

For the case of SDOF system (2.1), the FRF of the steady-state displacement of the system due to harmonic excitation can be expressed as

$$H(\omega) \triangleq \left.\frac{X(s)}{F(s)}\right|_{s=j\omega} = \frac{1}{m\left(\omega_{\text{n}}^2 - \omega^2 + 2j\zeta\omega_{\text{n}}\omega\right)} = |H(\omega)|\,\text{e}^{-j\phi} \tag{2.18}$$

where

$$|H(\omega)| = \frac{1}{k\sqrt{((1-r^2)^2 + (2\zeta r)^2)}}, \quad \phi = \tan^{-1}\left(\frac{2\zeta r}{1-r^r}\right) \tag{2.19}$$

As mentioned earlier, the FRF and especially its magnitude can be a very helpful representative of vibration response of a dynamic system. In order to better visualize

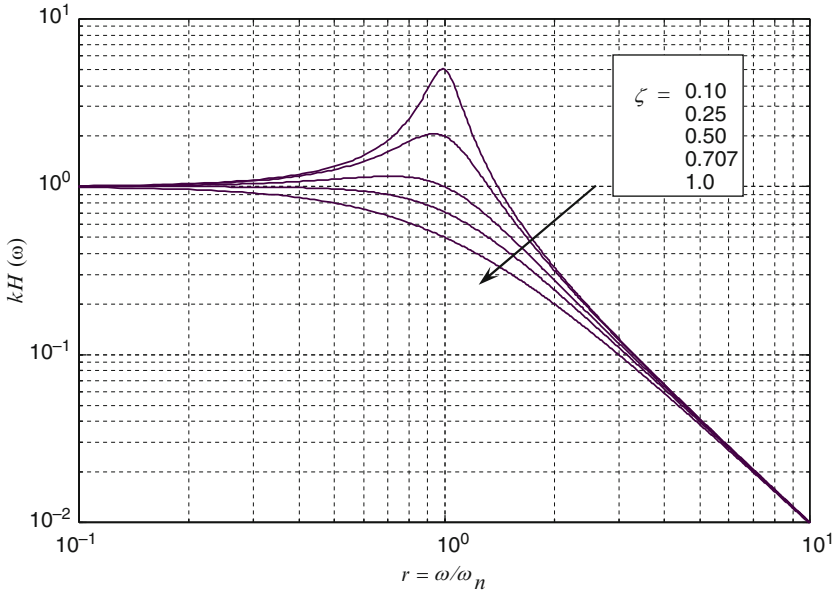

Fig. 2.2 Normalized frequency response plot of system (2.1) for different values of damping ratio

this, the plot of non-dimensional magnitude of the FTF of (2.19) for different values of damping ratio ζ is shown in Fig. 2.2. This plot can be utilized when designing vibration-control systems. For example, for vibration attenuation in system (2.1), one can easily see the effect of changing system damping ratio on the steady-state response $|X(j\omega)|$.

2.3 Vibrations of Multi-Degree-of-Freedom Systems

Consider the n-DOF system shown in Fig. 2.3 in which $x_1(t)$ through $x_n(t)$ represent the displacements of masses m_1 through m_n, respectively. As shown, it is assumed that each mass is acted upon an external force in general. Since the governing equations of motion can be easily obtained for this linear system, we prefer not to include any details in this regard as the expressions are lengthy and extensive. Subsequently, we resort to the following matrix representation of the equations that can be easily determined which has a general form of

$$\mathbf{M}\ddot{\mathbf{x}}(t) + \mathbf{C}\dot{\mathbf{x}}(t) + \mathbf{K}\mathbf{x}(t) = \mathbf{f}(t) \tag{2.20}$$

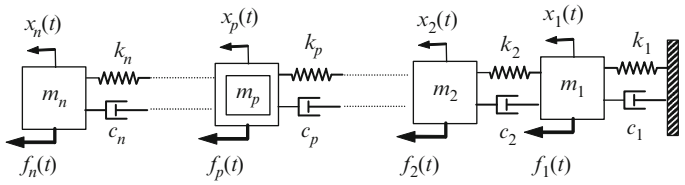

Fig. 2.3 Schematic diagram of an n-DOF mass-spring-damper system

where $\mathbf{x} = \{x_1, x_2, x_3, \ldots, x_n\}^T$, $\mathbf{f} = \{f_1, f_2, f_3, \ldots, f_n\}^T$, and $\mathbf{M}$, $\mathbf{C}$ and $\mathbf{K}$ are all real symmetric matrices made up of system physical parameters. In addition, it is assumed that $\mathbf{M}$ is a positive definite matrix, and hence, can be written as

$$\mathbf{M} = \mathbf{N}^T\mathbf{N} \tag{2.21}$$

2.3.1 Eigenvalue Problem and Modal Matrix Representation

Similar to SDOF systems, the complete solution to general (2.20) can be obtained by superimposing the solution to initial conditions (zero-input response) and solution to input excitation (zero-state response). For this, we will first concentrate on the solution to initial conditions, or the so-called "free and undamped" vibration. For this, the following solution is assumed

$$\mathbf{x} = \mathbf{X}\mathrm{e}^{j\omega t} \tag{2.22}$$

and substituted in the free (i.e., $\mathbf{f} = \mathbf{0}$) and undamped (i.e., $\mathbf{C} = \mathbf{0}$) version of (2.20) to obtain

$$(\mathbf{K} - \omega^2\mathbf{M})\mathbf{X} = 0 \tag{2.23}$$

where $\mathbf{X} = \{X_1, X_2, X_3, \ldots, X_n\}$ and ω is, at this stage, an unknown parameter to be determined.

Substituting property (2.21) into (2.23), one can write

$$\mathbf{A}\mathbf{Y} = \omega^2\mathbf{Y} \tag{2.24}$$

where

$$\mathbf{Y} \triangleq \mathbf{N}\mathbf{X}, \quad \mathbf{A} = \mathbf{N}^{-T}\mathbf{K}\mathbf{N}^{-1} \tag{2.25}$$

in which $\mathbf{A}$ can be shown to be a real symmetric matrix. Equation (2.24) is known as the *eigenvalue problem*.

From either solving the eigenvalue problem (2.24) or setting the determinant of coefficient $\mathbf{X}$ in (2.23) to zero (i.e., $\det(\mathbf{K} - \omega^2\mathbf{M}) = 0$), one can obtain an nth order algebraic equation in terms of ω^2. Since $\mathbf{A}$ is a real symmetric matrix, all solutions ω_i are real. The index i is also referred to as the mode number. These

solutions, in a similar fashion to SDOF systems, are referred to as "eigenvalues" or "natural frequencies" of the n-DOF system (2.20).

Substituting the solution $\omega = \omega_i$ into (2.23) or the eigenvalue problem (2.24), we get

$$\begin{aligned} &\left(\mathbf{K} - \omega_i^2 \mathbf{M}\right) \mathbf{X}_i = 0 \quad \text{or} \\ &\mathbf{A}\mathbf{Y}_i = \omega_i^2 \mathbf{Y}_i \rightarrow \left(\mathbf{A} - \omega_i^2 \mathbf{I}\right) \mathbf{Y}_i = 0, \quad i = 1, 2, \ldots, n \end{aligned} \tag{2.26}$$

which can be solved to obtain either $\mathbf{X}_i$ or $\mathbf{Y}_i$ [notice $\mathbf{X}_i$ and $\mathbf{Y}_i$ are related through (2.25)]. $\mathbf{X}_i$ or $\mathbf{Y}_i$ are referred to as "eigenvectors" of the system. Having determined both eigenfrequencies ω_i, and eigenvectors $\mathbf{X}_i$, the complimentary or solution to the free and undamped vibration (2.20) is now finalized. These solutions form the fundamental basis for obtaining the solution to the forced and damped version of (2.20) (i.e., the most complete case), as discussed in the next section.

Orthogonality Conditions: If $\mathbf{Y}_i$ represents the eigenvector associated with eigenvalue ω_i and $\mathbf{Y}_j$ denotes the eigenvector associated with eigenvalue ω_j, then based on eigenvalue problem (2.24) we have

$$\omega_i^2 \mathbf{Y}_i = \mathbf{A}\mathbf{Y}_i \tag{2.27a}$$

$$\omega_j^2 \mathbf{Y}_j = \mathbf{A}\mathbf{Y}_j \tag{2.27b}$$

Pre-multiplying (2.27a) and (2.27b) by $\mathbf{Y}_j^T$ and $\mathbf{Y}_i^T$, respectively, yields

$$\omega_i^2 \mathbf{Y}_j^T \mathbf{Y}_i = \mathbf{Y}_j^T \mathbf{A}\mathbf{Y}_i \tag{2.28a}$$

$$\omega_j^2 \mathbf{Y}_i^T \mathbf{Y}_j = \mathbf{Y}_i^T \mathbf{A}\mathbf{Y}_j \tag{2.28b}$$

Taking into account the symmetry property matrix $\mathbf{A}$ (*see* its definition in 2.25), transposing both sides of (2.28a) and subtracting (2.28b) from the resultant expression yields

$$\left(\omega_i^2 - \omega_j^2\right) \mathbf{Y}_i^T \mathbf{Y}_j = 0 \tag{2.29}$$

Since $\omega_i^2 \neq \omega_j^2$ (i.e., it is assumed that i and j represent two different and distinct modes), then (2.29), while using property (2.21) and definition (2.25), results in

$$\mathbf{Y}_i^T \mathbf{Y}_j = 0 \Rightarrow \mathbf{X}_i^T \mathbf{N}^T \mathbf{N} \mathbf{X}_j = 0 \Rightarrow \mathbf{X}_i^T \mathbf{M} \mathbf{X}_j = 0 \quad \text{for} \quad i \neq j \tag{2.30}$$

By substituting the result of (2.30) into the eigenvalue problem (2.23), one can obtain the so-called orthogonality conditions

$$\mathbf{X}_i^T \mathbf{M} \mathbf{X}_j = 0, \quad \mathbf{X}_i^T \mathbf{K} \mathbf{X}_j = 0, \quad \text{for} \quad i \neq j \tag{2.31}$$

That is, the eigenvectors are orthogonal with respect to both mass and stiffness matrices **M** and **K**. It must be noted that such properties result form the symmetry features of the matrices involved. We will elaborate more on this symmetry property and its relationship to orthogonality conditions in Chap. 4, where we introduce the self-adjointness property of both mass and stiffness operators in continuous systems.[2]

Remark 2.1. It must be noted that the symmetry conditions on mass and stiffness matrices are only imposed at this stage. We will illustrate, later in Sect. 2.3.3, that these restrictions can be relaxed. The ever-present asymmetry in mass or stiffness matrices can come from many sources including predominantly gyroscopic and/or circularly effects.

Remark 2.2. It must be noted that since the determinant of the coefficient $\mathbf{X}_i$ or $\mathbf{Y}_i$ in (2.26) is set to zero, the n components of $\mathbf{X}_i$ (for each i) become linearly dependent. Hence, there is always one free choice for one of the components of $\mathbf{X}_i$. In order to obtain unique solutions as well as facilitate the subsequent forced vibration analysis, one can normalize the eigenvectors using the so-called orthonormality conditions:

$$\mathbf{X}_i^T \mathbf{M} \mathbf{X}_i = 1, \quad \mathbf{X}_i^T \mathbf{K} \mathbf{X}_i = \omega_i^2 \tag{2.32}$$

This normalization is possible since **M** is assumed to be positive definite (*see* 2.21).

Now that the complimentary solution or the solution to the eigenvalue problem has been finalized, we need to focus on obtaining the solution to (2.20) where both force excitation and damping terms are present. For this, we utilize the normalized eigenvectors of the free and undamped vibration obtained so far and propose the following change of variable:

$$\mathbf{x} = \mathbf{\Phi} \mathbf{q} \tag{2.33}$$

where $\mathbf{\Phi} = [\mathbf{X}_1, \mathbf{X}_2, \ldots, \mathbf{X}_n]$ is referred to as modal matrix, $\mathbf{X}_i$ are the normalized eigenvectors of the system, and $\mathbf{q} = \{q_1, q_2, \ldots, q_n\}^T$ is the modal coordinate in new system. Once the modal coordinates q_i have been obtained, the solutions to displacement x_i can be consequently obtained using (2.33). Since this solution to this problem depends on the nature of the damping matrix **C** in (2.20), we will consider the following two cases.

2.3.2 Classically Damped Systems

A system is said to be "classically damped" or "proportionally damped" or "Rayleigh damped" if the damping matrix is proportional to mass and stiffness matrices. That is, a system with damping matrix **C** is classically damped, if **C** can be expressed as a linear function of mass matrix **M** and stiffness matrix **K** as

[2] These operators in continuous systems reduce to mass and stiffness matrices in discrete systems.

$$\mathbf{C} = \alpha\mathbf{M} + \beta\mathbf{K} \tag{2.34}$$

where α and β are constants.

Under this assumption, by substituting the change of coordinate (2.33) into the original forced and damped vibration problem (2.20), it yields

$$\mathbf{M\Phi\ddot{q}} + \mathbf{C\Phi\dot{q}} + \mathbf{K\Phi q} = \mathbf{f} \tag{2.35}$$

Now, pre-multiplying (2.35) from left by $\mathbf{\Phi}^T$ results in

$$\mathbf{\Phi}^T\mathbf{M\Phi\ddot{q}} + \mathbf{\Phi}^T\mathbf{C\Phi\dot{q}} + \mathbf{\Phi}^T\mathbf{K\Phi q} = \mathbf{\Phi}^T\mathbf{f} \tag{2.36}$$

Taking into account the classically damped condition (2.34) as well as the orthonormality conditions (2.32) in the matrix form

$$\mathbf{\Phi}^T\mathbf{M\Phi} = \mathbf{I}, \quad \mathbf{\Phi}^T\mathbf{K\Phi} = \text{diag}\left(\omega_i^2\right), \quad \mathbf{\Phi}^T\mathbf{C\Phi} = \text{diag}\left(\alpha + \beta\omega_i^2\right) \tag{2.37}$$

Equation (2.36) reduces to

$$\mathbf{I\ddot{q}} + \left[\text{diag}(\alpha + \beta\omega_i^2)\right]\mathbf{\dot{q}} + \left[\text{diag}(\omega_i^2)\right]\mathbf{q} = \mathbf{\Phi}^T\mathbf{f} \tag{2.38}$$

which can be represented in the following decoupled equations

$$\ddot{q}_i(t) + 2\zeta_i\omega_i\dot{q}_i(t) + \omega_i^2 q_i(t) = \bar{f_i}(t), \quad i = 1, 2, \ldots, n \tag{2.39}$$

In (2.39), the modal damping ratio ζ_i and forcing function $\bar{f_i}$ are defined as

$$\zeta_i = \frac{\alpha + \beta\omega_i^2}{2\omega_i}, \quad \bar{f_i}(t) = \mathbf{X}_i^T\mathbf{f} \tag{2.40}$$

As clearly seen from (2.39), the resultant n ODEs are all decoupled and can be easily and independently solved using the complete solution given in (2.13) for SDOF systems. It must be noted that the initial conditions from the original coordinates can be transferred into this modal coordinates using relation (2.33). That is,

$$\mathbf{q}(0) = \mathbf{\Phi}^T\mathbf{M}\mathbf{x}(0), \quad \mathbf{\dot{q}}(0) = \mathbf{\Phi}^T\mathbf{M\dot{x}}(0) \tag{2.41}$$

Hence, (2.39–2.41) can be used to obtain the solution for $q_i(t), i = 1, 2, \ldots, n$, and consequently $\mathbf{q}(t)$ in the modal coordinates. Once this solution is obtained, relationship (2.33) can be utilized to transfer this solution back to the original coordinates $\mathbf{x}(t)$, and consequently obtain the solution for each of the displacement coordinates $x_i(t), i = 1, 2, \ldots, n$ in Fig. 2.2.

2.3.3 Non-proportional Damping

As mentioned in the preceding subsection, in many vibration problems the classically damped assumption cannot be made or mass and stiffness matrices are not symmetric such as in most gyroscopic and circularly systems. Hence, there is a need to treat (2.20) in its most general case, that is, when mass and stiffness matrices are not necessarily symmetric or property (2.34) is not valid.

To handle this situation, the trivial equation

$$-\mathbf{K}\dot{\mathbf{x}}(t) + \mathbf{K}\dot{\mathbf{x}}(t) = 0 \tag{2.42}$$

is added to (2.20) to form the following set of equations

$$\begin{pmatrix} \mathbf{M} & \mathbf{0} \\ \mathbf{0} & -\mathbf{K} \end{pmatrix} \begin{Bmatrix} \ddot{\mathbf{x}}(t) \\ \dot{\mathbf{x}}(t) \end{Bmatrix} + \begin{pmatrix} \mathbf{C} & \mathbf{K} \\ \mathbf{K} & \mathbf{0} \end{pmatrix} \begin{Bmatrix} \dot{\mathbf{x}}(t) \\ \mathbf{x}(t) \end{Bmatrix} = \begin{Bmatrix} \mathbf{f}(t) \\ \mathbf{0} \end{Bmatrix} \tag{2.43}$$

which can be further compacted into the following more suitable form

$$\dot{\mathbf{y}} = \mathbf{A}\mathbf{y} + \mathbf{g} \tag{2.44}$$

where

$$\mathbf{y} = \begin{Bmatrix} \dot{\mathbf{x}}(t) \\ \mathbf{x}(t) \end{Bmatrix}, \mathbf{g} = \begin{Bmatrix} \mathbf{M}^{-1}\mathbf{f} \\ \mathbf{0} \end{Bmatrix}, \mathbf{A} = \begin{pmatrix} -\mathbf{M}^{-1}\mathbf{C} & -\mathbf{M}^{-1}\mathbf{K} \\ \mathbf{I} & \mathbf{0} \end{pmatrix} \tag{2.45}$$

Similar to classically damped system, we can now follow the same decoupling procedure we adopted in Sect. 2.3.2. However, one must note that the dimension of the eigenvalue problem has increased from n (i.e., n second-order differential equations in 2.39) to $2n$ (i.e., $2n$ first-order differential equations, *see* 2.44). Along this line, we first seek the complimentary solution, that is, the zero-input response of the system in the following form

$$\mathbf{y} = \mathbf{Y}\mathrm{e}^{st} \tag{2.46}$$

Substituting solution (2.46) into homogenous version of (2.44), that is, $\mathbf{g} = \mathbf{0}$, results in

$$\mathbf{A}\mathbf{Y} = s\mathbf{Y} \rightarrow [\mathbf{A} - s\mathbf{I}]\,\mathbf{Y} = \mathbf{0} \tag{2.47}$$

In order to have nontrivial solution for $\mathbf{Y}$, one must impose

$$\det(\mathbf{A} - s\mathbf{I}) = 0 \tag{2.48}$$

As mentioned before, the dimension of the eigenvalue problem has increased from n to $2n$, hence, (2.48) yields $2n$ eigenvalues $s_1, s_2, \ldots, s_{2n}$. Substituting these $2n$ eigenvalues into (2.47), a total of $2n$ eigenvectors $\mathbf{Y}_1, \mathbf{Y}_2, \ldots, \mathbf{Y}_{2n}$ can be obtained. These eigenvalues and eigenvectors are called the *right eigenvalues* and eigenvectors of matrix $\mathbf{A}$.

Since we have relaxed the symmetry restriction on mass and stiffness matrices, matrix $\mathbf{A}$ can be, in general, asymmetric, and hence, $\mathbf{A}^T \neq \mathbf{A}$. The need to discuss the properties of $\mathbf{A}^T$ arises from the fact that we may need to pre-multiply the equations by this matrix, similar to the procedure we followed in the preceding section for classically damped systems. Since the determinants of a matrix and its transpose are the same, we expect to have the same eigenvalues for both $\mathbf{A}$ and $\mathbf{A}^T$. However, due to the fact that $\mathbf{A}^T \neq \mathbf{A}$, the eigenvalue problem for $\mathbf{A}^T$ does not necessarily produce the same eigenvectors as for $\mathbf{A}$. Subsequently, representing the eigenvectors of $\mathbf{A}^T$ as $\mathbf{Z}_i$, the following eigenvalue problem is formed.

$$\mathbf{A}^T\mathbf{Z} = s\mathbf{Z} \rightarrow \mathbf{A}^T\mathbf{Z}_i = s_i\mathbf{Z}_i, \quad i = 1, 2, \ldots, 2n \tag{2.49}$$

The eigenvectors $\mathbf{Z}_1, \mathbf{Z}_2, \ldots, \mathbf{Z}_{2n}$ of $\mathbf{A}^T$ are also called the *left* eigenvectors of $\mathbf{A}$. Using (2.47) and (2.49), it can be easily shown that the left and right eigenvectors, $\mathbf{Z}_i$ and $\mathbf{Y}_j$, are orthogonal if $i \neq j$ (Nayfeh and Pai 2004). That is,

$$\Sigma^T\Psi = \mathbf{I} \text{ and } \Sigma^T\mathbf{A}\Psi = \text{diag}\{s_i\} = \begin{pmatrix} s_1 & & 0 \\ & \ddots & \\ 0 & & s_{2n} \end{pmatrix} \tag{2.50}$$

where $\Sigma = \{\mathbf{Z}_1, \mathbf{Z}_2, \ldots, \mathbf{Z}_{2n}\}$ and $\Psi = \{\mathbf{Y}_1, \mathbf{Y}_2, \ldots, \mathbf{Y}_{2n}\}$ are modal matrices corresponding to left and right eigenvectors, respectively. Using this property, the coupled equation of motion in its most general form, that is, (2.44) can be easily decoupled. For this, let us take the following change of variables similar to classically damped systems

$$\mathbf{y} = \Psi\mathbf{q} \tag{2.51}$$

and substitute it into the original (2.44) to yield

$$\Psi\dot{\mathbf{q}} = \mathbf{A}\Psi\mathbf{q} + \mathbf{g} \tag{2.52}$$

Pre-multiplying (2.52) by Σ^T from left and using properties (2.50), we have

$$\dot{\mathbf{q}} = [\mathbf{s}]\mathbf{q} + \mathbf{h}, \quad \mathbf{h} = \Sigma^T\mathbf{g} \tag{2.53}$$

Or in a more useful form,

$$\dot{q}_i(t) = s_i q_i(t) + h_i(t), \quad i = 1, 2, \ldots, 2n \tag{2.54}$$

Expression (2.54) represents a set of $2n$ first-order ODEs that are conveniently decoupled, and one can give the exact solution to these equations as

$$q_i(t) = q_i(0)\mathrm{e}^{s_i t} + \int_0^t \mathrm{e}^{-s_i(\tau - t)} h_i(\tau)\mathrm{d}\tau, \quad i = 1, 2, \ldots, 2n \tag{2.55}$$

Similar to classically damped systems, once the solutions in terms of modal coordinates $\mathbf{q} = \{q_1, q_2, \ldots, q_{2n}\}$ have been obtained, the solutions $\mathbf{y} = \{y_1, y_2, \ldots, y_{2n}\}$ can be readily obtained by utilizing the coordinate transformation (2.51).

2.4 Illustrative Example from Vibration of Discrete Systems

Although the procedures outlined in the preceding sections are easy to follow and relatively straightforward, it is worthy to demonstrate these steps in a more detailed fashion and through an example case study. For this, consider the 3DOF system shown in Fig. 2.4 where m_1, m_2 and m_3; k_1, k_2, k_3 and k_4; and c_1, c_2, c_3 and c_4 are system masses, spring constants and damping coefficients, respectively. We would like to derive the equations of motion and represent the system in matrix format. For the numerical parts, the following values are taken: $m_1 = m_2 = m_3 = m = 1$, $k_1 = k_2 = k_3 = 3$, $k_4 = 0$, and a damping matrix proportional to the stiffness matrix, $\mathbf{C} = 0.01\,\mathbf{K}$ (i.e., $c_i = 0.01\,k_i, i = 1, 2, 3, 4$).

For the free and undamped vibration, we would like to obtain the natural frequencies, mode shapes, and modal matrix, and further normalize the natural modes with respect to the mass matrix and draw the mode shapes. For the forced vibration analysis, a unit-impulse force is applied at mass 3, and it is desired to determine the response of the system for mass 1, that is, $x_1(t)$. Using modal transformation, we would like to decouple the equations of motion. Although the system considered here is a *classically damped* system (i.e., proportional damping), we would like to transfer the original equations of motion into a set of first-order ODE. This transformation is performed to obtain a new set of equations as well as the coefficients matrices (*see* Sect. 2.3.3). A comparison between the eigenvalues of the system in this case with the natural frequencies (modal frequencies) obtained previously is given to show that the frequency response of the system is similar to the one obtained before.

Solution: The system is a linear system that can be readily shown to be governed by the following ODE as in (2.20).

$$\mathbf{M}\ddot{\mathbf{x}}(t) + \mathbf{C}\dot{\mathbf{x}}(t) + \mathbf{K}\mathbf{x}(t) = \mathbf{f}(t) \tag{2.56}$$

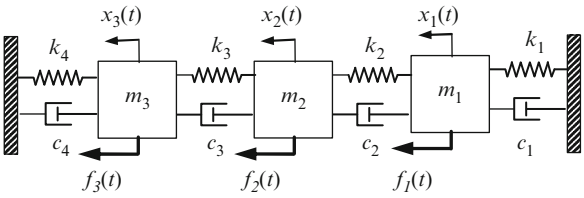

Fig. 2.4 An example case study for vibration analysis of discrete systems

where

$$\mathbf{M} = \text{diag}(m_1, m_2, m_3), \quad \mathbf{f} = [f_1 \quad f_2 \quad f_3]^T$$
$$\mathbf{C} = \begin{pmatrix} c_1 + c_2 & -c_2 & 0 \\ -c_2 & c_2 + c_3 & -c_3 \\ 0 & -c_3 & c_3 + c_4 \end{pmatrix}, \quad \mathbf{K} = \begin{pmatrix} k_1 + k_2 & -k_2 & 0 \\ -k_2 & k_2 + k_3 & -k_3 \\ 0 & -k_3 & k_3 + k_4 \end{pmatrix} \tag{2.57}$$

As mentioned earlier, to obtain the natural frequencies of the system, the determinant of the coefficient $\mathbf{X}$ in free and undamped version of (2.56), that is, (2.23), is set to zero. For the numerical values given, the resulting expression is given by

$$\omega^6 - 15\omega^4 + 54\omega^2 - 27 = 0 \tag{2.58}$$

which results in the three natural frequencies as

$$\omega_1 = 0.7708, \quad \omega_2 = 2.1598, \quad \omega_3 = 3.1210 \tag{2.59}$$

Substituting $\omega = \omega_i,\ i = 1, 2, 3$ from (2.59) into (2.23) or the eigenvalue problem (2.24) results in modal vectors $\mathbf{X}_i, i = 1, 2, 3$. Upon normalizing these vectors with respect to mass matrix using property (2.32), they can be expressed as

$$X_1 = \begin{pmatrix} 0.3280 \\ 0.5910 \\ 0.7370 \end{pmatrix}, \ X_2 = \begin{pmatrix} 0.7370 \\ 0.3280 \\ -0.5910 \end{pmatrix}, \ X_3 = \begin{pmatrix} 0.5910 \\ -0.7370 \\ 0.3280 \end{pmatrix} \tag{2.60}$$

and subsequently the modal matrix $\mathbf{\Phi}$ can be obtained as

$$\mathbf{\Phi} = \begin{bmatrix} X_1 & X_2 & X_3 \end{bmatrix} = \begin{pmatrix} 0.3280 & 0.7370 & 0.5910 \\ 0.5910 & 0.3280 & -0.7370 \\ 0.7370 & -0.5910 & 0.3280 \end{pmatrix} \tag{2.61}$$

Consequently, the mode shapes can be drawn as shown in Fig. 2.5.

Using the numerical values for the damping and stiffness matrices (i.e., $\mathbf{C} = \beta\mathbf{K} = 0.01\,\mathbf{K}$), it is obvious that this system is classically damped and hence the procedure outlined in Sect. 2.3.2 can be adopted to arrive at the forced vibration

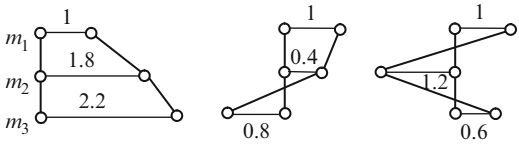

Fig. 2.5 Mode shapes of the 3DOF system of example case study; (*left*) first or fundamental mode $\omega_1 = 0.7708$, (*middle*) second mode $\omega_2 = 2.1598$ and (*right*) third mode $\omega_3 = 3.1210$

analysis and solution to the differential equations. For this, a solution in the form of (2.33) is selected that results in the decoupled equations as in (2.39) and (2.40).

$$\begin{gathered}\ddot{q}_i(t) + 2\zeta_i\omega_i\dot{q}_i(t) + \omega_i^2 q_i(t) = \mathbf{b}_i\mathbf{f}(t), \quad i = 1,2,3 \\ \mathbf{y} = \mathbf{D}\dot{\mathbf{q}}(t), \quad \dot{\mathbf{q}}(t) = [q_1(t) \quad q_2(t) \quad q_3(t)]^T, \\ \mathbf{f}(t) = [f_1(t) \quad f_2(t) \quad f_3(t)]^T\end{gathered} \tag{2.62}$$

where $\mathbf{b}_i$ is the ith row of $\mathbf{B}$ (*see* below), and $\mathbf{D}$ and modal damping ζ_i (*see* 2.40) are defined as

$$\mathbf{B} = \mathbf{\Phi}^T \begin{bmatrix} 0 & 0 & 1 \end{bmatrix}^T, \quad \mathbf{D} = \begin{pmatrix} 0 & 0 & 0 \\ 1 & 0 & 0 \\ 0 & 0 & 0 \end{pmatrix} \mathbf{\Phi}, \quad \zeta_i = 0.5\beta\omega_i \tag{2.63}$$

with the values of modal damping ratio calculated per (2.63) as

$$\zeta_1 = 0.0039, \quad \zeta_2 = 0.0108, \quad \zeta_3 = 0.0156 \tag{2.64}$$

Using (2.62), the transfer function of a mode can be calculated as

$$G_i(\omega) = \frac{j\omega\mathbf{b}_i\mathbf{D}_i}{\omega_i^2 - \omega^2 + 2j\zeta_i\omega_i\omega}, \quad i = 1,2,3 \tag{2.65}$$

where $\mathbf{D}_i$ is the ith column of $\mathbf{D}$ defined in (2.63). Consequently, the transfer function of the structure, as the sum of modal transfer functions, can be obtained as

$$G(\omega) = \sum_{i=1}^{3} G_i(\omega) \tag{2.66}$$

Figures 2.6 and 2.7 depict the frequency response plots of this system for both individual modes and the entire structure.

If one assumes that the system is not classically damped, the procedure outlined in Sect. 2.3.3 can be adopted here. For this, the equation of motion (2.56) can be readily transferred to (2.44). Subsequently, the eigenvalue problem (2.47) can be formed and the frequency (2.48) can be solved to result in the following six eigenvalues.

$$\begin{aligned} s_1 &= -0.0030 + j0.7708, \quad s_4 = \bar{s}_1 \\ s_2 &= -0.0233 + j2.1598, \quad s_5 = \bar{s}_2 \\ s_3 &= -0.0487 + j3.1207, \quad s_6 = \bar{s}_3 \end{aligned} \tag{2.67}$$

As discussed in Sect. 2.3.3, the imaginary part of these eigenvalues is the frequency of the system that matches exactly the results obtained in (2.59), while the real part

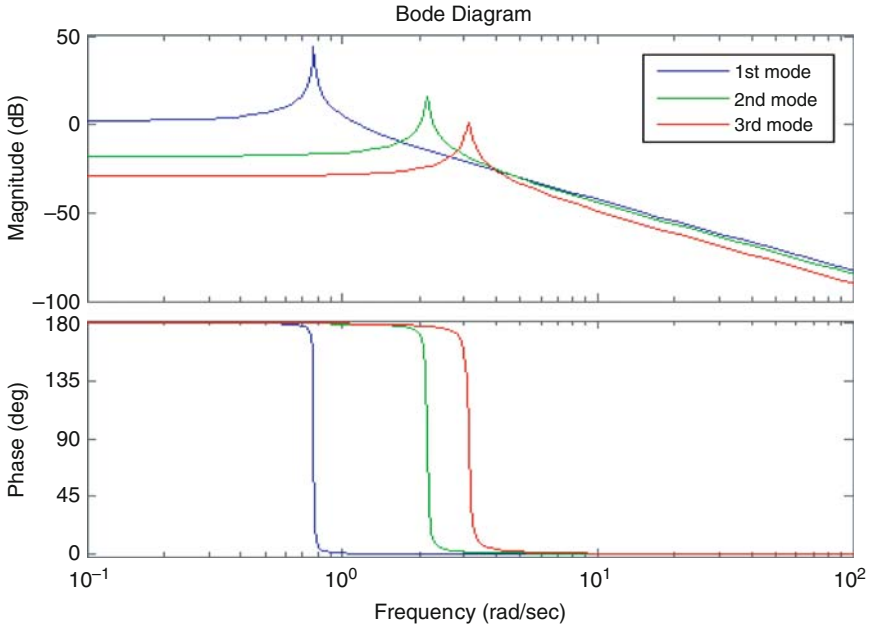

Fig. 2.6 Individual modal frequency response (2.64)

(absolute value) corresponds to the rate of decay, that is, $\zeta_i \omega_i$. Hence, the modal damping ratios can be obtained from the real parts of the eigenvalues in (2.67) as

$$\zeta_i = \text{abs}\left(Re\{s_i\}\right)/\omega_i \Rightarrow \tag{2.68}$$
$$\zeta_1 = 0.0030/0.7708 = 0.0039,\ \zeta_2 = 0.0108 \text{ and } \zeta_3 = 0.0156$$

It can be shown that the equations of motion in this form (similar to 2.54), when solved, can result in the same frequency and time responses as given in Figs. 2.6 and 2.7.

Summary

A brief, but essential overview of vibrations of lumped-parameter systems was given in this chapter. In order to focus on the discussion, a generalized treatment of these systems including modal matrix representation and decoupling strategies for the governing equations of motion was provided. The reader is able to follow the steps required in analyzing vibrations of discrete systems. The important outcomes given in this chapter such as proportional and non-proportional damping and their coupling are crucial in the equations of motion governing the vibrations of continuous system. We will demonstrate, Chapt. 4, how the equations of motion governing

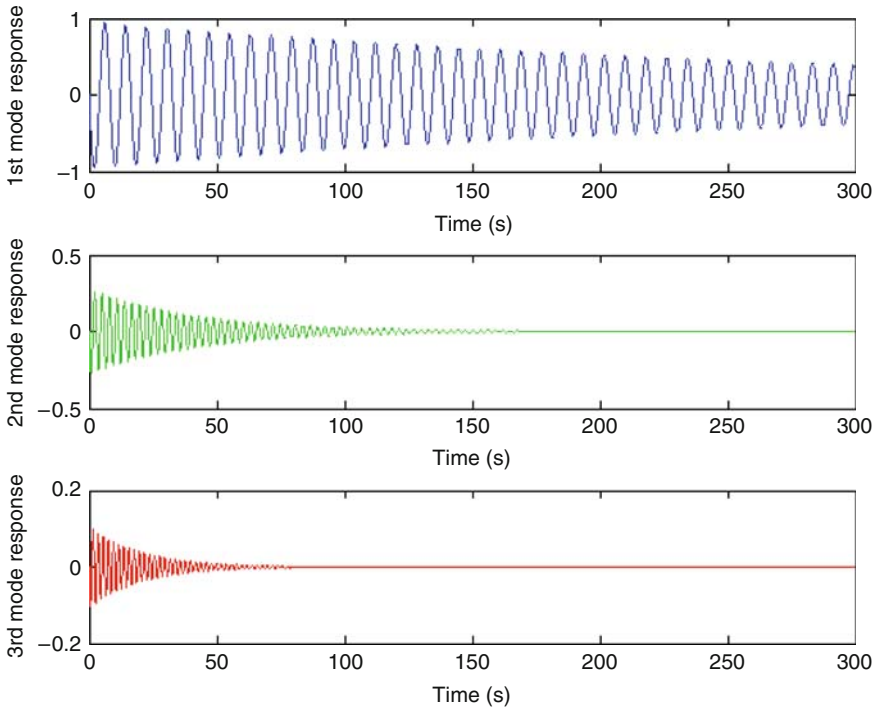

Fig. 2.7 Time response of the mass 1 in response to a unit impulse force applied at mass 3

continuous systems can be reduced to discrete model representation, and hence, solvable using the results given here.

Exercises[3]

2.2 Vibrations of SDOF Systems

2.1. The mass-spring systems, shown in Fig. 2.8, are all vibrating in the horizontal plane. Frictions in links and contact points are neglected and the linkages in configurations (b) and (c) are massless. For configurations (a), (b) and (c)

(a) Derive the equation of motion of mass m via Newtonian approach.
(b) Find the natural frequency of the system for each configuration.

[3] The exercises denoted by asterisk (*) refer to problems that require extensive use of numerical solvers such as Matlab/Simulink.

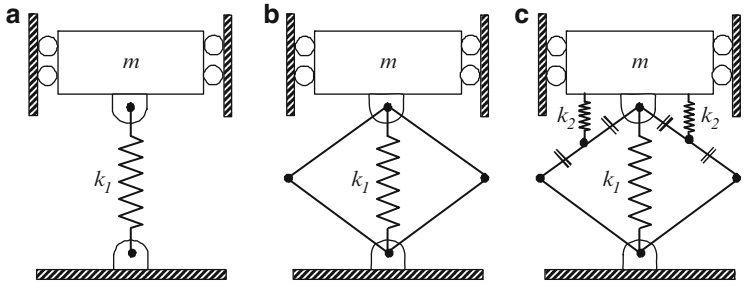

Fig. 2.8 The mass-spring systems of Exercise 2.1

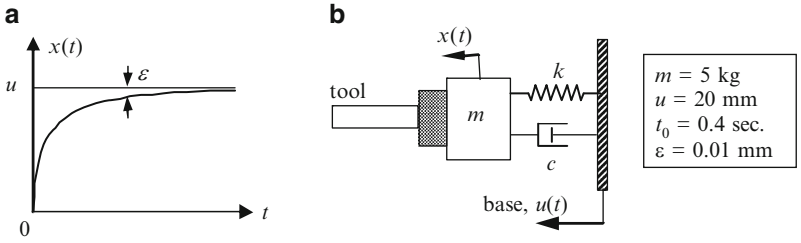

Fig. 2.9 A simple model of CNC machine tool (**b**) and its desired behavior (**a**)

2.2. A simple model of a CNC machine tool is shown in Fig. 2.9b. The vibration characteristics of the tool can be determined using a base excitation where tool is modeled as a SDOF system. m, k and c denote the equivalent mass, spring and damping coefficients of the tool, respectively. It is desired to select the values of k and c such that

(a) With a tool base step motion of u, the tool response has the behavior shown in Fig. 2.9a.
(b) The error $x - u$ at $t = t_0$ should not be greater than ε.

Determine the values of k and c to satisfy both conditions (a) and (b) above.

2.3 Vibrations of MDOF Systems

2.3. A vehicle suspension system can be modeled, in one of its simplest configurations, as a so-called *bicycle* model as shown in Fig. 2.10. Assume linear and small vibrations. Assume also that the system is at equilibrium at rest (hence, the effect of gravity is neglected as the equations are written from the equilibrium states).

(a) Derive the equations of motion for vertical (x) and angular (θ) displacements.
(b) For the following relationships, find the natural frequencies and mode shapes. $J = mK^2$ (where K is the radius of gyration and equals 0.5), $2l_1 = l_2 = 2l$ and $2k_1 = k_2 = 2k$.

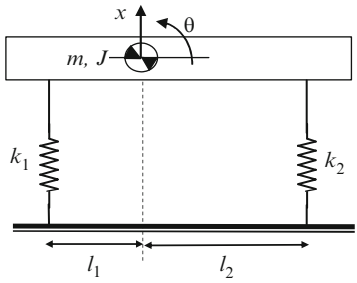

Fig. 2.10 Simple bicycle model of the vehicle suspension

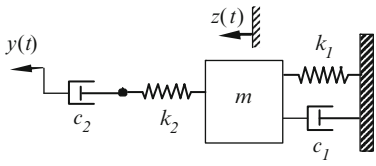

Fig. 2.11 Mass-spring-damper system with spring and damper in series

(c) Are the equations obtained in part (a) coupled? What is the nature of their coupling, static coupling or dynamic coupling? What are the conditions for which the equations can be decoupled? If these conditions cannot be met, are there any ways for these equations to be decoupled?

2.4. In some applications of passive vibration absorbers, a combination of damper and stiffness elements in series is most desirable. Derive the equations of motion for the system shown in Fig. 2.11, where dashpot c_2 is in series with spring k_2. Find the differential equations relating input $y(t)$ to the output $z(t)$. There is no friction between mass m and ground.

Hint: Define a new mass (M, for instance) at the point between spring k_2 and dashpot c_2. Define variable $x(t)$ to the left for this new mass. Treat the problem like a 2DOF system and derive the equations of motion. After the equations are obtained, simply put $M = 0$ and reduce the number of equations to one.

2.5. In many mechanical systems, a small element is used to move a much larger object through proper mechanical coupling. Figure 2.12 depicts this application in which a force f is applied to a small mass m in order to move large mass M. A combination of linear spring and damper in parallel is used to model the elastic coupling between the two masses. Derive the equations of motion governing this system and identify input, output and system variables.

2.6. Typically, automobile dynamics is analyzed using what is called *quarter* car models. One such structure is given in the Fig. 2.13. m_1 represents the $1/4$ car body and referred to as *sprung mass*, while m_2 is the rim of the wheel and attached parts and referred to as *unsprung mass*. The tire properties are given with a subscript 2, while the car suspension is shown with subscript 1. Given the particular structural absorption and stiffness properties, it is desired to design an active suspension system so that, the riding comfort of the vehicle is satisfactory to some requirements. One of the first steps in performing this task, is the derivation of the governing equations of motion.

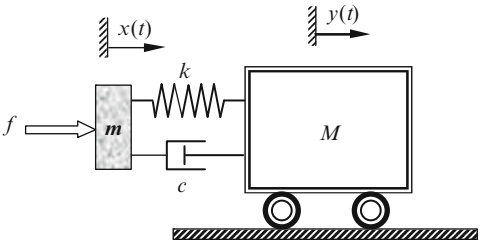

Fig. 2.12 2DOF system of Exercise 2.5

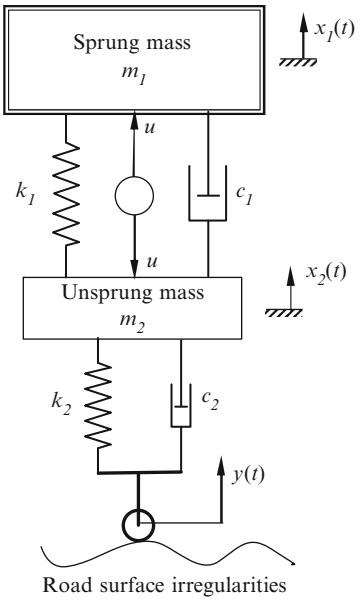

Fig. 2.13 Simple quarter car model equipped with active suspension system

(a) Assuming no external input to the suspension system, i.e., $u = 0$ in Fig. 2.13, derive the equations of motion for both unsprung and sprung masses.
(b) Repeat part (a) for the case where a PD controller in the form of $u(t) = -K_p\,(x_1(t) - x_2(t)) - K_D\,(\dot{x}_1(t) - \dot{x}_2(t))$ is applied as active element of the suspension. What differences are observed between the equations of motion for active (this part) and passive [part (a)] vibration absorbers? Which configuration is tunable in real time?

2.7. It is desired to control the position of a spring-driven cart, as shown in Fig. 2.14-top. The powered cart (on the left) is coupled to an un-powered cart (on the right) using a linear compression spring, k (*see* Fig. 2.14-bottom). The effects of structural damping in the spring and other types of frictions are all combined into an equivalent linear damper, c, parallel to spring k as shown in Fig. 2.14-bottom.

(a) Set the equations governing the dynamics of this system. Classify these equations and identify the input force F, and output-driven cart position, x_2, as the input and output variables, respectively.

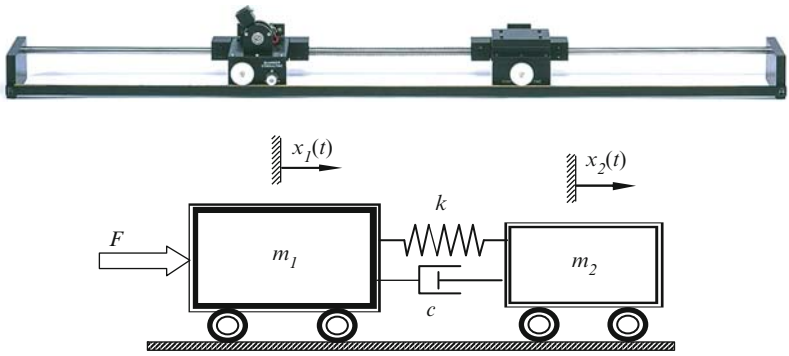

Fig. 2.14 Linear flexible joint system (www.quanser.com) (*top*), and its schematic representation (*bottom*)

(b) Represent the dynamics in the state-variable form (a set of first-order differential equations) and identify the states. Identify the system coefficient and input force matrices.
(c) Assuming zero initial conditions, transfer the governing equations developed in Part (c) into Laplace domain and find the transfer function of the system, $TF(s) = X_2(s)/F(s)$.
(d) Extract the characteristic equation from Part (b) or (c), and determine whether the system is stable or not (using characteristic roots). What is the order of system?
(e) What is the position of the driven cart as $t \to \infty$ (steady-state error) in response to a unit input force? Does this agree with the stability results of Part (d)?

Chapter 3
A Brief Introduction to Variational Mechanics

Contents

3.1 An Overview of Calculus of Variations 35
3.1.1 Concept of Variation 36
3.1.2 Properties of Variational Operator δ 38
3.1.3 The Fundamental Theorem of Variation 39
3.1.4 Constrained Minimization of Functionals 43
3.2 A Brief Overview of Variational Mechanics 45
3.2.1 Work–Energy Theorem and Extended Hamilton's Principle 45
3.2.2 Application of Euler Equation in Analytical Dynamics 49
3.3 Steps in Deriving Equations of Motion via Analytical Method 51
Summary
Exercises

This chapter presents a brief overview of some of the mathematical preliminaries and tools that will be used throughout the book, especially in Chaps. 4–9. These include an introduction to calculus of variation which is used for the derivation of equations of motion using analytical approach, as well as a brief overview to variational mechanics and steps in deriving equations of motion of a dynamical system. These brief, but important preliminaries shall facilitate the derivations of the constitutive equations of piezoelectric materials and systems given in Part II of the book.

3.1 An Overview of Calculus of Variations

The subject of typical college calculus deals with functions. When the arguments of a function themselves become functions of other variables, then this subject is expanded to what is referred to as "variational calculus" or "calculus of variation." The variational calculus forms the basic mathematical tools in analytical dynamics, especially for many energy-based modeling frameworks for continuous systems. Hence, a brief overview of this mathematical tool is given in this section to enable further development of the equations of motion for a variety of dynamic systems studied in this book.

N. Jalili, *Piezoelectric-Based Vibration Control*,
DOI 10.1007/978-1-4419-0070-8_3,

© Springer Science+Business Media LLC 2010

3.1.1 Concept of Variation

Function and functional: A function $y = f(x)$ is a correspondence between a set of independent input values x and a set of output values y, where x could be either constant or variable. Functional is, however, a function of function (i.e., the arguments of the functionals are also functions of other independent variables). For example, in $g = f\ (x(t))$, the argument of f, that is, $x(t)$, itself is a function of the time variable t.

Variational and infinitesimal displacements: Consider a system of interconnected elements with a set of fixed geometric constraints as depicted in Fig. 3.1. Assume that link OA in this system is going to be subjected to some small displacements. We encounter two scenarios, the first one being that link OA is subjected to an *infinitesimal* displacement regardless of the geometric constraint shown in Fig. 3.1, so the constraint may be violated (see Fig. 3.2). We denote this infinitesimal displacement of Point B with dx as shown in Fig. 3.2. In the second scenario, this link is subjected to an infinitesimal displacement that is compliant with the geometric constraints. We call this displacement of Point B an "*admissible variation*" and denote it with δx, see Fig. 3.3. We will demonstrate, next, how the concept of variation of a function can be described using these definitions of infinitesimal and variational displacements.

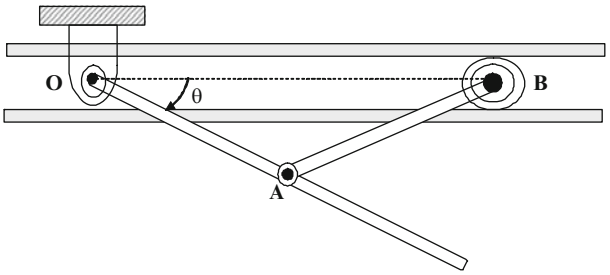

Fig. 3.1 A system of interconnected elements

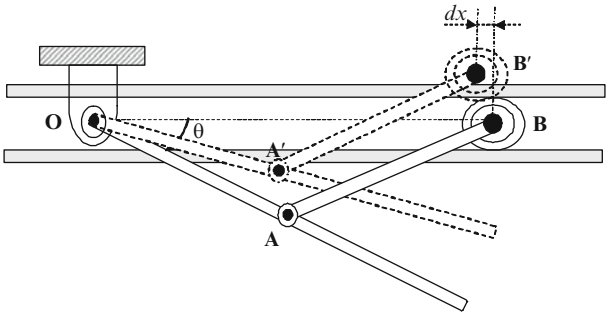

Fig. 3.2 A system of interconnected particles subjected to an infinitesimal displacement

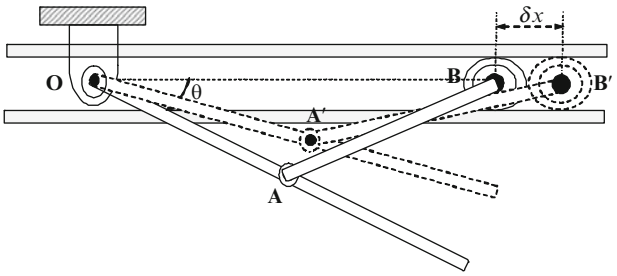

Fig. 3.3 A system of interconnected particles subjected to an "admissible variation"

Fig. 3.4 Concept of variation

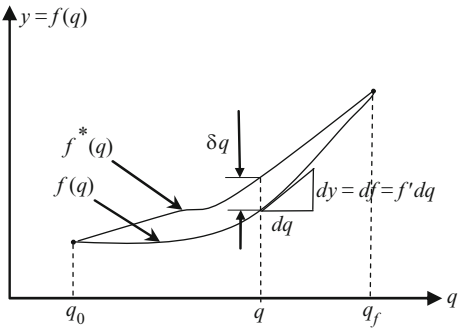

Remark 3.1. It must be noted that all variational displacements considered here are assumed to be admissible, that is, they are compliant with the fixed geometrical constraints. In other words, the variational displacements at the fixed boundaries always vanish. There is, however, an exception to this scenario in which we encounter free or natural boundaries at which the variations do not necessarily vanish. These important exceptions are discussed in detail later in this section.

Definition of variational operator: Consider $f(q)$ to be a function of independent variable q. Assume that this function can be slightly varied to a new function, named $f^*(q)$ as shown in Fig. 3.4. Since this is assumed to be an admissible variation, both $f(q)$ and $f^*(q)$ possess the same values at the boundaries (q_0 and q_f in Fig. 3.4).

Now, the variation of this function is defined as the difference between $f(q)$ and $f^*(q)$. That is,

$$\delta f(q) = \delta y \triangleq f^*(q) - f(q) \tag{3.1}$$

where δf is a change to a different curve with the independent variable q fixed. As clearly seen from Fig. 3.4, this variation is different from derivative of the function, *df*, at this point. The key point here is that "δ" is treated as an "operator." That is, when the variational operator δ operates on function f, it produces δf. Based on this conceptual definition of variation, we will, next, define the increment of a function and functional.

Increment of function and functional: The increment of function $f = f(\mathbf{q})$, $\mathbf{q} \in \mathbb{R}^n$ is defined as

$$df(\mathbf{q}) \triangleq f(\mathbf{q} + d\,\mathbf{q}) - f(\mathbf{q}) \tag{3.2}$$

While, the increment of a functional $J = J(\mathbf{x})$, $\mathbf{x} = \mathbf{x}(t) \in \Omega$ is defined as

$$\delta J(\mathbf{x}) \triangleq J(\mathbf{x} + \delta\mathbf{x}) - J(\mathbf{x}) \tag{3.3}$$

where $\delta J(\mathbf{x})$ is the variation of function $\mathbf{x}(t)$. Notice that based on the concept of variation established earlier, the variation δ operates only on functions [in this case $\mathbf{x}(t)$] and not on the independent variables (in this case t). This is an important concept and needs careful attention when expanding terms involving variations of functionals with multiple functions or independent variables.

3.1.2 Properties of Variational Operator δ

As discussed earlier, δ is viewed as an operator, and hence, possesses some properties similar to other operators (e.g., Laplace operator). We only list here the properties that will be frequently used in this book and leave the rest to dedicated books on calculus of variation cited in this chapter (e.g., Hildebrand 1965).

The derivative and variational operator δ can be interchanged with each other. Mathematically, this can be expressed as

$$\delta\left(\frac{\mathrm{d}f}{\mathrm{d}x}\right) = \frac{\mathrm{d}}{\mathrm{d}x}(\delta f) \tag{3.4}$$

Similar to derivative, integral and variational operator δ can be interchanged, that is,

$$\delta \int f(q)\,\mathrm{d}q = \int \delta f(q)\,\mathrm{d}q \tag{3.5}$$

Using previous property, it can be shown that

$$\text{If } F(q) = \int f(q)\mathrm{d}q, \quad \text{then} \quad \delta F(q) = f(q)\delta q \tag{3.6}$$

Free versus forced boundary conditions: It must be noted that we have, so far, restricted the variations of function $f(q)$ at the boundaries [i.e., $\delta f(q_0) = \delta f(q_f) = 0$ in Fig. 3.4]. That is, if we denote $\delta f(q) = \varepsilon\lambda(q)$ where $\lambda(q)$ is a function with continuous first derivatives and ε is a small parameter, then $\lambda(q_0) = \lambda(q_f) = 0$ in which q_0 and q_f are the boundary values shown in Fig. 3.4. This situation is referred to as "forced or geometrical" boundary conditions. We will show later in this section that these restrictions on $\lambda(q)$ can be relaxed which results in the so-called "free or natural" boundary conditions.

3.1.3 The Fundamental Theorem of Variation

Let us assume function $\mathbf{x}(t) \in \Omega$ and functional $J(\mathbf{x}(t))$ are differentiable and in addition function $\mathbf{x}(t)$ is not limited. Then, if $\mathbf{x}^*(t)$ is an extremal (minimal or maximal), variation J must vanish on $\mathbf{x}^*(t)$, that is,

$$\delta J(\mathbf{x}^*(t), \delta\mathbf{x}) = 0, \quad \text{for all admissible } \delta\mathbf{x} \tag{3.7}$$

Proof. See cited references on variational calculus in this chapter (e.g., Hildebrand 1965; Kirk 1970).

Euler equations: Using the fundamental theorem of variation, the so-called *Euler equation* can be obtained which has numerous applications in analytical dynamics including derivation of the Lagrange's equations.

For the sake of brevity and undue complication, assume $x(t)$ to be a scalar function of t in the class of functions with continuous first derivatives. We would like to find function $x^*(t)$ for which functional

$$J\,(x(t)) = \int_{t_0}^{t_f} g(x(t), \dot{x}(t), t)\mathrm{d}t,\ x(t_0) = x_0,\ x(t_f) = x_f \tag{3.8}$$

has a relative extremum.[1] In order to solve for $x^*(t)$, one can use the results of (3.7) and perform the variation over J. For this, we can use the definition of the variation of a functional (or increment) given by (3.3) to obtain

$$\delta J = J(x + \delta x) - J(x) = \int_{t_0}^{t_f} [g(x + \delta x, \dot{x} + \delta\dot{x}, t) - g(x, \dot{x}, t)]\mathrm{d}t \tag{3.9}$$

We can now use Taylor's series expansion for $J(x + \delta x)$ and expand the first integrant term on the right side of (3.9). Notice, this is a two-dimensional Taylor's expansion since functional g is a function of two functions [i.e., $x(t)$ and $\dot{x}(t)$]. Note that also as mentioned earlier, the variation does not operate on the independent variable t here. Hence, using the first-order Taylor's series approximation, we obtain

$$g(x + \delta x, \dot{x} + \delta\dot{x}, t) = g(x, \dot{x}, t) + \left.\frac{\partial g}{\partial x}\right|_{x,\dot{x},t} \delta x + \left.\frac{\partial g}{\partial \dot{x}}\right|_{x,\dot{x},t} \delta\dot{x} + \text{HOT} \tag{3.10}$$

[1] Note that we may frequently refer to t_0 and t_f as boundary conditions as "t" is treated as an independent variable only and not necessarily the "time" variable here. Similarly, $\mathrm{d}/\mathrm{d}t$ does not necessarily imply temporal derivative in this section.

Substituting (3.10) into (3.9) and after some manipulations, we get

$$\delta J = \int_{t_0}^{t_f} (g_x \delta x + g_{\dot{x}} \delta \dot{x}) \mathrm{d}t \tag{3.11}$$

where $(\,)_x \triangleq \dfrac{\partial(\,)}{\partial x}$.

Recall the first property of variational operator δ, that is, (3.4), we can write

$$\delta \dot{x} = \delta \left(\frac{\mathrm{d}x}{\mathrm{d}t} \right) = \frac{\mathrm{d}}{\mathrm{d}t} (\delta x) \tag{3.12}$$

Using integral by part (A.3) and property (3.12), expression (3.11) can be further simplified. For this, we take the second term in the integrant of (3.11) and expand it as follows:

$$\int_{t_0}^{t_f} g_{\dot{x}} \delta \dot{x} \mathrm{d}t = \int_{t_0}^{t_f} g_{\dot{x}} \delta \left(\frac{\mathrm{d}x}{\mathrm{d}t} \right) \mathrm{d}t = \int_{t_0}^{t_f} g_{\dot{x}} \frac{\mathrm{d}}{\mathrm{d}t} (\delta x) \mathrm{d}t = g_{\dot{x}} \delta x |_{t_0}^{t_f} - \int_{t_0}^{t_f} \frac{\mathrm{d}}{\mathrm{d}t} (g_{\dot{x}}) \delta x \mathrm{d}t \tag{3.13}$$

Recall from our assumptions in (3.8), the boundary conditions were considered to be fixed [i.e., $x(t_0) = x_0$, $x(t_f) = x_f$], hence their variations must vanish. That is,

$$\delta x(t_0) = \delta x(t_f) = 0 \tag{3.14}$$

Substituting these into (3.13), and subsequently into (3.11) yields

$$\delta J = \int_{t_0}^{t_f} \left\{ \left(g_x - \frac{\mathrm{d}}{\mathrm{d}t} (g_{\dot{x}}) \right) \delta x \right\} \mathrm{d}t \tag{3.15}$$

Using the fundamental theorem of calculus of variation and stated objectives, we are seeking solution $x^*(t)$ for which $\delta J = 0$. For δJ in (3.15) to vanish, the integral on the right-hand side must vanish, and for the integral to vanish, the integrant must vanish. That is,

$$\left(g_x - \frac{\mathrm{d}}{\mathrm{d}t} (g_{\dot{x}}) \right) \delta x = 0 \tag{3.16}$$

For expression (3.16) to vanish independent of δx (since $\delta x \neq 0$), we must have

$$g_x - \frac{\mathrm{d}}{\mathrm{d}t} (g_{\dot{x}}) \Big|_{x^*, \dot{x}^*} = 0 \tag{3.17}$$

And in expanded form

$$\frac{\partial}{\partial x} g(x^*, \dot{x}^*, t) - \frac{\mathrm{d}}{\mathrm{d}t}\left(\frac{\partial}{\partial \dot{x}} g(x^*, \dot{x}^*, t)\right) = 0 \tag{3.18}$$

Expression (3.18) is referred to as the so-called *Euler equation*. This is an important result that can be used for the derivation of equations of motion in many areas of analytical dynamics as well as optimal control theory.

Free boundary conditions: As mentioned in the preceding subsection, the boundary conditions have been taken to be fixed (or geometrical) so far. As will be shown later in this book, many flexible structures experience natural or free boundary conditions as part of their functionality or arrangements for a specific application. Hence, it is important to consider these types of boundary conditions. For this, assume that the boundary conditions given in (3.8) can be made free, hence, $\delta x(t_0) \neq 0$ and/or $\delta x(t_f) \neq 0$. Then, revisit the integral by part section of the derivation of Euler equation, that is, (3.13), and expand it as

$$\begin{aligned} \int_{t_0}^{t_f} g_{\dot{x}} \delta \dot{x}\, \mathrm{d}t &= g_{\dot{x}} \delta x|_{t_0}^{t_f} - \int_{t_0}^{t_f} \frac{\mathrm{d}}{\mathrm{d}t}(g_{\dot{x}}) \delta x \mathrm{d}t \\ &= g_{\dot{x}}|_{t_f}\, \delta x(t_f) - g_{\dot{x}}|_{t_0}\, \delta x(t_0) - \int_{t_0}^{t_f} \frac{\mathrm{d}}{\mathrm{d}t}(g_{\dot{x}}) \delta x \mathrm{d}t \end{aligned} \tag{3.19}$$

Substituting this expression into (3.11) results in

$$\delta J = \int_{t_0}^{t_f} \left(g_x - \frac{\mathrm{d}}{\mathrm{d}t}(g_{\dot{x}})\right) \mathrm{d}t\, \delta x + g_{\dot{x}}|_{t_f}\, \delta x(t_f) - g_{\dot{x}}|_{t_0}\, \delta x(t_0) \tag{3.20}$$

Similar to our earlier discussions, for δJ in (3.20) to vanish, the coefficients of δx, $\delta x(t_0)$ and $\delta x(t_f)$ must vanish since all of these variations could take any arbitrarily value independently. Hence, the Euler equation in this case is recast as

$$\begin{aligned} &\delta x \rightarrow \frac{\partial}{\partial x} g(x^*, \dot{x}^*, t) - \frac{\mathrm{d}}{\mathrm{d}t}\left(\frac{\partial}{\partial \dot{x}} g(x^*, \dot{x}^*, t)\right) = 0 \\ &\delta x(t_0) \rightarrow \frac{\partial}{\partial \dot{x}}\, g(x^*, \dot{x}^*, t)|_{t=t_0} = 0 \\ &\delta x(t_f) \rightarrow \frac{\partial}{\partial \dot{x}}\, g(x^*, \dot{x}^*, t)|_{t=t_f} = 0 \end{aligned} \tag{3.21}$$

Remark 3.2. If there is any fixed boundary condition, then the variation of the function at that boundary condition will vanish. For example, if the boundary condition at t_0 is a fixed boundary condition, then $x(t_0) = x_0$, and hence, $\delta x(t_0) = 0$.

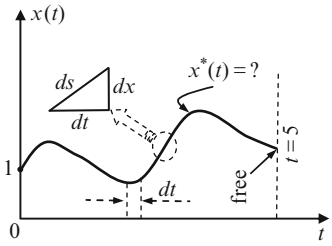

Fig. 3.5 Plot of $x(t)$ versus t of Example 3.1.

Example 3.1. Finding the smallest length between two points.

To demonstrate the use of Euler equation in optimization problem, let us consider the problem of finding a smooth curve of smallest length connecting point $x(0) = 1$ to line $t = 5$ (see Fig. 3.5).

Solution. Denote the length of the sought curve as ℓ, which can be expressed as (see Fig. 3.5)

$$\ell = \int_{t_0}^{t_f} \mathrm{d}s = \int_{t_0}^{t_f} \sqrt{\mathrm{d}t^2 + \mathrm{d}x^2} = \int_{t_0}^{t_f} \mathrm{d}t \sqrt{1 + (\mathrm{d}x/\mathrm{d}t)^2} = \int_{t_0}^{t_f} \sqrt{1 + \dot{x}^2}\mathrm{d}t \tag{3.22}$$

Hence, we want to find an extremum for ℓ. Comparing this expression with the general expression (3.8), one can conclude that

$$g(x, \dot{x}, t) = \sqrt{1 + \dot{x}^2} \tag{3.23}$$

Now, we want to find an extremum for $x(t)$, named here $x^*(t)$, such that $\delta\ell = 0$. For this, we shall use the Euler equation (3.21) with functional g given by (3.23). Since functional g in (3.23) is not explicitly function of x, the Euler equation reduces to

$$\frac{\mathrm{d}}{\mathrm{d}t}(g_{\dot{x}}) = 0 \Rightarrow g_{\dot{x}} = C = \text{constant} \tag{3.24}$$

Substituting (3.23) into (3.24) yields

$$g_{\dot{x}} = \frac{\dot{x}}{\sqrt{1 + \dot{x}^2}} = C \Rightarrow \dot{x} = C_1 \Rightarrow x(t) = C_1 t + C_2 \tag{3.25}$$

The results obtained in (3.25) for the general form of $x(t)$ reveals that the curve of the shortest length must be a line, which was expected from our own intuition.

Constants C_1 and C_2 are obtained using the boundary conditions. At $x(t_0)$, we have a fixed boundary condition. Hence, substituting $x(0) = 1$ in (3.25) results in $C_2 = 1$. At $x(t_f)$, the end of the curve could be on any point along the line $t = 5$, so this is a free boundary condition (see Fig. 3.5). Using the relationship for the free

boundary conditions [third equation in (3.21)] while using (3.25), one can write

$$g_{\dot{x}}|_{t=5} = 0 \Rightarrow \frac{\dot{x}}{\sqrt{1+\dot{x}^2}} = \frac{C_1}{\sqrt{1+C_1^2}} = 0 \Rightarrow C_1 = 0 \tag{3.26}$$

By determining constants C_1 and C_2, the final expression for $x^*(t)$ can be given as

$$x^*(t) = 1 \tag{3.27}$$

As expected, this is a straight line perpendicular to line $t = 5$.

3.1.4 Constrained Minimization of Functionals

In many cases, we would like to find conditions under which a function is stationary (i.e., attains its extremum, minimal or maximal). If (x_0, y_0) is a stationary point of function $f(x, y)$ where x and y are two independent variables, then $f(x, y)$ can be extended around this stationary point as

$$f(x,y) = f(x_0,y_0) + (x-x_0)\left.\frac{\partial f}{\partial x}\right|_{x_0,y_0} + (y-y_0)\left.\frac{\partial f}{\partial y}\right|_{x_0,y_0} + HOT \tag{3.28}$$

The condition for point (x_0, y_0) to be stationary is that its first-order derivatives in (3.28) must vanish. This results in $f(x, y) = f(x_0, y_0)$.

If there are some constraints, then this condition is more difficult to be met. Let us assume $h(x, y) = 0$ be an algebraic constraint augmented with function $f(x, y)$. Then, the derivatives of this constraint can be written as

$$\frac{\mathrm{d}h}{\mathrm{d}x} = \frac{\partial h}{\partial x} + \frac{\partial h}{\partial y}\frac{\mathrm{d}y}{\mathrm{d}x} \tag{3.29}$$

Since $h(x, y) = 0$, then $\mathrm{d}h/\mathrm{d}x = 0$ naturally. Using this fact and the results obtained in (3.29), we can get

$$\frac{\mathrm{d}h}{\mathrm{d}x} = 0 \rightarrow \frac{\partial h}{\partial x} + \frac{\partial h}{\partial y}\frac{\mathrm{d}y}{\mathrm{d}x} = 0 \rightarrow \frac{\mathrm{d}y}{\mathrm{d}x} = -\frac{\partial h/\partial x}{\partial h/\partial y} \tag{3.30}$$

Considering our search for stationary conditions on function $f(x, y(x))$, its implicit derivative must vanish, that is, $\mathrm{d}f/\mathrm{d}x = 0$, for instance, which yields

$$\frac{\mathrm{d}f}{\mathrm{d}x} = \frac{\partial f}{\partial x} + \frac{\partial f}{\partial y}\frac{\mathrm{d}y}{\mathrm{d}x} = 0 \rightarrow \frac{\mathrm{d}y}{\mathrm{d}x} = -\frac{\partial f/\partial x}{\partial f/\partial y} \tag{3.31}$$

Comparing (3.30) with (3.31), it yields

$$\frac{\partial f/\partial x}{\partial h/\partial x} = \frac{\partial f/\partial y}{\partial h/\partial y} = \text{constant} = -\lambda \tag{3.32}$$

Consequently, one can rewrite expression (3.32) as

$$\frac{\partial f}{\partial x} + \lambda \frac{\partial h}{\partial x} = 0, \quad \frac{\partial f}{\partial y} + \lambda \frac{\partial h}{\partial y} = 0, \tag{3.33}$$

which are the conditions that a function of three variables x, y and λ defined as

$$f_a(x, y, \lambda) = f(x, y) + \lambda h(x, y) \tag{3.34}$$

must be satisfied to be stationary. Constant λ is called the *Lagrange multiplier*.

In summary, in the case of constraints, one can augment the original function (here, f) with an appropriate number of Lagrange multipliers according to the number of constraints and seek stationary points for the augmented function (in this case, f_a). These conditions along with the constraints themselves can be solved simultaneously to obtain the stationary points for the problem.

Using the concept of Lagrange multipliers, one can study the constrained minimization of functional. That is, if the minimization problem of functional is combined with some constraints, one can use the method of Lagrange multipliers to augment the functional. For this, the minimization problem

$$J(x(t)) = \int_{t_0}^{t_f} g(x(t), \dot{x}(t), t)\mathrm{d}t \tag{3.35}$$

subject to n constraints or relationships

$$f_i(x, \dot{x}, t) = 0, \quad i = 1, 2, \ldots, n \tag{3.36}$$

could be expanded as minimizing the augmented functional J_a

$$J_\mathrm{a}(x, \mathbf{P}) = \int_{t_0}^{t_f} \left(g + \mathbf{P}(t) \cdot \mathbf{f}^T\right) \mathrm{d}t \tag{3.37}$$

where $\mathbf{P} = \{P_1, P_2, \ldots, P_n\}$ is a vector of n Lagrange multipliers and $\mathbf{f} = \{f_1, f_2, \ldots, f_n\}$. Consequently, the variation of this new functional becomes

$$\begin{aligned}\delta J_\mathrm{a} = \int_{t_0}^{t_f} &[g(x + \delta x, \dot{x} + \delta\dot{x}, t) + (\mathbf{P}(t) + \delta\mathbf{P}(t)) \cdot \mathbf{f}^T(x + \delta x, \dot{x} + \delta\dot{x}, t) \\ &-(g(x, \dot{x}, t) + \mathbf{P}(t) \cdot \mathbf{f}^T(x, \dot{x}, t))]\mathrm{d}t\end{aligned} \tag{3.38}$$

Similar to the unconstrained problem presented in the previous section, we can use the Taylor's series expansion to expand and simplify this expression. After some manipulations, it can be shown that this yields to the following modified Euler equation for constrained problem:

$$\frac{\partial}{\partial x} g_{\mathrm{a}}(x^*, \dot{x}^*, t) - \frac{\mathrm{d}}{\mathrm{d}t}\left(\frac{\partial}{\partial \dot{x}} g_{\mathrm{a}}(x^*, \dot{x}^*, t)\right) = 0 \tag{3.39}$$

where

$$g_{\mathrm{a}} = g(x, \dot{x}, t) + \mathbf{P}(t) \cdot \mathbf{f}^T(x, \dot{x}, t) \tag{3.40}$$

Equation (3.39) along with the constraints (3.36) can be simultaneously solved to obtain the extremum solution $x^*(t)$ and n Lagrange multipliers P_1 through P_n.

Now that the necessary mathematical backgrounds in calculus of variation have been briefly presented we would like to implement the fundamental law of calculus of variation in analytical dynamics, and especially to Hamilton's principle. We will give, next, an overview of Hamilton's principle and its derivations.

3.2 A Brief Overview of Variational Mechanics

In this section, the concept of work–energy relationship is briefly reviewed along with presenting the extended Hamilton's principle. In order to maintain the focus of the chapter, the development of the relationships and derivations are presented using a simple particle system instead of complex 3D flexible structures. Once this relationship is established and the Hamilton's principle is derived, the results can be extended to more complicated systems. We refer interested readers on these extensions to the cited references in this chapter.

3.2.1 Work–Energy Theorem and Extended Hamilton's Principle

As mentioned earlier and without undue complication, let us consider a particle with mass m moving along the path (solid line) shown in Fig. 3.6. It is assumed that the particle is acted on by a variable resultant force $\mathbf{f}(\mathbf{x}(t), t) \in \mathbb{R}^3$ and can be described by generalized displacement $\mathbf{x}(t) \in \mathbb{R}^3$. Note the dependency of resultant force $\mathbf{f}$ on both time and particle generalized coordinate.

Applying the second Newton's law to this particle yields

$$\mathbf{f}(\mathbf{x}, t) = \frac{\mathrm{d}\mathbf{p}(t)}{\mathrm{d}t},\ \mathbf{p}(t) \triangleq m\frac{\mathrm{d}\mathbf{x}(t)}{\mathrm{d}t} \tag{3.41}$$

Separating the resulting force $\mathbf{f}(t)$ into internal and external forces, (3.41) is recast as

$$\mathbf{f}^{\mathrm{int}} + \mathbf{f}^{\mathrm{ext}} = \frac{\mathrm{d}\mathbf{p}}{\mathrm{d}t} \tag{3.42}$$

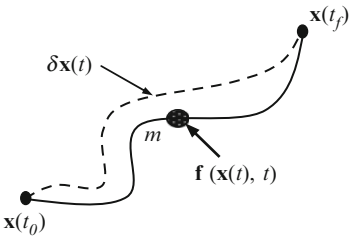

Fig. 3.6 A particle with mass m moving along an arbitrary path $\mathbf{x}(t)$

where $\mathbf{f}^{\text{int}}$ and $\mathbf{f}^{\text{ext}}$ represent internal and external forces, respectively, and the arguments of functions were dropped for simplicity of the derivations.

Now let us consider the varied path $\delta\mathbf{x}(t)$ as shown in Fig. 3.6 (dashed lines), and apply an admissible variation to (3.42). Following the concept of variational operator discussed in Sect. 3.1, this would result in

$$\mathbf{f}^{\text{int}}\delta\mathbf{x} + \mathbf{f}^{\text{ext}}\delta\mathbf{x} = \frac{\mathrm{d}\mathbf{p}}{\mathrm{d}t}\delta\mathbf{x} \tag{3.43}$$

Recall the definition of work done by external force $\mathbf{f}$ on a particle as $W = \int_{\mathbf{x}} \mathbf{f}\cdot\mathrm{d}\mathbf{x}$ and using the variational property (3.6), (3.43) can be rewritten in the following form:

$$\delta W^{\text{int}} + \delta W^{\text{ext}} = m\frac{\mathrm{d}\dot{\mathbf{x}}}{\mathrm{d}t}\delta\mathbf{x} \tag{3.44}$$

where δW^{int} and δW^{ext} denote the virtual works done by internal and external forces, respectively.

The internal work is typically related to a *potential energy* of the corresponding internal force. Hence, we can write

$$\delta W^{\text{int}} \triangleq -\delta U(\mathbf{x}) \tag{3.45}$$

where $U(\mathbf{x})$ represents the potential function of the internal force $\mathbf{f}^{\text{int}}$. Using this definition, (3.44) can be rewritten as

$$\delta W^{\text{ext}} - \delta U - m\frac{\mathrm{d}\dot{\mathbf{x}}}{\mathrm{d}t}\delta\mathbf{x} = 0 \tag{3.46}$$

Integrating (3.46) over the entire path on Fig. 3.6 from t_0 to t_f yields

$$\int_{t_0}^{t_f} \left(\delta W^{\text{ext}} - \delta U\right)\mathrm{d}t - \int_{t_0}^{t_f} m\frac{\mathrm{d}\dot{\mathbf{x}}}{\mathrm{d}t}\delta\mathbf{x}\,\mathrm{d}t = 0 \tag{3.47}$$

Using integral by part discussed in Appendix A, the last term of (3.47) can be simplified as

$$\int_{t_0}^{t_f} m\frac{\mathrm{d}\dot{\mathbf{x}}}{\mathrm{d}t}\delta\mathbf{x}\,\mathrm{d}t = m\dot{\mathbf{x}}(t)\delta\mathbf{x}(t)|_{t_0}^{t_f} - \int_{t_0}^{t_f} m\dot{\mathbf{x}}(t)\frac{\mathrm{d}}{\mathrm{d}t}(\delta\mathbf{x})\mathrm{d}t \tag{3.48}$$

Without loss of generality, we assume fixed boundary conditions (as evidenced from Fig. 3.6), hence $\delta\mathbf{x}(t_0) = \delta\mathbf{x}(t_f) = 0$. It is not too difficult to expand the results here to free boundary conditions as demonstrated in Sect. 3.1. Using this assumption and taking into account the variational operator property (3.4), (3.48) reduces to

$$\int_{t_0}^{t_f} m\frac{\mathrm{d}\dot{\mathbf{x}}}{\mathrm{d}t}\delta\mathbf{x}\,\mathrm{d}t = -\int_{t_0}^{t_f} m\dot{\mathbf{x}}(t)\delta\dot{\mathbf{x}}(t)\,\mathrm{d}t \tag{3.49}$$

Utilizing the concept of variational operator δ, one can write

$$\delta\left(\frac{1}{2}m\dot{\mathbf{x}}^2(t)\right) = m\dot{\mathbf{x}}(t)\delta\dot{\mathbf{x}}(t) \triangleq \delta T(\dot{\mathbf{x}}) \tag{3.50}$$

where T is defined as the *kinetic energy* of the particle given by (3.50). Substituting the results obtained in (3.49) and (3.50) into (3.47), it yields

$$\int_{t_0}^{t_f} \big(\delta W^{\text{ext}} - \delta U + \delta T\big)\mathrm{d}t = 0 \tag{3.51}$$

Defining *Lagrangian* $L = T - U$, (3.51) can be rewritten in the following form

$$\int_{t_0}^{t_f} \big(\delta L + \delta W^{\text{ext}}\big)\mathrm{d}t = 0 \tag{3.52}$$

which is referred to as *extended Hamilton's principle* in its most general form.

Remark 3.3. It must be noted that the procedure presented here can be followed for a system of particles as well as rigid and flexible bodies to arrive at the same expression. We defer this to cited references (Meirovitch 1997; Baruh 1999).

Remark 3.4. The works of all internal forces that have a corresponding potential are already included in the potential energy U [i.e., (3.45)] in the Hamilton's expression (3.52). These forces for which there exists a potential function are referred to as *conservative* forces. The works of external or non-conservative forces are included in the external work W^{ext} in (3.52). The following example better clarifies this remark.

Example 3.2. Potential energy of a uniform bar subject to axial loading.

Calculate the potential energy of a uniform rod clamped at one end and subjected to a slowly increasing axial load P (see Fig. 3.7).

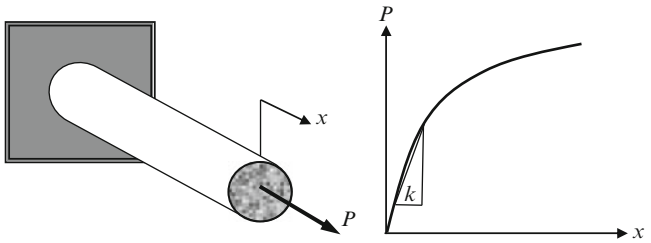

Fig. 3.7 The uniform rod of Example 3.2. subjected to a slowly varying tip load P

The work done by load P as the rod elongates can be easily calculated as

$$W_P = \int_0^x P(x)\mathrm{d}x \tag{3.53}$$

Assuming linear and elastic deformation (see the linear portion of load-deformation curve in Fig. 3.7), load P can be related to deformation x by linear relationship

$$P = kx \tag{3.54}$$

where k is a constant representative of the material's stiffness. Substituting (3.54) into (3.53) results in the potential energy or often referred to as *strain* energy of the rod subjected to axial load as

$$U_P = \int_0^x kx\,\mathrm{d}x = \frac{1}{2}kx^2 \tag{3.55}$$

Remark 3.5. In the absence of external or non-conservative forces, the Hamilton's principle (3.52) reduces to

$$\int_{t_0}^{t_f} (\delta L(\mathbf{x}, \dot{\mathbf{x}}, t))\,\mathrm{d}t = \delta \int_{t_0}^{t_f} L(\mathbf{x}, \dot{\mathbf{x}}, t)\,\mathrm{d}t = 0 \tag{3.56}$$

which is exactly in the form of minimization of a functional discussed in Sect. 3.1, that is, $L \equiv g$ in (3.8). This equation simply states that the variation of integral of the Lagrangian vanishes. This is a powerful result that can be used to conveniently derive the governing equations of any dynamic systems without the need for typical system decomposition used in Newtonian approach. It is worthy to note that using this method, a single scalar function (i.e., Lagrangian) is used to derive the equations of motion. This exercise is briefly demonstrated, next, for a simplified configuration, that is, a non-conservative system. This assumption is made here for simplicity and will be relaxed later in the solution.

3.2.2 Application of Euler Equation in Analytical Dynamics

To demonstrate the application of Euler equation and fundamental law of calculus in analytical dynamics, we present the derivation of Lagrange equations from Hamilton's principle. Without loss of generality and in order to avoid undue complication, we assume that x in Hamilton's equation (3.56) is scalar. It is now very easy to see that expression (3.56) is in the standard form of minimization of a functional that we have been working on, that is, $L \equiv g$ in (3.8). We are looking for an optimum path or trajectory $x^*(t)$ such that functional (3.56) vanishes. Without repeating the aforementioned details, we can see that this leads to Euler equation in the form of

$$\frac{\partial}{\partial x} L(x^*, \dot{x}^*, t) - \frac{\mathrm{d}}{\mathrm{d}t}\left(\frac{\partial}{\partial \dot{x}} L(x^*, \dot{x}^*, t)\right) = 0 \tag{3.57}$$

For most dynamic systems considered in this book, we can assume that

$$T(x, \dot{x}, t) = T(\dot{x}), \text{ (e.g., } T = \frac{1}{2} m\dot{x}^2) \tag{3.58}$$

$$U(x, \dot{x}, t) = U(x), \text{ (e.g., } U = \frac{1}{2} kx^2) \tag{3.59}$$

We will show, later, that these assumptions can be relaxed to arrive at the most general form of Lagrange's equations. Using these assumptions, the partial derivatives of L used in (3.57) can be obtained as

$$\begin{aligned} \frac{\partial L}{\partial x} &= \frac{\partial}{\partial x}\left(T(\dot{x}) - U(x)\right) = -\frac{\partial U(x)}{\partial x} \\ \frac{\partial L}{\partial \dot{x}} &= \frac{\partial}{\partial \dot{x}}\left(T(\dot{x}) - U(x)\right) = \frac{\partial T(\dot{x})}{\partial \dot{x}} \end{aligned} \tag{3.60}$$

Substituting partial derivatives obtained in (3.60) into (3.57) yields

$$\frac{\mathrm{d}}{\mathrm{d}t}\left(\frac{\partial T}{\partial \dot{x}}\right) + \frac{\partial U}{\partial x} = 0 \tag{3.61}$$

For cases in which the kinetic energy T is a function of both x and $\dot{x}$, that is, $T = T(x, \dot{x})$, the first partial derivative in (3.60) is extended to

$$\frac{\partial L}{\partial x} = \frac{\partial}{\partial x}\left(T(x, \dot{x}) - U(x)\right) = \frac{\partial T(x)}{\partial x} - \frac{\partial U(x)}{\partial x} \tag{3.62}$$

By substituting this new expression into (3.57), we get

$$\frac{\mathrm{d}}{\mathrm{d}t}\left(\frac{\partial T}{\partial \dot{x}}\right) - \frac{\partial T}{\partial x} + \frac{\partial U}{\partial x} = 0 \tag{3.63}$$

which is referred to as the so-called *Lagrange's equation* for conservative systems. For dynamic systems with a non-conservative force Q, one can write the non-conservative work done by Q as

$$W_{\text{nc}} = \int_x Q \mathrm{d}x \tag{3.64}$$

Using the third property of the variational operator δ given in (3.6), the variation of (3.64) can be simplified to

$$\delta W_{\text{nc}} = Q\, \delta x \tag{3.65}$$

On the other hand, the Hamilton's principle for a non-conservative system was obtained earlier as [see (3.52)]

$$\delta \int_{t_0}^{t_f} (L(x, \dot{x}, t) + W_{\text{nc}}) \mathrm{d}t = 0 \tag{3.66}$$

Substituting (3.65) into (3.66) reduces the Hamilton's principle for a non-conservative system to

$$\int_{t_0}^{t_f} (\delta L(x, \dot{x}, t) + Q \delta x) d\mathrm{t} = 0 \tag{3.67}$$

Following the same procedure discussed in the preceding subsection, expression (3.67) is rewritten as

$$\int_{t_0}^{t_f} \left(\frac{\partial}{\partial x} L(x, \dot{x}, t) - \frac{\mathrm{d}}{\mathrm{d}t} \left(\frac{\partial}{\partial \dot{x}} L(x, \dot{x}, t) \right) + Q \right) \delta x \, \mathrm{d}t = 0 \tag{3.68}$$

Following similar argument given earlier, since δx can take any value, the coefficient of δx must vanish. This yields

$$\frac{\mathrm{d}}{\mathrm{d}t} \left(\frac{\partial L}{\partial \dot{x}} \right) - \frac{\partial L}{\partial x} = Q \tag{3.69}$$

Or, using the partial derivatives of L obtained before, it yields

$$\frac{\mathrm{d}}{\mathrm{d}t} \left(\frac{\partial T}{\partial \dot{x}} \right) - \frac{\partial T}{\partial x} + \frac{\partial U}{\partial x} = Q \tag{3.70}$$

This is the Lagrange's equation in its most general form for non-conservative systems. It is not a difficult task to expand the results obtained here to MDOF systems. We leave this exercise to interested readers.

3.3 Steps in Deriving Equations of Motion via Analytical Method

As mentioned in the preceding section, using (extended) Hamilton's principle (3.52) or (3.56), one can easily derive the equations of motion. To this end, two different approaches can be taken. The first approach is to perform the variation on either (3.52) or (3.56) for a general system to arrive at the governing equations of motion for individual generalized coordinates, which is referred to as *Lagrange's equations*. The Lagrange equations can then be utilized for any given problem to determine the governing differential (typically ordinary) equations of motion (please see Sect. 3.2.2). This method is more suitable for lumped-parameters systems as demonstrated in Chap. 2.

The second method is to form the Lagrangian function L (i.e., expressing both kinetic and potential energies) and then performing the variation for the given problem to arrive at the differential (typically partial) equations of motions. The second method is the preferred method in this book, due to the nature of distributed-parameters systems considered here. These steps are summarized below, which are exercised and demonstrated extensively in Chap. 4.

1. Select a set of independent DOF or coordinates, referred to as generalized coordinates, such that they can fully represent the motion of the system.
2. Identify external, non-conservative and conservative forces. For the external and non-conservative forces, calculate their works and collect them into a single term named W^{ext}. For the conservative forces, such as elasticity, strain and gravity, calculate their energy and collect them into a single term called potential energy U. These two terms, W^{ext} and U, are written as functions of the generalized coordinates defined in Step 1.
3. Determine the kinetic energy of the system (T) as a function of generalized coordinates and their derivatives.
4. Perform the variation on W^{ext}, U and T used in the Hamilton's principle. It is recommended to keep these variation expressions inside the integral (3.52) or (3.56) in order to be able to switch between temporal and spatial integrals when needed. This will be clarified later in Chap. 4 through a number of illustrative examples.
5. Group the variations of similar generalized coordinates and assuming that these variations are independent, use the same procedure outline in Sect. 3.2.2 to arrive at equations of motions and boundary conditions simultaneously.

As seen from the above steps, we are almost ready to derive the governing equations of motion of any dynamic systems as long as we can determine a single scalar term, that is, the Lagrangian function L. This function is composed of potential and kinetic energies. For the kinetic energy calculations, we prefer not to include any detailed materials as these calculations can be easily performed using our elementary or intermediate dynamics background. The potential energy is, however, more involved and needs careful attention as it forms the basis for many vibrating flexible systems with strain and other types of energy storage capabilities. Along this line of

reasoning, we will present, in Chap. 4, the work of a deformable body in 3D. However, this requires the development of the differential equations of equilibrium first. These are discussed in detail in Chap. 4.

Summary

A brief overview of calculus of variation along with the fundamental theorem of variation was presented. This powerful tool was used in the derivation of Lagrange equations from Hamilton's principle, an important step in deriving the equations of motion of a dynamic system in general.

Exercises

3.1. Calculus of Variations

3.1. Find the extremals $x^*(t)$ for the following functionals:

a) $J(x) = \int_1^4 \left[x^2(t) + 2x(t)\,\dot{x}(t) + \dot{x}^2(t)\right] \mathrm{d}t, \quad x(1) = 0, x(4) = -2$

b) $J(x) = \int_0^2 \left[\frac{1}{2}\dot{x}^2(t) + x(t)\,\dot{x}(t) + \dot{x}(t) + x(t)\right] \mathrm{d}t,\ x(0) = 0,\ x(1) = \text{free}$

3.2. Consider the functional

$$J(x) = \int_{t_o}^{t_f} g\left(x(t),\ \dot{x}(t),\ \ldots,\ \frac{\mathrm{d}^r x(t)}{\mathrm{d}t^r},\ t\right) \mathrm{d}t$$

where t_0 and t_f are fixed, and $2r$ boundary conditions $\left(x(t_0), x(t_f)\right)$ and the first $(r-1)$ derivatives of x at t_0 and t_f are all given and fixed. Show that the Euler equation for this functional becomes

$$\sum_{k=0}^{r} (-1)^k \frac{\mathrm{d}^k}{\mathrm{d}t^k}\left[\frac{\partial g}{\partial x^{(k)}}\left(x^*(t),\ \ldots,\ \frac{\mathrm{d}^r x^*(t)}{\mathrm{d}t^r},\ t\right)\right] = 0$$

where $x^{(k)}$ denotes $\frac{\mathrm{d}^k x(t)}{\mathrm{d}t^k}$.

3.3. Use the Euler equation to find extremals for the functional:

$$J(x) = \int_0^1 \left[x(t)\dot{x}(t) + \ddot{x}^2(t)\right] \mathrm{d}t;\ \ x(0) = 0, \dot{x}(0) = 1, x(1) = 2 \text{ and } \dot{x}(1) = 4$$

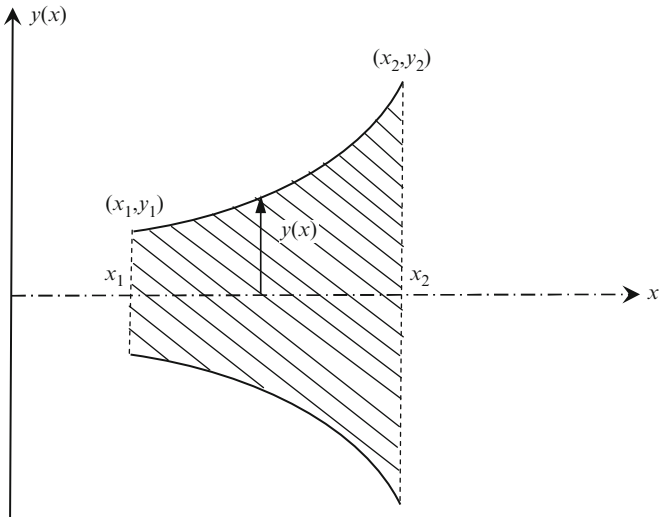

Fig. E3.1 Surface of revolution of Problem 3.5

3.4. A particle of unit mass moves on the surface $f(w_1(t), w_2(t), w_3(t)) = 0$ from point (w_{10}, w_{20}, w_{30}) to (w_{1f}, w_{2f}, w_{3f}) in fixed time T. Show that if the particle moves in such a way that the integral of the kinetic energy is minimized, then the motion satisfies the following equations:

$$\frac{\ddot{w}_1}{\dfrac{\partial f}{\partial w_1}} = \frac{\ddot{w}_2}{\dfrac{\partial f}{\partial w_2}} = \frac{\ddot{w}_3}{\dfrac{\partial f}{\partial w_3}}$$

3.5. A plane curve $y(x)$ is used to connect points (x_1, y_1) and (x_2, y_2) with $x_1 < x_2$. The curve $y(x)$ is rotated about the x-axis to generate a surface of revolution in the range $x_1 \leq x \leq x_2$ (see Fig. E3.1). Formulate the problem of finding the curve $y(x)$ that corresponds to minimum area of the surface of revolution in the xy plane.

3.6. Consider the Lagrangian functional L, given by

$$L = \int_0^\ell \frac{\rho A}{2}\left(\frac{\partial u}{\partial t}\right)^2 \mathrm{d}x - \int_0^\ell \frac{AE}{2}\left(\frac{\partial u}{\partial x}\right)^2 \mathrm{d}x + \int_0^\ell f\,u\,\mathrm{d}x + F\,u(\ell, t)$$

This functional corresponds to axial vibration of a bar with $u(x, t)$ being axial displacement. Find the first variation of the functional L with $\delta u(0, t) = \delta u(x, t_1) = \delta u(x, t_2) = 0$.

Chapter 4
A Unified Approach to Vibrations of Distributed-Parameters Systems

Contents

4.1 Equilibrium State and Kinematics of a Deformable Body 56
4.1.1 Differential Equations of Equilibrium 56
4.1.2 Strain–Displacement Relationships 58
4.1.3 Stress–Strain Constitutive Relationships 62
4.2 Virtual Work of a Deformable body 64
4.3 Illustrative Examples from Vibrations of Continuous Systems 69
4.3.1 Longitudinal Vibration of Bars 70
4.3.2 Transverse Vibration of Beams 74
4.3.3 Transverse Vibration of Plates 81
4.4 Eigenvalue Problem in Continuous Systems 86
4.4.1 Discretization of Equations and Separable Solution 87
4.4.2 Normal Modes Analysis 97
4.4.3 Method of Eigenfunctions Expansion 100
Summary
Exercises

This chapter provides a brief overview of vibrations of distributed-parameter systems. The treatment offered in this chapter follows a unified approach in which an energy-based modeling framework is adopted to describe the system behavior. As mentioned earlier in Chap. 1, the interactions between different fields (e.g., electrical, mechanical, magnetic) in active materials and especially in piezoelectrics materials can be conveniently established and presented using this method. This is especially important as the piezoelectric-based vibration-control systems considered in this book fall into this category of interacting different field systems. Hence, the materials presented here shall form the basis for the subsequent modeling and control developments for both piezoelectric-based systems and vibration-control systems discussed in Chaps. 8 and 9, respectively.

On the basis of the brief overview of work–energy relationship and Hamilton's principle in Chap. 3, the differential equations of a deformable body in 3-dimensional (3D) space are presented. Once these relationships are established, Hamilton's principle is utilized to derive the equations of motion of flexible continuous systems. The chapter ends with some illustrative examples from the vibrations of continuous systems including longitudinal vibration of bars and transverse vibration of beams and plates. These example case studies are purposefully selected as most of the piezoelectric-based actuators and sensors discussed in the subsequent chapters could be modeled using these systems.

N. Jalili, *Piezoelectric-Based Vibration Control*,
DOI 10.1007/978-1-4419-0070-8_4,

© Springer Science+Business Media LLC 2010

4.1 Equilibrium State and Kinematics of a Deformable Body

As mentioned in Sect. 3.3, to derive the equations of motion of a continuous system, one needs to determine the potential energy terms (mostly strain energy for vibration-control systems). For this, we will start with presenting the differential equations of motion in this section, followed by the relationships between strain and displacement and stress–strain constitutive relationships.

4.1.1 Differential Equations of Equilibrium

Recall from elementary mechanics of materials that the stress σ_{pq} or strain S_{pq}[1] denotes the stress or strain acting on face or plane p along the q-axis (see Fig. 4.1). Note also that a stress acting on a face or plane in the same direction of that plane (i.e., σ_{pp} or σ_{qq}) is called a *normal* stress and denoted by σ, while other components of the stress in the same plane or face are referred to as *shear* stress and denoted, typically, by τ.

Now consider a small rectangular parallelepiped of dimensions $\mathrm{d}x$, $\mathrm{d}y$, and $\mathrm{d}z$ along the x-, y-, and z-axes, respectively, in a deformed continuum subjected to a general stress–strain field. Using these notations, the components of the stress field acting on the rear surfaces are built as shown in Fig. 4.2a.

On the front surfaces, these components can be represented using first-order Taylor's series expansion as shown in Fig. 4.2b. To keep this figure readable, only

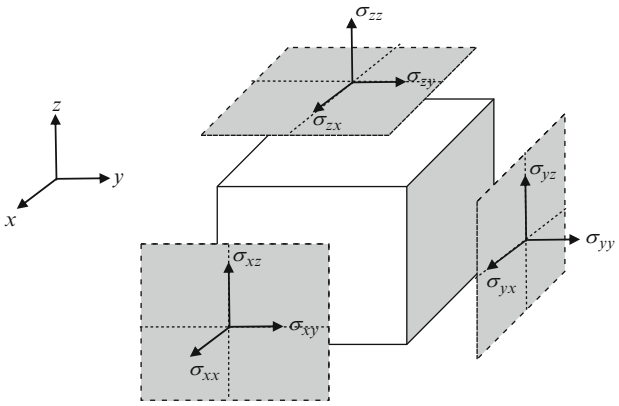

Fig. 4.1 The detailed notation of stress/strain components

[1] The standard symbol ε or γ commonly used for strain is replaced here with S for consistency in notations when using constitutive equations of piezoelectric materials discussed later in Parts II and III.

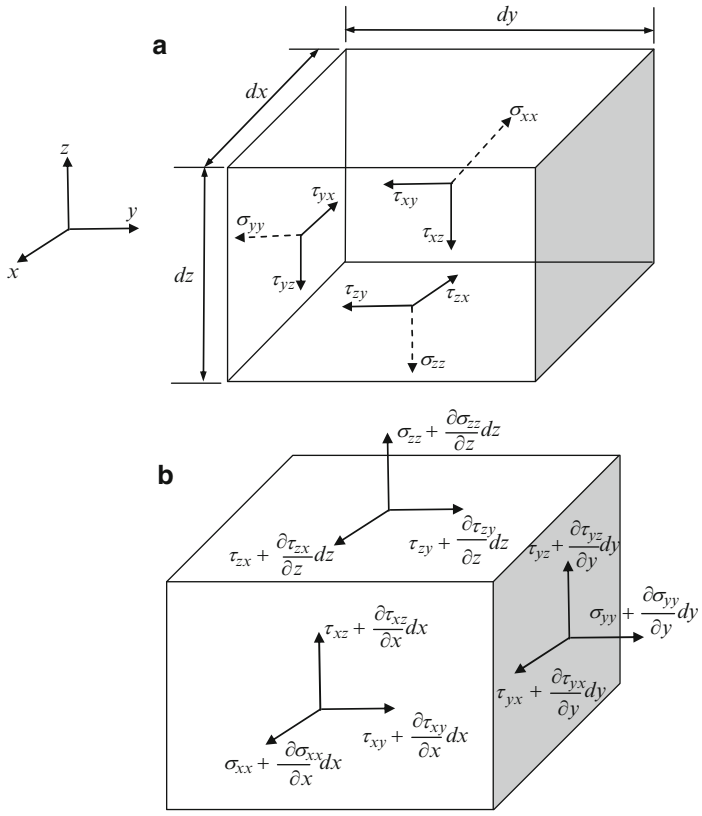

Fig. 4.2 Components of the stress field acting on (**a**) rear and (**b**) front faces

demonstrable components are shown in this figure, as the other components can be easily obtained with the same manner. It must be noted that these stresses are applied simultaneously on this continuum; however, they are drawn separately on rear and front faces to make the drawings clear and readable.

Assuming that F_x, F_x, and F_x denote the components of a resultant body force per unit volume (not shown in Fig. 4.2), for this continuum to be in equilibrium state, the summation of all forces acting in the x-direction must vanish, that is,

$$\left(\sigma_{xx} + \frac{\partial \sigma_{xx}}{\partial x}\mathrm{d}x\right)\mathrm{d}y\mathrm{d}z - \sigma_{xx}\mathrm{d}y\mathrm{d}z + \left(\tau_{yx} + \frac{\partial \tau_{yx}}{\partial y}\mathrm{d}y\right)\mathrm{d}x\mathrm{d}z - \tau_{yx}\mathrm{d}x\mathrm{d}z + \left(\tau_{zx} + \frac{\partial \tau_{zx}}{\partial z}\mathrm{d}z\right)\mathrm{d}x\mathrm{d}y - \tau_{zx}\mathrm{d}x\mathrm{d}y + F_x\mathrm{d}x\mathrm{d}y\mathrm{d}z = 0 \tag{4.1}$$

Simplifying this equation and taking into account the fact that the relationship holds for any arbitrary elemental volume $\mathrm{d}V = \mathrm{d}x\mathrm{d}y\mathrm{d}z$, we obtain

$$\frac{\partial \sigma_{xx}}{\partial x} + \frac{\partial \tau_{yx}}{\partial y} + \frac{\partial \tau_{zx}}{\partial z} + F_x = 0 \tag{4.2}$$

While condition (4.2) may guarantee that the continuum stays stationary in the x-direction, it cannot prevent its rotation. Hence, for the continuum to be truly at the equilibrium state, one shall consider the balance of the moments as well. For this, if we force the summation of the moments to be zero about an axis parallel to the x-axis and passing through the center of the continuum, it results in, after some manipulations and simplifications,

$$\tau_{yz} = \tau_{zy} \tag{4.3}$$

Similar procedure can be followed for the other two directions to yield the complete differential equations of equilibrium of an arbitrary deformable continuum as:

$$\begin{aligned}
&\frac{\partial \sigma_{xx}}{\partial x} + \frac{\partial \tau_{xy}}{\partial y} + \frac{\partial \tau_{xz}}{\partial z} + F_x = 0 \\
&\frac{\partial \tau_{yx}}{\partial x} + \frac{\partial \sigma_{yy}}{\partial y} + \frac{\partial \tau_{yz}}{\partial z} + F_y = 0 \\
&\frac{\partial \tau_{zx}}{\partial x} + \frac{\partial \tau_{zy}}{\partial y} + \frac{\partial \sigma_{zz}}{\partial z} + F_z = 0
\end{aligned} \tag{4.4}$$

where the symmetry of shear stresses has been taken into account (i.e., $\tau_{xy} = \tau_{yx}$, $\tau_{xz} = \tau_{zx}$, and $\tau_{yz} = \tau_{zy}$). These equations are valid for any conditions as no assumptions have been made regarding the size, shape, or displacement of the continuum. We shall be using these important results for representing the work of a deformable body in 3D, as discussed in the next section.

Using indicial notations given in Appendix A, one can rewrite the differential equations of equilibrium (4.4) in a more compact form. If we represent the coordinate system xyz and the components of the stress field shown in Fig. 4.2 with $x_1x_2x_3$ where x_1 denotes the x-axis and so on, then (4.4) in indicial format notation reduces to:

$$\frac{\partial \sigma_{ij}}{\partial x_j} + F_i = 0, \quad i = 1, 2, 3 \tag{4.5}$$

where subscripts 1, 2, and 3 in the stress components represent x, y, and z, respectively. It will be shown later in the chapter that such simplified expressions can significantly reduce the derivations and presentation of the equations.

4.1.2 Strain–Displacement Relationships

The conditions for which a deformed continuum is at equilibrium were obtained in the preceding subsection. While these conditions were concerned with forces and stresses acting on the continuum, the motion of the continuum was not considered. To complete the task of studying a deformed continuum in 3D, one needs to establish relationship between strain and displacement, the subject that is referred to as kinematics and presented next.

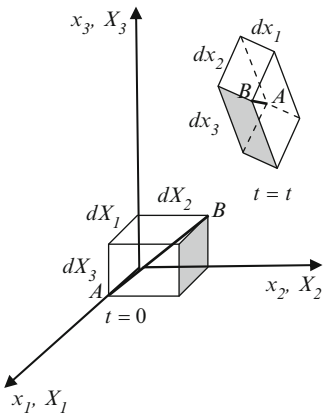

Fig. 4.3 Kinematics of a small rectangular parallelepiped continuum in undeformed ($t = 0$) and deformed ($t = t$) states

Since there are numerous definitions for strain (e.g., Eulerian strain, engineering strain, Lagrangian strain, and Green strain), we shall use an appropriate *measure* of strain that can capture the essence of strain in all these definitions. For this, we use a representative length in the continuum and define a measure of the difference between this length in the deformed and the undeformed states. To better describe this, let us consider the small rectangular parallelepiped shown in Fig. 4.3. in its undeformed state at $t = 0$ and deformed state at $t = t$.

To distinguish between undeformed and deformed configurations, as shown in Fig. 4.3, we denote the position vector of the continuum in undeformed state with block letters X_1, X_2, and X_3, while we use the small letters x_1, x_2, and x_3 to represent the position vector of the continuum in the deformed state. Hence, the position vector of the continuum in deformed state ($t = t$) can be represented as a function of its position in the undeformed state ($t = 0$) and vice versa, that is,

$$\mathbf{x} = \mathbf{x}(\mathbf{X}, t) \text{ or } \mathbf{X} = \mathbf{X}(\mathbf{x}, t) \tag{4.6}$$

where $\mathbf{x} = \{x_1\ x_2\ x_3\}^{\mathrm{T}}$ and $\mathrm{X} = \{X_1\ X_2\ X_3\}^{\mathrm{T}}$.

In order to come up with the sought measure of the strain, line AB of the continuum at hand is considered to be used for strain measurement (see Fig. 4.3). Denoting the length of line AB in Fig. 4.3 before deformation as $\mathrm{d}L$ and after deformation as $\mathrm{d}\ell$, one can write these lengths, using indicial notation, as

$$(\mathrm{d}L)^2 = \mathrm{d}X_m \mathrm{d}X_m, \quad (\mathrm{d}\ell)^2 = \mathrm{d}x_m \mathrm{d}x_m, \tag{4.7}$$

Consequently, an appropriate measure of the strain can be represented as the difference between these two lengths

$$(\mathrm{d}\ell)^2 - (\mathrm{d}L)^2 = \mathrm{d}x_m \mathrm{d}x_m - \mathrm{d}X_m \mathrm{d}X_m \tag{4.8}$$

However, the differentials used in (4.8) in the undeformed and the deformed configurations can be expressed as functions of each other through utilizing relationship (4.6). Since the current configuration or deformed state is of concern, we can express

the complete differentials $\mathrm{d}X_m$ in terms of elemental positions $\mathrm{d}x_m$. That is, using the second relationship in (4.6), we can write:

$$\mathrm{d}X_m = \frac{\partial X_m}{\partial x_j}\mathrm{d}x_j, \quad m = 1, 2, 3 \tag{4.9}$$

Substituting (4.9) into (4.8) and observing the indicial notation convention (i.e., not to repeat a summation index more than twice[2]), (4.8) can be rewritten as:

$$(d\ell)^2 - (dL)^2 = \left(\delta_{ij} - \frac{\partial X_m}{\partial x_i}\frac{\partial X_m}{\partial x_j}\right)\mathrm{d}x_i\mathrm{d}x_j \triangleq 2e_{ij}\mathrm{d}x_i\mathrm{d}x_j \tag{4.10}$$

where e_{ij} is defined as the *Eulerian* strain.

As briefly mentioned in Sect. 1.3, in order to describe the motion of a continuous system, the *displacement* variables are used instead of the position variables. This converts an infinite number of ODEs governing the motion of the system to a finite number of PDEs. To benefit from such convenience, we shall represent the position of the deformed continuum at hand, using displacement variables which are defined as:

$$u_m = x_m - X_m, \quad m = 1, 2, 3 \tag{4.11}$$

Rewriting X_m from (4.11) in terms of displacement variables and the deformed positions of the continuum (i.e., $X_m = x_m - u_m$) and substituting it in the Eulerian strain (4.10) yields

$$e_{ij} = \frac{1}{2}\left(\delta_{ij} - \left(\delta_{mi} - \frac{\partial u_m}{\partial x_i}\right)\left(\delta_{mj} - \frac{\partial u_m}{\partial x_j}\right)\right) \tag{4.12}$$

Using the property of Kronecker delta in indicial notation expressions (see Appendix A and the associated example therein), (4.12) can be simplified as:

$$e_{ij} = \frac{1}{2}\left(\frac{\partial u_i}{\partial x_j} + \frac{\partial u_j}{\partial x_i} - \frac{\partial u_m}{\partial x_i}\frac{\partial u_m}{\partial x_j}\right) \tag{4.13}$$

The Eulerian strain (4.13) is a complete form in the sense that no approximation has been made (not even a second-order approximation). For classical strain theory and small displacements considered in this book, however, only the linear terms of this strain are retained, i.e.,

$$e_{ij} = \frac{1}{2}\left(\frac{\partial u_i}{\partial x_j} + \frac{\partial u_j}{\partial x_i}\right) \tag{4.14}$$

Using standard engineering notation, one can convert the indicial notation back to the standard notation (i.e., $1 \to x$, $2 \to y$, $3 \to z$, $x_1 \to x$, $x_2 \to y$, $x_3 \to z$, $u_1 \to u$, $u_2 \to v$ and $u_3 \to w$) at this final stage to represent the strain components as:

[2] Please see Appendix A, Example A.2, for an exercise on this important substitution of indices.

$$e_{xx} \triangleq S_{xx} = \frac{\partial u}{\partial x},\ e_{yy} \triangleq S_{yy} = \frac{\partial v}{\partial y},\ e_{zz} \triangleq S_{zz} = \frac{\partial w}{\partial z}$$
$$e_{xy} \triangleq S_{xy} = \frac{\partial v}{\partial x} + \frac{\partial u}{\partial y},\ e_{xz} \triangleq S_{xz} = \frac{\partial w}{\partial x} + \frac{\partial u}{\partial z},\ e_{yz} \triangleq S_{yz} = \frac{\partial w}{\partial y} + \frac{\partial v}{\partial z} \tag{4.15}$$

where the coefficient 1/2 in the shear stresses is removed in the *engineering strain* notation used here.

Remark 4.1. It is obvious that if the three components of displacement, i.e., u, v, and w are prescribed, then the strain components can be easily obtained from relationships (4.15). However, if the components of strain field are prescribed instead, only three equations out of the six equations (4.15) will be needed to solve for the unknown displacements. This results in an overdetermined system that needs attention. In order to uniquely determine the three components of the displacement field, appropriate equations, which are referred to as strain compatibility conditions, are needed. These conditions for a general continuum are extensive and lengthy (Wallerstein 2002; Eringen 1952). However, the following example is given here to demonstrate the establishment of these conditions for a simple 2D displacement field.

Example 4.1. Strain compatibility conditions for 2D stress–strain field. Derive the compatibility conditions for a 2D displacement field.

Solution. For a 2D displacement field, the strain components (4.15) reduce to

$$S_{xx} = \frac{\partial u}{\partial x} \tag{4.16a}$$

$$S_{yy} = \frac{\partial v}{\partial y} \tag{4.16b}$$

$$S_{xy} = \frac{\partial u}{\partial y} + \frac{\partial v}{\partial x} \tag{4.16c}$$

In this case, if the three components of strain are prescribed, then the three equations (4.16) form an overdetermined system for the only two unknowns u and v. Hence, there should be one compatibility equation to relate the three components of the strain. This equation can be obtained through the following procedure.

Taking partial derivatives of (4.16a) and (4.16b) yields

$$\frac{\partial S_{xx}}{\partial y} = \frac{\partial^2 u}{\partial x \partial y} \rightarrow \frac{\partial^2 S_{xx}}{\partial y^2} = \frac{\partial^3 u}{\partial x \partial y^2} \tag{4.17a}$$

$$\frac{\partial S_{yy}}{\partial x} = \frac{\partial^2 v}{\partial x \partial y} \rightarrow \frac{\partial^2 S_{yy}}{\partial x^2} = \frac{\partial^3 v}{\partial x^2 \partial y} \tag{4.17b}$$

Now taking partial derivatives of (4.16c) with respect to x, first, and then with respect to y results in

$$\frac{\partial S_{xy}}{\partial x} = \frac{\partial^2 u}{\partial x \partial y} + \frac{\partial^2 v}{\partial x^2} \rightarrow \frac{\partial^2 S_{xy}}{\partial x \partial y} = \frac{\partial^3 u}{\partial x \partial y^2} + \frac{\partial^3 v}{\partial x^2 \partial y} \tag{4.18}$$

Substituting (4.17a) and (4.17b) into right-hand side of (4.18) results in

$$\frac{\partial^2 S_{xy}}{\partial x \partial y} = \frac{\partial^2 S_{xx}}{\partial y^2} + \frac{\partial^2 S_{yy}}{\partial x^2} \rightarrow \frac{\partial^2 S_{xx}}{\partial y^2} + \frac{\partial^2 S_{yy}}{\partial x^2} - \frac{\partial^2 S_{xy}}{\partial x \partial y} = 0 \tag{4.19}$$

which is the sought compatibility equation relating the three components of the strain field. Although (4.19) is only a necessary condition on the strain, its sufficiency can be proved. We leave the detailed proof to cited references in this chapter (e.g., Wallerstein 2002).

4.1.3 Stress–Strain Constitutive Relationships

As mentioned in Sect. 3.3, the stress–strain relationships must be utilized in order to arrive at useful governing equations of motion that can be further utilized in the subsequent controller design and developments. For this, we briefly review the constitutive relationship between stress and strain from mechanics of materials. We refer much of the details to the cited references (e.g., Malvern 1969).

In general, the stress and strain fields can be related using material behavior as:

$$\boldsymbol{\sigma} = \boldsymbol{\sigma}(\mathbf{S}) \tag{4.20}$$

where $\boldsymbol{\sigma}$ and $\mathbf{S}$ denote column matrices of stress and strain components, respectively. While there are many versions of this relationship depending on material nonlinearity, without undue complication we consider a linear relationship, or what is referred to as *Hooke's law*

$$\sigma_{ij} = c_{ijkl} S_{kl}, \quad i, j = 1, 2, 3 \tag{4.21}$$

where c_{ijkl} represents a fourth-order elastic stiffness tensor. As given in Appendix A, for this fourth-order tensor with the range of indices given in (4.21), there are a total of $3^4 = 81$ constants.

Referring the details to the cited references, it can be shown that when taking into account the stress/strain symmetry (see Sect. 4.1.2), the total number of constants reduces to only 36. Moreover, when the strain compatibilities mentioned in Remark 4.1 along with strain energy considerations are taken into account, the total number of constants further reduces to 21. This type of material is the most general material, which is referred to as *anisotropic* (e.g., concrete, glass). Depending on the number of planes of material symmetry, the number of constants can be further reduced to 13 for materials with one plane of symmetry (referred to as

monoclinic materials such as some synthetic composites), and to 9 for materials with two or three planes of symmetry (referred to as *orthotropic* materials such as Barytes and wood). In the case of three planes of symmetry as well as one isotropic plane, the number of constants reduces to only 6. These materials are referred to as *triagonal syngony* materials such as calcite and quartz (SiO_2). When the material's elastic properties are invariant with respect to rotation of any angle about a given axis, the total number reduces to 5. These materials are referred to as *transversely isotropic* material and include, for example, Beryl and piezoelectric materials especially piezoceramics. The materials with the lowest possible number of elastic constants are referred to as *isotropic* materials where the material's properties are symmetric with respect to any rotation or reflection. The number of elastic constants in these materials is only two and most metals are considered to belong to this group.

We refer the details of constitutive strain–stress relations of transversely isotropic materials such as piezoelectrics, which form the basis of this book, to Chap. 6 where physical principles and constitutive models of piezoelectric materials are reviewed. For the sake of demonstration of this strain–stress relationship in this section, however, let's consider a linear isotropic material with only two elastic constants. These elastic constants can be expressed, in the engineering notation, as Young's modulus of elasticity E and Poisson's ratio υ. Hence, (4.21) in this case reduces to (Malvern 1969):

$$\begin{Bmatrix} S_{xx} \\ S_{yy} \\ S_{zz} \\ S_{xy} \\ S_{yz} \\ S_{xz} \end{Bmatrix} = \frac{1}{E} \begin{pmatrix} 1 & -\upsilon & -\upsilon & 0 & 0 & 0 \\ -\upsilon & 1 & -\upsilon & 0 & 0 & 0 \\ -\upsilon & -\upsilon & 1 & 0 & 0 & 0 \\ 0 & 0 & 0 & 2(1+\upsilon) & 0 & 0 \\ 0 & 0 & 0 & 0 & 2(1+\upsilon) & 0 \\ 0 & 0 & 0 & 0 & 0 & 2(1+\upsilon) \end{pmatrix} \begin{Bmatrix} \sigma_{xx} \\ \sigma_{yy} \\ \sigma_{zz} \\ \tau_{xy} \\ \tau_{yz} \\ \tau_{xz} \end{Bmatrix} \tag{4.22}$$

For a plane stress, relationship (4.22) reduces to:

$$\begin{Bmatrix} S_{xx} \\ S_{yy} \\ S_{xy} \end{Bmatrix} = \frac{1}{E} \begin{pmatrix} 1 & -\upsilon & 0 \\ -\upsilon & 1 & 0 \\ 0 & 0 & 2(1+\upsilon) \end{pmatrix} \begin{Bmatrix} \sigma_{xx} \\ \sigma_{yy} \\ \tau_{xy} \end{Bmatrix} \tag{4.23a}$$

$$\begin{Bmatrix} \sigma_{xx} \\ \sigma_{yy} \\ \tau_{xy} \end{Bmatrix} = \frac{E}{1-\nu^2} \begin{pmatrix} 1 & \upsilon & 0 \\ \upsilon & 1 & 0 \\ 0 & 0 & (1-\upsilon)/2 \end{pmatrix} \begin{Bmatrix} S_{xx} \\ S_{yy} \\ S_{xy} \end{Bmatrix} \tag{4.23b}$$

And finally, for a one-dimensional stress–strain field, this relationship reduces to its most simplified version as:

$$S = \frac{\sigma}{E} \tag{4.24}$$

in which all the subscripts have been dropped for simplicity.

Table 4.1 Assignment of compressed notations from tensor form to matrix form

Indices used for tensors *ij* or *kl*	Equivalent compressed notation *p* or *q*
11 or *xx*	1
22 or yy	2
33 or *zz*	3
23 or 32 or yz or *zy*	4
13 or 31 or xz or *zx*	5
12 or 21 or *xy* or *yx*	6

Remark 4.2. As mentioned earlier when taking into account the stress/strain symmetry (see Sect. 4.1.1), the total number of constants reduces to 36. In conventional mechanics, it is typically preferred to write the tensor form of strain–strain relation (4.21) in matrix form. For this, a compressed notation is developed to replace the double indices (e.g., *ij*) to single index (e.g., *p*). Table 4.1 summarizes these abbreviations.

Using these compressed notations, Hooke's law (4.21) is recast in the following more compact form.

$$\sigma_p = c_{pq} S_q, \quad p, q = 1, \ldots, 6 \tag{4.25}$$

4.2 Virtual Work of a Deformable body

So far in this chapter, we have completed the derivations of differential equations governing the equilibrium states of a continuum along with the strain–displacement relationships. These important developments shall now pave the pathway toward the determination of variational terms required in the extended Hamilton's principle (3.52) for a deformable body in 3D. This important process is covered in this section.

Let's consider the deformable body of Fig. 4.2 and described by (4.4) in its equilibrium state. It is now desired to determine the virtual work done on this body by both internal and external forces. Recalling the definitions and procedure discussed in Chap. 3 for calculation of the total virtual work of internal and external forces, one can take the corresponding variations of each equations in (4.4) in their respective directions, integrate over the volume of the continuum and sum them to arrive at the following total virtual work of the deformable body moving in 3D.

$$\begin{aligned}\delta W \triangleq & \int_V \left(\frac{\partial \sigma_{xx}}{\partial x} + \frac{\partial \tau_{xy}}{\partial y} + \frac{\partial \tau_{xz}}{\partial z} + F_x \right) \delta u \, dV + \int_V \left(\frac{\partial \tau_{yx}}{\partial x} + \frac{\partial \sigma_{yy}}{\partial y} \right. \\ & \left. + \frac{\partial \tau_{yz}}{\partial z} + F_y \right) \delta v \, \mathrm{d}V + \int_V \left(\frac{\partial \tau_{zx}}{\partial x} + \frac{\partial \tau_{zy}}{\partial y} + \frac{\partial \sigma_{zz}}{\partial z} + F_z \right) \delta w \, dV = 0\end{aligned} \tag{4.26}$$

where δu, δv, and δw are admissible variations along x, y, and z axes, respectively. It is easy from (4.26) to see the components of both internal (stress components) and external (body force F) works.

Although one can extract the components of both internal and external works from the definition (4.20), the use of this equation in deriving the equations of equilibrium or motion is not very convenient and requires calculation and relating the variations δu, δv, and δw to other variables (e.g., stress or strain components). Using Green's and Divergence theorems (see Appendix A), we can simplify this expression to arrive at a more useful virtual work for the follow-up derivation of the equations of motion.

For brevity, we only show the detailed procedure for x-component in (4.26) and leave the other directions to interested readers. Consequently, we can rewrite the first block in this equation as:

$$\begin{aligned} A &\triangleq \int_V \left(\frac{\partial \sigma_{xx}}{\partial x} + \frac{\partial \tau_{xy}}{\partial y} + \frac{\partial \tau_{xz}}{\partial z} \right) \delta u \, \mathrm{d}V + \int_V F_x \delta u \, \mathrm{d}V \\ &= \int_V \left(\vec{\nabla}^T \cdot \vec{\sigma}_x \right) \delta u \, \mathrm{d}V + \int_V F_x \delta u \, \mathrm{d}V \end{aligned} \tag{4.27}$$

where $\vec{\nabla} = \begin{Bmatrix} \partial/\partial x \\ \partial/\partial y \\ \partial/\partial z \end{Bmatrix}$ and $\vec{\sigma}_x = \begin{Bmatrix} \sigma_{xx} \\ \tau_{xy} \\ \tau_{xz} \end{Bmatrix}$. Using the variational operator property (3.4), we can write:

$$\vec{\nabla}^T \cdot \left(\vec{\sigma}_x \delta u \right) = \delta u \left(\vec{\nabla}^T \cdot \vec{\sigma}_x \right) + \vec{\sigma}_x \cdot \vec{\nabla} \delta u \tag{4.28}$$

Insertion of (4.28) into (4.27) yields

$$A = \int_V \left(\vec{\nabla}^T \cdot \left(\vec{\sigma}_x \delta u \right) \right) \mathrm{d}V - \int_V \left(\vec{\sigma}_x \cdot \left(\vec{\nabla} \delta u \right) \right) \mathrm{d}V + \int_V F_x \delta u \, \mathrm{d}V \tag{4.29}$$

The Divergence theorem (A.8) can now be used to transfer the first integral in (4.29) as:

$$\int_V \left(\vec{\nabla}^T \cdot \left(\vec{\sigma}_x \delta u \right) \right) \mathrm{d}V = \oint_{\partial V} \left(\vec{\sigma}_x \delta u \right) \cdot \mathrm{d}\vec{s} = \oint_{\partial V} \left(\vec{\sigma}_x \delta u \right) \cdot \vec{n} \mathrm{d}s \tag{4.30}$$

where ∂V is the total boundary volume, $\mathrm{d}\vec{s} = \vec{n}\mathrm{d}s$, and $\vec{n}$ is the normal to the surface of the deformable body (see Fig. 4.4) with the following components:

$$\vec{n} = \begin{Bmatrix} l \\ m \\ p \end{Bmatrix} \tag{4.31}$$

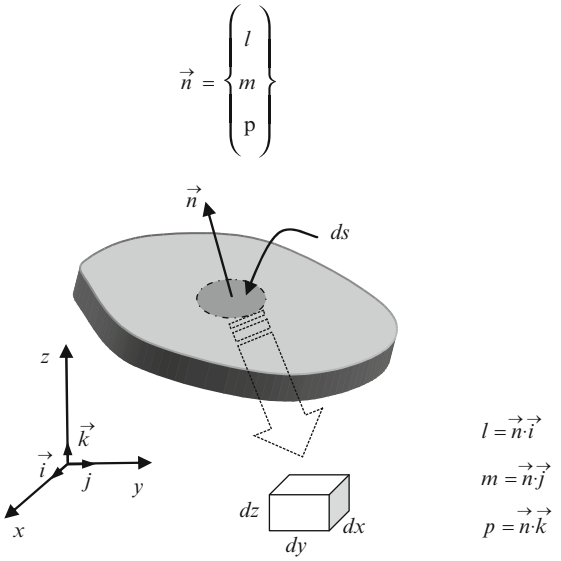

Fig. 4.4 Normal surface vector for a deformable body

Hence, utilizing (4.30) in (4.29) and substituting the result in expression (4.27) yields:

$$A = \oint_{\partial V} \left(\vec{\sigma}_x \cdot \vec{n}\right) \delta u \mathrm{d}s - \int_V \left(\vec{\sigma}_x \cdot \vec{\nabla} \delta u\right) \mathrm{d}V + \int_V F_x \delta u \, \mathrm{d}V \tag{4.32}$$

Following the same procedure on other blocks of (4.26), one can easily show that other terms in this equation can be simplified as:

$$\begin{aligned} B &\triangleq \int_V \left(\frac{\partial \tau_{yx}}{\partial x} + \frac{\partial \sigma_{yy}}{\partial y} + \frac{\partial \tau_{yz}}{\partial z} \right) \delta v \, \mathrm{d}V + \int_V F_y \delta v \, \mathrm{d}V \\ &= \oint_{\partial V} \left(\vec{\sigma}_y \cdot \vec{n}\right) \delta v \mathrm{d}s - \int_V \left(\vec{\sigma}_y \cdot \vec{\nabla} \delta v\right) \mathrm{d}V + \int_V F_y \delta v \, \mathrm{d}V \end{aligned} \tag{4.33}$$

$$\begin{aligned} C &\triangleq \int_V \left(\frac{\partial \tau_{zx}}{\partial x} + \frac{\partial \tau_{zy}}{\partial y} + \frac{\partial \sigma_{zz}}{\partial z} \right) \delta w \, \mathrm{d}V + \int_V F_z \delta w \, \mathrm{d}V \\ &= \oint_{\partial V} \left(\vec{\sigma}_z \cdot \vec{n}\right) \delta w \mathrm{d}s - \int_V \left(\vec{\sigma}_z \cdot \vec{\nabla} \delta w\right) \mathrm{d}V + \int_V F_z \delta w \, \mathrm{d}V \end{aligned} \tag{4.34}$$

where $\vec{\sigma}_y = \begin{Bmatrix} \tau_{yx} \\ \sigma_{yy} \\ \tau_{yz} \end{Bmatrix}$ and $\vec{\sigma}_z = \begin{Bmatrix} \tau_{zx} \\ \tau_{zy} \\ \sigma_{zz} \end{Bmatrix}$.

Let's consider the fact that inner product of stress vectors $\vec{\sigma}_x$, $\vec{\sigma}_y$, and $\vec{\sigma}_z$ with the surface normal vector $\vec{n}$ produces the following forces

$$\begin{aligned}
\vec{\sigma}_x \cdot \vec{n} &= l\sigma_{xx} + m\tau_{xy} + p\tau_{xz} \triangleq P_x, \\
\vec{\sigma}_y \cdot \vec{n} &= l\tau_{yx} + m\sigma_{yy} + p\tau_{yz} \triangleq P_y, \\
\vec{\sigma}_z \cdot \vec{n} &= l\tau_{zx} + m\tau_{zy} + p\sigma_{zz} \triangleq P_z
\end{aligned} \tag{4.35}$$

where P_x, P_y, and P_w are defined as *surface forces* acting on the boundary of the continuum.

So far, these are the results of expanding the first integral of (4.29) and similar terms in other directions. Now expanding the other terms used, i.e., the second integral in (4.29), (4.33) and (4.34), it yields

$$\begin{aligned}
\vec{\sigma}_x \cdot \vec{\nabla}\delta u &= \sigma_{xx}\frac{\partial}{\partial x}\delta u + \tau_{xy}\frac{\partial}{\partial y}\delta u + \tau_{xz}\frac{\partial}{\partial z}\delta u \\
\vec{\sigma}_y \cdot \vec{\nabla}\delta v &= \tau_{yx}\frac{\partial}{\partial x}\delta v + \sigma_{yy}\frac{\partial}{\partial y}\delta v + \tau_{yz}\frac{\partial}{\partial z}\delta v \\
\vec{\sigma}_z \cdot \vec{\nabla}\delta w &= \tau_{zx}\frac{\partial}{\partial x}\delta w + \tau_{zy}\frac{\partial}{\partial y}\delta w + \sigma_{zz}\frac{\partial}{\partial z}\delta w
\end{aligned} \tag{4.36}$$

Now utilizing the strain–displacement relationships (4.15) and taking into account the first property of variational operator δ given by (3.4), i.e.,

$$\delta\left(\frac{\partial(.)}{\partial p}\right) = \frac{\partial}{\partial p}\delta(.),$$

the relationships given in (4.36) reduce to:

$$\begin{aligned}
\sigma_{xx}\frac{\partial}{\partial x}\delta u + \tau_{xy}\frac{\partial}{\partial y}\delta u + \tau_{xz}\frac{\partial}{\partial z}\delta u &= \sigma_{xx}\delta\left(S_{xx}\right) + \tau_{xy}\delta\left(\frac{\partial u}{\partial y}\right) + \tau_{xz}\delta\left(\frac{\partial u}{\partial z}\right) \\
\tau_{yx}\frac{\partial}{\partial x}\delta v + \sigma_{yy}\frac{\partial}{\partial y}\delta v + \tau_{yz}\frac{\partial}{\partial z}\delta v &= \tau_{yx}\delta\left(\frac{\partial v}{\partial x}\right) + \sigma_{yy}\delta\left(S_{yy}\right) + \tau_{yz}\delta\left(\frac{\partial v}{\partial z}\right) \\
\tau_{zx}\frac{\partial}{\partial x}\delta w + \tau_{zy}\frac{\partial}{\partial y}\delta w + \sigma_{zz}\frac{\partial}{\partial z}\delta w &= \tau_{zx}\delta\left(\frac{\partial w}{\partial x}\right) + \tau_{zy}\delta\left(\frac{\partial w}{\partial y}\right) + \sigma_{zz}\delta\left(S_{zz}\right)
\end{aligned} \tag{4.37}$$

Taking into account the symmetry property of shear stresses (i.e., $\tau_{ij} = \tau_{ji}$) when substituting relations (4.37) into expressions (4.29), (4.33), and (4.34), as well as substituting findings of (4.35) into (4.29), (4.33), and (4.34) and summing all the terms and collecting similar terms, it can be easily shown that the virtual work (4.26) can be recast in the following more suitable form:

$$\begin{aligned}\delta W = &\left[-\int_V \left\{\sigma_{xx}\delta\left(S_{xx}\right) + \sigma_{yy}\left(\delta S_{yy}\right) + \sigma_{zz}\left(\delta S_{zz}\right) + \tau_{xy}\left(\delta S_{xy}\right)\right.\right. \\ &\left.\left. + \tau_{xz}\left(\delta S_{xz}\right) + \tau_{yz}\left(\delta S_{yz}\right)\right\} \mathrm{d}V \right] + \left[\int_V \left(F_x\delta u + F_y\delta v + F_z\delta w\right) \mathrm{d}V \right. \\ &\left. + \oint_{\partial \mathrm{V}} \left(P_x\delta u + P_y\delta v + P_z\delta w\right) \mathrm{d}s \right] \\ &= \delta W^{int} + \delta W^{\mathrm{ext}} \end{aligned} \tag{4.38}$$

The results obtained in (4.38) are very important and useful in the derivation of equations of motion of a deformable body such as the very vibration-control systems considered here. It must be noted that since the total work presented in this expression is, indeed, a virtual work, the distributions of internal and external (both body and surface forces) remain unchanged by the resulting virtual displacements (the first principle assumption in virtual work theory).

As defined in (4.38), the first integral (inside first square bracket) represents the total internal virtual work δW^{int}, while the remaining two integrals (inside second square brackets) represent the virtual work done by external body and surface forces, so they are collected into one single virtual work δW^{ext}. Hence, (4.38) can be rewritten as:

$$\delta W = \delta W^{\mathrm{int}} + \delta W^{\mathrm{ext}} = 0 \rightarrow -\delta W^{\mathrm{int}} \triangleq \delta U = \delta W^{\mathrm{ext}} \tag{4.39}$$

where U is defined as the potential energy of the body. Equation (4.39) reveals an important conclusion, i.e., for a deformable body to be in equilibrium, the total internal virtual work must balance the total external virtual work for every admissible virtual displacement.

Although the results presented in this section and the preceding section are for the deformable body at equilibrium state, one must note that the total internal virtual work done on the body will remain unchanged regardless of whether the deformable body is at equilibrium or in motion. In fact, as mentioned at the end of Chap. 3, this important internal work or energy is what we were looking for in order to complete the process of derivation of the equations of motion for a deformable body using Hamilton's principle. Hence, to complete this task, recall the definition of potential energy (3.45), then the total internal virtual work in (4.38) can be expressed as:

$$\begin{aligned} -\delta W^{\mathrm{int}} \triangleq \delta U \; = &\int_V \left\{\sigma_{xx}\delta\left(S_{xx}\right) + \sigma_{yy}\left(\delta S_{yy}\right) + \sigma_{zz}\left(\delta S_{zz}\right) + \tau_{xy}\left(\delta S_{xy}\right)\right. \\ &\left. + \tau_{xz}\left(\delta S_{xz}\right) + \tau_{yz}\left(\delta S_{yz}\right)\right\} \mathrm{d}V \end{aligned} \tag{4.40}$$

Equation (4.40) is the most general form of potential (strain) energy of a deformable body in 3D, which will be used extensively throughout this book. Similarly, the total potential energy (4.40) can be rewritten in its compressed notation as:

$$\delta U = \int_V \sigma_p \delta S_p \mathrm{d}V, \quad p = 1, \ldots, 6 \tag{4.41}$$

Remark 4.3. It must be noted that in the derivation of (4.38) or consequently (4.40), no assumptions or approximations have been made regarding material stress–strain constitutive relationships, or small- or large-displacement motions.

We have now completed all the steps mentioned in Chap. 3 for deriving the equations of motion of a general deformable body in its most general configuration. That is, for kinetic energy we shall utilize standard dynamics of deformable bodies to arrive at the expressions for this energy. It can be shown that depending on the nature of the problem at hand and the level of complexity of motion, this task can become tedious and extensive. Although these complicated dynamics do not form the fundamental contributions of this book, we provide a brief overview of systems undergoing complex motions such as coupled bending-torsion and/or vibrating flexible systems subjected to general rotation. These are given in Part III of this book. On the calculation of potential energy, we are now completely equipped with the necessary tools as expression (4.40) or (4.41) with the associated stress–strain relationship (4.20). As a result, the required Lagrangian L used in the extended Hamilton's principle (3.52) can be determined, and consequently, the governing equations of motion and associated boundary conditions can be derived by expanding the variations involved with this principle. These steps are better illustrated through numerous examples from vibration of continuous systems as presented next.

4.3 Illustrative Examples from Vibrations of Continuous Systems

In this section, several important examples from vibration of continuous systems are presented to demonstrate the effectiveness of the modeling framework described in the preceding subsections. As the subject of vibration of continuous systems could be extensive and one could provide endless discussions and treatment, we prefer not to go over this route. Instead, a number of important distributed-parameters systems are selectively targeted in this section that form the building blocks of vibration-control systems discussed later in the book. For this, the following three classes of systems are considered; a) bars as representatives of many piezoelectric stack and axial actuators and sensors, b) flexible beams as models of piezoelectric patch or bender-type actuators and sensors, and c) plates as enhanced models of flexible beams where Poisson's effect cannot be neglected (this is the case in many piezoelectric micro- and nano-cantilevers that will be discussed in Chap. 11).

4.3.1 Longitudinal Vibration of Bars

A bar is a mechanical element that is typically under axial (compression or tension) loads and nothing else. To study this element, consider a bar of mass per unit length $\rho(x)$[3] and variable area $A(x)$ under external axial load per unit length $P(x,t)$, see Fig. 4.5. To quantify the longitudinal vibrations of this structure, we associate displacement $u(x,t)$ to each element in the bar at the arbitrary location x (see Fig. 4.5).

Since this is a 1D strain–stress field, (4.16a) and (4.24) can be used to arrive at:

$$S_{xx} = \frac{\partial u}{\partial x}, \quad \sigma_{xx} = E S_{xx} = E \frac{\partial u}{\partial x} \tag{4.42}$$

On the other hand, employing the general expression for potential energy (4.40) and taking into account that the only nonzero term in this expression is the first term, the potential energy for this system can be expressed as:

$$\begin{aligned} \delta U &= \int_V \sigma_{xx} \delta\left(S_{xx}\right) \mathrm{d}V = \int_x E \varepsilon_{xx} \delta\left(S_{xx}\right) A(x) \mathrm{d}x = \int_0^L E A(x) S_{xx} \delta\left(S_{xx}\right) \mathrm{d}x \\ &= \int_0^L \left\{ E A(x) \frac{\partial u(x,t)}{\partial x} \delta\left(\frac{\partial u(x,t)}{\partial x}\right) \right\} \mathrm{d}x \end{aligned} \tag{4.43}$$

It can be easily seen that how convenient and thorough is the process adopted here for the derivation of the potential energy. The kinetic energy due to axial vibration of the same element can also be determined as:

$$T = \tfrac{1}{2} \int_0^L \left\{ \rho(x) \left(\frac{\partial u(x,t)}{\partial t}\right)^2 \right\} \mathrm{d}x \tag{4.44}$$

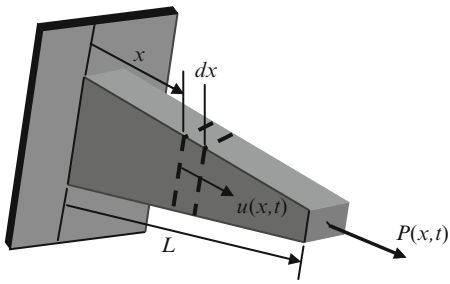

Fig. 4.5 A general bar in longitudinal vibrations

[3] The (volumetric) density of the bar is then expressed as $m(x) = \rho(x)/A(x)$.

with its variation given as:

$$\delta T = \int_0^L \left\{ \rho(x) \frac{\partial u(x,t)}{\partial t} \delta \left(\frac{\partial u(x,t)}{\partial t} \right) \right\} \mathrm{d}x \tag{4.45}$$

Now, the extended Hamilton's principle (3.52)

$$\int_{t_1}^{t_2} \left(\delta L + \delta W^{\text{ext}} \right) \mathrm{d}t = 0 \tag{4.46}$$

can be expanded to simplify different terms in the integration and obtain the governing equations of motion. Notice in (4.46), δW^{ext} represents the virtual work generated by external force $P(x,t)$ and given by:

$$\delta W^{\text{ext}} = \int_0^L (P(x,t)\delta u(x,t)) \mathrm{d}x \tag{4.47}$$

Now that all the terms in the Lagrangian expression have been identified, we start with expanding this expression for the work of external forces. For this, we substitute expressions (4.43), (4.45), and (4.47) into Hamilton's principle (4.46). This yields:

$$\int_{t_1}^{t_2} \left[\int_0^L \left\{ \rho(x) \frac{\partial u(x,t)}{\partial t} \delta \left(\frac{\partial u(x,t)}{\partial t} \right) \right\} \mathrm{d}x - \int_0^L \left\{ EA(x) \frac{\partial u(x,t)}{\partial x} \delta \left(\frac{\partial u(x,t)}{\partial x} \right) \right\} \mathrm{d}x + \int_0^L (P(x,t)\delta u(x,t)) \mathrm{d}x \right] \mathrm{d}t = 0 \tag{4.48}$$

Taking the first term in expression (4.48), we interchange temporal and spatial integrations to arrive at:

$$\begin{aligned} C &\triangleq \int_{t_1}^{t_2} \left[\int_0^L \left\{ \rho(x) \frac{\partial u(x,t)}{\partial t} \delta \left(\frac{\partial u(x,t)}{\partial t} \right) \right\} \mathrm{d}x \right] \mathrm{d}t \\ &= \int_0^L \left\{ \int_{t_1}^{t_2} \left[\rho(x) \frac{\partial u(x,t)}{\partial t} \delta \left(\frac{\partial u(x,t)}{\partial t} \right) \right] \mathrm{d}t \right\} \mathrm{d}x = \int_0^L \{C_1\} \mathrm{d}x \end{aligned} \tag{4.49}$$

Now the integrant of spatial integration (4.49) can be further simplified using variational property (3.4) and integral-by-part (A.3) to arrive at:

$$C_1 = \int_{t_1}^{t_2} \rho(x) \frac{\partial u(x,t)}{\partial t} \frac{\partial}{\partial t} (\delta u(x,t))\, \mathrm{d}t = \rho(x) \frac{\partial u(x,t)}{\partial t} \delta u(x,t) \Big|_{t_1}^{t_2} - \int_{t_1}^{t_2} \rho(x) \frac{\partial}{\partial t} \left(\frac{\partial u(x,t)}{\partial t} \right) \delta u(x,t) \mathrm{d}t \tag{4.50}$$

Considering the fact that $\delta u(x,t_1) = \delta u(x,t_2) = 0$ and using abbreviated notions, (4.50) reduces to:

$$C_1 = -\int_{t_1}^{t_2} \rho(x) \frac{\partial^2 u}{\partial t^2} \delta u \mathrm{d}t \tag{4.51}$$

Similarly, the second term in (4.48) can be rewritten as:

$$B = \int_{t_1}^{t_2} \left[\int_0^L \left\{ EA(x) \frac{\partial u(x,t)}{\partial x} \delta \left(\frac{\partial u(x,t)}{\partial x} \right) \right\} \mathrm{d}x \right] \mathrm{d}t = \int_{t_1}^{t_2} [B_1] \mathrm{d}t \Rightarrow$$

$$B_1 = \int_0^L \left\{ EA(x) \frac{\partial u(x,t)}{\partial x} \frac{\partial}{\partial x} (\delta u(x,t)) \right\} \mathrm{d}x \tag{4.52}$$

Upon implementation of the integral-by-part (A.3) to (4.52) it reduces to:

$$B_1 = EA(x) \frac{\partial u(x,t)}{\partial x} \delta u(x,t) \Big|_0^L - \int_0^L \frac{\partial}{\partial x} \left(EA(x) \frac{\partial u(x,t)}{\partial x} \right) \delta u(x,t) \mathrm{d}x \tag{4.53}$$

Substituting (4.51) and (4.53) into (4.48), collecting and sorting different terms we get:

$$\int_{t_1}^{t_2} \left[\int_0^L \left\{ \frac{\partial}{\partial x} \left(EA(x) \frac{\partial u(x,t)}{\partial x} \right) - \rho(x) \frac{\partial^2 u(x,t)}{\partial t^2} + P(x,t) \right\} \delta u(x,t) \mathrm{d}x - \left(EA(x) \frac{\partial u(x,t)}{\partial x} \right) \delta u(x,t) \Big|_0^L \right] \mathrm{d}t = 0 \tag{4.54}$$

Similar to the argument we made in Chap. 3 in (3.15) or (3.20), for (4.54) to vanish, the integrant must vanish, and for the integrant to vanish we must have:

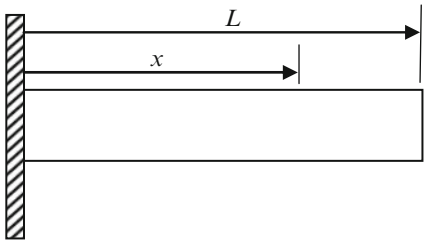

Fig. 4.6 A fixed-free uniform bar under axial vibrations

$$\rho(x)\frac{\partial^2 u(x,t)}{\partial t^2} - \frac{\partial}{\partial x}\left(EA(x)\frac{\partial u(x,t)}{\partial x}\right) = P(x,t) \tag{4.55a}$$

$$\left(EA(x)\frac{\partial u(x,t)}{\partial x}\right)\delta u(x,t)\Big|_0^L = 0 \tag{4.55b}$$

where we have used the fact that $\delta u(x,t)$ is arbitrary in the interval $0 < x < L$. Equations (4.55a) and (4.55b), respectively, represent the PDE governing the axial vibrations of a nonuniform bar along with the associated boundary conditions.

Example 4.2. Free vibration of a fixed-free uniform bar.

Consider the free vibration of a uniform bar shown in Fig. 4.6.

The governing equation (4.55a) can be simplified for this particular configuration as:

$$EA\frac{\partial^2 u(x,t)}{\partial x^2} - \rho\frac{\partial^2 u(x,t)}{\partial t^2} = 0 \;\rightarrow\; u_{xx}(x,t) = \frac{1}{c^2}u_{tt}(x,t) \tag{4.56}$$

which is in the form of standard wave equation with the wave velocity $c^2 = E/m$ (recall that $\rho = mA$). The subscripts in (4.56) represent partial derivatives with respect to the arguments.

Consequently, the boundary conditions (4.55b) can be simplified for this particular configuration as:

$$EA\left(\frac{\partial u(x,t)}{\partial x}\right)\delta u(x,t)\Big|_0^L = 0 \;\rightarrow\; EA\left(\frac{\partial u(L,t)}{\partial x}\right)\delta u(L,t) - A\left(\frac{\partial u(0,t)}{\partial x}\right)\delta u(0,t) = 0 \tag{4.57}$$

With the given geometry, the displacement at the fixed end is zero, i.e., $u(0,t) = 0$ (and hence, $\delta u(0,t) = 0$). Substituting this into (4.57) results in:

$$EA\left(\frac{\partial u(L,t)}{\partial x}\right)\delta u(L,t) = 0 \tag{4.58}$$

Since $EA = \text{constant} \neq 0$ and the fact that the tip displacement $u(L,t)$ can take any arbitrary value, it yields $\delta u(L,t) \neq 0$. Taking these into consideration in (4.58),

we get

$$\frac{\partial u(L,t)}{\partial x} = 0 \tag{4.59}$$

The boundary condition (4.59) physically makes sense as there is no stress or consequently strain at the free end. That is,

$$\sigma_{xx}(L,t) = 0 \;\rightarrow\; \sigma_{xx}(L,t) = ES_{xx}(L,t) = E\frac{\partial u(L,t)}{\partial x} = 0 \rightarrow \frac{\partial u(L,t)}{\partial x} = 0 \tag{4.60}$$

Hence, the governing equations and associated boundary conditions for this problem become:

$$u_{xx}(x,t) = \frac{1}{c^2}u_{tt}(x,t),\; u(0,t) = 0 \text{ and } \frac{\partial u(L,t)}{\partial x} = 0 \tag{4.61}$$

4.3.2 Transverse Vibration of Beams

A beam is a mechanical element that can withstand transverse and shear forces, and hence bending moments, as well as axial forces. Beams are 1D model of structures in which one dimension is much longer than others. Examples of beam elements could include aircraft wings, turbine and rotor blades, robotic manipulators, and many more. Recent advances in MEMS and NEMS have made the beam-like systems as the most frequently used and mass produced elements. These examples include microbeams for biological sensors, vibrating beam microgyroscopes, and cantilever beam resonators. As mentioned earlier, we will overview some of these MEMS and NEMS examples with their fast-growing applications in today's technological advances in Chaps. 10–12.

Beam Theories: Depending on the level of modeling accuracy, the beam theories can be divided into several groups some of which include: (1) Euler–Bernoulli theory, (2) shear–deformable or Timoshenko theory, and (3) 3D beam theory (Nayfeh and Pai 2004). Without undue complication, we will heavily concentrate on the first theory and only mention the second and the third theories with most of their details for advanced beam systems considered in Part III. More specifically, Chap. 11 will cover the third theory for microbeams where both in-plane and out-of-plane motions become equally important, and hence the effects of 3D stresses must be fully considered.

Euler-Beam Theory: In this, although simplest but most commonly used, beam theory, only axial strain is considered. It is also assumed that the beam cross-section remains undistorted after the deformation, i.e., the effect of shear deformation as well as the warping of the cross-section are ignored (see Fig. 4.7). A measure of validity of these assumptions is the slenderness of the beam. Practically speaking and as a rule of thumb, when the largest dimension of the cross-section to beam length is less than 1/10, these assumptions are mostly valid. In order to derive the governing equations of motion of a beam element under these assumptions, we

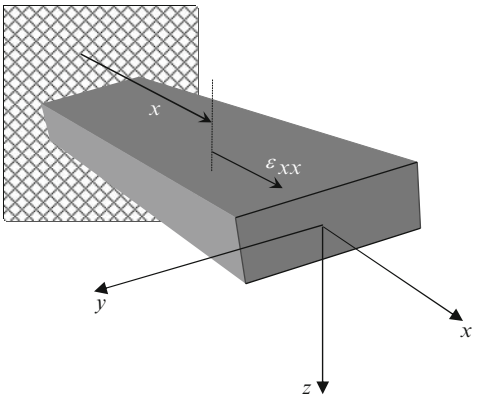

Fig. 4.7 A beam element under only axial strain (Euler–Bernoulli beam theory)

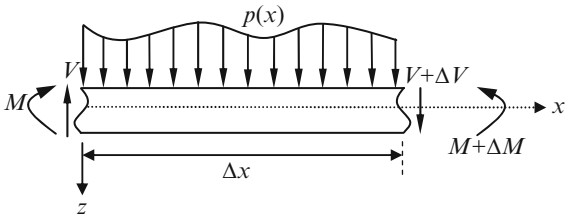

Fig. 4.8 A segment of beam under general loading when considering transverse displacement along the z-axis

briefly review, next, the beam theory from classical strength of materials (Beer and Johnson 1981).

A Brief Review of Simple Beam Theory: Before we can develop the equations of motion for a beam element, it is necessary to review some of the basic materials from mechanics of materials in transverse displacement and strain relationship. For this, let's consider the segment of the beam in equilibrium state as shown in Fig. 4.8. $p(x)$ is a distributed load per unit length, V is the internal shear force, and M is the internal bending moment all at distance x measured from the origin (not shown in Fig. 4.8). It is assumed that the cross-section of the beam is symmetric in xy plane.

From the equilibrium of this segment in z direction as well as the moments about the right edge of the segment as $\Delta x \to 0$, we get:

$$\frac{\mathrm{d}\,V}{\mathrm{d}x} = -p(x), \ \frac{\mathrm{d}M}{\mathrm{d}x} = V \tag{4.62}$$

Now, considering the beam under transverse vibrations and taking into account the Euler–Bernoulli beam assumptions, the total axial displacement induced by bending of the beam based on the kinematics shown in Fig. 4.9 can be expressed as:

$$u = -z\sin(\phi) \tag{4.63}$$

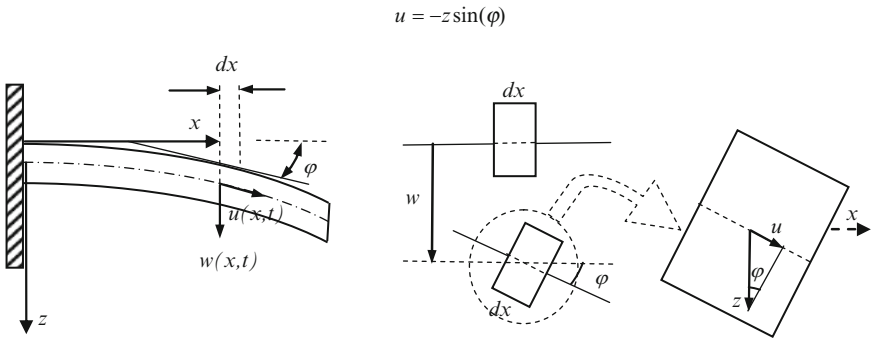

Fig. 4.9 Kinematics of deformation of an Euler–Bernoulli beam

Remark 4.4. Notice the axial displacement u in (4.63) is the so-called bending-induced axial displacement and does not include the external elongation of the beam along the x-axis. That is, we are assuming the beam is extensible, but the amount of external axial extension is negligible compared to transverse displacement w. This is a very important fact that must be fully understood. We provide, later in Part III (Chap. 11), cases where this external elongation is comparable to transverse vibration, and hence, both axial and transverse displacements must be considered as independent DOF for the beam.

For small vibrations assumption, one can relate the slope φ to the transverse displacement w as:

$$\sin(\varphi) \approx \varphi = \frac{\partial w}{\partial x} \tag{4.64}$$

Describing the displacement field as u, $v = 0$, and w, one can calculate the 2D strain components (4.16) for this beam as:

$$S_{xx} = \frac{\partial u}{\partial x} = \frac{\partial}{\partial x}(-z\varphi) = \frac{\partial}{\partial x}\left(-z\frac{\partial w}{\partial x}\right) = -z\frac{\partial^2 w}{\partial x^2} \tag{4.65a}$$

$$S_{yy} = \frac{\partial v}{\partial x} = 0,\ S_{xy} = \frac{\partial u}{\partial y} + \frac{\partial v}{\partial x} = 0 \tag{4.65b}$$

Once the strain–displacement relationships for the beam have been established, we are ready to proceed with calculation of energy terms for this system for the derivation of the equations of motion. However, we can use the results (4.65a) to calculate the internal bending moment M to normal stress (and consequently to strain and deflection), which can be used later in many bender-type piezoelectric sensors and actuators modeling described in Chap. 8. For this and using the schematic of Fig. 4.10, we can write:

$$M = \int_A z\sigma_{xx}dA = \int_A zES_{xx}dA = \int_A zE\left(-z\frac{\partial^2 w}{\partial x^2}\right)dA = -EI\frac{\partial^2 w}{\partial x^2} \tag{4.66}$$

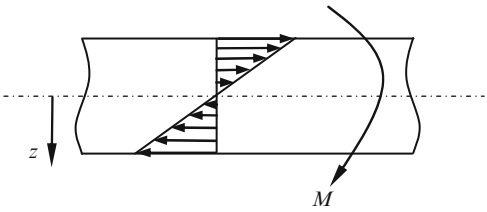

Fig. 4.10 Schematic of internal moment and normal stress distribution

where

$$I \triangleq \int_A z^2 dA \tag{4.67}$$

Substituting the results of (4.65a) and (4.66) into the stress–strain relationship (4.24), we can relate the normal stress at distance z from the beam neutral axis (see Fig. 4.10) to this internal bending moment as:

$$\sigma_{xx} = E S_{xx} = E\left(-z\frac{\partial^2 w}{\partial x^2}\right) = \frac{Mz}{I} \tag{4.68}$$

Derivation of the Equations of Motion for Beams: Now that we are equipped with basic preliminaries and background from mechanics of materials, we can express the kinetic and potential energies for the beams. For kinetic energy and based on the Euler–Bernoulli assumptions, this energy due to the only motion of the beam (i.e., transverse deflection) can be written as:

$$T = \tfrac{1}{2}\int_0^L \rho(x)\left(\frac{\partial w(x,t)}{\partial t}\right)^2 dx \tag{4.69}$$

where $\rho(x)$ is the beam linear density (mass per unit length). Notice that other kinetic energies such as the kinetic energy due to rotary inertia and or external axial deformation are ignored when compared with (4.69).

Subsequently, the strain energy due to normal stress–strain can be determined as (see (4.40)):

$$\begin{aligned}\delta U &= \int_V \sigma_{xx}\delta\left(S_{xx}\right)\mathrm{d}V = \int_V E S_{xx}\delta\left(S_{xx}\right)\mathrm{d}V = \tfrac{1}{2}\int_V E\delta\left(S_{xx}\right)^2\mathrm{d}V \\ &= \tfrac{1}{2}\delta\int_V E\left(S_{xx}\right)^2\mathrm{d}V\end{aligned} \tag{4.70}$$

Now substituting (4.65a) into (4.70) and considering $\mathrm{d}V = \mathrm{d}A\ \mathrm{d}x$, (4.70) can be simplified as:

$$\delta U = \tfrac{1}{2}\delta \int_V E\left(-z\frac{\partial^2 w}{\partial x^2}\right)^2 \mathrm{d}V = \tfrac{1}{2}\delta \int_0^L E\left(\int_A z^2 \mathrm{d}A\right)\left(\frac{\partial^2 w}{\partial x^2}\right)^2 \mathrm{d}x$$
$$= \tfrac{1}{2}\delta \int_0^L EI(x)\left(\frac{\partial^2 w(x,t)}{\partial x^2}\right)^2 \mathrm{d}x \tag{4.71}$$

where $I(x)$ is the moment of inertia and defined as:

$$I(x) = \int_A z^2 dA \tag{4.72}$$

Assuming also that distributed load $P(x,t)$ is acting on the beam, its virtual work can be written as:

$$\delta W^{\text{ext}} = \int_0^L P(x,t)\delta w(x,t)\mathrm{d}x \tag{4.73}$$

Similar to Sect 4.3.1, by substituting energy terms (4.69) and (4.71) along with the virtual work of external force (4.73) into Hamilton's principle (3.52), we obtain:

$$\int_{t_1}^{t_2}\left[\int_0^L \left\{\rho(x)\frac{\partial w(x,t)}{\partial t}\delta\left(\frac{\partial w(x,t)}{\partial t}\right)\right\}\mathrm{d}x - \int_0^L \left\{EI(x)\frac{\partial^2 w(x,t)}{\partial x^2}\delta\left(\frac{\partial^2 w(x,t)}{\partial x^2}\right)\right\}\mathrm{d}x\right.$$
$$\left. + \int_0^L (P(x,t)\delta w(x,t))\mathrm{d}x\right]\mathrm{d}t = 0 \tag{4.74}$$

The first term in (4.74) is similar to the first term in axial vibrations of bar (4.48) and the same procedures as in (4.49–4.51) can be followed to arrive at:

$$C = \int_{t_1}^{t_2}\left[\int_0^L \left\{\rho(x)\frac{\partial w(x,t)}{\partial t}\delta\left(\frac{\partial w(x,t)}{\partial t}\right)\right\}\mathrm{d}x\right]\mathrm{d}t$$
$$= -\int_{t_1}^{t_2}\left[\int_0^L \left\{\rho(x)\frac{\partial^2 w(x,t)}{\partial t^2}\delta w(x,t)\right\}\mathrm{d}x\right]\mathrm{d}t \tag{4.75}$$

For the second term in (4.74), we again adopt the same procedure as in axial vibration of bars but implementing the integral-by-part twice. Consequently, this term can be rewritten as:

$$B = \int_{t_1}^{t_2} \left[\int_0^L \left\{ EI(x) \frac{\partial^2 w(x,t)}{\partial x^2} \delta \left(\frac{\partial^2 w(x,t)}{\partial x^2} \right) \right\} \mathrm{d}x \right] \mathrm{d}t$$

$$= \int_{t_1}^{t_2} \left[\int_0^L \left\{ EI(x) \frac{\partial^2 w(x,t)}{\partial x^2} \frac{\partial}{\partial x} \left[\delta \left(\frac{\partial w(x,t)}{\partial x} \right) \right] \right\} \mathrm{d}x \right] \mathrm{d}t = \int_{t_1}^{t_2} [B_1] \mathrm{d}t \tag{4.76}$$

And then,

$$B_1 = EI(x) \frac{\partial^2 w}{\partial x^2} \delta \left(\frac{\partial w}{\partial x} \right) \Big|_0^L - \int_0^L \left\{ \frac{\partial}{\partial x} \left(EI(x) \frac{\partial^2 w}{\partial x^2} \right) \delta \left(\frac{\partial w}{\partial x} \right) \right\} \mathrm{d}x \tag{4.77}$$

Implementing another integral-by-part on the second term in (4.77) results in:

$$B_2 = \int_0^L \left\{ \frac{\partial}{\partial x} \left(EI(x) \frac{\partial^2 w}{\partial x^2} \right) \delta \left(\frac{\partial w}{\partial x} \right) \right\} \mathrm{d}x = \int_0^L \left\{ \frac{\partial}{\partial x} \left(EI(x) \frac{\partial^2 w}{\partial x^2} \right) \frac{\partial}{\partial x} (\delta w) \right\} \mathrm{d}x$$

$$= \frac{\partial}{\partial x} \left(EI(x) \frac{\partial^2 w}{\partial x^2} \right) \delta w \Big|_0^L - \int_0^L \left\{ \frac{\partial^2}{\partial x^2} \left(EI(x) \frac{\partial^2 w}{\partial x^2} \right) \delta w \right\} \mathrm{d}x \tag{4.78}$$

Substituting expressions (4.73) and (4.75–4.78) into the Hamilton principle (4.74), we get:

$$\int_{t_1}^{t_2} \left[\int_0^L \left\{ -\rho(x) \frac{\partial^2 w(x,t)}{\partial t^2} - \frac{\partial^2}{\partial x^2} \left(EI(x) \frac{\partial^2 w(x,t)}{\partial x^2} \right) + P(x,t) \right\} \mathrm{d}x \delta w(x,t) \right.$$

$$\left. - EI(x) \frac{\partial^2 w(x,t)}{\partial x^2} \delta \left(\frac{\partial w(x,t)}{\partial x} \right) \Big|_0^L + \frac{\partial}{\partial x} \left(EI(x) \frac{\partial^2 w(x,t)}{\partial x^2} \right) \delta w(x,t) \Big|_0^L \right] \mathrm{d}t = 0 \tag{4.79}$$

Similar to (4.54) for axial vibration of bars, for (4.79) to vanish for any arbitrary value of $\delta w(x,t)$, one must have:

$$\rho(x) \frac{\partial^2 w(x,t)}{\partial t^2} + \frac{\partial^2}{\partial x^2} \left(EI(x) \frac{\partial^2 w(x,t)}{\partial x^2} \right) = P(x,t) \tag{4.80}$$

$$\left[EI(x) \frac{\partial^2 w(x,t)}{\partial x^2} \right] \delta \left(\frac{\partial w(x,t)}{\partial x} \right) \Big|_0^L = 0 \tag{4.81}$$

$$\left[\frac{\partial}{\partial x} \left(EI(x) \frac{\partial^2 w(x,t)}{\partial x^2} \right) \right] \delta w(x,t) \Big|_0^L = 0 \tag{4.82}$$

Remark 4.5. Equations (4.81) and (4.82) *mathematically* represent a total of eight equations (four equations at $x = 0$ and four equations at $x = L$) for any arbitrary values of $\delta w(0,t)$, $\delta w(L,t)$, $\delta w_x(0,t)$, and $\delta w_x(L,t)$. However, in order for the physical system at hand to have realistic, yet nonconflicting constraints, *either* displacement/slope *or* shear force/bending moment can be prescribed. In other words, in (4.81) and (4.82) either the term in the square brackets or the variations must vanish at each end of the beam, but not both simultaneously. As seen from (4.81), the term in the bracket represents the bending moment (see (4.66)), while the variation of the argument represents the slope at that end. Hence, either bending moment or slope can be prescribed at any given end of the beam. Similarly, the term in the bracket in (4.82) represents shear force (see the combination of (4.62) and (4.66)), while the variation of the argument represents the deflection. Hence, either shear force or deflection at any given end of the beam can be prescribed. As a results, only four boundary conditions can be prescribed for the beam, which are to be associated with the fourth-order PDE of (4.80).

The boundary conditions associated with geometry such as displacement and slope are referred to as *geometrical* or *essential* boundary conditions, while the ones related to forces and moments are so-called *natural* or *dynamic* boundary conditions. It is clear the former boundary conditions appear as either the transverse displacement or its first derivative, while the latter boundary conditions are related to second (for moments) or third (for forces) derivatives of the transverse displacement. This is an important observation that will be more generalized in the next section. The following example case studies will better demonstrate these observations.

Example 4.3. Conventional boundary conditions for uniform beams in transverse vibrations.

Consider the geometries shown in Fig. 4.11 for a uniform beam (i.e., $EI(x) = EI$, $\rho(x) = \rho$) and express the boundary conditions at each end using (4.81) and (4.82).

(a) *Cantilever or Clamped End:* A clamped or fixed end is defined as the boundary condition where no displacement or rotation can take place for all time. Hence, for Fig. 4.11a, one can simplify (4.81) and (4.82) to arrive at:

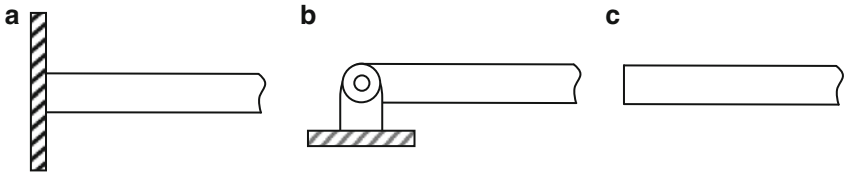

Fig. 4.11 Different boundary conditions for a uniform beam under transverse vibration $w(x,t)$; (**a**) cantilever or clamped end, (**b**) hinged end and (**c**) free end

$$w(0,t) = 0,\ \frac{\partial w(0,t)}{\partial x} = \phi(0,t) = 0^4 \tag{4.83}$$

(b) *Hinged End:* A hinged end does not allow displacement, and cannot withstand any bending moment and hence permits rotation. Similar to case (a), (4.81) and (4.82) can be simplified to:

$$w(0,t) = 0,\ EI\frac{\partial^2 w(0,t)}{\partial x^2} = M(0,t) = 0, \tag{4.84}$$

(c) *Free End:* A free end does not have resistance against either bending moment or shear force; hence, (4.81) and (4.82) reduce to:

$$\begin{aligned} M(0,t) &= EI\frac{\partial^2 w(0,t)}{\partial x^2} = 0 \ \rightarrow\ \frac{\partial^2 w(0,t)}{\partial x^2} = 0 \\ V(0,t) &= \frac{\partial}{\partial x}\left(EI\frac{\partial^2 w(x,t)}{\partial x^2}\right)\Big|_{x=0} = 0 \ \rightarrow\ \frac{\partial^3 w(0,t)}{\partial x^3}0, \end{aligned} \tag{4.85}$$

Remark 4.6. The boundary conditions considered in Example 4.3 are referred to as *conventional* boundary conditions. Any combination of these boundary conditions could be used to make beams with different configurations. We will also review, later in this chapter, some of the *unconventional* boundary conditions that find applications in many beam-like systems such as beams with tip mass, spring or damper element.

Remark 4.7. Although we have derived the equations of motion of thin beams for a relatively general case, we have not included many effects and issues. As these will require extensive discussions and may disturb the focus of the book, we prefer not to add any additional materials and refer to cited references and textbooks. Although these additional considerations are not discussed here, they are worth being mentioned. These extensions and effects could include: (1) shear-deformable beam theory or the effect of beam cross-sectional distortion, (2) the effect of shear warping, (3) rotary inertia of the kinetic energy due to beam cross-sectional rotation, (4) beams with initial curves, (5) effects of thermal strain in both straight and curved beams, (6) thin-walled beams, (7) effects of geometrical nonlinearities, (8) inextensible beams, and finally (9) combined motions such as coupled bending/torsion, bending/axial and bending/axial/torsion motions.

4.3.3 Transverse Vibration of Plates

Plates are the 2D extension of beams and have many applications in structural engineering and mechanics. Such extension in dimension of the problem is in line with

[4] Notice the short notation $\partial w(x_p,t)/\partial x$ used here, which is meant to imply $\left.\frac{\partial w(x,t)}{\partial x}\right|_{x=x_p}$.

our interests in this book in micro- and nanoscale piezoelectric sensors and actuators. That is, as we move from macroscale to micro- and nanoscale media, the effect of vibration of other dimensions that are typically ignored in macroscale becomes important. This is referred to as Poisson's effect and has an important role in modeling many micro- and nanoscale continuous systems. We will provide a comprehensive treatment of such microscale continuous systems such as microcantilevers later in Chap. 11.

The derivations of equations of motion of plates are very extensive in general case and are outside the scope of this book. However, as a demonstrable example of a 2D continuous system we consider the most basic plate model, i.e., a uniform rectangular thin plate. The axial strains are also ignored and only bending-induced strains are considered similar to the beam theory in the previous subsection. We are also ignoring the effect of shear deformation and rotary inertia. We refer the interested readers to Rao (2007) for these cases and configurations.

Referring to Fig. 4.12 and following the same conventions as for the beam, we can associate, to each element in the cross-section of the beam, displacement $w(x, y, t)$ as shown in Fig. 4.12.

Similar to beam kinematics, the bending-induced axial strain in the x-direction can be related to plate transverse displacement as:

$$u(x, y, t) = -z \sin \phi = -z \sin \left(\frac{\partial w(x, y, t)}{\partial x} \right) \approx -z \frac{\partial w(x, y, t)}{\partial x} \tag{4.86}$$

Similarly, we can relate the bending-induced axial strain in the y-direction to plate transverse displacement as:

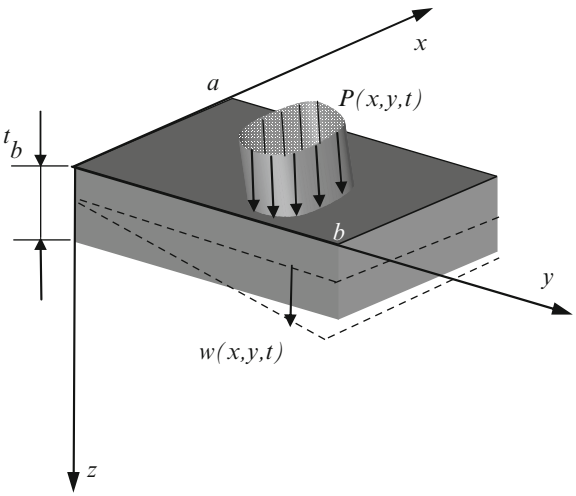

Fig. 4.12 Schematic of a plate in transverse vibration subject to distributed force per unit area of $P(x, y, t)$

$$v(x,y,t) = -z\sin\psi = -z\sin\left(\frac{\partial w(x,y,t)}{\partial y}\right) \approx -z\frac{\partial w(x,y,t)}{\partial y} \tag{4.87}$$

Now, describing the displacement field as $u(x,y,t)$, $v(x,y,t)$, and $w(x,y,t)$, one can calculate the 2D strain components (4.16) for this beam as:

$$S_{xx} = \frac{\partial u}{\partial x} = \frac{\partial}{\partial x}\left(-z\frac{\partial w}{\partial x}\right) = -z\frac{\partial^2 w}{\partial x^2} \tag{4.88a}$$

$$S_{yy} = \frac{\partial v}{\partial y} = \frac{\partial}{\partial y}\left(-z\frac{\partial w}{\partial y}\right) = -z\frac{\partial^2 w}{\partial y^2} \tag{4.88b}$$

$$S_{xy} = \frac{\partial u}{\partial y} + \frac{\partial v}{\partial x} = \frac{\partial}{\partial y}\left(-z\frac{\partial w}{\partial x}\right) + \frac{\partial}{\partial x}\left(-z\frac{\partial w}{\partial y}\right) = -2z\frac{\partial^2 w}{\partial x \partial y} \tag{4.88c}$$

Notice from (4.88c) that the shear strain component is not zero because of the dependency of transverse displacement w on both x and y. This is a very important fact and reveals that although shear stresses are not directly considered for the plates, the 2D nature of this system creates an inherent shear strain, and hence, shear stress.

Once the strain–displacement relationships (4.88) for the plate have been established, these strains can be related to stresses using stress–strain relationships (4.23b), i.e.,

$$\sigma_{xx} = \frac{E}{1-\nu^2}\left(S_{xx} + \nu S_{yy}\right) = \frac{-Ez}{1-\nu^2}\left(\frac{\partial^2 w}{\partial x^2} + \nu\frac{\partial^2 w}{\partial y^2}\right) \tag{4.89a}$$

$$\sigma_{yy} = \frac{E}{1-\nu^2}\left(S_{yy} + \nu S_{xx}\right) = \frac{-Ez}{1-\nu^2}\left(\frac{\partial^2 w}{\partial y^2} + \nu\frac{\partial^2 w}{\partial x^2}\right) \tag{4.89b}$$

$$\tau_{xy} = \frac{E}{2(1+\nu)}S_{xy} = \frac{-Ez}{1+\nu}\frac{\partial^2 w}{\partial x \partial y} \tag{4.89c}$$

Now that the relationships (4.89) are established, we are ready to proceed with calculation of energy terms for this plate system for the derivation of the equations of motion. The strain energy (4.40) for this 2D problem is represented as:

$$\delta U = \int_V \left[\sigma_{xx}\delta\left(S_{xx}\right) + \sigma_{yy}\delta\left(S_{yy}\right) + \tau_{xy}\delta\left(S_{xy}\right)\right]\mathrm{d}V \tag{4.90}$$

The kinetic energy is simply the same as in the case of the beam, with the only difference being the geometry for which it is integrated over. That is,

$$T = \tfrac{1}{2}\int_0^a \int_0^b \rho(x,y)\left(\frac{\partial w(x,y,t)}{\partial t}\right)^2 \mathrm{d}x\mathrm{d}y \tag{4.91}$$

where $\rho(x, y)$ is the plate density (mass per unit area). Notice that similar to the beam problem, other kinetic energies such as the kinetic energy due to rotary inertia and or external axial deformation are ignored. The virtual work of external force $P(x, y, t)$ can also be expressed as:

$$\delta W^{\text{ext}} = \int_0^a \int_0^b P(x, y, t)\delta w(x, y, t)\mathrm{d}x\mathrm{d}y \tag{4.92}$$

Substituting stress–strain relationships (4.89) into the strain energy (4.90) and inserting the results along with the kinetic energy (4.91) and virtual work (4.92) into Hamilton's principle (3.52) and after some manipulations similar to the steps followed in beam problem, we get the plate governing equation of motion for transverse vibration as:

$$\rho t_b \frac{\partial^2 w(x, y, t)}{\partial t^2} + D\left(\frac{\partial^4 w(x, y, t)}{\partial x^4} + 2\frac{\partial^4 w(x, y, t)}{\partial x^2 \partial y^2} + \frac{\partial^4 w(x, y, t)}{\partial y^4}\right) = P(x, y, t) \tag{4.93}$$

where $D = Et_b^3/12(1 - \nu^2)$ is called the flexural rigidity of the plate and t_b is the thickness of the plate as shown in Fig. 4.12. The associated boundary conditions, for a given edge $x = a$ (for instance), can be represented as (Rao 2007):

$$D\left[\nabla^2 w - (1 - \nu)w_{,yy}\right]\Big|_{x=a,y} \triangleq M_y = 0 \quad \text{or} \quad w_{,x}|_{x=a,y} = 0 \tag{4.94a}$$

$$D\left[\left(\nabla^2 w\right)_{,x} + (1 - \nu)w_{,xyy}\right]\Big|_{x=a,y} \triangleq V_y = 0 \quad \text{or} \quad w|_{x=a,y} = 0 \tag{4.94b}$$

where Laplacian ∇^2 is defined as:

$$\nabla^2(\,) = \frac{\partial^2}{\partial x^2}(\,) + \frac{\partial^2}{\partial y^2}(\,) \tag{4.95}$$

and the subscripts after the commas in expression (4.94) represent partial derivative with respect to the argument. The boundary conditions (4.94) have the same meaning as in the ones for beams. That is, either the bending moment or slope can be prescribed at a given edge but not both (see (4.94a)). Similarly, as seen from (4.94b), either shear force or deflection can be prescribed at any given edge but not both. Hence, (4.94a) and (4.94b) provide only two boundary conditions. By identifying the boundary conditions for the other three edges, a total of eight boundary conditions can be obtained in order to solve the 2D partial differential equation (4.93).

Using the short notion, (4.93) can be rewritten as:

$$\rho t_b \frac{\partial^2 w(x, y, t)}{\partial t^2} + D\nabla^4 w(x, y, t) = P(x, y, t) \tag{4.96}$$

where ∇^4 is called the *biharmonic* operator defined as:

$$\nabla^4(\,) = \frac{\partial^4}{\partial x^4}(\,) + 2\frac{\partial^4}{\partial x^2 \partial y^2}(\,) + \frac{\partial^4}{\partial y^4}(\,) \tag{4.97}$$

The boundary conditions for plates are classified into geometrical and natural boundary conditions similar to beams. While we obtained, using extended Hamilton's principle, both these types for conventional boundary condition for the beams in most general form (see (4.81) and (4.82)), the derivation of the boundary conditions for the plates from Hamilton's principle is extensive and outside the scope of this book. However, we can use our intuition and the similarity between beams and plates to arrive at some of these boundary conditions. For this, we present, next, an example case study to study some of the most commonly used conventional boundary conditions for plates.

Example 4.4. Conventional boundary conditions for transversally vibrating uniform plates.

Consider a uniform rectangular plate as shown in Fig. 4.13 with several conventional boundary conditions and obtain the corresponding expressions for these boundary conditions.

(a) Plate with clamped edge at $x = a$: In this case, the displacement along the y-axis at $x = a$ as well as slope of the plate in this direction at this edge must vanish. That is,

$$w(x, y, t)|_{x=a,y} = 0, \ \left.\frac{\partial w(x, y, t)}{\partial x}\right|_{x=a,y} = 0 \tag{4.98}$$

(b) Plate with simply supported edge at $x = a$: In this case, the displacement along the y-axis at $x = a$ must vanish as well as the bending moment about the y-axis. That is,

$$w(x, y, t)|_{x=a,y} = 0, \ M_y\big|_{x=a,y} = 0 \tag{4.99}$$

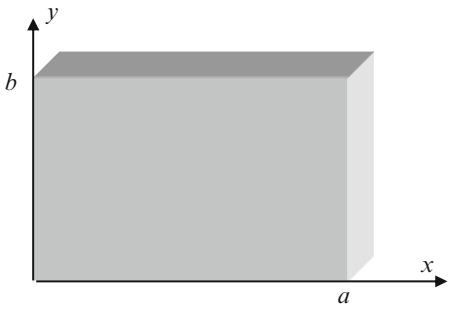

Fig. 4.13 Schematic of uniform rectangular plate of Example 4.4

Similar to beam problem for relation between bending moment M and displacement w in (4.66), this relationship can be extended for plate as (Rao 2007):

$$M_y = -D\left(\frac{\partial^2 w}{\partial x^2} + \nu\frac{\partial^2 w}{\partial y^2}\right)\Big|_{x=a,y} = 0 \tag{4.100}$$

However, if edge $x = a$ is simply supported, then

$$\frac{\partial^2 w}{\partial y^2}\Big|_{x=a,y} = 0.$$

This basically comes from the fact that edge $x = a$ cannot have any displacement or slope (derivatives of the displacement) along the y-axis due to its simply supported nature. Inserting this into (4.100), one can conclude that for the simply supported edge $x = a$ we have also

$$\frac{\partial^2 w}{\partial x^2}\Big|_{x=a,y} = 0 \tag{4.101}$$

Hence, (4.99) and (4.101) represent the boundary conditions of a simply supported plate at edge $x = a$.

(c) Plate with free edge at $x = a$: In this case, the bending moment and shear force along the y-axis and at $x = a$ must vanish. Extending the definition of bending moment and shear deformation for plate (Rao 2007), one can write

$$\begin{aligned} M_y &= D\left(\frac{\partial^2 w}{\partial x^2} + \nu\frac{\partial^2 w}{\partial y^2}\right)\Big|_{x=a,y} = 0, \\ V_y &= D\Big[\left(\nabla^2 w\right)_{,x} + (1-\nu)w_{,xyy}\Big]\Big|_{x=a,y} = 0 \end{aligned} \tag{4.102}$$

4.4 Eigenvalue Problem in Continuous Systems

Now that we have illustrated several examples from vibration of continuous systems ranging from simple 1D wave equation for axial vibration of bars to complex 2D transverse vibration of plates, one can express the equations of motion and the associated boundary conditions into the following generalized operator form:

$$\mathrm{M}\left[w_{,tt}\right] + \mathrm{K}\left[w\right] = P \tag{4.103a}$$

$$\Gamma_i\left[w\right] = 0 \quad i = 1, 2, \ldots, 2n-1 \tag{4.103b}$$

where P is a generalized external force, M is a mass partial differential operator of order $2m$, K is a stiffness partial differential operator of order $2n$, and Γ_i is partial differential operators of order $2n-1$.

Using this generalization, the classification between geometrical and natural boundary conditions can be made very easily and systematically. That is, the boundary conditions involving spatial derivatives of up to order $n-1$ are the geometric or essential boundary conditions, while the other boundary conditions are referred to as natural or dynamic boundary conditions. The following example better demonstrates these representations of equations of motion and boundary conditions of continuous systems.

Example 4.5. Representation of equations of motion of continuous systems in operator forms.

Determine the mass and stiffness partial differential operators for axial vibration of bars and transverse vibration of beams.

Solution. Comparing (4.55a) and (4.103a), we can write these operators for the axial vibration of bars as:

$$\mathrm{M}\,[w_{,tt}] = \rho(x)\,[w_{,tt}] \Rightarrow \mathrm{M} = \rho(x) \text{ and } m = 0 \tag{4.104a}$$

$$\mathrm{K}\,[w] = -\frac{\partial}{\partial x}\left(EA(x)\frac{\partial}{\partial x}\right)[w] \Rightarrow \mathrm{K} = -\frac{\partial}{\partial x}\left(EA(x)\frac{\partial}{\partial x}\right) \text{ and } n = 1 \tag{4.104b}$$

Similarly, comparing (4.80) and (4.103a), these operators for the transverse vibration of beams can be expressed as:

$$\mathrm{M}\,[w_{,tt}] = \rho(x)\,[w_{,tt}] \Rightarrow \mathrm{M} = \rho(x) \text{ and } m = 0 \tag{4.105a}$$

$$\mathrm{K}\,[w] = \frac{\partial^2}{\partial x^2}\left(EI(x)\frac{\partial^2}{\partial x^2}\right)[w] \Rightarrow \mathrm{K} = \frac{\partial^2}{\partial x^2}\left(EI(x)\frac{\partial^2}{\partial x^2}\right) \text{ and } n = 2 \tag{4.105b}$$

4.4.1 Discretization of Equations and Separable Solution

Now that we have obtained the differential equations of a continuous system in its most generalized form, one needs to explore possible solutions to these equations for follow-up vibration-control purposes. While there are several methods that lead to discretization of the governing PDE of continuous systems, we shall highlight the most elementary assumption regarding the solutions; that is, the solution is *separable* in spatial and temporal coordinates.

$$\begin{aligned} w(x,t) &= W(x)T(t) \text{ for 1D continua, and} \\ w(x,y,t) &= W(x,y)T(t) \text{for 2D continua} \end{aligned} \tag{4.106}$$

where W and T are the respective spatial and temporal functions and imply that the behavior in time and space is independent. This is in line with the same concept of eigenvalue problem utilized in MDOF systems in Chap. 2.

To better demonstrate this concept and avoid undue complication, we shall utilize the three elementary continua that were discussed in the previous subsection. That is, the axial vibration of bars serves as representative of wave equations (a second-order stiffness operator problem, see (4.104b)), the transverse vibration of beams represents a fourth-order stiffness operator problem in 1D (see (4.105b)), and finally the transversally vibrating plates serve as 2D continuous problems with fourth-order stiffness operator.

Axial Vibration of Bars: Implementing assumption (4.106) into the homogeneous version[5] of the governing equation of motion of axial vibration of bars (4.55a) results in

$$\frac{\partial}{\partial x}\left(EA(x)W'(x)T(t)\right) = \rho(x)W(x)\ddot{T}(t) \tag{4.107}$$

Equation (4.107) can be rewritten in the following separable time-dependent and space-dependent configurations:

$$\frac{1}{\rho(x)W(x)}\frac{\mathrm{d}}{\mathrm{d}x}(EA(x)W'(x)) = \frac{\ddot{T}(t)}{T(t)} \triangleq -\omega^2 \tag{4.108}$$

The left side of (4.108) is only function of spatial variable x, while its right side is only function of temporal variable. Hence, for such equality to hold true, the two sides of this equation must equal to a constant, say $-\omega^2$. The reason for negative sign of this constant is to assure boundedness of the temporal solution $T(t)$ as detailed later in this chapter. Therefore, (4.108) can be recast as:

$$\ddot{T}(t) + \omega^2 T(t) = 0, \text{ temporal component} \tag{4.109a}$$

$$-\frac{\mathrm{d}}{\mathrm{d}x}(EA(x)W'(x)) = \omega^2\rho(x)W(x), \text{spatial component} \tag{4.109b}$$

The spatial component (4.109b) must be satisfied over the domain $0 \leq x \leq L$ with the associated boundary conditions, while the temporal component (4.109a) is associated with some initial conditions. The key to the spatial solution is satisfying the boundary conditions and, as will be demonstrated later, the behavior of the system is quite different for different boundary conditions. In satisfying these conditions, the modal solutions and consequently natural frequencies will result. The following example demonstrates this.

Example 4.6. Axial vibration of uniform bar with elastic boundary condition.

In many practical applications, a continuous system may interact with elastic elements (e.g., support points of structures). Consider the uniform bar fixed at one

[5] This is a similar practice as in MDOF systems, where the eigenvalues and eigenvectors were determined using free and undamped vibration analysis.

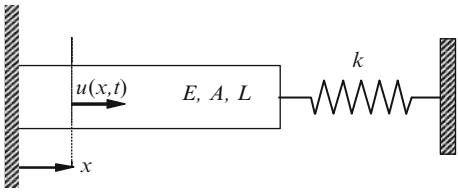

Fig. 4.14 Axial vibration of a uniform bar clamed at one end and attached to an external stiffness at the other end

end and having an external stiffness k at the other end as shown in Fig. 4.14. Use the concept of separation of variables to obtain the frequency equation for this system.

Solution. The modeling steps described in Sect. 4.3.1 can be followed to derive both the governing equations of motion and boundary conditions. For this problem, we only highlight the new changes in the strain energy due to the addition of spring k. Hence, the total strain energy (4.43) is extended to include the strain energy of discrete spring k as:

$$\delta U = \delta U_{\text{beam}} + \delta U_{\text{spring}\,k} = \int_0^L \left\{ EA(x)\frac{\partial u(x,t)}{\partial x}\delta\left(\frac{\partial u(x,t)}{\partial x}\right)\right\} \mathrm{d}x + \tfrac{1}{2}k\,(u(L,t))^2 \tag{4.110}$$

Substituting this expression for δU and variation of kinetic energy (4.45) into Hamilton's principle (4.46) when taking into account the fact that for this problem, $\delta W^{\text{ext}} = 0$, and after some manipulations it yields

$$\int_{t_1}^{t_2}\left[\int_0^L \left\{\frac{\partial}{\partial x}\left(EA(x)\frac{\partial u(x,t)}{\partial x}\right) - \rho(x)\frac{\partial^2 u(x,t)}{\partial t^2} + P(x,t)\right\}\delta u(x,t)\mathrm{d}x \right.$$
$$\left. -ku(L,t)\delta u(L,t) - \left(EA(x)\frac{\partial u(x,t)}{\partial x}\right)\delta u(x,t)\Big|_0^L\right]\mathrm{d}t = 0 \tag{4.111}$$

Similar to the argument we made previously, for (4.111) to vanish, the integrant must vanish, and for the integrant to vanish we must have:

$$\rho(x)\frac{\partial^2 u(x,t)}{\partial t^2} - \frac{\partial}{\partial x}\left(EA(x)\frac{\partial u(x,t)}{\partial x}\right) = P(x,t) \tag{4.112a}$$

$$\left(ku(L,t) + EA\frac{\partial u(L,t)}{\partial x}\right)\delta u(L,t) - \left(EA\frac{\partial u(0,t)}{\partial x}\right)\delta u(0,t) = 0 \tag{4.112b}$$

Considering the geometry shown in Fig. 4.14, $u(0,t) = 0$ and $\delta u(L,t)$ must be free. Substituting these into (4.112b) results in the two required boundary conditions as:

$$\left(ku(L,t) + EA\frac{\partial u(L,t)}{\partial x}\right) = 0 \rightarrow EA\frac{\partial u(L,t)}{\partial x} = -ku(L,t) \text{ and } u(0,t) = 0 \tag{4.113}$$

Now that the boundary conditions are obtained for this problem, we can utilize the separable equation (4.109b) as:

$$\frac{\mathrm{d}^2}{\mathrm{d}x}(W(x)) + \beta^2 W(x) = 0,\ \beta^2 = \rho\omega^2/EA \tag{4.114}$$

The solution to this simple ODE can be expressed as:

$$W(x) = C_1 \sin\beta x + C_2 \cos\beta x \tag{4.115}$$

Substituting the separable form (4.106) into the boundary conditions (4.113), we obtain:

$$u(0,t) = W(0)T(t) = 0 \rightarrow W(0) = 0 \tag{4.116a}$$

$$EA\frac{\partial u(L,t)}{\partial x} = -ku(L,t) \rightarrow EAW'(L) = -kW(L) \tag{4.116b}$$

Substituting (4.116a) into general expression (4.115) for $W(x)$, it yields $C_2 = 0$, and hence

$$W(x) = C_1 \sin\beta x \tag{4.117}$$

Now substituting (4.116b) into expression (4.117), it yields:

$$W'(L) = \frac{-k}{EA}W(L) \rightarrow C_1\beta\cos(\beta L) = \frac{-k}{EA}C_1\sin(\beta L) \tag{4.118}$$

or in a simplified form as:

$$\tan(\beta L) = \frac{-\beta EA}{k} \tag{4.119}$$

Equation (4.119) is referred to as the *eigenfrequency equation*.

Remark 4.8. The obtained frequency equation (4.119) is transcendental in nature, so it possesses infinitely many solutions, which are referred to as *eigenfrequencies* or *eigenvalues* of continuous systems. Throughout this subsection, it will be shown that all the frequency equations obtained for the vibration of continuous systems are transcendental, and hence, possess infinitely many solutions. To highlight this important feature, these eigenfrequencies are denoted by β_r where $r = 1, 2, \ldots, \infty$. Substituting these eigenfrequencies into the expression for the spatial solution results, to what is referred to as, eigenfunctions, i.e., W_r.

Since the frequency equation (4.119) is an implicit function of frequency β, one needs to numerically solve this equation. For instance, if we take $k = EA$ and $L = 1$, then the eigenfrequency (4.119) reduces to

$$\tan\beta = -\beta \tag{4.120}$$

with the first few solutions as:

$$\beta_r = 0,\ 2.03,\ 4.91,\ \ldots \tag{4.121}$$

Using the relationship between natural frequency and β_r of (4.114), the natural frequencies can be expressed as:

$$\omega_r^2 = \beta_r^2 \frac{EA}{\rho} \tag{4.122}$$

Substituting either β_r or ω_r in the general eigenfunction (4.117) results in

$$W_r(x) = C_r \sin \beta_r x = C_r \sin\left(\sqrt{\frac{\rho}{EA}}\omega_r x\right) \tag{4.123}$$

which form the basis functions for the overall solution

$$w(x,t) = W(x)T(t) = \sum_r^{\infty} W_r(x)T_r(t) \tag{4.124}$$

We will discuss, later in this chapter, the use of these basis functions (or here eigenfunctions) in obtaining the ultimate solution of the axial vibrations.

Transverse Vibration of Beams: Similar to vibration of bars, implementing assumption (4.106) into the homogeneous version of the governing equation of transverse vibration of beams (4.80), i.e.,

$$\frac{\partial^2}{\partial x^2}\left(EI(x)\frac{\partial^2 w(x,t)}{\partial x^2}\right) = -\rho(x)\frac{\partial^2 w(x,t)}{\partial t^2} \tag{4.125}$$

results in

$$\frac{1}{\rho(x)W(x)}\frac{\mathrm{d}^2}{\mathrm{d}x^2}\left(EI(x)W''(x)\right) = -\frac{\ddot{T}(t)}{T(t)} \triangleq \omega^2 \tag{4.126}$$

Similar to vibration problem of bars, the separated differential equations governing temporal and spatial functions can be expressed as:

$$\ddot{T}(t) + \omega^2 T(t) = 0 \tag{4.127a}$$

$$\frac{\mathrm{d}^2}{\mathrm{d}x^2}\left(EI(x)W''(x)\right) = \omega^2 \rho(x)W(x) \tag{4.127b}$$

For a complete solution to system of (4.127), two initial conditions are required for the temporal differential equation, while a total of four boundary conditions are required for the fourth-order spatial differential equation. The following example case study overviews the required steps in obtaining the eigenfrequency and eigenfunctions for a uniform beam.

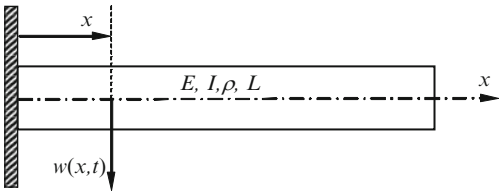

Fig. 4.15 Transversally vibrating uniform cantilever beam

Example 4.7. Transversally vibrating uniform cantilever beam.

Consider the problem of transverse vibration of a uniform (i.e., $EI(x) = EI$, $\rho(x) = \rho$) cantilever (clamped-free) beam as shown in Fig. 4.15.

Equation (4.127b) for this uniform beam can be simplified as:

$$EI\frac{\mathrm{d}^4W(x)}{\mathrm{d}x^4} = \omega^2\rho W(x) \rightarrow W''''(x) - \beta^4 W(x) = 0 \tag{4.128}$$

where

$$\beta^4 = \rho\omega^2/EI \tag{4.129}$$

The solution to differential (4.128) can be given as

$$W(x) = C_1 \sin\beta x + C_2 \cos\beta x + C_3 \sinh\beta x + C_4 \cosh\beta x \tag{4.130}$$

For the clamped-free boundary conditions, the results of Example 4.3 ((4.83) and (4.85)) can be used to write:

$$\begin{aligned} &w(0,t) = W(0)T(t) = 0 \rightarrow W(0) = 0 \\ &w'(0,t) = W'(0)T(t) = 0 \rightarrow W'(0) = 0 \\ &w''(L,t) = W''(L)T(t) = 0 \rightarrow W''(L) = 0 \\ &w'''(L,t) = W'''(L)T(t) = 0 \rightarrow W'''(L) = 0 \end{aligned} \tag{4.131}$$

The first two relationships of (4.131) can be used in (4.130) to yield:

$$\begin{aligned} &W(0) = 0 \rightarrow C_2 + C_4 = 0 \text{ or } \mathrm{C}_4 = -C_2 \\ &W'(0) = 0 \rightarrow C_1 + C_3 = 0 \text{ or } C_3 = -C_1 \end{aligned} \tag{4.132}$$

Hence, (4.130) is rewritten as:

$$W(x) = C_1\,(\sin\beta x - \sinh\beta x) + C_2\,(\cos\beta x - \cosh\beta x) \tag{4.133}$$

Now, applying the last two boundary conditions (4.131) to expression (4.133) results in a linear system of equations in terms of unknowns C_1 and C_2 as

$$C_1(\sin\beta L + \sinh\beta L) + C_2(\cos\beta L + \cosh\beta L) = 0$$
$$C_1(\cos\beta L + \cosh\beta L) - C_2(\sin\beta L - \sinh\beta L) = 0 \tag{4.134}$$

Or

$$\begin{bmatrix} \sin\beta L + \sinh\beta L & \cos\beta L + \cosh\beta L \\ \cos\beta L + \cosh\beta L & -\sin\beta L + \sinh\beta L \end{bmatrix} \begin{Bmatrix} C_1 \\ C_2 \end{Bmatrix} = \begin{Bmatrix} 0 \\ 0 \end{Bmatrix} \tag{4.135}$$

To arrive at a nontrivial solution for $W(x)$, the determinant of the coefficients (4.135) must vanish. Simplifying this determinant and after some manipulations, we obtain the following frequency equation for a uniform cantilever beam in terms of nondimensional frequency β,

$$\cos(\beta L)\cosh(\beta L) = -1 \tag{4.136}$$

Similar to axial vibration of bars, this frequency equation is transcendental in nature, and hence, results in infinitely many solutions. Numerically solving this equation, one can obtain the following first few solutions

$$\beta_r L = 1.875,\ 4.694,\ 7.855,\ \ldots \tag{4.137}$$

Using definition (4.129), the natural frequencies can now be obtained as:

$$\omega_1 = (1.875)^2\sqrt{\frac{EI}{\rho L^4}},\ \omega_2 = (4.694)^2\sqrt{\frac{EI}{\rho L^4}},\ \ldots \tag{4.138}$$

Since the determinant of the coefficients (4.135) has been forced to be zero, the two equations are linearly dependent and only one of them can be used. Using any of these equations, constant C_2 can be related to C_1, and hence, the general expression for the eigenfunction $W(x)$ can be obtained as:

$$W_r(x) = \frac{C_r}{\sin\beta_r L - \sinh\beta_r L}\Big[(\sin\beta_r L - \sinh\beta_r L)(\sin\beta_r x - \sinh\beta_r x) + (\cos\beta_r L + \cosh\beta_r x)(\cos\beta_r x - \cosh\beta_r x)\Big] \tag{4.139}$$

And finally, the complete solution can be obtained as:

$$w(x,t) = \sum_r^{\infty} W_r(x)T_r(t) \tag{4.140}$$

Transverse Vibration of Plates: Similar to the previous two continuous systems, substituting the 2D version of separable form (4.106) into the homogeneous version of the governing equation of transverse vibration of plates (4.93) results in

$$\rho t_b W(x,y)\ddot{T}(t) + DT(t)\nabla^4 W(x,y) = 0 \tag{4.141}$$

Or in a separable form as

$$\frac{D}{\rho t_b}\frac{\nabla^4 W}{W} = -\frac{\ddot{T}(t)}{T(t)} \triangleq \omega^2 \tag{4.142}$$

Hence, the separated differential equations governing temporal and spatial functions can be expressed as:

$$\ddot{T}(t) + \omega^2 T(t) = 0 \tag{4.143a}$$
$$\nabla^4 W - \beta^4 W = 0 \tag{4.143b}$$

where the nondimensional frequency β is defined as

$$\beta^4 = \omega^2 \rho t_b / D \tag{4.144}$$

Since we are interested in the spatial part of the solution, (4.143b) can be further simplified to

$$\left(\nabla^2 + \beta^2\right)\left(\nabla^2 - \beta^2\right) W = 0 \tag{4.145}$$

Equation (4.145) has two solutions $W = W_1$ and $W = W_2$ that satisfy

$$\left(\nabla^2 + \beta^2\right) W_1 = 0,\ \left(\nabla^2 - \beta^2\right) W_2 = 0 \tag{4.146}$$

and can be superimposed as $W = W_1 + W_2$ to give the complete solution.

We will first concentrate on solution $W(x, y) = W_1(x, y)$. For this, we need a further separation on spatial coordinates x and y. That is, W_1 is taken as:

$$W_1(x, y) = X(x)Y(y) \tag{4.147}$$

Substituting the separable form (4.147) into the first expression in (4.146) and dividing the resulting equation by XY, it yields

$$\frac{X''}{X} + \frac{Y''}{Y} + \beta^2 = 0 \rightarrow \frac{X''}{X} = -\frac{Y''}{Y} - \beta^2 \triangleq -\alpha^2 = \text{constant} \tag{4.148}$$

The sign of α^2 in (4.148) is selected such that the solutions to $X(x)$ and $Y(y)$ both would yield bounded responses (i.e., harmonic). Hence, the individual differential equation governing $X(x)$ and $Y(y)$ can be rewritten as

$$X''(x) + \alpha^2 X(x) = 0,\ Y''(y) + \gamma^2 Y(y) = 0 \tag{4.149}$$

where

$$\gamma^2 = \beta^2 - \alpha^2 \tag{4.150}$$

The solutions to (149), similar to the wave equations in axial vibration of bars, can be given as:

$$\begin{aligned} X(x) &= A_1 \sin \alpha x + A_2 \cos \alpha x, \\ Y(y) &= A_3 \sin \gamma y + A_4 \cos \gamma y \end{aligned} \tag{4.151}$$

Hence, using (4.147) and these solutions, the final form of W_1 can be expressed as:

$$\begin{aligned} W_1(x, y) \; &= C_1 \sin(\alpha x) \sin(\gamma y) + C_2 \sin(\alpha x) \cos(\gamma y) \\ &+ C_3 \cos(\alpha x) \sin(\gamma y) + C_4 \cos(\alpha x) \cos(\gamma y) \end{aligned} \tag{4.152}$$

Similarly, the solution $W = W_2$ satisfying the second expression of (4.146) can be expressed as:

$$\begin{aligned} W_2(x, y) = C_5 \sinh(\bar{\alpha} x) \sinh(\bar{\gamma} y) + C_6 \sinh(\bar{\alpha} x) \cosh(\bar{\gamma} y) \\ + C_7 \cosh(\bar{\alpha} x) \sinh(\bar{\gamma} y) + C_8 \cosh(\bar{\alpha} x) \cosh(\bar{\gamma} y) \end{aligned} \tag{4.153}$$

where

$$\bar{\gamma}^2 = \bar{\beta}^2 - \bar{\alpha}^2 \tag{4.154}$$

with $\overline{\alpha}$ and $\overline{\beta}$ being some constants similar to α and β. In (4.152) and (4.153), constants C_1 through C_8 are determined using the required eight boundary conditions. Now that both solutions W_1 and W_2 have been determined, the complete spatial solution can be obtained as $W = W_1 + W_2$. The following example overviews the required steps to obtain the eigenfrequencies and eigenfunctions for a uniform rectangular plate.

Example 4.8. Transversally vibrating uniform simply-supported rectangular plates.

Consider the problem of transverse vibration of a uniform plate which is hinged at all the four edges as shown in Fig. 4.16.

In Example 4.4, (4.99) and (4.101) provided the boundary conditions for a plate simply supported at edge $x = a$. Extending this to all four edges for this problem,

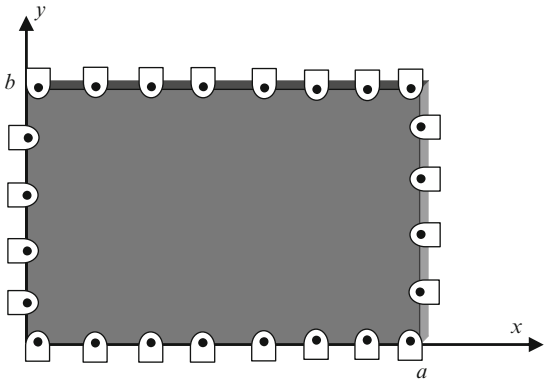

Fig. 4.16 Transversally vibrating uniform rectangular plate hinged at all four edges

the following required eight boundary conditions are obtained

$$w(x,y,t)|_{x=0,y}=0,\ w(x,y,t)|_{x,y=0}=0,\quad w(x,y,t)|_{x=a,y}=0,\ w(x,y,t)|_{x,y=b}=0, \tag{4.155a}$$

$$\left.\frac{\partial^2 w}{\partial x^2}\right|_{x=0,y}=0,\ \left.\frac{\partial^2 w}{\partial y^2}\right|_{x,y=0}=0,\ \left.\frac{\partial^2 w}{\partial x^2}\right|_{x=a,y}=0,\ \left.\frac{\partial^2 w}{\partial y^2}\right|_{x,y=b}=0, \tag{4.155b}$$

Inserting these boundary conditions into the separable form (4.106) results in:

$$W(0,y)=0,\ W(x,0)=0,\ W(a,y)=0,\ W(x,b)=0, \tag{4.156a}$$

$$\frac{\partial^2 W(0,y)}{\partial x^2}=0,\ \frac{\partial^2 W(x,0)}{\partial y^2}=0,\ \frac{\partial^2 W(a,y)}{\partial x^2}=0,\ \frac{\partial^2 W(x,b)}{\partial y^2}=0, \tag{4.156b}$$

Without going into the details, inserting the solutions (4.152) and (4.153) into these boundary conditions, it can be shown that all constants C_1 through C_8 vanish, except for C_1. Hence, the spatial function $W(x,y)$ will take the following form

$$W(x,y)=C_1\sin(\alpha x)\sin(\gamma y) \tag{4.157}$$

Now using the last two boundary conditions in (4.156a) and the fact that we are looking for a nontrivial solution, it yields:

$$\begin{matrix}\sin(\alpha a)=0\rightarrow\alpha_m=\frac{m\pi}{a}\\ \sin(\gamma b)=0\rightarrow\gamma_n=\frac{n\pi}{b}\end{matrix},\quad m,n=1,2,\ldots,\infty \tag{4.158}$$

Using these findings and relationship (4.150), the nondimensional eigenfrequency β can be represented as:

$$\beta_{mn}^2=\alpha_m^2+\gamma_n^2=\pi^2\left(\frac{m^2}{a^2}+\frac{n^2}{b^2}\right) \tag{4.159}$$

Now using relationship (4.144), the plate eigenfrequencies can be finally obtained as:

$$\omega_{\mathrm{mn}}=\beta_{mn}^2\sqrt{D/\rho t_b}=\pi^2\sqrt{D/\rho t_b}\left(\frac{m^2}{a^2}+\frac{n^2}{b^2}\right) \tag{4.160}$$

Notice the dependency of the eigenfrequencies on two arguments rather than one in the 1D vibration problems. That is, there are many configurations for the modes, such as ω_{11}, ω_{23}, ω_{33}, and so on. Due to this arrangement, there is a possibility that two modes could have the same eigenfrequency which is an interesting situation. For instance, if the plate is square, i.e., $a=b$, then $\omega_{jk}=\omega_{kj}$.

Similar to 1D vibration problems, once the eigenfrequencies have been obtained, the eigenfunctions can be determined. In this case, the eigenfunctions (4.157) take the form:

$$W_{mn}(x, y) = C_{mn} \sin\left(\frac{m\pi x}{a}\right) \sin\left(\frac{n\pi y}{b}\right) \tag{4.161}$$

Also, the temporal part of the solution can be expressed (see (4.143a))

$$T_{mn}(t) = B_{mn} \cos(\omega_{mn} t) + \bar{B}_{mn} \sin(\omega_{mn} t) \tag{4.162}$$

Consequently, the complete solution $w(x, y, t)$ can be obtained as:

$$\begin{aligned} w(x, y, t) &= \sum_{m=1}^{\infty} \sum_{n=1}^{\infty} W_{mn}(x, y) T_{mn}(t) \\ &= \sum_{m=1}^{\infty} \sum_{n=1}^{\infty} \Bigg(C_{mn} \sin\left(\frac{m\pi x}{a}\right) \sin\left(\frac{n\pi y}{b}\right) \\ &\quad \times \left(B_{mn} \cos(\omega_{mn} t) + \bar{B}_{mn} \sin(\omega_{mn} t) \right) \Bigg) \end{aligned} \tag{4.163}$$

where constant C_{mn} can be selected freely or through some sorts of normalization of modes that will be discussed later in this chapter, and B_{mn} and $\overline{B}_{mn}$ are obtained using the two initial conditions for the problem.

4.4.2 Normal Modes Analysis

Similar concept in modal analysis of discrete systems discussed in Chap. 2 can be adopted for continuous systems using eigenfunctions instead of mode shapes in discrete systems. Before we demonstrate this, we first briefly review the self-adjointness property of functions.

Self-adjoint Functions: Two functions f and g are called self-adjoint if they are as many times differentiable as the highest order of stiffness operator (see (4.103)) and the following relationships hold

$$\begin{aligned} \langle \{f\} \cdot \mathrm{M}\{g\} \rangle &= \langle \{g\} \cdot \mathrm{M}\{f\} \rangle \\ \langle \{f\} \cdot \mathrm{K}\{g\} \rangle &= \langle \{g\} \cdot \mathrm{K}\{f\} \rangle \end{aligned} \tag{4.164}$$

where K and M are the stiffness and mass operators, respectively, defined earlier in (4.103). The properties (4.164) simply imply the interchangeability feature of these functions with respect to the operator. Therefore, we can think of this property as the counterpart to the symmetry of the mass and stiffness matrices in MDOF systems.

Orthogonality Conditions: It can be easily shown that properties (4.164) simply imply modal (or here eigenfunction) orthogonality with respect to mass and stiffness operators, similar to discrete systems (see (2.31) and (2.32) as well as Remark 2.2).

Without loss of generality and in order to keep the discussion focused, we only show these results for axial vibration of bars where the stiffness operator is of second order.

Considering (4.109b)

$$\frac{\mathrm{d}}{\mathrm{d}x}\left(EA(x)\frac{\mathrm{d}W(x)}{\mathrm{d}x}\right) = -\omega^2\rho(x)W(x) \tag{4.165}$$

and taking into account the fact that all eigenfunctions must satisfy this equation including, for instance, the two arbitrary eigenfunctions $W_r(x)$ and $W_s(x)$, i.e.,

$$\frac{\mathrm{d}}{\mathrm{d}x}\left(EA(x)\frac{\mathrm{d}W_r(x)}{\mathrm{d}x}\right) = -\omega_r^2\rho(x)W_r(x) \tag{4.166}$$

$$\frac{\mathrm{d}}{\mathrm{d}x}\left(EA(x)\frac{\mathrm{d}W_s(x)}{\mathrm{d}x}\right) = -\omega_s^2\rho(x)W_s(x) \tag{4.167}$$

Premultiplying (4.166) by $W_s(x)$ and integrating over the system length L yield,

$$\int_0^L W_s(x)\frac{\mathrm{d}}{\mathrm{d}x}\left(EA(x)\frac{\mathrm{d}W_r(x)}{\mathrm{d}x}\right)\mathrm{d}x = -\omega_r^2\int_0^L \rho(x)W_s(x)W_r(x)\mathrm{d}x \tag{4.168}$$

Similarly, premultiplying (4.167) by $W_r(x)$ and integrating over length L results

$$\int_0^L W_r(x)\frac{\mathrm{d}}{\mathrm{d}x}\left(EA(x)\frac{\mathrm{d}W_s(x)}{\mathrm{d}x}\right)\mathrm{d}x = -\omega_s^2\int_0^L \rho(x)W_r(x)W_s(x)\mathrm{d}x \tag{4.169}$$

Now, subtracting (168) from (169) yields

$$\int_0^L \left[W_r(x)\frac{\mathrm{d}}{\mathrm{d}x}\left(EA(x)\frac{\mathrm{d}W_s(x)}{\mathrm{d}x}\right) - W_s(x)\frac{\mathrm{d}}{\mathrm{d}x}\left(EA(x)\frac{\mathrm{d}W_r(x)}{\mathrm{d}x}\right)\right]\mathrm{d}x$$

$$= \left(\omega_r^2 - \omega_s^2\right)\int_0^L \rho(x)W_r(x)W_s(x)\mathrm{d}x \tag{4.170}$$

Performing integration by part on each of the term inside the square bracket on the left side of (4.170) results

$$EA(x)W_r(x)W_s'(x)\Big|_0^L - EA(x)W_r'(x)W_s(x)\Big|_0^L$$

$$= \left(\omega_r^2 - \omega_s^2\right)\int_0^L \rho(x)W_r(x)W_s(x)\mathrm{d}x \tag{4.171}$$

It can be shown the left side of (4.171) vanishes for any combination of conventional[6] boundary conditions, and therefore,

$$\left(\omega_r^2 - \omega_s^2\right) \int_0^L \rho(x) W_r(x) W_s(x) \mathrm{d}x = 0 \tag{4.172}$$

Taking into account the fact that $\omega_r \neq \omega_s$ if $r \neq s$, then (4.172) reduces to

$$\int_0^L \rho(x) W_r(x) W_s(x) dx = 0, \quad \text{for} \quad r \neq s \tag{4.173}$$

Equation (4.173) implies orthogonality property of eigenfunctions with respect to mass operator and can be rewritten in a more useful form as

$$\int_0^L \rho(x) W_r(x) W_s(x) \mathrm{d}x = \delta_{rs} \tag{4.174}$$

where δ_{rs} is the Kronecker delta.

Substituting orthogonality condition (4.174) into (4.168) and integrating by part the left side of the equation, while again considering conventional boundary conditions, yields

$$\int_0^L EA(x) W_r'(x) W_s'(x) \mathrm{d}x = \omega_r^2 \delta_{rs} \tag{4.175}$$

which is referred to as orthogonality condition between eigenfunctions in axially vibrating bars with respect to stiffness operator.

Following the same procedure for the problem of transverse vibration of beams, it can be shown that property (4.174) remains unchanged for the beams (this was expected as the mass operator in axial vibration of bars is the same as transverse vibration of beams), while the orthogonality with respect to stiffness operator changes to

$$\int_0^L EI(x) W_r''(x) W_s''(x) \mathrm{d}x = \omega_r^2 \delta_{rs} \tag{4.176}$$

[6] Please refer to the definition of the conventional boundary conditions given earlier in this section. These restrictions, however, can be relaxed for nonconventional boundary conditions and corresponding orthogonality conditions can be obtained. We refer interested readers to cited references as well as Exercise 4.16 in this chapter.

The orthogonality conditions (4.174) and (4.175) or (4.176) facilitate the complete solution of the boundary value problem in continuous systems, much like the coordinate transformation using normal modes matrix in discrete systems. We will briefly review this technique in the next subsection.

4.4.3 Method of Eigenfunctions Expansion

Now that the boundary value problem for the free and undamped vibration problem has been solved and the system eigenfrequencies and eigenfunctions have resulted, one can utilize the orthogonality conditions obtained in the preceding subsection to completely solve the problem of forced vibration. For this, we consider two scenarios, (1) when the eigenfunctions can be obtained relatively easily (e.g., when the boundary conditions are conventional and/or the continuum possesses simple and uniform geometry), and (2) when the eigenfunctions cannot be obtained (i.e., extracting exact solution to the boundary value problem of free and undamped vibration becomes nontrivial). For the latter case, we resort to what are referred to as *trial* functions which do not necessarily satisfy the equations of motion and only need to satisfy all or some of the boundary conditions. If these trial functions satisfy all the boundary conditions, they are referred to as *comparison* functions and are called *admissible* functions if they only satisfy the geometrical or essential boundary conditions.

Brief Introduction to Expansion Theorem: The eigenfunctions $W_r(x)$ constitute a complete set in the sense that any comparison function $Y(x)$ can be expanded as a uniformly convergent series of the eigenfunctions as

$$Y(x) = \sum_{r=1}^{\infty} a_r W_r(x) \tag{4.177}$$

The coefficients a_r can be easily found by multiplying (4.177) by $\rho(x)W_s(x)$ and integrating over the domain and use the orthogonality condition with respect to mass operator (4.174) to arrive at:

$$a_r = \int_0^L \rho(x) W_r(x) Y(x) \mathrm{d}x \tag{4.178}$$

which is very similar to Fourier series expansion. Equations (4.177) and (4.178) form the fundamental basis of expansion theorem, using which the modal equations of motion can be derived. Hence, expanding based on this concept, the solution of vibration displacement $w(x,t)$ can be expressed as:

$$w(x,t) = \sum_{r=1}^{\infty} q_r(t) W_r(x) \tag{4.179}$$

in which the coefficients of the eigenfunctions $W_r(x)$ in (4.177) are expanded from constants to time-dependent terms. $q_r(t)$ are referred to as *generalized coordinates* or *modal coordinates*.

This expansion can be implanted at two stages in vibration problem of continuous systems; (1) after the step at which the partial differential equations of motion have been derived and implement this expansion to discretize equations, or (2) at the energy expressions derivation stage so as to reduce Hamilton's principle to Lagrangian equations and directly obtain the discretized equations of motion. These two cases are discussed next and appropriate techniques to handle each scenario are briefly reviewed.

Eigensolution and Discretization of Equations of Motion: To demonstrate this method, let's consider a simply supported Euler–Bernoulli beam with uniform properties which is governed by:

$$EI\frac{\partial^4 w(x,t)}{\partial x^4} + c\frac{\partial w(x,t)}{\partial t} + \rho\frac{\partial^2 w(x,t)}{\partial t^2} = p(x,t) \tag{4.180}$$

where c is the linear distributed damping material property and $p(x,t)$ is a distributed external force. Substituting expansion solution (4.179) into (4.180) results

$$\sum_{r=1}^{\infty}\left(EI\frac{\mathrm{d}^4 W_r(x)}{\mathrm{d}x^4}q_r(t) + cW_r(x)\dot{q}_r(t) + \rho W_r(x)\ddot{q}_r(t)\right) = p(x,t) \tag{4.181}$$

Or in indicial notation form

$$EI\frac{\mathrm{d}^4 W_r(x)}{\mathrm{d}x^4}q_r(t) + cW_r(x)\dot{q}_r(t) + \rho W_r(x)\ddot{q}_r(t) = p(x,t) \tag{4.182}$$

On the other hand, $W_r(x)$ are the eigenfunctions and satisfy the free and undamped vibration problem (4.128),

$$EI\frac{\mathrm{d}^4 W_r(x)}{\mathrm{d}x^4} = \omega_r^2 \rho W_r(x) \tag{4.183}$$

Now, substituting (4.183) into (4.182), premultiply the resulting expression by eigenfunction $W_s(x)$ and integrating over the domain while utilizing the orthogonality conditions between eigenfunction $W_r(x)$ and $W_s(x)$ yields

$$\omega_r^2\delta_{rs}q_r(t) + \frac{c}{\rho}\delta_{rs}\dot{q}_r(t) + \delta_{rs}\ddot{q}_r(t) = \frac{1}{\rho}\int_0^L W_s(x)\,p(x,t)\mathrm{d}x \tag{4.184}$$

Using the property of Kronecker delta in indicial notation expressions revealed in Example A.3, (4.184) can be easily simplified to:

$$\ddot{q}_r(t) + 2\zeta_r\omega_r\dot{q}_r(t) + \omega_r^2 q_r(t) = Q_r(t), \quad r = 1, 2, \ldots \tag{4.185}$$

where modal damping ratio ξ_r and generalized force $Q_r(t)$ are defined as:

$$\zeta_r = \frac{c}{2\rho\omega_r}, \quad Q_r(t) = \frac{1}{\rho}\int_0^L W_r(x)\,p(x,t)\mathrm{d}x \tag{4.186}$$

Equation (4.185) is in the form of a well-known system of decoupled equations for MDOF systems (2.39) with the solution given by the following convolution integral

$$q_r(t) = \int_0^t Q_r(\tau)g_r(t-\tau)\mathrm{d}\tau = \frac{1}{\rho}\int_0^t \left(\int_0^L W_r(\lambda)\,p(\lambda,\tau)\mathrm{d}\lambda\right) g_r(t-\tau)\mathrm{d}\tau \tag{4.187}$$

where $g_r(t)$ is the impulse response function for a damped oscillator derived earlier in Sect. 2.2. To obtain the complete solution, (4.187) is substituted into the expansion form (4.179) to have:

$$w(x,t) = \sum_{r=1}^{\infty} W_r(x)q_r(t) = \frac{1}{\rho}\sum_{r=1}^{\infty} W_r(x)\left\{\int_0^t \left(\int_0^L W_r(\lambda)\,p(\lambda,\tau)d\lambda\right) \times g_r(t-\tau)d\tau\right\} \tag{4.188}$$

Equation (4.188) is the complete zero-state response solution. If the transient response to nonzero initial conditions is required, then it must be added to this solution in a similar manner as SDOF systems (see Sect. 2.2).

Assumed Modes Methods: As mentioned earlier in the introduction part of this subsection, when eigenfunctions are difficult to obtain for a given problem, the trial functions either in the form of comparison or admissible functions can be utilized. For this, we extend the expansion solution (4.179) to replace the eigenfunctions W_r with trial functions Ψ_r as

$$w(x,t) = \sum_{r=1}^{\infty} q_r(t)\Psi_r(x) \tag{4.189}$$

where the restriction on self-adjointness on mass or stiffness operators can be relaxed in order to apply this powerful method to such problems including systems with nonproportional damping or even nonlinear PDE. The solution (4.189) is referred to as *Galerkin Approximation*. While the convergence of the solution (4.189) can be guaranteed when the number of trial functions, and accordingly generalized coordinates, is infinity, the problem becomes practically difficult to deal

with. Hence, we resort to a truncated version of this solution, the so-called *assumed mode method* (AMM):

$$w(x,t) = \sum_{r=1}^{n} q_r(t)\Psi_r(x) \tag{4.190}$$

where a finite number of modes (or terms) is considered instead of infinitely many in (4.189). In order to demonstrate the applicability of this method, and at the same time, provide an example case study regarding implementing this discretization at the energy expressions level, we will consider the following example.

Example 4.9. Derivation of equations of motion for transverse vibration of beams using assumed mode method.

Consider an undamped Euler–Bernoulli beam under conventional boundary conditions and derive the equations of motion using AMM and Lagrangian approach.

The kinetic and potential energies for this beam can be written as (see (4.69) and (4.71))

$$T = \tfrac{1}{2}\int_0^L \rho(x)\left(\frac{\partial w(x,t)}{\partial t}\right)^2 \mathrm{d}x,\; U = \tfrac{1}{2}\int_0^L EI(x)\left(\frac{\partial^2 w(x,t)}{\partial x^2}\right)^2 \mathrm{d}x \tag{4.191}$$

Now, substituting solution (4.190) for $w(x,t)$ into energy expressions (4.191), while using indicial notation convention, (4.191) is expanded to:

$$\begin{aligned} T &= \tfrac{1}{2}\int_0^L \rho(x)\left(\Psi_r(x)\dot{q}_r(t)\right)\left(\Psi_s(x)\dot{q}_s(t)\right)\mathrm{d}x \\ &= \tfrac{1}{2}\dot{q}_r(t)\dot{q}_s(t)\int_0^L \rho(x)\Psi_r(x)\Psi_s(x)\mathrm{d}x = \tfrac{1}{2}\dot{q}_r(t)\dot{q}_s(t)m_{rs} \end{aligned} \tag{4.192a}$$

$$\begin{aligned} U &= \tfrac{1}{2}\int_0^L EI(x)\left(\Psi_r''(x)q_r(t)\right)\left(\Psi_s''(x)q_s(t)\right)\mathrm{d}x \\ &= \tfrac{1}{2}q_r(t)q_s(t)\int_0^L EI(x)\Psi_r''(x)\Psi_s''(x)\mathrm{d}x = \tfrac{1}{2}q_r(t)q_s(t)k_{rs} \end{aligned} \tag{4.192b}$$

where m_{rs} and k_{rs} are self-explanatory in (4.192) and referred to as generalized mass and stiffness coefficients, respectively.

The work of external force $p(x,t)$, using indicial notation, can also be easily calculated as:

$$\delta W^{\text{ext}} = \int_0^L p(x,t)\delta w(x,t)\mathrm{d}x = \int_0^L p(x,t)\delta\left(\Psi_r(x)q_r(t)\right)\mathrm{d}x$$
$$= \int_0^L p(x,t)\Psi_r(x)\delta q_r(t)dx = \delta q_r(t)\int_0^L p(x,t)\Psi_r(x)dx = \delta q_r(t)Q_r(t) \tag{4.193}$$

where generalized force $Q_r(t)$ is self-explanatory in (4.193).

Now that both kinetic and potential energies as well as virtual work of external force $p(x,t)$ have been derived based on generalized coordinate $q_r(t)$, one can resort to Lagrangian equation (3.70) as

$$\frac{\mathrm{d}}{\mathrm{d}t}\left(\frac{\partial T}{\partial \dot{q}_r}\right) - \frac{\partial T}{\partial q_r} + \frac{\partial U}{\partial q_r} = Q_r(t), \quad r = 1,2,\ldots,n \tag{4.194}$$

Substituting (4.192) and (4.193) into Lagrangian (4.194) leads to the following n coupled differential equations of motion.

$$\mathbf{M}\ddot{\mathbf{q}}(t) + \mathbf{K}\mathbf{q}(t) = \mathbf{Q}(t), \quad r = 1,2,\ldots n \tag{4.195}$$

where $\mathbf{q}(t)$ is a column vector containing generalized coordinates $q_r(t)$, i.e., $\mathbf{q}(t) = \{q_1(t)\ q_2(t)\ \cdots\ q_n(t)\}^{\mathrm{T}}$, $\mathbf{Q}(t) = \{Q_1(t) \quad Q_2(t)\ \cdots\ Q_n(t)\}^{\mathrm{T}}$ is the vector of generalized forces, and $\mathbf{M}$ and $\mathbf{K}$ are the generalized mass and stiffness matrices defined as $\mathbf{M} = \{m_{rs}\} \in \mathbb{R}^{n\times n}$ and $\mathbf{K} = \{k_{rs}\} \in \mathbb{R}^{n\times n}$, respectively, with m_{rs} and k_{rs} defined earlier in (4.192).

It is now straightforward to apply the general procedure developed for the MDOF systems in Sect. 2.3 to the discretized set of equations (4.195). Whether the mass or stiffness matrices are symmetric or not, or whether the system is classically damped or has nonproportional damping makes no difference in the overall procedure as all these conditions can be handled as shown in Sect. 2.3.

Convergence Issues: As mentioned earlier, for an exact representation of solution to the boundary value problem of distributed-parameters systems, an infinitely many number of trial functions are needed in expansion form (4.189). However, this is not possible in practice and one shall resort to a reduced order or truncated version (4.190). Such approximated solution and finite series of trial functions is mathematically equivalent to placing constraints on a distributed-parameters system. That is, reducing the infinitely many degrees of freedom of a naturally continuous system to a finite number of degrees of freedom makes the system more constrained, and hence, stiffer with higher values of eigenvalues; hence, the exact eigenvalues are always lower bound to the approximate values.

The overall convergence of the solution, when utilizing the truncated version (4.190), depends on the type and the number of trial functions in the series. In general and as a rule of thumb, if an n number of trial functions are used, then it

is expected that the first $n/2$ of the eigenvalues are fairly accurate. However, the number of accurate eigenvalues reduces when simple polynomials-type are used.

Summary

Through this important chapter, we provided readers with a unified approach to vibrations of distributed-parameters systems using an energy-based modeling approach. After a brief overview of work–energy relationship and Hamilton's principle, the differential equations of a deformable body in 3D were presented, in which both strain–displacements as well as strain–stress relationships were established. To demonstrate the effectiveness of the modeling framework, a select number of illustrative examples from vibration of continuous systems including longitudinal vibration of bars, transverse vibrations of beams and plates were presented. These example case studies were purposefully selected as most piezoelectric-based actuators and sensors discussed in the subsequent chapters could be modeled using these systems. The materials presented in this chapter shall form the basis for the subsequent modeling and control developments for both piezoelectric-based systems and vibration-control systems discussed in Chaps. 8 and 9, respectively.

Exercises[7]

4.1. Equilibrium State and Kinematics of a Deformable Continuum

4.1. The differential equations of equilibrium of a deformable continuum are expressed as:

$$\frac{\partial \sigma_{xx}}{\partial x} + \frac{\partial \tau_{xy}}{\partial y} + \frac{\partial \tau_{xz}}{\partial z} + F_x = 0$$

$$\frac{\partial \tau_{yx}}{\partial x} + \frac{\partial \sigma_{yy}}{\partial y} + \frac{\partial \tau_{yz}}{\partial z} + F_y = 0$$

$$\frac{\partial \tau_{zx}}{\partial x} + \frac{\partial \tau_{zy}}{\partial y} + \frac{\partial \sigma_{zz}}{\partial z} + F_z = 0$$

[7] The exercises denoted by asterisk (∗) refer to problems that require extensive use of numerical solvers such as Matlab/Simulink.

where σ_{pq} or τ_{pq} denotes the stress components and F_x, F_y, and F_z are the components of the body force $\mathbf{F}$. By substituting coordinate system xyz with $x_1x_2x_3$, represent these equations using a single expression in indicial notation convention.

4.2. Assume that the position vectors of a deformable continuum in Cartesian coordinate $x_1x_2x_3$ in undeformed and deformed states are denoted as $\mathbf{X} = \{X_1 \quad X_2 \quad X_3\}^{\mathrm{T}}$ and $\mathbf{x} = \{x_1 \quad x_2 \quad x_3\}^{\mathrm{T}}$, respectively. Now, expand the following complete differentials written in the indicial notation.

$$dX_m = \frac{\partial X_m}{\partial x_j} dx_j, \quad m, j = 1, 2, 3$$

Hint: Note that $\mathbf{X} = \mathbf{X}(\mathbf{x}, t)$.

4.3. If the deformed and undeformed position vectors of the continuum in Exercise 4.2 can be represented in terms of displacement variables $u_m = x_m - X_m$, $m = 1, 2, 3$, then expand the complete differentials $\mathrm{d}X_m$ of Exercise 4.2 by substituting $X_m = x_m - u_m$.

4.4. Using the property of Kronecker delta in indicial notation expressions, simplify the following expression

$$A = \left(\delta_{mi} - \frac{\partial u_m}{\partial x_i}\right)\left(\delta_{mj} - \frac{\partial u_m}{\partial x_j}\right), \quad m, ij = 1, 2, 3$$

4.2. Virtual Work of a Deformable Body

4.5. Let's revisit Exercise 3.6 in which the following Lagrangian functional L was considered.

$$L = \int_0^\ell \frac{\rho A}{2}\left(\frac{\partial u}{\partial t}\right)^2 \mathrm{d}x - \int_0^\ell \frac{AE}{2}\left(\frac{\partial u}{\partial x}\right)^2 \mathrm{d}x + \int_0^\ell f\, u\, \mathrm{d}x + F\, u(\ell, t)$$

This functional corresponds to axial vibration of a bar with $u(x, t)$ being axial displacement.

(a) Find the first variation of the functional L with

$$\delta u(0, t) = \delta u\,(x, t_1) = \delta u\,(x, t_2) = 0.$$

(b) Derive the equations of motion for the conditions given in part (a).

Hint: The boundary condition at $x = \ell$ is not fixed.

4.6. Consider a nonuniform bar of cross-sectional area $A(x)$ and length l which is subjected to an axially distributed load $p(x)$ as well as axial temperature distribution

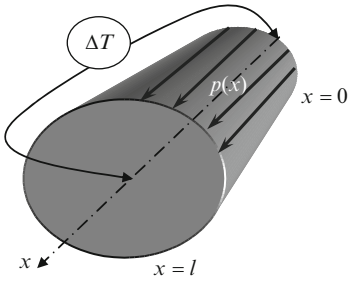

Fig. 4.17 Nonuniform bar subjected to axial load and temperature distribution

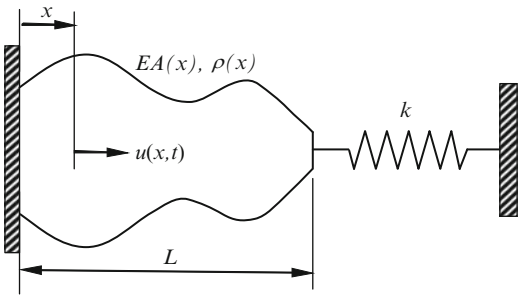

Fig. 4.18 An axially vibrating nonuniform bar clamed at one end and attached to a discrete spring at the other end

$\Delta T = T(x) - T_0$, as shown in Fig. 4.17. Derive the differential equation of motion for the bar in terms of axial displacement $u(x, t)$.
Hint: Use the general equation of virtual work for a deformable body in equilibrium (the results of (4.40) for 1D stress/strain relationship $S_{xx} = \frac{\partial u}{\partial x} = \frac{\sigma}{E(x)} + \alpha\, \Delta T(x)$, where α is the coefficient of thermal expansion).

4.3. Illustrative Examples from Vibration of Continuous Systems

4.7. Using the variational principle, derive the equations of motion and boundary conditions of the axially vibrating nonuniform bar shown in Fig. 4.18. The following properties hold: $E\ A(x) = E\ A\ (1 - x/L)$, and $\rho(x) = \rho\ (1 - x/L)$ (ρ is measured as mass per until length). Reduce your derivations for the case where $k = 0$.

4.8. Many vibrating beams may undergo both lateral and axial loadings. Our interest in this problem lies in establishing the added effect of the axial force on the equation of motion of a laterally vibrating beam. To highlight this effect, we are adopting the Euler–Bernoulli assumptions with general boundary conditions. To formulate the problem, consider the simple transverse vibration of a beam when subjected to a varying axial load $Q(x)$ and derive the equations of motion and the associated general (conventional) boundary conditions.

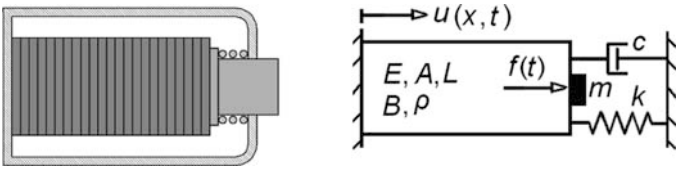

Fig. 4.19 Piezostack stage (*left*) and its rod-like representation (*right*)

Hint: Start with calculating the strain energy, and note the additional moment term due to the axial force when relating the internal (induced) bending moment to the transverse deflection.

4.9. Figure 4.19 depicts a typical piezostack flexural stage configuration utilized in many nanopositioning systems. $u(x,t)$ is the axial displacement; ρ, E, A, B, and L are the mass per unit length, Young modulus of elasticity, cross-sectional area, structural damping, and length of the stage, respectively; m, c, and k represent the inertia, damping, and stiffness of the boundary elements, respectively. Since the stack is prestressed by the spring at its boundary, the layers do not separate during the operation. Hence, it can be considered as a uniform bar structure with mass-spring-damper boundary condition. The excitation force $f(t)$ acting at the boundary is generated through the piezostack actuator (stage).

(a) Derive the governing partial differential equation and the boundary conditions for this system.
(b) To overcome the problem of nonhomogeneous boundary condition at $x = L$, apply a change of variable to homogenize the boundary condition in order for it to become appropriate for the subsequent separation of variables.
(c) Alternative to Part (b), an infinitely small equivalent distribution of force $f(t)$ can be used in the partial differential equation to produce a homogeneous boundary condition.

Hint: Use the dirac Delta function to generate a distributed forcing function which is applied to the equation of motion.

4.10. Use extended Hamilton principle to derive the boundary conditions for the transversally vibrating thin beams of Fig. 4.20(a–c).

4.11. To demonstrate the importance of boundary conditions, consider the effect of the degree of fixity of the supports. As mentioned in Remark 4.6, conventional boundary conditions are defined as fixed, hinged, or free. However, in practice, the ideal clamped or fixed boundary conditions become somewhere between fixed and hinged as shown in Fig. 4.21 (Olgac and Jalili 1998). Considering the Euler–Bernoulli beam theory, develop the equations of motion for the transversally vibrating beam shown in Fig. 4.21 and derive, directly using extended Hamilton principle, the associated boundary equations.

4.12. Most of the boundary conditions considered in this section were homogeneous. As a well-known fact, for nonhomogeneous boundary conditions, the separation of

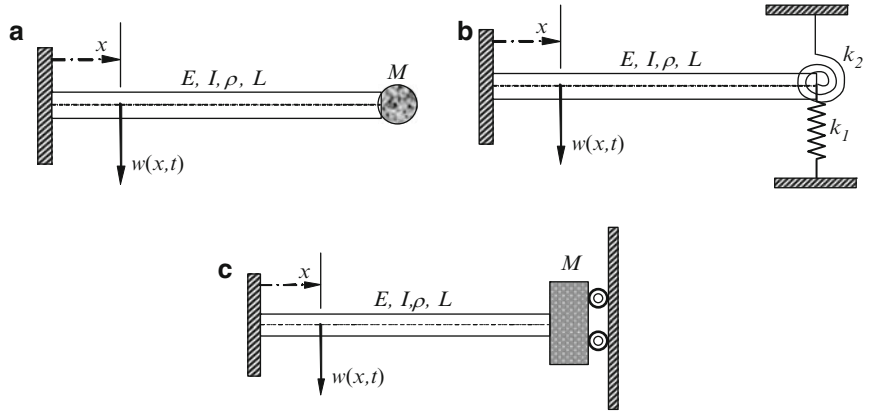

Fig. 4.20 Transversally vibrating beam with (**a**) end mass, (**b**) elastic supports and (**c**) end roller

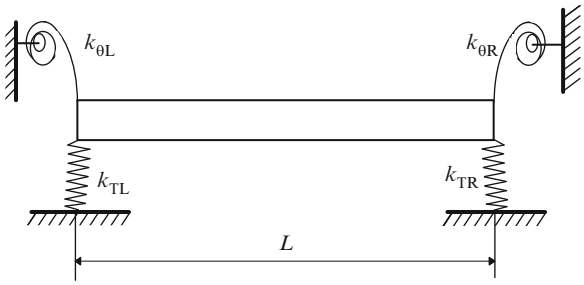

Fig. 4.21 Beam with elastic boundaries

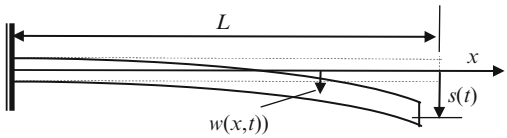

Fig. 4.22 Cantilever beam subject to nonharmonic displacement at the free end

variables fails not in the equation of motion but rather in the boundary conditions (Benaroya 1998, Jalili et al. 2004). A remedy to this is to transform the original homogeneous differential equation with nonhomogeneous boundary condition into a nonhomogeneous differential equation with homogeneous boundary conditions that can be solved by modal analysis techniques. Consider a cantilever beam subjected to an arbitrary transverse time-dependent displacement ($w(L,t) = s(t)$) at the free end (see Fig. 4.22).

(a) Assuming that beam obeys Euler–Bernoulli theory, derive the equations of motion and associated boundary conditions using energy method. Assume zero initial conditions.

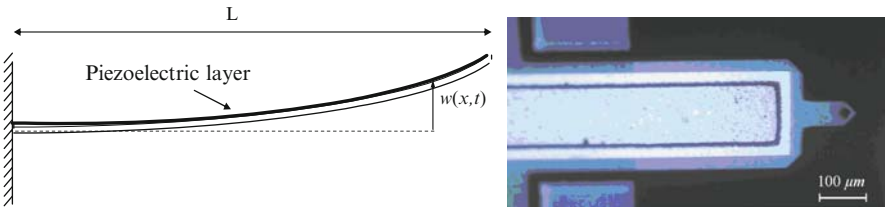

Fig. 4.23 Schematic of the flexible beam covered with piezoelectric patch actuator (*left*), and actual image of a piezoelectrically driven microbeam under microscope covered with ZnO actuator layer (right)
Source: Salehi-Khojin et al. 2008, with permission

(b) Using the transformation $w(x,t) = z(x,t) + s(t)\ g(x)$, convert the original equations of motion and show that the boundary conditions can become homogeneous in the new transformed coordinate $z(x,t)$. Select a polynomial-type function for $g(x)$ and give its detailed expression.
(c) Alternative to method (b), use the Laplace transformation and try to transform the boundary conditions into Laplace domain and give direction on how to solve for eigenfrequencies and eigenfunctions. See a similar treatment for a vibrating gyroscopic system in Esmaeili et al. (2007).

4.13. Consider a uniform flexible cantilever beam with a piezoelectric actuator bonded on its top surface. As shown in Fig. 4.23, one end of the beam is free and the other end is vertically clamped into a fixed base. The beam has total thickness t_b, width b, and length L, while the piezoelectric film possesses thickness t_p and the same length as beam. The piezoelectric actuator is perfectly bonded on the beam. Using the Euler–Bernoulli beam theory for the beam, one can extend the stress/strain relationship within the beam layer

$$\sigma_x = E_b S_x$$

to the following relationship within the piezoelectric layer as (Dadfarnia et al. 2004a,b)

$$\sigma_x = E_p S_x - E_p d_{31} \frac{V_a(t)}{t_p}$$

where E_b is the beam Young's modulus of elasticity, E_p is the piezoelectric Young's modulus of elasticity, d_{31} is the piezoelectric constant, and $V_a(t)$ is the applied voltage to piezoelectric layer. Using the Hamilton's principle, derive the governing dynamics for the system and the associated boundary conditions.

4.4. Eigenvalue Problem in Continuous Systems

4.14. In many practical applications, a continuous system may interact with discrete damping elements (e.g., support points of structures). Consider a uniform bar fixed at one end, and having an external damper c at the other end (see Fig. 4.24).

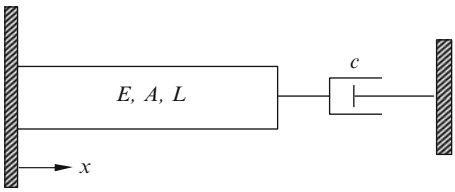

Fig. 4.24 An axially vibrating uniform bar clamped at one end and attached to a discrete damper at the other end

(a) Using the variational principle, derive the equation of motion and associated boundary conditions.
(b) Using the concept of separation of variables, i.e., $u(x,t) = U(x)T(t)$, obtain the frequency equation for this system.
(c) Assume $c = 0$ and $c \to \infty$ and reduce your frequency equation obtained in Part (b) to the standard fixed-free and fixed-fixed bar vibrations, and crossverify your frequency equation.
(d) For the following numerical values;

$$L = 2\,\text{m},\ \rho = 1\,\text{kg/m}^3,\ E = 10^6\,\text{Pa},\ A = 0.025\,\text{m}^2$$

numerically solve the frequency equation (obtained in Part b) and determine the eigenfrequencies for the following three damping coefficients: $c = 5\,\text{kg/sec}$, $c = 10\,\text{kg/sec}$, and $c = 25\,\text{kg/sec}$. Explain physically what is happening when $c = 25\,\text{kg/sec}$. Do you obtain any values for the natural frequencies for this value of c? Why?

4.15. Revisit Exercise 4.14 where a uniform bar was fixed at one end and attached to an external damper c at the other end (see Fig. 4.24).

(a) Show that the equation of motion and the associated boundary conditions can be expressed as.

$$\rho\frac{\partial^2 u(x,t)}{\partial t^2} - EA\frac{\partial^2 u(x,t)}{\partial x^2} = 0,\ u(0,t) = 0,\ EA\frac{\partial u(L,t)}{\partial x} = -c\frac{\partial u(L,t)}{\partial t}$$

(b) Alternative to the approach you adopted for taking into account the effect of discrete damping c in the equation of motion, use the method described in Exercise 4.9c to replace the damping term in the boundary condition with a distributed force applied to the equation of motion.
(c) Now, use the expansion theorem to assume the following solution for the displacement $u(x,t)$

$$u(x.t) = \sum_{i=1}^{n} U_i(x)q_i(t)$$

where $U_i(x)$ and $q_i(t)$ are the i-th eigenfunction and generalized coordinate, respectively. Substitute this solution into the equation of motion modified in Part (b) and

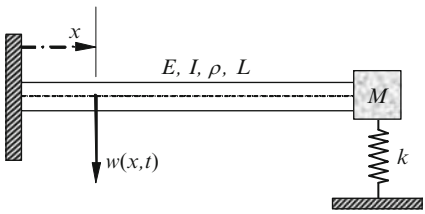

Fig. 4.25 Transversally vibrating beam with end mass and supported on linear spring

use the orthogonality conditions to arrive at an ODE for the generalized coordinates $q_i(t)$.

4.16. Derive the orthogonality relationship of the normal modes, $W_i(x)$ and $W_j(x)$, for a transversally vibrating uniform beam clamed at one end and carrying tip mass M and supported by linear spring k at the other end (see Fig. 4.25).

Part II
Piezoelectric-Based Vibration-Control Systems

This second part of the book presents the fundamentals of piezoelectric-based systems with an emphasis to their constitutive modeling, followed by vibration absorption and control techniques using piezoelectric actuators and sensors. The five chapters in this part are organized as follows. The first chapter in this part (Chap. 5) provides a brief introduction to active materials utilized in smart structures. The working principles along with the constitutive equations are briefly reviewed for these materials, followed by their practical applications and representative examples of both natural and synthetic materials. Specifically, the following materials are covered in this section: piezoelectric and pyroelectric materials, electrorheological and magnetorheological fluids, electrostrictive and magnetostrictive materials, and shape memory alloys. The second chapter in this part (Chap. 6) provides an overview and more detailed discussion on physical principles and constitutive models of piezoelectric materials. Starting with an elementary level in fundamentals of piezoelectricity, this chapter transitions into constitutive models of piezoelectric materials, their hysteresis and other nonlinear characteristics, and finally their engineering applications with an emphasis to piezoelectric-based actuators and sensors. Chapter 7 provides a brief, but self-contained discussions for dealing with hysteresis and compensation techniques for this material-level nonlinearity. Chapter 8 presents the required material for dealing with piezoelectric-based systems modeling and control including both lumped-parameters and distributed-parameters representations. Building based on the material presented in this chapter, Chap. 9 presents what this book is about, i.e., vibration control using piezoelectric actuators and sensors. Benefiting from all the preceding sections, this chapter provides a comprehensive treatment for active vibration absorption as well as vibration control using piezoelectric materials for a variety of systems. The materials presented in this part shall form the basis for the advanced topics in piezoelectric-based micro/nano actuators and sensors discussed in Part III of the book.

Chapter 5
An Overview of Active Materials Utilized in Smart Structures

Contents

5.1 Piezoelectric Materials 116
5.1.1 Piezoelectricity Concept 116
5.1.2 Basic Behavior and Constitutive Models of Piezoelectric Materials 116
5.1.3 Practical Applications of Piezoelectric Materials 118
5.2 Pyroelectric Materials 119
5.2.1 Constitutive Model of Pyroelectric Materials 119
5.2.2 Common Pyroelectric Materials 120
5.3 Electrorheological and Magnetorheological Fluids 120
5.3.1 Electrorheological Fluids 120
5.3.2 Magnetorheological Fluids 121
5.4 Shape Memory Alloys (SMAs) 123
5.4.1 SMA Physical Principles and Properties 123
5.4.2 Commercial Applications of SMAs 124
5.5 Electrostrictive and Magnetostrictive Materials 125
5.5.1 Electrostrictive Materials 125
5.5.2 Magnetostrictive Materials 126
Summary

This chapter provides a brief overview of working principles, physical properties, constitutive models and the practical applications of a few select active materials as the building blocks of many smart structures. More specifically, the following active materials are discussed in this chapter: piezoelectric and pyroelectric materials, electrorheological and magnetorheological fluids, electrostrictive and magnetostrictive materials, and finally shape memory alloys (SMA). In order not to disturb the focus of the book, only selective but essential materials are reviewed in this chapter. We refer interested readers to cited references and other dedicated books on smart materials and structures (e.g., Srinviasan and MacFarland 2001; Culshaw 1996; Gandhi and Thompson 1992; Banks et al. 1996; Clark et al. 1998; Suleman 2001; Leo 2007; Preumont 2002; Janocha 1999; Tzou and Anderson 1992; Gabert and Tzou 2001), vibration control (Moheimani and Fleming 2006; Gawronski 2004; Tao and Kokotovic 1996), sensors and actuators (Busch-Vishniac 1999) and piezoelectric (Yang 2005; Moheimani and Fleming 2006; Ballas 2007).

N. Jalili, *Piezoelectric-Based Vibration Control*,
DOI 10.1007/978-1-4419-0070-8_5,

© Springer Science+Business Media LLC 2010

While studying these and other active materials, piezoelectric materials stand out as the most commonly used active materials in many mechatronic and vibration-control systems, the areas that are of great importance to the subject of this book. Consequently, two separate chapters are dedicated to these materials and present, in much more detail, the concept of piezoelectricity and constitutive models of piezoelectric materials along with their practical applications as sensors and actuators (Chap. 6 and 7).

5.1 Piezoelectric Materials[1]

5.1.1 Piezoelectricity Concept

Piezoelectricity refers to an electromechanical phenomenon in particular solid-state materials that demonstrates a coupling between their electrical, mechanical, and thermal states generated by applying mechanical stress to dielectric crystals (Cady 1964). The word "piezo" originates from a Greek word meaning pressure. The first experimental demonstration of a connection between the macroscopic piezoelectric phenomenon and the crystallographic structure was reported in 1880 by Curie brothers (Curie and Curie, 1880). It was demonstrated that when these materials undergo mechanical deformation (stress/strain), an electric charge can be produced (direct effect). Conversely, when an electric field is applied to these materials, it results in mechanical stress or strain (converse effect). Such bidirectional application makes these materials ideal for use as both sensors (direct effect) and actuators (converse effects). These applications will be extensively discussed in Chap. 6.

5.1.2 Basic Behavior and Constitutive Models of Piezoelectric Materials

To better illustrate the basic behavior of piezoelectric materials, Figs. 5.1 and 5.2 schematically depict the piezoelectric effect in both axial (e.g., piezoceramics) and laminar (e.g., polymeric piezoelectrics) configurations, respectively. For clarity, the magnitude of deflections in both cases has been exaggerated. Figure 5.1a demonstrates when a compressive load is applied to piezoelectric materials, a positive voltage, for instance, is generated because of coupling between electrical and mechanical fields. Similarly, when a tensile force is applied, a voltage with reverse polarity is generated (see Fig 5.1b). On the actuation side, Fig. 5.2 demonstrates that

[1] As mentioned earlier, an extensive discussion about piezoelectricity and piezoelectric materials will be given in the next two chapters, and only a brief overview is presented here.

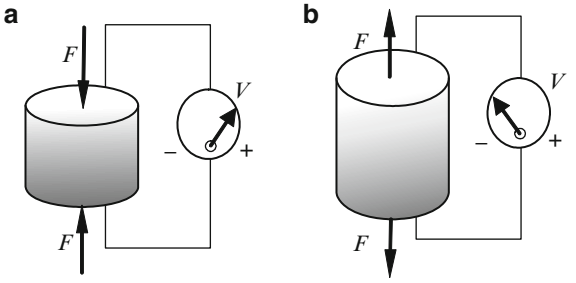

Fig. 5.1 Schematic of piezoelectric effect in axial configuration (e.g., piezoceramics)

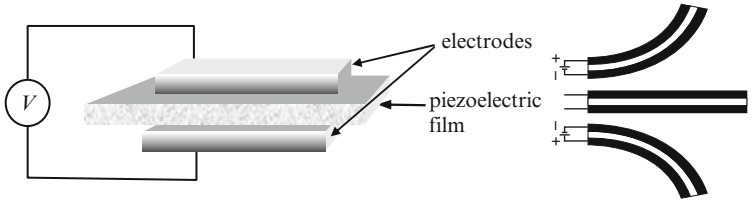

Fig. 5.2 Schematic of piezoelectric effect in laminar configuration (e.g., polymeric piezoelectric materials).

when a positive voltage is applied to a bender-type piezoelectric actuator, an upward bending is produced, again because of mechanical and electrical fields coupling. Application of a reverse voltage will produce the bending in the opposite direction.

Leaving much of the details to Chap. 6, it was discussed and shown briefly here that the behavior of piezoelectric materials involves the interaction between electrical and mechanical fields. From the elementary physics and under ideal case, the relationship[2] between dielectric displacement, D, in an unstressed linear medium under the influence of the electrical field ϵ can be given as:

$$D = \xi\epsilon \tag{5.1}$$

where ξ is the absolute dielectric permittivity of the medium in the units of Farads per meter [F/m]. On the other hand, the relationship between applied mechanical stress σ and the induced mechanical strain S in the same linear medium under zero electric field is:

$$S = s\sigma \tag{5.2}$$

[2] In order to maintain the focus of this chapter, we limit the derivations of the constitutive models to one-dimensional cases for all the active materials considered in this chapter. Otherwise, the required mathematical preliminaries and notations that must be covered for general three-dimensional medium will be very extensive and outside of the scope of this book.

where s denotes the compliance (simply speaking, inverse of the material stiffness) of the medium in the units of $\left[m^2/N\right] = C^{-1}$.

However, in piezoelectric materials there is a coupling between these interacting fields (mechanical and electrical). To a good approximation, this interaction can be represented by a linear relationship between these two fields. That is,

$$\begin{aligned} S &= s^{\epsilon}\sigma + d\epsilon \\ D &= d\sigma + \xi^{\sigma}\epsilon \end{aligned} \tag{5.3}$$

where d, which creates the electromechanical coupling in relationships (5.3), is referred to the so-called *piezoelectric charge constant*. This coupling is clearly observed by comparing the individual field equations (5.1) and (5.2) with the constitutive equation (5.3) for piezoelectric materials. The superscripts ϵ and σ in (5.3) imply that those quantities are measured at constant stress ($\sigma = 0$) or constant electric field ($\epsilon = 0$). It is worthy to note that the first equation in (5.3) represents the converse effect (i.e., actuation mechanism) while the second equation denotes the direct effect (i.e., sensing mechanism). The two equations in (5.3) can be combined in any particular way to yield a customized relationship between the field variables ϵ and σ and materials properties ξ and d. This process that can ease the derivation of equations of motion in piezoelectric actuators and sensors will be more elaborated and detailed in Chap. 6.

5.1.3 Practical Applications of Piezoelectric Materials

Piezoelectricity exists in materials either naturally or synthetically. Quartz, Rochelle salt, ammonium phosphate, paraffin, bone and even wood are some of the common natural piezoelectric materials. On the other hand, synthetic piezoelectric materials include, but not limited to, lead zirconate titanate ($PbZrTiO_3$–$PbTiO_3$, known as PZT), barium titanate, barium strontium titanate (BaSTO), lead lanthinum zirconate titanate (PLZT), lithium sulfate, and polyvinylidene fluoride (PVDF) and PVDF copolymers (Tzou et al. 2004). Most raw synthetic piezoelectric materials are naturally isotropic and do not have the dipole effect to produce piezoelectricity. Hence, they will have to go through an important process called *polling*, in which a strong electric field is applied to align the molecular dipoles in the materials. More details about this process and dipole alignment and orientation will be given in Chap. 6.

From structural viewpoint, piezoelectric materials could also be divided into ceramic and polymeric forms. The most popular piezoelectric ceramics are compounds of PZT, the properties of which can be optimized to suit specific applications by appropriate adjustment of the zirconate-titanate ratio. Their mechanical properties make them ideal for a variety of electromechanical transducers such as generators (e.g., spark ignition, solid-state batteries), sensors (e.g., accelerometers and pressure transducers), and actuators (e.g., pneumatic and hydraulic valves). Today, PZT ceramics are the most widely used of all ceramic materials because

of their excellent properties (Berlincourt 1981). Although much of the work carried out from the 1960s to present has been on developing applications for PZT materials, research activities continue into the development of new materials with exciting potential as piezoelectrics such as discovery of giant piezoelectric effect in strontium titanate ($SrTiO_3$) at very low temperatures (Damjanovic 1998), or recent piezoelectricity in boron nitride nanotubes (Mele and Kral 2002; Jalili 2003; Salehi-Khojin and Jalili 2008a,b; Salehi-Khojin et al. 2009a).

5.2 Pyroelectric Materials

In piezoelectric materials, a temperature change can also sometime affect materials' electric polarization, hence, temperature and mechanical fields can be coupled. This phenomenon is referred to as "pyroelectric" effect and defined as an instantaneous polarization of crystals in response to a temperature change (Tzou and Ye 1996). These materials are also referred to as "thermopiezoelectric" materials. Hence, it is safe to say that all pyroelectric materials are considered a subgroup of piezoelectric materials (Cady 1964).

5.2.1 Constitutive Model of Pyroelectric Materials

In order to obtain the constitutive model of linear pyroelectric materials, the induced mechanical strain in piezoelectric materials can be conveniently replaced by the temperature-induced strain in the medium. For this, we need to recast the first equation of piezoelectric constitutive model (5.3) such that the independent field variable σ can be written as a function of other variables. That is,

$$S = s^{\epsilon}\sigma + d\epsilon \rightarrow \sigma = \frac{1}{s^{\epsilon}}S - \frac{d}{s^{\epsilon}}\epsilon = c^{D}S - h^{T}\epsilon \tag{5.4}$$

where the new material properties in (5.4), i.e., elastic stiffness c^D and piezoelectric constant h, are self-explanatory. As these constants are seldom used in practice, they can be defined as quotients of other practical constants (see Chap. 6 for more details).

Now, replacing the mechanical strain S with $S - \alpha(\theta - \theta_0)$ in (5.4) yields the following constitutive model (converse effect)

$$\sigma = c^{D}S - h^{T}\epsilon - \lambda(\theta - \theta_0) \tag{5.5}$$

where $\lambda = c^{D}\alpha$ is the stress temperature module and α is the material's coefficient of thermal expansion (Mindlin 1961).

Although the model presented in (5.5) must be coupled with other constitutive relations such as heat flux and the balance of internal energy to arrive at the complete constitutive models for pyroelectric materials, we refer such expansions to the cited references. Our main objective from such brief introduction to the constitutive model in these materials is to demonstrate coupling of temperature gradient ($\Delta\theta = \theta - \theta_0$), electrical field ($\epsilon$) and mechanical field ($S$ or σ) which is clearly evident by inspecting (5.5).

5.2.2 Common Pyroelectric Materials

Common pyroelectric materials include triglycine sulfate, strontium barium niobate, lithium tantalate, PVDF and ceramic materials based on lead zirconate (Tzou et al. 2004; Porter 1981; Lang 1982; Tzou and Ye 1996). Similar to piezoelectric materials, the converse pyroelectricity is the creation of temperature differential using electrical field (Cady 1964). This property is referred to as *electrocaloric* effect. Although this is very small change for most pyroelectric crystals, it is considerable in some materials such as Rachelle salt. Pyroelectric-based structures and devices find applications in temperature related measurements and infrared detection (Dyer and Srinivasan 1989; Batt 1981; Hussain et al. 1995; Hofmann et al. 1991; Munch and Thiemann 1991).

5.3 Electrorheological and Magnetorheological Fluids[3]

5.3.1 Electrorheological Fluids

Electrorheological (ER) fluids are materials which undergo significant instantaneous reversible changes in material characteristics when subjected to electric potentials. The most significant change is associated with complex shear moduli of the material, and hence, ER fluids can be usefully exploited in many semi-active vibration-control systems and suspensions where variable rate dampers are utilized. These materials contain suspensions of micron size particles that can polarize and align themselves upon application of electric filed. This results in fluids that can change from a liquid to a solid-like structure almost instantly (Carlson et al. 1989). Originally, the idea of applying ER damper to vibration control has been initiated in automobile suspensions, followed by other applications (Petek et al. 1995; Austin 1993).

The flow motion of an ER fluid-based damper can be classified by shear mode, flow mode, or squeeze mode. However, the rheological properties (i.e., yield stress, plasticity and elasticity) of ER fluid are evaluated in the shear mode (Choi 1999).

[3] Most parts of this section may have come directly from our book chapter on the subject matter (Jalili and Esmailzadeh 2005).

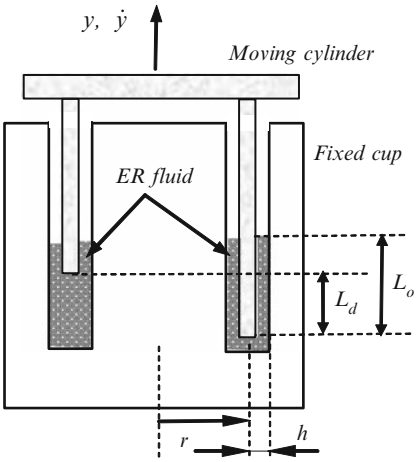

Fig. 5.3 A Schematic configuration of an ER damper

Under the electrical potential, the constitutive equation of an ER fluid damper has the form of Bingham plastic (Ginder and Ceccio 1995)

$$\tau = \eta\,\dot{\gamma} + \tau_y(\epsilon), \text{ and } \tau_y(\epsilon) = \alpha_1 \epsilon^{\alpha_2} \tag{5.6}$$

where τ is the shear stress, η is the fluid viscosity, γ is shear rate and $\tau_y(\epsilon)$ is the yield stress of the ER fluid which is a function of the electric filed ϵ. The coefficients α_1 and α_2 are intrinsic values, which are functions of particle size, concentration and polarization factors.

Consequently, the variable damping force in shear mode can be obtained as

$$F_{\text{ER}} = 4\pi r L_d \{\eta\,\dot{y}/h + \alpha_1 \epsilon^{\alpha_2}\,\text{sgn}(\dot{y})\} \tag{5.7}$$

where h is the electrode gap, L_d is the electrode length of the moving cylinder, r is the mean radius of the moving cylinder, $\dot{y}$ is the transverse velocity of the ER damper, and sgn $(\cdot)$ represents the signum function (see Fig. 5.3). As a result, the ER fluid damper provides an adaptive viscous and frictional damping for use in many engineering applications of vibration-control and suspension systems such as clutches, brakes, engine mounts and valves (Jalili 2001b; Wang et al. 1994; Dimarogonas-Andrew and Kollias 1993; Weiss et al. 1994; Duclos 1988; Carlson 1994).

5.3.2 Magnetorheological Fluids

Magnetorheological (MR) fluids are the magnetic analogs of ER fluid and typically consist of micron-sized, magnetically polarizable particles dispersed in a carrier

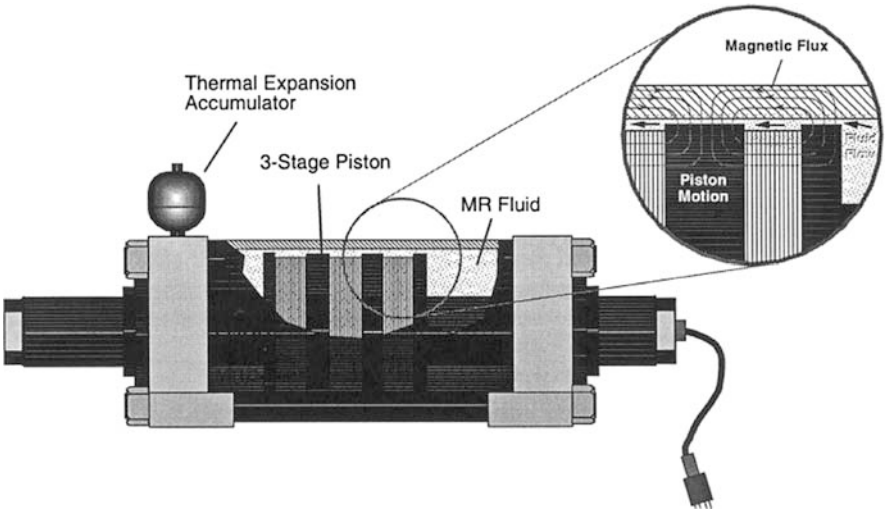

Fig. 5.4 A Schematic configuration of an MR damper
Source: Spencer et al. 1998, *with permission*

medium such as mineral or silicon oil. When a magnetic filed is applied, particle chains form and the fluid becomes a semi-solid, exhibiting plastic behavior similar to that of ER fluids (see Fig. 5.4). Transition to rheological equilibrium can be achieved in a few milliseconds, providing devices with high bandwidth (Spencer et al. 1998, Lord Corporation).

Similar to Bigham's plasticity model of (5.6), the behavior of controllable fluid is represented by

$$\tau = \eta \dot{\gamma} + \tau_y(H) \tag{5.8}$$

where H is the magnetic filed. Most devices that use MR fluids can be classified as having either fixed poles (pressure driven flow mode) or relatively movable poles (direct shear mode). In a like manner as ER dampers, the variable force developed by MR damper in direct-shear mode is

$$F_{\mathrm{MR}} = \eta\, A\, \dot{y}/h + \tau_y(H)A \tag{5.9}$$

where $\dot{y}$ is the relative pole velocity, $A = Lw$ is the shear (pole) area and the rest of the parameters are similar to those in ER notations used in Fig. 5.3.

The major difference between ER and MR fluids is in the level of applied field, that is, the ER fluids can only be activated by high-voltage and low-current electric fields, while MR fluids do not need the high voltage that ER fluids need since they respond to magnetic fields. This limits ER fluids utilization in engineering applications due to safety and packaging concerns. On the other hand, MR fluids can

produce much higher shear stress compared to ER fluids and exhibit very low shear resistance and hysteresis. As a result, they are more practical for use in many controllable applications of fluids such as active vibration isolation, shock absorbers and dampers (Tzou et al. 2004).

5.4 Shape Memory Alloys (SMAs)

5.4.1 SMA Physical Principles and Properties

These active materials undergo shape change and deformation when heated or cooled, coupling thermal and mechanical fields. When their temperature is raised above a certain point, they can be mechanically deformed significantly. If the applied heat is removed, the SMAs possess the ability to return to their original shape and state. At low temperature, the SMA crystalline structure exhibits a monoclinic lattice structure, called *martensite*, whereas when heated they have a strong cubic structure called *austenite* (see Fig 5.5). It is this different crystalline structure at low (martensite) and high (austenite) temperatures that produces the *shape-memory* effect (Tzou et al. 2004). In many SMAs, a temperature change of only about 10°C is enough to initiate the phase change between martensite and austenite crystalline structures.

The martensitic phase is relatively soft and can be easily deformed. Due to this relatively soft molecular structure at this phase (i.e., low temperature), the material tends to exhibit a self-accommodating behavior called "twinned" crystalline structure as shown in Fig. 5.6b. This molecular structure reorients or "detwins" when stress is applied and material is deformed (see Fig. 5.6c). When the material is heated, the reoriented martensitic phase will revert to austenitic phase, which is the stronger phase of SMA, and hence, the original shape of the material will be retained. Figure 5.7 depicts the entire process of transformation between high and low temperatures while also taking into account the effect of loading and unloading the materials. Instead of going through extensive modeling steps, we shall resort to this schematic (Fig 5.7) as the representative constitutive relationship between the crystallographic changes and stress-strain-temperature in SMA.

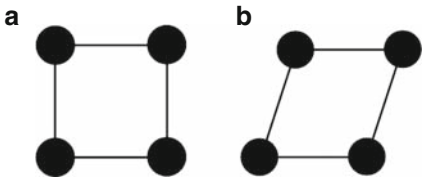

Fig. 5.5 Crystalline structure of SMA at: (**a**) high (austenite), (**b**) low (martensite) temperatures

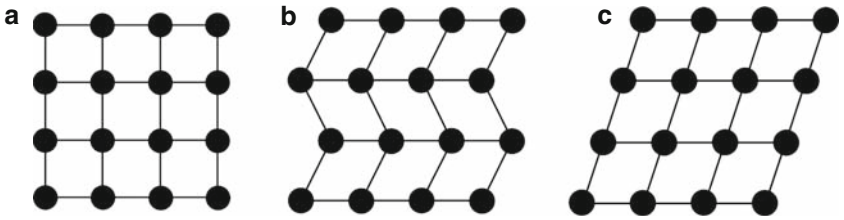

Fig. 5.6 Atomic rearrangement of SMAs at; (**a**) high temperature, (**b**) low temperature under no stress, and (**c**) low temperature when deformed

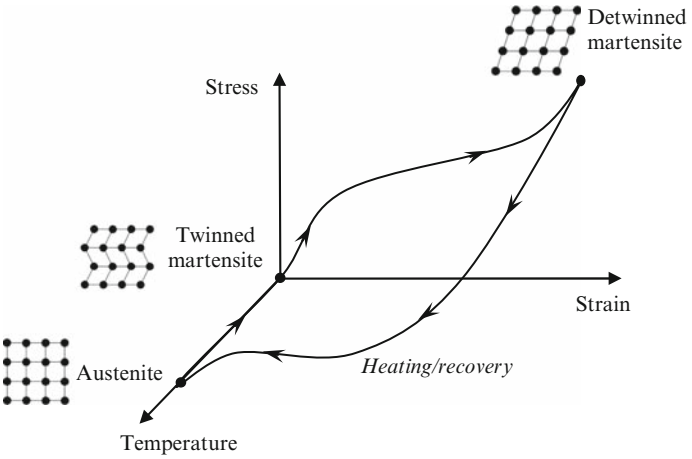

Fig. 5.7 Schematic of crystallographic changes and three-way relationship between stress, strain and temperature in shape memory effect

5.4.2 Commercial Applications of SMAs

The shape-memory effect was first observed in a sample of gold cadmium (AuCd) in 1932, and later in brass (copper–zinc) alloys in 1938. It was not until 1962 that researchers at Naval Ordinance Labs observed significant shape-memory effect in a series of nickel–titanium alloys. Today, nickel–titanium and its doped alloys, called Nitinol (NiTi) are considered as the most commercially known SMAs (Hodgoson 1988). Although the shape-memory effect is predominantly found in metal alloys, certain ceramics and polymeric materials possess this shape-memory effect. Leaving much of the details to the cited references, SMAs can be made into many shapes including especially straight wires, helical springs, torsion bars and wires, and beam-like structures for use in many engineering applications such as wing morphing, medical instruments, prosthetic members, shock absorber valve control, thermal expanders in automotives, and seals and fasteners (Suleman 2001).

5.5 Electrostrictive and Magnetostrictive Materials

5.5.1 Electrostrictive Materials

Electrostriction originates from mechanical strain induced through electric field, which in turn, resembles the converse piezoelectric effect in piezoelectric materials mentioned earlier in Sect. 5.1. In fact, both electrostriction and piezoelectricity phenomena belong to ferroelectric materials. However, the difference between electrostrictive and piezoelectric materials is in the nature and effect of electric and mechanical fields coupling. That is, in piezoelectric materials this coupling is a first-order effect, i.e., the strain is proportional to the electric field (see (5.3)), whereas in electrostrictive materials this effect is of secondary nature where the induced strain is proportional to the square of the electric field as shown in Fig. 5.8.

Due to nonlinear strain response and frequency-dependent nature of the electromechanical response in these materials, there exist a number of constitutive relationships for electrostrictive materials (Hu et al. 2000; Jiang and Kuang 2004; Bar-Cohen et al. 2001; Piquette and Forsythe 1998; Chen et al. 2001; Ren et al. 2002; Hu et al. 2004; Lee 1999). To maintain our briefness, we only present one of the most commonly used constitutive models for converse effect in electrostrictive materials as given by the following relationship:

$$S = s^{\epsilon}\sigma + d\epsilon + m\epsilon^2 \tag{5.10}$$

where m is the electrostrictive coefficient of the material in the units of $[m^2/V^2]$, and the rest of the variables are the same as piezoelectric constitutive model of (5.3). Similar to piezoelectric materials and without loss of generality, we limit the constitutive model to one-dimensional problem and leave the general cases to the cited references in this chapter. Depending upon the crystalline structure of the electrostrictive material, the dielectric polarization (the third term on right-hand side of (5.10)) may dominate the effect of piezoelectric (the second term on right-hand side

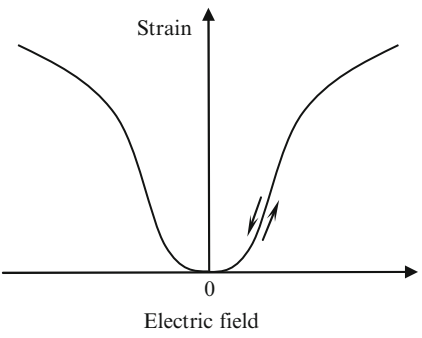

Fig. 5.8 Typical strain vs. electrical filed in electrostrictive materials

of (5.10)). Hence, the constitutive model for these materials reduces to

$$S = s^{\epsilon}\sigma + m\epsilon^2 \tag{5.11}$$

Due to the quadratic relationship between the induced strain and electric field in (5.11), the electrostrictive materials are always under tension (positive strain) irrespective of the polarity of the applied electric field. However, a bias voltage can be used in order to obtain bidirectional operation (tension and compression).

The electrostriction is typically present in dielectric materials due to strong piezoelectric effect in these materials; however, the magnitude of the strain is very small and not useful. This is due to the fact that the first-order piezoelectric effect almost masks the secondary effect of electrostriction. However, materials with high dielectric constants or polarizations such as relaxor ferroelectrics can possess very large electrostriction effect. Among all electrostrictive materials, the compounds of lead magnesium niobate, $Pb(Mg_{1/3}Nb_{2/3})O_3$ (PMN) and their solid state solutions with lead titanate, $Pb\left(Mg_{1/3}Nb_{2/3}\right)O_3$-$PbTiO_3$ (PMN-PT) are the most significant relaxor ferroelectrics and exhibit a strong electrostrictive effect. PMN and PMN-PT have high strain electrostrictive strain capabilities with very low hysteresis properties. These materials are capable of producing strains that are comparable to strains generated by PZT, while also possessing a negligible hysteresis. Due to these attractive properties, there has been a growing interest in utilizing these materials in precision actuators and displacement transducers such as high-power sonar transducers, deformable mirrors and optical systems (Chai and Tzou 2002; Tzou et al. 2003).

5.5.2 Magnetostrictive Materials

Magnetostrictive materials are magnetic analogs of electrostrictive materials and possess secondary (quadratic) effect, i.e., the induced strain is proportional to the square of applied magnetic field. Magnetostriction (magnetically induced strain) and its complementary effect, stress-induced magnetization, originate from the coupling between interatomic spacing and magnetic moment orientation (DeSimone and James 2002). Magnetostrictive materials possess magnetic anisotropy in their atomic structure, and therefore, they undergo dimensional changes when placed in magnetic fields as a result of reorientation of the atomic magnetic moments.

Understanding the physical principles and mechanism of magnetostriction at an atomic level might be relatively difficult, but the basic behavior of these materials can be better understood by a simple model as shown in Fig 5.9. Similar to orienting dipoles in piezoelectric materials through applying electrical field (see extensive discussions on this later in Chap. 6), magnetization of a magnetostrictive material can rotate and align the magnetic moments, and subsequently resulting in a deformation or shape change as shown in Fig. 5.9a. This effect can be increased by preloading the material before applying the magnetic field (see Fig. 5.9b). To benefit from

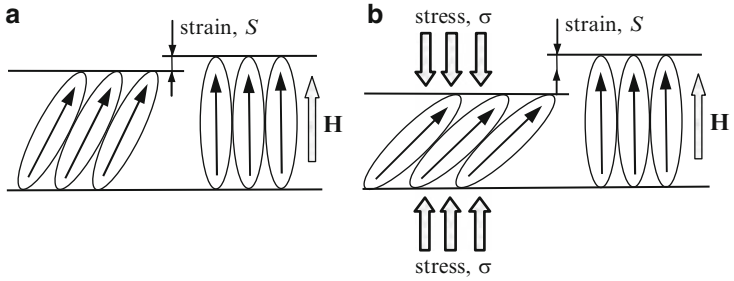

Fig. 5.9 Physical principle and basic operation of magnetostriction; (**a**) material under moderate or no preload, and (**b**) material under significant preload

this increased strain, most magnetostrictive-based actuators employ a preloading mechanism. Hence, the most common configurations for these actuators are rod or cylindrical element wrapped in an exciting coil (Suleman 2001).

Similar to electrostrictive materials, the one-dimensional constitutive model for converse effect in magnetostrictive materials can be represented as:

$$S = s^{\epsilon}\sigma + dH + mH^2 \tag{5.12}$$

where H is the magnetic field flux and m is the magnetostrictive coefficient of the material. As seen from constitutive model (5.12), the induced strain is always positive and independent of the direction of the applied magnetic field.

The first observation of magnetostriction was reported in nickel that exhibited microlevel strains. Later in 1972, an alloy made of terbium, dysprosium and iron generated large strains at room temperature and in the presence of only low magnetic fields. This alloy known as Terfelon-D can produce large forces, possesses fast and high-precision motion as well as high efficiency (Tzou et al. 2004). The only shortfalls of Terfelon-D are its flammability and brittleness. More recently, magnetostrictive Galfenol has been shown to possess key additional advantages; that is, unlike most active materials, Galfenol is malleable and machinable (Kellogg et al. 2004), and can be safely operated under simultaneous tension, compression, bending, and shock loads. As a consequence of the unique combination of metallurgical and mechanical properties of Galfenol, this material can enable smart load-carrying Galfenol devices and structures with innovative 3D manufactured by welding, extrusion, rolling, deposition, or machining. Furthermore, the unprescented control of anisotropies through manufacturing and post-processing methods made possible with Galfenol (Wun-Fogle et al. 2005) can lead to innovative devices with fully coupled 3D functionality (Wun-Fogle et al. 2006). Despite these advantages, Galfenol does exhibit magnetic saturation, magnetic hysteresis and magnetomechanical nonlinearities (Bashash et al. 2008c).

While studying these and other active materials, piezoelectric materials stand out as one of the most commonly used active materials. More specifically, with the widespread application of mechatronic concepts to dynamic systems in recent years,

interest has been focused on the substitution of piezoelectric materials (e.g., PZT) for conventional electrical motors and actuators (Jalili et al. 2003; Galvagni and Rawal 1991; Takagi 1996 and references therein). The properties of PZT materials, for instance, can be uniquely optimized to suit specific applications by appropriate adjustment of the zirconate-titanate ratio. Such capabilities make them ideal for a variety of electromechanical transducers such as generators (e.g., spark ignition, solid-state batteries), sensors (e.g., acceleration and pressure transducers), and actuators (e.g., pneumatic and hydraulic valves). Along this line, the rest of this book is dedicated to smart structures and systems made of piezoelectric materials in different forms and configurations. More detailed discussions and overview of piezoelectric materials and their applications in vibration-control systems will be given in Chap. 6–9.

Summary

This chapter presented a brief overview of physical principles and constitutive models of a few select active materials. These active materials, which form the building blocks of smart structures, were piezoelectric and pyroelectric materials, electrorheological and magnetorheological fluids, electrostrictive and magnetostrictive materials, and SMAs. After an easy-to-follow and single-source review style of these materials, piezoelectric materials, as the most commonly used active materials in many mechatronic and vibration-control systems, were selected to be studied in more detail. Through the following next chapters, we will present, in much more detailed and focused fashion, the concept of piezoelectricity and constitutive models of piezoelectric materials along with their practical applications as sensors and actuators used in a variety of vibration-control systems.

Chapter 6
Physical Principles and Constitutive Models of Piezoelectric Materials

Contents

6.1 Fundamentals of Piezoelectricity 130
6.1.1 Polarization and Piezoelectric Effects 130
6.1.2 Crystallographic Structure of Piezoelectric Materials 132
6.2 Constitutive Models of Piezoelectric Materials 134
6.2.1 Preliminaries and Definitions 134
6.2.2 Constitutive Relations 135
6.2.3 Nonlinear Characteristics of Piezoelectric Materials 139
6.3 Piezoelectric Material Constitutive Constants 140
6.3.1 General Relationships 140
6.3.2 Piezoelectric Coefficients 142
6.4 Engineering Applications of Piezoelectric Materials and Structures 148
6.4.1 Application of Piezoceramics in Mechatronic Systems 149
6.4.2 Motion Magnification Strategies for Piezoceramic Actuation 149
6.4.3 Piezoceramic-Based High Precision Miniature Motors 150
6.5 Piezoelectric-Based Actuators and Sensors 151
6.5.1 Piezoelectric-Based Actuator/Sensor Configurations 151
6.5.2 Examples of Piezoelectric-Based Actuators/Sensors 154
6.6 Recent Advances in Piezoelectric-Based Systems 156
6.6.1 Piezoelectric-Based Micromanipulators 156
6.6.2 Piezoelectrically Actuated Microcantilevers 156
6.6.3 Piezoelectrically Driven Translational Nano-Positioners 158
6.6.4 Future Directions and Outlooks 158
Summary

This chapter presents a detailed discussion on physical principles and constitutive models of piezoelectric materials and structures. Starting with an elementary level in the fundamentals of piezoelectricity, the constitutive models of piezoelectric materials are presented. To complete the chapter and provide the readers with practical information, the engineering applications of piezoelectric materials and structures with a special emphasis to piezoelectric-based actuators and sensors are presented. More specifically, the applications of piezoelectric actuators and sensors in ultrafine micro/nano-scale positioning and manipulation are reviewed briefly, leaving the details to Chaps. 10–12. Finally, a brief discussion on future directions and outlooks for piezoelectric materials and systems is given.

N. Jalili, *Piezoelectric-Based Vibration Control*,
DOI 10.1007/978-1-4419-0070-8_6,

© Springer Science+Business Media LLC 2010

6.1 Fundamentals of Piezoelectricity

6.1.1 Polarization and Piezoelectric Effects

As mentioned earlier, the word "piezo" originates from a Greek word meaning for pressure. Piezoelectricity refers to an electromechanical phenomenon in particular solid-state materials that relates macroscopic electric *polarization* to mechanical stress or strain. Electric polarization is generated when a dielectric material is placed in an electric field and microscopic charge redistribution between its molecules occurs (Yang 2005). Although microscopic polarization may occur differently and using different mechanisms (see, for example, electronic and orientational mechanisms shown in Fig. 6.1, Yang 2005), it does not result in different macroscopic polarization, **P**.

In certain materials, this macroscopic polarization can also be induced by means of mechanical deformation or loads, instead of crystallographic charge redistribution. The generated polarization can be in any direction depending on the material anisotropy (see Sect. 4.1.3), which could result in displacements of varying amplitude and direction. Utilizing this feature, a piezoelectric material can be manufactured in such a way that the resultant displacement can be selectively dominated in a specific direction. More details about this process will be given later in this chapter (see Sect. 6.2). Such a phenomenon in these materials, which is referred to as *direct piezoelectric* effect, was discovered in 1880 by Curie brothers, Pierre and Jacques, Fig. 6.2 (Curie and Curie 1880).

The Curie brothers experimentally observed that when these materials are subjected to a mechanical pressure, the crystals become electrically polarized. Subsequently, the tension and compression generate voltages of opposite polarity that are proportional to the applied force (see Fig. 6.3a). This relationship for the simple structure of Fig. 6.3a can be written as

$$V_s = -g\,(L/A)\,F \tag{6.1}$$

where g is referred to as the piezoelectric "voltage" or "charge" constant, and L and A are, respectively, the length and cross-sectional area of the structure measured along the poling direction (see Fig. 6.3).

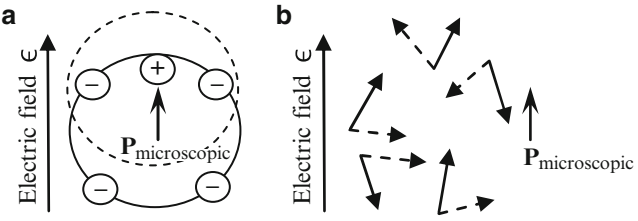

Fig. 6.1 Representative microscopic polarization mechanisms: (**a**) electronic, and (**b**) orientational (Yang 2005)

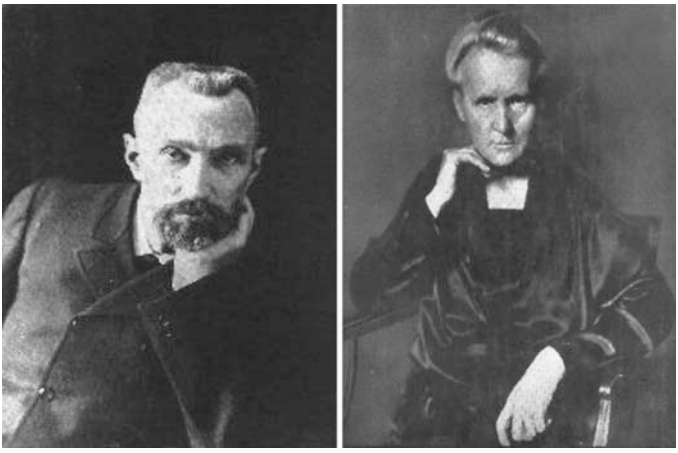

Fig. 6.2 Pierre and Jacques Curie (1880)
Source: http://www.piezoelectric.net

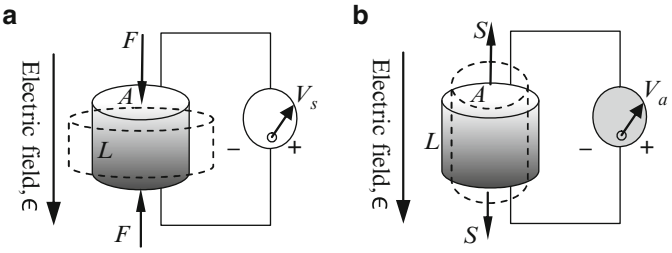

Fig. 6.3 Schematic demonstration of (**a**) direct, and (**b**) converse piezoelectric effects

It was verified later that when an electrical field is applied to a material possessing the direct piezoelectric effect, it leads to deformation of the material (see Fig. 6.3b). This effect is referred to as the *converse piezoelectric* effect. Similarly, for the simple one-dimensional structure of Fig. 6.3b, this relationship is expressed as

$$S = d(1/L)V_{\mathrm{a}} \tag{6.2}$$

where d is referred to as the piezoelectric "strain" constant.

As indicated in the configurations shown in Fig. 6.3, the electric field is parallel to the direction of polarization. As briefly mentioned in this section, the piezoelectric effect is anisotropic; hence, it exists only in materials with crystallographic asymmetry. The existence of this phenomenon in certain materials below a certain temperature (called Curie temperature) will be more discussed later in this chapter.

6.1.2 Crystallographic Structure of Piezoelectric Materials

As briefly mentioned in the preceding section, piezoelectric materials could be divided, from structural viewpoint, into ceramic and polymeric forms. The most popular piezoelectric ceramics (or in short, piezoceramics) are compounds of lead zirconate titanate (PZT), the properties of which can be optimized to suit specific applications by appropriate adjustment of the zirconate–titanate ratio. In order not to disturb our focus, only piezoceramics are discussed in this subsection. Other types of piezoelectric materials such as polymeric materials and composites will be discussed later in Sects. 6.4 and 6.5.

Piezoceramics typically have a tetragonal shape very close to cubic and are governed by the general formulation $A^{2+}B^{4+}O_3^{2-}$, where A denotes a large divalent metal ion such as lead or barium, B stands for a tetravalent metal ion such as zirconium or titanium, and O represents oxygen. Above a certain temperature, called the Curie temperature,[1] these materials have a symmetric cubic crystal structure as shown in Fig. 6.4a. Since the positive and negative charges coincide, the net charge induced dipole at microscale is zero resulting in no net macroscopic dipole. However, below the Curie temperature, the crystal structure of these materials becomes tetragonal (see Fig. 6.4b), resulting in a built-in microscopic electric dipole similar to the one shown in Fig. 6.1 ($\mathbf{P}_{\text{microscopic}}$); however, the net macroscopic electric dipole (Yang 2005)

$$\mathbf{P} = \lim_{\Delta V \to 0} \frac{\sum_{\Delta V} \mathbf{P}_{\text{microscopic}}}{\Delta V} \tag{6.3}$$

is still zero.

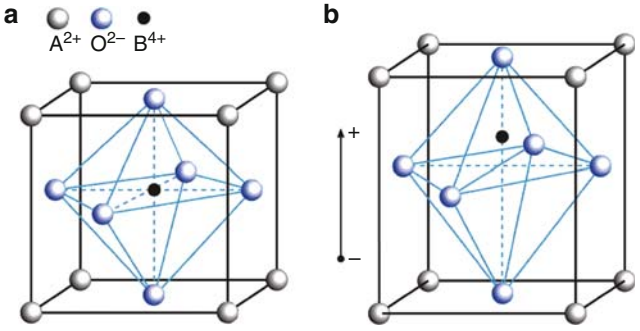

Fig. 6.4 Crystallographic structure of piezoceramics cell, (**a**) cubic lattice above Curie temperature, and (**b**) tetragonal lattice below Curie temperature
Source: Tutorial-Piezoelectrics in positioning contents, Physik Instrumente manual, www.pi.ws, with permission

[1] The Curie temperature is typically the result of a chemical process in the range of 300°C–400°C. While typically fixed, this range can be changed and tuned accordingly if needed.

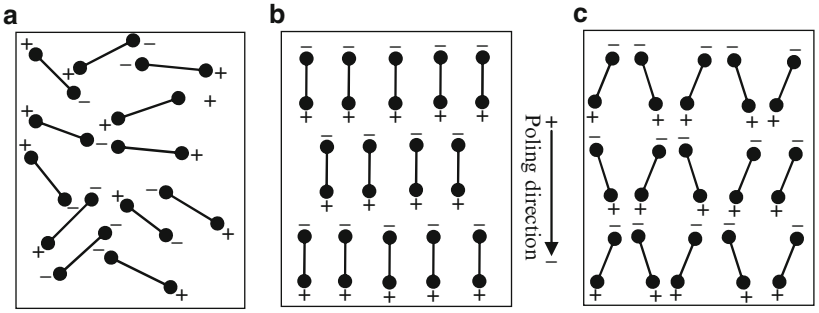

Fig. 6.5 Schematic representation of electric dipoles in *Weiss* domains: (**a**) before polarization, (**b**) during polarization, and (**c**) after polarization

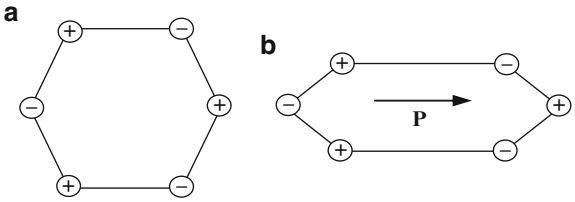

Fig. 6.6 Macroscopic polarization of a typical piezoelectric material when subjected to mechanical deformation: (**a**) before, and (**b**) after deformation

The dipoles in a material typically tend to form regions of local alignment, called *Weiss Domains*. Although within a domain, all the dipoles are aligned resulting in a net polarization, the neighboring *Weiss* domains within a crystalline differ by 90° or 180°, see Fig. 6.5a. Owing to random distribution of these Weiss domains throughout the material, no net polarization can be exhibited. However, when these materials are exposed to a strong field slightly below the Curie temperature, the dipoles tend to align to form regions of local alignment and leading to a non-zero macroscopic electric dipole (see Fig. 6.5b). After the removal of the electrical field, the dipoles cannot typically return to their original position, and give rise to what is refereed to as *remanent* polarization. In this case, permanent deformation occurs and the ceramic becomes anisotropic and permanently piezoelectric (see Fig. 6.5c) with the ability to lengthening when subjected to electric field (converse effect) or producing electric field when stressed or strained (direct effect). Figure 6.6 demonstrates an example of macroscopic polarization of a piezoelectric material when subjected to mechanical deformation.

Under the following severe conditions, a pizeoceramic can lose its piezoelectric effect; (1) application of a strong field in the opposite direction of polarization, (2) undergoing high mechanical stress resulting in distortion of dipoles alignment, and (3) heating the material above its Curie temperature. In most practical applications, the working temperature of piezoceramics is kept below half of the Curie temperature to avoid permanent damage to the material.

6.2 Constitutive Models of Piezoelectric Materials

Section 5.1.2 presented a brief overview of basic behavior of piezoelectric materials using elementary physics and under ideal case (5.1–5.3). This section provides a more detailed derivation of constitutive equations governing piezoelectric materials. To make the readers understand this better, we first provide some physical preliminaries, followed by 3D constitutive relations for a linear piezoelectric material in both the most general case and commonly used configurations in practical applications.

6.2.1 Preliminaries and Definitions

Electric charge and current intensity: The total accumulated charge Q for a continuum of volume V is defined as

$$Q = \int_V q \mathrm{d}V \tag{6.4}$$

where the total charge Q is measured in Coulombs (C) and q is the charge density in C/m^3. The current intensity, I, is defined as the rate of change of total charge Q as

$$I = \dot{Q} \tag{6.5}$$

Electric field: The electric field ϵ, the analog of a conservative force field in mechanics, can be related to electric potential φ, similar to the relationship between conservative potential function and force in mechanics, as

$$\boldsymbol{\epsilon} = -\vec{\nabla}\varphi \tag{6.6}$$

where the electric filed ϵ is measured in V/m.

Electric displacement: Similar to deformation of a continuum when subjected to a stress field,[2] when a continuum is subjected to an electric filed, charges undergo movement and redistribution, resulting in what is referred to as electric displacement. The total charge accumulated on the boundary of a continuum with volume V is given by

$$Q = \oint_{\partial V} \mathbf{D} \cdot \mathbf{n} \mathrm{d}A \tag{6.7}$$

where $\mathbf{D}$ is the electric displacement vector measured in C/m^2, and $\mathbf{n}$ is a unit vector normal to the boundary of continuum V (i.e., ∂V).

[2] $F = \oint_{\partial V} \boldsymbol{\sigma} \cdot \mathbf{n} \mathrm{d}A$, where $\mathbf{F}$ is the resulting force along vector $\mathbf{n}$ normal to surface, and $\boldsymbol{\sigma}$ is the stress vector.

Maxwell's equations: The application of Divergence theorem (A.8) to (6.7) and using the definition of total charge Q in (6.4) results into what is referred to as Maxwell equation:

$$q = \vec{\nabla} \cdot \mathbf{D} \triangleq \text{Div}\mathbf{D} \tag{6.8}$$

6.2.2 Constitutive Relations

Now that we have presented the necessary background materials in the preceding subsection, we would like to utilize our unified approach adopted in Chap. 4 (Sect. 4.2) to derive the electrical potential energy. This potential energy will be augmented with the developed strain energy (4.40) to form the total potential energy for piezoelectric materials, from which the constitutive equations will be derived.

The total electrical potential energy of the electrostatic filed ϵ (with potential φ), while neglecting losses, is equal to the work needed to move total charge Q in this field. This relationship in variational form can be simply given by

$$\delta U_{\text{e}} = \delta(\varphi Q) \tag{6.9}$$

where Ue is the total electric potential energy. Insertion of Maxwell's equation (6.8) for charge density q into the definition (6.4) for total charge Q, and substitution of the resultant expression in (6.9) yields

$$\delta U_{\text{e}} = \delta \int_V \varphi \, (\text{Div}\mathbf{D}) \, \text{d}V \tag{6.10}$$

Using the following relationship for divergence,

$$\text{Div}\,(\varphi\mathbf{D}) = \varphi \text{Div}\mathbf{D} + \mathbf{D} \cdot \vec{\nabla}\varphi \tag{6.11}$$

expression (6.10) can be rewritten as

$$\delta U_{\text{e}} = \delta \left(\int_V (\text{Div}\varphi\mathbf{D}) \, \text{d}V - \int_V \left(\mathbf{D} \cdot \vec{\nabla}\varphi \right) \text{d}V \right) \tag{6.12}$$

The application of divergence theorem on the first term in (6.12)[3] results in

$$\delta U_{\text{e}} = \delta \left(\oint_{\partial V} \varphi \mathbf{D} \cdot \vec{\mathbf{n}} \text{d}A - \int_V (\mathbf{D} \cdot \vec{\nabla}\varphi) \text{d}V \right) \tag{6.13}$$

[3] See a similar process for application of divergence theorem in Chap. 4 for (4.29–4.30).

Assuming either high-frequency applications or taking into account the fact that potential energy decreases at least with $1/r$ (where r is the distance) while also dielectric displacement D decreases at least with $1/r^2$ (Batra 2004; Ballas 2007), the first term in expression (6.13) can be safely ignored. Considering this fact and the definition of electric field $\boldsymbol{\epsilon}$ in (6.6), the electrical energy (6.13) reduces to

$$\delta U_e = \delta \int_V (\mathbf{D} \cdot \boldsymbol{\epsilon}) \mathrm{d}V \text{ or } \delta U_\mathrm{e} = \int_V (\boldsymbol{\epsilon} \cdot \delta \mathbf{D}) \mathrm{d}V \tag{6.14}$$

The electrical potential energy (6.14) can be recast in indicial notation form as

$$\delta U_\mathrm{e} = \int_V (\epsilon_i \delta D_i) \mathrm{d}V, \quad i = 1, 2, 3 \tag{6.15}$$

This electrical potential energy can now be augmented with the developed strain energy (4.41) to form the total potential energy as (Ballas 2007)

$$\delta U = \int_V \left(\sigma_p \delta S_p + \epsilon_i \delta D_i\right) \mathrm{d}V, \quad i = 1, 2, 3 \text{ and } p = 1, \ldots, 6 \tag{6.16}$$

Remark 6.1. It is clear that the total energy (6.16) does not take into account other coupled and interacting fields such as magnetomechanical, electromagnetic, thermoelectric, thermomagnetic, and thermomechanical couplings. As emphasized earlier, our primary objective here is to derive the constitutive relationships for standard piezoelectric materials in which the magnetic effects can be safely assumed negligible. It is also assumed that the thermal effects may be neglected; that is, either the heat exchange with the environment is assumed to be negligible (an adiabatic process) or the temperature is constant (an isothermal process). Although this is not a good assumption as most piezoelectric materials are virtually pyroelectric (see Sect. 5.2 where the effect of thermal and electrical coupling was shown), this is a common practice and could save a lot of undue complications. Our specific justification in this book, however, can be attributed to the effective compensation of this "unmodeled" dynamic through application of effective controllers when using this model for piezoelectric materials (see Chaps. 8 and 9 for more details).

Representing the total energy density (energy per volume V) as u_V, one can write (6.16) in the following density form

$$\delta u_V = \sigma_p \delta S_p + \epsilon_i \delta D_i \tag{6.17}$$

which, in comparison with (6.16), implies that total variation δu_V can be described as

$$\delta u_\mathrm{V} = \left(\frac{\partial u_\mathrm{V}}{\partial S_p}\right)_\epsilon \delta S_p + \left(\frac{\partial u_\mathrm{V}}{\partial D_i}\right)_\sigma \delta D_i \tag{6.18}$$

where the subscripts "ϵ" and "σ" imply that those values are measured at constant stress ($\sigma = 0$) or constant electrical field ($\epsilon = 0$). By comparing (6.17) and (6.18), one can relate the conjugated and dependent variables σ_p and ϵ_i as functions of independent variables S_p and D_i. That is,

$$\delta\sigma_p = \left(\frac{\partial\sigma_p}{\partial S_q}\right)_{\epsilon} \delta S_q + \left(\frac{\partial\sigma_p}{\partial D_i}\right)_{\sigma} \delta D_i, \tag{6.19a}$$

$$\delta\epsilon_i = \left(\frac{\partial\epsilon_i}{\partial S_p}\right)_{\epsilon} \delta S_p + \left(\frac{\partial\epsilon_i}{\partial D_j}\right)_{\sigma} \delta D_j, \tag{6.19b}$$

$i, j = 1, 2, 3$ and $p, q = 1, 2, \ldots, 6$

Alternatively, the conjugated and dependent variables S_p and D_i can be related to independent variables σ_p and ϵ_i as

$$\delta S_p = \left(\frac{\partial S_p}{\partial\sigma_q}\right)_{\epsilon} \delta\sigma_q + \left(\frac{\partial S_p}{\partial\epsilon_i}\right)_{\sigma} \delta\epsilon_i, \tag{6.20a}$$

$$\delta D_i = \left(\frac{\partial D_i}{\partial\sigma_p}\right)_{\epsilon} \delta\sigma_p + \left(\frac{\partial D_i}{\partial\epsilon_j}\right)_{\sigma} \delta\epsilon_j, \tag{6.20b}$$

$i, j = 1, 2, 3$ and $p, q = 1, 2, \ldots, 6$

Equations (6.19) and (6.20) are called *linear constitutive equations*. Defining the materials constants given in Table 6.1, these constitutive relationships can be recast in the following more useful form:

$$\begin{aligned} S_p &= s^{\epsilon}_{pq}\sigma_q + d_{pi}\epsilon_i \\ D_i &= d_{ip}\sigma_p + \xi^{\sigma}_{ij}\epsilon_j \end{aligned} \tag{6.21}$$

where the indices $i, j = 1, 2, 3$ and $p, q = 1, 2, \ldots, 6$ refer to different directions within the material coordinate systems as discussed in Chap. 4.

Remark 6.2. It must be noted that in constitutive relationships (6.21) or subsequent configurations (see next), the differentials in (6.19) or (6.20) have been replaced by the variables themselves. To justify this action, we have assumed that the nominal values of the variables used in either (6.19) or (6.20) are zero. Hence, the differentials are defined as the comparison between the variables themselves to these zero-value states.

In matrix form of (6.21), $\mathbf{S} \in R^{6\times1}$ is the strain vector, $\boldsymbol{\sigma} \in R^{6\times1}$ is the stress vector, $\boldsymbol{\epsilon} \in R^{3\times1}$ is the electrical field vector measured in V/m, and $\mathbf{D} \in R^{3\times1}$ is the displacement vector measured in $\mathrm{C/m^2}$.

Similar to 1D case in Chap. 5, the first relationship in (6.21) refers to converse piezoelectric effect (actuation), while the second equation describes the direct piezoelectric effect (sensing). These equations can be alternatively rewritten in the following form, which is mainly used for sensing applications:

Table 6.1 Definition of material constants used in the constitutive relationships (6.21) and (6.22)

Material constants	Notation	Units
$\left(\frac{\partial S_p}{\partial \sigma_q}\right)_{\epsilon} \triangleq s^{\epsilon}_{pq} \in R^{6\times 6}$	Compliance coefficients matrix (inverse of elastic coefficient matrix) under constant electric field	m^2/N
$\left(\frac{\partial D_i}{\partial \sigma_p}\right)_{\epsilon} = \left(\frac{\partial S_p}{\partial \epsilon_i}\right)_{\sigma} \triangleq d_{ip} \in R^{3\times 6}$	Matrix of piezoelectric strain constants relating electric displacement $\mathbf{D} \in R^{3\times 1}$ (measured in C/m^2) to stress under zero electric field (short-circuited electrodes)	m/V or C/N
$\left(\frac{\partial D_i}{\partial \epsilon_j}\right)_{\sigma} \triangleq \xi^{\sigma}_{ij} \in R^{3\times 3}$	Dielectric or permittivity constants matrix under constant stress	F/m (Farad, F = C/V),
$\left(\frac{\partial S_p}{\partial D_i}\right)_{\sigma} = -\left(\frac{\partial \epsilon_i}{\partial \sigma_p}\right)_{D} \triangleq g_{ip} \in R^{3\times 6}$	Matrix of piezoelectric voltage constants relating strain $\mathbf{S} \in R^{6\times 1}$ to electric filed under zero stress	Vm/N or m^2/C
$\left(\frac{\partial \epsilon_i}{\partial D_j}\right)_{\sigma} \triangleq \beta^{\sigma}_{ij} \in R^{3\times 3}$	Impermittivity constants matrix under constant stress	m/F
$-\left(\frac{\partial \epsilon_i}{\partial S_p}\right)_{D} = -\left(\frac{\partial \sigma_p}{\partial D_i}\right)_{S} \triangleq h_{ip} \in R^{6\times 3}$	Matrix of piezoelectric constants	V/m
$\left(\frac{\partial \sigma_p}{\partial S_q}\right)_{D} \triangleq c^{D}_{pq} \in R^{6\times 6}$	Elastic stiffness coefficients matrix under constant dielectric displacement	N/m^2
$\left(\frac{\partial D_i}{\partial S_p}\right)_{\epsilon} = -\left(\frac{\partial \sigma_p}{\partial \epsilon_i}\right)_{S} \triangleq e_{ip} \in R^{6\times 3}$	Matrix of piezoelectric constants	$V/m \cdot V$ or C/m^2

$$\begin{aligned} S_p &= s^{D}_{pq}\sigma_q + g_{pi}D_i \\ \epsilon_i &= -g_{ip}\sigma_p + \beta^{\sigma}_{ij}D_j \end{aligned} \tag{6.22}$$

where s^{D}_{pq} (in a similar manner to s^{ϵ}_{pq}) is the compliance coefficients matrix under constant dielectric displacement ($\mathbf{D} = 0$), see Table 6.1. Similar to constitutive relationships (6.21), the first equation in (6.22) refers to converse effect (i.e., actuation mechanism) while the second equation denotes the direct effect (i.e., sensing mechanism).

Alternatively, (6.22) can be manipulated to arrive at the following more suitable form for actuation applications:

$$\begin{aligned} \sigma_p &= c^{D}_{pq}S_q - h_{pi}D_i \\ \epsilon_i &= -h_{ip}S_p + \beta^{S}_{ij}D_j \end{aligned} \tag{6.23a}$$

$$\begin{aligned} \sigma_p &= c^{\epsilon}_{pq}S_q - e_{pi}\epsilon_i \\ D_i &= e_{ip}S_p + \xi^{S}_{ij}\epsilon_j \end{aligned} \tag{6.23b}$$

Table 6.2 Relationships between piezoelectric and material constants used in the constitutive relationships (6.21–6.3)

Material constants	Equations used
$\beta^S - \beta^\sigma = gh$	(6.22, 6.23)
$\xi^\sigma - \xi^S = de$	(6.21)
$c_{ijpq} s_{pqkl} = \delta_{(ij)(kl)}$	(6.20–6.23)
$c^D - c^\epsilon = eh$	(6.23)
$s^\epsilon - s^D = dg$	(6.21, 6.22)
$d = \xi^\sigma g = es^\epsilon$	(6.21, 6.22)
$e = \xi^S h = dc^\epsilon$	(6.21, 6.23)
$g = \beta^\sigma d = hs^D$	(6.21–6.23)
$h = \beta^S e = gc^D$	(6.22, 6.23)

Notice that the indices are dropped for brevity, unless needed

where c_{pq}^D is the elasticity coefficients matrix (see 4.21) under constant dielectric displacement ($\mathbf{D} = 0$), and $\mathbf{h}$ and $\mathbf{e}$ are the piezoelectric constants matrices defined in Table 6.1 (the superscript S in β_{ij}^S refers to constant or zero strain condition for the impermittivity constants matrix).

It is worthy to note that a set of relationships between material constants defined in (6.21) and (6.22) can be obtained by simple cross-insertion of these equations in each other. These relationships for some representative cases will be demonstrated later in this section.

To better realize the relationships between different constants used in (6.21–6.23) and Table 6.1, a summary of different and useful forms of these equations is given in Table 6.2. These relationships can be obtained simply by comparing different versions of the constitutive equations while also taking into account the definition of these constants given in Table 6.1.

6.2.3 Nonlinear Characteristics of Piezoelectric Materials

The constitutive relationships developed in the preceding subsection were based on linear elasticity (stress–strain relationship) and permittivity (dielectric displacement–electric filed relationship) assumptions. However, in practice, piezoelectric materials exhibit nonlinear characteristics such as hysteresis, creep, and other nonlinearities. Due to importance of hysteretic nonlinearity in piezoelectric materials and their subsequent utilization in vibration-control systems discussed in this book, a dedicated chapter (Chap. 7) is devoted to this phenomenon in piezoelectric materials along with a select number of compensation techniques. Hence, we leave all the details about this nonlinearity to Chap. 7.

In addition to hysteresis nonlinearity, piezoelectric actuators, especially piezoceramics, demonstrate undesirable *creep* nonlinearity in their response. Creep is defined as unwanted changes, in the form of plastic deformations and generally in logarithmic shape, in the displacement of piezoelectric actuator under constant

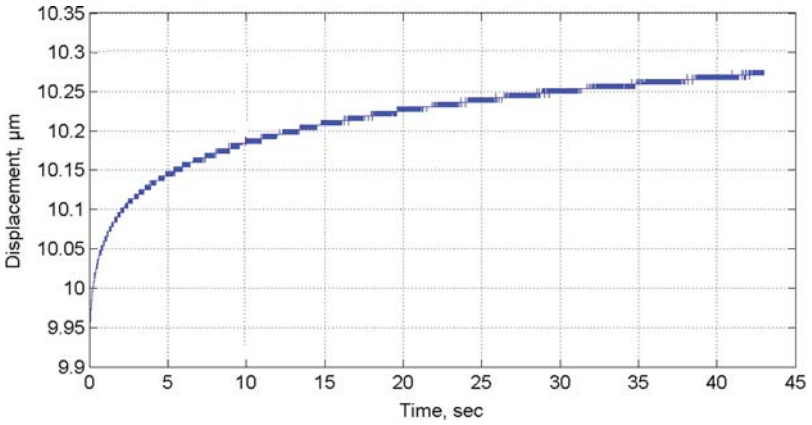

Fig. 6.7 Creep response of a piezoelectric actuator to a step input

electrical loads over time. This phenomenon is related to the effect of the applied voltage on the remanent polarization of the piezo ceramics. Generally, creep is the expression of the slow realignment of the crystal domains in a constant electric field over time (http://www.physikinstrumente.com). Figure 6.7 demonstrates a typical creep response of a piezoelectric actuator to a step input.

A good approximated model for creep can be given as (Krejci and Kuhnen 2001; Binnie et al. 1982)

$$\Delta S = \Delta S_0 \left[1 + \gamma \ln(t/0.1)\right] \tag{6.24}$$

where S_0 is the initial strain after 0.1 s, γ is the creep factor (typically between 0.01 and 0.02), and t is time. Although the effect of creep is considerably small when compared with the effect of hysteresis, this nonlinearity must be compensated for in order to ensure precise feedforward positioning, especially at low frequencies. That is, for low-frequency operation or static applications, creep nonlinearity must be taken into account, while it can be ignored either (1) at high frequencies, or (2) when actuators are under elastic constraints where prolong application of large electric fields cannot produce significant deflection over time.

6.3 Piezoelectric Material Constitutive Constants

6.3.1 General Relationships

To better visualize the material constants defined in the preceding subsection, the piezoelectric constitutive relations (6.21) can be written in matrix form as

$$\begin{Bmatrix} S_1 \\ S_2 \\ S_3 \\ S_4 \\ S_5 \\ S_6 \end{Bmatrix} = \begin{pmatrix} s_{11} & s_{12} & s_{13} & s_{14} & s_{15} & s_{16} \\ s_{21} & s_{22} & s_{23} & s_{24} & s_{25} & s_{26} \\ s_{31} & s_{32} & s_{33} & s_{34} & s_{35} & s_{36} \\ s_{41} & s_{42} & s_{43} & s_{44} & s_{45} & s_{46} \\ s_{51} & s_{52} & s_{53} & s_{54} & s_{55} & s_{56} \\ s_{61} & s_{62} & s_{63} & s_{64} & s_{65} & s_{66} \end{pmatrix} \begin{Bmatrix} \sigma_1 \\ \sigma_2 \\ \sigma_3 \\ \sigma_4 \\ \sigma_5 \\ \sigma_6 \end{Bmatrix} + \begin{pmatrix} d_{11} & d_{21} & d_{31} \\ d_{12} & d_{22} & d_{32} \\ d_{13} & d_{23} & d_{33} \\ d_{14} & d_{24} & d_{34} \\ d_{15} & d_{25} & d_{35} \\ d_{16} & d_{26} & d_{36} \end{pmatrix} \begin{Bmatrix} \epsilon_1 \\ \epsilon_2 \\ \epsilon_3 \end{Bmatrix} \tag{6.25a}$$

$$\begin{Bmatrix} D_1 \\ D_2 \\ D_3 \end{Bmatrix} = \begin{pmatrix} d_{11} & d_{12} & d_{13} & d_{14} & d_{15} & d_{16} \\ d_{21} & d_{22} & d_{23} & d_{24} & d_{25} & d_{26} \\ d_{31} & d_{32} & d_{33} & d_{34} & d_{35} & d_{36} \end{pmatrix} \begin{Bmatrix} \sigma_1 \\ \sigma_2 \\ \sigma_3 \\ \sigma_4 \\ \sigma_5 \\ \sigma_6 \end{Bmatrix} + \begin{pmatrix} \xi_{11} & \xi_{12} & \xi_{13} \\ \xi_{21} & \xi_{22} & \xi_{23} \\ \xi_{31} & \xi_{32} & \xi_{33} \end{pmatrix} \begin{Bmatrix} \epsilon_1 \\ \epsilon_2 \\ \epsilon_3 \end{Bmatrix} \tag{6.25b}$$

The matrix forms (6.25) are in the most general form; however, when the material's elastic properties are invariant with respect to rotation of any angle about a given axis, the total number of compliance coefficients reduces to 5. As mentioned in Chap. 4, these materials are referred to as *transversely isotropic*. As discussed earlier, piezoceramics belong to this class of materials. It is commonly assumed that the third axis or direction 3 is along the polarization direction which also coincides with the axis of transverse isotropy. Hence, (6.25) for these materials (piezoceramics) reduces to

$$\begin{Bmatrix} S_1 \\ S_2 \\ S_3 \\ S_4 \\ S_5 \\ S_6 \end{Bmatrix} = \begin{pmatrix} s_{11} & s_{12} & s_{13} & 0 & 0 & 0 \\ s_{12} & s_{11} & s_{13} & 0 & 0 & 0 \\ s_{13} & s_{13} & s_{33} & 0 & 0 & 0 \\ 0 & 0 & 0 & s_{44} & 0 & 0 \\ 0 & 0 & 0 & 0 & s_{44} & 0 \\ 0 & 0 & 0 & 0 & 0 & 2(s_{11}-s_{12}) \end{pmatrix} \begin{Bmatrix} \sigma_1 \\ \sigma_2 \\ \sigma_3 \\ \sigma_4 \\ \sigma_5 \\ \sigma_6 \end{Bmatrix} + \begin{pmatrix} 0 & 0 & d_{31} \\ 0 & 0 & d_{31} \\ 0 & 0 & d_{33} \\ 0 & d_{15} & 0 \\ d_{15} & 0 & 0 \\ 0 & 0 & 0 \end{pmatrix} \begin{Bmatrix} \epsilon_1 \\ \epsilon_2 \\ \epsilon_3 \end{Bmatrix} \tag{6.26a}$$

$$\begin{Bmatrix} D_1 \\ D_2 \\ D_3 \end{Bmatrix} = \begin{pmatrix} 0 & 0 & 0 & 0 & d_{15} & 0 \\ 0 & 0 & 0 & d_{15} & 0 & 0 \\ d_{31} & d_{31} & d_{33} & 0 & 0 & 0 \end{pmatrix} \begin{Bmatrix} \sigma_1 \\ \sigma_2 \\ \sigma_3 \\ \sigma_4 \\ \sigma_5 \\ \sigma_6 \end{Bmatrix} + \begin{pmatrix} \xi_{11} & 0 & 0 \\ 0 & \xi_{11} & 0 \\ 0 & 0 & \xi_{33} \end{pmatrix} \begin{Bmatrix} \epsilon_1 \\ \epsilon_2 \\ \epsilon_3 \end{Bmatrix} \tag{6.26b}$$

Equations (6.26) imply that for transversely isotropic piezoceramics, there are five elastic constants, three piezoelectric strain constants, and two dielectric or permittivity constants.

To better realize these relationships, we will explain, next, the physical meaning of piezoelectric strain constants d_{ij} and how they provide coupling between mechanical and electrical fields. Before we present such explanations, however, one can clearly see the transversely isotropic assumption for piezoceramics where an electric field applied in direction of polarization vector (ϵ_3 for instance) will result in same strains in 1 and 2 directions (see (6.26a) where $d_{31} = d_{32}$). This assumption, however, is not valid for nonisotropic piezoelectric materials such as PVDF where their piezoelectric strain constants matrix takes the form

$$\mathbf{d}^{\text{PVDF}} = \begin{pmatrix} 0 & 0 & d_{31} \\ 0 & 0 & d_{32} \\ 0 & 0 & d_{33} \\ 0 & d_{25} & 0 \\ d_{15} & 0 & 0 \\ 0 & 0 & 0 \end{pmatrix} \tag{6.27}$$

Equation (6.27) clearly demonstrates that the application of an electric field in the polarization direction for these piezoelectric materials results in different strains in directions 1 and 2 since $d_{31} \neq d_{32}$. As a matter of fact, PVDF films are highly anisotropic with $d_{31} \cong 5d_{32}$. Also, the dielectric strength of PVDF polymers is about 20 times higher than that of PZT, and hence, can endure much higher electric field compared to PZT materials. Part III will present some of the applications of PVDF as an excellent piezoelectric sensors when flexibility and lightweight attributes are required (see Chap. 12).

For both PZT and PVDF materials, piezoelectric strain constant d_{15} implies that the application of electric field ϵ_1 or ϵ_2 (normal to the polarization direction 3) produces a shear deformation S_5 ($S_{xz} = S_{zx}$) or S_4 $\left(S_{yz} = S_{zy}\right)$. Since d_{15} typically has the largest values among all piezoelectric constants, this property can be utilized to design effective shear actuators and sensors (Glazounov et al. 1998, www.physikinstrumente.com). To better provide a relative comparison between material constants for selected piezoelectric materials, Table 6.3 lists some of these constants for several piezoceramic types (PZT-4, PZT-5A, PZT-5H, and PMN-PT).

6.3.2 Piezoelectric Coefficients

Although piezoelectric coefficients were introduced in the preceding subsection, they were derived and utilized from structural mechanics and mathematical perspectives. To better provide an insight on their physical origin, this section justifies their presence from a totally different viewpoint. As mentioned in the preceding subsection, piezoelectric materials are generally anisotropic, and hence, their physical constants (e.g., piezoelectric constants, elasticity, permittivity) depend upon both the direction of the applied stress or strain and that of the applied field. Therefore, these constants were defined using two subscripts (please refer to the definitions

Table 6.3 Selective material constants for several commonly used piezoceramics

Quantity	Units	PZT-4	PZT-5A	PZT-5H	PMN-PT
s_{11}^{ϵ}	$10^{-12}\,\mathrm{m}^2/\mathrm{N}$	12.3	16.4	16.5	59.7
s_{12}^{ϵ}	$10^{-12}\,\mathrm{m}^2/\mathrm{N}$	−4.05	−5.74	–	–
s_{13}^{ϵ}	$10^{-12}\,\mathrm{m}^2/\mathrm{N}$	−5.31	−7.22	−9.1	−45.3
s_{33}^{ϵ}	$10^{-12}\,\mathrm{m}^2/\mathrm{N}$	15.5	18.8	20.7	86.5
s_{44}^{ϵ}	$10^{-12}\,\mathrm{m}^2/\mathrm{N}$	39.0	47.5	43.5	14.4
d_{33}	$10^{-12}\,C/N$	289	390	650	2,285
d_{31}	$10^{-12}\,C/N$	−123	−190	−320	−1,063
d_{15}	$10^{-12}\,C/N$	496	584		
ρ	$\mathrm{kg/m}^3$	7,500	7,800	7,800	8,050
κ_{33}	–	–	0.72	0.75	0.91

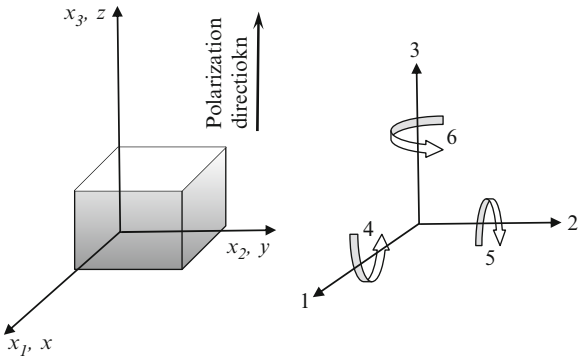

Fig. 6.8 Schematic representation of crystallographic axes and directions of deformation (1–3 indicate normal strain/stress, while 4–6 imply shear strain/stress)

of these constants in Table 6.1), one index for stress or strain (for elasticity) and the other for dielectric displacement or electric field (for permittivity), while also a superscript was used to indicate the quantity that is kept constant (constant electric field or constant stress).

Without loss of generality, we assume that the direction of positive polarization is along the z-axis or direction 3. As mentioned earlier, this is a common practice which will ease the subsequent derivations and definitions. To better review the physical meaning of these constants, Fig. 6.8 depicts a typical rectangular system of crystallographic axes x, y, and z with the positive polarization along the z-axis. Using this figure, we will, next, present some of the most important piezoelectric material constants, followed by some special cases and configurations.

Piezoelectric strain constants d_{ij}: As defined in Table 6.1, the piezoelectric strain (or sometime referred to as charge) constant is the ratio of the induced electric polarization per unit applied mechanical stress. Alternatively, it is defined as produced mechanical strain per unit applied electric field (see the second term in the first column in second row of Table 6.1). Therefore, representing this definition using the indicial notation, the piezoelectric strain constant d_{ij} can be defined as the generated

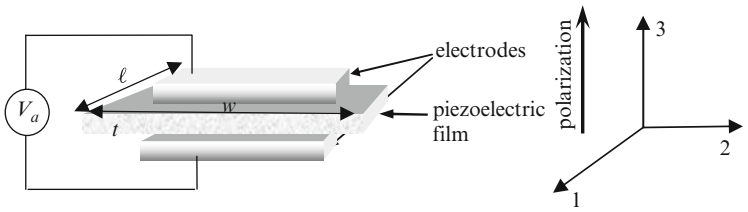

Fig. 6.9 Schematic of piezoelectric strain constant d_{31} configuration (laminar)

strain along j-axis due to a unit electric field applied along i-axis, provided that all external stresses are kept constant. For example, d_{31} is the induced strain in direction 1 due to a unit electric field in direction 3 (polarization direction), while the system is kept under a stress-free field (see Fig. 6.9).

Using the notations shown in Fig. 6.9 and definition d_{31}, one can express this constant as

$$d_{31} = \frac{S_1}{\epsilon_3} = \frac{\Delta\ell\,/\,\ell}{V_\mathrm{a}\,/\,t} = \frac{t\Delta\ell}{V_\mathrm{a}\ell} \tag{6.28}$$

The piezoelectric constant d_{31} is usually negative (see Table 6.3). As mentioned, another interpretation of d_{31} is the induced polarization per unit applied stress (applied force F along direction 3) under zero electric filed ($\epsilon = 0$). The induced polarization for this case equals to the short-circuited charge density, that is,

$$d_{31} = \frac{Q/\ell w}{F/tw} = \frac{C\,V_\mathrm{a}/\ell w}{F/tw} = \frac{C\,V_\mathrm{a}t}{F\ell} \triangleq \frac{V_\mathrm{a}}{F} K\xi_0 w \tag{6.29}$$

where ξ_0 is the permittivity of free space and the relative dielectric constant K is related to equivalent capacitance C of piezoelectric material (see 6.29) as

$$C = K\xi_0 \frac{\ell w}{t} \tag{6.30}$$

Piezoelectric voltage constants g_{ij}: Similar to strain constant, piezoelectric voltage constant g_{ij} is defined (see the definition of g in the first column of fourth row in Table 6.1) as the induced electric field (along direction i) per applied unit mechanical stress (along direction j). Alternatively, it is defined as the experienced mechanical strain (along direction j) due to application of unit electric displacement (along direction i). For example, g_{31} is the induced field in direction 3 due to applied unit stress in direction 1, while all other stresses are zero (see Fig. 6.10).

Using the notations shown in Fig. 6.10 and definition g_{31}, one can express this constant as

$$g_{31} = \frac{\epsilon_3}{\sigma_1} = \frac{V_\mathrm{a}/t}{F/wt} = \frac{V_\mathrm{a}}{F} w \tag{6.31}$$

Alternatively, g_{31} is the developed strain per unit applied charge density, hence, it can be expressed as

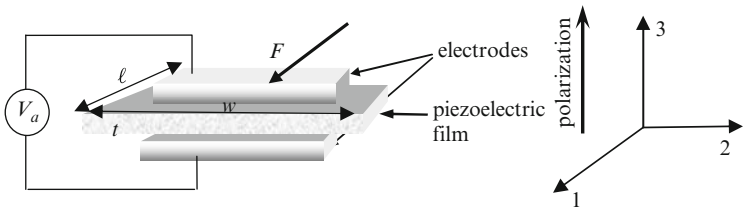

Fig. 6.10 Schematic of piezoelectric voltage constant g_{31} configuration (laminar)

$$g_{31} = \frac{\Delta\ell/\ell}{Q/\ell w} = \frac{\Delta\ell/\ell}{C V_a/\ell w} \triangleq \frac{\Delta\ell}{\ell}\frac{t}{V_a K \xi_0} \tag{6.32}$$

Piezoelectric dielectric (permittivity) constants ξ_{ij}: Based on the definition of permittivity given in Table 6.1, the absolute permittivity ξ_{ij} is defined as electric displacement or charge per unit area (along i-axis) per unit electric field (measured along j-axis). In most piezoelectric materials, the application of an electric field in a given direction only causes electric displacement in the same direction. Instead of the absolute value, most references provide values of relative permittivity, $K = \xi/\xi_0$, that is, the ratio of absolute permittivity to the permittivity of free space ($\xi_0 = 8.85 \times 10^{-12}$ F/m). As demonstrated earlier, the relative permittivity is related to material inherent capacity per relationship (6.30).

Elastic compliance s_{ij}: Again, according to the definition of elastic compliance given in Table 6.1, compliance s_{ij} is defined as the produced strain along i-axis due to a unit stress along j-axis. Similar to stress–strain relationship (4.21) where stress vector was related to strain vector using elastic stiffness tensor c, strain vector can be related to stress vector using this elastic compliance (inverse of stiffness).

Like any other material constants discussed here, the elastic compliance is measured under either constant field ($\epsilon = 0$) or short-circuited (SC) denoted by s^{ϵ}_{ij}, or under constant dielectric displacement ($D = 0$) or open-circuited (OC) denoted by s^{D}_{ij}. When the circuit is open (see Fig. 6.11-left), the electric field produces additional strain in piezoelectric material that results in increased value of s^{D}_{ij} compared to SC configuration as shown in Fig. 6.11-right (since $\epsilon = 0$, no additional strain is generated). That is, $s^{D}_{ij} > s^{\epsilon}_{ij}$. This difference in compliance values is generated only through a simple change in circuit configurations (i.e., from OC to SC and vice versa). On the other hand, the elastic stiffness is directly related to elastic compliance as (from elementary mechanics)

$$c^{D} = \frac{1}{s^{D}} \quad \text{or} \quad c^{\epsilon} = \frac{1}{s^{\epsilon}} \tag{6.33}$$

Therefore, by changing the circuit configurations from OC to SC, one can easily change the effective elastic stiffness without altering material properties. This observation, known as *piezoelectric shunting*, can be effectively used to design a novel semi-active vibration-control system that selectively changes the effective stiffness

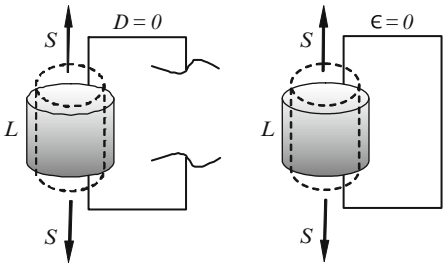

Fig. 6.11 Schematic of (*left*) open-circuit (OC or $D = 0$), and (*right*) short-circuit (SC or $\epsilon = 0$) configurations

of the structure to either absorb the vibration (in case of unwanted vibrations) or harvest energy from vibrating structures, depending on the control laws designed. More details about this concept will be presented in Chap. 9.

Piezoelectric coupling coefficients κ_{ij}: The electromechanical coupling in general quantifies that from an applied energy, how much remains in the materials rather than being converted into other forms. On the other hand, it is defined as the ratio of stored mechanical energy to applied electrical energy (for actuators) or the ratio of the stored electrical energy to applied mechanical energy (for sensors). That is, κ_{ij} is defined as

$$\kappa_{ij}^2 = \frac{\text{stored mechanical energy (stress andstrain) in direction } i}{\text{applied electrical energy (electricfield and electric displacement) in direction } j} \tag{6.34a}$$

or

$$\kappa_{ij}^2 = \frac{\text{stored electrical energy (electric field and electric displacement) in direction } j}{\text{applied mechanical energy (stress and strain) in direction } i} \tag{6.34b}$$

Equation (6.34a) is used for actuators, while (6.34b) is utilized for sensors.

It is this coupling that, indeed, signifies the importance of boundary conditions that exist when measuring stress, strain, dielectric displacement, or electric field in piezoelectric materials. Taking into account this fact and in order to relate this coupling coefficient to other piezoelectric material constants, a simple experiment utilizing OC configuration can be carried out. Before explaining the procedure here and without loss of generality, we revisit the scalar (1D) version of piezoelectric constitutive relationships (6.21) as

$$\begin{aligned} S &= s^{\epsilon}\sigma + d\epsilon \\ D &= d\sigma + \xi^{\sigma}\epsilon \end{aligned} \tag{6.35}$$

where all indices are dropped for the sake of simplicity in the derivations. By eliminating electric field ϵ from these equations, the following relationship results

$$S = s^{\epsilon}\left(1 - \frac{d^2}{s^{\epsilon}\xi^{\sigma}}\right)\sigma - \frac{d}{\xi^{\sigma}}D \tag{6.36}$$

Moreover, utilizing the scalar version of the first expression in (6.22), we get

$$S = s^D \sigma + gD \tag{6.37}$$

Now that we have established the required relationships, let us get back to the problem of determining coupling coefficient κ. When the circuit is OC (see Fig. 6.11-left), the dielectric displacement is zero (i.e., $D = 0$). Inserting this information into both (6.36) and (6.37), while noticing the left-hand side of these equations are the same, will result in

$$s^D = s^\epsilon \left(1 - \frac{d^2}{s^\epsilon \xi^\sigma}\right) \tag{6.38}$$

From (6.38), it is clear that second term inside the parentheses quantifies the change in the mechanical compliance $\left(s^D\right)$ as a function of electrical boundary condition ($D = 0$). It is also this very term that, if not present, the OC and SC configurations will generate the same values for the mechanical compliances s^D and s^ϵ. Hence, this term can be, indeed, viewed as an indicator of *coupling* between electrical and mechanical fields. For this, the square root of this term is referred to as the coupling coefficient and defined as

$$\kappa^2 = \frac{d^2}{s^\epsilon \xi^\sigma} \tag{6.39}$$

or in general form as

$$\kappa_{ij}^2 = \frac{d_{ij}^2}{s_{ij}^\epsilon \xi_{ij}^\sigma} \triangleq g_{ij} d_{ij} E_p \tag{6.40}$$

where E_p is the Young's modulus of elasticity of piezoelectric material. The coupling coefficient is always positive (based on the definition 6.39) and less than 1 (based on the fact that either mechanical or electrical compliance as per (6.38) become negative when changing boundary conditions), see Table 6.3 for this value for some representative piezoelectric materials. Hence,

$$0 < \kappa^2 < 1 \tag{6.41}$$

As mentioned earlier, the compliance s^D (or elastic stiffness c^D) corresponds to OC configuration, while compliance s^ϵ (or elastic stiffness c^ϵ) is associated with the SC configuration. Denoting the OC and SC elastic stiffness values as K_{OC} and K_{SC}, respectively, and considering (6.33) and (6.38), one can readily relate these stiffness values as

$$\frac{K_{\text{OC}}}{K_{\text{SC}}} = \frac{1}{1 - \kappa^2} \tag{6.42}$$

As seen from (6.42), the difference between elastic stiffness values for OC and SC configurations is a function of coupling coefficient. That is, the higher the value of this coefficient, the more difference between these stiffness values. For instance, the coupling coefficient in PZT is about 0.7, while this value is about 0.1 for PVDF. We will extensively discuss later in Chap. 9 that how a higher difference value between

K_{OC} and K_{SC} (or alternatively higher κ values) will result in a more effective vibration control.

6.4 Engineering Applications of Piezoelectric Materials and Structures

As briefly mentioned in the preceding chapter, piezoelectricity exists in materials either naturally or synthetically. If not all, most engineering applications of piezoelectric materials consist of synthetic piezoelectric materials such as compounds of lead zirconate titanate ($PbZrTiO_3$–$PbTiO_3$, or PZT), barium titanate, barium strontium titanate (BaSTO), lead lanthinum zirconate titanate (PLZT), lithium sulfate, and polyvinylidene fluoride (PVDF) and copolymers of PVDF (Tzou et al. 2004).

From structural viewpoint, piezoelectric materials are divided into polymeric and ceramic forms. Piezoelectricity effects in polymers such as elongated and poled PVDF have been observed for a number of decades. Although PVDF copolymers have found diverse uses in industrial applications such as ultrasonic transducers, hydrophones, microphones, and vibration damping (Fukada 2000; Baz and Ro 1996), their low stiffness and electromechanical coupling coefficients (when compared to ceramics like PZT, for instance) have limited their use.

The most popular piezoelectric ceramics are PZT because of their excellent properties as well the ability to optimize their properties to suit specific applications by appropriate adjustment of the zirconate–titanate ratio (Berlincourt 1981). Their mechanical properties make them ideal for a variety of electromechanical transducers such as generators (e.g., spark ignition, solid-state batteries), sensors (e.g., acceleration and pressure), and actuators (e.g., pneumatic and hydraulic valves). When used as generators, they covert mechanical impulse or pressure into electrical power (Audigier et al. 1994; Sodano et al. 2005). The most common sensor applications of piezoceramics are accelerometers and pressure sensors (Tomikawa and Okada 2003; Caliano et al. 1995). More specifically, when operated in high frequencies (>10 kHz), piezoceramics could be utilized as sonic and ultrasonic transducers to generate high-frequency sounds for different testing and measurement applications (Matsunaka et al. 1998; Billson and Hutchins 1993).

Although much of the work carried out from the 1960s to present has been on developing applications for PZT materials, research activities continue into the development of new materials with exciting potential as piezoelectrics such as discovery of giant piezoelectric effect in strontium titanate ($SrTiO_3$) at very low temperatures (Damjanovic 1998), or recent piezoelectricity in boron nitride nanotubes (Mele and Kral 2002; Jalili et al. 2003; Salehi-Khojin and Jalili 2008a,b; Salehi-Khojin et al. 2009a).

6.4.1 Application of Piezoceramics in Mechatronic Systems

With the widespread application of mechatronic concepts to dynamic systems in recent years, interest has been focused on the substitution of piezoceramics for conventional actuators. Generally, the anisotropic nature of the actuation in piezoceramics permits the design of actuators without relying on transmission of the actuation through structural coupling mechanisms.

Despite the recognized advantages of PZT actuation, use of these actuators present significant design restrictions. The primary limitations include small deformation and nonlinear behavior. The engineering challenges lie in the development and utilization of these actuators for practical applications where displacements with high force/torque capabilities are required. While many alternatives exist, the following subsections present some effective remedies to realize high-resolution capabilities of PZT elements for large position applications.

6.4.2 Motion Magnification Strategies for Piezoceramic Actuation

A review of existing concepts for PZT displacement magnification reveals that a multitude of methods and principles can be employed as shown in Fig. 6.12 (Giurgiutiu et al. 1995; Jalili et al. 2003). Considerable engineering experience has been accumulated in this field, since the problem is not limited to PZT actuator applications.

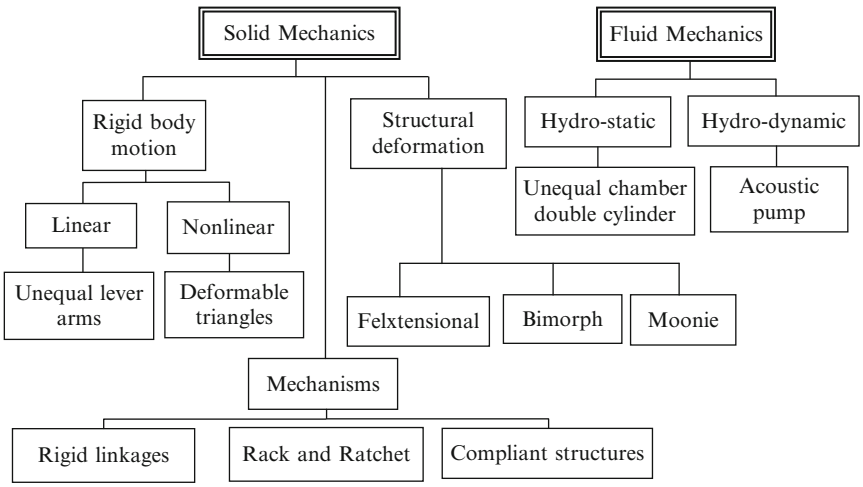

Fig. 6.12 Displacement amplification concepts for piezoelectric actuators
Source: Jalili et al. 2003, with permission

Piezoelectric actuators or positioning stages can be designed to integrate a lever motion amplifier such that the PZT displacement is increased by a factor of typically 2–20. To maintain sub-nanometer resolution with the increased travel range, the lever system must be stiff with minimal backlash and friction. Alternatively, a compliant mechanism can be used to amplify the PZT displacement and thus, provide a usable amount of stroke (Confield and Frecker 2000; Frecker et al. 1997; Kota et al. 1999). Due to the mechanism's inherent elasticity, it can provide a preload effect which is important in PZT stacked actuators (i.e., PZT stacks can sustain compression but not tension[4]).

The placement of PZT patches onto a beam structure can result in lateral motion that may be harvested using a compliant gear mechanism. For greater rotational resolution and torque production, a circular array of these composite beams may be considered which requires synchronization of the excitation voltages to simulate the motion at the proper time instance. From a deflection perspective, the composite beam's structural properties must be addressed to fully understand the beam's behavior for various operating conditions, for instance, axial and lateral loads with elevated temperatures. Furthermore, the interface with the compliant gear and beams' tips represents the area in which torque transmission occurs based on the frictional behavior.

6.4.3 Piezoceramic-Based High Precision Miniature Motors

Some manufacturing processes will need to evolve from fixed "macro" systems to portable flexible small-scale units capable of supporting milli- and micro-technologies. The increasing interest in mechanical system miniaturization for automation, micro-manipulation, precision micro-assembly, and medical technology (e.g., medical pump and instruments for minimal invasive therapy) is a driving factor. This has encouraged the development of new miniature actuators as driving units in these systems. A number of technical designs for miniature motors have been presented (Itoh 1993; Nakamura et al. 1995; Sato 1994; Vishnewsky and Glob 1996).

As shown in Fig. 6.13, the PZT actuators may be interfaced with a motion transformer or compliant mechanism which produces translational or rotational displacement. The small mechanical displacement produced by the PZT material (e.g., 20–100 μm and 1,000–10,000 N) may be harnessed into a translational and rotational motion. For this, two device configurations can be utilized. First, a stepping motion amplifier mechanism, coupled with integrated ratchet-type transmission linkage, transforms the step motion into a rotational displacement with high torque properties (Jalili et al. 2003). Second, the principle of friction is the basis for the compliant rotating stepwise mechanism (Jalili et al. 2003). This concept is based on

[4] Please refer to next subsection for detailed description and operational principle for these types of actuators.

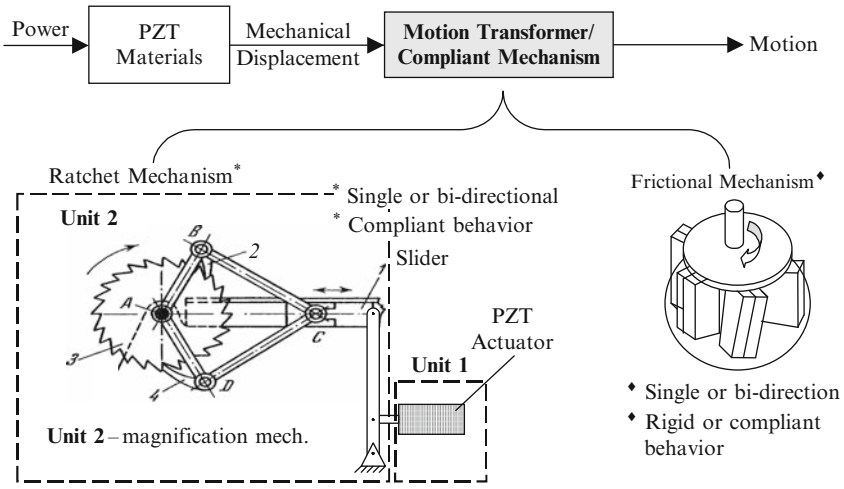

Fig. 6.13 PZT-based miniature motor with ratchet and frictional motion transformer concepts

quasi-static positioning of piezoceramic elements in contrast to ultrasonic motors based on resonance (Uhea and Tomikawa 1993). Although the ratchet mechanism offers tremendous opportunities, its motion is dependent on the ratchet's number of gear teeth.

6.5 Piezoelectric-Based Actuators and Sensors

6.5.1 Piezoelectric-Based Actuator/Sensor Configurations

There are two basic types of PZT actuator (or sensor) designs: stacked (i.e., axial actuation) and laminar (i.e., bender-type actuation). An axial actuator is composed of a stack of thin ceramic disks separated by metallic electrodes that are alternatively connected to the positive and negative terminals of a voltage source (see Fig. 6.14). In laminar actuator configuration, thin film of piezoelectric materials [e.g., active fiber composites (AFCs)] (Bent and Hagood 1993; Sodano et al. 2004; Wilkie et al. 2000), is either sandwiched between two electrodes (see Fig. 6.15) or attached to one side of the main structure (see Fig. 6.16). When the actuator is energized, the piezoelectric film strains, resulting in straining the main structure, thereby producing a motion proportional to the applied voltage. More details about the operational principles for these two configurations are given next.

Piezoelectric stack actuators/sensors: These types of actuators can produce extremely fine position changes, down to the sub-nanometer range, with large forces of up to several 10,000 N. They also offer very fast response time (i.e., microsecond time constants), and can reach their nominal displacement in approximately one-third of the resonant frequency period. Rise times on the order of microseconds,

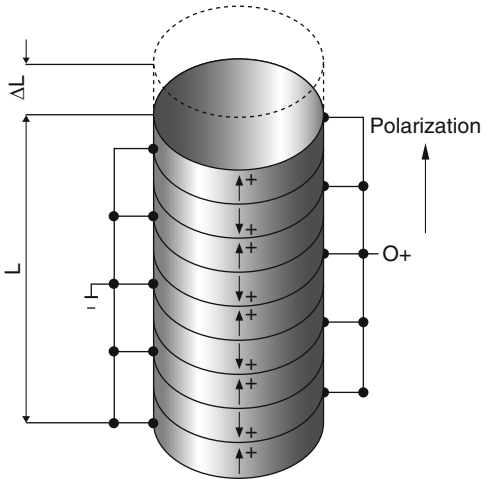

Fig. 6.14 Schematic of piezoelectric actuators in axial configuration separated with metallic electrodes (http://www.physikinstrumente.com)

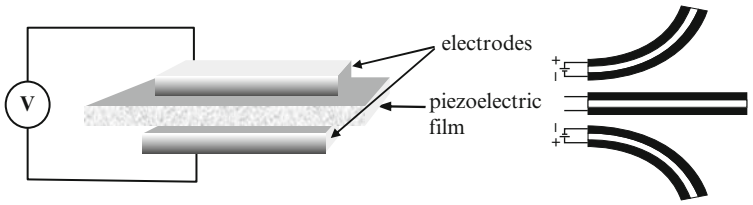

Fig. 6.15 Schematic of piezoelectric laminar actuator (piezoelectric film sandwiched between electrodes)

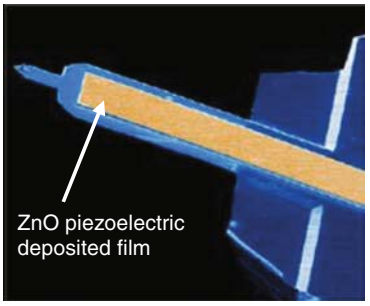

Fig. 6.16 Schematic of piezoelectric laminar actuator (piezoelectric deposited/appended on the main structure)
Source: Gurjar and Jalili 2007, with permission

and accelerations of more than 10,000 gs are possible under this configuration. This feature permits rapid switching applications and repeatable nanometer and sub-nanometer motion at high frequencies, because their motion is derived through solid state crystals. There are no moving parts, and hence no "stick–slip" motion occurs. These features collectively result in unlimited resolution in theory, making them advantageous tools for micro/nano-scale metrology and manipulation applications. Due to the importance of such advantages and features, Chap. 10 presents a detailed discussion along with the latest advances on piezoelectric-based micro- and nano-positioning systems.

For this configuration, the linear electromechanical coupling coefficient, d_{33}, dominates the other piezoelectric constants. Thus, the direction of expansion coincides with the electric field. For instance, for 1D configuration shown in Fig. 6.14, the linear electromechanical constitutive relations (6.21) reduce to

$$S_3 = d_{33}\epsilon_3 + \frac{1}{c}\sigma_3 \tag{6.43}$$

$$D_3 = \xi_{33}\epsilon_3 + d_{33}\sigma_3 \tag{6.44}$$

When an external load is absent, the change of length is related to the applied voltage by the approximate relationship

$$\Delta L \approx d_{33}\, n\, V_{\mathrm{a}} \tag{6.45}$$

where n is the number of disks in the stack and V_{a} is the applied voltage.

Despite the aforementioned advantages and as briefly reviewed in the preceding subsection, the most obvious disadvantages of piezoceramic stack actuators include: (1) relatively small strain on the order of 1/1,000 (0.1%), and (2) sensitivity to pulling forces. To address the first drawback, several amplification mechanisms, such as those listed in Fig. 6.12, could be utilized to increase the actuator displacement range by a factor of 2–20. To keep the sub-nanometer resolution, friction-free flexures are utilized (see Fig. 6.17 for some demonstrable examples of such mechanisms). On the other hand, in order to reduce the sensitivity of these actuators to pulling forces, they can be internally preloaded with spring configuration as shown in Fig. 6.18.

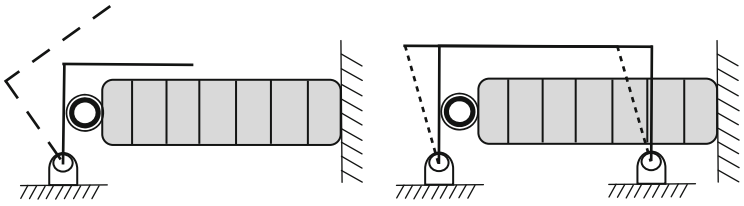

Fig. 6.17 Flexural mechanisms for amplification of piezoelectric actuator displacement

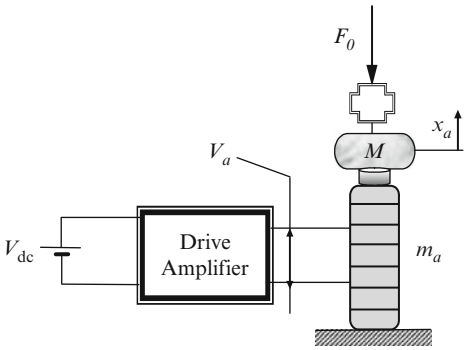

Fig. 6.18 Structure of piezoelectric stack actuators preloaded with spring

Piezoelectric patch actuator/sensor: For laminar actuators (or sensors), the active material consists of thin ceramic strips (see Figs. 6.15 or 6.16). The displacement of these actuators is perpendicular to the direction of polarization and the electric field. When the voltage is increased, the strip contracts. The maximum travel is a function of the length of the strips, while the number of strips arranged in parallel determines the element's stiffness and stability. The displacement ΔL of an unloaded single layer piezoelectric actuator can be estimated as

$$\Delta L \approx \pm \epsilon_3 \, d_{31} \, L_0 \tag{6.46}$$

where L_0 is the ceramic length and d_{31} is the piezoelectric strain coefficient which is related to the strain orthogonal to the polarization vector (i.e., width). The strip actuator is put to use by mounting the large flat area of the actuator directly to a flat area on the flexible structure. Application of a voltage will generate a piezoelectric stress within the actuator. The differential stress between the actuator and the structure will induce a bending moment which causes the structure to deform, as shown in Fig. 6.19. Since the derivations of the equations of motion for this configuration are more involved, we prefer not to include these materials here, and instead refer the reader to Chap. 8 for more details.

Similar to actuator configurations presented in Sect. 6.6.1, piezoelectric sensors are divided into axial and laminar configurations. The only significant difference between sensors and actuators is in the values of electromechanical piezoelectric coefficients.

6.5.2 Examples of Piezoelectric-Based Actuators/Sensors

PZT inertial actuators: the PZT inertial actuators are most commonly made out of two parallel piezoelectric plates. If a voltage is applied, one of the plates expands as the other one contracts, and hence, producing displacement that is proportional

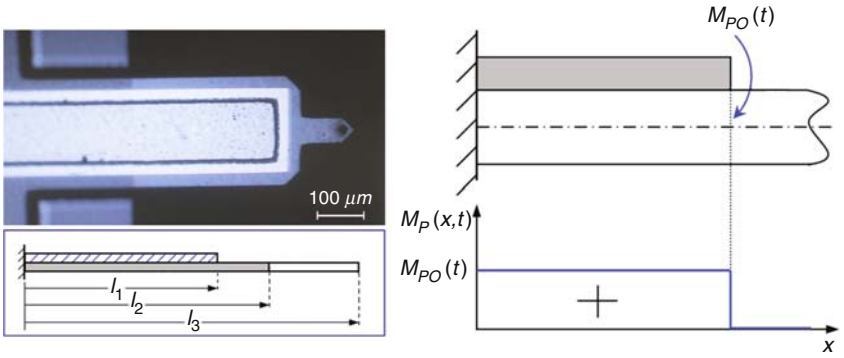

Fig. 6.19 (*left*) Piezoelectrically driven actuator with cross-sectional discontinuity (*top-right*), equivalent electromechanical moment due to piezoelectric excitation, and (*bottom-right*) uniform distribution of internal moment along the actuator length
Source: Salehi-Khojin et al. 2008, with permission

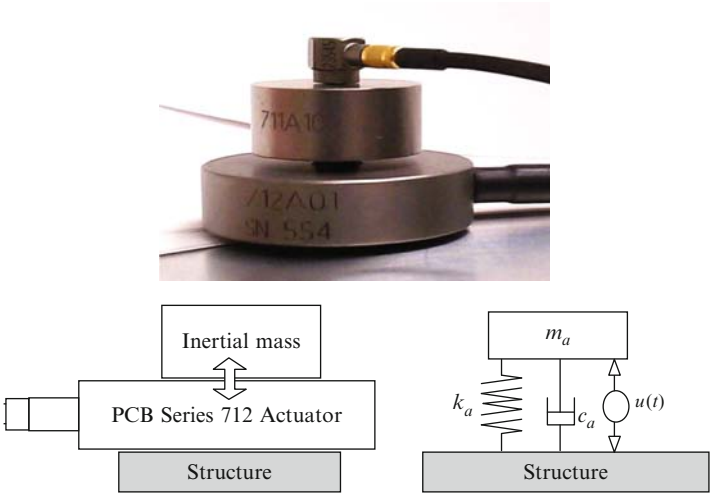

Fig. 6.20 A PCB (Active Vibration Control Instrumentation, A Division of PCB Piezotronics, Inc., www.pcb.com) series 712 PZT inertial actuator (*top*), schematic of operation (*lower left*), and a simple SDOF mathematical model (*lower right*)
Source: Jalili and Knowles 2004, with permission

to the input voltage. The resonance of such actuator can be adjusted by the size of the inertial mass (see Fig. 6.20). Increasing the size of the inertial mass will lower the resonance frequency and decreasing the mass will increase it. The resonance frequency of such actuator, f_r, can be expressed as

$$f_r = \frac{1}{2\pi}\sqrt{\frac{k_a}{m_a}} \tag{6.47}$$

where k_a is the effective stiffness of the actuator, and m_a is defined as

$$m_a = m_{e_{PZT}} + m_{inertial} + m_{acc} \tag{6.48}$$

$m_{e_{PZT}}$ is the PZT effective mass, $m_{inertial}$ is the inertial mass, and m_{acc} is the accelerometer mass. Using a simple SDOF system (see Fig. 6.20), the parameters of the PZT inertial actuators can be experimentally determined (Jalili and Knowles 2004; Knowles et al. 2001). This "parameter identification" problem is an inverse problem. We refer the interested readers to Banks and Ito (1988) and Banks and Kunisch (1989) for a general introduction to parameter estimation or inverse problem governed by differential equations.

6.6 Recent Advances in Piezoelectric-Based Systems

Piezoelectric actuators and sensors, with their ultra-fine resolution and fast frequency response, find applications in many micro/nano-scale applications. Leaving much of the details for these application to Part III of book where this topic is extensively discussed, we briefly review some representative applications here. In general, the applications of piezoelectric actuators and sensors can be divided into the following four disciplines: (1) life science, medicine, and biology (e.g., scanning microscopy, gene manipulation, cell penetration, and microdispersing); (2) semiconductors and microelectronics (e.g., wafer and mask positioning and alignment, microlithography and nanolithography); (3) optics and photonics (e.g., fiber optic alignment and switching, image stabilization, adaptive optics, laser tuning, and mirror positioning); and (4) precision machines (e.g., fast tool servos, micro/nano-positioning, and micro-engraving systems).

6.6.1 Piezoelectric-Based Micromanipulators

Figure 6.21 demonstrates a three-link micromanipulator which is being utilized for nanofiber grasping and manipulation applications in our research group (Saeidpourazar and Jalili 2008a, b). However, the precision positioning is limited due to lack of feedback sensors (manufacturer's hardware limitation) in addition to existence of the hysteresis nonlinearity in the manipulator's actuators. Therefore, an accurate hysteresis model for use in an inverse feedforward hysteresis compensation technique is the only solution for such a precise system.

6.6.2 Piezoelectrically Actuated Microcantilevers

Piezoelectrically actuated microcantilevers have recently emerged as an effective means for label-free chemical and biological species detection (Chen et al. 1995;

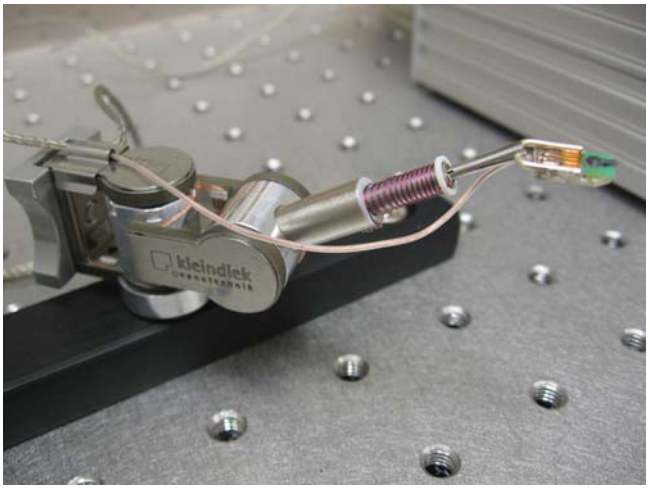

Fig. 6.21 MM3A® piezoelectrically driven micromanipulator for nanofiber grasping
Source: Saeidpourazar and Jalili 2008a, b, with permission

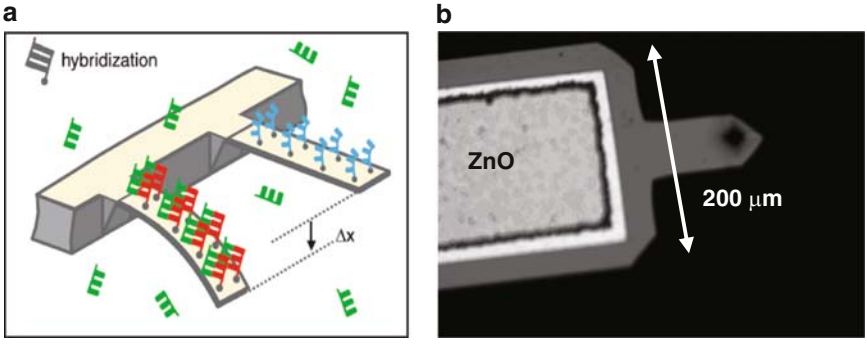

Fig. 6.22 (**a**) microcantilever-based DNA detection and (**b**) Piezoelectrically driven microcantilever
Source: Sepaniak et al. 2002, with permission

Afshari and Jalili 2007a, b, 2008; Mahmoodi et al. 2008a). These sensors operate through the adsorption of species on the functionalized surface of cantilevers (Fig. 6.22a). Studies are being performed for estimating the surface stress arising from the antigen–antibody interactions on the surface of the microcantilever (Afshari and Jalili 2008; Mahmoodi et al. 2008a; Salehi-Khojin et al. 2009b; Mahmoodi et al. 2008b). Figure 6.22b depicts a commercial piezoelectrically driven microcantilever, currently used for biological species detection in our research group. The hysteresis nonlinearity in the piezoelectric layer (ZnO layer highlighted in Fig. 6.22b), within the electromechanical voltage-to-force conversion, must be first detected and then mitigated to ensure accurate mass detection.

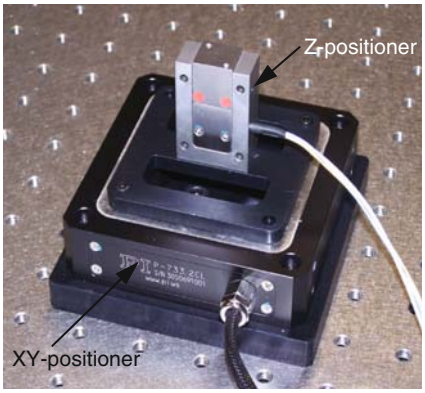

Fig. 6.23 3D Physik Instrumente® PZT-driven translational positioner in our research group

6.6.3 Piezoelectrically Driven Translational Nano-Positioners

Piezoelectrically driven translational positioners convert electrical energy into strain-induced energy resulting in translational displacements (Berlincourt 1981). Typically, they employ stacks of piezoelectric ceramic disks. The use of PZT-driven positioners has greatly expanded in recent years, and they offer a viable alternative which can lead to improvements in such applications as scanning probe microscopy (Schitter and Stemmer 2004; Xu and Meckl 2004), optical-memory devices (Park et al. 1995; Aoshima et al. 1992), microrobotics and microassembly (Hesselbach et al. 1998; Schmoeckel et al. 2000), nanoscale metrology (Haitjema 1996), and biomedical instruments (Meldrum 1997). However, hysteresis nonlinearity limits their ability to precisely control their micro- and nanoscale motions, which in turn limits their practical applications (Hu et al. 2005; Hu and Ben-Mrad 2003; Goldfarb and Celanovic 1997a, b; Bashash and Jalili 2007a, b, 2008). Figure 6.23 demonstrates a 3D PZT translational positioner which is being utilized for a number of micro- and nanopositioning applications in our research group (Bashash and Jalili 2006a, b, 2007a, b, 2008).

6.6.4 Future Directions and Outlooks

The day-to-day growth of applications of piezoelectric-based systems in general has evolved during past decade in part by focusing on more computer-controlled design, and machining operations for greater precision and tolerances. The evolution of select manufacturing processes from fixed "macro" systems to mobile "micro/nano" systems represents an exciting area for utilization of these systems due to their attractive features. As mentioned repeatedly in this chapter, one exciting thrust for actuator/sensor development, to facilitate the manufacturing and machining processes, is the application of piezoelectric materials (especially piezoceramics) to

realize innovative miniature motors capable of large torque and precision position/speed.

Although these materials have received well attention, there are some areas that could be seen as challenging subjects which may need further investigation and development. These could include (1) development of new materials and novel enhancement techniques to produce piezoelectric materials with higher expansion, strength, stability, repeatability and durability; (2) development of more robust and easy-to-implement feedforward and feedback positioning control frameworks; and (3) development of dedicated hardware and high-speed signal processing platforms for demanding application of piezoelectric-based systems in areas such as ultrafast scanning probe microscopy (e.g., AFM), ultrahigh precision positioning and manufacturing, and complex manipulation tasks at small scales.

Summary

This chapter presented a detailed discussion on physical principles and constitutive models of piezoelectric materials. Starting with an elementary level in fundamentals of piezoelectricity, the constitutive models of piezoelectric materials were derived, in the most possible general form, based on the unified energy approach discussed in Chap. 4. Important and practical parameters for piezoelectric materials along with the most common configurations of piezoelectric sensors and actuators were then presented. The engineering applications of piezoelectric materials and structures with an emphasis to piezoelectric-based actuators and sensors were discussed. The materials presented in this chapter shall form the basis for the subsequent modeling and control developments for both piezoelectric-based systems and vibration-control systems discussed in Chaps. 8 and 9, respectively.

Chapter 7
Hysteretic Characteristics of Piezoelectric Materials

Contents

7.1 The Origin of Hysteresis 161
7.1.1 Rate-Independent and Rate-Dependent Hysteresis 162
7.1.2 Local versus Nonlocal Memories 163
7.2 Hysteresis Nonlinearities in Piezoelectric Materials 163
7.3 Hysteresis Modeling Frameworks for Piezoelectric Materials 164
7.3.1 Phenomenological Hysteresis Models 165
7.3.2 Constitutive-based Hysteresis Models 170
7.4 Hysteresis Compensation Techniques 179
Summary

This chapter presents a brief but self-contained discussion on the origin of hysteresis in piezoelectric materials, some select modeling frameworks and effective compensation techniques. The materials given in this chapter shall prepare the readers for vibration-control systems using piezoelectric actuators and sensors discussed in Chaps. 9 and 10.

7.1 The Origin of Hysteresis

The constitutive relationships developed in the preceding subsection were based on linear elasticity (stress–strain relationship) and permittivity (dielectric displacement–electric field relationship) assumptions. However, in practice, piezoelectric materials exhibit nonlinear characteristic including, most importantly, hysteresis nonlinearity. The hysteresis phenomenon is encountered in many different areas of science and is not limited to piezoelectric materials only. Examples of such materials and systems include shape memory alloys, viscoelastic materials, electro-active polymers, magnetostrictive materials, electro/magneto-rheological fluids, concrete reinforced structures, and gear systems. Figure 7.1 depicts typical examples of hysteresis nonlinearity in three different materials.

Although hysteresis phenomenon has been around for many years, it is still the subject of many research and investigations in different fields. This is mainly due to its ubiquitous and complex structure. In order to avoid confusion and ambiguity and

N. Jalili, *Piezoelectric-Based Vibration Control*,
DOI 10.1007/978-1-4419-0070-8_7,

© Springer Science+Business Media LLC 2010

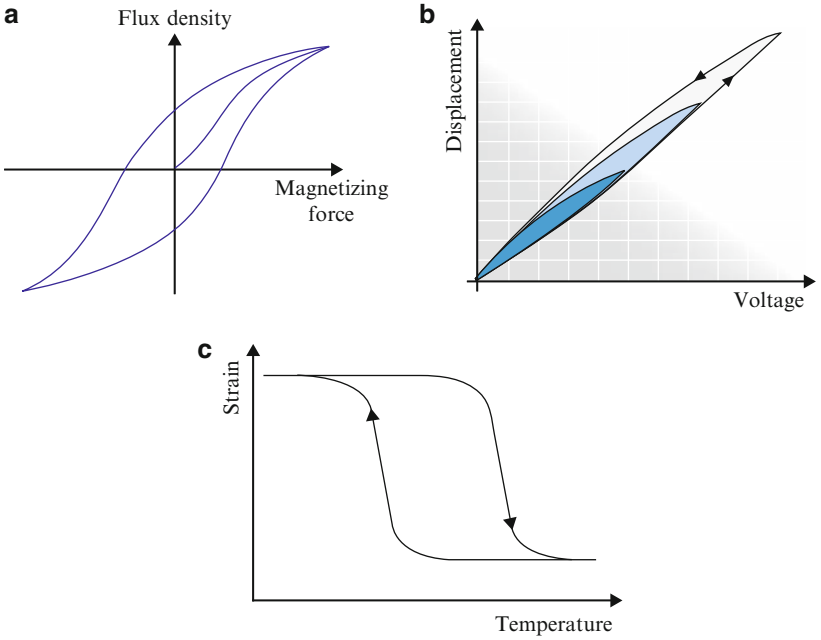

Fig. 7.1 Hysteresis nonlinearity in (**a**) magnetic materials, (**b**) piezoelectric materials, and (**c**) shape memory alloys

for the readers' convenience, a simple, yet general, mathematical representation is given here for this phenomenon. On the basis of this description, the hysteresis operator is referred to as a multi-branch nonlinear input/output relationship, for which the future value of output depends not only on the instantaneous values of the input but also on the history (past or memory) of its operation, especially the extremum values, *see* Fig. 7.1 (Krasnosel'skii and Pokrovskii 1989; Bashash and Jalili 2006a, 2007a and 2008). Hence, the hysteresis operator belongs to a more general nonlinear multi-valued family of operators.

7.1.1 Rate-Independent and Rate-Dependent Hysteresis

The "rate-independent" hysteresis refers to a family of multi-branch nonlinearities that *rate*, *speed* or *type* of variations between instantaneous or past extremum points of input signal do not influence the values of the output. Many hysteresis models based on this type have been developed and verified to be effective experimentally, especially for magnetic and piezoelectric hysteresis (Tao and Kokotovic 1996; Mayergoyz 2003 and reference therein). This type of modeling framework indicates that the time effects on the input/output relationship are negligible. Hence, this type of hysteresis is sometime referred to as "static" relationship. However, for very fast input variations, time effects cannot be ignored and must be taken

into account, since they lead to complicated and sometime cumbersome hysteresis models (Mayergoyz 2003; Ang et al. 2003). In order to avoid such complication, in practice, however, the rate-independent model of hysteresis can be augmented with effective control and compensation techniques, which can greatly enhance the performance of a variety of systems with dominant rate-dependent hysteresis nonlinearity (Bashash and Jalili 2007b).

7.1.2 Local versus Nonlocal Memories

The rate-independent hysteresis nonlinearities could be divided into two categories: (1) nonlinearities with "local" memories and (2) nonlinearities with "nonlocal" memories. As mentioned earlier in the definition of the hysteresis operator, the values of input may provoke several values of output, since this is a multi-valued, multi-branch nonlinearity. In hysteresis with local memories, the influence of history or past (or "memory") on future values of output is seen only through the current value of output. However, in hysteresis model with nonlocal memories, the future values of output depend not only on the current values of input but also on the past extremum values of input.

7.2 Hysteresis Nonlinearities in Piezoelectric Materials

As mentioned in the preceding subsection, while ferromagnetic hysteresis is the best-known type of hysteresis, many other materials experience such multi-branch nonlinearities. Especially, piezoelectric materials suffer from material-level hysteresis nonlinearity that drastically degrades their performance and may cause operational instability in feedback control applications. While the origin of such nonlinearity in piezoelectric materials is still the subject of many research studies, one widely accepted theory signifies the existence of hysteresis in these materials due to internal sliding in material crystalline polarization. In other words, upon the application of a varying input, residual misalignment of crystal grains in the poled materials causes an internal energy dissipation (Ge and Jouaneh 1995; Ikeda 1996). Although it seems that this phenomenon is less evident for inputs with low variations, the presence of residual strains (even upon removal of the electric field) can be quite important. Figure 7.2 demonstrates a typical hysteresis response of a piezoelectric actuator to an alternating triangular input profile with nine turning points, where the direction of input is changed (Bashash and Jalili 2006a).

While the original meaning word "hysteresis" refers to "lagging behind," this definition should not be interpreted as "phase lag" in many linear systems such as viscous-type memory (Moheimani and Fleming 2006). In piezoelectric materials, the hysteresis response exhibits sharp turns at extremum values of inputs similar to the plots shown in Fig. 7.2. This behavior is totally different in linear systems with phase lag in the sense that the output values change more smoothly at the

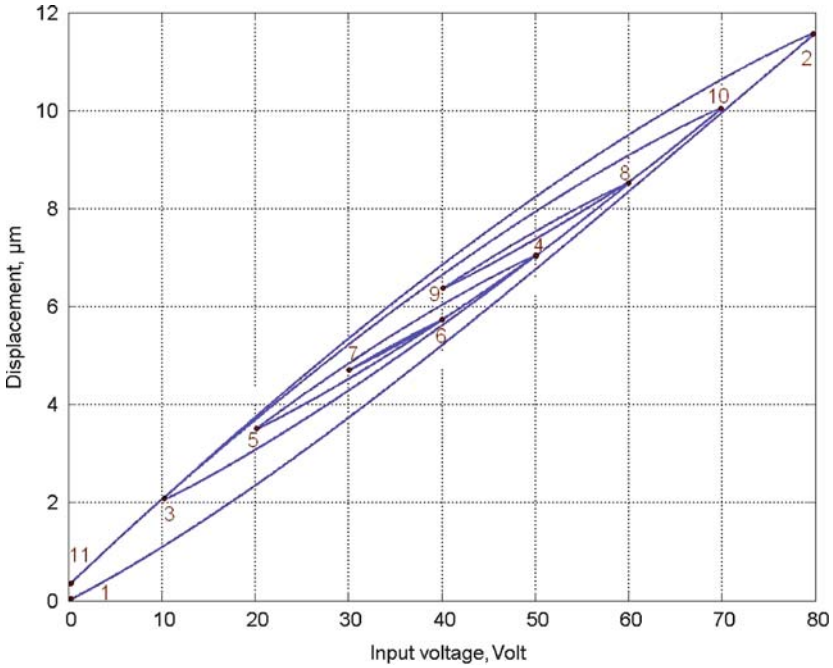

Fig. 7.2 Hysteresis response of a piezoelectric actuator to an alternating triangular input
Source: Bashash and Jalili 2006a, with permission

extremum values of input. Having said that, the apparent similarity between these two behaviors has been utilized to develop hysteresis models using an unmodeled phase lag (Washington 2006).

7.3 Hysteresis Modeling Frameworks for Piezoelectric Materials[1]

Conceptually, hysteresis models can be classified into two different types: (1) *constitutive-based* approaches inspired from the underlying physics of the phenomenon and derived based on some empirical observations, and (2) *phenomenological* approaches utilizing mathematical models describing the phenomenon without considering its underlying physics.

It is clear that covering all the models developed for hysteresis is impossible and outside of the scope in this book. However, in an effort to provide the reader with useful background in this regard, a brief, yet self-contained overview of some of the select models is given in this subsection. Without going too much

[1] The materials in this section may have come, collectively or directly, from our publications in this area as properly cited in the text.

into the details, this brief overview includes both phenomenological and constitutive methodologies with a comparative study on their computational efficiency and practical implementation issues.

7.3.1 Phenomenological Hysteresis Models

Phenomenological approaches for hysteresis modeling have been extensively developed (Gorbet et al. 2001; Visintin 1994; Brokate and Sprekels 1996). The most well-known approaches in this category, known as the Preisach model and its variations (Ge and Jouaneh 1997; Galinaitis 1999), have received general acceptance in modeling hysteresis in piezoelectric materials especially piezoceramics. A simplified subclass of the Preisach model, the Prandtl-Ishlinskii (PI) hysteresis operator, has been also developed (Chaghai et al. 2004; Ang et al. 2003). We briefly outline, next, these models as the most commonly used phenomenological methods.

Preisach Hysteresis Model: The Preisach model, a purely intuitive method (Preisach 1935) and primarily used in magnetic field modeling (Mayergoyz 2003), has been extensively implemented in numerous applications in superconductive, magnetic and ferroelectric materials (Ge and Jouaneh 1997; Hughes and Wen 1997; Bobbio et al. 1997). In this model, the actuator expansion is related to input voltage as (Ge and Jouaneh 1997)

$$x(t) = H_{VD}\{V_a(t)\} = \iint_{\alpha \geq \beta} \mu(\alpha, \beta)\gamma_{\alpha\beta}[V_a(t)]\mathrm{d}\alpha\mathrm{d}\beta \tag{7.1}$$

where $x(t)$ is the piezoelectric material output (e.g., expansion) and $V_a(t)$ is the input voltage. $\gamma_{\alpha\beta}[\cdot]$ are the elementary two-position relay operators as shown in Fig. 7.3a, and α and β correspond to "up" and "down" switching values of input, respectively (*see* Fig. 7.3a). As seen, the classical Preisach model represents the hysteresis as a continuous weighted superposition of a set of two-position relay operators. $\mu(\alpha, \beta)$, often referred to as the Preisach function, is a weighting function which is numerically calculated using a triangle method shown in Fig. 7.3b (Mayergoyz 2003). We refer interested readers to Mayergoyz (2003) for a complete and comprehensive overview of this model and its analogy to functional analysis (Friedman 1982) in which a complicated operator can be represented as a superposition of simpler elementary operators. It must be noted that although elementary hysteresis operators $\gamma_{\alpha\beta}[\cdot]$ are typically based on local memories, it can be proved that the nonlocal memory effect can be captured by this type of modeling (Mayergoyz 2003).

Although Preisach model provides a purely mathematical tool for modeling complex hysteresis loops, it does not provide a physical insight into the phenomenon. Furthermore, the numerical implementation of this model requires considerable numerical efforts, and hence, constitutive approaches are sometime preferred. These types of modeling frameworks will be discussed later at the end of this subsection.

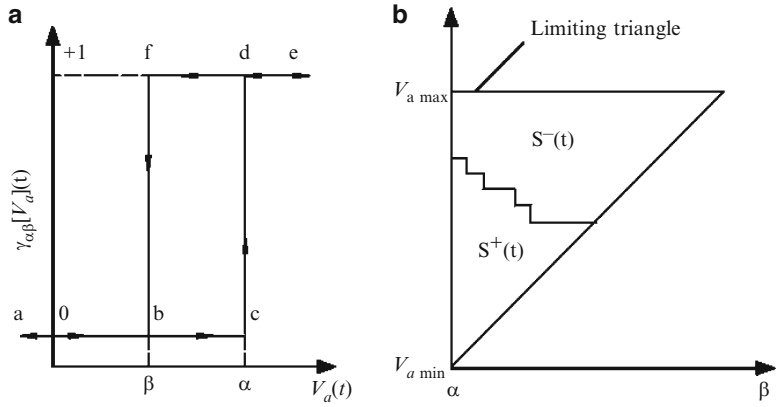

Fig. 7.3 **(a)** Hysteresis operators, and **(b)** triangle method for calculating the weighting function

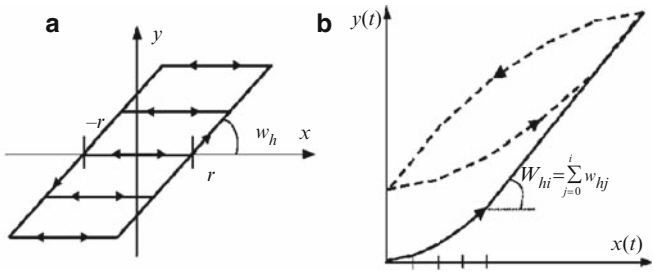

Fig. 7.4 **(a)** Generalized backlash operator with threshold r and weighting value w_h, and **(b)** hysteresis loop consisting of linear superposition of many backlash operators

Prandtl-Ishlinskii (PI) Hysteresis Model: Among the phenomenological methods, Prandtl-Ishlinskii (PI) hysteresis operator has attracted significant attention due to its ease of implementation as well as existence of its inverse model analytically (Kuhnen and Janocha 2001; Bashash and Jalili 2007b). This model is a discretized subclass of Preisach operator which nearly presents the same level of accuracy in practice (*see* Fig. 7.4a). Through superposing a set of weighted backlash operators with different threshold values, the PI operator attempts to predict the multi-branch hysteresis response. From a physical viewpoint, this combination constructs models of elasto-plasticity with strain-hardening nonlinearity (Visintin 1994).

In short, the expression for a generalized backlash operator is given by

$$y(t) = H_{r,w_h}[x, y_0](t) = w_h \max\{x(t) - r, \min\{x(t) + r, y(t - T)\}\} \qquad (7.2)$$

with

$$y_0 = y(0) = w_h \max\{x(0) - r, \min\{x(0) + r, y(0)\}\} \qquad (7.3)$$

where $x(t)$ is the input, $y(t)$ is the operator output, r is the control input threshold value of the magnitude of the backlash, w_h is the weighing value, and T is the

sampling period. Complex hysteretic nonlinearity can then be modeled using a linearly weighted superposition of many backlash operators with different threshold and weight values as (*see* Fig. 7.4b)

$$y(t) = \sum_{i=0}^{n} H^{i}_{r,w_h}[x, y_0](t) = \sum_{i=0}^{n} w^{i}_{h} \max\{x(t) - r^{i}, \min\{x(t) + r^{i}, y(t-T)\}\} \tag{7.4}$$

with the weight vector $\vec{H}_{r,w_h}[x, \vec{y}_0](t) = [H^{0}_{r,w_h}[x, y^{0}_{0}](t), \ldots, H^{n}_{r,w_h}[x, y^{n}_{o}](t)]^T$, $\vec{w}_h = [w^{0}_{h}, \ldots, w^{n}_{h}]^T$, threshold vector $\vec{r} = [r^0, \ldots, r^n]^T$ and $r^0 < r^1 < \cdots < r^{n-1} < r^n$.

Figure 7.5 depicts a typical hysteresis response obtained from the superposition of four backlash operators with different threshold and weighting values.

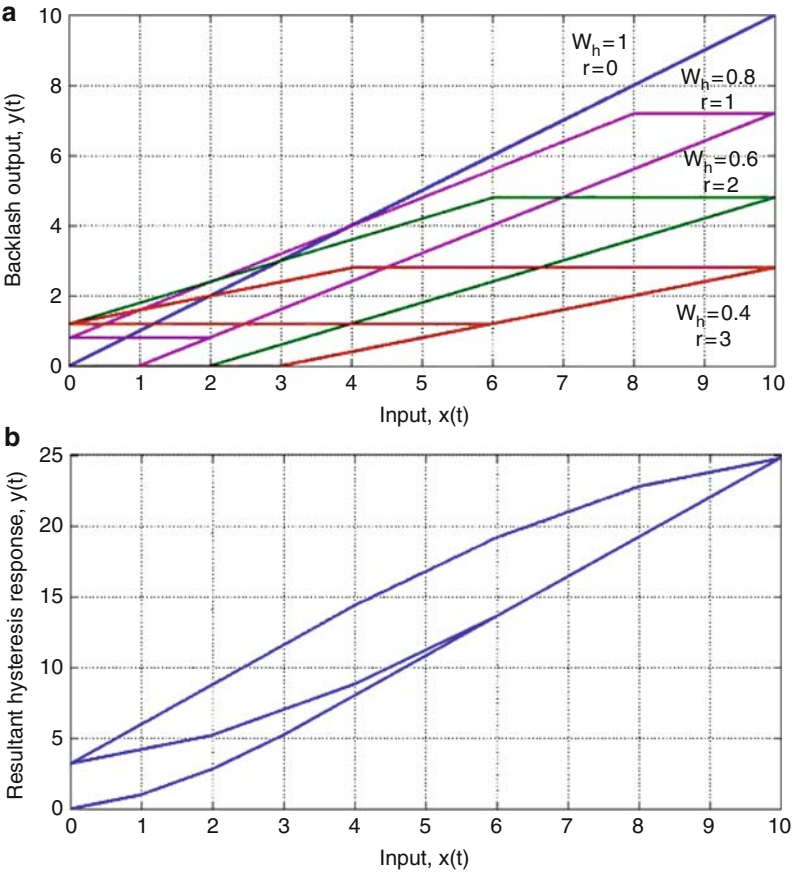

Fig. 7.5 A representative example of hysteresis obtained by superposition of four backlash operators with different threshold values and weighting values
Source: Bashash and Jalili 2007b, with permission

Due to its phenomenological nature, the PI operator suffers from its rigid structure which may lead to inaccuracy. Consequently, several modifications have been proposed to improve this methodology (Bashash and Jalili 2007b; Ang et al. 2003), including some recent ones (Bashash and Jalili 2007a, b, 2008). The need for such improvements is better realized when the symmetry property around the center of the loop for this and other phenomenological approaches (e.g., Preisach) is utilized in precision positioning applications. However, the actual hysteretic response of piezoelectric actuators does not exhibit such symmetric property. This deficiency results in precision inaccuracy and degrades the performance of piezoceramic actuators, especially when utilized in precision positioning applications. To address this, several remedies have been proposed including modified PI hysteresis model as briefly described next (Chaghai et al. 2004).

Modified Prandtl-Ishlinskii (PI) Hysteresis Model: In addition to aforementioned mismatch between the proposed and actual symmetry property around the center of the loop, PI operator suffers from lack of accuracy in adjusting the residual displacement around the origin. One solution is to design and combine new operators with the PI operator in order to compensate for the described deficiencies. However, this increases the modeling complexity and limits its practical implementation (Ang et al. 2003).

To address this, a recent modification in the describing equation of the backlash operator has been proposed to simultaneously compensate the symmetry and residual displacement requirements (Bashash and Jalili 2007b). More specifically, a new parameter $\eta > 0$ is introduced to be interleaved in the primary backlash operators of the PI hysteresis model (7.4) as

$$y(t) = \sum_{i=0}^{n} {H_{r,\eta,w_h}}^i[x, y_0^i](t) = w_h^i \max\{x(t) - r^i, \min\{x(t) + \eta^i r^i, y(t-T)\}\}$$
$$y_0^i(0) = y^i(0) = w_h^i \max\{x(0) - r^i, \min\{x(0) + \eta^i r^i, y^i(0)\}\} \quad (7.5)$$

The parameter η (or η^i) alters the threshold of the backlash in the descending state; the larger the η is chosen, the more delay in the descending state. With proper values of η for every individual backlash operator, the flexibility and accuracy of the model can be significantly enhanced. Figure 7.6 demonstrates the response of the modified backlash operator with different values of η. The modified PI hysteresis operator is then written as (Bashash and Jalili 2007b)

$$y(t) = \sum_{i=0}^{n} w_h^i \max\{x(t) - r^i, \min\{x(t) + \eta^i r^i, y(t-T)\}\} \quad (7.6)$$

Leaving much of the details to Bashash and Jalili (2007b), to demonstrate the effectiveness of the modified PI operator over the conventional approach, the proposed model and conventional operator are both implemented on a Physik Instrumente P-753.11CPZT-driven nano-positioner with high-resolution capacitive position sensor (*see* Fig. 7.7).

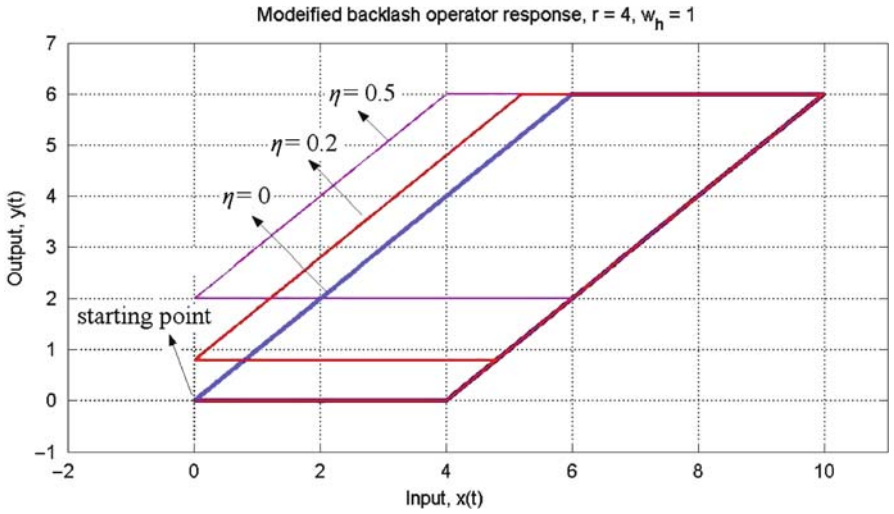

Fig. 7.6 Modified backlash operator with different delay values for the descending state
Source: Bashash and Jalili 2007b, with permission

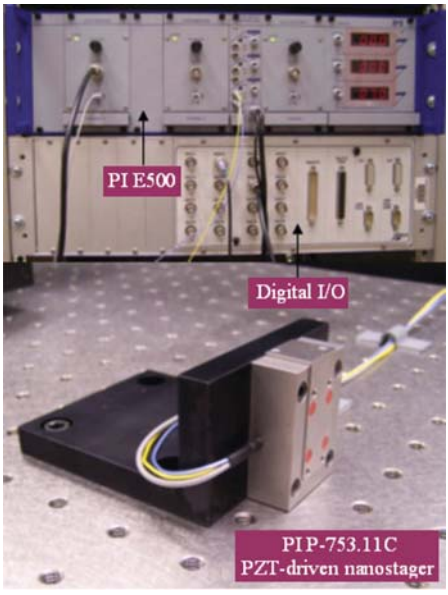

Fig. 7.7 Experimental setup of the Physik Instrumente P-753.11C PZT-driven nano-positioner
Source: Bashash and Jalili 2006a, with permission

To identify the weighting parameters and appropriate values of η, 26 backlash operators are exploited here to cover the input voltage range of 0–60 V. This number of backlash operators ensures a minimal error between the experimental results and model response. The threshold values are chosen in an orderly increasing sequence, with fine intervals for the initial inputs and coarse intervals for the last inputs. Figure 7.8 depicts the identification outcomes for both experimental results and identified model. As seen from both system output response (Fig. 7.8a) and hysteresis curves (Figs. 7.8b and c), the proposed modified PI is capable of identifying the hysteresis very well.

To demonstrate the effectiveness of the modified PI model over the conventional approach, a representative model for the conventional approach is developed by setting η^i equal to zero in (7.6). The same number of backlash elements with the same threshold values are utilized, and for the sake of accuracy, an adjustable offset is added to the operator to locate the hysteresis loops as close as possible to the actual response. Figure 7.9b depicts the hysteresis response of the conventional PI model to the input shown in Fig. 7.8a. By comparing the modeling errors between the conventional and the modified approaches, the error signature shown in Fig. 7.9b, it is clearly observed that the modified PI model demonstrates improved response over the conventional approach.

7.3.2 Constitutive-based Hysteresis Models

As mentioned earlier, due to the symmetrical property of the operators used in the Preisach model, the hysteresis loops become symmetric around the center of the loop. However, this is not the case for actual hysteretic response of piezoelectric materials, especially PZT actuators and positioners. Moreover, numerical implementation of this model requires considerable effort in calculating the weighting function (Hu and Ben-Mrad 2003; Ge and Jouaneh 1997; Hughes and Wen 1997). Similar to the Preisach operator, the Prandtl-Ishlinskii model also had the drawback of symmetry (Bashash and Jalili 2006b; Ang et al. 2003), and limited flexibility in adjusting the residual displacement around the origin (Bashash and Jalili 2006b).

To remedy these issues associated with phenomenological approaches, extensive research work has been carried out to develop effective hysteresis models using constitutive approaches. For instance, an electromechanical model combined with nonlinear first order differential equations has been proposed to describe both hysteresis and the systems dynamics (Aderiaens et al. 2000). A generalized Maxwell resistive capacitor model was also utilized as a lumped-parameters casual representation of hysteresis by Goldfarb et al. (Goldfarb and Celanovic 1997a, b). However, the constitutive approaches have limited performance characteristics as the underlying physics of the hysteresis phenomenon has not been completely understood.

In an attempt to enable a more precise modeling and control of hysteresis, Bashash and Jalili (2006a) recently proposed the development of memory-dominant properties of hysteresis (Bashash and Jalili 2007a, 2008). Without giving much

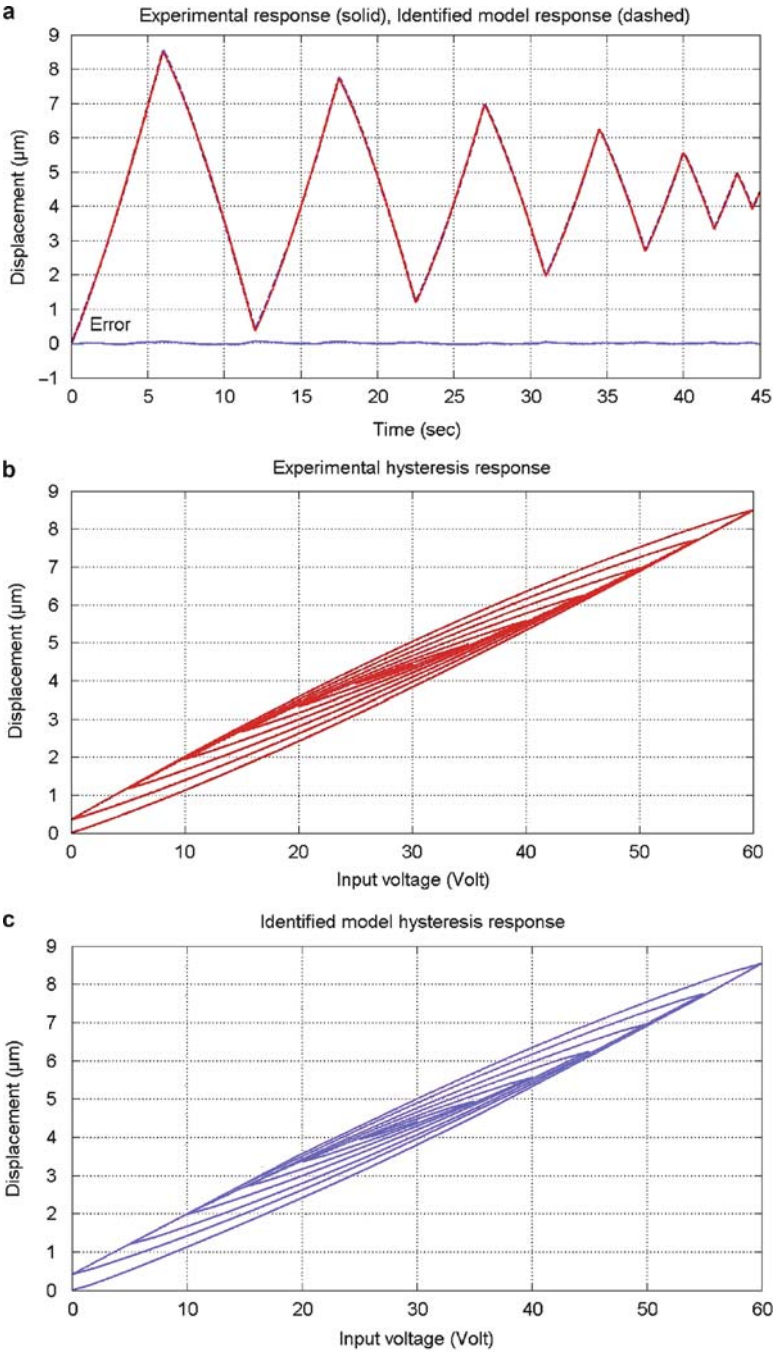

Fig. 7.8 **(a)** Input signal to PZT-driven nano-positioner and experimental and identified model response $[y(t)]$, and hysteresis response $[y(t)$ vs. $V_a(t)]$ of **(b)** piezoelectric actuator and **(c)** identified model
Source: Bashash and Jalili 2007b, with permission

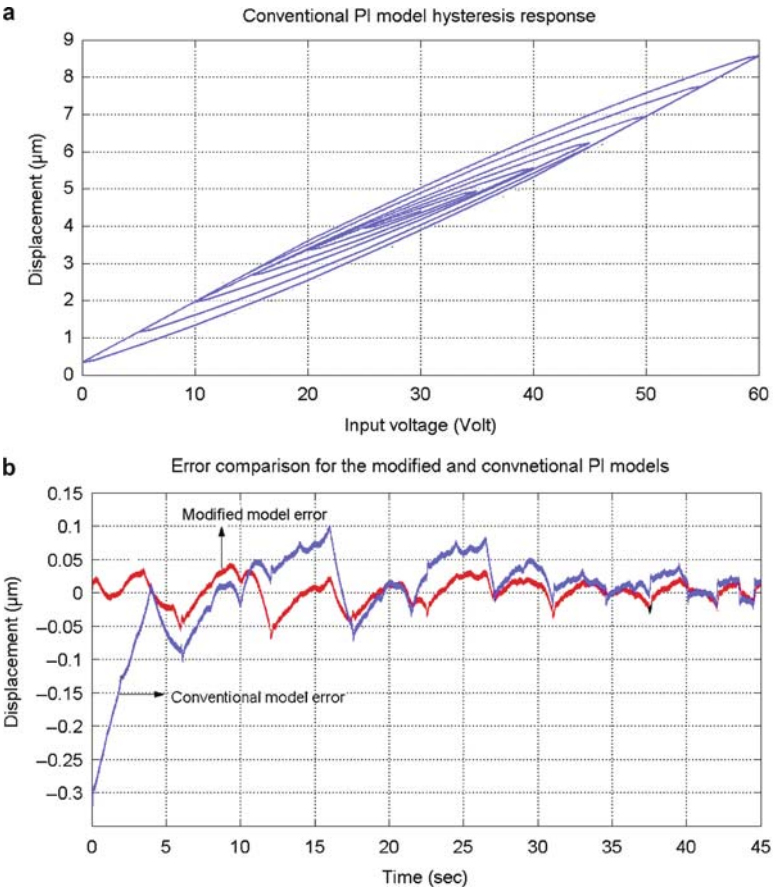

Fig. 7.9 **(a)** Hysteretic response of the conventional PI model, and **(b)** modeling error comparisons for the conventional and modified PI models
Source: Bashash and Jalili 2007b, with permission

details and in an effort to keep the book focused, we only highlight, next, the key features of this method and provide comparative results with conventional phenomenological approaches.

Memory-dominant Hysteresis Modeling: Although hysteresis nonlinearity appears to be unpredictable in nature, our extensive experiments and observations have enabled the realization of the underlying physics of its intrinsic behavior, and observe an intellectual harmony in the manner in which this phenomenon behaves. More specifically, three properties, namely, *targeting* turning points, curve *alignment* and *wiping-out* effect, exist in these materials based on empirical observations (Bashash and Jalili 2006a). That is, the locations of turning points can be detected and recorded for the prediction of future hysteresis trajectory. The ascending and the descending curves are then separated and the loading or major curves are approximated through a function with exponential form and two shaping parameters. An

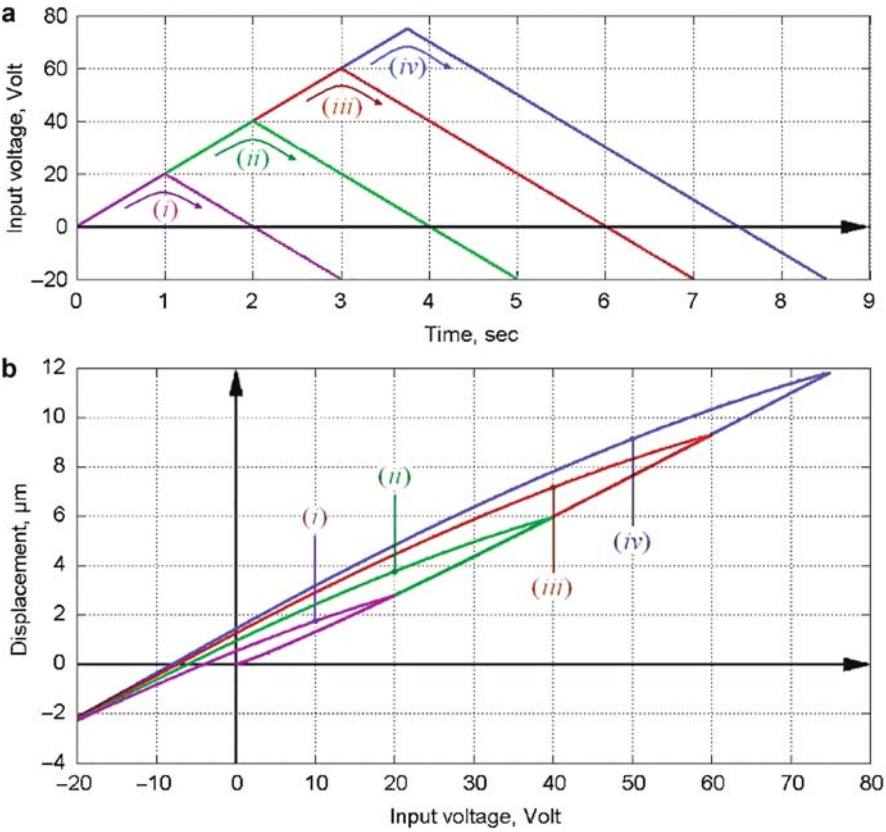

Fig. 7.10 Hysteresis response of the actuator to triangular input signals; **(a)** input signals and **(b)** actuator response
Source: Bashash and Jalili 2006a, with permission

internal trajectory can then be assumed to follow a multiple-segment path via a continuous connection of several curves passing through every two consequent turning points. These curves adopt their shapes from the reference hysteresis curves with exponential and polynomial configurations. The internal hysteresis path can then be identified through a mapping technique between a set of untouched internal turning points that indicate the trace of hysteresis trajectory (Bashash et al. 2008).

In order to better describe the memory-dominant properties of hysteresis, a set of experimental tests on a Physik Instrumente PZT-driven positioner (*see* Fig. 7.7) is performed (Bashash and Jalili 2006a, 2007b). Figure 7.10 demonstrates the hysteretic response of the actuator to a set of four alternating continuous quasi-static input profiles. Hysteresis curves are encompassed by two so-called "major" or "reference" curves. All ascending curves starting from zero follow an identical path on the ascending reference curve. All the descending curves branching from different locations are similar in shape and approach a particular converging point.

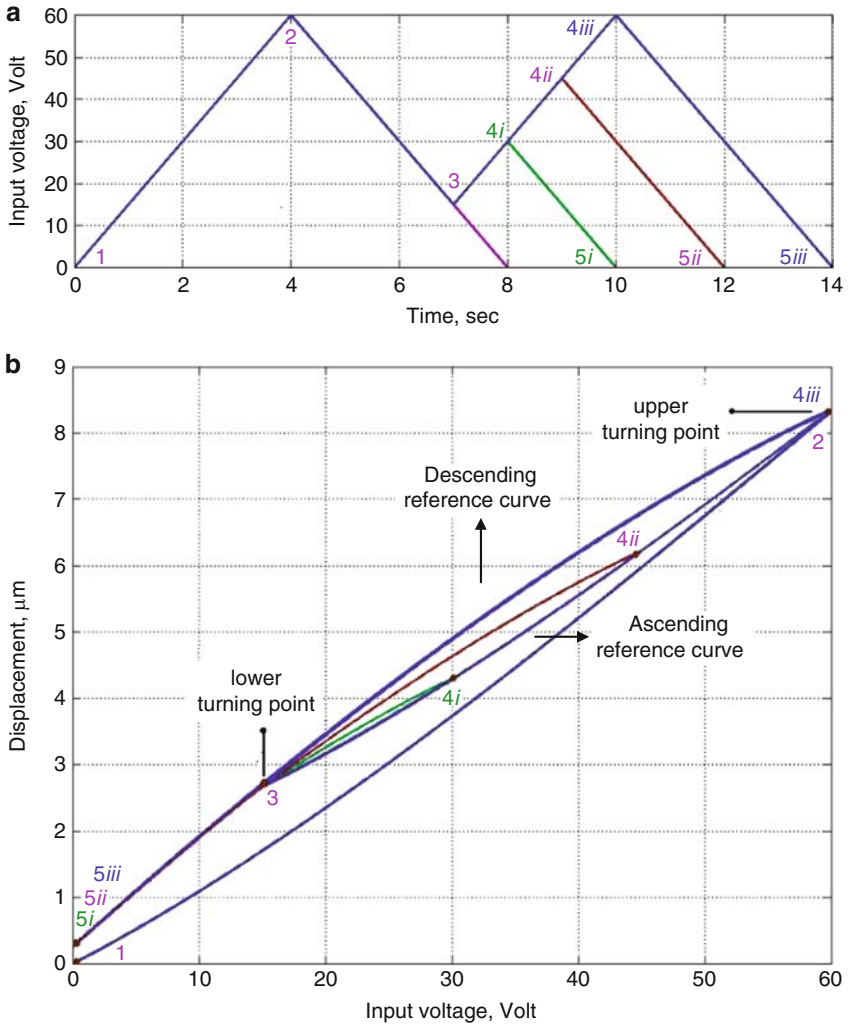

Fig. 7.11 Hysteresis response to a set of four alternating continuous input profiles; **(a)** input signals and **(b)** stage response
Source: Bashash and Jalili 2006a, with permission

Recording Turning Points (Bashash and Jalili 2006a): Three out of four input signals have four segments. After moving up to point #2 the direction of the input is changed, where the upper turning point is recorded (*see* Fig. 7.11). The input signal then descends to point #3 where the lower turning point is recorded. The input again rises to point #4 and finally descends to its zero ending point (point #5). A closer look at Fig. 7.11b clearly demonstrates that the hysteresis track, branching from a turning point approaches the previous turning point, so that the configuration of the

curve remains similar to the related reference curve. For example, tracks originating from points #3 and #4 in Fig. 7.11b approach points #2 and #3, respectively.

Curve Alignment (Bashash and Jalili 2006a): This is the key property of hysteresis; the direction of hysteresis path slightly changes after hitting and overtaking a turning point. Hence, curves approaching point #3 from three different points marked as #4 merge together after hitting the turning point, and continue on an identical path. The physical interpretation of this hysteresis property is most interesting: There is no way for an internal path to break the hysteresis bounds and escape from the borders sketched by other hysteresis trails; all hysteresis tracks arriving to a turning point unite together and align themselves to the previously broken curve associated with that turning point. After curve alignment in a crossed turning point, the new trajectory continues the path of previously broken track toward the intact target point. Therefore, for precise prediction of hysteresis trajectory, the location of turning points must be stored within the so-called "model memory unit."

Wiping-out Effect (Bashash and Jalili 2006a): Based on this property, only the alternating series of dominant internal loops, which are not crossed by other hysteresis tracks, are stored in the memory. All other loops are "wiped out." Figure 7.12 illustrates the wiping-out property when the input signal surpasses a dominant extremum. Dominant extrema are the maximum or minimum points that have, respectively, larger or smaller values than the subsequent values of input signal. Therefore, the first and second wipe-outs occur between points #7 and #8, where the input exceeds extrema #6 and #4, respectively. The third wipe-out occurs between points #9 and #10, where the input exceeds extremum #8. We remark that the wiping-out effect coincides with the curve alignment effect, where the hysteresis trajectory hits and surpasses a turning point. Wiping-out is a unique property of hysteresis that permits evacuating the memory unit from the unused turning points associated with the loop that has been wiped out.

Memory-dominant Hysteresis Modeling Paradigm: Now that we have established the required foundations and experimentally validated the memory-based properties of hysteresis, an exponential expression is proposed to appropriately fit a uniform hysteresis curve between two arbitrary points (y_1, x_1) and (y_2, x_2) in output–input plane (Bashash and Jalili 2006a, 2008)

$$x(y) = F(y, y_1, x_1, y_2, x_2) = k(1 + ae^{-\tau(y-y_1)})(y - y_1) + x_1 \tag{7.7}$$

where a and τ are constant parameters that shape the hysteresis curves, and k represents the slope of exponential hysteresis mapping between two initial and ultimate points given by

$$k = \frac{x_2 - x_1}{y_2 - y_1}(1 + ae^{-\tau(y_2-y_1)})^{-1} \tag{7.8}$$

Parameters a and τ are identified for the ascending and the descending reference curves and kept unchanged for any other internal curves, while parameter k is calculated for every individual curve between two initial and ultimate points. Based on

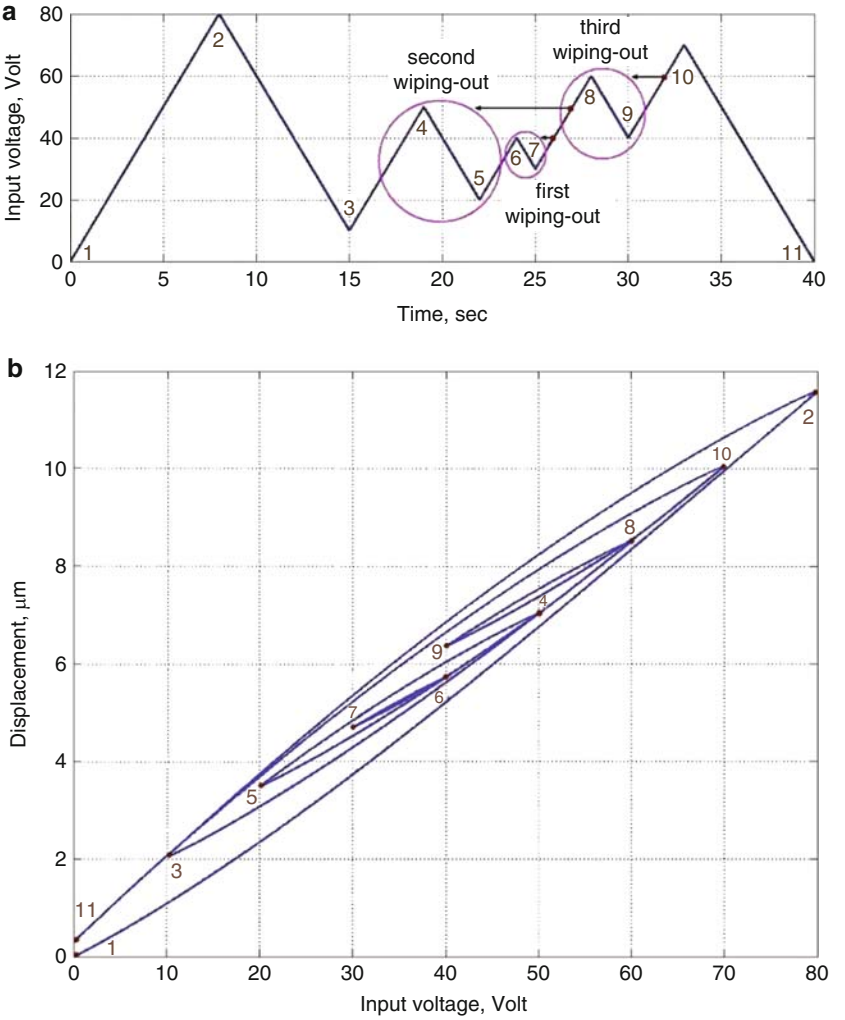

Fig. 7.12 Wiping-out and curve alignment properties of hysteresis: **(a)** arbitrarily alternating input profile, and **(b)** the resultant hysteresis response
Source: Bashash and Jalili 2006a, with permission

this mapping technique, the hysteresis path becomes predictable for any trajectory between known initial and target turning points.

Figure 7.13 demonstrates a typical hysteretic response consisting of n internal loops. Lower and upper turning points are labeled by L and U subscripts, while the ascending and descending curves are labeled with A and D subscripts, respectively. The numbering sequence starts from the smallest internal loop to the largest surrounding loop. Regarding the curve alignment in the turning points, for the ascending curve starting from point (y_{L1}, x_{L1}) and shown with a dashed

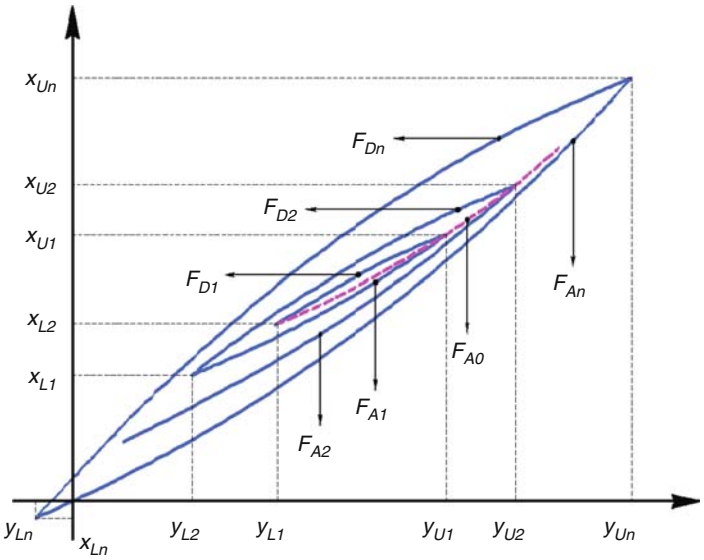

Fig. 7.13 Typical input/output hysteresis response with n internal loops
Source: Bashash, Jalili 2006a, with permission

configuration and labeled by F_{A0} in Fig. 7.12, the prediction of hysteresis path is expanded to the following expression:

$$\begin{aligned} x_A(y) &= F_{A0}(y) = F(y, y_{L1}, x_{L1}, y_{U1}, x_{U1})\, G(y, y_{L1}, y_{U1}) \\ &\quad + \sum_{i=1}^{n} F_{Ai}(y)\, G(y, y_{Ui}, y_{U(i+1)}) \end{aligned} \tag{7.9}$$

where n is the number of intact internal loops, and G represents the Heaviside function expressed as

$$G(x, a, b) = 1(\text{for}\, a \le x \le b), \text{ and } 0\ (\text{for}\ x > b\ or\ x < a) \tag{7.10}$$

Equation (7.9) states that hysteresis path is composed of a sequential set of different hysteretic curves that are separated by intervals and distinguished by turning points. Similarly, for a descending curve starting from (y_{U1}, x_{U1}), the hysteresis path is expressed as

$$\begin{aligned} x_D(y) &= F(y, y_{U1}, x_{U1}, y_{L1}, x_{L1})\, G(y, y_{L1}, y_{U1}) \\ &\quad + \sum_{i=1}^{n} F_{Di}(y)\, G(y, y_{L(i+1)}, y_{Li}) \end{aligned} \tag{7.11}$$

To demonstrate the model performance, a $\pm$ 10 V/s input profile is designed so that the model requires at least three memory units for the accurate prediction of

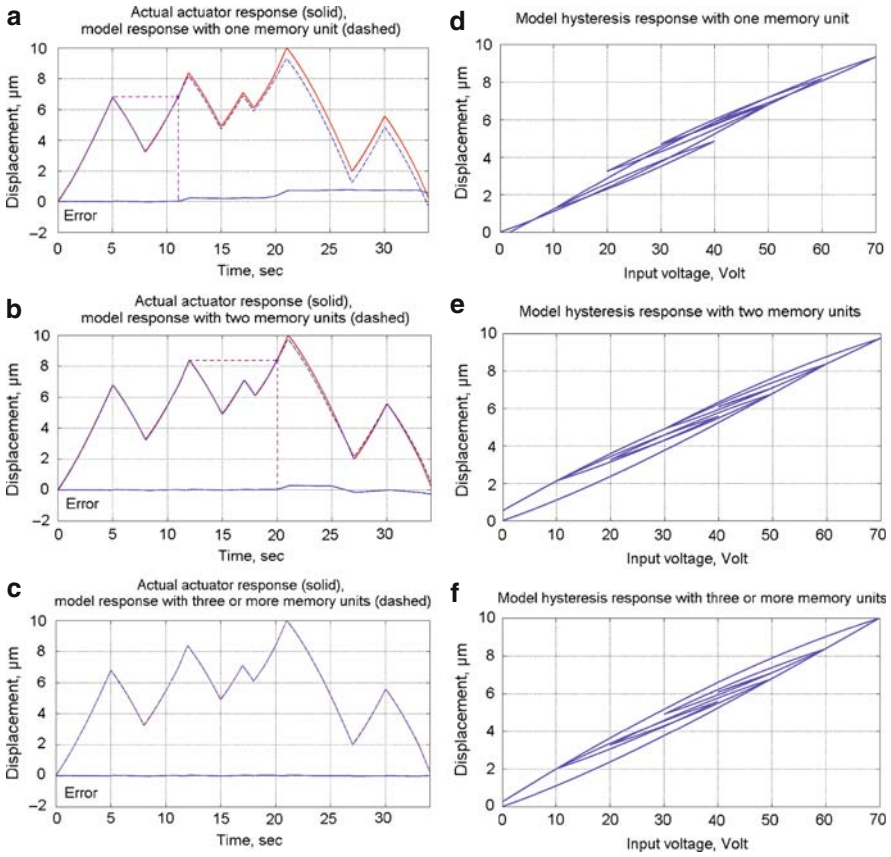

Fig. 7.14 Experimental verification of the memory-dominant hysteresis model; system responses with **(a)** one, **(b)** two, and **(c)** three memory units; hysteresis response with **(d)** one, **(e)** two, and **(f)** three memory units
Source: Bashash and Jalili 2006a, with permission

hysteresis trajectory. The developed model is simulated with one, two and three memory units separately. Figure 7.14 depicts both the simulation and experimental results (Bashash and Jalili 2006a). As previously predicted, model response with one memory unit (Fig. 7.14a) diverges from the actual hysteresis response after input passes the first dominant extremum, in the same manner that the model response with two memory units (Fig. 7.14b) diverges as the input overtakes the second dominant extremum. Models with three or more memory units (Fig. 7.14c) demonstrate impeccable performances with an insignificant modeling error. Figures 7.14d–7.14f demonstrate the hysteresis evolution, as the number of memory units increases to a minimum value. It is, therefore, concluded that an accurate prediction of hysteresis requires a sufficient number of memory units to be explicitly included in the model.

We remark that once the parameters for shaping hysteresis (a and τ in (7.7), (7.9) and (7.11)) are identified for an actuator, they remain constant if the actuator is not subjected to large temperature variations or intense impacts. However, the aging effect may gradually change the parameters over time. Therefore, the actuator parameters must be calibrated on a monthly or yearly basis, depending upon the number of actuation cycles.

To compare the memory-based hysteresis model response with phenomenological approaches, the Prandtl-Ishlinskii (PI) hysteresis operator is used. A bias is added to the operator output to adjust the hysteresis loops in a proper location, and 26 backlash operators (similar to the PI operator results in the preceding subsection) are employed to maintain the continuity of the response. Figure 7.15 shows that the PI model response to the same input applied in the previous simulation has 0.29% maximum and 0.054 μm average modeling errors values, while the proposed memory-based model yields only 0.05% maximum and 0.013 μm average modeling error values. This clearly demonstrates the advantage of the memory-based framework over the widely utilized PI model and its variations.

7.4 Hysteresis Compensation Techniques

As clearly demonstrated in the preceding subsections, hysteresis models typically have complicated structures due to the multi-branch and memory-dependent behavior (past history) of the phenomenon. As the input voltage changes, the area bounded by the hysteresis loop proportionally changes leading to proportional energy loss (Mayergoyz 2003). A promising approach to avoid hysteresis is to use charge-driven circuits such that an input charge can be applied in a controlled way. It has been demonstrated that the relation between applied charge and displacement is linear in piezoelectric materials (Newcomb and Filnn 1982; Furutani et al. 1998); however, the need for expensive instrumentation, amplification of the measurement noise, and reduction in the system responsiveness are the main drawbacks of charge-driven strategy (Moheimani and Fleming 2006; Salah et al. 2007). Therefore, many applications prefer to utilize voltage-driven strategy and compensate hysteresis effect with inverse models through either feedforward or feedback controllers.

Feedforward controllers generally employ an inverse hysteresis model and are traditionally used for low-frequency and less-accurate positioning and precision applications, while feedback controllers are used for accurate positioning and tracking of high-frequency trajectories. However, a feedforward hysteresis compensator can significantly improve the stability of the overall feedback controller. We argue that by integrating the dynamics of the system into the inverse hysteresis model, a more accurate feedforward controller is achievable that can enhance the performance of the piezoelectric actuators in a wide frequency range (*see* Fig. 7.16a). Furthermore, a robust feedback control approach can be implemented for integration into the inverse hysteresis model to stabilize the closed-loop system against

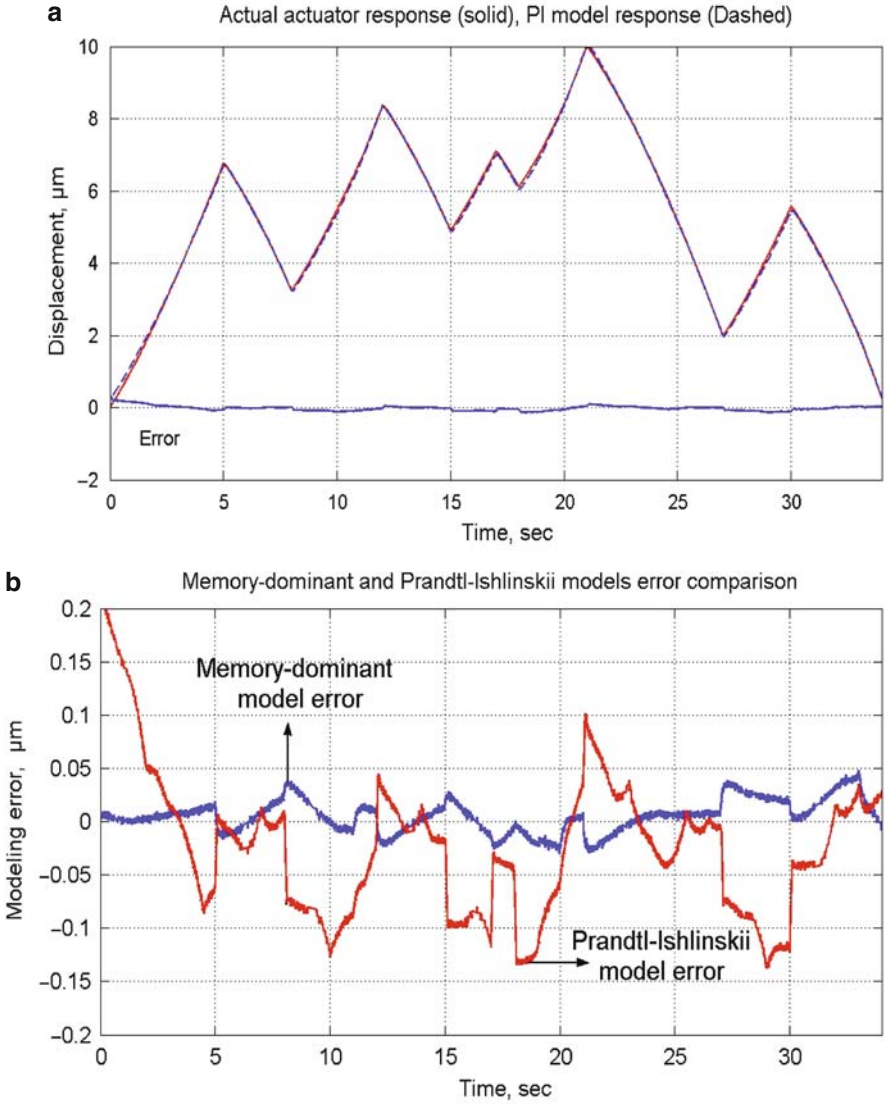

Fig. 7.15 Comparison between Prandtl-Ishlinskii (PI) and memory-based hysteresis modeling frameworks: **(a)** PI model output, and **(b)** modeling error comparison between the two methods *Source:* Bashash and Jalili 2007b, with permission

ever-present unmodeled dynamics and external disturbances (*see* Fig. 7.16b). Based on the various hysteresis models, see for examples the models presented in the preceding section, a variety of feedforward and feedback strategies could be adopted (Bashash and Jalili 2007b, 2008). However, we prefer to give the details of these two compensatory techniques for control of single-axis piezoelectric nanopositioning systems later in Chap. 10 (*see* Sect. 10.3).

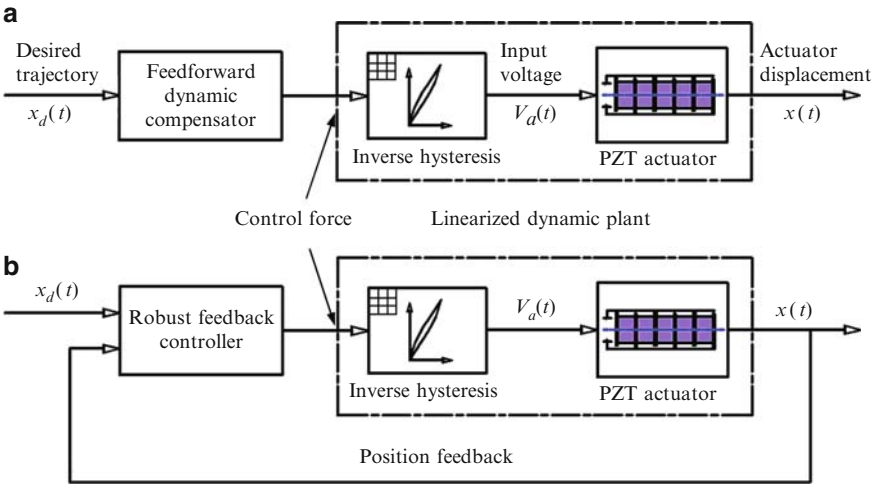

Fig. 7.16 Control schemes for position control of piezoelectric actuators: **(a)** inverse model-based feedforward, and **(b)** robust variable structure feedback controllers

Summary

This chapter provided a relatively comprehensive, but condensed modeling frameworks for piezoelectric-based systems contaminated with hyesteresis nonlinearity. Both modeling frameworks and compensatory techniques for hysteresis were discussed. The materials presented here can be used when designing controllers for a variety of piezoelectric-based systems (especially actuators), some of which are extensively discussed and detailed in Chap. 10.

Chapter 8
Piezoelectric-Based Systems Modeling

Contents

8.1 Modeling Preliminaries and Assumptions 183
8.2 Modeling Piezoelectric Actuators in Axial (Stacked) Configuration 185
8.2.1 Piezoelectric Stacked Actuators under No External Load 186
8.2.2 Piezoelectric Stacked Actuators with External Load 189
8.2.3 Vibration Analysis of Piezoelectric Actuators in Axial Configuration – An Example Case Study 192
8.3 Modeling Piezoelectric Actuators in Transverse (Bender) Configuration 198
8.3.1 General Energy-based Modeling for Laminar Actuators 198
8.3.2 Vibration Analysis of a Piezoelectrically Actuated Active Probe® – An Example Case Study 205
8.3.3 Equivalent Bending Moment Actuation Generation 213
8.4 A Brief Introduction to Piezoelectric Actuation in 2D 219
8.4.1 General Energy-based Modeling for 2D Piezoelectric Actuation 219
8.4.2 Equivalent Bending Moment 2D Actuation Generation 224
8.5 Modeling Piezoelectric Sensors 226
8.5.1 Piezoelectric Stacked Sensors 227
8.5.2 Piezoelectric Laminar Sensors 229
8.5.3 Equivalent Circuit Models of Piezoelectric Sensors 230
Summary

Building upon the preceding chapters in this part, we present a comprehensive treatment of piezoelectric-based systems modeling including lumped-parameters and distributed-parameters representations for both stacked and laminar configurations. The materials given in this chapter shall prepare the readers for vibration-control systems using piezoelectric actuators and sensors discussed extensively in Chap. 9.

8.1 Modeling Preliminaries and Assumptions

On the basis of unified approach discussed in Chap. 4 and 6, the total potential energy of a linear piezoelectric material is expressed as (see Sect. 6.2.2, (6.16)):

N. Jalili, *Piezoelectric-Based Vibration Control*,
DOI 10.1007/978-1-4419-0070-8_8,

© Springer Science+Business Media LLC 2010

$$\delta U = \int_V \left(\sigma_p \delta S_p + \epsilon_i \delta D_i\right) \mathrm{d}V,\ i = 1, 2, 3 \text{ and } p = 1, \ldots, 6 \tag{8.1}$$

By substituting the piezoelectric constitutive relationships (6.21), (6.22), or (6.23), the potential energy (8.1) reduces to appropriate relationships depending on the nature of the problem at hand. For instance, for actuator applications, substituting constitutive equation (6.23a) into energy (8.1) results in:

$$\delta U = \int_V \left(\left(c_{pq}^D S_q - h_{ip} D_i\right) \delta S_p + \left(-h_{ip} S_p + \beta_{ij}^S D_j\right) \delta D_i\right) \mathrm{d}V,\ i, j = 1, 2, 3 \text{ and } p, q = 1, \ldots, 6 \tag{8.2}$$

Equation (8.2) can be further simplified to:

$$\delta U = \int_V \left(c_{pq}^D S_p \delta S_q - h_{ip} \delta \left(D_i S_p\right) + \beta_{ij}^S D_j \delta D_i\right) \mathrm{d}V,\ i, j = 1, 2, 3 \text{ and } p, q = 1, \ldots, 6 \tag{8.3}$$

Clearly, (8.3) can be separated into three parts: a purely mechanical term (elastic energy), a purely electrical term (dielectric energy), and a combined term (coupled energy).

It must be noted that the electrical kinetic energy is still ignored in the calculations (see Chap. 6 for a discussion about this assumption and its practical validity and limitation, Liu et al. 2002). However, the electrical virtual work due to application of electrical voltage in piezoelectric material will be considered in Hamilton's formulation as discussed in the next section (Sect. 8.2). Alternatively, one could represent the total potential energy U on the basis of electrical enthalpy as:

$$\delta U = \int_V H_e \mathrm{d}V \tag{8.4a}$$

where

$$H_e = \frac{1}{2} c_{pq}^{\epsilon} S_p S_q - e_{ip} \epsilon_i S_p - \frac{1}{2} \beta_{ij}^S \epsilon_j \epsilon_i \tag{8.4b}$$

is the electrical enthalpy or electric Gibbs energy. While either approach could be exercised here, we prefer to adopt the first approach, i.e., utilizing (8.3) combined with electrical virtual work into the Hamilton's formulation.

In the following sections, several common configurations of piezoelectric-based systems in the form of either actuators or sensors are considered and extensively discussed.

8.2 Modeling Piezoelectric Actuators in Axial (Stacked) Configuration

Piezoelectric actuators in axial or stacked configuration (see Fig. 8.1) are the key elements of many micro- and nanopositioning systems. With their ultrahigh resolution and accuracy, they are utilized in a variety of applications including scanning probe microscopy (Giessibl 2003; Gonda et al. 1999), microsurgery (Lopez et al. 2001), microassembly, and micromanufacturing (Hesselbach et al. 1998; Schmoeckel et al. 2000).

The simplified version of the constitutive equation (6.23a) for this one-dimensional actuator can be expressed as

$$\begin{aligned} \sigma_3 &= c_{33}^D S_3 - h_{33} D_3 \Rightarrow \boldsymbol{\sigma} = c^D\, S - h D \\ \epsilon_3 &= -h_{33} S_3 + \beta_{33}^S D_3 \Rightarrow \boldsymbol{\epsilon} = -hS + \beta^S\, D \end{aligned} \tag{8.5}$$

where all subscripts (i.e., $()_{33}$ and $()_3$) in (8.5) are dropped for brevity. Substituting this simplified form into the potential energy (8.3), noticing that the kinetic energy of this bar-like or rod-like structure can be written as (see Sect. 4.3.1, (4.44)),

$$T = \frac{1}{2} \int_0^L \left\{ \rho(x) \left(\frac{\partial u(x,t)}{\partial t} \right)^2 \right\} \mathrm{d}x, \tag{8.6}$$

and using the extended Hamilton's principle (see also Sect. 3.2)

$$\int_{t_1}^{t_2} \left(\delta L + \delta W^{\text{ext}} \right) \mathrm{d}t = 0 \tag{8.7}$$

the equations of motion for this actuator can be readily obtained. As mentioned earlier, since the kinetic energy of the electrical field is typically very small compared to the mechanical kinetic energy (especially in moderate- to high-frequency applications), the electrical kinetic energy is neglected (Ge et al. 1998a, b, 1999).

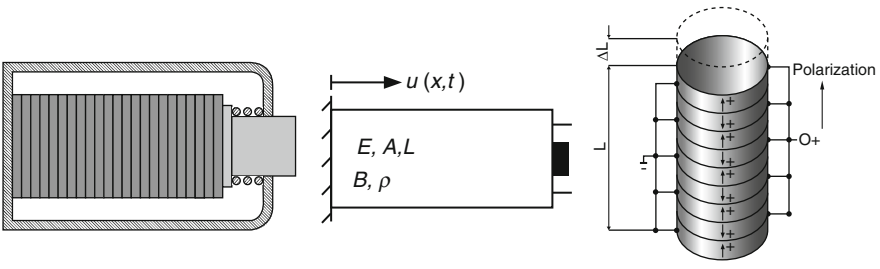

Fig. 8.1 (*left*) Schematic of an *n*-layer solid-state actuator, and (*right*) its representative rod model

Similar to potential and kinetic energies, the virtual work of external forces in (8.7) is also composed of mechanical virtual work (due to, for example, external nonconservative forces and damping forces) as well as electrical virtual work (due to input voltage to piezoelectric actuator). That is,

$$\delta W^{\text{ext}} = \delta W_m^{\text{ext}} + \delta W_e^{\text{ext}} \tag{8.8}$$

On the basis of applications of axial actuators, two cases can be encountered: actuator under no external load (or negligible load such as many optical positioning systems), or when the actuator is used under external load. For readers' convenience, these two cases will be discussed separately in the following subsections.

The electrical virtual work is, however, generated regardless of the existence of this external (mechanical) load. That is, an applied electrical voltage $V_a(x,t)$ causes a change in charge Q. To make the calculation of this virtual work as general as possible, the applied voltage is considered to be a function of both spatial and temporal variables x and t, respectively. This spatial dependency is especially important when the size of the actuator or sensor is comparable to the size of the host structure to which this piezoelectric material is attached. Hence, on the basis of these facts and the actuator configuration considered in Fig. 8.1, the electrical virtual work δW_e^{ext}, to cause a change in total charge Q over the actuator length L, is expressed as:

$$\delta W_e^{ext} = \int_0^L (V_a(x,t)\delta Q)dx \tag{8.9}$$

where $V_a(x,t)$ is the input voltage per unit length (i.e., normalized based on the distance between the electrodes). By substituting the 1D version of total charge-dielectric displacement relationship (6.7) into (8.9), the electrical virtual work (8.9) reduces to:

$$\delta W_e^{\text{ext}} = \int_0^L V_a(x,t) \left(\oint_{\partial V} \delta D(x,t) \mathrm{d}A \right) \mathrm{d}x = \int_0^L A(x) V_a(x,t) \delta D(x,t) \mathrm{d}x \tag{8.10}$$

where $A(x)$ is the variable cross-section of piezoelectric actuator (see Fig. 8.1-right). Notice that on the basis of the unit of input voltage $V_a(x,t)$, the number of layers, n in Fig. 8.1-right, has already been included in the input voltage.

8.2.1 Piezoelectric Stacked Actuators under No External Load

In this case, the only external mechanical work done by nonconservative forces is due to the internal damping of the structure with the expression for the mechanical virtual work given by (Dadfarnia et al. 2004a)

$$\delta W_m^{\text{ext}} = -\int_0^L B\left(\frac{\partial u(x,t)}{\partial t}\right)\delta u(x,t)\mathrm{d}x \tag{8.11}$$

where B is the equivalent linear viscous (air) damping. Insertion of the relationship (8.5) into the potential energy (8.1), while noticing the strain-displacement relationship $S = \partial u/\partial x$, and the resultant expression, along with kinetic energy (8.6), electrical virtual work (8.10), and mechanical virtual work (8.11), into Hamilton's principle (8.7) yields

$$\begin{aligned}\int_{t_1}^{t_2}\Bigg[\int_0^L\left\{\rho(x)\frac{\partial u(x,t)}{\partial t}\delta\left(\frac{\partial u(x,t)}{\partial t}\right)\right\}\mathrm{d}x - \int_0^L\Bigg\{c^D A(x)\frac{\partial u(x,t)}{\partial x}\delta\left(\frac{\partial u(x,t)}{\partial x}\right)\\ - hA(x)\frac{\partial u(x,t)}{\partial x}\delta D(x,t) - hA(x)D(x,t)\delta\left(\frac{\partial u(x,t)}{\partial x}\right)\\ + \beta^S A(x)D(x,t)\delta D(x,t)\Bigg\}\,\mathrm{d}x + \int_0^L (A(x)V_a(x,t)\delta D(x,t))\mathrm{d}x\\ - \int_0^L B\left(\frac{\partial u(x,t)}{\partial t}\right)\delta u(x,t)\mathrm{d}x\Bigg]\mathrm{d}t = 0\end{aligned} \tag{8.12}$$

Following similar procedures as in Chap. 4 (e.g., interchanging the temporal and spatial integrations for the first term, subsequent application of integral-by-part, standard assumptions that the variations vanish at the two end points corresponding to $t = t_1$ and $t = t_2$, and collecting similar variational terms), one can simplify (8.12) as follows:

$$\begin{aligned}\int_{t_1}^{t_2}\Bigg[\int_0^L\Bigg\{\left(-\rho(x)\frac{\partial^2 u(x,t)}{\partial t^2} + \frac{\partial}{\partial x}\left(c^D A(x)\frac{\partial u(x,t)}{\partial x}\right) - \frac{\partial}{\partial x}\left(hA(x)D(x,t)\right)\right.\\ \left. - B\frac{\partial u(x,t)}{\partial t}\right)\delta u(x,t) + \left(hA(x)\frac{\partial u(x,t)}{\partial x} - \beta^S A(x)D(x,t) + A(x)V_a(x,t)\right)\\ \delta D(x,t)\Bigg\}\,\mathrm{d}x + \left(hA(x)D(x,t) - c^D A(x)\frac{\partial u(x,t)}{\partial x}\right)\delta u(x,t)\Big|_0^L\Bigg]\mathrm{d}t = 0\end{aligned} \tag{8.13}$$

Similar to the argument we made in Sect. 3.1.3 in (3.20), for (8.13) to vanish regardless of the independent variations $\delta u(x,t)$ and $\delta D(x,t)$, the integrant must vanish, and for the integrant to vanish we must have:

for $\delta u(x,t)$,

$$\rho(x)\frac{\partial^2 u(x,t)}{\partial t^2} - \frac{\partial}{\partial x}\left(c^D A(x)\frac{\partial u(x,t)}{\partial x}\right) + B\frac{\partial u(x,t)}{\partial t} + \frac{\partial}{\partial x}\left(hA(x)D(x,t)\right) = 0 \tag{8.14a}$$

for $\delta D(x,t)$,

$$h\frac{\partial u(x,t)}{\partial x} - \beta^S D(x,t) + V_a(x,t) = 0 \tag{8.14b}$$

along with the boundary conditions,

$$\left(hA(x)D(x,t) - c^D A(x)\frac{\partial u(x,t)}{\partial x}\right)\delta u(x,t)\Big|_0^L = 0 \tag{8.14c}$$

Equation (8.14a) represents the distributed-parameters equation of actuator, coupled dynamically with dielectric displacement, (8.14b) indicates a static coupling between piezoelectric actuator and structure, and finally (8.14c) denotes the boundary conditions that need to be satisfied.

By substituting dielectric displacement $D(x,t)$ from (8.14b) into both (8.14a) and boundary conditions (8.14c), one can obtain a single PDE governing the piezoelectric actuator in axial configuration in response to input voltage $V_a(x,t)$ as:

$$\begin{aligned}\rho(x)\frac{\partial^2 u(x,t)}{\partial t^2} - \frac{\partial}{\partial x}\left(A(x)\left(c^D - \frac{h^2}{\beta^S}\right)\frac{\partial u(x,t)}{\partial x}\right) + B\frac{\partial u(x,t)}{\partial t}\\ = -\frac{\partial}{\partial x}\left(\frac{h}{\beta^S}A(x)V_a(x,t)\right)\end{aligned} \tag{8.15a}$$

$$\left(\left(\frac{h^2}{\beta^S} - c^D\right)A(x)\frac{\partial u(x,t)}{\partial x} + \frac{h}{\beta^S}A(x)V_a(x,t)\right)\delta u(x,t)\Big|_0^L = 0 \tag{8.15b}$$

Considering the relationships between piezoelectric constants defined in Tables 6.1 and 6.2, one can simplify the coupling term $c^D - h^2/\beta^S$ appeared in both (8.15a) and (8.15b) to the following;

$$\begin{aligned}c^D - \frac{h^2}{\beta^S} &= c^D - \frac{(\beta^S d c^\epsilon)^2}{\beta^S} = c^D - \beta^S d^2 (c^\epsilon)^2 = c^D - \beta^S c^\epsilon (d^2 c^\epsilon)\\ &= c^D - \beta^S c^\epsilon \kappa^2 \xi^\sigma = c^D - \beta^S c^\epsilon \kappa^2 \frac{e s^\epsilon}{g} = c^D - (\beta^S e) c^\epsilon \kappa^2 \frac{s^\epsilon}{g}\\ &= c^D - (g c^D) c^\epsilon \kappa^2 \frac{s^\epsilon}{g} = c^D (1 - \kappa^2)\end{aligned} \tag{8.16a}$$

where κ is the piezoelectric coupling factor defined in Chap. 6 (please note that since the indices were dropped, this coupling factor is actually $\kappa = \kappa_{33}$, see 6.40). Similarly, term h/β^S appeared in the right-hand side of (8.15a) can be substituted

with:

$$\frac{h}{\beta^S} = \frac{\beta^S dc^\epsilon}{\beta^S} = dc^\epsilon = d\left(c^D(1-\kappa^2)\right) \tag{8.16b}$$

With the results of (8.16), one can readily observe the influence or coupling of piezoceramic material on material elastic stiffness. The higher the coupling factor, the less equivalent stiffness of the material (i.e., $c^D(1-\kappa^2)$), and hence softer in nature and desire to move. This is a very important conclusion, which can be utilized in the design of piezoelectric actuators and sensors.

8.2.2 Piezoelectric Stacked Actuators with External Load

As discussed briefly in Chap. 6, most piezoceramic actuators can only sustain axial loads (expect those designed for shear modes), and hence, care must be taken when applying external loads to these actuators. In practice and in order to avoid unintentional damage to the internal structure of these actuators, compliant mechanisms or flexures in different forms and configurations are used (see Physik Instrumente catalog for an extensive designs and adaptors for this purpose).

One common practice is a spring-damper compliant adaptor whose schematic is shown in Fig. 8.2. As shown in Fig. 8.2, the stacked actuator of Fig. 8.1 with linear mass density ρ, Young's modulus of elasticity E, viscous damping coefficient B, length L, and cross-sectional area A is augmented with a compound boundary condition of a mass M, damper c, and spring k as well as external load F_0 as shown in Fig. 8.2.

To derive the equations of motion for this case, one needs to simply augment the potential and kinetic energies (8.1 and 8.6) as well as virtual works (8.11) with the addition of compliant flexure and external load F_0. That is, these relationships change accordingly to:

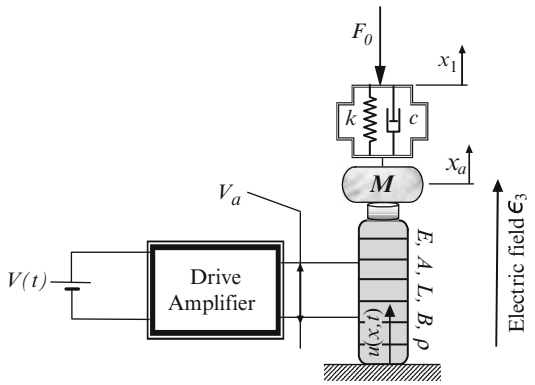

Fig. 8.2 Piezoelectric actuator in axial (stacked) configuration under external load and complaint flexure, note $x_a(t) = u(L,t)$

$$\delta U = \int_0^L A(x)\left(c^D S\delta S - h\delta(DS) + \beta^S D\delta D\right)\mathrm{d}x + \tfrac{1}{2}k\left(u(L,t) - x_l(t)\right)^2 \tag{8.17}$$

$$T = \frac{1}{2}\int_0^L \left\{\rho(x)\left(\frac{\partial u(x,t)}{\partial t}\right)^2\right\}\mathrm{d}x + \frac{1}{2}M\left(\frac{\partial u(L,t)}{\partial t}\right)^2 \tag{8.18}$$

$$\delta W_m^{\text{ext}} = -F_0 x_l(t) - \int_0^L B\left(\partial u(x,t)\,/\,\partial t\right)\delta u(x,t)\mathrm{d}x - c\left(\partial u(L,t)\,/\,\partial t - \dot{x}_l(t)\right)\delta\left(u(L,t) - x_l(t)\right) \tag{8.19}$$

Substituting these new expressions along with the electrical virtual work (8.10) into the extended Hamilton's principle (8.7), and after some manipulations and collecting similar variational terms, the equations of motion for the actuator in this configuration can be obtained using the same procedure adopted in the preceding section. That is,
for $\delta u(x,t)$:

$$\rho(x)\frac{\partial^2 u(x,t)}{\partial t^2} - \frac{\partial}{\partial x}\left(c^D A(x)\frac{\partial u(x,t)}{\partial x}\right) + B\frac{\partial u(x,t)}{\partial t} + \frac{\partial}{\partial x}\left(hA(x)D(x,t)\right) = 0 \tag{8.20a}$$

for $\delta D(x,t)$:

$$h\frac{\partial u(x,t)}{\partial x} - \beta^S D(x,t) + V_a(x,t) = 0 \tag{8.20b}$$

for $\delta x_l(t)$:

$$c\dot{x}_l(t) + kx_l(t) - c\frac{\partial u(L,t)}{\partial x} - ku(L,t) + F_0 = 0 \tag{8.20c}$$

$$\left\{hA(L)D(L,t) - c^D A(L)\frac{\partial u(L,t)}{\partial x} - M\frac{\partial^2 u(L,t)}{\partial t^2} - k\left(u(L,t) - x_l(t)\right) - c\left(\frac{\partial u(L,t)}{\partial t} - \dot{x}_l(t)\right)\right\}\delta u(L,t) = 0 \tag{8.20d}$$

$$\left(c^D A(0)\frac{\partial u(0,t)}{\partial x} - hA(0)D(0,t)\right)\delta u(0,t) = 0 \tag{8.20e}$$

Similar to the preceding section, by substituting dielectric displacement $\delta D(x,t)$ from (8.20b) into both (8.20a) and boundary conditions (8.20d and 8.20e), one can obtain a single PDE governing this piezoelectric actuator in axial configuration in response to input voltage $V_a(x,t)$ as:

$$\rho(x)\frac{\partial^2 u(x,t)}{\partial t^2} - \frac{\partial}{\partial x}\left(c^D A(x)(1-\kappa^2)\frac{\partial u(x,t)}{\partial x}\right) + B\frac{\partial u(x,t)}{\partial t} = -\frac{\partial}{\partial x}\left(\mathrm{d}c^D A(x)(1-\kappa^2)V_a(x,t)\right) \tag{8.21a}$$

$$c\dot{x}_l(t) + kx_l(t) - c\frac{\partial u(L,t)}{\partial x} - ku(L,t) + F_0 = 0 \tag{8.21b}$$

$$\left\{dc^D(1-\kappa^2)A(L)V_a(L,t) - c^D(1-\kappa^2)A(L)\frac{\partial u(L,t)}{\partial x} - M\frac{\partial^2 u(L,t)}{\partial t^2} - k\left(u(L,t)-x_l(t)\right) - c\left(\frac{\partial u(L,t)}{\partial t} - \dot{x}_l(t)\right)\right\}\delta u(L,t) = 0 \tag{8.21c}$$

$$\left(dc^D(1-\kappa^2)A(0)V_a(0,t) - c^D(1-\kappa^2)A(0)\frac{\partial u(0,t)}{\partial x}\right)\delta u(0,t) = 0 \tag{8.21d}$$

Remark 8.1. The input voltage for most piezoelectric actuators in practice is considered to be independent of spatial coordinate x. One simple and widely accepted voltage profile that satisfies this condition is $V_a(x,t) \cong V_a(t)$, (Dadfarnia et al. 2004a, b). Considering this and assuming uniform cross-section for the actuator, the governing equations of motion (8.21) reduce to:

$$\rho(x)\frac{\partial^2 u(x,t)}{\partial t^2} - E_p A\frac{\partial^2 u(x,t)}{\partial x^2} + B\frac{\partial u(x,t)}{\partial t} = 0 \tag{8.22a}$$

$$c\dot{x}_l(t) + kx_l(t) - c\frac{\partial u(L,t)}{\partial x} - ku(L,t) + F_0 = 0 \tag{8.22b}$$

$$\left\{dE_p AV_a(t) - E_p A\frac{\partial u(L,t)}{\partial x} - M\frac{\partial^2 u(L,t)}{\partial t^2} - k\left(u(L,t)-x_l(t)\right) - c\left(\frac{\partial u(L,t)}{\partial t} - \dot{x}_l(t)\right)\right\}\delta u(L,t) = 0 \tag{8.22c}$$

$$\left(dE_p AV_a(t) - E_p A\frac{\partial u(0,t)}{\partial x}\right)\delta u(0,t) = 0 \tag{8.22d}$$

where the equivalent piezoelectric stiffness E_p used in these expressions is defined as:

$$E_p \triangleq c^D\left(1-\kappa^2\right) \tag{8.23}$$

Notice again here that the coupling factor κ in (8.23) is actually κ_{33} for this configuration where the subscripts are dropped for brevity. For the fixed-sprung boundary conditions given in Fig. 8.2, we have $\delta u(L,t) \neq 0$ and $u(0,t) = 0$. Hence, the boundary equations (8.22c) and (8.22d) reduce to:

$$M\frac{\partial^2 u(L,t)}{\partial t^2} + E_p A\frac{\partial u(L,t)}{\partial x} + c\left(\frac{\partial u(L,t)}{\partial t} - \dot{x}_l(t)\right) + k\left(u(L,t) - x_l(t)\right) = dE_p A V_a(t) \tag{8.24a}$$

$$u(0,t) = 0 \tag{8.24b}$$

Equation (8.24a) forms the fundamental relationship between actuator input voltage $V_a(t)$ and actuator tip deflection $u(L,t)$. The application of this relationship in vibration analysis of piezoelectric actuators in axial configuration is better demonstrated next.

8.2.3 Vibration Analysis of Piezoelectric Actuators in Axial Configuration – An Example Case Study

Figure 8.3 depicts the schematic configuration as well as representative model of a typical axial piezoelectric actuator. The compliance arrangement given in Fig. 8.3b is a typical configuration for many axial piezoceramic actuators, especially in precision positioning applications. The equations of motion and boundary conditions can be readily deduced from actuator governing (8.22a) and simplified version of boundary conditions (8.24a) and (8.24b) by simply substituting $x_l(t) = 0$. That is, the governing equations of motion and boundary equations become

$$\rho(x)\frac{\partial^2 u(x,t)}{\partial t^2} - E_p A\frac{\partial^2 u(x,t)}{\partial x^2} + B\frac{\partial u(x,t)}{\partial t} = 0 \tag{8.25a}$$

$$M\frac{\partial^2 u(L,t)}{\partial t^2} + E_p A\frac{\partial u(L,t)}{\partial x} + c\frac{\partial u(L,t)}{\partial t} + ku(L,t) = f(t) \tag{8.25b}$$

$$u(0,t) = 0 \tag{8.25c}$$

where equivalent actuation force $f(t)$ is defined as (see 8.24a):

$$f(t) = dE_p A V_a(t)$$

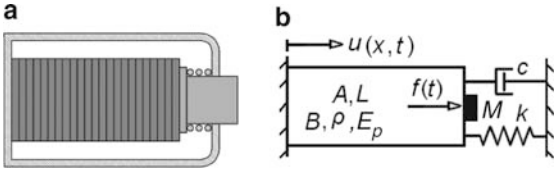

Fig. 8.3 (**a**) Schematic of a piezoelectric axial actuator, and (**b**) its representative model
Source: Vora et al. 2008, with permission

Modal Analysis: The standard modal analysis described in Chap. 4 is performed here for the free and undamped version of (8.25a):

$$\rho\left(\frac{\partial^2 u(x,t)}{\partial t^2}\right) = E_p A\left(\frac{\partial^2 u(x,t)}{\partial x^2}\right) \tag{8.26}$$

By assuming that the solution of (8.26) is separable in time and space domains, the longitudinal displacement $u(x,t)$ can be written as:

$$u(x,t) = \phi(x)q(t) \tag{8.27}$$

where $\phi(x)$ is known as the spatial modal function and $q(t)$ is the generalized time-dependant coordinate. Substituting (8.27) into (8.26) and after some standard manipulations similar to the vibrations of bar in Sect. 4.3.1, it results

$$\left(\frac{\ddot{q}(t)}{q(t)}\right) = \left(\frac{E_p A}{\rho}\right)\frac{\phi''(x)}{\phi(x)} = -\omega^2 \tag{8.28}$$

Note that the generation of mode-dependent modal eigenfunctions and frequencies (i.e., $\phi_r(x)$ instead of $\phi(x)$ or ω_r instead of ω) comes from the transcendental nature of the frequency equation similar to the argument made in Chap. 4. Hence, the solution to eigenfunction can be simply given by:

$$\phi_r(x) = C_r \sin\beta_r x + D_r \cos\beta_r x \tag{8.29}$$

where

$$\beta_r^2 = \frac{\rho\omega_r^2}{E_p A} \tag{8.30}$$

At the fixed boundary, we have $\phi_r(0) = 0$ (see 8.25c) which results in $D_r = 0$ in (8.29). Hence, eigenfunctions $\phi_r(x)$ reduce to:

$$\phi_r(x) = C_r \sin\beta_r x \tag{8.31}$$

Utilization of the boundary condition at actuator end ($x = L$), while taking into the account the separable form (8.27) and ignoring discrete damping c, yields

$$M\phi_r(L)\ddot{q}_r(t) + E_p A\phi_r'(L)q_r(t) + k\phi_r(L)q_r(t) = 0 \tag{8.32}$$

By substituting temporal part of (8.28) and (8.31) into (8.32) and with further simplifications, the characteristics equation of system is obtained as:

$$-\left(ME_p A/\rho\right)\beta_r^2 + E_p A\beta_r \cot(\beta_r L) + k = 0 \tag{8.33}$$

The numerical solution of (8.33) yields infinitely many solutions for β_r and natural frequencies according to (8.30). For the rth mode shape of system given by:

$$\phi_r(x) = C_r \sin\left(\sqrt{\frac{\rho}{E_p A}}\omega_r x\right) \tag{8.34}$$

coefficient C_r is calculated using a orthonormality condition with respect to mass (refer to Sect. 4.4.2 for more information) as:

$$\rho \int_0^L \phi_r(x)\phi_s(x)\mathrm{d}x + M\phi_r(L)\phi_s(L) = \delta_{rs} \tag{8.35}$$

Substituting (8.34) into (8.35) and simplifying it, the following explicit expression is obtained:

$$C_r = \left[\rho \int_0^L \sin^2\left(\sqrt{\rho/E_p A}\omega_r x\right)\mathrm{d}x + M\sin^2\left(\sqrt{\rho/E_p A}\omega_r L\right)\right]^{-\frac{1}{2}} \tag{8.36}$$

Now that the equations and expressions for system natural frequencies and mode shapes have been derived, the forced motion analysis of system can be presented. For this, the effects of excitation force and damping are taken back into account to form the final solution to the problem.

Forced Vibration Analysis: As extensively discussed in Chap. 4, the modal eigenfunctions and natural frequencies obtained through the earlier free motion analysis can now be expanded to form the longitudinal displacement function $u(x,t)$ as:

$$u(x,t) = \sum_{r=1}^{\infty} \phi_r(x)q_r(t) \tag{8.37}$$

By this assumption, the partial differential equation of motion (8.25a) is recast as an infinite series:

$$\sum_{r=1}^{\infty} \left\{\rho\phi_r(x)\ddot{q}_r(t) - E_p A\phi_r''(x)q_r(t) + B\phi_r(x)\dot{q}_r(t)\right\} = 0 \tag{8.38}$$

Adopting the standard modal analysis described in Chap. 4, utilizing boundary conditions, orthonormality of modal functions with respect to both mass and stiffness, the equation of motion can be obtained as:

$$\ddot{q}_r(t) + \sum_{s=1}^{\infty} \{\zeta_{rs}\dot{q}_s(t)\} + \omega_r^2 q_r(t) = f_r(t) \tag{8.39}$$

where

$$\zeta_{rs} = B\int_0^L \phi_r(x)\phi_s(x)\mathrm{d}x + c\phi_r(L)\phi_s(L),\ \ f_r(t) = \phi_r(L)f(t) \tag{8.40}$$

The truncated p-mode description of (8.39) can be presented in the following matrix form:

$$\mathbf{M}\ddot{\mathbf{q}}(t) + \boldsymbol{\zeta}\dot{\mathbf{q}}(t) + \mathbf{K}\mathbf{q}(t) = \mathbf{F}u \tag{8.41}$$

where

$$\mathbf{M} = [\delta_{rs}]_{p\times p}\,, \boldsymbol{\zeta} = [\zeta_{rs}]_{p\times p}\,, \mathbf{q} = \left[q_1(t), q_2(t), \ldots, q_p(t)\right]^T_{p\times 1}\,,$$

$$\mathbf{K} = \left[\omega_r^2\delta_{rs}\right]_{p\times p}\,, \mathbf{F} = \left[\phi_1(L), \phi_2(L), \ldots..., \phi_p(L)\right]^T_{p\times 1}\,, u = f(t) \tag{8.42}$$

Eventually, (8.42) can be converted into the following state-space representation:

$$\dot{\mathbf{x}}(t) = \mathrm{A}\mathbf{x}(t) + \mathbf{B}u(t), \mathbf{y}(t) = \mathbf{C}\mathbf{x}(t) \tag{8.43}$$

where

$$\mathbf{A} = \begin{bmatrix} \mathbf{0} & \mathbf{I} \\ -\mathbf{M}^{-1}\mathbf{K} & -\mathbf{M}^{-1}\boldsymbol{\zeta} \end{bmatrix}_{2p\times 2p}, \mathbf{B} = \begin{bmatrix} \mathbf{0} \\ \mathbf{M}^{-1}\mathbf{F} \end{bmatrix}_{2p\times 1}, \mathbf{x}(t) = \begin{Bmatrix} \mathbf{q}(t) \\ \dot{\mathbf{q}}(t) \end{Bmatrix}_{2p\times 1} \tag{8.44}$$

and considering actuator's displacement at $x = L$ as the system output, i.e., $y(t) = u(L, t)$, the output matrix is given by:

$$\mathbf{C} = [\phi_1(L), \phi_2(L), \ldots, \phi_p(L), 0, \ldots, 0]_{1\times 2p} \tag{8.45}$$

according to the truncated p-mode approximation of (8.37).

Numerical Simulations: A set of numerical simulations are carried out in this section to assess different aspects of the developed modeling framework. The initial simulations investigate the effects of boundary mass and spring on the natural frequencies and eigenfunctions of system. The first four natural frequencies are plotted versus different values of spring k, while setting M to zero, in Fig. 8.4a, and versus boundary mass M, while taking k as zero, in Fig. 8.4b. Other parameters used for these simulations are taken as: $\rho = 6000\,\mathrm{kg/m^3}$, $d_a = 0.01\,\mathrm{m}$ (actuator diameter), $L = 0.1\,\mathrm{m}$, and $E_p = 100\,\mathrm{GPa}$. These values may represent those of a real solid-state micropositioning actuator.

It can be observed from Fig. 8.4 that as the stiffness of the boundary spring increases, the natural frequencies of all modes increase exponentially, but eventually converge to particular values. This is because of the fact that actuator with a hard spring at the boundary behaves similar to that of clamped-clamped one. Hence, further increase in the spring stiffness will not affect the natural frequencies much.

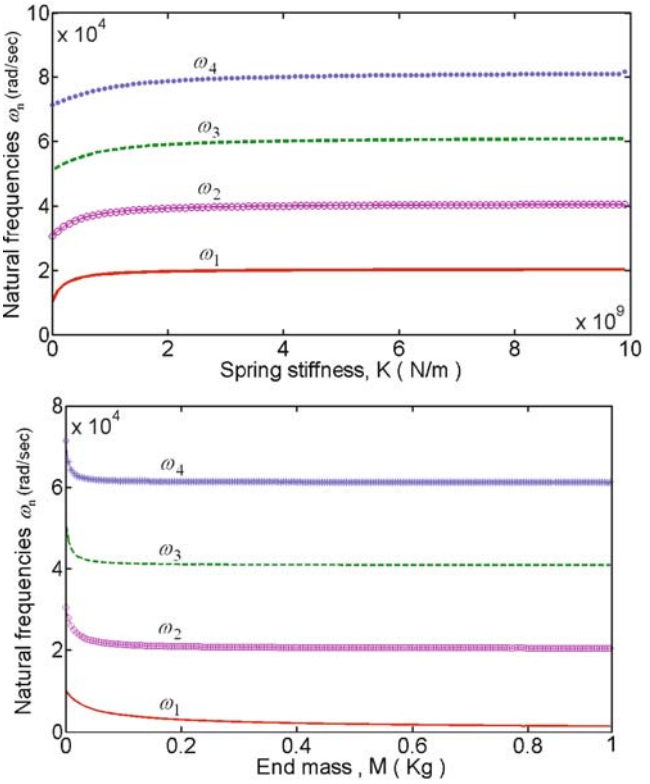

Fig. 8.4 First four natural frequencies of actuator versus (**a**) boundary spring stiffness k and (**b**) boundary mass M
Source: Vora et al. 2008, with permission

Similar phenomenon occurs in a reverse way with increasing the values of boundary mass. That is, the natural frequencies decrease as the value of boundary mass increases until they get saturated at particular values. Interestingly, the natural frequencies of the actuator with a hard spring at boundary are close to those of the rod with a heavy mass at the boundary with one mode ahead. For instance, the first and the second natural frequencies of the actuator with a hard boundary spring are near the second and the third natural frequencies, respectively, of an actuator with a heavy boundary mass (Vora et al. 2008).

To study the behavior of mode shapes with the change in the values of boundary spring and mass, the first four modal functions are plotted for four different configurations: (C1) $M = 0$ with high k, (C2) $M = 0$, with $k = 0$, (C3) moderate M with moderate k, and (C4) high M with high k. The selected parameters for the simulations are given in Table 8.1 and the results are depicted in Fig. 8.5. The significant changes in all the four modal functions are observed from one configuration to another. By carefully observing the modal functions, one can see modal functions

Table 8.1 Parameters used for numerical simulations to calculate mode shapes

Configuration	M (kg)	k (N/m)	ω_1 (kHz)	ω_2 (kHz)	ω_3 (kHz)	ω_4 (kHz)
C1	0	10^{10}	20.25	40.5	60.76	81
C2	0	0	10.21	30.62	51.03	71.44
C3	0.02	10^4	7.31	24.09	43.04	62.79
C4	1	10^{10}	1.39	20.5	40.87	61.27

Other actuator parameters: Actuator's damping coefficient: $B = 0.1(\mathrm{N \cdot s/m^2})$, Discrete damping coefficient: $c = 0.05(\mathrm{N \cdot s/m})$
Source: Vora et al. 2008, with permission

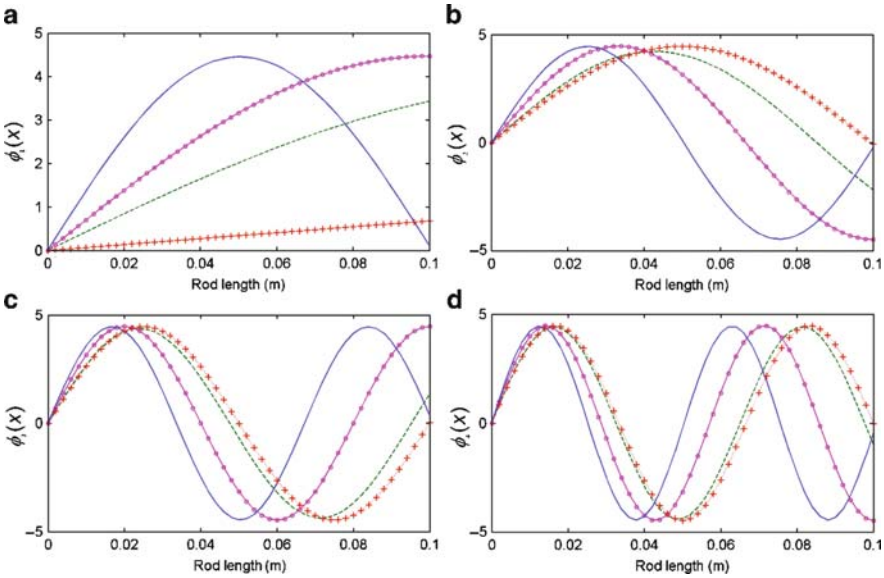

Fig. 8.5 (a) First, (b) second, (c) third, and (d) fourth modal functions of rod for four different configurations of boundary mass and spring (C1: ——, C2: —o—, C3: – – –, C4: ··+··)

of the actuator with boundary configuration C1 ($M = 0$ with high k) are similar to those of the actuator with both ends clamped. It can also be seen from the figures that the modal functions of configuration C1 follow those of configuration C4 (high M and k) with one mode advanced (e.g., the first mode shape of C1 is similar to the second mode shape of C4), Vora et al. (2008).

The Bode diagram of configuration C3 (moderate M with moderate k), which seems to be a more realistic case, for the first four modes is depicted in Fig. 8.6. As expected, a uniform multimodal frequency response is seen from this diagram which could indicate the validity of the developed modeling.

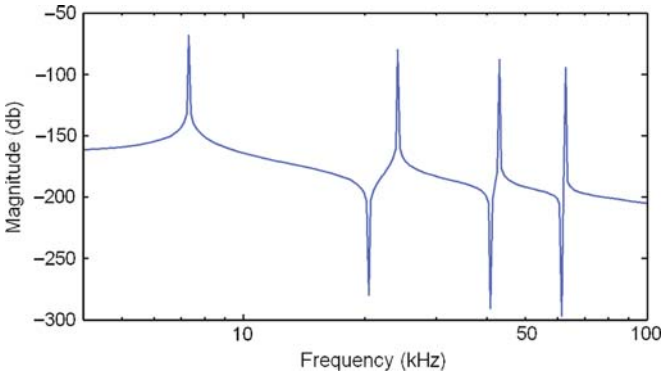

Fig. 8.6 Bode plot of system with four modes and boundary condition of configuration C3
Source: Vora et al. 2008, with permission

8.3 Modeling Piezoelectric Actuators in Transverse (Bender) Configuration

Many structural vibration-control systems utilize piezoceramic materials that are typically implemented in the form of monolithic wafers. The term "monolithic" refers to a piezoceramic material which is free from added materials or augmenting structural components. While the axial configuration described in Sect. 8.2 is mainly used for positioning applications, the laminar configuration is typically utilized in structural vibration control and sensing applications. As briefly noted in Chap. 6, this mode of actuation or sensing relies on in-plane actuation and sensing, i.e., induced stresses and strains parallel to the structure's surfaces (see Fig. 8.7). As a result, the piezoceramic wafers operate in d_{31} mode (see Fig. 6.15). Using this approach, in-plane strains can be readily measured with an attached piezoceramic. As briefly noted in Table 6.3, the values of d_{31} are typically lower than those of d_{33}.

8.3.1 General Energy-based Modeling for Laminar Actuators

For the purpose of model development and undue complications, a uniform flexible beam with piezoelectric patch actuator bonded on its top surface is considered. As shown in Fig. 8.8, the beam has total thickness t_b, and length L, while the piezoelectric film possesses thickness and length t_p and $(l_2 - l_1)$, respectively. We assume that both the actuator and beam have the same width, b. It is also assumed that the piezoelectric actuator is perfectly bonded on the beam at distance l_1 measured from the beam support. As also mentioned in Remark 8.1, the input voltage $V_a(t)$ applied to the piezoelectric actuator is considered to be independent of spatial coordinate x and serves as the only external effect.

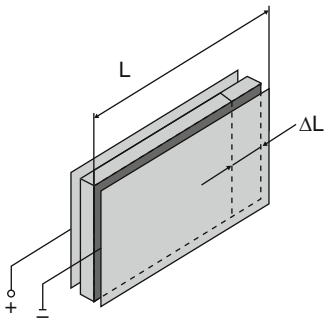

Fig. 8.7 Piezoelectric patch actuator

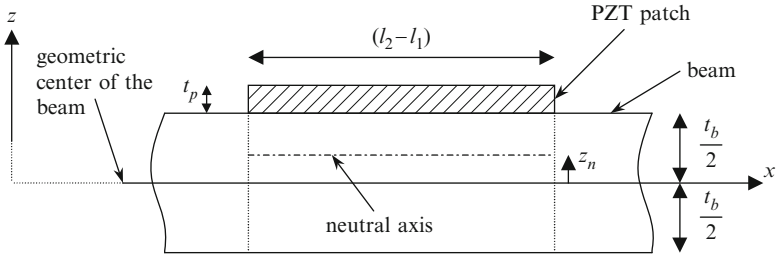

Fig. 8.8 Coordinate system and detailed descriptions of the attachment

To establish a coordinate system for the beam, the x-axis is taken in the longitudinal direction and the z-axis is specified in the transverse direction of the beam with midplane of the beam to be $z = 0$ as shown in Fig. 8.8.

Similar to axial configuration, the simplified version of the constitutive equation (6.23a) for this configuration can be expressed as:

$$\begin{aligned} \boldsymbol{\sigma}_1 &= c_{11}^D S_1 - h_{31} D_3 \\ \epsilon_3 &= -h_{31} S_1 + \beta_{33}^S D_3 \end{aligned} \tag{8.46}$$

Notice that for this configuration, the strain-displacement relationship (4.65a) is utilized as:

$$S_1 = S_{xx} = -z \frac{\partial^2 w(x,t)}{\partial x^2} \tag{8.47}$$

where $w(x,t)$ is the transverse displacement of the neutral axis. Before utilizing (8.46) and (8.47) into the potential energy (8.3), care must be taken for the multimaterial and nonuniform nature of the system. For this, the original form of the potential energy (8.1) is a better choice when dealing with this variable geometry structure, i.e., this energy is written for three parts: the section before piezoelectric

patch starts (0 to l_1), the zone where patch is affixed (l_1 to l_2), and the zone after patch (l_2 to L).

It must also be noted that in the segment of the beam where the piezoelectric patch is attached, the material properties change along the height (or z-axis); hence, both strain equation (8.47) and potential energy (8.1) need to be modified. That is, wherever the piezoelectric patch is not attached on the beam (i.e., $x < l_1$ or $x > l_2$), the neutral surface is the geometric center of the beam ($z = 0$) and strain equation (8.47) holds. For the portions where the piezoelectric patch is attached (i.e., $l_1 < x < l_2$), the strain equation (8.47) is modified to

$$S_1 = -(z - z_n)\frac{\partial^2 w(x,t)}{\partial x^2} \tag{8.48}$$

where z_n is the neutral surface (see Fig. 8.8). This new neutral surface can be calculated by setting the sum of all forces in x-direction over the entire cross-section zero as (Ballas 2007; Dankert and Dankert 1995)

$$b \int_{-\frac{t_b}{2}}^{\frac{t_b}{2}} \boldsymbol{\sigma}_1^b(z)\mathrm{d}z + b \int_{\frac{t_b}{2}}^{\frac{t_b}{2}+t_p} \boldsymbol{\sigma}_1^p(z)\mathrm{d}z = 0 \tag{8.49}$$

where $\boldsymbol{\sigma}_1^b$ and $\boldsymbol{\sigma}_1^p$ are referred to as stresses induced in beam and piezoelectric material segments, respectively. Utilizing Hook's law (4.24) for each segment, while substituting strain relationship (8.48), yields

$$\int_{-\frac{t_b}{2}}^{\frac{t_b}{2}} c_b^D(z - z_n)\mathrm{d}z + \int_{\frac{t_b}{2}}^{\frac{t_b}{2}+t_p} c_p^D(z - z_n)\mathrm{d}z = 0 \tag{8.50}$$

where c_b^D and c_p^D are the respective Young's moduli of elasticity for beam and piezoelectric materials. Upon simplifying (8.50), the neutral axis z_n can be readily obtained as:

$$z_n = \frac{c_p^D t_p(t_p + t_b)}{2\left(c_b^D t_b + c_p^D t_p\right)} \tag{8.51}$$

In order to deal with the material dissimilarity and geometrical nonuniformity, the integral for the potential energy (8.1) for this configuration is also broken into several integrals, based on the location of the piezoelectric actuator. Hence, (8.1) is recast in the following form.

$$\delta U = b\left\{\int_0^{l_1}\int_{-\frac{t_b}{2}}^{\frac{t_b}{2}}\left(c_b^D S_1\delta S_1\right)\mathrm{d}z\mathrm{d}x + \int_{l_1}^{l_2}\int_{-\frac{t_b}{2}}^{\frac{t_b}{2}}\left(c_b^D S_1\delta S_1\right)\mathrm{d}z\,\mathrm{d}x\right.$$
$$+\int_{l_1}^{l_2}\int_{\frac{t_b}{2}}^{\frac{t_b}{2}+t_p}\left(\left(c_p^D S_1 - h_{31}D_3\right)\delta S_1 + \left(-h_{31}S_1 + \beta_{33}^S D_3\right)\delta D_3\right)\mathrm{d}z\mathrm{d}x$$
$$\left.+\int_{l_2}^{L}\int_{-\frac{t_b}{2}}^{\frac{t_b}{2}}\left(c_b^D S_1\delta S_1\right)\mathrm{d}z\mathrm{d}x\right\} \tag{8.52}$$

Note that in (8.52), strain S_1 from (8.47) is used in the first two and last integrals, while strain S_1 from (8.48) is used in the third integral. Similar to potential energy, the kinetic energy associated with this nonuniform configuration can be expressed as (notice that similar to axial configuration, the electrical kinetic energy is neglected):

$$T = \frac{1}{2}b\left\{\int_0^{l_1}\rho_b t_b\left(\dot{w}(x,t)\right)^2 dx + \int_{l_1}^{l_2}\left(\rho_b t_b + \rho_p t_p\right)\left(\dot{w}(x,t)\right)^2 dx\right.$$
$$\left.+\int_{l_2}^{L}\rho_b t_b\left(\dot{w}(x,t)\right)^2 dx\right\} = \frac{1}{2}\int_0^L \rho(x)\left(\dot{w}(x,t)\right)^2 dx \tag{8.53}$$

where

$$\begin{aligned}\rho(x) &= [\rho_b t_b + G(x)\rho_p t_p]b\\ G(x) &= H(x-l_1) - H(x-l_2)\end{aligned} \tag{8.54}$$

and $H(x)$ is the Heaviside function, ρ_b and ρ_p are the respective beam and piezoelectric volumetric densities.

Considering both viscous and structural damping mechanisms for beam material, the total mechanical virtual work can be given by:

$$\delta W_m^{\text{ext}} = -B\int_0^L\left(\frac{\partial w(x,t)}{\partial t}\right)\delta w(x,t)\mathrm{d}x - C\int_0^L\left(\frac{\partial^2 w(x,t)}{\partial x\partial t}\right)\delta w(x,t)\mathrm{d}x \tag{8.55}$$

where B and C are the viscous and structural damping coefficients, respectively (Dadfarnia et al. 2004c). In a very similar fashion to axial configuration, the electrical virtual work due to input voltage to piezoelectric patch is given by:

$$\delta W_e^{\text{ext}} = b \int_0^L V_a(x,t)\delta D_3(x,t)\mathrm{d}x \tag{8.56}$$

Notice that for generalization, we again assume that the input voltage to piezoelectric actuator is a function of both spatial and temporal coordinates as presented in (8.56). At this stage, all the intermediate steps in deriving different expressions for use in the extended Hamilton's principle (8.7) have been completed. By insertion of (8.47) and (8.48) into energy equation (8.52), and inserting the results along with kinetic energy (8.53) and total virtual works (8.55) and (8.56) into (8.7), and after some manipulations, we get

$$\int_{t_1}^{t_2}\Bigg[\int_0^L \left\{\rho(x)\frac{\partial w(x,t)}{\partial t}\delta\left(\frac{\partial w(x,t)}{\partial t}\right)\right\}\mathrm{d}x - \int_0^L \left\{c(x)\frac{\partial^2 w(x,t)}{\partial x^2}\delta\left(\frac{\partial^2 w(x,t)}{\partial x^2}\right)\right.$$

$$+\beta_1 D_3(x,t)\delta D_3(x,t) + h_1\frac{\partial^2 w(x,t)}{\partial x^2}\delta D_3(x,t)$$

$$\left. + h_1 D_3(x,t)\delta\left(\frac{\partial^2 w(x,t)}{\partial x^2}\right)\right\}\mathrm{d}x + b\int_0^L V_a(x,t)\delta D_3(x,t)\mathrm{d}x$$

$$-B\int_0^L \frac{\partial w(x,t)}{\partial x}\delta w(x,t)\mathrm{d}x - C\int_0^L \frac{\partial^2 w(x,t)}{\partial x\partial t}\delta w(x,t)\mathrm{d}x\Bigg]\mathrm{d}t = 0 \tag{8.57}$$

Where

$$c(x) = \frac{b}{3}\left\{\left(\frac{c_b^D t_b^3}{4}\right) + G(x)\left[3c_b^D t_b z_n^2 + c_p^D\left(t_p^3 + 3t_p(\frac{t_b}{2} - z_n)^2\right.\right.\right.$$

$$\left.\left.\left. +3t_p^2\left(\frac{t_b}{2} - z_n\right)\right)\right]\right\}$$

$$h_1 = h_{31}t_p b(t_p + t_b - 2z_n)/2, \beta_1 = \beta_{33}^{\varepsilon} b t_p \tag{8.58}$$

Following similar procedures in preceding section and after similar manipulations adopted for (8.12), one can simplify (8.57) as follows:

$$\int_{t_1}^{t_2}\left[\int_0^L\left\{\left(-\rho(x)\frac{\partial^2 w(x,t)}{\partial t^2}-\frac{\partial}{\partial x}\left(c(x)\frac{\partial^2 w(x,t)}{\partial x^2}\right)-h_1\frac{\partial^2 D_3(x,t)}{\partial x^2}-B\frac{\partial w(x,t)}{\partial t}\right.\right.\right.$$
$$\left.-C\frac{\partial^2 w(x,t)}{\partial x\partial t}\right)\delta w(x,t)+\left(-\beta_1 D_3(x,t)-h_1\frac{\partial^2 w(x,t)}{\partial x^2}+bV_a(x,t)\right)\delta D_3(x,t)\Bigg\}\,\mathrm{d}x$$
$$-\left(c(x)\frac{\partial^2 w(x,t)}{\partial x^2}+h_1 D_3(x,t)\right)\delta\left(\frac{\partial w(x,t)}{\partial x}\right)\Bigg|_0^L-\left(\frac{\partial}{\partial x}\left(c(x)\frac{\partial^2 w(x,t)}{\partial x^2}\right)\right.$$
$$\left.\left.+h_1\frac{\partial D_3(x,t)}{\partial x}\right)\delta w(x,t)\Bigg|_0^L\right]\mathrm{d}t=0 \tag{8.59}$$

Similar to the argument we made earlier, for (8.59) to vanish regardless of independent variations $\delta u(x,t)$ and $\delta D(x,t)$, the integrant must vanish, and for the integrant to vanish we must have:

for $\delta w(x,t)$,

$$\rho(x)\frac{\partial^2 w(x,t)}{\partial t^2}+\frac{\partial^2}{\partial x^2}\left(c(x)\frac{\partial^2 w(x,t)}{\partial x^2}\right)+h_1\frac{\partial^2 D_3(x,t)}{\partial x^2}$$
$$+B\frac{\partial w(x,t)}{\partial t}+C\frac{\partial^2 w(x,t)}{\partial x\partial t}=0 \tag{8.60a}$$

for $\delta D_3(x,t)$,

$$\beta_1 D_3(x,t)+h_1\frac{\partial^2 w(x,t)}{\partial x^2}=bV_a(x,t) \tag{8.60b}$$

along with the boundary conditions,

$$\left(c(x)\frac{\partial^2 w(x,t)}{\partial x^2}+h_1 D_3(x,t)\right)\delta\left(\frac{\partial w(x,t)}{\partial x}\right)\Bigg|_0^L=0$$
$$\left(\frac{\partial}{\partial x}\left(c(x)\frac{\partial^2 w(x,t)}{\partial x^2}\right)+h_1\frac{\partial D_3(x,t)}{\partial x}\right)\delta w(x,t)\Bigg|_0^L=0 \tag{8.60c}$$

Similar to stacked actuator, (8.60a) represents the distributed-parameters equation of beam coupled with the dielectric displacement, (8.60b) indicates a static coupling between piezoelectric actuator and structure and finally (8.60c) presents the boundary conditions that need to be satisfied.

Substituting the dielectric displacement $D_3(x,t)$ from (8.60b) into both (8.60a) and boundary conditions (8.60c), one can obtain the PDE governing this type of

actuator in response to input voltage $V_a(x,t)$ as:

$$\rho(x)\frac{\partial^2 w(x,t)}{\partial t^2}+\frac{\partial^2}{\partial x^2}\left(\left(c(x)-\frac{h_1^2}{\beta_1}\right)\frac{\partial^2 w(x,t)}{\partial x^2}\right)$$
$$+B\frac{\partial w(x,t)}{\partial t}+C\frac{\partial^2 w(x,t)}{\partial x\partial t}=\frac{-bh_1}{\beta_1}\frac{\partial^2 V_a(x,t)}{\partial x^2} \tag{8.61a}$$

$$\left[\left(c(x)-\frac{h_1^2}{\beta_1}\right)\frac{\partial^2 w(x,t)}{\partial x^2}+\frac{bh_1}{\beta_1}V_a(x,t)\right]\delta\left(\frac{\partial w(x,t)}{\partial x}\right)\Bigg|_0^L=0 \tag{8.61b}$$

$$\left[\frac{\partial}{\partial x}\left(\left(c(x)-\frac{h_1^2}{\beta_1}\right)\frac{\partial^2 w(x,t)}{\partial x^2}\right)+\frac{bh_1}{\beta_1}\frac{\partial V_a(x,t)}{\partial x}\right]\delta w(x,t)\Bigg|_0^L=0 \tag{8.61c}$$

Due to geometrical nonuniformity arising from piezoelectric patch attachment, the coupling term $c(x)-h_1^2/\beta_1$ appearing in (8.61) cannot be further simplified at this stage. We will demonstrate, later in this section, that for some special or simple arrangements this expression can be further simplified in a similar manner to axial actuators. However, expression $-bh_1/\beta_1$ in (8.61) can be simplified, in a similar manner to axial actuator, to:

$$\begin{aligned}\frac{-bh_1}{\beta_1}&=\frac{-bh_{31}t_p b\left(t_p+t_b-2z_n\right)}{2\beta_{33}^S bt_p}=-\frac{1}{2}b(t_p+t_b-2z_n)\frac{h_{31}}{\beta_{33}^S}\\&=-\frac{1}{2}b\left(t_p+t_b-2z_n\right)c_p^D\left(1-\kappa_{31}^2\right)d_{31}\\&=-\frac{1}{2}b\left(t_p+t_b-2z_n\right)E_p d_{31}\end{aligned} \tag{8.62}$$

where E_p is the equivalent stiffness of the piezoelectric actuator in laminar configuration defined as (see (8.62) to extract this):

$$E_p=c_p^{\in}=c_p^D\left(1-\kappa_{31}^2\right) \tag{8.63}$$

Remark 8.2. A widely accepted assumption for laminar piezoelectric actuator is to assume a uniform input voltage wherever the actuator is attached on the beam, and naturally zero input voltage elsewhere. To mathematically describe this voltage profile, $V_a(x,t)$ can be expressed as:

$$V_a(x,t)=V_a(t)G(x) \tag{8.64}$$

where $G(x)$ was defined earlier in (8.54) and $V_a(t)$ is the input voltage to the actuator.

Inserting the input voltage profile (8.64) and property (8.62) into (8.61), while noticing that $G(x = 0) = G(x = L) = 0$ in boundary equations (8.61b and 8.61c) yields

$$\rho(x)\frac{\partial^2 w(x,t)}{\partial t^2} + \frac{\partial^2}{\partial x^2}\left(EI^{\text{eqv}}(x)\frac{\partial^2 w(x,t)}{\partial x^2}\right) + B\frac{\partial w(x,t)}{\partial t} + C\frac{\partial^2 w(x,t)}{\partial x \partial t} = M_{p_0} G''(x) V_a(t) \tag{8.65}$$

$$\left(\frac{\partial^2 w(x,t)}{\partial x^2}\right)\delta\left(\frac{\partial w(x,t)}{\partial x}\right)\Bigg|_0^L = 0 \tag{8.66a}$$

$$\left[\frac{\partial}{\partial x}\left(\frac{\partial^2 w(x,t)}{\partial x^2}\right)\right]\delta w(x,t)\Bigg|_0^L = 0 \tag{8.66b}$$

where

$$EI^{\text{eqv}}(x) = c(x) - \frac{h_1^2}{\beta_1},\ M_{P_0} = -\frac{1}{2}b\left(t_p + t_b - 2z_n\right)E_p d_{31} \tag{8.67}$$

Equation (8.65) and boundary conditions (8.66a) and (8.66b) represent the governing equations describing piezoelectric laminar actuators. They form the fundamental ground from which many vibration-control systems can be designed for these types of actuators. These will be extensively covered later in Chap. 9. A practical example case study is, however, presented next to demonstrate the application of these results in modeling commercial piezoelectric actuator in laminar configuration.

8.3.2 *Vibration Analysis of a Piezoelectrically Actuated Active Probe® – An Example Case Study*[1]

Background and Preliminaries: This example case study presents the application of piezoelectric laminar actuators described here using, what is referred to as, NanoMechanical Cantilever (NMC) probes (Salehi-Khojin et al. 2008). With their structural flexibility, sensitivity to atomic and molecular forces, and ultrafast responsiveness, NMC probes have recently attracted widespread attention in variety of applications including atomic force and friction microscopy (Jalili and

[1] The materials in this section may have come directly from our recent publication (Salehi-Khojin et al. 2008).

Laxminarayana 2004; Jalili et al. 2004; Nagashima et al. 1996; Gahlin and Jacobson 1998; Miyahara et al. 1999), biomass sensing (Ziegler 2004; Dareing and Thundat 2005; McFarland et al. 2005; Ren and Zhao 2004; Wu et al., 2001; Braun et al. 2005), thermal scanning microscopy (Thundat et al. 1994; Berger et al. 1996; Grigorov et al. 2004; Susuki 1996; Majumdar et al. 1995; Shi et al. 2000), and MEMS switches (Lee et al. 2007; Chu et al. 2007). For instance, in the Atomic Force Microscopy (AFM), the NMC oscillates at or near its resonant frequency. The shift in the natural frequency due to the tip-sample interaction is used to quantitatively characterize the topography of the surface (Jalili et al. 2004; Jalili and Laxminarayana 2004). In the biosensing applications, the NMC surface is functionalized to adsorb desired biological species which induce surface stress on the NMC. In this application, the added mass of species is estimated from the shift in the resonant frequency of the system away from that of the original NMC (Mahmoodi et al. 2008b; Afshari and Jalili 2008). More detailed discussions about these systems will be provided in Chap. 11. We only present the modeling and vibration analysis steps related to these types of laminar actuators in this section.

An Active Probe® is typically covered by a piezoelectric layer (e.g., ZnO) on the top surface (see Fig. 8.9). To develop an accurate dynamic model for NMCs with jump discontinuities in cross-section (see Fig. 8.9), a comprehensive framework has been recently developed (Bashash et al. 2008a; Bashash 2008). It has been shown that the effects of added mass and stiffness on the beam mode shapes and natural frequencies are significant. Also, results from forced vibration analysis indicate that the system frequency response is affected by geometrical discontinuities of the structure. More details will be provided in this regard later in Part III; however, it is experimentally shown that assuming uniform geometry and configuration for the dynamic analysis of the current NMC Active Probes® is not a valid assumption since it oversimplifies the problem and creates significant error in measurements.

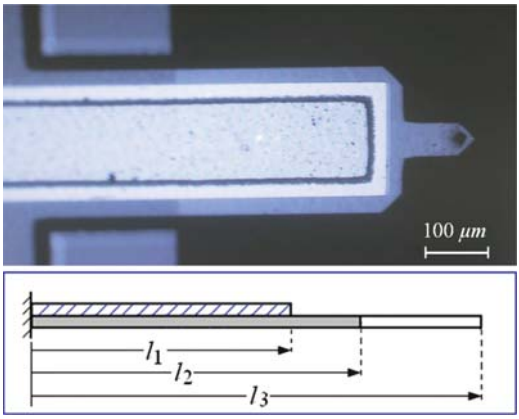

Fig. 8.9 Piezoelectrically driven NMC beam with cross-sectional discontinuity
Source: Salehi-Khojin et al. 2008, with permission

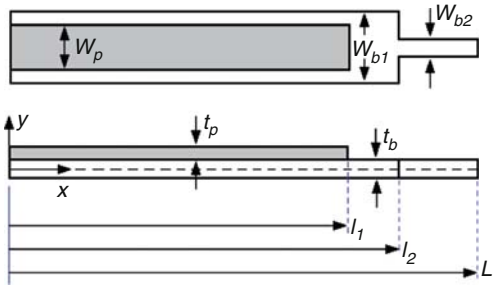

Fig. 8.10 Schematic representation of NMC with an attached piezoelectric layer on its top surface
Source: Salehi-Khojin et al. 2008, with permission

Development of a Comprehensive Model for NMC Active Probes®: Consider a piezoelectrically driven discontinuous NMC beam with its geometrical parameters depicted in Fig. 8.10. Utilizing the results of Remark 8.2, the equations of motion governing this system can be simply given by Eq. (8.66), with the only difference being in a simpler form of $G(x) = 1 - H(x - l_1)$, as well as slight modification to expression $\rho(x)$ in (8.54) due to different widths for piezoelectric and beam materials (see Fig. 8.10).

For the current configuration of Active Probe®, the variable mass per unit length, stiffness, and moment of inertia are given as:

$$EI^{\text{eqv}}(x) = \begin{cases} (EI^{\text{eqv}})_1 = c_b^D \left(I_p + I_{b1}\right), & 0 < x \le l_1 \\ (EI^{\text{eqv}})_2 = c_b^D I_{b1}, & l_1 < x \le l_2 \\ (EI^{\text{eqv}})_3 = c_b^D I_{b2}, & l_2 < x \le L \end{cases} \tag{8.68}$$

where similar to derivations presented in Sect. 8.3.1,

$$\begin{aligned} I_p &= z_n^2 \left(t_b W_{b1} + \eta t_p W_p\right) - \eta \left[\left(t_p^2 + t_b t_p\right) z_n + \frac{1}{3} t_p^3 + \frac{1}{2} t_b t_p^2 + \frac{1}{4} t_b^2 t_p\right] W_p \\ I_{b1} &= \frac{W_{b1} t_b^3}{12}, I_{b2} = \frac{W_{b2} t_b^3}{12}; z_n = \frac{c_p^D t_p W_p \left(t_p + t_b\right)}{2\left(c_p^D t_p W_p + c_b^D t_b W_{b1}\right)}, \eta = \frac{c_p^D}{c_b^D} \end{aligned} \tag{8.69}$$

and

$$m(x) = \begin{cases} m_1 = \rho_p W_p t_p + \rho_b W_{b1} t_b, & 0 < x \le l_1 \\ m_2 = \rho_b W_{b1} t_b, & l_1 < x \le l_2 \\ m_3 = \rho_b W_{b2} t_b, & l_2 < x \le L \end{cases} \tag{8.70}$$

where z_n is the neutral axis of the beam on the composite portion, ρ_b and ρ_p are the densities of the beam and piezoelectric layer, respectively, and the rest of the parameters were defined before. Moreover, from our past experience with this system, the distribution of damping can be safely assumed to be uniform in the entire length of the cantilever (Salehi-Khojin et al. 2008).

Following the same modal analysis procedure presented in Sect. 4.4, the free and undamped conditions associated with the transverse vibration of NMC are given by:

$$\frac{\partial^2}{\partial x^2}\left(EI^{\text{eqv}}(x)\frac{\partial^2 w}{\partial x^2}\right) = -m(x)\frac{\partial^2 w}{\partial t^2} \tag{8.71}$$

Assuming that the solution of (8.71) is separable in the form of $w(x,t) = \phi(x)q(t)$, (8.71) can be rewritten in the form of

$$\frac{d^2}{dx^2}\left(EI^{\text{eqv}}(x)\frac{d^2\phi(x)}{dx^2}\right) = \omega^2 m(x)\phi(x) \tag{8.72}$$

where ω is the natural frequency of the system. In order to obtain an analytical solution for (8.72), the entire length of NMC is divided into three uniform segments (see Fig. 8.10) with two sets of continuity conditions at stepped points. Therefore, (8.72) can be divided into three equations given by:

$$(EI^{\text{eqv}})_n\frac{d^4\phi_n(x)}{dx^4} = \omega^2 m_n\phi_n(x)\,, l_{n-1} < x < l_n; n = 1,2,3; l_0 = 0 \text{ and } l_3 = L \tag{8.73}$$

where $\phi_n(x)$, $(EI)_n$, and m_n are mode shapes, flexural stiffness, and mass per unit length of beam at the nth segment, respectively[2].

The general solution for (8.73) can be written as:

$$\phi_n(x) = A_n \sin\beta_n x + B_n \cos\beta_n x + C_n \sinh\beta_n x + D_n \cosh\beta_n x \tag{8.74}$$

where $\beta_n^4 = \omega^2 m_n/(EI^{eqv})_n$, and A_n, B_n, C_n, and D_n are the constants of integration to be obtained by solving the characteristics equation of the system. For this purpose, the boundary conditions for NMC as well as the continuity conditions at the stepped points must be applied. The clamped-free boundary conditions of NMC require:

$$\phi_1(0) = \frac{d\phi_1(0)}{dx} = 0 \tag{8.75}$$

$$\frac{d^2\phi_3(L)}{\mathrm{d}x^2} = \frac{d^3\phi_3(L)}{\mathrm{d}x^3} = 0 \tag{8.76}$$

and the respective conditions for the continuity of deflection, slope of the deflection, bending moment, and shear force of NMC at the nth stepped point, where $n = 1, 2,$

[2] $(\,)_n$ denotes the mode shape or parameter value for the nth cross-section, while $(\,)^{(r)}$, which will be used later in the analysis, denotes the mode shape or parameter value of the rth mode; though ω_r which represents the rth natural frequency is an exception.

are given by:

$$\phi_n(l_n) = \phi_{n+1}(l_n) \tag{8.77}$$

$$\frac{d\varphi_n(l_n)}{\mathrm{d}x} = \frac{d\varphi_{n+1}(l_n)}{\mathrm{d}x} \tag{8.78}$$

$$(EI^{\mathrm{eqv}})_n \frac{d^2\varphi_n(l_n)}{\mathrm{d}x^2} = (EI^{\mathrm{eqv}})_{n+1} \frac{d^2\varphi_{n+1}(l_n)}{\mathrm{d}x^2} \tag{8.79}$$

$$(EI^{\mathrm{eqv}})_n \frac{d^3\varphi_n(l_n)}{\mathrm{d}x^3} = (EI^{\mathrm{eqv}})_{n+1} \frac{d^3\varphi_{n+1}(l_n)}{\mathrm{d}x^3} \tag{8.80}$$

Applying (8.75–8.80) into (8.74), the characteristics matrix equation of system can be formed, with its detailed derivations given in Bashash (2008). Setting the determinant of the characteristics matrix to zero leads to finding the system natural frequencies. The mode shape coefficients at each natural frequency can be obtained by solving the characteristics equation and using a normalization condition with respect to mass as follows:

$$\int_{l_0}^{l_n} m(x)\phi^{(r)}(x)\phi^{(s)}(x)\mathrm{d}x = \delta_{rs} \text{ or } \int_{l_0}^{l_n} m(x)\left(\phi^{(r)}(x)\right)^2\mathrm{d}x = 1 \tag{8.81}$$

where δ_{rs} is the Kronecker delta, and $\phi^{(r)}(x)$ and $\phi^{(s)}(x)$ are rth and sth mode shapes corresponding to the rth and sth natural frequency of NMC. For instance, $\phi^{(r)}(x)$ is expressed as:

$$\phi^{(r)}(x) = \begin{cases} \phi_1^{(r)}(x) = A_1^{(r)} \sin\beta_1^{(r)}x + B_1^{(r)} \cos\beta_1^{(r)}x \\ \qquad\qquad + C_1^{(r)} \sinh\beta_1^{(r)}x + D_1^{(r)} \cosh\beta_1^{(r)}x,\ 0 \le x \le l_1 \\ \phi_2^{(r)}(x) = A_2^{(r)} \sin\beta_2^{(r)}x + B_2^{(r)} \cos\beta_2^{(r)}x \\ \qquad\qquad + C_2^{(r)} \sinh\beta_2^{(r)}x + D_2^{(r)} \cosh\beta_2^{(r)}x,\ l_1 \le x \le l_2 \\ \phi_3^{(r)}(x) = A_3^{(r)} \sin\beta_3^{(r)}x + B_3^{(r)} \cos\beta_3^{(r)}x \\ \qquad\qquad + C_3^{(r)} \sinh\beta_3^{(r)}x + D_3^{(r)} \cosh\beta_3^{(r)}x,\ l_2 \le x \le L \end{cases} \tag{8.82}$$

The obtained natural frequencies and mode shapes are utilized to derive the governing equations of motion for the forced vibration of the system. According to the eigenfunctions expansion method detailed in Chap. 4, the response of system can be expressed in the form of:

$$w(x,t) = \sum_{r=1}^{\infty} \phi^{(r)}(x)q^{(r)}(t), \tag{8.83}$$

where $\phi^{(r)}(x)$ and $q^{(r)}(t)$ are the eigenfunction and generalized time-dependent coordinates for the rth mode for each section. Substituting (8.83) into (8.65), and

carrying out the forced vibration analysis described in Sect. 4.4.3, the equation of motion of the system can be expressed in the following form

$$\ddot{q}^{(r)}(t) + \sum_{s=1}^{\infty} \left\{ \zeta_{rs} \dot{q}^{(s)}(t) \right\} + \omega_r^2 q^{(r)}(t) = f^{(r)}(t), r = 1, 2, \ldots, \infty \tag{8.84}$$

where

$$\begin{aligned} \zeta_{rs} &= \int_0^L c(x)\phi^{(r)}(x)\phi^{(s)}(x)\mathrm{d}x \\ &= c \left\{ \int_0^{l_1} \phi_1^{(r)}(x)\phi_1^{(s)}(x)\mathrm{d}x + \int_{l_1}^{l_2} \phi_2^{(r)}(x)\phi_2^{(s)}(x)\mathrm{d}x + \int_{l_2}^{L} \phi_3^{(r)}(x)\phi_3^{(s)}(x)\mathrm{d}x \right\} \end{aligned} \tag{8.85}$$

$$\begin{aligned} f^{(r)}(t) &= M_{P_0} V_a(t) \int_0^L G''(x)\phi^{(r)}(x)\mathrm{d}x \\ &= \frac{1}{2} W_p E^{\text{piezo}} d_{31} (t_b + t_p - 2z_n) V_a(t) \int_0^L G''(x - l_1)\phi^{(r)}(x)\mathrm{d}x \end{aligned} \tag{8.86}$$

For the second distributional derivative of the Heaviside function used in (8.86), we can write[3] (Abu-Hilal 2003):

$$\int_0^L H''(x - l_1)\phi^{(r)}(x)dx = \int_0^L \delta'(x - l_1)\phi^{(r)}(x)dx = -\frac{d}{dx}\left(\phi^{(r)}(x)\right)\Big|_{x=l_1} \tag{8.87}$$

where $\delta(\cdot)$ represents the Dirac delta function. Substituting (8.87) into (8.86) yields:

$$f^{(r)}(t) = \bar{f}^{(r)} V_a(t) \text{ where } \bar{f}^{(r)} = -\frac{1}{2}\phi'^{(r)}(l_1) W_p E_p d_{31} (t_b + t_p - 2z_n) \tag{8.88}$$

The truncated p-mode description of the NMC model of (8.84) can now be presented in the following matrix form:

$$\mathbf{M}\ddot{\mathbf{q}} + \boldsymbol{\zeta}\dot{\mathbf{q}} + \mathbf{K}\mathbf{q} = \mathbf{F}u \tag{8.89}$$

[3] In this simplification, we have utilized the following property of Dirac delta function, $\int_{-\infty}^{\infty} \delta^{(n)}(x - x_0) f(x)dx = (-1)^n f^{(n)}(x_0)$.

where

$$\mathbf{M} = I_{p\times p}, \boldsymbol{\zeta} = [\zeta_{rs}]_{p\times p}, \mathbf{K} = [\omega_r^2 \delta_{rs}]_{p\times p}, \mathbf{F} = \left[\bar{f}^{(1)}, \bar{f}^{(2)}, \ldots, \bar{f}^{(p)}\right]^T_{p\times 1}$$
$$\mathbf{q} = [q^{(1)}(t), q^{(2)}(t), \ldots, q^{(p)}(t)]^T_{p\times 1}, u = V_a(t) \tag{8.90}$$

Consequently, the state-space representation of (8.89) can be expressed as:

$$\dot{\mathbf{X}} = \mathbf{A}\mathbf{X} + \mathbf{B}u \tag{8.91}$$

where

$$\mathbf{A} = \begin{bmatrix} \mathbf{0} & \mathbf{I} \\ -\mathbf{M}^{-1}\mathbf{K} & -\mathbf{M}^{-1}\boldsymbol{\zeta} \end{bmatrix}_{2p\times 2p}, \mathbf{B} = \begin{bmatrix} \mathbf{0} \\ \mathbf{M}^{-1}\mathbf{F} \end{bmatrix}_{2p\times 1}, \mathbf{X} = \begin{Bmatrix} \mathbf{q} \\ \dot{\mathbf{q}} \end{Bmatrix}_{2p\times 1} \tag{8.92}$$

Theoretical and Experimental Vibration Analyses Comparisons: For experimental verification, a commercial NMC Active Probe®, the DMASP manufactured by Veeco Instruments Inc., is used to study the dynamic response of the probe. For this purpose, an experimental setup is built using a state-of-the-art microsystem analyzer, the MSA-400 manufactured by Polytec Inc. MSA-400 employs the laser Doppler vibrometry and stroboscopic video microscopy to measure the 3D dynamic response of MEMS and NEMS (see Fig. 8.11). It features picometer displacement resolution for out-of-plane measurement, as well as measures frequencies as high as 20 MHz. The NMC, shown in Fig. 8.12a, is covered by a piezoelectric layer containing a stack of 0.25 μm Ti/Au, 3.5 μm ZnO, and 0.25 μm Ti/Au. The Ti/Au layers

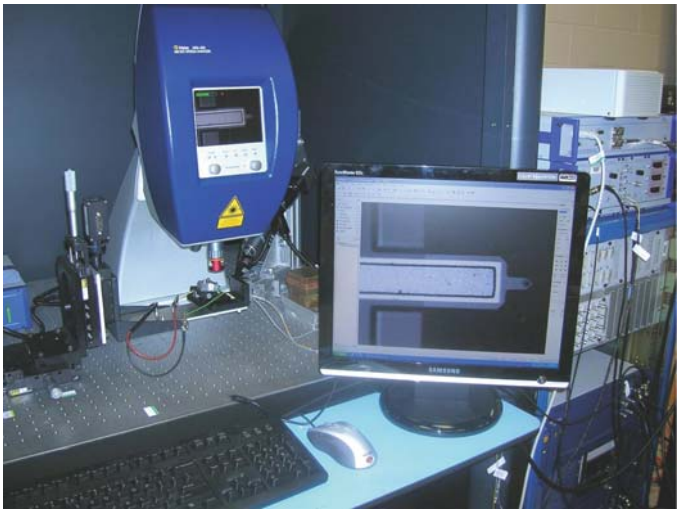

Fig. 8.11 Experimental setup for NMC characterization under Microsystem Analyzer (MSA-400) at Clemson University Smart Structures and NEMS Laboratory
Source: Salehi-Khojin et al. 2008, with permission

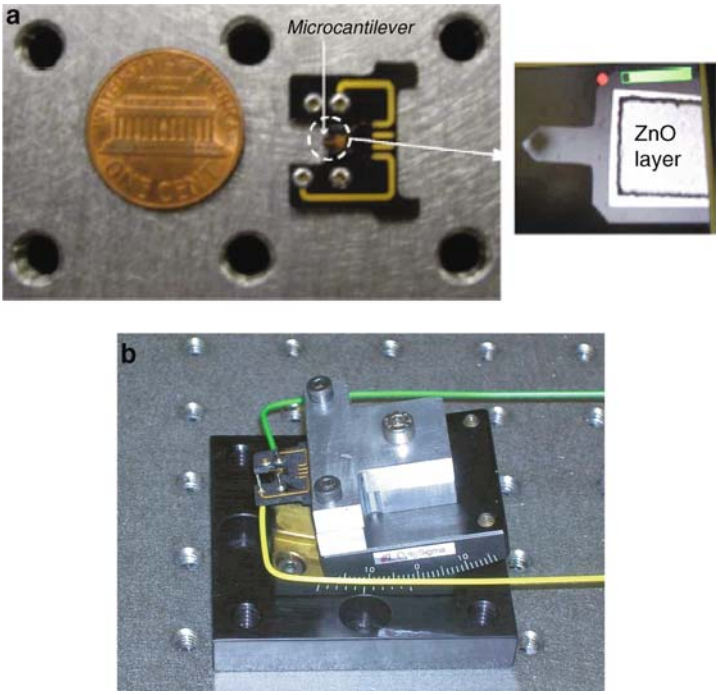

Fig. 8.12 (**a**) Comparison of the Veeco DMASP NMC beam size with a US penny, (**b**) *XYZ* microstage for adjusting laser light reflecting form NMC tip
Source: Salehi-Khojin et al. 2008, with permission

on the top and beneath ZnO layer act as electrodes which, along with the silicon cantilever, construct a bimorph actuator. As the input voltage is applied to the pads at the fixed end of the beam, the expansion and contraction of the ZnO layer results in the transversal vibration of the NMC.

The NMC assembled on a chip is mounted on a *XYZ* stage to be adjusted within the laser light focus for measuring of beam motion (Fig. 8.12b). Using an optical microscope, the desired points on the surface of NMC are precisely chosen to be scanned. When the electrical signals are applied to the system, the laser Doppler vibrometer measures the beam velocity at any given points through collecting and processing of backscattered laser light. In this study, a 10-Volt AC chirp signal with 500-kHz bandwidth is applied to the piezoelectric layer as the source of excitation.

To compare the experimental mode shapes and natural frequencies with those obtained from the developed model, exact values of system parameters are required. Although some of the parameters are given in the product catalog, and some others can be measured through precision measurement devices such as the MSA-400, the presence of uncertainties associated with the parameters may drastically degrade model accuracy. Therefore, a system identification procedure was carried out here to fine-tune the parameter values for precise comparison with the experimentally

Table 8.2 System parameters used in system identification; approximate parameter values, upper and lower bounds, and optimal solution for uniform and discontinuous NMC beam models

Parameters	Lower bound	Upper bound	Initial value	Optimal solution
$L(\mu m)$	475	485	480	**477.9**
$l_1(\mu m)$	315	330	325	**321.6**
$l_2(\mu m)$	350	370	360	**360.8**
$(EI^{eqv})_1$ [N · μm^2]	200	2,000	1,000	**1352.5**
$(EI^{eqv})_2$ [N · μm^2]	100	500	200	**208.6**
$(EI^{eqv})_3$ [N · μm^2]	10	100	50	**23.3**
m_1 [mg/m]	5.00	15.00	10.00	**10.2**
m_2 [mg/m]	2.00	5.00	3.00	**3.6**
m_3 [mg/m]	–	–	0.51	–
m_e [ng]	0.1	2.0	0.5	**1.3**
μ_1	100	800	500	**148.2**
μ_2	1000	10000	5000	**2719.9**
μ_3	1000	10000	5000	**3788.6**

Source: Salehi-Khojin et al. 2008, with permission

obtained data. The objective of system identification is to minimize a constructed error function between the model and the actual system mode shapes and natural frequencies. The details of the identification procedure are not given here for brevity. The interested readers are referred to Salehi-Khojin et al. 2008, 2009b for more details.

Table 8.2 demonstrates the initial (approximate) values of optimization variables, their imposed upper and lower bounds, and optimal values for the uniform and discontinuous NMC models, respectively. Figure 8.13 depicts the first three mode shapes of the actual NMC beam along with those of the theoretical models. As seen from Fig. 8.13, the mode shapes of the proposed discontinuous model match with the experimental data very closely when compared to those of the uniform model. Furthermore, the modal frequency responses show more accurate estimation of the system natural frequencies using the discontinuous beam theory (see Fig. 8.14). Since the uniform beam assumption fails to accurately model the actual response of the NMC Active Probe® for a multiple-mode operation, the discontinuous beam assumptions must be taken into account for the sake of modeling precision.

8.3.3 Equivalent Bending Moment Actuation Generation

Although the comprehensive treatment and analytical approach (energy-based) described in the preceding sections shall provide the necessary basis for the development of models for piezoelectric actuators, it might be worth rederiving some of the equations, especially for the laminar actuators, from conventional Newtonian

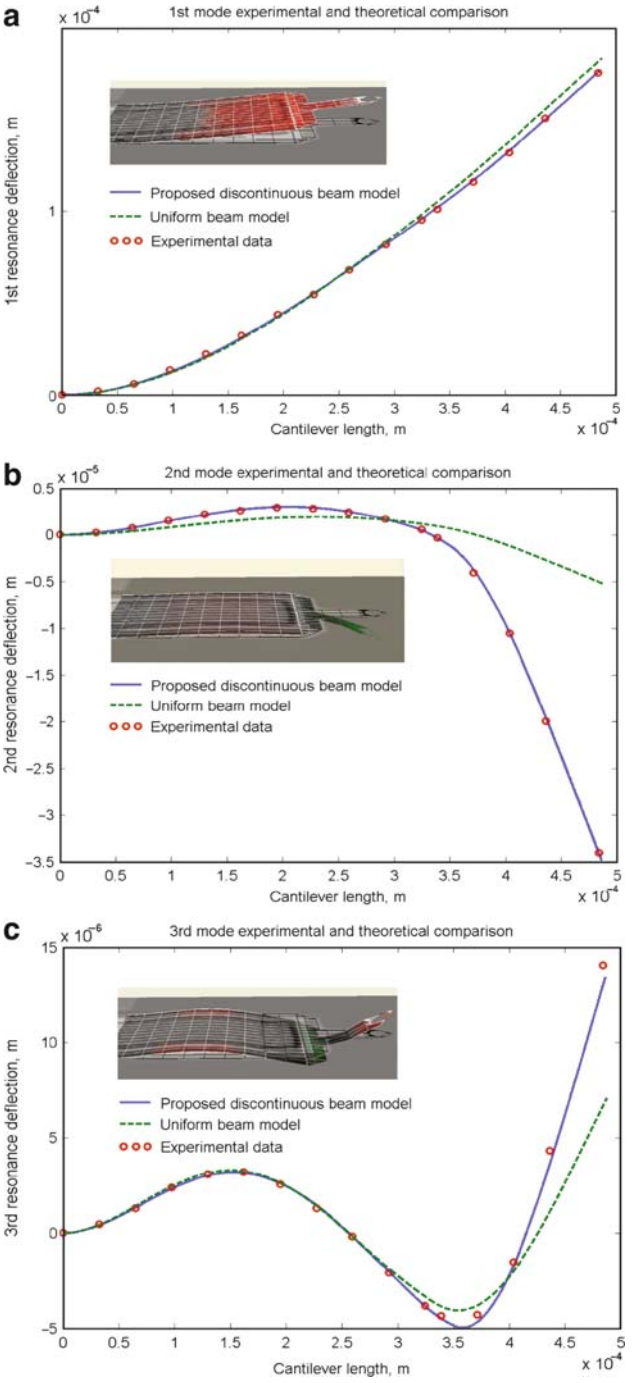

Fig. 8.13 Modal response experimental and theoretical comparisons for both uniform and discontinuous beam models: (**a**) first mode shape, (**b**) second mode shape, and (**c**) third mode shape
Source: Salehi-Khojin et al. 2008, with permission

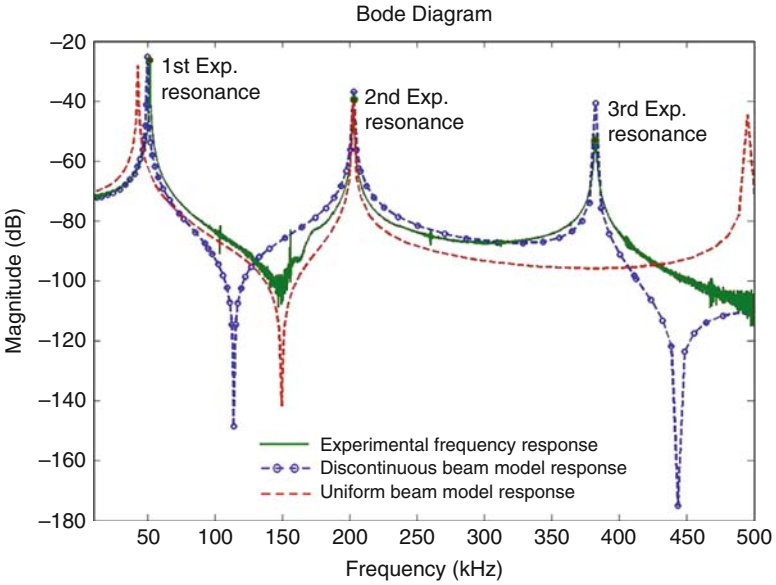

Fig. 8.14 Modal frequency response comparisons (solid blue lines: proposed model, dashed red lines: uniform model). The vertical dashed lines show actual values obtained experimentally *Source:* Salehi-Khojin et al. 2008, with permission

approach. For this, the first equation in the constitutive relationship (6.21) is written for the laminar configuration given in Figs. 8.7 and 8.8. That is, setting $p = q = 1$ and $i = 3$ in the first expression of (6.21), while also considering the relationships between different material constants given in Table 6.2, yields the following stress and strain expressions for the segment that piezoelectric patch actuator is attached

$$\sigma_1 = \frac{1}{s_{11}^{\epsilon}} S_1 - \frac{d_{31}}{s_{11}^{\epsilon}} \epsilon_3 = c_p^{\epsilon} \left(S_1 - d_{31} \epsilon_3 \right) \tag{8.93a}$$

$$S_1 = -(z - z_n) \frac{\partial^2 w(x,t)}{\partial x^2} \tag{8.93b}$$

Since we are only interested in the effect of added piezoelectric actuator on the beam, only the induced stress and strain in the piezoelectric material (i.e., 8.93) are considered in the bending moment calculations. It can be easily shown that if one also takes the following standard stress and strain expressions

$$\sigma_1 = \frac{1}{s_{11}^{\epsilon}} S_1 = c_b^{\epsilon} S_1 \tag{8.94a}$$

$$S_1 = -z \frac{\partial^2 w(x,t)}{\partial x^2} \tag{8.94b}$$

for the segments that piezoelectric material is not attached, then the complete governing equations of motion (i.e., the left-hand side of (8.65) can be obtained). As mentioned earlier, our intention here is not to rederive the equations of motion using this method, instead, we are interested in the bending moment generated due to the addition of piezoelectric materials.

While there are several models to represent the distribution of strains within both beam and piezoelectric materials (e.g., pin-force model of Fig. 8.15a, enhanced pin-force model of Fig. 8.15b, and Euler-Bernoulli model of Fig. 8.15c), we only consider the most accurate model that assumes correct curvatures and constraints compatibilities, i.e., the Euler-Bernoulli model of Fig. 8.15c.

Therefore, for the Euler-Bernoulli model of Fig. 8.15c, one can express the strain S_1 along the thickness using (8.93b) or (8.94b). As discussed earlier, the electrical field in piezoelectric materials is also assumed to be uniform, i.e.,

$$\epsilon_3 = \frac{V_a(t)}{t_p} \tag{8.95}$$

within the piezoelectric layer (i.e., $\frac{t_b}{2} < z < t_p + \frac{t_b}{2}$). Substituting strain (8.93b), while adopting the Euler-Bernoulli model Fig. 8.15c, and electric field (8.95) into stress (8.93a) and inserting the resultant stress into bending moment expression (4.66) and integrating over the entire length (for the beam section where only

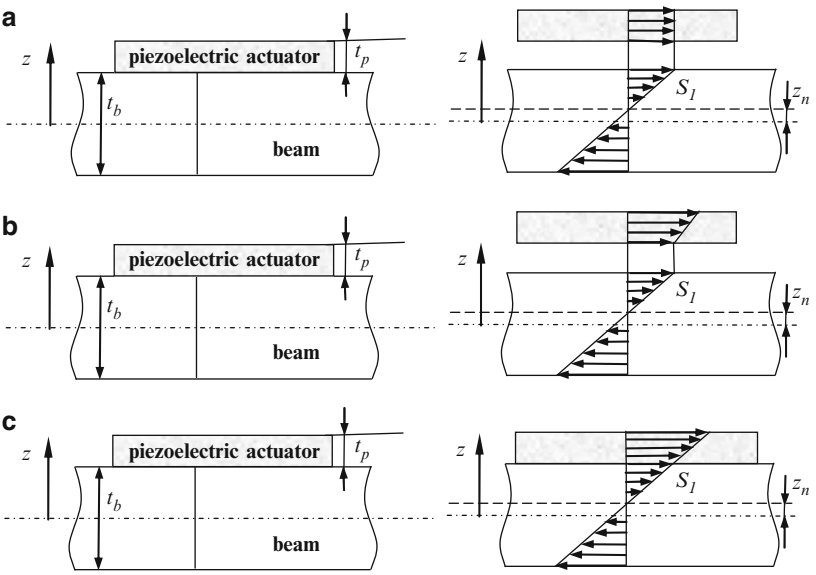

Fig. 8.15 Schematic of different strains distribution in laminar actuators; (*left*) beam and piezoelectric configuration, and (*right*) strain profiles for; (**a**) pin-force model, enhanced pin-force model, and (**c**) Euler-Bernoulli model

piezoelectric actuator is attached) yields

$$M_{\text{piezo}}(x,t) = -\int_A \boldsymbol{\sigma}_1 z dA$$
$$= -b\int_{\frac{t_b}{2}}^{\frac{t_b}{2}+t_p} \times\left[c_p^{\epsilon}\left(-(z-z_n)\frac{\partial^2 w(x,t)}{\partial x^2} - \frac{d_{31}}{t_p}V_a(t)\right)\right](z-z_n)\mathrm{d}z \quad (8.96)$$

Notice that the equivalent moment is calculated from the new neutral axis z_n in (8.96). Simplifying this integral, the induced bending moment in piezoelectric actuator can be expressed as:

$$M_{\text{piezo}}(x,t) = \underbrace{\left(E_p I^{\text{eqv}}\right)\frac{\partial^2 w(x,t)}{\partial x^2}}_{\boldsymbol{M}_{\text{piezo}}^{\text{nonactive}}} \underbrace{+\tfrac{1}{2}bE_p d_{31}(t_p+t_b-2z_n)V_a(t)}_{\boldsymbol{M}_{\text{piezo}}^{\text{active}}} \quad (8.97)$$

where the equivalent cross-sectional area moment of inertia I^{eqv} is defined as

$$I^{\text{eqv}} = I_p - bz_n t_p\left(t_p + t_b - z_n\right), \text{ and } I_p = b\int_{\frac{t_b}{2}}^{\frac{t_b}{2}+t_p} z^2\mathrm{d}z \quad (8.98)$$

Adopting the standard equilibrium equation of a classical Euler-Bernoulli beam

$$\rho A w_{tt}(x,t) = -\frac{\partial^2 M(x,t)}{\partial x^2} \quad (8.99)$$

where $M(x,t)$ is the total (i.e., when the bending moment (8.96) is integrated over the entire length) cross-sectional bending moment acting at distance x. By performing this integral, the equation of motion can be obtained consequently.

As mentioned earlier, our intention here is not to exercise this model development, instead investigate the influence of the addition of the piezoelectric materials on this total bending moment. To this end, a closer look at (8.97) reveals that the addition of piezoelectric actuator generates a standard induced bending moment ($M_{\text{piezo}}^{\text{nonactive}}$ term in 8.97) due to the added material (i.e., the nonactive part of the piezoelectric materials) as well as a uniform bending moment on the segment of the beam where piezoelectric patch actuator is attached ($M_{\text{piezo}}^{\text{active}}$ term in 8.97). Comparing this moment with expression (8.67), it yields

$$M_{\text{piezo}}^{\text{active}} = \tfrac{1}{2}E_p d_{31}(t_p+t_b-2z_n)V_a(t) = -M_{P_0}V_a(t) \quad (8.100)$$

which demonstrates that the addition of the laminar piezoelectric actuator is equivalent to adding concentrated moments $M_{\text{piezo}}^{\text{active}}$ at the boundaries of the actuator as shown in Fig. 8.16.

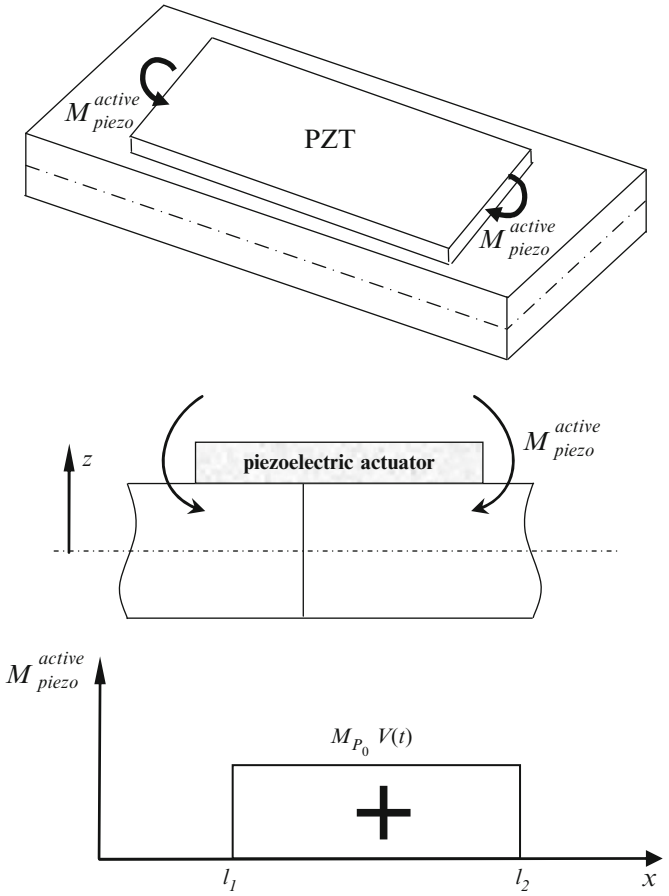

Fig. 8.16 Equivalent induced bending moment due to piezoelectric patch attachment (*top*), and uniform distribution of internal moment along the beam length (*bottom*)

Now that the effect of added piezoelectric on the internal bending moment is realized, one could consider this induced bending moment as an external load and consequently calculate the resultant electrical virtual work as:

$$\delta W^{\text{ext}}_{\text{piezo}} = \int_0^L \frac{\partial^2}{\partial x^2}\left(M^{\text{active}}_{\text{piezo}} G(x)\right)\delta w(x,t)\mathrm{d}x = -M_{P_0} V_a(t)\int_0^L G''(x)\delta w(x,t)\mathrm{d}x \tag{8.101}$$

Then, adding this virtual work to the total mechanical virtual work (8.55) and substituting the result into Hamilton's principle will yield the governing equations of motion similar to the ones obtained in the preceding section.

8.4 A Brief Introduction to Piezoelectric Actuation in 2D

As mentioned in Sect. 4.3.3, many engineering structures, especially those for use in distributed actuation and sensing, are really 2D systems such as plates and membranes. Such extension from 1D to 2D structures was also briefly justified in micro- and nanoscale applications of piezoelectric actuators and sensors. The added "Poisson's effect" in these systems complicates the analysis in general case. Despite this, the comprehensive and general treatment presented so far in this book shall provide the necessary tools for the developments of piezoelectric systems for plates and other 2D structures.

8.4.1 General Energy-based Modeling for 2D Piezoelectric Actuation

To provide an example case study, while also presenting the results for a typical and commonly used configuration, we present modeling steps for a Kirchhoff plate with a piezoelectric laminar actuator attached to its surface (see Fig. 8.17).

In order to avoid undue complications in the following derivations, it is assumed that there is another piezoelectric patch, identical to the one shown in Fig. 8.17, and attached to the opposite side of the plate (not shown in Fig. 8.17). This is done for the convenience in the derivation of the strain equations in this relatively complicated 2D configuration. For single piezoelectric patch attachment or asymmetric arrangement, similar procedure performed for beam in Sect. 8.3.1 (see 8.48 and 8.51) can be adopted here. We leave the exhaustive derivations for this case to interested readers.

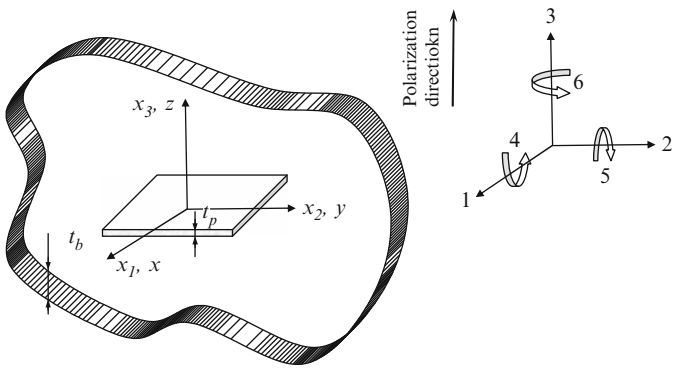

Fig. 8.17 Schematic representation of plate with piezoelectric actuator attachment and directions of deformation and polarization

Based on these assumptions and the configurations shown in Fig. 8.17, the total internal energy (8.3) reduces to

$$\delta U = \int_V \Big\{ c_{11}^D S_1 \delta S_1 + c_{12}^D S_1 \delta S_2 + c_{21}^D S_2 \delta S_1 + c_{22}^D S_2 \delta S_2 + c_{16}^D S_1 \delta S_6 + c_{26}^D S_2 \delta S_6 - h_{31} \delta (D_3 S_1) - h_{32} \delta (D_3 S_2) - h_{36} \delta (D_3 S_6) + \beta_{33}^S D_3 \delta D_3 \Big\} \mathrm{d}V \tag{8.102}$$

The total energy (8.102) is in its most general case for any type of plate and piezoelectric actuator. For instance, for an isotropic plate and piezoceramic actuator, there are only 5 elastic constants, 3 piezoelectric strain constants, and 2 dielectric or permittivity constants (see Sect. 6.3.1 and 6.25–6.26). Based on this assumption and taking into account the stress–strain relationships (4.25 and 4.23), we have

$$c_{11}^D = c_{22}^D = \frac{E}{1-\upsilon^2}, c_{12}^D = c_{21}^D = \frac{\upsilon E}{1-\upsilon^2}, c_{16}^D = c_{26}^D = 0, h_{31} = h_{32}, h_{36} = 0 \tag{8.103}$$

Substituting values of material constants (8.103) into energy (8.102) yields:

$$\delta U = \int_V \left\{ \frac{E}{1-\upsilon^2} S_1 \delta S_1 + \frac{\upsilon E}{1-\upsilon^2} S_1 \delta S_2 + \frac{\upsilon E}{1-\upsilon^2} S_2 \delta S_1 + \frac{E}{1-\upsilon^2} S_2 \delta S_2 - h_{31} \Big[\delta (D_3 S_1) + \delta (D_3 S_2) \Big] + \beta_{33}^S D_3 \delta D_3 \right\} \mathrm{d}V \tag{8.104}$$

Expanding energy equation (8.104) for the uniform plate with the geometry shown in Fig. 8.18 and noticing different materials' properties (plate and piezoelectric) yields:

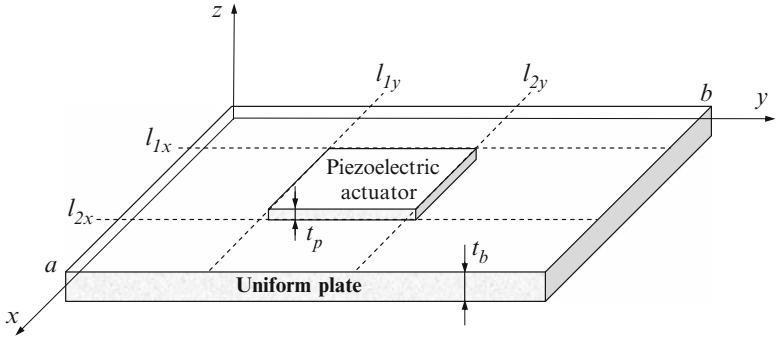

Fig. 8.18 Geometry of rectangular plate with symmetric piezoelectric attachment

$$
\begin{aligned}
\delta U = & \int_0^{l_{1x}} \int_0^{b} \int_{-\frac{t_b}{2}}^{\frac{t_b}{2}} \left\{ \frac{E_b}{1-\upsilon_b^2} S_1 \delta S_1 + \frac{\upsilon_b E_b}{1-\upsilon_b^2} S_1 \delta S_2 + \frac{\upsilon_b E_b}{1-\upsilon_b^2} S_2 \delta S_1 \right. \\
& \left. + \frac{E_b}{1-\upsilon_b^2} S_2 \delta S_2 \right\} \mathrm{d}x\mathrm{d}y\mathrm{d}z + \int_{l_{1x}}^{l_{2x}} \int_0^{l_{1y}} \int_{-\frac{t_b}{2}}^{\frac{t_b}{2}} \left\{ \frac{E_b}{1-\upsilon_b^2} S_1 \delta S_1 \right. \\
& \left. + \frac{\upsilon_b E_b}{1-\upsilon_b^2} S_1 \delta S_2 + \frac{\upsilon_b E_b}{1-\upsilon_b^2} S_2 \delta S_1 + \frac{E_b}{1-\upsilon_b^2} S_2 \delta S_2 \right\} \mathrm{d}x\mathrm{d}y\mathrm{d}z \\
& + \int_{l_{1x}}^{l_{2x}} \int_{l_{1y}}^{l_{2y}} \int_{-\frac{t_b}{2}-t_p}^{-\frac{t_b}{2}} \left\{ \frac{E_p}{1-\upsilon_p^2} S_1 \delta S_1 + \frac{\upsilon_p E_p}{1-\upsilon_p^2} S_1 \delta S_2 + \frac{\upsilon_p E_p}{1-\upsilon_p^2} S_2 \delta S_1 \right. \\
& \left. + \frac{E_p}{1-\upsilon_p^2} S_2 \delta S_2 - h_{31} \Big[\delta(D_3 S_1) + \delta(D_3 S_2) \Big] + \beta_{33}^S D_3 \delta D_3 \right\} \mathrm{d}x\mathrm{d}y\mathrm{d}z \\
& + \int_{l_{1x}}^{l_{2x}} \int_{l_{1y}}^{l_{2y}} \int_{-\frac{t_b}{2}}^{\frac{t_b}{2}} \left\{ \frac{E_b}{1-\upsilon_b^2} S_1 \delta S_1 + \frac{\upsilon_b E_b}{1-\upsilon_b^2} S_1 \delta S_2 + \frac{\upsilon_b E_b}{1-\upsilon_b^2} S_2 \delta S_1 \right. \\
& \left. + \frac{E_b}{1-\upsilon_b^2} S_2 \delta S_2 \right\} \mathrm{d}x\mathrm{d}y\mathrm{d}z + \int_{l_{1x}}^{l_{2x}} \int_{l_{1y}}^{l_{2y}} \int_{\frac{t_b}{2}}^{\frac{t_b}{2}+t_p} \left\{ \frac{E_p}{1-\upsilon_p^2} S_1 \delta S_1 \right. \\
& + \frac{\upsilon_p E_p}{1-\upsilon_p^2} S_1 \delta S_2 + \frac{\upsilon_p E_p}{1-\upsilon_p^2} S_2 \delta S_1 + \frac{E_p}{1-\upsilon_p^2} S_2 \delta S_2 \\
& \left. - h_{31} \Big[\delta(D_3 S_1) + \delta(D_3 S_2) \Big] + \beta_{33}^S D_3 \delta D_3 \right\} \mathrm{d}x\mathrm{d}y\mathrm{d}z \\
& + \int_{l_{1x}}^{l_{2x}} \int_{l_{2y}}^{b} \int_{-\frac{t_b}{2}}^{\frac{t_b}{2}} \left\{ \frac{E_b}{1-\upsilon_b^2} S_1 \delta S_1 + \frac{\upsilon_b E_b}{1-\upsilon_b^2} S_1 \delta S_2 + \frac{\upsilon_b E_b}{1-\upsilon_b^2} S_2 \delta S_1 \right. \\
& \left. + \frac{E_b}{1-\upsilon_b^2} S_2 \delta S_2 \right\} \mathrm{d}x\mathrm{d}y\mathrm{d}z + \int_{l_{1x}}^{a} \int_0^{b} \int_{-\frac{t_b}{2}}^{\frac{t_b}{2}} \left\{ \frac{E_b}{1-\upsilon_b^2} S_1 \delta S_1 \right. \\
& \left. + \frac{\upsilon_b E_b}{1-\upsilon_b^2} S_1 \delta S_2 + \frac{\upsilon_b E_b}{1-\upsilon_b^2} S_2 \delta S_1 + \frac{E_b}{1-\upsilon_b^2} S_2 \delta S_2 \right\} \mathrm{d}x\mathrm{d}y\mathrm{d}z \qquad (8.105)
\end{aligned}
$$

where E_b and E_p are the respective Young's modulus of elasticity for plate and piezoelectric, υ_b and υ_p are the respective Poisson's ratios for plate and piezoelectric, and lower and upper bounds for the integrals are depicted in Fig. 8.18.

Similar to beam kinetic energy, the kinetic energy associated with this plate can be expressed, see (4.91), as (notice that similar to beam problem, the electrical kinetic energy is neglected):

$$\begin{aligned} T = {} & \tfrac{1}{2}\int_0^{l_{1x}}\int_0^{b}\left(\rho_b t_b \dot{w}^2(x,y,t)\right)\mathrm{d}x\mathrm{d}y + \tfrac{1}{2}\int_{l_{1x}}^{l_{2x}}\int_0^{l_{1y}}\left(\rho_b t_b \dot{w}^2(x,y,t)\right)\mathrm{d}x\mathrm{d}y \\ & + \tfrac{1}{2}\int_{l_{1x}}^{l_{2x}}\int_{l_{1y}}^{l_{2y}}\left((\rho_b t_b + 2\rho_p t_p)\dot{w}^2(x,y,t)\right)\mathrm{d}x\mathrm{d}y \\ & + \tfrac{1}{2}\int_{l_{1x}}^{l_{2x}}\int_{l_{2y}}^{b}\left(\rho_b t_b \dot{w}^2(x,y,t)\right)\mathrm{d}x\mathrm{d}y + \tfrac{1}{2}\int_{l_{1x}}^{a}\int_0^{b}\left(\rho_b t_b \dot{w}^2(x,y,t)\right)\mathrm{d}x\mathrm{d}y \end{aligned} \tag{8.106}$$

or in short,

$$T = \tfrac{1}{2}\int_0^a\int_0^b \rho(x,y)\left(\frac{\partial w(x,y,t)}{\partial t}\right)^2 \mathrm{d}x\mathrm{d}y \tag{8.107}$$

where $\rho(x,y)$ is the variable density of the combined piezoelectric and plate materials defined as:

$$\rho(x,y) = \rho_b t_b + \rho_p 2 t_p G(x,y) \tag{8.108}$$

with the piezoelectric/beam section indicator function $G(x,y)$ given by:

$$G(x,y) = \big(H(x-l_{1x}) - H(x-l_{2x})\big)\big(H(y-l_{1y}) - H(y-l_{2y})\big) \tag{8.109}$$

Similar to the beam problem, considering both viscous and structural damping mechanisms for plate, the total mechanical virtual work can be given by:

$$\begin{aligned} \delta W_m^{\text{ext}} = {} & -B\int_0^a\int_0^b\left(\frac{\partial w(x,y,t)}{\partial t}\right)\delta w(x,y,t)\mathrm{d}x\mathrm{d}y x \\ & - C\int_0^a\int_0^b\left(\frac{\partial^3 w(x,t)}{\partial x\partial y\partial t}\right)\delta w(x,y,t)\mathrm{d}x\mathrm{d}y \end{aligned} \tag{8.110}$$

where B and C are the viscous and structural damping coefficients, respectively (Dadfarnia et al. 2004c). In a very similar fashion to 1D configuration, the electrical virtual work due to input voltage to piezoelectric patch is given by:

$$\delta W_e^{\text{ext}} = \int_0^a \int_0^b V_a(x,y,t)\delta D_3(x,y,t)\mathrm{d}x\mathrm{d}y \tag{8.111}$$

Finally, at this stage substituting the strain-displacement relationships (4.88) into (8.105), taking the variation of kinetic energy (8.107) and inserting the resultant expressions for both δU and δT along with total virtual work $\delta W^{\text{ext}}(= \delta W_m^{\text{ext}} + \delta W_e^{\text{ext}})$ into the extended Hamilton's principle yields two PDEs, one for plate vibrations and the other one for static relationship for dielectric displacement $D_3(x,y,t)$, along with eight boundary conditions. As it is very obvious, the expressions and derivations are extremely extensive and lengthy. We leave the detailed derivations to the interested readers, although with the help of advanced mathematical tools (e.g., Maple or Mathematica) one could obtain the following PDE for the plate transverse vibration with the symmetric arrangement of piezoelectric as:

$$\begin{aligned}
&\rho t_b \frac{\partial^2 w}{\partial t^2} + \frac{\partial^2}{\partial x^2}\left[b\left\{[R + R_1(x,y)]\left(\frac{\partial^2 w}{\partial x^2} + v_b\frac{\partial^2 w}{\partial y^2}\right)\right\}\right.\\
&\qquad \left. + (l_{2y} - l_{1y})R_2(x,y)\left(\frac{\partial^2 w}{\partial x^2} + v_p\frac{\partial^2 w}{\partial y^2}\right)\right]\\
&\qquad + \frac{\partial^2}{\partial y^2}\left[a\left\{[R + R_1(x,y)]\left(\frac{\partial^2 w}{\partial y^2} + v_b\frac{\partial^2 w}{\partial x^2}\right)\right\}\right.\\
&\qquad \left. + (l_{2x} - l_{1x})R_2(x,y)\left(\frac{\partial^2 w}{\partial y^2} + v_p\frac{\partial^2 w}{\partial x^2}\right)\right]\\
&\qquad + \frac{\partial^2}{\partial x\partial y}\left((1 - v_b)[R + R_1(x,y)]\frac{\partial^2 w}{\partial x\partial y} + (1 - v_p)R_2(x,y)\frac{\partial^2 w}{\partial x\partial y}\right)\\
&\qquad = -\frac{\partial^2}{\partial x^2}\Big((l_{2y} - l_{1y})\left\{B(t)G(x,y)(d_{31} + v_p d_{32})\right\}\Big)\\
&\qquad\quad - \frac{\partial^2}{\partial y^2}\Big((l_{2x} - l_{1x})\left\{B(t)G(x,y)(d_{32} + v_p d_{31})\right\}\Big)
\end{aligned} \tag{8.112}$$

where

$$\begin{aligned}
&R = \frac{E_b t_b^3}{12(1 - v_b^2)},\ R_1(x,y) = G(x,y)\frac{E_b t_b^3}{12(1 - v_b^2)},\\
&R_2(x,y) = G(x,y)\frac{E_p}{12(1 - v_p^2)}\left(\frac{t_p^3}{3} + \frac{t_b^2 t_p}{4} + \frac{t_b t_p^2}{2}\right),\\
&B(t) = \frac{E_p V_a(t)}{2(1 - v_p^2)}(t_p + t_b)
\end{aligned} \tag{8.113}$$

8.4.2 Equivalent Bending Moment 2D Actuation Generation

Similar to 1D actuation, the results of Sect. 8.3.3 can be extended to plate. For this, we review briefly the moment equations for the plate vibration (notice that due to our energy-based approach, these materials were not provided in Chap. 4).

In a similar fashion to treatment in Sect. 8.3.3, the constitutive relationships (6.26a) can be written for this 2D stress-strain state within the piezoelectric layer as:

$$\begin{aligned} S_1 &= s_{11}^S \sigma_1 + s_{12}^S \sigma_2 + d_{31}\epsilon_3 \\ S_2 &= s_{12}^S \sigma_1 + s_{11}^S \sigma_2 + d_{32}\epsilon_3 \\ S_6 &= 2\left(\mathrm{s}_{11}^S - \mathrm{s}_{12}^S\right)\sigma_6 \end{aligned} \tag{8.114}$$

where we have assumed that the piezoelectric material used here, in general, is non-isotropic (i.e., $d_{31} \neq d_{32}$, see Sect. 6.3.1). The compliance coefficients s_{pq}^S in (8.114) can be related to engineering constants for the plate as (see 4.23):

$$s_{11}^S = 1/E_p, \quad s_{12}^S = -\nu_p/E_p \tag{8.115}$$

By converting the indicial notations used in (8.114) to engineering notations (i.e., $1 \rightarrow xx$, $2 \rightarrow yy$ and $6 \rightarrow xy$) and solving for the stresses σ_{xx}, σ_{yy}, and σ_{xy}, it yields:

$$\begin{aligned} \sigma_{xx} &= \frac{E_p}{1-\nu_p^2} S_{xx} + \frac{\nu_p E_p}{1-\nu_p^2} S_{yy} - \frac{E_p}{1-\nu_p^2}\left(d_{31} + \nu_p d_{32}\right)\frac{V_a(t)}{t_p} \\ \sigma_{yy} &= \frac{\nu_p E_p}{1-\nu_p^2} S_{xx} + \frac{E_p}{1-\nu_p^2} S_{yy} - \frac{E_p}{1-\nu_p^2}\left(d_{31}\nu_p + d_{32}\right)\frac{V_a(t)}{t_p} \\ \sigma_{xy} &= \frac{E_p}{2(1+\nu_p)} S_{xy} \end{aligned} \tag{8.116}$$

where the uniform electric field $\epsilon_3 = V_a(t)/t_p$ within the piezoelectric material is assumed.

Similar to 1D configuration, the bending moment expression (8.96), for the section of the plate where only piezoelectric material is attached, can be expressed as:

$$M_x^{\text{piezo}} = -(l_{2y} - l_{1y}) \int_{\frac{t_b}{2}}^{\frac{t_b}{2}+t_p} \sigma_{xx} z \mathrm{d}z \tag{8.117a}$$

$$M_y^{\text{piezo}} = -(l_{2x} - l_{1x}) \int_{\frac{t_b}{2}}^{\frac{t_b}{2}+t_p} \sigma_{yy} z \mathrm{d}z \tag{8.117b}$$

$$M_{xy}^{\text{piezo}} = \iint_A \sigma_{xy} z \mathrm{d}A \tag{8.117c}$$

Notice that due to symmetry arrangement of piezoelectric patch actuator and sensor, $z_n = 0$ in (8.117) when compared to its analogous 1D expression (8.96). Inserting the 2D strain components (4.88) into the stress components (8.116), substituting the resultant expressions into the bending moments (8.117) and after some manipulations and simplifications yields:

$$M_x^{\text{piezo}}(x,y,t) = \underbrace{\left(l_{2y}-l_{1y}\right) R_2(x,y)\left(\frac{\partial^2 w}{\partial x^2}+\nu_p\frac{\partial^2 w}{\partial y^2}\right)}_{M_{x,\text{nonactive}}^{\text{piezo}}} + \underbrace{\frac{E_p}{2\left(1-\nu_p^2\right)}\left(l_{2y}-l_{1y}\right)\left(t_b+t_p\right)\left(d_{31}+\nu_p d_{32}\right)V_a(t)}_{M_{x,\text{active}}^{\text{piezo}}} \tag{8.118a}$$

$$M_y^{\text{piezo}}(x,y,t) = \underbrace{\left(l_{2x}-l_{1x}\right) R_2(x,y)\left(\frac{\partial^2 w}{\partial y^2}+\nu_p\frac{\partial^2 w}{\partial x^2}\right)}_{M_{y,\text{nonactive}}^{\text{piezo}}} + \underbrace{\frac{E_p}{2\left(1-\nu_p^2\right)}\left(l_{2x}-l_{1x}\right)\left(t_b+t_p\right)\left(d_{32}+\nu_p d_{31}\right)V_a(t)}_{M_{y,\text{active}}^{\text{piezo}}} \tag{8.118b}$$

$$M_{xy}^{\text{piezo}}(x,y,t) = \underbrace{\left(\frac{1-\nu_p}{2}\right) R_2(x,y)\frac{\partial^2 w}{\partial x\partial y}}_{M_{xy,\text{nonactive}}^{\text{piezo}}} \tag{8.118c}$$

Note $G(x,y) = 1$ in $R_2(x,y)$ that was defined earlier in (8.113) since we only consider the section of the plate where only piezoelectric patch is attached.

Now considering the standard equilibrium equation of a classical Kirchhoff plate (Rao 2007)

$$\rho t_b\frac{\partial^2 w}{\partial t^2} = \frac{\partial^2 M_x}{\partial x^2}+\frac{\partial^2 M_y}{\partial y^2}+2\frac{\partial^2 M_{xy}}{\partial x\partial y} \tag{8.119}$$

and by substituting the active parts of bending moments (8.118) into (8.119) reveals

$$\begin{aligned} M_{x,\text{active}}^{\text{piezo}}(x,y,t) &= \frac{E_p}{2\left(1-\nu_p^2\right)}\left(l_{2y}-l_{1y}\right)\left(t_b+t_p\right)\left(d_{31}+\nu_p d_{32}\right)V_a(t) \\ &= -M_{P_{0x}}V_a(t) \end{aligned} \tag{8.120a}$$

$$\begin{aligned} M_{y,\text{active}}^{\text{piezo}}(x,y,t) &= \frac{E_p}{2\left(1-\nu_p^2\right)}\left(l_{2x}-l_{1x}\right)\left(t_b+t_p\right)\left(d_{32}+\nu_p d_{31}\right)V_a(t) \\ &= -M_{P_{0y}}V_a(t) \end{aligned} \tag{8.120b}$$

which demonstrates, similar to 1D configuration, that the addition of the laminar piezoelectric actuator is equivalent to adding two concentrated moments $M^{\text{piezo}}_{\text{x, active}}$ and $M^{\text{piezo}}_{\text{y, active}}$ at the boundaries of the actuator. Similar to 1D configuration, calculating the electrical virtual work due to these added external moments (i.e., in place of expression 8.111), and following the same procedure for calculating the total mechanical virtual work (8.110) and other steps as highlighted in Sect. 8.4.1, one can obtain the equations of motion. After some manipulations as well as extensive substitutions, it can be shown that the equations of motion identical to (8.112) will result.

8.5 Modeling Piezoelectric Sensors

As generally discussed in Chap. 6, when piezoelectric materials are used as sensors, they generate voltage proportional to the mechanical stress or strain. This phenomenon is governed, as discussed extensively in Chap. 6, by the direct piezoelectric effect (second expression in both 6.21 and 6.22). Superior signal-to-noise ratio and high-frequency noise rejection are among attractive features of piezoelectric sensors, when compared to conventional strain gauges (Moheimani and Fleming 2006).

When piezoelectric sensors are subject to a stress field, under zero applied electric field (i.e., $\epsilon_i = 0$ or short circuited), the second expression in (6.21) can be utilized to express the total dielectric displacement D as a function of the applied stress. That is,

$$D_i = d_{ip}\sigma_p, i = 1, 2, 3 \text{ and } p = 1, 2, \ldots, 6 \tag{8.121}$$

Alternatively, when piezoelectric sensors are subject to a stress field under zero displacement, i.e., $D_i = 0$ (or open circuit) in the second equation in (6.22), the generated electric field can be obtained as:

$$\epsilon_i = -g_{ip}\sigma_p, i = 1, 2, 3 \text{ and } p = 1, 2, \ldots, 6 \tag{8.122}$$

Hence, the total generated charge can be determined from (6.7) as

$$Q = \oint_{\partial V} \mathbf{D}.\mathbf{n}\mathrm{d}A \tag{8.123}$$

Depending on the circuits designed for capturing the output voltage from piezoelectric sensor, the generated voltage can be accordingly related to total charge Q. Similar to actuator configurations considered in the preceding subsection, both axial and laminar configurations are discussed for piezoelectric sensors.

8.5.1 Piezoelectric Stacked Sensors

As briefly discussed in Chap. 6, piezoelectric sensors in axial (or stacked) configuration proportionally convert mechanical energy into electrical energy (see Fig. 8.19). As discussed earlier, piezoelectric sensors can operate in two configurations, short circuited and open circuit. These two configurations are discussed next.

General Modeling and Preliminaries: Very similar to piezoelectric stacked actuator, a similar procedure presented in Sect. 8.2.1 can be adopted in order to obtain the equations of motion for piezoelectric sensors in axial configuration (see Fig. 8.19). For this, the same kinetic and potential (both electrical and mechanical) energies for the axial sensor can be expressed as given in (8.6) and (8.3). Due to absence of electrical virtual work (8.10) for the sensor case, the equations of motion for the axial sensor, similar to actuator equations (8.14), can be obtained by substituting these energies and ever-present mechanical virtual work (8.11) into Hamilton's principle (8.7). After some manipulations and simplifications, the equations of motion can be obtained as:

for $\delta u(x,t)$,

$$\rho(x)\frac{\partial^2 u(x,t)}{\partial t^2} - \frac{\partial}{\partial x}\left(c^D A(x)\frac{\partial u(x,t)}{\partial x}\right) + B\frac{\partial u(x,t)}{\partial t} + \frac{\partial}{\partial x}\left(hA(x)D(x,t)\right) = 0 \tag{8.124a}$$

for $\delta D(x,t)$,

$$h\frac{\partial u(x,t)}{\partial x} - \beta^S D(x,t) = 0 \tag{8.124b}$$

along with the boundary conditions,

$$\left(hA(x)D(x,t) - c^D A(x)\frac{\partial u(x,t)}{\partial x}\right)\delta u(x,t)\Big|_0^L = 0 \tag{8.124c}$$

where, similar to piezoelectric axial actuator, h and β^S are piezoelectric sensor constants. Utilizing (8.124b), the dielectric displacement $D(x,t)$ can be obtained as:

$$D(x,t) = \frac{h}{\beta^S}\frac{\partial u(x,t)}{\partial x} \tag{8.125}$$

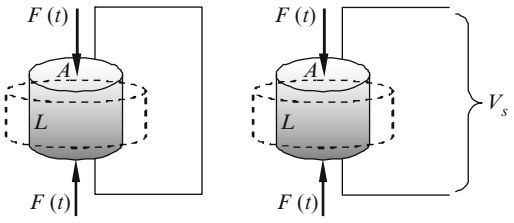

Fig. 8.19 Schematic demonstration of piezoelectric sensor in axial configuration under; (*left*) zero applied electric field ($\epsilon = 0$ or short circuited), and (*right*) zero displacement ($D = 0$ or open circuit)

Consequently, the total generated charge can be determined from Eq. (8.123) by substituting dielectric displacement (8.125) into this charge equation and integrating over the sensor area to obtain:

$$Q = \oint_{\partial V} \mathbf{D}.\mathbf{n}\mathrm{d}A = \oint_{\partial V} \frac{h}{\beta^S} \frac{\partial u(x,t)}{\partial x}\mathrm{d}A = \frac{hA}{\beta^S} \frac{\partial \overline{u}(x,t)}{\partial x} = \frac{hA}{\beta^S} \overline{S}(x,t) \quad (8.126)$$

where we have assumed that the axial displacement is constant over the sensor cross-section. Substituting h/β^S with its equivalent expression as in (8.16b) and utilizing the strain-stress relationship (6.21), under zero applied electric field, (i.e., $S = s_{11}^{\epsilon}\boldsymbol{\sigma}$), (8.126) reduces to:

$$Q = d_{33}c^{\epsilon}A(-s^{\epsilon}\boldsymbol{\sigma}) = -d_{33}F(t) \quad (8.127)$$

where the negative sign in strain-stress relationship comes from the fact that axial force F is compression as shown in Fig. 8.19. For n layers (see Fig. 8.1-right), since this compressive force is simultaneously acting on all layers in the stack, the total charge (8.127) is modified to

$$Q = -nd_{33}F(t)$$

Open Circuit Configuration: The open circuit voltage $V_s(t)$ of the piezoelectric axial sensor shown in Fig. 8.19 can be calculated using simplified version of (8.122) for this configuration as:

$$\boldsymbol{\epsilon}_3 = -g_{33}\boldsymbol{\sigma}_3 \rightarrow \frac{V_s}{L} = -g_{33}\frac{F}{A} \rightarrow V_s(t) = -g_{33}\frac{L}{A}F \quad (8.128)$$

Using the relationships between piezoelectric constants given in Table 6.2, (8.128) reduces to

$$V_s(t) = -\frac{d_{33}}{\xi^{\sigma}}\frac{L}{A}F = -d_{33}\frac{F}{C_p^s}, C_p^s \triangleq \xi^{\sigma}\frac{A}{L} \quad (8.129)$$

where C_p^s is defined as the capacitance of the piezoelectric cylinder (in stacked configuration) and ξ^{σ} is the dielectric or permittivity constant at constant stress or pressure (see Table 6.1). Consequently, the total charge Q can be calculated as:

$$Q = C_p^s V_s(t) = -d_{33}F = -g\xi^{\sigma}F \quad (8.130)$$

As seen from (8.127) and (8.130), the induced charge Q is completely independent of actuator dimensions in contrast to the induced voltage V_s.

Force and Acceleration Sensors: Equation (8.128) or (8.129) can be used to measure applied forces to a piezoelectric material in stacked configuration, or measure acceleration of a vibrating structure. In the case of a force sensor, the application of axial force $F(t)$ in Fig. 8.19-right can be measured using the resulting voltage $V_s(t)$ based on (8.128).

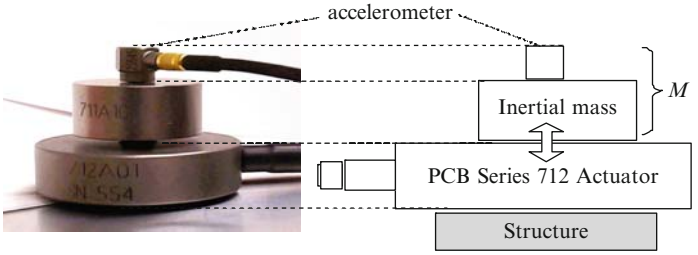

Fig. 8.20 Schematic demonstration of piezoelectric axial sensor for acceleration measurement

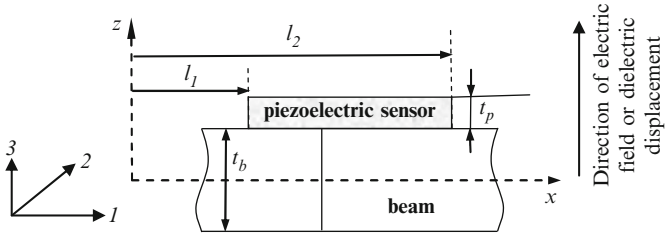

Fig. 8.21 Schematic of piezoelectric laminar sensor with detailed geometry

For the acceleration measurement, the induced inertial force F can be related to the generated acceleration a as $F = Ma$, and consequently output voltage $V_s(t)$ as (see Fig. 8.20)

$$V_s(t) = -g_{33}\frac{L}{A}F = -g_{33}\frac{L}{A}Ma = \left(-g_{33}\frac{L}{A}M\right)a = K_a a \tag{8.131}$$

Equation (8.131) simply demonstrates that the generated voltage is proportional to the acceleration.

8.5.2 Piezoelectric Laminar Sensors

In a similar manner to piezoelectric axial sensors, when a piezoelectric sensor in laminar configuration (see Fig. 8.21) is subjected to a stress field under zero applied electric field, the resulting dielectric displacement can be calculated from (8.121). However, we have already obtained comprehensive equation of motions involving laminar piezoelectric materials. That is, (8.60b) can be used under no external voltage (i.e., $V_a(x,t) = 0$ in (8.60b)) to obtain the dielectric displacement D_3 as

$$D_3(x,t) = -\frac{h_1}{\beta_1}\frac{\partial^2 w(x,t)}{\partial x^2} = -\frac{h_{31}t_p b(t_p + t_b - 2z_n)}{2\beta_{33}^S b t_p}\frac{\partial^2 w(x,t)}{\partial x^2} \tag{8.132}$$

Then, the total generated charge can be determined from Eq. (8.123) by substituting dielectric displacement (8.132) into the charge equation as:

$$Q = \oint_{\partial V} \mathbf{D}.\mathbf{n}\mathrm{d}A = b\int_{l_1}^{l_2} D_3 dx = -b\int_{l_1}^{l_2} \frac{h_{31}(t_p + t_b - 2z_n)}{2\beta_{33}^S} \frac{\partial^2 w(x,t)}{\partial x^2}\mathrm{d}x \tag{8.133}$$

Upon further simplification, (8.133) reduces to:

$$\begin{aligned} Q &= -b\frac{h_{31}(t_p + t_b - 2z_n)}{2\beta_{33}^S}\int_{l_1}^{l_2} \frac{\partial^2 w(x,t)}{\partial x^2}\mathrm{d}x \\ &= -b\frac{h_{31}t_{\mathrm{eq}}}{\beta_{33}^S}\int_{l_1}^{l_2} \frac{\partial^2 w(x,t)}{\partial x^2}\mathrm{d}x = -bE_p d_{31}t_{\mathrm{eq}}\int_{l_1}^{l_2} \frac{\partial^2 w(x,t)}{\partial x^2}\mathrm{d}x \\ &= -bE_p d_{31}t_{\mathrm{eq}}\left(\frac{\partial w(l_2,t)}{\partial x} - \frac{\partial w(l_1,t)}{\partial x}\right) \end{aligned} \tag{8.134}$$

which reveals the corresponding electrical charge. The equivalent thickness t_{eq} in this equation is defined as the distance between neutral axis of beam/sensor and that of midplane of beam and sensor

$$t_{\mathrm{eq}} = \tfrac{1}{2}(t_p + t_b) - z_n \tag{8.135}$$

If the thickness of the piezoelectric patch is small compared to that of beam (i.e., $t_p \ll t_b$), several substitutions for t_{eq} can be made such as $z_n = 0$ or $z_n = 0$ and $t_p = 0$ in (8.135).

8.5.3 Equivalent Circuit Models of Piezoelectric Sensors

In many sensing and actuation applications involving piezoelectric materials, it is desirable to replace the sensor or actuator with its electrical equivalent model. While there are numerous circuit models for this, we present only a simple, yet widely accepted electric circuit model used in practice (Preumont 2002). That is, the piezoelectric material can be modeled as a voltage source in series with a capacitor (see Fig. 8.22). In Fig. 8.22, C_p^l is the equivalent piezoelectric capacitance constant for laminar configuration and V_s is either the induced voltage in piezoelectric sensor or applied voltage in piezoelectric actuator.

Hence, the generated voltage V_s can be related to the charge (see Fig. 8.22) as:

$$V_s(t) = -\frac{Q}{C_p^l} \tag{8.136}$$

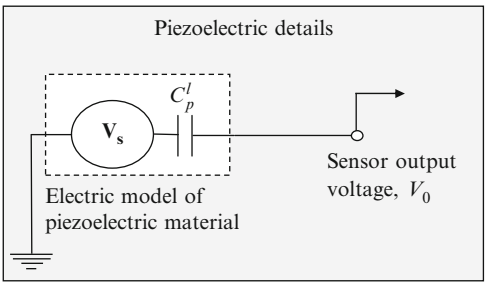

Fig. 8.22 Schematic diagram of electric model of piezoelectric material (i.e., a voltage source in series with capacitor)

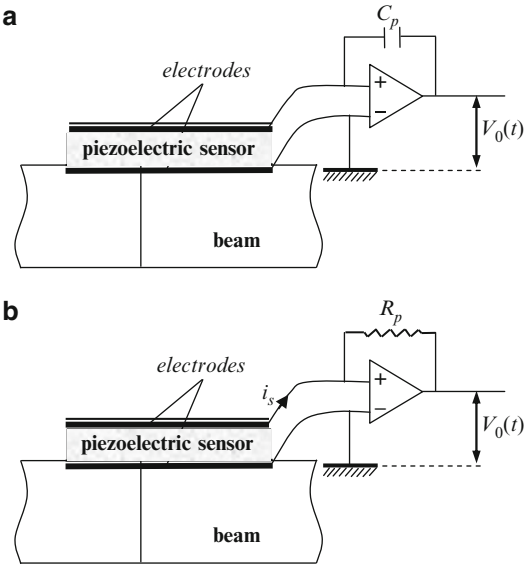

Fig. 8.23 Schematic of piezoelectric laminar sensor; (*a*) charge amplifier circuit, and (*b*) current amplifier circuit

Upon insertion of (8.134) into output voltage (8.136), the sensor output voltage is obtained as:

$$V_s(t) = \frac{bE_p d_{31} t_{\text{eq}}}{C_p^l} \left(\frac{\partial w(l_2, t)}{\partial x} - \frac{\partial w(l_1, t)}{\partial x} \right) \tag{8.137}$$

In practice, however, the piezoelectric output voltage is amplified through either a charge amplifier or a current amplifier (see Fig. 8.23). In case of charge amplification as shown in Fig. 8.23a, the output voltage is simply amplified proportionally to the induced voltage V_s as

$$V_0(t) = K_c V_s(t) \tag{8.138}$$

where K_c is the constant of charge amplifier, and V_0 is the output voltage of the circuit (see Fig. 8.23a).

In case of current amplifier (Fig. 8.23b) and under ideal assumption for the op-amp (i.e., infinite internal resistance), the sensor output V_0 can be obtained as:

$$V_0(t) = -R_p i_s(t) = -R_p \dot{Q} \tag{8.139}$$

where R_p is the constant of the amplifier. Upon insertion of (8.134) into output voltage (8.139), the sensor output voltage is obtained as:

$$V_0(t) = -R_p \dot{Q} = bE_p d_{31} t_{\text{eq}} R_p \left(\frac{\partial^2 w(l_2, t)}{\partial x \partial t} - \frac{\partial^2 w(l_1, t)}{\partial x \partial t} \right) \tag{8.140}$$

Remark 8.3. – Poisson's effect consideration for piezoelectric laminar sensors: Our primary assumption in deriving the voltage equation in laminar configuration is that the sensor is strained only in one direction (direction x or 1). However, in many practical applications, especially in micro- and nanoscale, this assumption becomes invalid and must be corrected to include the effect of strain in other directions. As extensively discussed in Chap. 11, this inclusion, referred to as "Poisson's effect," is one of the main differences between macroscale and micro/nanoscale piezoelectric sensing and actuation as other dimensions become comparable with the dimension of interest (e.g., along x-axis). Although this seems not to have been considered, a closer look at the 2D actuation using piezoelectric laminar actuator presented in Sect. 8.4.1 along with adopting the same procedure given in Sect. 8.5.2 can lead to determination of dielectric displacement $D_3(z, y, t)$ for plate similar to 1D expression (8.132). Then, the charge Q given in (8.133) can be used for plate to arrive at the sensor voltage. We leave this exercise to interested reader.

Summary

This chapter provided a comprehensive modeling of piezoelectric-based systems (actuators and sensors). Building based on the unified energy-based approach presented in the Chaps. 4 and 6, the governing equations of motion for both piezoelectric actuators and sensors in their most general forms were obtained. Both axial (or stacked) and transverse (or laminar) configurations were considered along with some special cases to demonstrate the effectiveness of modeling framework in handling different situations. The materials given in this chapter shall prepare the reader for vibration-control systems using piezoelectric actuators and sensors discussed in next chapter.

Chapter 9
Vibration Control Using Piezoelectric Actuators and Sensors

Contents

9.1 Notion of Vibration Control and Preliminaries 233
9.2 Active Vibration Absorption using Piezoelectric Inertial Actuators 235
9.2.1 Active Resonator Absorber 237
9.2.2 Delayed-Resonator Vibration Absorber 242
9.3 Piezoelectric-Based Active Vibration-Control Systems 251
9.3.1 Control of Piezoceramic Actuators in Axial Configuration 252
9.3.2 Vibration Control Using Piezoelectric Laminar Actuators 263
9.4 Piezoelectric-based Semi-active Vibration-Control Systems 284
9.4.1 A Brief Overview of Switched-Stiffness Vibration-Control Concept 286
9.4.2 Real-Time Implementation of Switched-Stiffness Concept 290
9.4.3 Switched-Stiffness Vibration Control using Piezoelectric Materials 293
9.4.4 Piezoelectric-Based Switched-Stiffness Experimentation 298
9.5 Self-sensing Actuation using Piezoelectric Materials 302
9.5.1 Preliminaries and Background 302
9.5.2 Adaptation Strategy for Piezoelectric Capacitance 304
9.5.3 Application of Self-sensing Actuation for Mass Detection 306
Summary

This chapter presents, through several example case studies and representative systems, the notion and implementation of vibration control using piezoelectric actuators and sensors. Using the modeling developments and derivations in the preceding chapters, a comprehensive treatment is provided for active vibration absorption as well as vibration control using piezoelectric materials for a variety of systems. These include the application of piezoelectric actuators and/or sensors in both axial and transverse configurations as well as piezoelectric control design using lumped-parameters and distributed-parameters representations.

9.1 Notion of Vibration Control and Preliminaries

As briefly mentioned in Chap. 1, control or otherwise cancellation of undesirable vibrations can be executed in three general forms: (a) vibration isolation, (b) vibration absorption, and (c) vibration control. In vibration isolation, either the source

N. Jalili, *Piezoelectric-Based Vibration Control*,
DOI 10.1007/978-1-4419-0070-8_9, © Springer Science+Business Media LLC 2010

of vibration is isolated from the system of concern, or the device is protected from vibration of its point of attachment (see Fig. 1.3). Unlike the isolator, a vibration absorber consists of a secondary system (usually mass-spring-damper trio) added to the primary device to protect it from vibrating. In vibration-control schemes, however, the driving forces or torques applied to the system are altered in order to regulate or track a desired trajectory while simultaneously suppressing the vibrational transients in the system. This control problem is rather challenging, since it must achieve the motion tracking objectives while stabilizing the transient vibrations in the system (Jalili and Esmailzadeh 2005).

As discussed earlier, vibration-control systems are classified into passive, active, and semi-active (see Fig. 1.5). This classification depends on the amount of external power required for the vibration-control system to perform its function. In *passive* vibration control, resilient member (e.g., stiffness) and an energy dissipator (e.g., damper) are utilized to either absorb vibratory energy or to load the transmission path of the disturbing vibration. In order to compensate for significant limitations of passive treatments in applications where broadband disturbances of highly uncertain nature are encountered, *active* vibration-control systems are utilized. With an additional active force introduced as a part of absorber subsection, the system is then controlled using different algorithms to make it more responsive to the source of disturbances (Jalili and Esmailzadeh 2005). A combination of active and passive treatments, the so-called *semiactive* vibration-control system, can be utilized to reduce the amount of external power necessary to achieve the desired performance characteristics, while also taking advantage of the variable nature of passive elements for effective vibration control despite ever-present disturbances and parameters uncertainties (Jalili 2000,2001b).

This chapter reviews the fundamental concepts, modeling frameworks, design and real-time control implementation of several vibration-control systems utilizing piezoelectric actuators and sensors. These systems are classified into two major categories of (a) vibration absorbers and (b) vibration-control systems. For the first category, active vibration absorption technique is implemented on both lumped- and distributed-parameters systems. Under the second category, both active and semi-active configurations are discussed for distributed-parameters systems in both axial and laminar configurations, along with some related practical developments in self-sensing actuation concepts in which unique properties of piezoelectric materials in dual actuation and sensing are utilized.

Remark 9.1. Before we proceed with the discussion in this chapter, we shall emphasize the importance of reviewing mathematical preliminaries given in Appendix A, especially Sects. A.3 and A.4 for some of the stability analyses and backgrounds needed in this chapter.

9.2 Active Vibration Absorption using Piezoelectric Inertial Actuators[1]

The active absorption concept offers a wide band of vibration attenuation frequencies as well as real-time tunability as two major advantages. In general, an active vibration absorber utilizes a resonator generation mechanism that forms the underlying concept. For this, a stable primary system (see Fig. 9.1 (top), for instance) is forced into a marginally stable one through the addition of a controlled force in the active unit (see Fig. 9.1, bottom). It is clear that the active control could be a destabilizing factor for the combined system, and therefore the stability of the combined system (i.e., primary and the absorber subsystems) must be assessed. The stability properties briefly reviewed in Appendix A shall be useful in this regard.

The conceptual design for generating such resonance condition is demonstrated in Fig. 9.2, where the system dominant characteristics roots (poles) are moved and placed on the imaginary axis. The absorber, then, is converted into a resonator

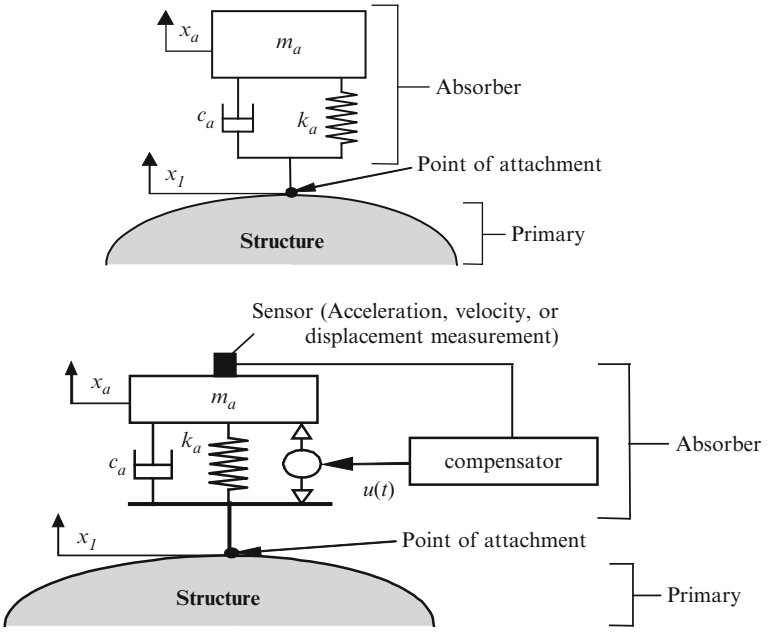

Fig. 9.1 A general primary structure with passive (*top*), and active (*bottom*) absorber settings *Source:* Jalili and Esmailzadeh (2005), with permission

[1] The materials in this section may have come directly or collectively from our publication (Jalili and Esmailzadeh 2005, Sect. 23.3.2).

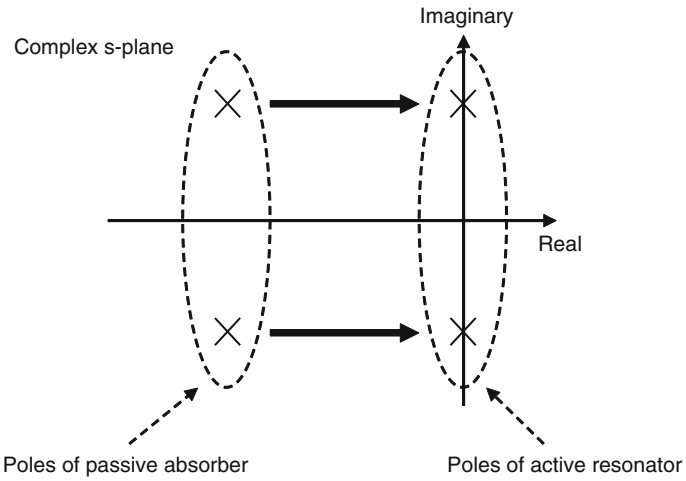

Fig. 9.2 Schematic of the active resonator absorber concept through placing the poles of the characteristic equation on the imaginary axis

capable of mimicking the vibratory energy from the primary system at the point of attachment. Although there seem to be many ways to generate such resonance, only two widely accepted practical vibration absorber resonators are discussed here for brevity.

A very important component of any active vibration absorber is the actuator unit. Advances in smart materials have led to the development of advanced actuators using piezoelectric ceramics, shape memory alloys, and magnetostrictive materials (Shaw 1998; Garcia et al. 1992). Over the past couple of decades, the piezoelectric ceramics have been utilized as potential replacements for conventional transducers. Specifically, a piezoelectric inertial actuator is an efficient and inexpensive solution to active structural vibration control including active vibration absorption. As briefly mentioned in Sect. 6.5.2 and shown in Fig. 6.20, it applies a point force to the structure to which it is attached.

These inertial actuators are made out of two parallel piezoelectric plates, and when a voltage is applied, one of the plates expands as the other one contracts, thereby producing displacement that is proportional to the input voltage. The resonance of such actuator can be adjusted by the size of the inertial mass (see Fig. 6.20). Increasing the size of the inertial mass will lower the resonance frequency and decreasing the mass will increase it. The details of resonance frequency, f_r, and effective actuator mass were given in Sect. 6.5.2. Using a simple SDOF system (see Fig. 6.20, lower-left), the parameters of the piezoelectric inertial actuators can be experimentally determined (Knowles et al. 2001; Jalili and Knowles 2004).

In the following subsections, two widely used active vibration absorber implementation schemes are described along with details of their modeling frameworks, controller design, stability analysis, and real-time control implementations issues.

9.2.1 Active Resonator Absorber

Active Resonator Vibration Absorber Concept: One novel implementation of the tuned vibration absorbers is the active resonator absorber (ARA) (Knowles et al. 2001; Jalili and Knowles 2004). Using a simple position (or velocity or acceleration) feedback control within the absorber section, it enforces the dominant characteristic roots of the absorber subsection to be on the imaginary axis, and hence leading to resonance. Once the ARA becomes resonant, it creates perfect vibration absorption at this frequency.

As demonstrated later in this subsection, the characteristic equation of the proposed control scheme is rational in nature and hence easier to implement when closed-loop stability of the system is concerned. The proposed ARA requires only one signal from the absorber mass, absolute or relative to the point of attachment (see Fig. 9.1, bottom). After the signal is processed through a compensator, an additional force is produced, for instance, by a PZT inertial actuator. By properly setting the compensator parameters, the absorber should behave as an ideal resonator at one or even more frequencies. As a result, the resonator will absorb vibratory energy from the primary mass at given frequencies. The frequency to be absorbed can be tuned in real time. Moreover if the controller or the actuator fails, the ARA will still function as a passive absorber; thus, it is inherently fail-safe. A similar vibration absorption methodology is given by Filipovic and Schroda (1999) for linear systems. The ARA, however, is not confined to the linear regime.

For the case of linear assumption for the PZT actuator, the dynamics of the ARA (Fig. 9.1, bottom) can be expressed as

$$m_a\ddot{x}_a(t) + c_a\dot{x}_a(t) + k_a x_a(t) - u(t) = c_a\dot{x}_1(t) + k_a x_1(t) \tag{9.1}$$

where $x_1(t)$ and $x_a(t)$ are the respective primary (at the absorber point of attachment) and absorber mass displacements. The mass m_a is given by (6.48), and the control $u(t)$ is designed to produce designated resonance frequencies within the ARA.

The objective of the feedback control, $u(t)$, is to convert the dissipative structure (Fig. 9.1, top) into a conservative or marginally stable one (Fig. 9.1, bottom) with a designated resonance frequency, ω_c. In other words, the control aims the placement of dominant poles at $\pm j\omega_c$ for the combined system, where $j = \sqrt{-1}$ (see Fig. 9.2). As a result, the ARA becomes marginally stable at particular frequencies in the determined frequency range. Using a simple position (or velocity, or acceleration) feedback within the absorber section (i.e., $U(s) = \overline{U}(s)X_a(s)$), the corresponding dynamics of the ARA given by (9.1) in the Laplace domain become

$$(m_a s^2 + c_a s + k_a)X_a(s) - \overline{U}(s)X_a(s) = (c_a s + k_a)X_1(s) \tag{9.2}$$

The compensator transfer function $\overline{U}(s)$ is then selected such that the primary system displacement, at the absorber point of attachment, is forced to be zero, i.e.,

$$C(s) \triangleq \left(m_a s^2 + c_a s + k_a\right) - \overline{U}(s) = 0. \tag{9.3}$$

The parameters of the compensator are determined through introducing resonance conditions to the absorber characteristic equation, $C(s)$. That is, equations $\mathrm{Re}\{\ C(j\omega_i)\} = 0$ and $\mathrm{Im}\{C(j\omega_i)\} = 0$ are simultaneously solved, where $i = 1, 2, \ldots, l$ and l is the number of frequencies to be absorbed. Using additional compensator parameters, the stable frequency range or other properties can be adjusted in real time.

Consider the case where $U(s)$ is taken as a proportional compensator with a single time constant based on the acceleration of the ARA given by

$$U(s) = \overline{U}(s) X_a(s) \quad \text{where} \quad \overline{U}(s) = \frac{g s^2}{1 + Ts}, \tag{9.4}$$

then, in the time domain, the control force $u(t)$ can be obtained from

$$u(t) = \frac{g}{T} \int_0^t e^{-(t-\tau)/T} \ddot{x}_a(\tau) \mathrm{d}\tau \tag{9.5}$$

where g and T are control gains to be selected and tuned online. To achieve ideal resonator behavior, two dominant roots of equation (9.3) are placed on the imaginary axis at the desired crossing frequency ω_c. Substituting $s = \pm j\omega_c$ into (9.3) and solving for the control parameters, g_c and T_c, one can obtain

$$g_c = m_a \left(\frac{c_a^2}{m_a^2 \left(\omega^2 - k_a/m_a\right)} - \frac{k_a}{m_a \omega^2} + 1 \right), \quad T_c = \frac{c_a \sqrt{k_a/m_a}}{\sqrt{m_a k_a} \left(\omega^2 - k_a/m_a\right)}, \quad \text{for} \quad \omega = \omega_c \tag{9.6}$$

The control parameters, g_c and T_c, are based on the physical properties of the ARA (i.e., c_a, k_a and m_a) as well as the frequency of the disturbance ω, illustrating that the ARA does not require any information from the primary system to which it is attached. However, when the physical properties of the ARA are not known within a high degree of certainty, a method to autotune the control parameters must be considered. The stability assurance of such autotuning proposition will bring primary system parameters into the derivations, and hence, the primary system cannot be totally decoupled. This issue will be discussed later in this subsection.

Application of ARA to Structural Vibration Control: In order to demonstrate the effectiveness of the proposed ARA, a simple SDOF primary system subjected to tonal force excitations is considered. As shown in Fig. 9.3, two PZT inertial actuators are used for both the primary (model 712-A01) and the absorber (model

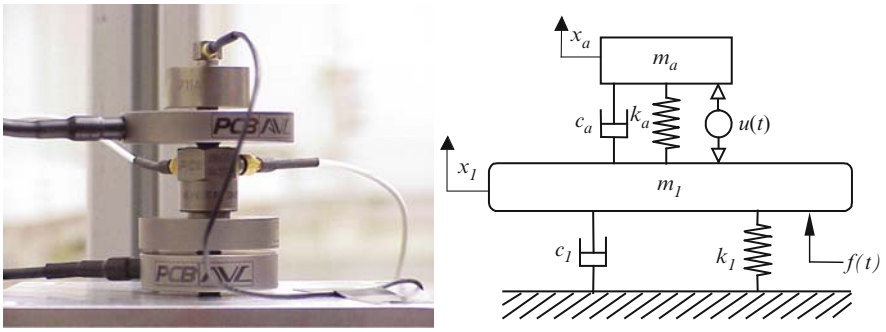

Fig. 9.3 Implementation of ARA concept using two PZT actuators (*left*) and its mathematical model (*right*)
Source: Jalili and Esmailzadeh (2005), with permission

Table 9.1 Experimentally determined parameters of PCB Series 712 PZT inertial actuators

PZT system parameters	PCB model 712-A01	PCB model 712-A02
Effective mass [gr], m_{ePZT}	7.199	12.14
Inertial mass [gr], m_{inertial}	100	200
Stiffness [kN/m]	$k_1 = 3,814.9$	$k_a = 401.5$
Damping [Ns/m]	$c_1 = 79.49$	$c_a = 11.48$

Source: Jalili and Esmailzadeh (2005), with permission

712-A02) subsections. Each system consists of passive elements (spring stiffness and damping properties of the PZT materials) and active compartment with the physical parameters listed in Table 9.1. The top actuator acts as the ARA with the controlled force $u(t)$, while the bottom one represents the primary system subjected to the force excitation f(t).

The governing dynamics for the combined system can be expressed as:

$$m_a\ddot{x}_a(t) + c_a\dot{x}_a(t) + k_a x_a(t) - u(t) = c_a\dot{x}_1(t) + k_a x_1(t) \tag{9.7}$$

$$\begin{aligned} m_1\ddot{x}_1(t)(c_1 + c_a)\dot{x}_1(t) + (k_1 + k_a)x_1(t) - \{c_a\dot{x}_a(t) \\ + k_a x_a(t) - u(t)\} = f(t) \end{aligned} \tag{9.8}$$

where $x_1(t)$ and $x_a(t)$ are the respective primary and absorber displacements.

Stability Analysis and Parameters Sensitivity: The sufficient and necessary condition for asymptotic stability is that all roots of the characteristic equation have negative real parts. For the linear system, (9.7)–(9.8) when utilizing controller (9.5), the characteristic equation of the combined system (Fig. 9.3, right) can be determined and the stability region for compensator parameters, g and T, can be readily obtained using Routh–Hurwitz method.

Autotuning Proposition: When using the proposed ARA configuration in real applications where the physical properties are not known or vary over time, the compensator parameters, g and T, only provide partial vibration suppression. In order to remedy this, a need exists for an autotuning method to adjust the

compensator parameters, g and T, by some quantities, say Δg and ΔT, respectively (Jalili and Olgac 1998b, 2000a). For the case of the linear compensator with a single time constant, given by (9.4), the transfer function between primary displacement, $X_1(s)$, and absorber displacement, $X_a(s)$, can be obtained as

$$G(s) = \frac{X_1(s)}{X_a(s)} = \frac{m_a s^2 + c_a s + k_a - \frac{g s^2}{1+Ts}}{c_a s + k_a} \tag{9.9}$$

The transfer function can be rewritten in the frequency domain for $s = j\omega$ as

$$G(j\omega) = \frac{X_1(j\omega)}{X_a(j\omega)} = \frac{-m_a\omega^2 + c_a\omega j + k_a + \frac{g\omega^2}{1+T\omega j}}{c_a\omega j + k_a} \tag{9.10}$$

where $G(j\omega)$ can be obtained in real time by convolution of accelerometer readings (Renzulli et al. 1999) or other methods (Jalili and Olgac 2000a). Following a similar procedure as utilized in Renzulli et al. (1999), the numerator of the transfer function (9.10) must approach zero in order to suppress primary system vibration. This is accomplished by setting

$$G(j\omega) + \Delta G(j\omega) = 0 \tag{9.11}$$

where $G(j\omega)$ is the real-time transfer function and $\Delta G(j\omega)$ can be written as a variational form of equation (9.10) as

$$\Delta G(\omega i) = \frac{\partial G}{\partial g}\Delta g + \frac{\partial G}{\partial T}\Delta T + \text{higher order terms} \tag{9.12}$$

Since the estimated physical parameters of the absorber (i.e., c_a, k_a and m_a) are within the vicinity of the actual parameters, Δg and ΔT should be small quantities and the higher order terms of (9.12) could be neglected. Using (9.11) and (9.12) and neglecting higher order terms, we get

$$\begin{aligned}
\Delta g &= Re[G(j\omega)]\left[\frac{2Tc_a\omega^2 - k_a + k_a T^2\omega^2}{\omega^2}\right] \\
&\quad + Im[G(j\omega)]\left[\frac{c_a - T^2\omega^2 c_a + 2k_a T}{\omega^2}\right] \\
\Delta T &= Re[G(j\omega)]\left[\frac{c_a - T^2\omega^2 c_a + 2k_a T}{g\omega^2}\right] \\
&\quad + Im[G(j\omega)]\left[\frac{k_a - 2Tc_a\omega^2 - k_a T^2\omega^2}{g\omega^3}\right] + \frac{T}{g}\Delta g
\end{aligned} \tag{9.13}$$

In these expressions, g and T are the current compensator parameters given by (9.6), c_a, k_a, and m_a are the estimated absorber parameters, ω is the absorber base excitation frequency, and $G(j\omega)$ is the transfer function obtained in real time. That is, the retuned control parameters, g and T, are determined as follows

$$g_{\text{new}} = g_{\text{current}} + \Delta g, \quad \text{and} \quad T_{\text{new}} = T_{\text{current}} + \Delta T \tag{9.14}$$

where Δg and ΔT are those given by (9.13). After compensator parameters, g and T, are adjusted by (9.14), the process can be repeated until $|G(j\omega)|$ falls within the desired level of tolerance. $G(j\omega)$ can be determined in real time by

$$G(j\omega) = |G(j\omega)|\, \mathrm{e}^{(j\varphi(j\omega))} \tag{9.15}$$

where the magnitude and the phase are determined assuming that the absorber and the primary displacements are harmonic functions of time given by

$$x_a(t) = X_a \sin(\omega t + \varphi_a), x_1(t) = X_1 \sin(\omega t + \varphi_1) \tag{9.16}$$

With the magnitudes and phase angles of (9.15), the transfer function can be determined from (9.15) and the following:

$$|G(j\omega)| = \frac{X_1}{X_a}, \quad \varphi(j\omega) = \varphi_1 - \varphi_a \tag{9.17}$$

Numerical Simulations and Discussions: To illustrate the feasibility of the proposed absorption methodology, an example case study is presented. The ARA control law is the proportional compensator with a single time constant as given in (9.5). The primary system is subjected to a harmonic excitation with unit amplitude and a frequency of 800 Hz. The ARA and primary system parameters are taken as those given in Table 9.1. The simulation was done using Matlab/Simulink® and the results for the primary system and the absorber displacements are given in Fig. 9.4.

As seen, vibrations are completely suppressed in the primary subsection after approximately 0.05 seconds at which the absorber acts as a marginally stable resonator. For this case, all physical parameters are assumed to be known exactly. However, these parameters are not known exactly in practice or vary with time, so the case with estimated system parameters must be considered.

To demonstrate the feasibility of the proposed autotuning method, the nominal system parameters (m_a, m_1, k_a, k_1, c_a, c_1) were fictitiously perturbed by 10% (i.e., representing the actual values) in the simulation. However, the nominal values of m_a, m_1, k_a, k_1, c_a, and c_1 were used for calculation of the compensator parameters, g and T. The results of the simulation using nominal parameters are given in Fig. 9.5. From Fig. 9.5a, the effect of parameter variation is shown as steady-state oscillations of the primary structure. This undesirable response will undoubtedly be encountered when the experiment is implemented. Thus, an autotuning procedure is needed.

The result of the first autotuning iteration is given in Fig. 9.5b, where the control parameters, g and T, are adjusted based on algorithm (9.14). One can see tremendous improvement in the primary system response with only one iteration (see Fig. 9.5b). A second iteration is performed, as shown in Fig. 9.5c. The response closely resembles that from Fig. 9.4, where all system parameters were assumed to be known exactly.

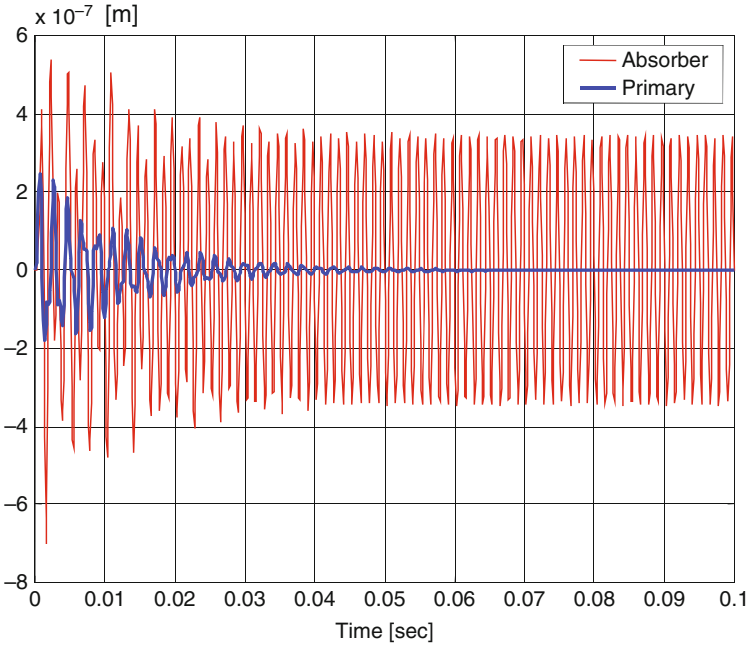

Fig. 9.4 Primary system and absorber displacements subjected to 800-Hz harmonic disturbance *Source:* Jalili and Esmailzadeh (2005), with permission

9.2.2 Delayed-Resonator Vibration Absorber

A novel approach to effectively sensitize the absorber subsection, the so-called Delayed Resonator (DR), was first introduced and implemented by Olgac and his research team back in 1994 (Olgac and Holm-Hansen 1994). The DR vibration absorber offers some attractive features in eliminating tonal vibrations from the objects to which it is attached (Olgac and Holm-Hansen 1994; Olgac 1995; Olgac and Jalili 1998; Renzulli et al. 1999), some of which are real-time tunability, stand-alone nature of the actively controlled absorber, and the simplicity of the implementation. Additionally, this SDOF absorber can also be tuned to handle multiple frequencies of vibration (Olgac et al. 1996). It is particularly important that the combined system, i.e., the primary structure and the absorber together, is asymptotically stable when the DR is implemented on the primary structure.

A Brief Overview of the DR Concept: An overview of DR is presented here to help the reader. The equation of motion governing the absorber dynamics (Fig. 9.1, bottom) is

$$m_a\ddot{x}_a(t) + c_a\dot{x}_a(t) + k_a x_a(t) - u(t) = 0, \quad u(t) = g\ddot{x}_a(t-\tau) \tag{9.18}$$

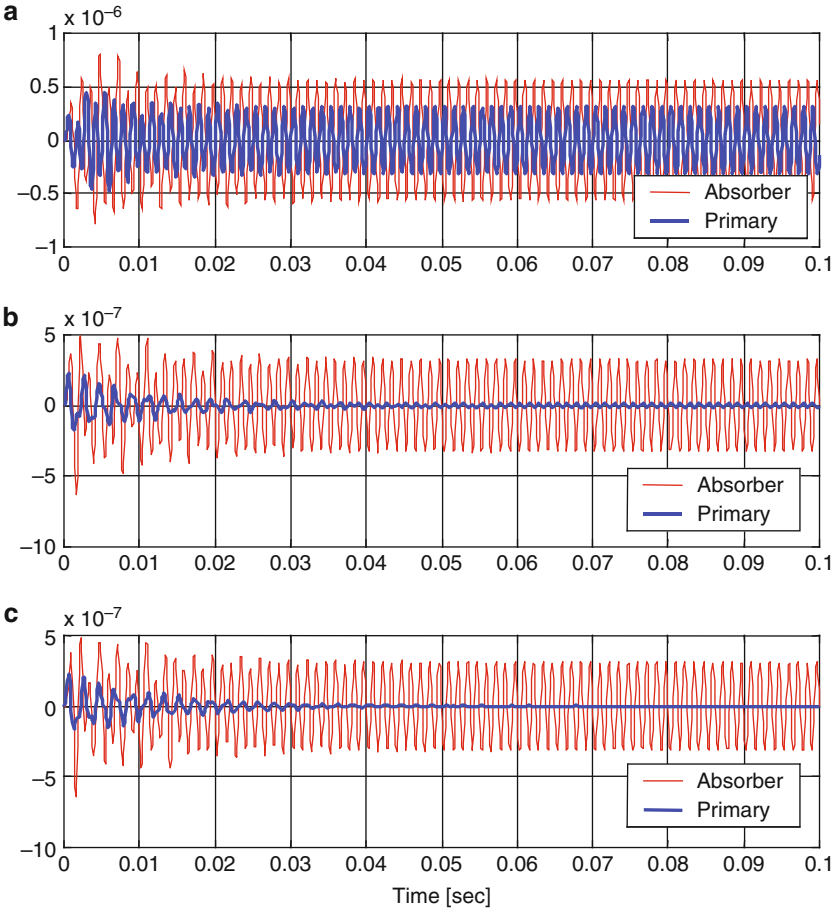

Fig. 9.5 System responses (displacement [m]) for (**a**) nominal absorber parameters, (**b**) after first autotuning procedure, and (**c**) after second autotuning procedure
Source: Jalili and Esmailzadeh (2005), with permission

where $u(t)$ represents the delayed acceleration feedback. The Laplace domain transformation of this equation yields the characteristics equation

$$m_a s^2 + c_a s + k_a - g s^2 e^{-\tau s} = 0 \tag{9.19}$$

Without feedback ($g = 0$), this structure is dissipative with two characteristic roots (poles) on the left half of the complex plane. For g and $\tau > 0$, however, these two finite stable roots are supplemented by infinitely many additional finite roots. Note that the characteristic roots (poles) of (9.19) are discretely located (say at $s = a + j\omega$), and the following relation holds.

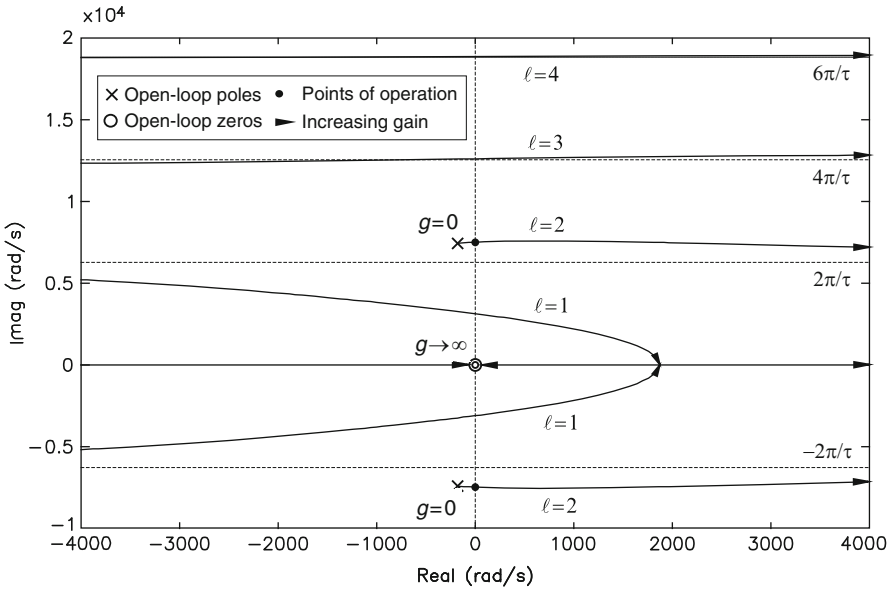

Fig. 9.6 A typical root locus plot for DR with acceleration feedback and fixed time delay τ
Source: Olgac and Jalili (1998), with permission

$$g = \frac{\left|m_a s^2 + c_a s + k_a\right|}{|s^2|} e^{\tau a} \tag{9.20}$$

where $|\bullet|$ denotes the magnitude of the argument.

Using (9.20), the following observation can be made:

For $g = 0$: there are two finite stable poles and all the remaining poles are at $a = -\infty$

For $g = +\infty$: there are two poles at $s = 0$, and the rest are at $a = +\infty$

Figure 9.6 depicts a typical root locus plot for DR with acceleration feedback and fixed time delay τ (Olgac and Jalili 1998). A closer look at Fig. 9.6 and taking into account the continuity of the root loci for a given time delay, τ, reveals that as g varies from 0 to ∞, it is obvious that the roots of (9.19) move from stable left half to the unstable right half of the complex plane. For a certain critical gain g_c, one pair of poles reaches the imaginary axis. At this operating point, the DR becomes a perfect resonator, and the imaginary characteristic roots are $s = \pm j\omega_c$, where ω_c is the resonance frequency and $j = \sqrt{-1}$. The subscript "c" implies the crossing of the root loci on the imaginary axis. The control parameters g_c and τ_c of concern can be found by substituting the desired $s = \pm j\omega_c$ into (9.19) as

$$g_c = \frac{1}{\omega_c^2}\sqrt{(c_a\omega_c)^2 + \left(m_a\omega_c^2 - k_a\right)^2},$$
$$\tau_c = \frac{1}{\omega_c}\left\{\tan^{-1}\left[\frac{c_a\omega_c}{m_a\omega_c^2 - k_a}\right] + 2(l-1)\pi\right\},\ l = 1, 2, \ldots \tag{9.21}$$

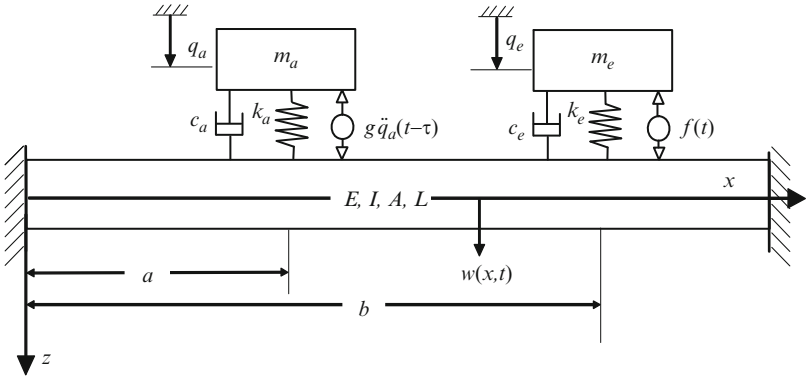

Fig. 9.7 Beam-absorber-exciter system configuration
Source: Olgac and Jalili 1998, with permission

The variable parameter ℓ, refers to the branch of root loci that happens to cross the imaginary axis at ω_c (see Fig. 9.6). Clearly, it does not have to be the first branch.

When these g_c and τ_c are used, the DR structure (Fig. 9.1, bottom) mimics a resonator at frequency ω_c. In turn, this resonator forms an *ideal absorber* of tonal vibration at ω_c. The objective of the control, therefore, is to maintain the DR absorber at this marginally stable point. On the DR stability, further discussions can be found in (Olgac and Holm-Hansen 1994; Olgac et al. 1997).

Vibration Absorber Application on Flexible Beams: To illustrate the application of active vibration absorber on distributed-parameters systems, we consider a general beam as the primary system with absorber attached to it and subjected to a harmonic force excitation, as shown in Fig. 9.7. The point excitation is located at b, and the absorber is placed at a. Uniform cross-section is considered for the beam and Euler–Bernoulli assumptions are made. The beam parameters are all assumed to be constant and uniform. The elastic deformation from the undeformed natural axis of the beam is denoted by $w(x,t)$, and in the derivations that follow, the dot "$\cdot$" and prime "$'$" indicate a partial derivative with respect to the time variable t and position variable x, respectively.

Under these assumptions, the kinetic energy of the system can be written as

$$T = \frac{1}{2}\rho \int_0^L \left(\frac{\partial w}{\partial t}\right)^2 \mathrm{d}x + \frac{1}{2}m_a\dot{q}_a^2 + \frac{1}{2}m_e\dot{q}_e^2 \tag{9.22}$$

The potential energy of this system using linear strain is given by

$$U = \frac{1}{2}EI \int_0^L \left(\frac{\partial^2 w}{\partial x^2}\right)^2 dx + \frac{1}{2}k_a \{ w(a,t) - q_a \}^2 + \frac{1}{2}k_e \{ w(b,t) - q_e \}^2 \tag{9.23}$$

Although the equations of motion can be simply obtained by Hamilton's principle, for the subsequent vibration absorption analysis as well as stability analysis, we resort to an assumed mode expansion. However, general treatment including the derivation of the controller for the original distributed-parameters representation is given later in the next subsection for vibration-control systems. For this discretization, specifically, w is written as a finite sum, the so-called assumed mode model (AMM) of (4.190)

$$w(x,t) = \sum_{i=1}^{n} W_i(x) q_{bi}(t) \tag{9.24}$$

The orthogonality conditions between these mode shapes can also be derived as (see 4.174 and 4.176)

$$\begin{aligned} &\int_0^L \rho W_r(x) W_s(x) \mathrm{d}x = \delta_{rs} \\ &\int_0^L E I W_r''(x) W_s''(x) \mathrm{d}x = \omega_r^2 \delta_{rs} \end{aligned} \tag{9.25}$$

The feedback laws for the absorber subsection, actuator excitation force, and damping dissipating forces in both absorber and exciter are considered as nonconservative forces in Lagrange's formulation (see Chap. 4). Consequently, the equations of motion are derived.

Absorber dynamics is governed by

$$\begin{aligned} m_a \ddot{q}_a(t) + c_a \left\{ \dot{q}_a(t) - \sum_{i=1}^{n} W_i(a) \dot{q}_{bi}(t) \right\} \\ + k_a \left\{ q_a(t) - \sum_{i=1}^{n} W_i(a) q_{bi}(t) \right\} - g \ddot{q}_a(t-\tau) = 0 \end{aligned} \tag{9.26}$$

and **exciter**

$$\begin{aligned} m_e \ddot{q}_e(t) + c_e \left\{ \dot{q}_e(t) - \sum_{i=1}^{n} W_i(b) \dot{q}_{bi}(t) \right\} \\ + k_e \left\{ q_e(t) - \sum_{i=1}^{n} W_i(b) q_{bi}(t) \right\} = -f(t) \end{aligned} \tag{9.27}$$

and finally **beam**

$$
\begin{aligned}
&N_i \ddot{q}_{bi}(t) + S_i q_{bi}(t) + c_a \left\{ \sum_{i=1}^{n} W_i(a)\dot{q}_{bi}(t) - \dot{q}_a(t) \right\} W_i(a) \\
&+ c_e \left\{ \sum_{i=1}^{n} W_i(b)\dot{q}_{bi}(t) - \dot{q}_e(t) \right\} W_i(b) \\
&+ k_a \left\{ \sum_{i=1}^{n} W_i(a) q_{bi}(t) - q_a(t) \right\} W_i(a) \\
&+ k_e \left\{ \sum_{i=1}^{n} W_i(b) q_{bi}(t) - q_e(t) \right\} W_i(b) \\
&+ g W_{\mathrm{i}}(a)\ddot{q}_a(t-\tau) = f(t) W_i(b) \quad i = 1, 2, \ldots, n
\end{aligned} \tag{9.28}
$$

Equations (9.26)–(9.28) form a system of $n + 2$ second-order coupled differential equations.

By proper selection of the feedback gain, the absorber can be tuned to the desired resonant frequency ω_c. This condition, in turn, forces the beam to be motionless at a, when the beam is excited by a tonal force at frequency ω_c. This conclusion is arrived by taking the Laplace transform of (9.24) and using feedback control law for the absorber. In short,

$$
\bar{W}(a, s) = \sum_{i=1}^{n} W_i(a) Q_{bi}(s) = 0 \tag{9.29}
$$

where $\bar{W}(a, s) = \Im\{w(a, t)\}$, $Q_a(s) = \Im\{q_a(t)\}$ and $Q_{bi}(s) = \Im\{q_{bi}(t)\}$. Equation (9.29) can be rewritten in time domain as,

$$
w(a, t) = \sum_{i=1}^{n} W_i(a) q_{bi}(t) = 0 \tag{9.30}
$$

which indicates that the steady-state vibration of the point of attachment of the absorber is eliminated. Hence, the absorber mimics a resonator at the frequency of excitation and absorbs all the vibratory energy at the point of attachment.

Stability of the Combined System: In the preceding section, we have derived the equations of motion for the beam-exciter-absorber system, in its most general form. As stated before, inclusion of the feedback control for active absorption is, indeed, an invitation to instability. This topic is treated next.

The Laplace domain representation of the combined system takes the form (Olgac and Jalili 1998)

$$
\mathbf{A}(s)\mathbf{Q}(s) = \mathbf{F}(s) \tag{9.31}
$$

where

$$\mathbf{Q}(s) = \begin{Bmatrix} Q_a(s) \\ Q_e(s) \\ Q_{b1}(s) \\ \vdots \\ Q_{bn}(s) \end{Bmatrix}_{(n+2)\times 1} \qquad \mathbf{F}(s) = \begin{Bmatrix} 0 \\ -F(s) \\ 0 \\ \vdots \\ 0 \end{Bmatrix}_{(n+2)\times 1}$$

$$\mathbf{A}(s) = \begin{pmatrix} m_a s^2 + c_a s + k_a - g s^2 e^{-\tau s} & 0 & -W_1(a)(c_a s + k_a) & \cdots & -W_n(a)(c_a s + k_a) \\ 0 & m_e s^2 + c_e s + k_e & -W_1(b)(c_e s + k_e) & \cdots & -W_n(b)(c_e s + k_e) \\ m_a W_1(a) s^2 & m_e W_1(b) s^2 & s^2 + cs + \omega_1^2(1 + j\delta) & \cdots & 0 \\ \vdots & \vdots & \vdots & \ddots & \vdots \\ m_a W_n(a) s^2 & m_e W_n(b) s^2 & 0 & \cdots & s^2 + cs + \omega_n^2(1 + j\delta) \end{pmatrix} \tag{9.32}$$

In order to assess the combined system stability, the roots of the characteristic equation, det(**A**(s)) = 0 are analyzed. The presence of feedback (transcendental delay term for this absorber) in the characteristic equations complicates this effort. The root locus plot observation can be applied to the entire system. It is typical that increasing feedback gain, causes instability as the roots move from left to right in the complex plane. This picture also yields the frequency range for stable operation of the combined system (Olgac and Jalili 1998).

Experimental Setting and Results: The experimental setup used to verify the findings is shown in Fig. 9.8. The primary structure is a $3/8'' \times 1'' \times 12''$ steel beam (2) clamped at both ends to a granite bed (1). A piezoelectric inertial actuator with a reaction mass (3 and 4) is used to generate the periodic disturbance on the beam. A similar actuator-mass setup constitutes the DR absorber (5 and 6). They are located symmetrically at one-quarter of the length along the beam from the center. The feedback signal used to implement the DR is obtained from the accelerometer (7) mounted on the reaction mass of the absorber structure. The other accelerometer (8) attached to the beam is only to monitor the vibrations of the beam and to evaluate the performance of DR absorber in suppressing them. The control is applied via a fast data acquisition card using a sampling of 10 kHz.

The numerical values for this beam-absorber-exciter setup are taken as:

Beam: $E = 210\,\text{GPa}$, $\rho = 1.8895\,\text{kg/m}$

Absorber: $m_a = 0.183\,\text{kg}$, $k_a = 10{,}130\,\text{kN/m}$, $c_a = 62.25\,\text{N.s/m}$, $a = L/4$

Exciter: $m_e = 0.173\,\text{kg}$, $k_e = 6{,}426\,\text{kN/m}$, $c_e = 3.2\,\text{N.s/m}$, $b = 3L/4$

Dynamic Simulations and Comparison with Experiments: For the experimental setup at hand, the natural frequencies are measured for the first two natural modes, ω_1 and ω_2. These frequencies are obtained much more precisely than those of higher order natural modes. Table 9.2 offers a comparison between the experimental (*real*) and analytical (*ideal*) clamped–clamped beam natural frequencies.

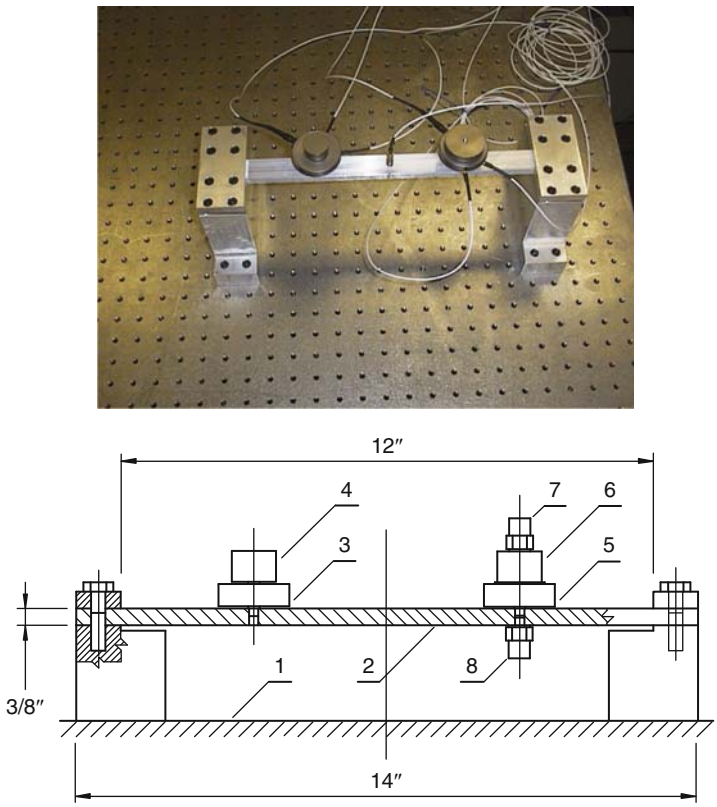

Fig. 9.8 Experimental structure (*top*), and schematic depiction of the setup (*bottom*)
Source: Olgac and Jalili 1998, with permission

Table 9.2 Comparison between experimental and theoretical beam natural frequencies (Hz)

Natural modes	Peak frequencies (experimental)	Natural frequencies (clamped–clamped)
First mode	466.4	545.5
Second mode	1,269.2	1,506.3

The discrepancies arrive from two sources: the experimental frequencies are structurally damped natural frequencies and they reflect the effect of partially clamped BCs. The theoretical frequencies, on the other hand, are evaluated for an undamped *ideal* clamped–clamped beam.

After observing the effect of the number of modes used on the beam deformation, a minimum of three natural modes are taken into account. We then compare the simulated time response versus the experimental results of vibration suppression. Fig. 9.9 shows a test with the excitation frequency $\omega_c = 1,270$ Hz. The corresponding theoretical control parameters are: $g_{c\,\text{theory}} = 0.0252$ kg and $\tau_{c\,\text{theory}} = 0.8269$ ms. The experimental control parameters for this frequency are found to be $g_{c\,\text{exp.}} = 0.0273$ kg and $\tau_{c\,\text{exp}} = 0.82$ ms. The exciter disturbs the beam for

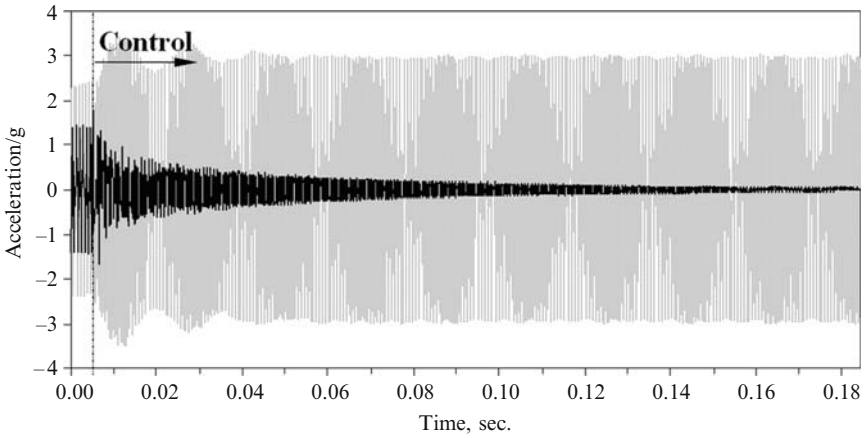

Fig. 9.9 Beam and absorber response to 1,270 Hz disturbance, analytical
Source: Olgac and Jalili 1998, with permission

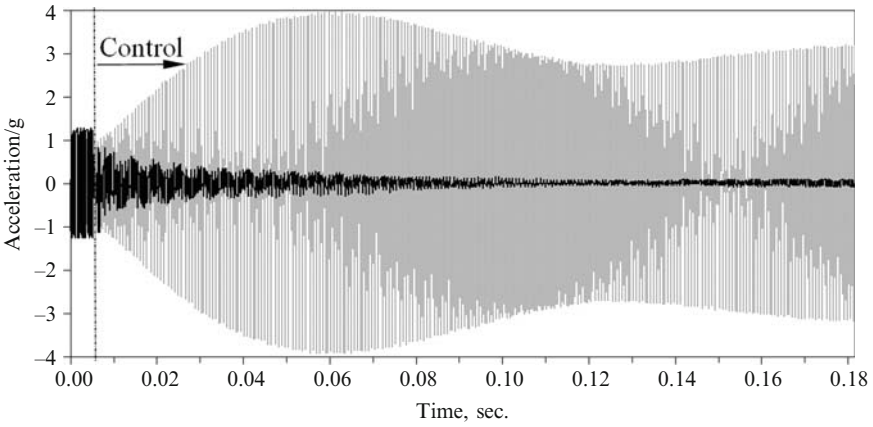

Fig. 9.10 Beam and absorber response to 1,270 Hz disturbance, experimental
Source: Olgac and Jalili 1998, with permission

5 ms; then the DR tuning is triggered. The acceleration of the beam at the point of attachment decays exponentially. For all intents and purposes, the suppression takes effect in approximately 200 ms. These results match very closely with the experimental data, Fig. 9.10. The only noticeable difference is in the frequency content of the exponential decay. This property is dictated by the dominant poles of the combined system. The imaginary part, however, is smaller in the analytical study. This difference is a small nuance which does not affect the earlier observations.

9.3 Piezoelectric-Based Active Vibration-Control Systems[2]

As discussed earlier, in vibration-control schemes the control inputs are altered in order to regulate or track a desired trajectory while simultaneously suppressing the vibrational transients in the system. As briefly highlighted in Chap. 1, all physical systems are naturally governed by partial differential equations (PDE) as a system of distributed-parameters, and therefore, possesses infinite number of dimensions. Due to the complexity of these equations and in order to facilitate the application of control strategies, discretization techniques are typically used to construct a finite-dimensional reduced model. Based on the resulting approximate model (assumed mode model (AMM) or finite element method (FEM), for instance) several controller design approaches are then applied (Ge et al. 1997; Yuh 1987; Bontsema et al. 1988). The problem associated with these model-based controllers is the truncation procedure used in the approximation. Due to ignored high-frequency dynamics (related to control spillovers) and high order of the designed controller (related to increased number of flexible modes utilized in the model), severe limitations occur in implementation of these controllers. To overcome these shortfalls, alternative approaches based on the infinite dimensional distributed (IDD) partial differential models have been developed (Lou 1993; Zhu et al. 1997; Jalili 2001a).

This subsection provides control design, development, and real-time implementation using piezoelectric actuators of two general configurations, i.e., axial and transverse configurations. For the axial configuration, the same piezoceramic actuator, extensively modeled and discussed in Sect. 8.2, is taken here and a novel controller is designed using this type of actuation. In order to be able to effectively highlight the control design and developments for this first example of vibration-control system, we resort to a discretized representation of the system and a lumped-parameters base controller (Sect. 9.3.1).

The second example is a bender-type piezoelectric actuator attached to a flexible beam, which forms a commonly used configuration in many piezoelectric actuators and sensors (Sect. 9.3.2). In order to highlight the complexity of the control implementation based on distributed-parameters representation of the system, the design, development, and real-time control implementation for these types of systems are discussed in detail and comparisons between both lumped- and distributed-parameters representations are provided. In this regard, the first vibration-control method is based on the lumped-parameters representation of the system, followed by the design and development of the vibration controller for the same system but based on the distributed-parameters representation of the system.

[2] The materials in this section may have come directly from our publication (Jalili and Esmailzadeh 2005, Sect. 23.3.2).

9.3.1 Control of Piezoceramic Actuators in Axial Configuration[3]

The modeling and the vibration analyses of piezoceramic actuators in axial configuration were given in Sect. 8.2. This subsection presents the development of a state-space controller for tracking control of this type of actuator which is used extensively in many positioning and vibration-control applications. To this end, we first present a brief overview of the state-space controller design, followed by its implementation on the piezoceramic actuator as well as covering practical control implementation issues such as control observer design in case of partial feedback and robust control design in case of parametric uncertainties and unmodeled dynamics.

An Overview of State-Space Controller Design: The piezoceramic actuator of Fig. 9.3 (see Sect. 8.2.3) is considered here. It is desirable for the actuator tip ($y(t) = u(L,t)$ see (8.43) to follow a two-time continuously differentiable desired trajectory, $y_d(t)$. Therefore, the tracking error is represented as:

$$e(t) = y_d(t) - y(t) \tag{9.33}$$

Taking the time derivative of (9.33) and using (8.43) yields:

$$\begin{aligned} \dot{e}(t) &= \dot{y}_d(t) - \dot{y}(t) = \dot{y}_d(t) - \mathbf{C}\dot{\mathbf{x}}(t) \\ &= \dot{y}_d(t) - \mathbf{CA}\mathbf{x}(t) - \mathbf{CB}u(t) \end{aligned} \tag{9.34}$$

It can be shown that for the present actuator or other flexible structures (e.g., beams, plates, shells) with inputs being applied forces and outputs being displacements, term $\mathbf{CB}$ is always zero. This implies that first-order state-space controller cannot be used for tracking of desired trajectories in the form of displacement. Letting $\mathbf{CB} = \mathbf{0}$ and differentiating one more time from the tracking error yields:

$$\begin{aligned} \ddot{e}(t) &= \ddot{y}_d(t) - \mathbf{CA}\dot{\mathbf{x}}(t) \\ &= \ddot{y}_d(t) - \mathbf{CA}^2\mathbf{x}(t) - \mathbf{CAB}u(t) \end{aligned} \tag{9.35}$$

Similarly, it can be shown that the term $\mathbf{CAB}$ in (9.35) becomes nonzero for the flexible mechanical structures. Hence, a second-order state-space control law presented in the next theorem can be utilized to control the actuator displacement.

Theorem 9.1. *For the SISO state-space system given in (8.43) which satisfies* $\mathbf{CB} = \mathbf{0}$ *and* $\mathbf{CAB} \neq \mathbf{0}$*, the following control law leads to asymptotic convergence of the tracking error, i.e.* $e \to 0$ *as* $t \to \infty$*, provided that all the signals are bounded.*

$$u(t) = \{\mathbf{CAB}\}^{-1}\left(\ddot{y}_d(t) - \mathbf{CA}^2\mathbf{x}(t) + k_1\dot{e}(t) + k_2 e(t)\right); \quad k_1,\ k_2 > 0 \tag{9.36}$$

[3] The materials presented here may have come, directly or collectively, from our recent publication (Vora et al. 2008).

Proof. Substituting the control law given by (9.36) into (9.35), an equation representing the error dynamics of system is obtained, that is:

$$\ddot{e}(t) + k_1\dot{e}(t) + k_2 e(t) = 0 \tag{9.37}$$

Since k_1 and k_2 are positive constants, (9.37) represents a stable second-order differential equation with the roots of its characteristics equation being located in the left side of the complex plane. This indicates that asymptotic convergence of the tracking error $e(t)$ is achieved (Vora et al. 2008).

State-Space Controller Simulation Results: The proposed control law is numerically implemented on the actuator model with configuration C3 (see Sect. 8.2.3), assuming that the system output and state vectors are measurable in real time. Two sinusoidal reference signals with amplitude of 10 μm at 1 kHz and 50 kHz frequencies are considered as the desired trajectories. A phase shift of 60 degrees has been applied to achieve a nonzero initial error value and assess the controller transient response. The values of k_1 and k_2 are selected as 70,000 and 1.225×10^9, respectively, so that a critically damped error dynamics with the natural frequency of 35,000 rad/s (5,573 kHz) is achieved. The sampling rate is set to 100 MHz to maintain the stability of numerical integrations. It is remarked that the critically damped error dynamics offers a suitable stability and performance because of its fast settling time without overshoot. Moreover, higher natural frequency of a critically damped error dynamics results in faster settling time; however, this value cannot be increased above a certain threshold in practice which is determined by the chatter effect.

Figure 9.11 depicts the tracking results which demonstrate that the controller is able to precisely track both low- and high-frequency trajectories with identical exponential convergence rates. There are small amplitude oscillations in the tracking error, particularly at the high-frequency trajectory, due to the ever-present approximation in the numerical integrations. While the system output converges to the desired trajectory within the first cycle of the low-frequency input, it takes a few cycles to converge to the high-frequency trajectory. However, this can be modified by increasing the control gains to achieve a desirable response.

Control Observer Design: In many practical applications, only actuator's tip displacement (system output $y(t) = u(L,t)$, see (9.43)) is measurable. This limits the implementation of the developed controller which requires full state feedback. Hence, the use of state estimators or observers in the feedback loop can be considered to effectively overcome this problem. Closed-loop state observers have been widely used in feedback control techniques when the direct measurements of states are not possible. Yet, the observability of the system must be investigated. Unfortunately, the present state-space model for the axial actuator does not agree with the observability condition, because the rank of observability matrix becomes less than the system order, meaning that it is not guaranteed to set the closed-loop observer poles at any desired locations. However, noting that the open-loop system is stable (which implies that the state vector is detectable) one can set the observer poles close enough to desired locations by optimally tuning the closed-loop observer gains.

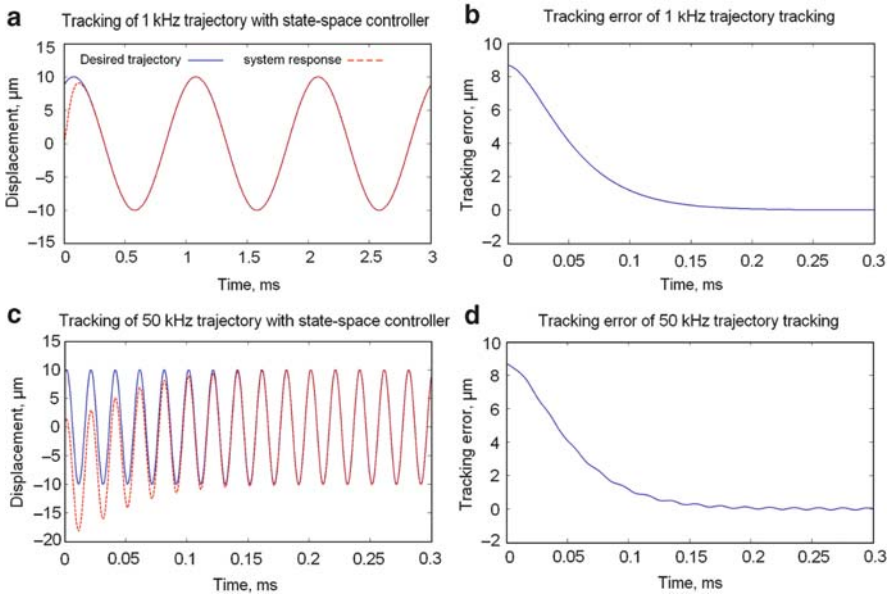

Fig. 9.11 Tracking control results using the proposed state-space control law: (**a**) 1-kHz sinusoidal trajectory tracking and (**b**) its tracking error; (**c**) 50-kHz sinusoidal trajectory tracking, and (**d**) its tracking error
Source: Bashash et al. 2008

The classical closed-loop observer for a linear system is given by:

$$\dot{\hat{\mathbf{x}}}(t) = \mathbf{A}\hat{\mathbf{x}}(t) + \mathbf{B}u(t) + \mathbf{L}\left(y(t) - \mathbf{C}\hat{\mathbf{x}}(t)\right) \tag{9.38}$$

where $\hat{\mathbf{x}}(t)$ is the observed state vector and $\mathbf{L}$ is the observer gain matrix. To obtain the observer error dynamics, the state observation error is defined as:

$$\tilde{\mathbf{x}}(t) = \mathbf{x}(t) - \hat{\mathbf{x}}(t) \tag{9.39}$$

Taking the time derivative of (9.39) and using (8.43) and (9.38) yields:

$$\dot{\tilde{\mathbf{x}}}(t) = (\mathbf{A} - \mathbf{LC})\,\tilde{\mathbf{x}}(t) \tag{9.40}$$

Equation (9.40) is a first-order differential equation representing the observer error dynamics. The only condition for its asymptotic stability is for the eigenvalues of matrix $(\mathbf{A} - \mathbf{LC})$ to be located in the left side of the complex plane. The simplest choice would be setting $\mathbf{L} = \mathbf{0}$ and using an open-loop observer since the eigenvalues of matrix $\mathbf{A}$ for the present system have negative real parts. However, the possible presence of uncertainties and disturbances in the system and the poor transient response of open-loop observer due to system inherent low damping necessitate the use of a closed-loop observer. The objective is to choose the gain

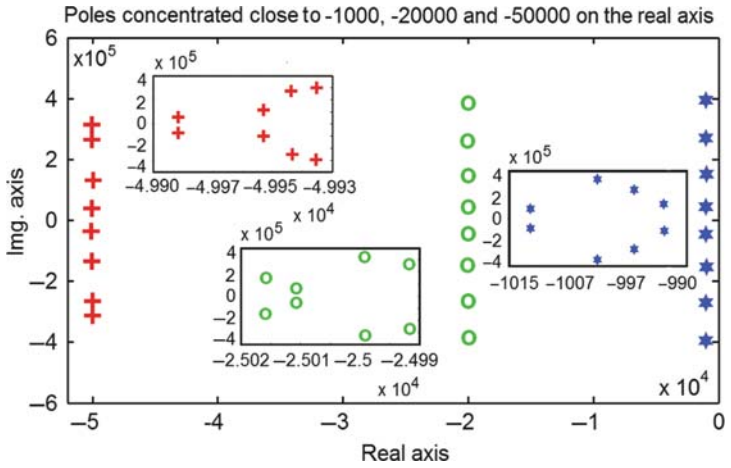

Fig. 9.12 Optimal location of the observer poles around $-1,000$, $-20,000$ and $-50,000$ on the real axis
Source: Bashash et al. 2008b

matrix $\mathbf{L}$ such that a stable error dynamics is achieved with its eigenvalues are all pushed toward left and concentrated around the real axis to enhance both stability and transient response of observation. It is remarked that the observer eigenvalues cannot be moved more leftward than a certain value in practice because of the need for smaller sampling time to solve the observer differential equation in real time than that digital signal processing systems could offer.

A random optimization algorithm is utilized to optimally locate the observer poles around the desired locations. The advantage of the random optimization over the gradient-based methods is in its seeking for the global extremum of the given objective function (Matyas 1965). Figure 9.12 depicts three different sets of optimal locations of observer poles for the desired locations being set to $-1{,}000$, $-20{,}000$, and $-50{,}000$ on the real axis. Although the observer poles can be moved leftward leading to more stable configuration, they cannot be all located on the real axis to yield a desired transient response. However, the poles have been attempted to be squeezed around the real axis through the proposed optimization algorithm within the constraints of the problem, most important of which is the lack of the observability condition. Nevertheless, desirable steady-state responses are expected.

To assess the performance of the observer in estimating the state vector, a set of simulations is carried out by setting the observer poles around $-50,000$ on the real axis and applying an initial condition and an input force at 20 kHz on the system. The results are depicted in Fig. 9.13, where all the eight state observation errors converge to zero. There are limited oscillations at the beginning, but the steady-state responses are all excellent.

Controller and Observer Integration: The designed observer can now be integrated with the proposed state-space controller to effectively solve the problem associated with the unavailability of state feedback in practice. By integrating

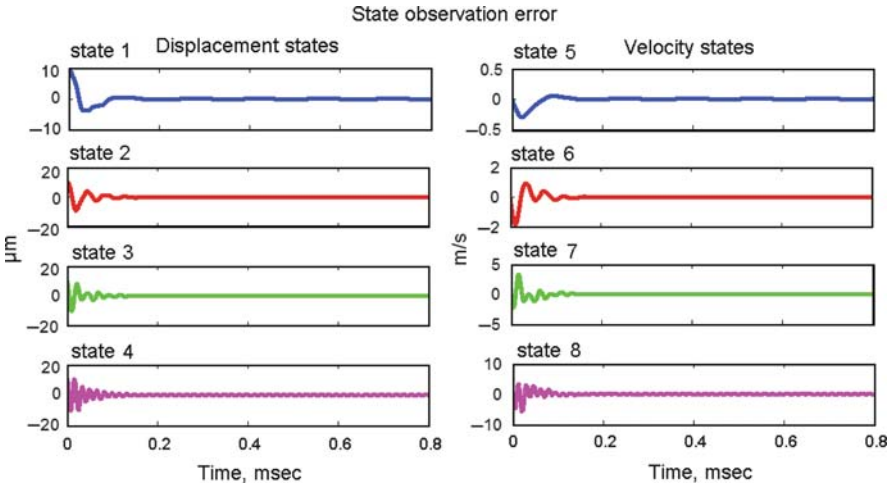

Fig. 9.13 Convergence of the state observer errors to zero despite a 20 kHz input excitation, for the observer poles located around $-50,000$ on the real axis
Source: Bashash et al. 2008b

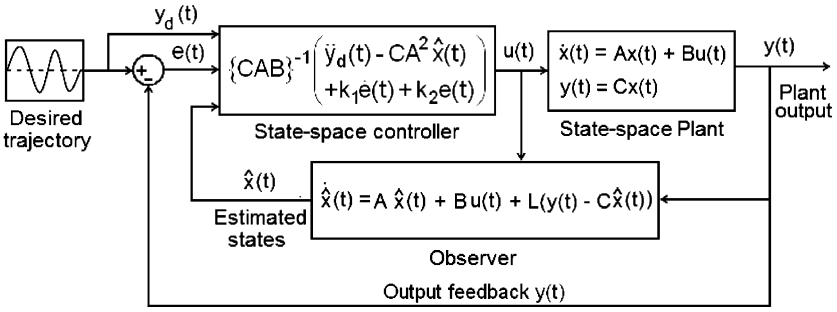

Fig. 9.14 Integrated state-space controller/observer diagram for practical control of rod-type actuators
Source: Bashash et al. 2008

(9.36) with (9.38), the state-space control law with the observer integration can be given by:

$$u(t) = \{\mathbf{CAB}\}^{-1}\left(\ddot{y}_d(t) - \mathbf{CA}^2\hat{\mathbf{x}}(t) + k_1\dot{e}(t) + k_2 e(t)\right); \quad k_1, k_2 > 0$$
$$\dot{\hat{\mathbf{x}}}(t) = \mathbf{A}\hat{\mathbf{x}}(t) + \mathbf{B}u(t) + \mathbf{L}\left(y(t) - \mathbf{C}\hat{\mathbf{x}}(t)\right) \tag{9.41}$$

Figure 9.14 demonstrates the block diagram of the control structure. As seen, the observer receives plant input and output, and feeds the estimated states back to the controller. Using this strategy, the simulations of tracking control for 1 and 50 kHz desired trajectories are repeated here. Results are depicted in Fig. 9.15, where both transient and steady-state responses are about the same as those of the case when system exact state feedback is utilized. These simulations indicate the practicability of the proposed controller/observer strategy.

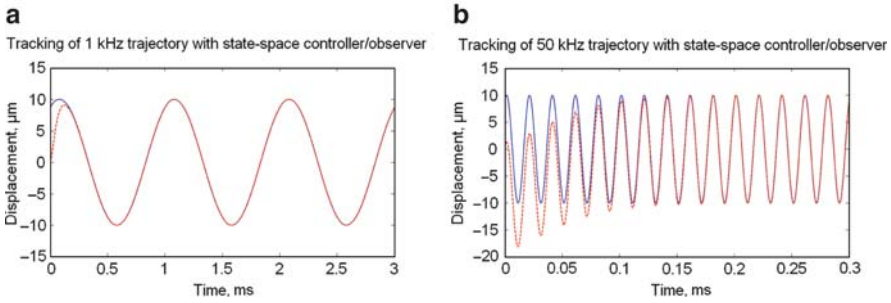

Fig. 9.15 Tracking control of (**a**) 1 kHz and (**b**) 50 kHz sinusoidal trajectories using the combined controller/observer strategy
Source: Bashash et al. 2008b

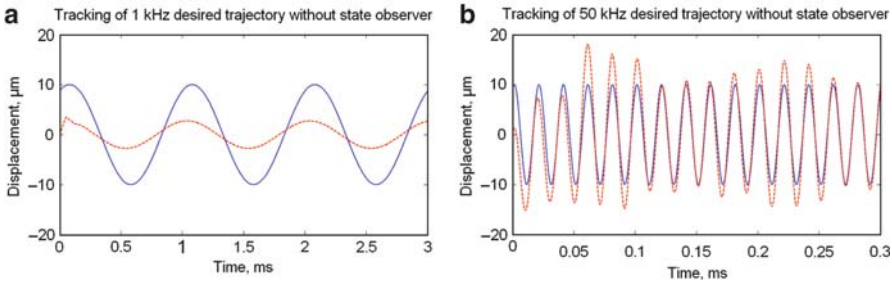

Fig. 9.16 Tracking control of (**a**) 1 kHz and (**b**) 50 kHz sinusoidal trajectories without using the state feedback
Source: Bashash et al. 2008

With almost identical tracking results of state-space controller with exact state feedback (Fig. 9.11) and with observed state feedback (Fig. 9.15), one may argue that the effects of state feedback can be negligible compared to other terms in the control law. To clarify this doubt, the state observer is disconnected from controller and the simulations are repeated. As seen from Fig. 9.16, poor tracking results prove the importance of the state observer integration.

Assessment of Controller Bandwidth: One of the main objectives in any vibration-control schemes, such as this one, is to achieve a high bandwidth tracking controller for piezoelectric axial solid-state actuators for any desired frequency ranges. In the present framework and because of the practical limitations, the effects of higher modes are neglected. Hence, a truncated model has been utilized based on which the controller is formulated. However, a real actuator has infinite number of modes and the truncation may lead to considerable tracking errors. Along this line of reasoning, we study, next, how the modes truncation affects the controller performance and bandwidth.

A four-mode actuator model with configuration C3 is assumed here to represent an actual plant. Four different controllers are formed based on one-, two-, three-, and four-mode approximation of the plant, respectively. It is expected that the controllers with higher number of modes offer better tracking bandwidth. A 10μm

amplitude desired trajectory is applied to the system with its frequency incrementally changed from 1 to 80 kHz to cover all the plant resonant frequencies. The steady-state tracking error amplitude is plotted versus frequency to continuously demonstrate the performance of the proposed controller/observer over the frequency range of interest. Plant limited-mode approximations as well as their corresponding tracking results are depicted in Fig. 9.17. It is seen that the controller is able to only subside the tracking error for the included modes. For instance, the controller with one-mode approximation is able to precisely track the desired trajectory only below the second resonance; except for the first resonance, tracking error suffers from the unexpected large peaks of the higher modes. As the number of included modes in the controller increases, the tracking bandwidth increases as well. For the controller with full four-mode approximation, the tracking error demonstrates smooth and small variations in the entire frequency range. Hence, it can be concluded that for a real actuator with infinite modes, the tracking bandwidth of the developed controller depends on the number of included modes. For any desired bandwidth, accurate tracking can be guaranteed provided that all the modes up to the frequency of interest have been included in the controller.

There are, however, small peaks within the covered frequencies due to the truncation of higher modes. These peaks can be flattened by increasing the control gains. This has been demonstrated in Fig. 9.18, where the error level as well as its small unwanted peak at around 20 kHz has been attenuated by choosing larger control gains. In general, for a plant with uncertainties, larger control gains lead to lower tracking error amplitude. The most limiting factor in practice could be the chatter phenomenon for the controllers with very large gain values.

Robust State-Space Control Development: Uncertainties are unavoidable in practice. The effects of neglected dynamics, external disturbances, system nonlinearities, parametric uncertainties, and the environmental changes would affect the closed-loop system performance. Hence, the controller must be made robust against these effects to result in high-performance tracking. In this section, a Lyapunov-based robust variable structure control is developed for the present state-space system to reduce the degrading effects of uncertainties on the system performance. Variable structure (e.g., sliding mode) control has been widely used in variety of control applications since its invention (Utkin 1977, Slotine 1984, Slotine and Sastry 1983).

The modified state-space equations of system by including a disturbance terms is given by:

$$\begin{aligned} \dot{\mathbf{x}}(t) &= \mathbf{A}\mathbf{x}(t) + \mathbf{B}u(t) + \mathbf{G}d(t) \\ y(t) &= \mathbf{C}\mathbf{x}(t) \end{aligned} \tag{9.42}$$

where $\mathbf{G}_{2p\times 1}$ is the disturbance matrix and $d(t)$ is a bounded time-varying term representing the collective effects of disturbances on the system. The objective of robust control is to force the system output to track desired trajectories despite the

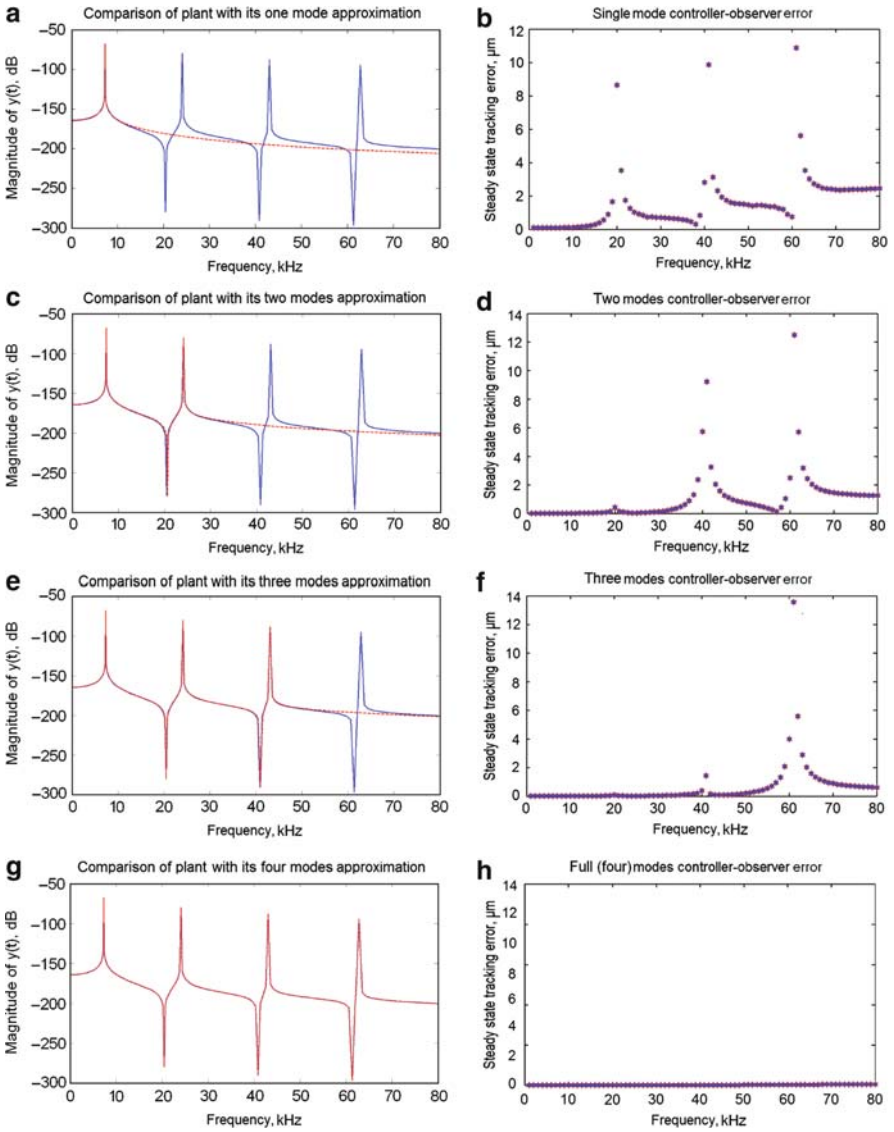

Fig. 9.17 Different approximations and tracking control results for a four-mode plant model. (**a, b**) one-mode, (**c, d**) two-mode, (**e, f**), three-mode and (**g, h**) four (full)-mode approximations and tracking control results
Source: Bashash et al. 2008b

effects of unknown disturbances on the system. The first-order time derivative of (9.33) for the system described by (9.42) becomes:

$$\begin{aligned}\dot{e}(t) &= \dot{y}_d(t) - \dot{y}(t) = \dot{y}_d(t) - \mathbf{C}\dot{\mathbf{x}}(t) \\ &= \dot{y}_d(t) - \mathbf{CAx}(t) - \mathbf{CB}u(t) - \mathbf{CG}\mathrm{d}(t)\end{aligned} \tag{9.43}$$

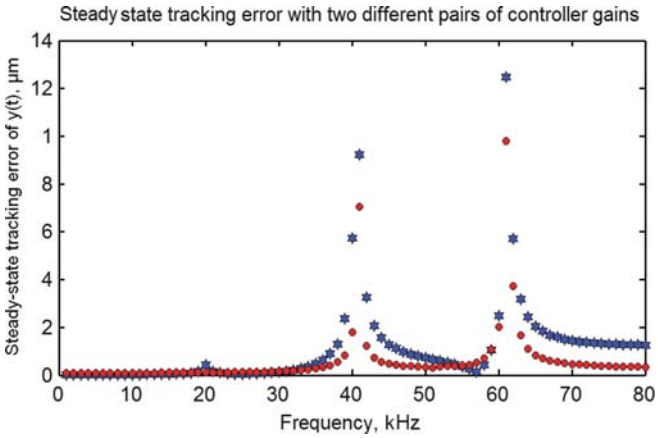

Fig. 9.18 Steady-state tracking error comparisons for two sets of gains for controller/observer based on two-mode approximation (data with the circle legend correspond to the controller with larger gain values)
Source: Bashash et al. 2008b

As discussed earlier, term **CB** becomes zero for the present system. Therefore, the first-order state-space controller cannot be used for the tracking of actuator tip displacement. It can also be shown that the term **CG** becomes zero in many cases such as in the presence of parametric uncertainties and external disturbances. However, to develop a more general strategy, we assume a nonzero value for this term. The second-order time derivative of the tracking error represented in (9.43) is then given by:

$$\ddot{e}(t) = \ddot{y}_d(t) - \mathbf{CA}^2\mathbf{x}(t) - \mathbf{CAB}u(t) - \mathbf{CAG}d(t) - \mathbf{CG}\dot{d}(t) \tag{9.44}$$

To achieve both robustness and tracking control of system simultaneously, the sliding manifold is defined as:

$$s(t) = \dot{e}(t) + \sigma e(t) \tag{9.45}$$

with σ being a positive constant representing the slope of the sliding line. Now, consider the following control law:

$$u(t) = \{\mathbf{CAB}\}^{-1}\left(\ddot{y}_d(t) - \mathbf{CA}^2\mathbf{x}(t) + \sigma\dot{e}(t) + \eta_1 s(t) + \eta_2 \mathrm{sgn}\left(s(t)\right)\right); \eta_1, \eta_2 > 0 \tag{9.46}$$

where η_1 and η_2 are the control gains, and η_2 satisfies the robustness condition given by:

$$\|\mathbf{CG}\mathrm{d}(t) + \mathbf{CAG}\mathrm{d}(t)\| \leq \eta_2 \tag{9.47}$$

which requires $\mathbf{CG}\dot{d}(t)$ be bounded, meaning either **CG** is zero or d(t) is one time continuously differentiable.

Theorem 9.2. *For the plant given by (9.42), control law (9.46) guarantees the asymptotic convergence of sliding trajectory $s(t)$, tracking error $e(t)$, and its time derivative $\dot{e}(t)$, i.e., $s(t)$, $e(t)$, $\dot{e}(t) \to 0$ as $t \to \infty$, in the sense that all signals are bounded.*

Proof. Substitution of the control law (9.46) into the second-order error dynamics, (9.44), yields:

$$\ddot{e}(t) + \sigma\dot{e}(t) + \eta_1 s(t) + \eta_2 sgn(s(t)) + \mathbf{CAG}\mathrm{d}(t) + \mathbf{CG}\dot{\mathrm{d}}(t) = 0 \tag{9.48}$$

We now define a positive definite Lyapunov function V as:

$$V = \frac{1}{2}s^2(t) \tag{9.49}$$

Its first-order time derivative is obtained as:

$$\dot{V}(t) = s(t)\dot{s}(t) = s(t)(\ddot{e}(t) + \sigma\dot{e}(t)) \tag{9.50}$$

Substituting the second-order time derivative of tracking error from (9.48), into (9.50) yields:

$$\begin{aligned}\dot{V}(t) &= -\eta_1 s^2(t) - \eta_2 s(t)\mathrm{sgn}(s(\mathrm{t})) - (\mathbf{CAG}\mathrm{d}(\mathrm{t}) + \mathbf{CG}\dot{\mathrm{d}}(t))s(t) \\ &= -\eta_1 s^2(t) - \eta_2 |s(t)| - (\mathbf{CAG}\mathrm{d}(t) + \mathbf{CG}\dot{\mathrm{d}}(t))s(t)\end{aligned} \tag{9.51}$$

If the controller gains are chosen in such a way that the robustness condition given by (9.47) is satisfied, then the time derivative of the Lyapunov function given by (9.51) results in:

$$\dot{V}(t) \leq -\eta_1 s^2(t) \leq 0 \tag{9.52}$$

This ensures the asymptotic convergence of $s(t)$ yielding asymptotic convergence of $e(t)$ and $\dot{e}(t)$ as well.

It is well known that the sliding trajectory $s(t)$ of the sliding mode control has finite-time convergence property. That is, after a finite time, the sliding trajectory intersects with the sliding line corresponding to $\dot{e}(t) + \sigma e(t) = 0$, and slides along it toward the origin. In the reaching phase, there is a smooth transition of the sliding trajectory toward the sliding line; however, in the sliding phase, where the input switches between two values with infinite frequency, system suffers from the chatter effect. Chatter has been recognized to derive the system into instability in practice and needs to be eliminated or otherwise reduced. One of the widely used methods to reduce the chatter is to replace the hard switching signum function in the control law with a soft switching saturation function as:

$$u(t) = \{\mathbf{CAB}\}^{-1}\left(\ddot{y}_d(t) - \mathbf{CA}^2\mathbf{x}(t) + \sigma\dot{e}(t) + \eta_1 s(t) + \eta_2 \mathrm{sat}\left(s(t)/\varepsilon\right)\right) \tag{9.53}$$

where $\varepsilon > 0$ is a small number determining the switching rate of the saturation function defined as:

$$sat\,(s/\varepsilon) = \begin{cases} s/\varepsilon; & |s| < \varepsilon \\ sgn(s); |s| \geq \varepsilon \end{cases} \tag{9.54}$$

Utilizing the proposed modification, the chatter effect can be eliminated; accordingly, the asymptotic convergence property of the controller is degraded as well. However, a globally uniformly ultimately bounded response is achieved with the steady-state error amplitude being bounded by a combination of control gains given by (Bashash and Jalili 2009):

$$|e_{ss}(t)| \leq \frac{\eta_2 \varepsilon}{\sigma(\eta_1 \varepsilon + \eta_2)} \tag{9.55}$$

The smaller ε is chosen, the smaller becomes the error amplitude, and the more likely chatter occurs in practice. There should be a tradeoff between the chatter and the tracking performance to effectively tune this parameter.

Two simulations are performed here to demonstrate the performance of the proposed variable structure controller with both signum and saturation functions. The nominal parameters for the controller are perturbed by 5% from the actual plant parameters to induce uncertainties in the closed-loop system. Figure 9.19 demonstrates the tracking results for a 5-μm amplitude desired trajectory with frequency of 50 kHz. Both controllers are able to effectively track the desired trajectory. The control input of the sliding mode control with the signum function demonstrates

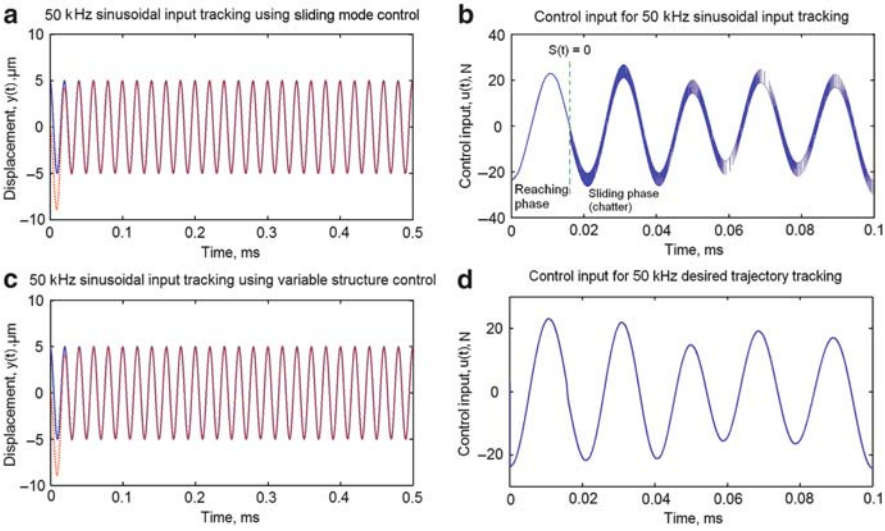

Fig. 9.19 Robust tracking control of 50-kHz desired trajectory. Sliding mode control: (**a**) tracking, and (**b**) control input; soft-switching mode control, (**c**) tracking, and (**d**) control input
Source: Bashash et al. 2008b

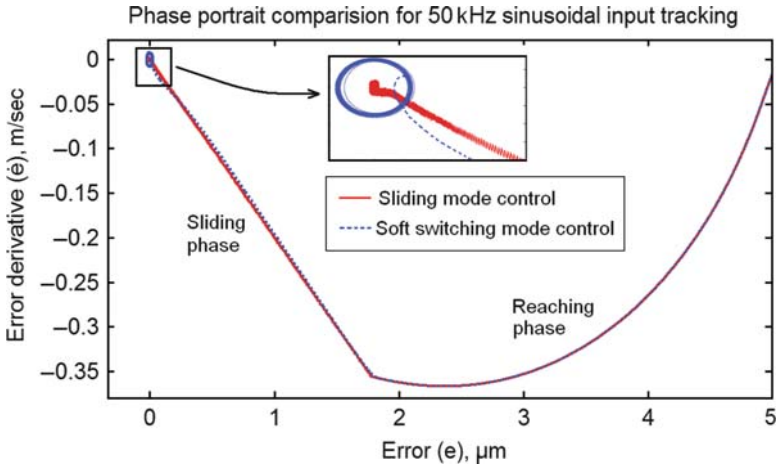

Fig. 9.20 Phase portrait comparison of sliding mode and soft switching mode variable structure controllers
Source: Bashash et al. 2008b

the chatter effect in the sliding phase (Fig. 9.19b,) while this effect is not seen in Fig. 9.19d where the saturation function is used. Figure 9.20 demonstrates the phase portrait of the controllers, in which both portraits demonstrate similar responses with differences being the small amplitude error cycles around the origin but removal of the chatter effect using the soft switching controller.

9.3.2 Vibration Control Using Piezoelectric Laminar Actuators

As mentioned earlier, the bender-type or laminar configuration of piezoelectric-based sensors and actuators is a commonly used configuration in many vibration-control systems, sensing and switching applications, and very recently in vibration-based energy harvesting systems. Along this line, we present in this section a comprehensive vibration-control design along with real-time implementation for these systems. The control design is divided into two different frameworks, (1) based on lumped-parameters, and (2) distributed-parameters representations of the system. Both methods are comprehensively treated, and a comparative study on their features and attributes is given.

Preliminaries and Vibration-Control Objectives: To implement these two controllers, the regulation problem of a flexible beam attached to a moving base is considered here (see Fig. 9.21). The base motion is controlled utilizing an electrodynamic shaker, while a piezoelectric patch actuator is bonded on the surface of the flexible beam for suppressing residual arm vibrations (see Fig. 9.21). The control objective here is to regulate the arm base movement, while simultaneously suppressing the vibration transients in the arm.

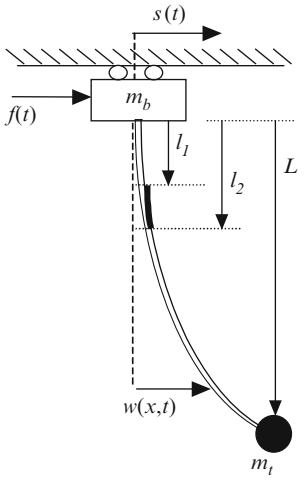

Fig. 9.21 Schematic of the moving flexible beam with piezoelectric actuator attachment

For the first control framework based on lumped-parameters representation of the system, a simple PD control strategy is selected for the regulation of the movement of the base and a Lyapunov-based controller for the piezoelectric voltage signal. The selection of the proposed energy-based Lyapunov function naturally results in velocity-related signals which are not physically measurable (Dadfarnia et al. 2004a). To remedy this, a reduced-order observer is designed to estimate the velocity-related signals. For this, the control structure is designed based on the truncated two-mode beam model.

For the second control framework designed based on the distributed-parameters representation of the same system (Fig. 9.21), the control objective here is to exponentially regulate the beam base movement, while simultaneously suppressing the vibration transients in the beam. To achieve this, we take advantage of the two typical types of damping forms, namely viscous and structural damping terms, which are inherently present in the beam structure (Dadfarnia et al. 2004c). Through a Lyapunov-based approach for both the arm base control force and piezoelectric input voltage control, it is demonstrated that the base motion can be regulated and the closed-loop system shows exponential stability performance.

Mathematical Modeling: The system considered here is a uniform flexible cantilever beam with piezoelectric actuator bonded on its top surface. As shown in Fig. 9.21, one end of the beam is clamped into a moving base with the mass of m_b, and a tip mass, m_t, is attached to the free end of the beam. The beam has total thickness t_b, and length L, while the piezoelectric film possesses thickness and length t_b and $(l_2 - l_1)$, respectively. We assume that the piezoelectric and the beam have the same width, b. The piezoelectric actuator is perfectly bonded on the beam at distance l_1 measured from the beam support. Force $f(t)$ acting on the base and input voltage $V_a(t)$ applied to the piezoelectric actuator are the only external effects.

For the purpose of model development, we refer to our extensive modeling treatment given in Sect. 8.3.1. The only change to the modeling is the added base motion, tip mass, and their associated kinetic energy as well as the nonconservative work calculation due to the external force at the base. That is, the kinetic energy (8.53) is modified to

$$T = \frac{1}{2}\left\{\int_0^L \rho(x)\left(\dot{s}(t)+\dot{w}(x,t)\right)^2 dx + m_b\dot{s}(t)^2 + m_t\left(\dot{s}(t)+\dot{w}(L,t)\right)^2\right\} \tag{9.56}$$

in order to include the kinetic energy associated with the base motion. Similarly, the mechanical virtual work (8.55) is slightly altered to include the work due to base motion as:

$$\delta W_m^{\text{ext}} = f(t)\delta s(t) - B\int_0^L \left(\frac{\partial w(x,t)}{\partial t}\right)\delta w(x,t)\mathrm{d}x - C\int_0^L \left(\frac{\partial^2 w(x,t)}{\partial x \partial t}\right)\delta w(x,t)\mathrm{d}x \tag{9.57}$$

In a similar procedure as presented in Chap. 8, insertion of energy equation (8.52), kinetic energy (9.56) and total virtual works (9.57) and (8.56) into (8.7), and after some manipulations (including the omission of dielectric displacement $D_3(x,t)$ from the resulting equations), the equations of motion result as

$$\left(m_b + m_t + \int_0^L \rho(x)\mathrm{d}x\right)\ddot{s}(t) + \int_0^L \rho(x)\ddot{w}(x,t)\mathrm{d}x + m_t\ddot{w}(L,t) = f(t) \tag{9.58a}$$

$$\rho(x)\left(\ddot{s}(t) + \frac{\partial^2 w(x,t)}{\partial t^2}\right) + \frac{\partial^2}{\partial x^2}\left(EI^{\text{eqv}}(x)\frac{\partial^2 w(x,t)}{\partial x^2}\right) + B\frac{\partial w(x,t)}{\partial t} + C\frac{\partial^2 w(x,t)}{\partial x \partial t} = M_{p_0}G''(x)V_a(t) \tag{9.58b}$$

$$w(0,t) = 0, w'(0,t) = 0, w''(L,t) = 0,$$
$$EI^{\text{eqv}}(L)w'''(L,t) = m_t\left(\ddot{s}(t) + \ddot{w}(L,t)\right) \tag{9.58c}$$

where

$$EI^{\text{eqv}}(x) = c(x) - \frac{h_1^2}{\beta_1}, \quad M_{P_0} = -\frac{1}{2}b\left(t_p + t_b - 2z_n\right)E_p d_{31} \tag{9.59}$$

Now that the equations of motion have been obtained for piezoelectric actuators appended on flexible beam in their most general case, they can be utilized to develop the control law for effective trajectory tracking while also simultaneously control the vibrations. As mentioned earlier, two different frameworks for the design

and development of the controller are considered based on lumped-parameters or distributed-parameters representations. The following two example case studies are given to extensively discuss these methods and provide general guidelines for control design and development and real-time implementation issues.

Example 9.1. Lumped-Parameters base Piezoelectric Vibration Control of Translating Flexible Beams (Jalili and Esmailzadeh 2005).

In this first example case study, the general partial differential equations of motion (9.58) are discretized using the assumed mode model (AMM) discussed in Chap. 4. For this, the beam deflection can be written as

$$w(x,t) = \sum_{i=1}^{\infty} \varphi_i(x) q_i(t) \tag{9.60}$$

$$P(x,t) = s(t) + w(x,t)$$

Implementing the same procedure as extensively discussed in Chap. 4, the discretized version of (9.58) can be represented as:

$$\left[m_b + m_t + \int_0^L \rho(x)dx\right] \ddot{s}(t) + \sum_{i=1}^{\infty} m_i \ddot{q}_i(t) = f(t) \tag{9.61a}$$

$$m_i \ddot{s}(t) + m_{di} \ddot{q}_i(t) + \omega_i^2 m_{di} q_i(t) - \frac{h_1^2 \left(\phi_i'(l_2) - \phi_i'(l_1)\right)}{\beta_1 (l_2 - l_1)} \sum_{j=1}^{\infty} \left\{ \left(\phi_j'(l_2) - \phi_j^{\mid\prime}(l_1)\right) q_j(t) \right\} = -\frac{h_1 b \left(\phi_i'(l_2) - \phi_i'(l_1)\right)}{\beta_1} V_a(t)$$

$$i = 1, 2, \ldots \tag{9.61b}$$

where

$$m_{di} = \int_0^L \rho(x) \phi_i^2(x)\, \mathrm{d}x + m_t \phi_i^2(L) \tag{9.62}$$

$$m_i = \int_0^L \rho(x) \phi_i(x)\, \mathrm{d}x + m_t \phi_i(L)$$

Remark 9.2. For this first example case and in order to keep the subsequent controller development steps more manageable and compact, we have ignored the effect of damping in the beam. Although this does not make the treatment any less general,

we will include the effect of damping dissipation in the second example case study (Example 9.2) following this example.

Derivation of the Controller: As mentioned earlier, one of the assumptions in the control development using lumped-parameters representation was to assume a finite number of modes. For this and in order to being able to experimentally implement the controller, we resort to only two modes. This selection of number of modes will be more elaborated later in this section. Hence, utilizing (9.61) and (9.62), the truncated two-mode beam with piezoelectric model reduces to

$$\left[m_b + m_t + \int_0^L \rho(x)dx\right] \ddot{s}(t) + m_1\ddot{q}_1(t) + m_2\ddot{q}_2(t) = f(t) \tag{9.63a}$$

$$m_1\ddot{s}(t) + m_{d1}\ddot{q}_1(t) + \omega_1^2 m_{d1} q_1(t) - \frac{h_1^2\left(\phi_1'(l_2) - \phi_1'(l_1)\right)}{\beta_1(l_2 - l_1)}\left\{\left(\phi_1'(l_2) - \phi_1'(l_1)\right)\right.$$
$$\left.\times q_1(t) + \left(\phi_2'(l_2) - \phi_2'(l_1)\right) q_2(t)\right\} = -\frac{h_1 b(\phi_1'(l_2) - \phi_1'(l_1))}{\beta_1} V_a(t) \tag{9.63b}$$

$$m_2\ddot{s}(t) + m_{\mathrm{d}2}\ddot{q}_2(t) + \omega_2^2 m_{\mathrm{d}2} q_2(t) - \frac{h_1^2(\phi_2'(l_2) - \phi_2'(l_1))}{\beta_1(l_2 - l_1)}$$
$$\times\left\{\left(\phi_1'(l_2) - \phi_1'(l_1)\right) q_1(t) + \left(\phi_2'(l_2) - \phi_2'(l_1)\right) q_2(t)\right\}$$
$$= -\frac{h_1 b(\phi_2'(l_2) - \phi_2'(l_1))}{\beta_1} V_a(t) \tag{9.63c}$$

Equations (9.63) can be written in the following more compact form

$$\mathbf{M}\ddot{\boldsymbol{\Delta}} + \mathbf{K}\boldsymbol{\Delta} = \mathbf{F}_e \tag{9.64}$$

where

$$\mathbf{M} = \begin{bmatrix} \psi & m_1 & m_2 \\ m_1 & m_{\mathrm{d}1} & 0 \\ m_2 & 0 & m_{\mathrm{d}2} \end{bmatrix}, \quad \mathbf{K} = \begin{bmatrix} 0 & 0 & 0 \\ 0 & k_{11} & k_{12} \\ 0 & k_{12} & k_{22} \end{bmatrix}, \quad \mathbf{F}_e = \begin{Bmatrix} f(t) \\ \tau_1 V_a(t) \\ \tau_2 V_a(t) \end{Bmatrix}, \quad = \begin{Bmatrix} s(t) \\ q_1(t) \\ q_2(t) \end{Bmatrix} \tag{9.65}$$

and

$$\psi = m_b + m_t + \int_0^L \rho(x)\mathrm{d}x$$

$$\tau_1 = -\frac{h_1 b}{\beta_1}\left(\phi_1'(l_2) - \phi_1'(l_1)\right), \tau_2 = -\frac{h_1 b}{\beta_1}(\phi_2'(l_2) - \phi_2'(l_1))$$

$$k_{11} = \omega_1^2 m_{\mathrm{d}1} - \frac{h_1^2}{\beta_1(l_2 - l_1)}\left(\phi_1'(l_2) - \phi_1'(l_1)\right)^2$$

$$k_{12} = -\frac{h_1^2}{\beta_1 (l_2 - l_1)} \left(\phi_1' (l_2) - \phi_1' (l_1)\right) \left(\phi_2' (l_2) - \phi_2' (l_1)\right) \tag{9.66}$$

$$k_{22} = \omega_2^2 m_{d2} - \frac{h_1^2}{\beta_1 (l_2 - l_1)} \left(\phi_2'(l_2) - \phi_2' (l_1)\right)^2$$

Theorem 9.3. *For the system described by (9.64), if the control laws for the arm base force and piezoelectric voltage generated moment are selected as*

$$f(t) = -k_p \Delta s - k_d \dot{s}(t) \tag{9.67}$$

$$V_a(t) = -k_v (\tau_1 \dot{q}_1(t) + \tau_2 \dot{q}_2(t)) \tag{9.68}$$

where k_p and k_d are positive control gains, $\Delta s = s(t) - s_d$, s_d is the desired set-point position, and $k_v > 0$ is the voltage control gain, then the closed-loop system is stable, and in addition

$$\lim_{t \to \infty} \{q_1(t), q_2(t), \Delta s\} = 0.$$

Proof. See Appendix B (Sect. B.1) for detailed proof.

Controller Implementation: The control input $V_a(t)$ requires the information from the velocity-related signals $\dot{q}_1(t)$ and $\dot{q}_2(t)$, which are usually not measurable. Solved the problem by integrating the acceleration signals measured by the accelerometers. However, such controller structure may result in unstable closed-loop system in some cases. To remedy this, a reduced-order observer is designed to estimate the velocity signals $\dot{q}_1$ and $\dot{q}_2$. For this, we utilize three available signals: base displacement $s(t)$, arm tip deflection $P(L, t)$, and beam root strain $S(0, t)$. That is,

$$y_1 = s(t) = x_1 \tag{9.69a}$$

$$y_2 = P(L, t) = x_1 + \phi_1(L)x_2 + \phi_2(L)x_3 \tag{9.69b}$$

$$y_3 = S(0, t) = \frac{t_b}{2} \left(\phi_1''(0)x_2 + \phi_2''(0)x_3\right) \tag{9.69c}$$

It can be seen that the first three states ($x_1 = s(t), x_2 = q_1(t), x_3 = q_2(t), x_4 = \dot{s}(t), x_5 = \dot{q}_1(t), x_6 = \dot{q}_2(t)$) can be obtained by:

$$\begin{Bmatrix} x_1 \\ x_2 \\ x_3 \end{Bmatrix} = \mathbf{C}_1^{-1} \mathbf{y} \tag{9.70}$$

Since this system is observable, we can design a reduced-order observer to estimate the velocity-related state signals. Defining $\mathbf{X}_1 = \begin{bmatrix} x_1 & x_2 & x_3 \end{bmatrix}^{\mathrm{T}}$ and $\mathbf{X}_2 = \begin{bmatrix} x_4 & x_5 & x_6 \end{bmatrix}^{\mathrm{T}}$, the estimated value for $\mathbf{X}_2$ can be designed as

$$\hat{\mathbf{X}}_2 = \mathbf{L}_r \mathbf{y} + \hat{\mathbf{z}} \tag{9.71}$$

$$\dot{\hat{\mathbf{z}}} = \mathbf{F}\hat{\mathbf{z}} + \mathbf{G}\mathbf{y} + \mathbf{H}\mathbf{u} \tag{9.72}$$

where $\mathbf{L}_r \in R^{3\times 3}$, $\mathbf{F} \in R^{3\times 3}$, $\mathbf{G} \in R^{3\times 3}$, and $\mathbf{H} \in R^{3\times 2}$ will be determined by the observer pole placement. Defining the estimation error as

$$\mathbf{e}_2 = \mathbf{X}_2 - \hat{\mathbf{X}}_2 \tag{9.73}$$

the derivative of the estimation error becomes

$$\dot{\mathbf{e}}_2 = \dot{\mathbf{X}}_2 - \dot{\hat{\mathbf{X}}}_2 \tag{9.74}$$

Substituting the state-space equations of the system (9.71) and (9.72) into (9.74) and simplifying, we get

$$\begin{aligned}\dot{\mathbf{e}}_2 = {} & \mathbf{F}\mathbf{e}_2 + (\mathbf{A}_{21} - \mathbf{L}_r\mathbf{C}_1\mathbf{A}_{11} - \mathbf{G}\mathbf{C}_1 + \mathbf{F}\mathbf{L}_r\mathbf{C}_1)\,\mathbf{X}_1 \\ & + (\mathbf{A}_{22} - \mathbf{L}_r\mathbf{C}_1\mathbf{A}_{12} - \mathbf{F})\,\mathbf{X}_2 + (\mathbf{B}_2 - \mathbf{L}_r\mathbf{C}_1\mathbf{B}_1 - \mathbf{H})\,\mathbf{u}\end{aligned} \tag{9.75}$$

In order to force the estimation error $\mathbf{e}_2$ to go to zero, matrix $\mathbf{F}$ should be selected to be Hurwitz and the following relations must be satisfied (Liu et al. 2002; Dadfarnia et al. 2004a):

$$\mathbf{F} = \mathbf{A}_{22} - \mathbf{L}_r\mathbf{C}_1\mathbf{A}_{12} \tag{9.76}$$

$$\mathbf{H} = \mathbf{B}_2 - \mathbf{L}_r\mathbf{C}_1\mathbf{B}_1 \tag{9.77}$$

$$\mathbf{G} = (\mathbf{A}_{21} - \mathbf{L}_r\mathbf{C}_1\mathbf{A}_{11} + \mathbf{F}\mathbf{L}_r\mathbf{C}_1)\,\mathbf{C}_1^{-1} \tag{9.78}$$

Matrix $\mathbf{F}$ can be chosen by the desired observer pole placement requirement. Once $\mathbf{F}$ is known, $\mathbf{L}_r$, $\mathbf{H}$, and $\mathbf{G}$ can be determined utilizing (9.76–9.78). The velocity variables $\hat{\mathbf{X}}_2$ can now be estimated by (9.71) and (9.72).

Numerical Simulations: In order to show the effectiveness of the controller, the flexible beam structure in Fig. 9.21 is considered with the piezoelectric actuator attached on beam surface. The system parameters are listed in Table 9.3.

First, we consider the beam without piezoelectric control. The PD control gains are taken to be $k_p = 120$, $k_d = 20$. Fig. 9.22 shows the results for the beam without piezoelectric control (i.e., only with PD force control for the base movement). To investigate the effect of piezoelectric controller on the beam vibration, we consider the voltage control gain to be $k_v = 2 \times 10^7$. The system responses to the proposed controller with piezoelectric actuator based on the two-mode model are shown in Fig. 9.23. The comparison between the tip displacement, Figs. 9.22 and 9.23, shows that the beam vibration can be suppressed significantly utilizing the piezoelectric actuator.

Control Experiments: In order to better demonstrate the effectiveness of the controller, an experimental setup is constructed and used to verify the numerical results. The experimental apparatus consists of a flexible beam with piezoelectric actuator and strain sensor attachments, data acquisition, amplifier, signal conditioner, and the

Table 9.3 System parameters used in numerical simulations and experimental setup for translational beam

Properties	Symbol	Value	Unit
Beam Young's modulus	c_b^D	69×10^9	N/m^2
Beam thickness	t_b	0.8125	mm
Beam and PZT width	b	20	mm
Beam length	L	300	mm
Beam volumetric density	ρ_b	3,960.0	kg/m^3
PZT Young's modulus	c_p^D	66.47×10^9	N/m^2
PZT coupling parameter	h_{31}	5×10^8	V/m
PZT impermittivity	β_{33}	4.55×10^7	m/F
PZT thickness	t_p	0.2032	mm
PZT length	$l_2 - l_1$	33.655	mm
PZT position on beam	l_1	44.64	mm
PZT volumetric density	ρ_p	7,750.0	kg/m^3
Base mass	m_b	0.455	kg
Tip mass	m_t	0.01	kg
PZT piezoelectric constant	d_{31}	-180.0×10^{-12}	C/N
PZT capacitance	C_p^l	103.8	nF
Beam viscous damping coefficient	B	0.1	kg/ms
Beam structural damping coefficient	C	0.04	kg/s
PZT modulus of elasticity – high	$E_{\text{high}}^{\text{piezo}}$	72.59×10^9	N/m^2
PZT modulus of elasticity – low	$E_{\text{low}}^{\text{piezo}}$	60.98×10^9	N/m^2

control software. As shown in Fig. 9.24, the plant consists of a flexible aluminum beam with a strain sensor and piezoelectric patch actuator bounded on each side of the beam surface. One end of the beam is clamped to the base with a solid clamping fixture which is driven by a shaker. The shaker is connected to the arm base by a connecting rod. The experimental setup parameters are listed in Table 9.3.

Figure 9.25 shows the high-level control block diagram of the experiment, where the shaker provides the input control force to the base and the piezoelectric applies a controlled moment on the beam. Two laser sensors measure the position of the base and the beam tip displacement. A strain gauge sensor, which is attached near the base of the beam, is utilized for the dynamic strain measurement. These three signals are fed back to the computer through the MultiQ data acquisition card. The remaining required signals for the controller (9.67) and (9.68) are determined as explained in the preceding section.

The experimental results for both cases (i.e., without piezoelectric and with piezoelectric control) are depicted in Figs. 9.26 and 9.27. The results demonstrate that with piezoelectric control, the arm vibration is eliminated in less than 1 sec., while the arm vibration lasts for more than 6 sec. when piezoelectric control is not used. The experimental results are in agreement with the simulation results except for some differences at the beginning of the motion. The slight overshoot and discrepancies at the beginning of the motion are due to the limitation of the experiment (e.g., shaker saturation limitation) and unmodeled dynamics in the modeling

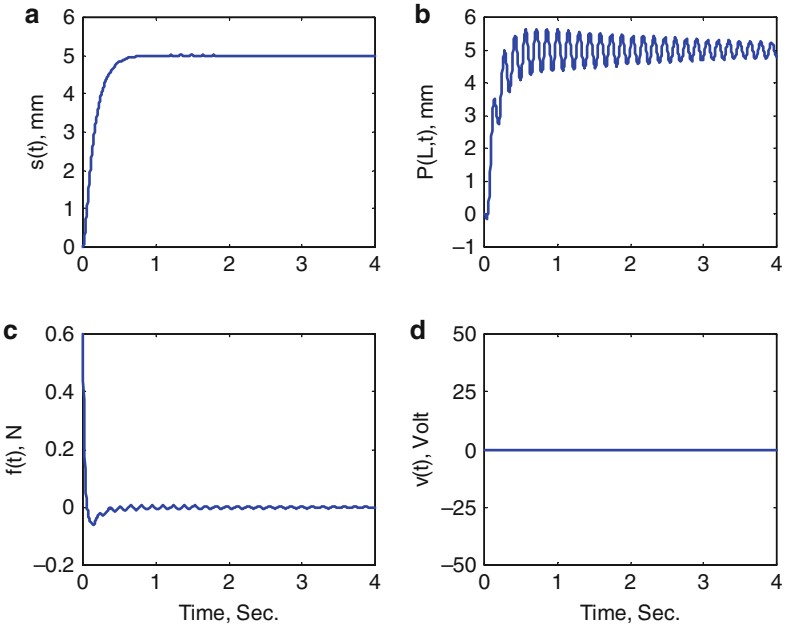

Fig. 9.22 Numerical simulations for the case without piezoelectric control; (**a**) base motion, (**b**) tip displacement, (**c**) control force, and (**d**) piezoelectric voltage
Source: Jalili and Esmailzadeh (2005), with permission

(e.g., friction modeling). However, it is still very apparent that the piezoelectric voltage control can substantially suppress the arm vibration despite such limitations and modeling imperfections.

Example 9.2. Distributed-Parameters base Piezoelectric Vibration Control of Translating Flexible Beams (Dadfarnia et al. 2004b).

The previous example case study demonstrated, in detail, the simultaneous control development and vibration cancellation using lumped-parameters representation of the system. While the results showed satisfactory performance even experimentally, it was limited to only two modes due to sensors limitation for the arrangement at hand. Through the following example case study, we demonstrate the steps and overall procedure for the design and real-time piezoelectric-based vibration-control development based on the original distributed-parameters representation of the system. Although the control development steps become more complicated and cumbersome, it is shown that many issues associated with the truncated model of the systems such as control spillovers and sensors limitation could be avoided.

Considering the same configuration as the one shown in Fig. 9.21, the primary control objective is to design the control force $f(t)$ and the piezoelectric input voltage $V_a(t)$ to drive the arm base to the set-point position s_d ($s_d > 0$) while forcing

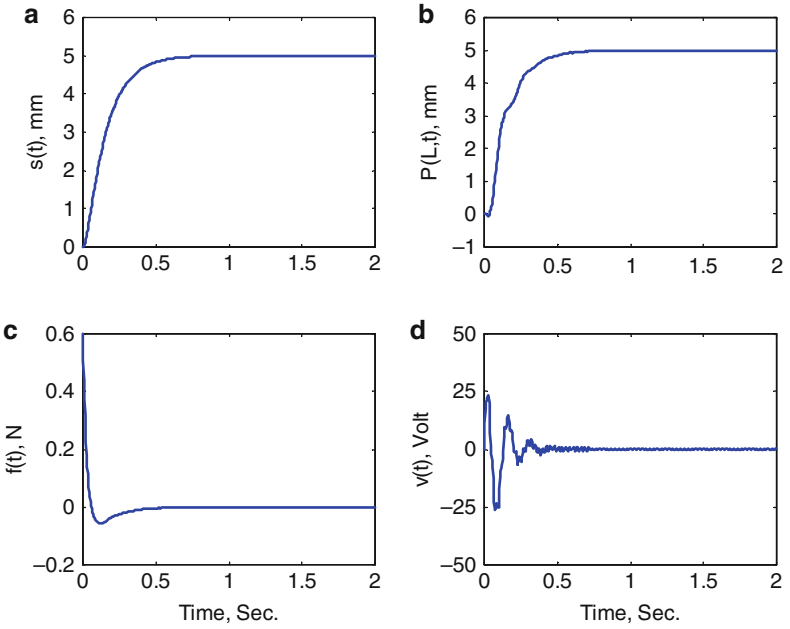

Fig. 9.23 Numerical simulations for the case with piezoelectric control: (**a**) base motion, (**b**) tip displacement, (**c**) control force, and (d) piezoelectric voltage
Source: Jalili and Esmailzadeh (2005), with permission

the beam displacement $w(x,t)$, $\forall x \in [0, L]$ to approach zero exponentially. For this, we define an auxiliary signal $s_1(t) \in \Re$ as

$$s_1(t) = s(t) - s_d \tag{9.79}$$

thus, $\dot{s}_1(t) = \dot{s}(t)$ and $\ddot{s}_1(t) = \ddot{s}(t)$. To facilitate the control design and the subsequent stability analysis, we define also an auxiliary signal $u(x,t) \in \Re$ as

$$u(x,t) = s_1(t) + w(x,t) \tag{9.80}$$

The following equations hold for the partial derivatives of $u(x,t)$ with respect to the time variable t and spatial variable x:

$$\begin{aligned} u(0,t) &= s_1(t) \\ \dot{u}(x,t) &= \dot{w}(x,t) + \dot{s}(t), \quad \dot{u}(0,t) = \dot{s}(t) \\ \ddot{u}(x,t) &= \ddot{w}(x,t) + \ddot{s}(t), \quad \ddot{u}(0,t) = \ddot{s}(t) \end{aligned} \tag{9.81}$$

$$\begin{aligned} u'(x,t) &= w'(x,t), \qquad u''(x,t) = w''(x,t) \\ u'''(x,t) &= w'''(x,t), \qquad u''''(x,t) = w''''(x,t) \end{aligned} \tag{9.82}$$

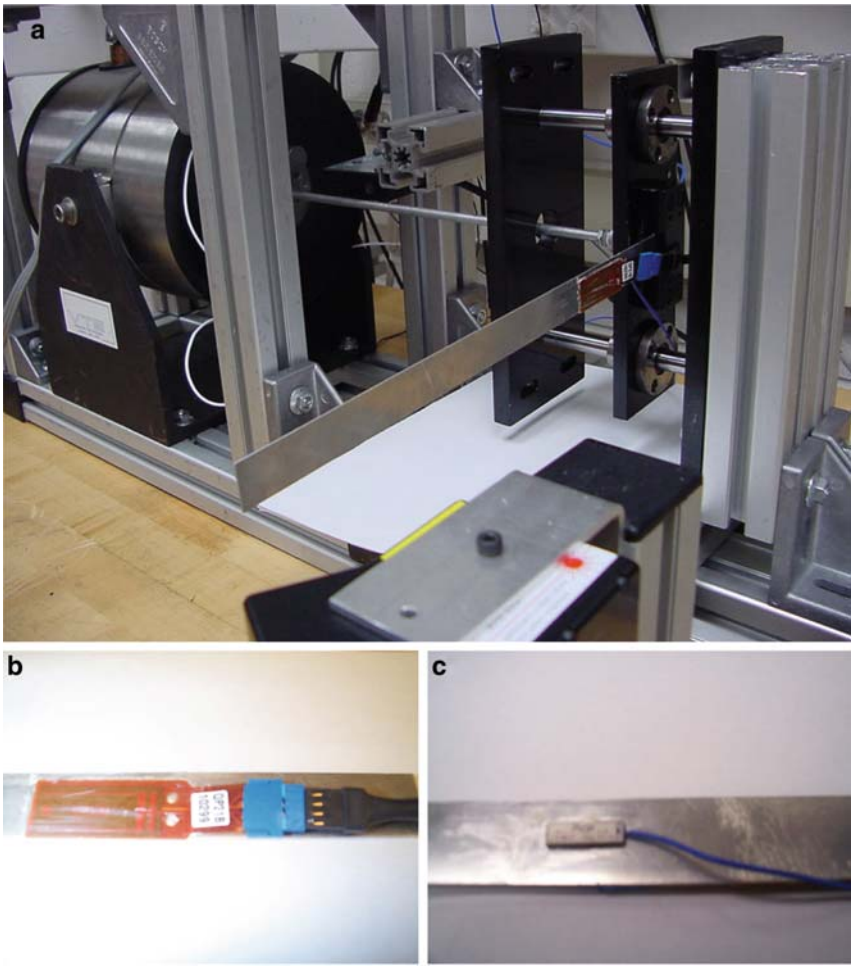

Fig. 9.24 The experimental set up: (**a**) the whole system, (**b**) PZT actuator, ACX model No. QP21B, (**c**) dynamic strain sensor (attached on the other side of the beam), model No. PCB 740B02 *Source:* Jalili and Esmailzadeh (2005), with permission

Now utilizing relationships (9.81) and (9.82), the beam field equations and boundary conditions (9.58a–c) can be recast in the following forms

$$m_b\ddot{u}(0,t) + \int_0^L \rho(x)\ddot{u}(x,t)\mathrm{d}x + m_t\ddot{u}(L,t) = f(t) \tag{9.83}$$

$$\rho(x)\ddot{u}(x,t) + B\dot{u}(x,t) + C\dot{u}'(x,t) + \frac{\partial^2}{\partial x^2}[EI^{\mathrm{eqv}}(x)u''(x,t)] = M_{p0}V_a(t)G''(x) + B\dot{u}(0,t) \tag{9.84}$$

$$u'(0,t) = 0, u''(L,t) = 0,\ m_t\ddot{u}(L,t) - EI^{\mathrm{eqv}}(L)u'''(L,t) = 0 \tag{9.85}$$

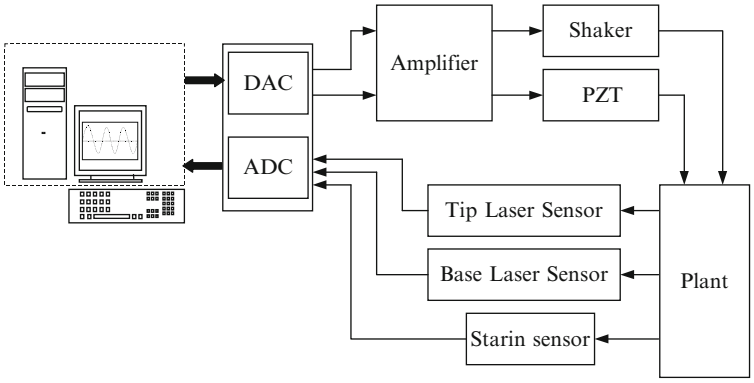

Fig. 9.25 High-level control block diagram
Source: Jalili and Esmailzadeh (2005), with permission

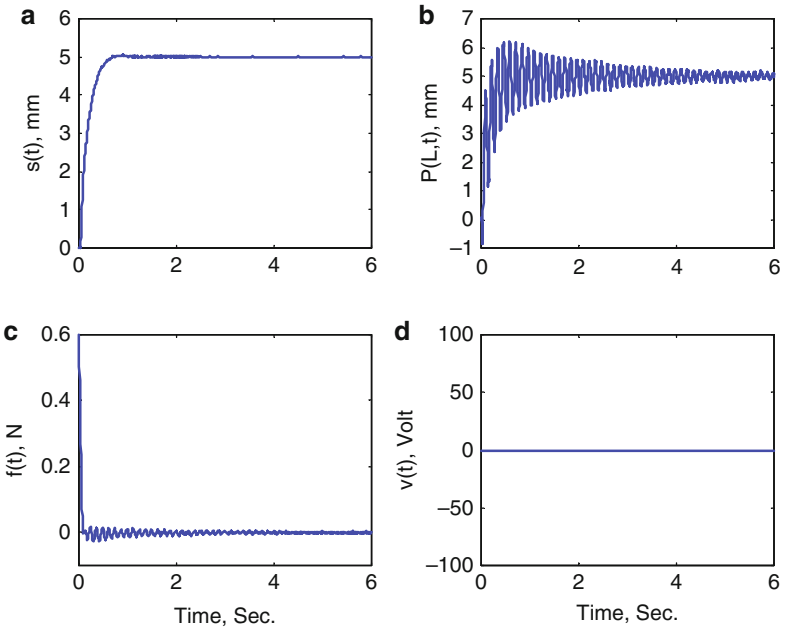

Fig. 9.26 Experimental results for the case without piezoelectric control: (**a**) base motion, (**b**) tip displacement, (**c**) control force, and (**d**) piezoelectric voltage
Source: Jalili and Esmailzadeh (2005), with permission

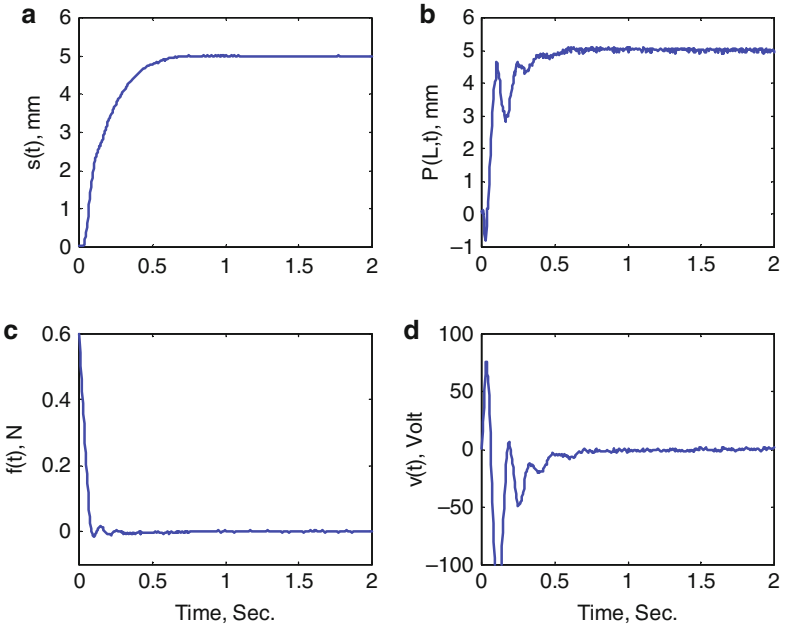

Fig. 9.27 Experimental results for the case with piezoelectric control: (**a**) base motion, (**b**) tip displacement, (**c**) control force, and (**d**) piezoelectric voltage
Source: Jalili and Esmailzadeh (2005), with permission

Substituting (9.84) into (9.83) and after some manipulations, the arm base equation (9.83) reduces to

$$m_b\ddot{u}(0,t) + (BL + C)\dot{u}(0,t) - B\int_0^L \dot{u}(x,t)\mathrm{d}x + EI^{\mathrm{eqv}}(0)u'''(0,t) - C\dot{u}(0,t) = f(t) \tag{9.86}$$

Equations (9.84) and (9.86) along with the boundary conditions (9.85) form the basis for the controller derivation and stability proof of the closed-loop system.

Remark 9.3. During the subsequent stability analysis, we will utilize the following inequalities:

$$w^2(x,t) \le L\int_0^L w'^2(x,t)\mathrm{d}x,\ w^2(x,t) \le L^3\int_0^L w''^2(x,t)\mathrm{d}x,$$
$$w'^2(x,t) \le L\int_0^L w''^2(x,t)\mathrm{d}x, \forall x \in [0,L] \tag{9.87}$$

$$\int_0^L w^2(x,t)\mathrm{d}x \le L^2 \int_0^L w'^2(x,t)\mathrm{d}x \le L^4 \int_0^L w''^2(x,t)\mathrm{d}x \tag{9.88}$$

$$\int_0^L u'^2(x,t)\mathrm{d}x \le L^2 \int_0^L u''^2(x,t)\mathrm{d}x \tag{9.89}$$

$$\frac{z^2}{\delta} + \delta y^2 \ge |zy|, \forall z, y, \delta \in \Re \quad \text{and} \quad \forall \delta > 0, \tag{9.90}$$

$$z^2 + y^2 \ge 2zy, -(z^2 + y^2) \le 2|\, zy\, | \forall z, y \in \Re \tag{9.91}$$

$$\int_0^L f(x,t)g(x,t)\mathrm{d}x \le \left(\sqrt{\int_0^L f^2(x,t)\mathrm{d}x}\right)\left(\sqrt{\int_0^L g^2(x,t)\mathrm{d}x}\right),$$
$$f(x,t), g(x,t) \in \Re \; \forall x \in [0, L] \tag{9.92}$$

Remark 9.4. If the potential energy given by:

$$U = \frac{1}{2}\int_0^L EI^{\mathrm{eqv}}(x)u''^2(x,t)\mathrm{d}x \tag{9.93}$$

is bounded for $\forall t \in [0, \infty)$, then $\frac{\partial^n u(x,t)}{\partial x^n}$ is bounded for $n = 2, 3, 4, \forall x \in [0, L]$ and $\forall t \in [0, \infty)$. In addition, if the kinetic energy given by:

$$T = \frac{1}{2}m_b\dot{u}^2(0,t) + \frac{1}{2}\int_0^L \rho(x)\dot{u}^2(x,t)\mathrm{d}x + \frac{1}{2}m_t\dot{u}^2(L,t) \tag{9.94}$$

is bounded for $\forall\, t \in [0, \infty)$, then $\frac{\partial^n \dot{u}(x,t)}{\partial x^n}$ is bounded for $n = 0, 1, 2, 3, \forall\, x \in [0, L]$ and $\forall\, t \in [0, \infty)$.

Controller Design: Utilizing a Lyapunov-based approach, we define the following non-negative function $V_1(t) \in \Re$

$$V_1(t) = \frac{1}{2}\int_0^L \rho(x)\dot{u}^2(x,t)\mathrm{d}x + \frac{1}{2}\int_0^L EI^{\mathrm{eqv}}(x)u''^2(x,t)\mathrm{d}x \tag{9.95}$$

Taking the time derivative of (9.95), substituting (9.84) into the resulting expression and simplifying yield

$$\dot{V}_1(t) = -B\int_0^L \dot{u}^2(x,t)\mathrm{d}x + B\dot{u}(0,t)\int_0^L \dot{u}(x,t)\mathrm{d}x - \frac{C}{2}\dot{u}^2(L,t) + \frac{C}{2}\dot{u}^2(0,t)$$
$$-EI^{\mathrm{eqv}}(L)\dot{u}(L,t)u'''(L,t) + EI^{\mathrm{eqv}}(0)\dot{u}(0,t)u'''(0,t)$$
$$-M_{p0}V_a(t)[\dot{u}'(l_1,t) - \dot{u}'(l_2,t)] \tag{9.96}$$

Dadfarnia et al. (2004b) details the derivations. Now, we define a scalar function $V_2(t)$ as

$$V_2(t) = \int_0^L \rho(x)u(x,t)\dot{u}(x,t)\mathrm{d}x + \frac{B}{2}\int_0^L u^2(x,t)\mathrm{d}x + C\int_0^L u(x,t)\,u'(x,t)\mathrm{d}x \tag{9.97}$$

Differentiating (9.97) and using field equations (9.84) and (9.86) along with the boundary conditions (9.85) yield

$$\dot{V}_2(t) = \int_0^L \rho(x)\dot{u}^2(x,t)dx - EI^{\mathrm{eqv}}(L)u(L,t)u'''(L,t)$$
$$+EI^{\mathrm{eqv}}(0)u(0,t)u'''(0,t) - \int_0^L EI^{\mathrm{eqv}}(x)u''^2(x,t)\mathrm{d}x$$
$$+B\dot{u}(0,t)\int_0^L u(x,t)dx + C\int_0^L \dot{u}(x,t)u'(x,t)dx$$
$$-M_{p_0}V_a(t)[u'(l_1,t) - u'(l_2,t)] \tag{9.98}$$

Dadfarnia et al. (2004b) provides the detailed derivations. We define a new scalar function candidate $V_3(t)$ as

$$V_3(t) = V_1(t) + \beta_0 V_2(t) \tag{9.99}$$

where β_0 is a positive control gain. Substituting (9.96) and (9.98) into the time derivative of (9.99) results in

$$\dot{V}_3(t) = \int_0^L (\beta_0\rho(x) - B)\dot{u}^2(x,t)\mathrm{d}x + B\dot{u}(0,t)\int_0^L \dot{u}(x,t)\mathrm{d}x - \beta_0\int_0^L EI^{\mathrm{eqv}}(x)u''^2(x,t)\mathrm{d}x$$
$$+B\beta_0\dot{u}(0,t)\int_0^L u(x,t)\mathrm{d}x + C\beta_0\int_0^L \dot{u}(x,t)\,u'(x,t)dx - \frac{C}{2}\dot{u}^2(L,t)$$
$$+\frac{C}{2}\dot{u}^2(0,t) - EI^{\mathrm{eqv}}(L)\gamma_L(t)\,u'''(L,t) + EI^{\mathrm{eqv}}(0)\gamma_0(t)\,u'''(0,t)$$
$$+M_{p_0}V_a(t)(\beta_0 g(t) + \dot{g}(t)) \tag{9.100}$$

where the auxiliary signals $\gamma_0(t)$, $\gamma_L(t)$, and $g(t) \in \Re$ are defined as

$$\gamma_0(t) = \dot{u}(0,t) + \beta_0 u(0,t) \tag{9.101}$$
$$\gamma_L(t) = \dot{u}(L,t) + \beta_0 u(L,t) \tag{9.102}$$
$$g(t) = u'(l_2,t) - u'(l_1,t) \tag{9.103}$$

Based on the structure of (9.100), the piezoelectric input voltage $V_a(t)$ is designed as

$$V_a(t) = -\frac{K_v}{M_{p_0}}(\beta_0 g(t) + \dot{g}(t)) \tag{9.104}$$

where K_v is a positive control gain. To obtain the dynamics of $\gamma_0(t)$, we take the time derivative of (9.101), multiply the result by m_b, and then use (9.86) to get the following open-loop equation

$$\begin{aligned} m_b\dot{\gamma}_0(t) = &-(BL + C)\dot{u}(0,t) + B\int_0^l \dot{u}(x,t)\mathrm{d}x - EI^{\mathrm{eqv}}(0)u'''(0,t) \\ &+ C\dot{u}(L,t) + f(t) + m_b\beta_0\dot{u}(0,t) \end{aligned} \tag{9.105}$$

The control force $f(t)$ can now be designed as

$$f(t) = -(m_b\beta_0 - BL - C)\dot{u}(0,t) - K_r\gamma_0(t) - K_p u(0,t) \tag{9.106}$$

where K_r and K_p are positive control gains. Substituting (9.106) into (9.105) results in the closed-loop system of $\dot{\gamma}_0(t)$ as

$$m_b\dot{\gamma}_0(t) = B\int_0^L \dot{u}(x,t)\mathrm{d}x + C\dot{u}(L,t) - EI^{\mathrm{eqv}}(0)u'''(0,t) - K_r\gamma_0(t) - K_p u(0,t) \tag{9.107}$$

Stability Analysis: We now use Lyapunov's stability theory to prove that the control objectives stated in the preceding section have been met under the proposed control law. The main result of this section is summarized by the following theorem.

Theorem 9.4. *The control law given by (9.104) and (9.106) ensures that the base movement is exponentially regulated in the sense that*

$$|s_1(t)| \le \sqrt{\frac{2\lambda_3\kappa_0}{K_p}\exp\left(-\frac{\lambda_5}{\lambda_3}t\right)} \tag{9.108a}$$

and the beam displacement is exponentially regulated in the sense that

$$|w(x,t)| \le \sqrt{\frac{\lambda_3\kappa_0 L^3}{\lambda_4}\exp\left(-\frac{\lambda_5}{\lambda_3}t\right)} \quad \forall\, x \in [0,L] \tag{9.108b}$$

provided that the control gains K_p and K_r are selected to satisfy the following conditions

$$K_p > m_t\beta_0 + 2B\delta_6 L^2 + \frac{2B\beta_0}{\delta_5} + \frac{2B\beta_0^2}{\delta_6} + C\beta_0$$

$$K_r > \frac{B}{\delta_3} + \frac{C}{\delta_4} + \frac{2B}{\delta_5} + \frac{2B\beta_0}{\delta_6} + C \tag{9.108c}$$

$$K_r > \frac{B}{\delta_3} + \frac{C}{\delta_4} + \frac{2B}{\delta_5} + \frac{2B\beta_0}{\delta_6} + C \tag{9.108d}$$

where λ_3, λ_4, λ_5, β_0, δ_3, δ_4, δ_5, and δ_6 are positive bounding constants, and the positive constant κ_0 is given by:

$$\kappa_0 = \int_0^L \dot{u}^2(x,0)\mathrm{d}x + u^2(0,0) + \gamma_0^2(0) + \dot{u}^2(L,0) + \int_0^L u'^2(x,0)\mathrm{d}x \tag{9.108e}$$

Proof. See Appendix B (Sect B.2) for detailed proof.

Remark 9.5. From (B.20), (B.21), (B.22), (B.24), and (B.29), we can state that $\int_0^L \dot{u}^2(x,t)\mathrm{d}x$, $\int_0^L u'^2(x,t)\mathrm{d}x$, $u(0,t)$, $\gamma_0(t)$, $\gamma_L(t)$ are all bounded for $\forall t \in [0,\infty)$. It is easy to show that $\dot{u}(0,t)$ and $\dot{u}(L,t)$ are also bounded for $\forall t \in [0,\infty)$ from the definition of $\gamma_0(t)$ and $\gamma_L(t)$, respectively. Consequently, the kinetic and potential energies of the mechanical system are bounded. Hence, we can use (B.30), (9.87) and the properties discussed in Remark 9.4 to state that $\frac{\partial^n u(x,t)}{\partial x^n}$ for $n = 0,1,2,3,4$, and $\frac{\partial^n \dot{u}(x,t)}{\partial x^n}$ for $n = 0,1,2,3$, $\forall x \in [0,L]$ and $\forall t \in [0,\infty)$ are bounded. Using equation (9.86), it can be seen that $\ddot{u}(0,t)$ or $\ddot{s}(t)$ is bounded $\forall t \in [0,\infty)$. Then, it can be shown that $\ddot{w}(x,t)$ is also bounded for $\forall x \in [0,L]$ and $\forall t \in [0,\infty)$ by dividing the beam equation (9.58b) into three closed sets: (1) $x \in [0,l_1]$, (2) $x \in [l_1,l_2]$, and (3) $x \in [l_2,L]$ and considering the boundedness of $\ddot{w}(x,t)$ in each part. From this information, we can now state that all the signals in the control law of (9.104) and (9.106) and the mechanical system given by (9.58a–c) remain bounded for $\forall t \in [0,\infty)$, during the closed-loop operation.

Numerical Simulations: For the numerical simulations only, we utilize assumed mode model expansion to truncate the original partial differential equations. The implementation issues are discussed and the results are presented in this section. Similar to the previous example case study, we adopt the AMM expansion (9.60) for the beam vibration analysis. The equations of motion can now be obtained similar to example case study 9.1 with only difference being in the added damping term in the model and numerical analysis. That is the governing equation (9.61) is modified here to:

$$\left[m_b + m_t + \int_0^l \rho(x)\mathrm{d}x\right]\ddot{s}(t) + \sum_{j=1}^{n} m_j \ddot{q}_j(t) = f(t) \tag{9.109a}$$

$$\begin{aligned} m_i\ddot{s}(t) + \sum_{j=1}^{n} m_{ij}\ddot{q}_j(t) + \sum_{j=1}^{n} \zeta_{ij}\dot{q}_j(t) + \sum_{j=1}^{n} k_{ij}\ddot{q}_j(t) \\ = M_{p_0}\big(\phi_i(l_2) - \phi_i(l_1)\big)V_a(t) \quad i = 1\,2\,\ldots \end{aligned} \tag{9.109b}$$

where

$$m_i = \int_0^L \rho(x)\phi_i(x)\,\mathrm{d}x + m_t\phi_i(L)$$

$$m_{ij} = \int_0^L \rho(x)\phi_i(x)\phi_j(x)\,\mathrm{d}x + m_t\phi_i(L)\phi_j(L)$$

$$\zeta_{ij} = \int_0^L \phi_i(x)\big[B\phi_j(x) + C\phi_j'(x)\big]\,\mathrm{d}x$$

$$k_{ij} = \int_0^L EI^{\mathrm{eqv}}(x)\phi_i''(x)\phi_j''(x)\,\mathrm{d}x$$

Consequently, the truncated n-mode description of the beam equations in (9.109) can be recast as

$$\mathbf{M}\ddot{\boldsymbol{\Delta}} + \boldsymbol{\zeta}\dot{\boldsymbol{\Delta}} + \mathbf{K}\boldsymbol{\Delta} = \mathbf{F}\mathbf{u} \tag{9.110}$$

where

$$\mathbf{M} = \begin{bmatrix} \psi & m_1 & m_2 & \cdots & m_n \\ m_1 & m_{11} & m_{12} & \cdots & m_{1n} \\ m_2 & m_{12} & m_{22} & \cdots & m_{2n} \\ \vdots & \vdots & \vdots & \ddots & \vdots \\ m_n & m_{1n} & m_{2n} & \cdots & m_{nn} \end{bmatrix}, \quad \boldsymbol{\zeta} = \begin{bmatrix} 0 & 0 & 0 & \cdots & 0 \\ 0 & \zeta_{11} & \zeta_{12} & \cdots & \zeta_{1n} \\ 0 & \zeta_{21} & \zeta_{22} & \cdots & \zeta_{2n} \\ \vdots & \vdots & \vdots & \ddots & \vdots \\ 0 & \zeta_{n1} & \zeta_{n2} & \cdots & \zeta_{nn} \end{bmatrix}$$

$$\mathbf{K} = \begin{bmatrix} 0 & 0 & 0 & \cdots & 0 \\ 0 & k_{11} & k_{12} & \cdots & k_{1n} \\ 0 & k_{12} & k_{22} & \cdots & k_{2n} \\ \vdots & \vdots & \vdots & \ddots & \vdots \\ 0 & k_{1n} & k_{2n} & \cdots & k_{nn} \end{bmatrix}, \quad \boldsymbol{\Delta} = \begin{Bmatrix} s(t) \\ q_1(t) \\ q_2(t) \\ \vdots \\ q_n(t) \end{Bmatrix}, \quad \mathbf{F} = \begin{bmatrix} 1 & 0 \\ 0 & \tau_1 \\ 0 & \tau_2 \\ \vdots & \vdots \\ 0 & \tau_n \end{bmatrix}, \quad \mathbf{u} = \begin{Bmatrix} f(t) \\ V_a(t) \end{Bmatrix}$$

$$\psi = m_b + m_t + \int_0^L \rho(x)\mathrm{d}x$$
$$\tau_i = M_{p_0}(\phi_i'(l_2) - \phi_i'(l_1)) \quad i = 1, 2, \ldots, n \tag{9.111}$$

Equation (9.109) can be expressed in the following state-space form

$$\dot{\mathbf{X}} = \mathbf{A}\mathbf{X} + \mathbf{B}\,\mathbf{u} \tag{9.112}$$

where

$$\mathbf{A} = \begin{bmatrix} \mathbf{0} & \mathbf{I} \\ -\mathbf{M}^{-1}\mathbf{K} & -\mathbf{M}^{-1}\mathbf{C} \end{bmatrix}, \quad \mathbf{B} = \begin{Bmatrix} \mathbf{0} \\ \mathbf{M}^{-1}\mathbf{F} \end{Bmatrix}, \quad \mathbf{X} = \begin{Bmatrix} \Delta \\ \dot{\Delta} \end{Bmatrix} \tag{9.113}$$

to be solved using Matlab software programming.

Implementation Issues: The proposed controller in equation (9.104) for the piezoelectric input voltage requires the measurement of $g(t)$ given in (9.103). Utilizing the relationship (9.82), we can get

$$g(t) = w'(l_2, t) - w'(l_1, t) \tag{9.114}$$

Comparing (9.114) and the piezoelectric sensor equation given in (8.137), we can write

$$g(t) = \frac{C_p^l}{bE_p d_{31} t_{eq}} V_s(t) \tag{9.115}$$

Having obtained $g(t)$, we can use appropriate numerical differentiation methods to get the time derivative of the signal in order to be used in the piezoelectric control voltage (9.104).

Numerical Results: In order to show the effectiveness of the proposed controller, the flexible beam depicted in Fig. 9.21 is considered with the system parameters listed in Table 9.3. The desired set-point, s_d, is taken to be 5 mm. We select the control gains to be $K_p = 120$, $K_r = 16$, and also $\beta_0 = 0.01$. Figure 9.28 shows the system response for the case without piezoelectric control (i.e., only with force control acting on the base). The beam tip displacement, base motion, and control force are shown in Figs. 9.28a–c, respectively. The system response to the controller with piezoelectric actuator based on the eight-mode model is shown in Fig. 9.29. The control gain for the piezoelectric input voltage is chosen to be $K_v = 0.5$. The results demonstrate that the beam vibration can be suppressed using the piezoelectric actuator. The piezoelectric input voltage signal $V_a(t)$ is shown in Fig. 9.29b, in which the voltage signal is in the practical and implementable range of −100V to 100V. The base motion and the force control are also depicted in Figs. 9.29c, d, respectively.

In order to show the effectiveness of the proposed controller, we compare our controller with a reduced-order observer-based controller presented in example

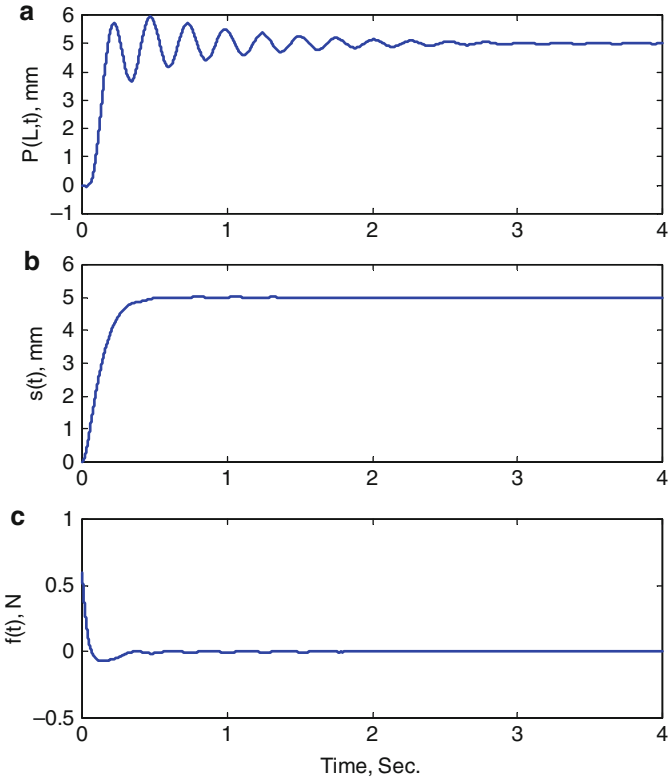

Fig. 9.28 System responses for the case without piezoelectric control: (**a**) beam tip displacement, (**b**) base motion, and (**c**) base control force
Source: Dadfarnia et al. (2004b), with permission

case study 9.1, wherein a simple PD controller was selected for the moving base regulation, while an observer-based controller was utilized for the piezoelectric input voltage to make the closed-loop system energy dissipative and hence stable. Fig. 9.30 shows the comparison between the tip displacement of the beam for both the controller developed in this example and the observer-based controller of (9.67) and (9.68) of Example 9.1. The results show no significant difference for the two-mode model case. However, when considering three-mode model in the simulations, the tip displacement depicted in Fig. 9.31 results for both controllers. The controller developed here results in a stable operation, while the observer-based controller (9.67) and (9.68) causes instability in the system which is the result of the spillover effect. It also demonstrates that the spillover effect becomes more evident when increasing the piezoelectric voltage control gain (K_v). Contrary to the reduced-order controller, increasing the number of modes in the current controller does not affect the stability properties of the system (as shown in Fig. 9.29) since the controller

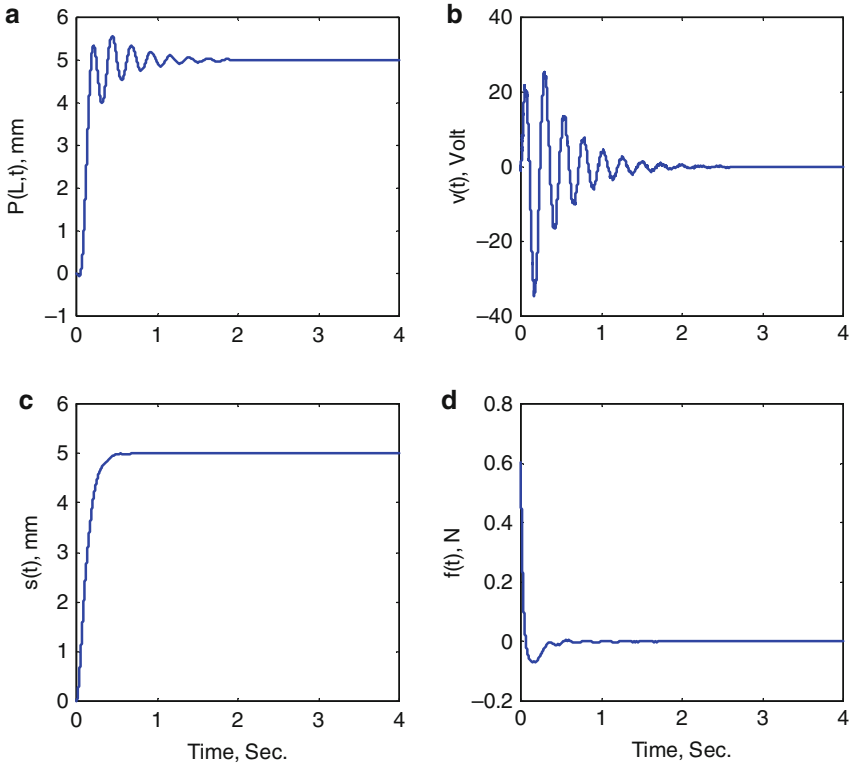

Fig. 9.29 System responses for the case with piezoelectric control: (**a**) beam tip displacement, (**b**) piezoelectric voltage, (**c**) base motion, and (**d**) base control force
Source: Dadfarnia et al. (2004b), with permission

developed here (9.104) is based on the infinite dimensional distributed equations of motion.

Comparing the results given in Figs. 9.29 and 9.31, it can be seen that if we consider only the first couple of modes, the vibration of truncated model of the beam can be suppressed very quickly with the piezoelectric actuator. However, considering the higher mode model of the beam causes the vibration of the beam to last longer. The piezoelectric actuator cannot effectively suppress the higher modes of the vibration since the higher modes have nodes where piezoelectric attached on the beam. Using additional piezoelectric actuators on different locations on the beam can suppress vibration of these modes.

Control Experiments: In order to better demonstrate the effectiveness of the controller, an experimental setup, similar to the setup in example case study 9.1, is constructed and used to verify the numerical results (see Fig. 9.24). The high-level control block diagram of the experiment is also similar to the one in Fig. 9.25, in which the shaker provides the input control force to the base and the PZT applies a controlled moment on the beam.

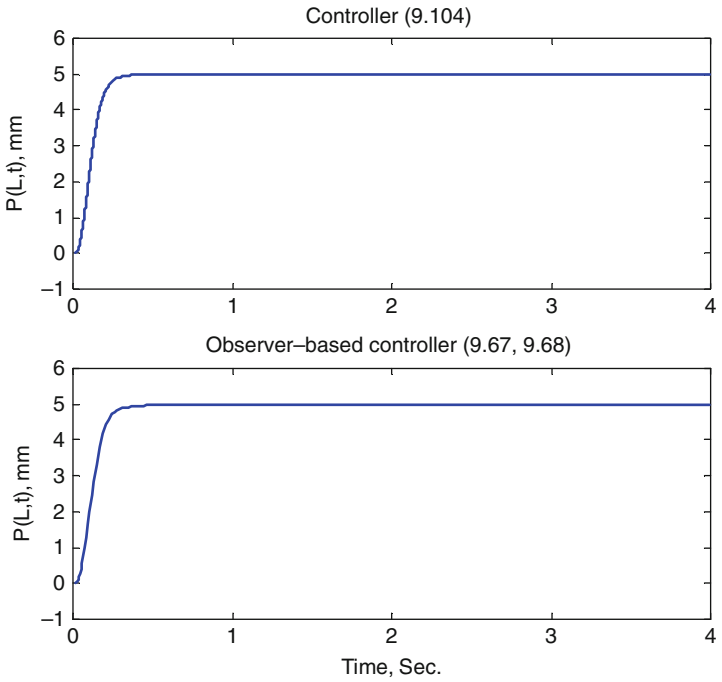

Fig. 9.30 Comparison between the tip displacement of two-mode model in response to the proposed controller here and the observer-based controller of (9.67) and (9.68), Fig. 9.23b

The experimental results for both cases (i.e., without and with piezoelectric controller) are depicted in Fig. 9.32 and 9.33, respectively. It is demonstrated that with piezoelectric controller, the arm vibration is eliminated in less than a second, while the arm vibration lasts for more than 3 s when piezoelectric controller is not used.

The experimental results are generally in agreement with those of simulation results. Fig. 9.34 and 9.35 show the comparison between tip displacement in numerical simulations and experiment for the cases without and with piezoelectric controller, respectively. The slight overshoot and discrepancies are due to the limitation of the experiment (e.g., shaker saturation limitation) and unmodeled dynamics in the plant (e.g., friction modeling and other nonlinearities). However, it is still very apparent that the piezoelectric input voltage control can suppress the arm vibration despite such limitations and modeling imperfections.

9.4 Piezoelectric-based Semi-active Vibration-Control Systems

As mentioned in Chap. 1 and briefly at the beginning of this chapter, semi-active vibration-control systems are those which otherwise passively generated damping or spring forces are modulated according to a parameter tuning policy with only

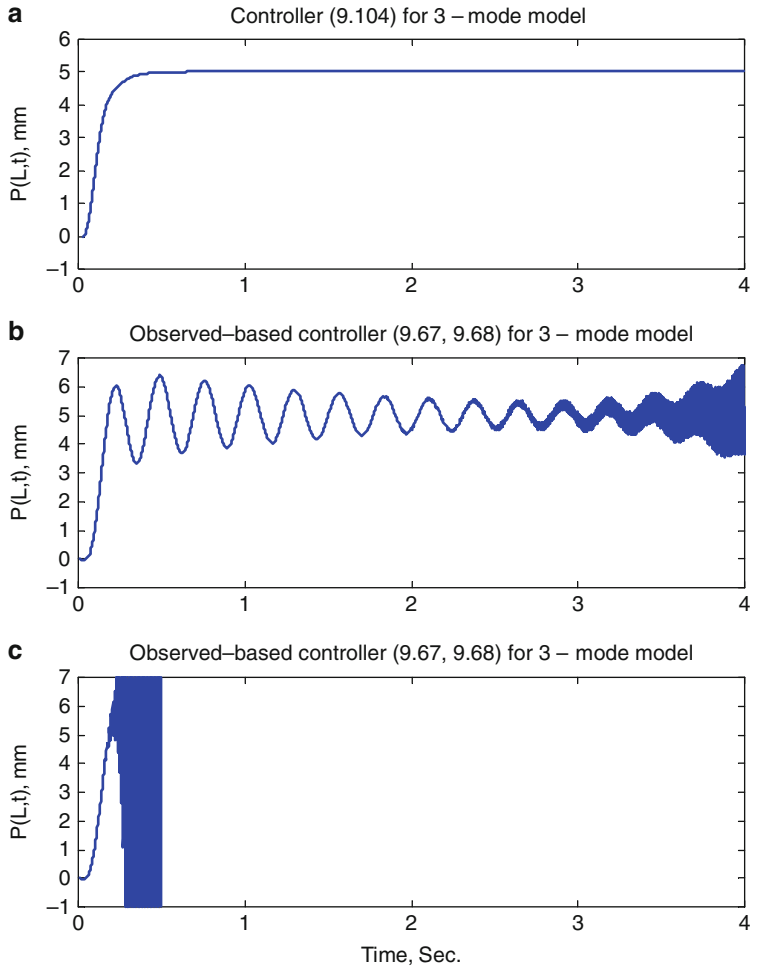

Fig. 9.31 Comparison between the tip displacement of three-mode model in response to (**a**) the proposed controller developed here, and the observer-based controller (9.67) and (9.68) for (**b**) $K_v = 0.01$, and (**c**) $K_v = 0.15$
Source: Dadfarnia et al. (2004b), with permission

a small amount of control effort. These vibration-control systems, as their name implies, fill the gap between purely passive and fully active vibration-control systems and offer the reliability of passive systems, yet maintain the versatility and adaptability of fully active systems. During recent years there has been considerable interest toward practical implementation of these vibration-control systems for their low energy requirement and cost. Along this line of reasoning, this subsection presents the basic theoretical concepts, design, and implementation issues for a representative semi-active system, the so-called switched-stiffness vibration-control system using piezoelectric materials.

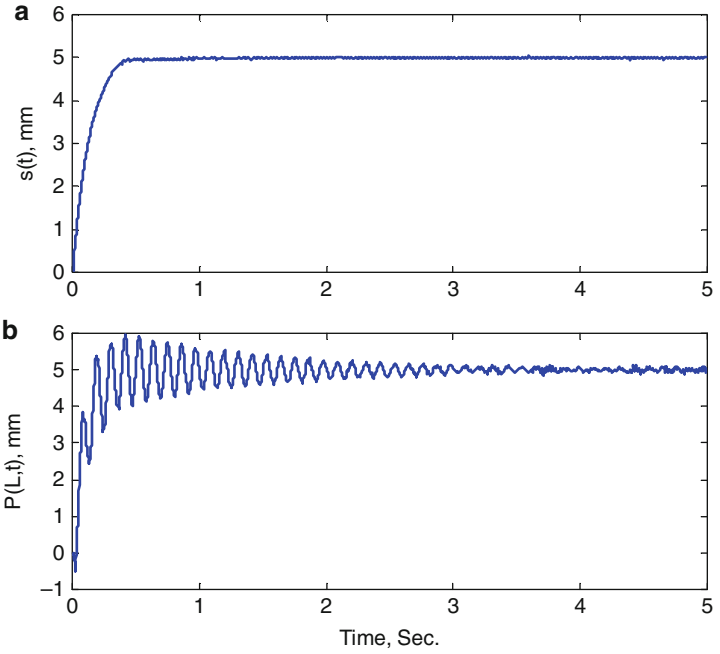

Fig. 9.32 Experimental results for the case without piezoelectric control: (**a**) base motion and (**b**) tip displacement
Source: Dadfarnia et al. (2004b), with permission

9.4.1 A Brief Overview of Switched-Stiffness Vibration-Control Concept[4]

As briefly mentioned earlier in Sect. 6.3.2, the switched stiffness method is a semi-active vibration-control method, where the energy of the system is dissipated by switching the values of the stiffness of the spring between two different values, namely, low and high values (Clark 2000; Ramaratnam et al. 2004a,b; Ramaratnam et al. 2003; Ramaratnam and Jalili 2006). A simple control law, based on the position and velocity feedback, is designed to switch the stiffness of the spring in order to increase the energy dissipation from the system. The spring should possess two distinct stiffness values, referred to as high stiffness and low stiffness. The high stiffness state is used when the system is moving away from its equilibrium such that the potential energy stored in the system is maximized. The spring is switched to low stiffness state when the system has reached its maximum stored potential energy, which occurs when the system has attained its maximum amplitude of vibration for

[4] The materials presented in this section may have come directly from our publication (Ramaratnam and Jalili 2006).

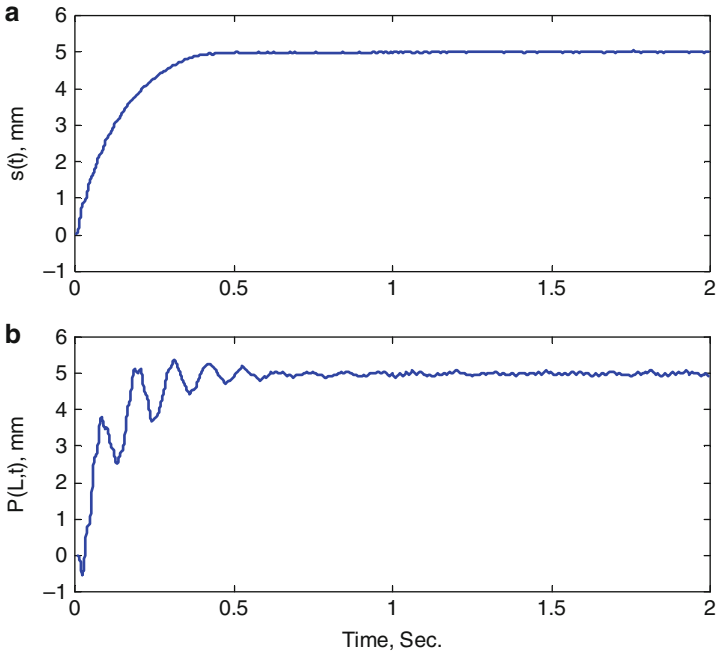

Fig. 9.33 Experimental results for the case with piezoelectric control: (**a**) base motion and (**b**) tip displacement
Source: Dadfarnia et al. (2004b), with permission

that half cycle. Thus, the stiffness switching results in the loss of some of the potential energy. The energy is dissipated in the system by this loss of potential energy. The reduced potential energy is then converted to kinetic energy that is lower than the kinetic energy during the previous cycle due to the lost energy by changing the spring stiffness.

This energy dissipation method can be used for vibration suppression of transient and continuously excited systems. However, limitations for implementation of this type of vibration attenuation are the velocity measurement requirement of the system under study and availability of a bistiffness spring configuration in practice. Expensive velocity sensors and noisy differentiators make the first limitation even more noticeable. This problem can be overcome by implementing an output feedback velocity observer, for instance, by Xian et al. (2003).

The concept of switched stiffness vibration-control system can be easily implemented using piezoelectric materials, as these materials possess the ability to change their equivalent effective stiffness according to the type of circuit connection, see Sect. 6.3.2 (Ramaratnam and Jalili 2006; Richard et al. 1999). More specifically, when connected in an open circuit, the piezoelectric material exhibits a particular stiffness and when short circuited, it exhibits different value, typically lower stiffness. This ability of the piezoelectric materials to change their stiffness is due to their

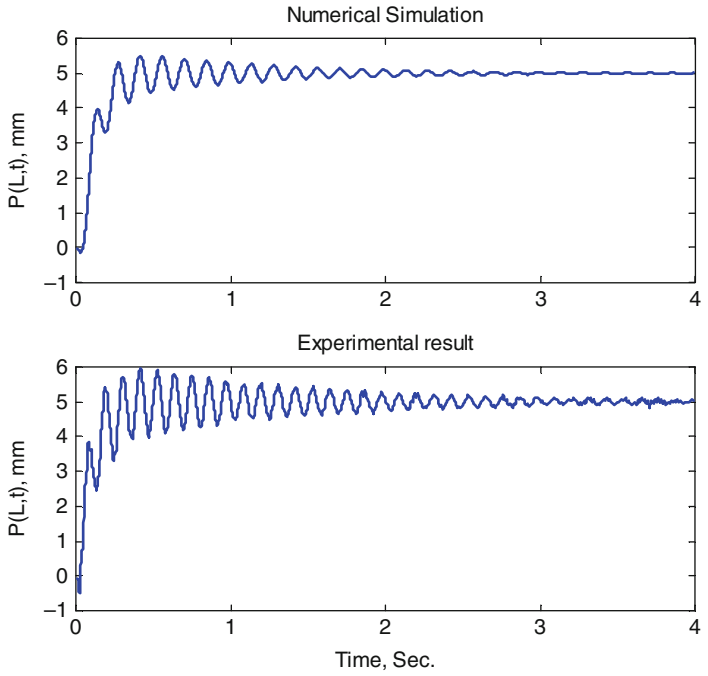

Fig. 9.34 Comparison between beam tip displacement in numerical simulations and experimental results for the case without piezoelectric control

ability to change their mechanical compliance, caused by changes in their electrical impedance when connected in open or short circuit (Ramaratnam et al. 2004b).

Switched-Stiffness Vibration-Control on A SDOF Mass-Spring System: In order to better explain the switched-stiffness concept, a SDOF mass-spring system is taken as shown in Fig. 9.36. The governing equation is simply given by:

$$m\ddot{y}(t) + k(t)y(t) = f(t) \tag{9.116}$$

where $y(t)$ is the system output (i.e., the signal that is to be attenuated), m is the mass, $k(t)$ is the stiffness, and $f(t)$ is the external force acting on the system. The spring is assumed to possess a step-variable stiffness setting in the sense that it can be switched between two distinct values, namely high and low stiffness values. As the external force $f(t)$ causes the mass to move away from its equilibrium position, the stiffness of the spring $k(t)$ is kept at the high value. The maximum potential energy at maximum mass displacement is simply $1/2 k_{\text{high}}\, y_{\text{max}}^2$. At this point ($y_{\text{max}}$), the stiffness is switched to low value and kept at this value until the mass reaches the equilibrium point again. Therefore, the potential energy at y_{max} becomes $1/2 k_{\text{low}} y_{\text{max}}^2$. The loss in potential energy can be given as $1/2 \Delta k\, y_{\text{max}}^2$, where $\Delta k = k_{\text{high}} - k_{\text{low}}$.

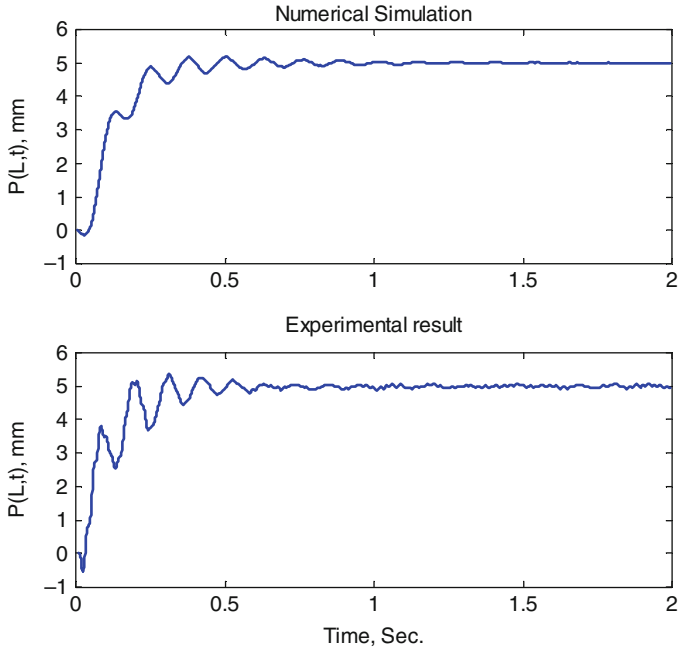

Fig. 9.35 Comparison between beam tip displacement in numerical simulations and experimental results for the case with piezoelectric control

Fig. 9.36 The SDOF mass-spring system with variable stiffness

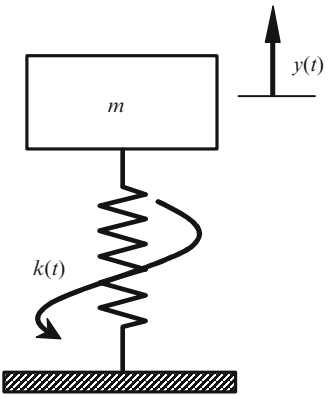

The decrease in potential energy given by $^1/_2 \Delta k \; y_{\max}^2$ will consequently result in decrease in converted kinetic energy, thereby introducing energy dissipation in the system. The stiffness is then switched back to the high value when the system moves away from its equilibrium, thus switching stiffness from low to high in a periodic manner to gradually dissipate system energy. The SDOF system is no more conservative due to the dependence of the stiffness with time. Hence, the system becomes a parametric system (with quasi time-varying parameters) and the work done by such nonconservative spring force is the means of energy dissipation (Meirovitch 2001).

Control Law for Switching Stiffness: A heuristic control law was suggested to essentially switch the stiffness values through a hard switching or on-off (relay) control (Clark 2000). The control law is based on the position of the system with respect to the equilibrium state. The control law can be stated as

$$\begin{cases} k(t) = k_{\text{high}} & \text{for} \quad y\dot{y} \geq 0 \\ k(t) = k_{\text{low}} & \text{for} \quad y\dot{y} < 0 \end{cases} \tag{9.117}$$

The control law can also be expressed in the following more compact form,

$$k(t) = \bar{K}_1 + \bar{K}_2 \,\text{sgn}(y\dot{y}), \quad \text{for} \quad k_{\text{low}} \leq k \leq k_{\text{high}} \tag{9.118}$$

where

$$\bar{K}_1 = \frac{(k_{\text{high}} + k_{\text{low}})}{2}, \bar{K}_2 = \frac{(k_{\text{high}} - k_{\text{low}})}{2}$$

For numerical simulations, the spring stiffness value is changed such that the potential energy is dissipated at maximum deflection, resulting in the "step down" of total system energy, and hence, suppressing the displacement as shown in Fig. 9.37. The amount of dissipated energy over a particular period is proportional to the difference between high and low values (Δk as explained earlier in this section). When the stiffness is switched as per control law given in (9.118), it results in significant vibration suppression (Ramaratnam et al. 2004b).

9.4.2 Real-Time Implementation of Switched-Stiffness Concept

The control law (9.118) can be implemented by measuring the position and velocity of the mass-spring system. However, due to the unavailability (or complication of implementation) of velocity sensors, velocity cannot be measured directly, thus hindering the implementation of the control law. Also, acquiring acceleration signals using accelerometers and integrating them to get both displacement and velocity may not provide clean and useful measurements. In order to overcome this dilemma, a simple solution would be to measure the position and numerically differentiate it to find the required velocity signal. A classical problem associated with this approach is the resulting noise accompanying the differentiated signal leading to erroneous results. To prevent this, a robust velocity observer scheme can be utilized to observe the velocity and help implement the control law as developed in Xian et al. (2003) and implemented and utilized by Ramaratnam and Jalili (2006). This control law is briefly explained next. This observer may also be considered as an inexpensive replacement for the velocity sensors.

Velocity Observer Design Overview: This section briefly explains the variable structure velocity observer for a class of unknown nonlinear systems of the form

$$\ddot{y} = h(y, \dot{y}) + G(y, \dot{y})u \tag{9.119}$$

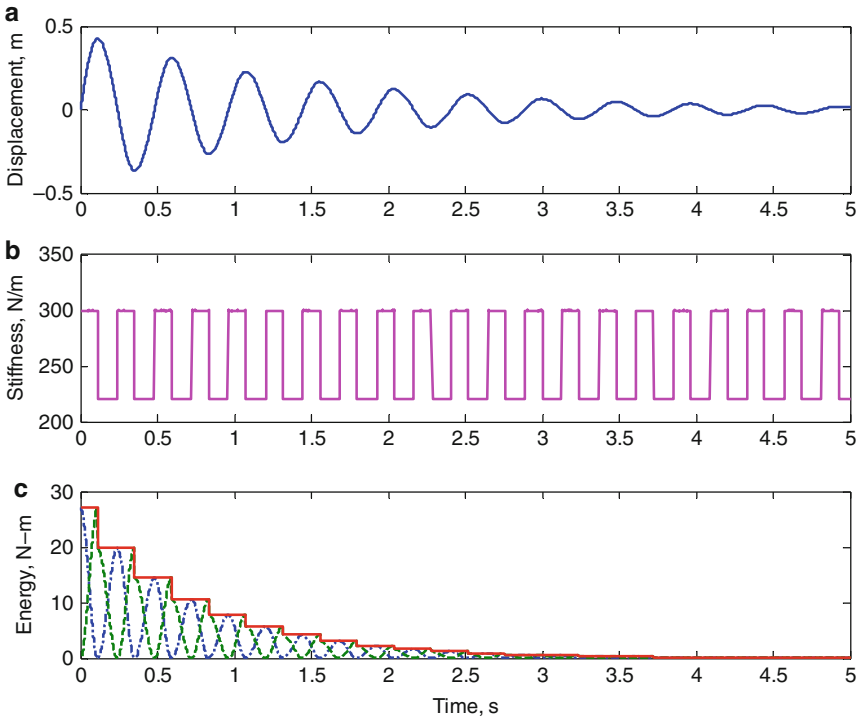

Fig. 9.37 Illustration of the stiffness switching concept for a SDOF system with $m = 1.5\,\text{kg}$, $k_{low} = 220\,\text{N/m}$, and $k_{high} = 300\,\text{N/m}$. In Fig. 9.37c; dashed-dotted lines (-.-.-.) represent kinetic energy, dashed lines (- - -) represent potential energy, and solid lines (——) represent total energy *Source:* Ramaratnam and Jalili (2006), with permission

where $y(t) \in \Re^n$ is the system output, $u(t) \in \Re^n$ is the control input, $h(y, \dot{y}) \in \Re^n$, and $G(y, \dot{y}) \in \Re^n$ are system nonlinear functions. The following assumptions are made in order to design the observer:

- The system states are always bounded.
- $h(y, \dot{y})$ and $G(y, \dot{y})$ are first-order differentiable such that their derivatives exist.
- The control input $u(t)$ is first-order differentiable.

If $\dot{\hat{y}}(t)$ is the observed velocity, then the error due to the velocity observation can be given as,

$$\dot{\tilde{y}} = \dot{y} - \dot{\hat{y}} \tag{9.120}$$

Therefore, to observe velocity accurately, the error should go to zero, i.e., $\dot{\tilde{y}} \to 0$, as $t \to \infty$. In order to achieve this, a second-order filter whose structure is motivated by the Lyapunov-type stability analysis is adopted as follows to generate the needed velocity as:

$$\dot{\hat{y}} = p + K_0 \tilde{y} \tag{9.121}$$

$$\dot{p} = K_1 \,\text{sgn}(\tilde{y}) + K_2 \tilde{y} \tag{9.122}$$

where $p(t)$ is an auxiliary variable, sgn(.) denotes the standard signum function, K_0, K_1 and K_2 are positive-definite constant diagonal matrices. The stability analysis using this observer can be performed. However, we prefer not to add additional details here and refer the interested reader to Xian et al. (2003) for more information.

Modified Velocity Observer Design for Switched Stiffness: In order to prove the stability of the observer based switched stiffness system, the observer with the structure given in (9.121) and (9.122) are modified to satisfy the stability criterion as follows,

$$\dot{\hat{y}} = p + K_{01}\tilde{y} \tag{9.123}$$

$$\dot{p} = -\frac{2\bar{K}_2}{m} y \,\mathrm{sgn}(y\dot{\hat{y}}) - \frac{\bar{K}_1}{m} y + K_{02}\tilde{y} \tag{9.124}$$

where K_{01} and K_{02} are positive-definite constant diagonal matrices. The stability analysis of this structure is explained next.

Theorem 9.5. *The homogenous version of the quasi time-variant linear system ((9.116) with $f(t) = 0$) with the variable-rate stiffness k(t) given by control law (9.118) and velocity observer system (9.123) and (9.124) is globally asymptotically stable in the sense that $y(t) \to 0$ as $t \to \infty$.*

Proof. See Appendix B (Sect. B.3) for details.

Numerical Simulations for SDOF System (Proof of Concept): The switched stiffness control concept is implemented using the position and the estimated velocity via the output feedback observer explained earlier. The SDOF system of Fig. 9.36 is revisited here again with the velocity observer presented in the preceding subsection for the simulation. Appropriate values for the control gains K_{01} and K_{02} are selected as listed in Table 9.4. The results for a given initial velocity are obtained as shown in Figs. 9.38 and 9.39. The velocity observation error goes to zero (see Fig. 9.39), as a result of which the observed velocity corresponds to the actual velocity. It must be noted that although the observer does not yield accurate results for some cases, the direction (sign) of the observed signal and the actual signal are in agreement. Such agreement will be more than enough for implementing the switched stiffness control law proposed here. Notice the control law (9.118) requires accurate measurement of the velocity signs and not the actual velocity itself.

Table 9.4 System parameters of the mass-spring system

System parameters	Value	Unit
Mass	1.5	Kg
High spring stiffness	300	N/m
Low spring stiffness	220	N/m
K_{01}	2,300	–
K_{02}	2,500	–

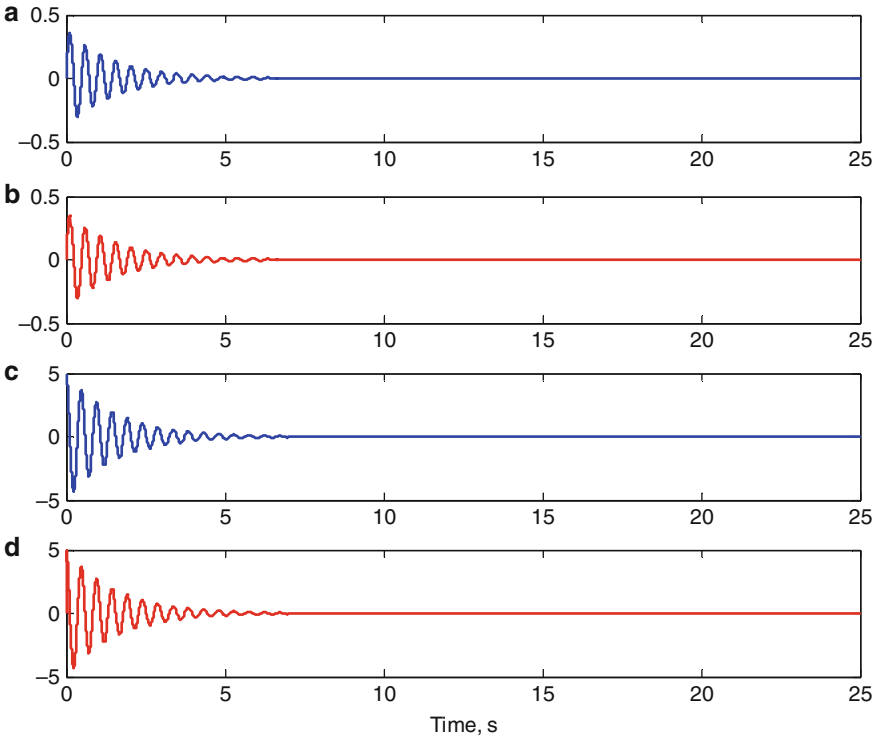

Fig. 9.38 Velocity observer performance for the switched stiffness method implemented on the SDOF system of Fig. 9.36; (**a**) position $y(t)$ in [m], (**b**) observed position $\hat{y}(t)$ in [m], (**c**) velocity $\dot{y}(t)$ in [m/s], and (**d**) observed velocity $\dot{\hat{y}}(t)$ in [m/s]
Source: Ramaratnam and Jalili (2006), with permission

9.4.3 Switched-Stiffness Vibration Control using Piezoelectric Materials

As demonstrated earlier in Chap. 6, when a piezoelectric material (e.g., a laminar piezoelectric patch actuator) is attached to a vibrating elastic body, changing the circuit configurations from open to short circuited, for example, results in different equivalent stiffness values. Denoting the elastic stiffness c^D corresponding to OC (open circuit) configuration, while naming elastic stiffness c^E as the SC (short circuited) configuration elastic stiffens, these two elastic stiffness values were related as per (6.38) and (6.42) as

$$c^E = c^D\left(1 - \kappa^2\right) \tag{9.125}$$

As seen from (9.125), when the piezoelectric material is connected in an open circuit, the material exhibits a particular stiffness and when short circuited, it exhibits different, typically lower stiffness (due to the fact that $\kappa < 1$). The ability of the

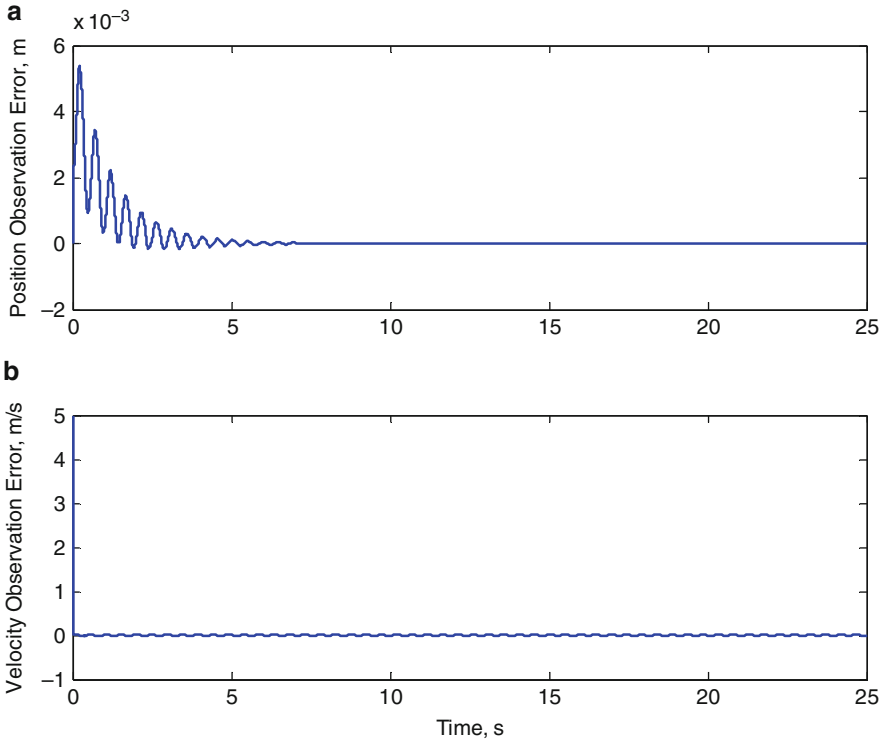

Fig. 9.39 Position and velocity observation error of the results in Fig. 9.38
Source: Ramaratnam and Jalili 2006, with permission

piezoelectric actuators to change their stiffness is due to their ability to change their mechanical compliance, caused by changes in their electrical impedance when connected in open or short circuit.

As also demonstrated in Chap. 8, a piezoelectric actuator or sensor can be considered equivalent to a voltage source and a capacitor in series. During open circuit, the piezoelectric actuator is able to store more potential energy due to its higher stiffness and inherent capacitance. When switched to low stiffness (i.e., short circuited), it is able to dissipate the energy effectively as the capacitor is shunted to short circuited and the stiffness becomes lower. The different piezoelectric circuit configurations are shown in Fig. 9.40. By changing the circuit connection of the piezoelectric material electrodes, the stiffness of the piezoelectric material can be changed. If the piezoelectric material is shunted to a resistive (R) or resistive-inductive (R-L) circuit, the resistor dissipates electrical energy in the form of heat energy (Hagood and Flotow 1991). Passively shunted systems provide better performance than the simple open-closed type systems (Moheimani and Fleming 2006); however, they tend to show inconsistency and poor performance if not optimally tuned.

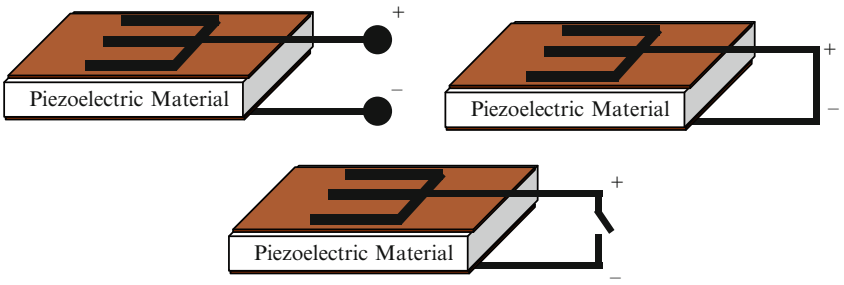

Fig. 9.40 Different configurations of piezoelectric materials: (*top left*) open-circuit, (*top right*) short-circuited, and (*bottom*) switched-circuited configuration. (Ramaratnam, 2004)

Piezoelectric Switched-Stiffness Vibration Control for Flexible Beams: In order to implement the switched-stiffness vibration control using piezoelectric materials, we revisit the bender-type configuration of system considered in Chap. 8 (8.63), where the piezoelectric modulus of elasticity E_p was defined as

$$E_p = c_p^E = c_p^D \left(1 - \kappa_{31}^2\right) \tag{9.126}$$

Notice the switched stiffness method is a semi-active method and the piezoelectric material attached to the beam acts as energy dissipating mechanism rather than an active control system. When short circuited, Young's modulus is E_p, while in open circuit, it is $E_p/\left(1-\kappa_{31}^2\right)$, thereby introducing a change in equivalent stiffness (here κ_{31} is the electromechanical coupling coefficient as defined in Chap. 6).

Similar to the control law for the SDOF system (see (9.118)), the beam tip deflection $w(L,t)$ is used as the system output. Consequently, the control law (9.118) can be modified for the beam as:

$$E_p = \begin{cases} E_p^{\text{high}} = E_p/\left(1-\kappa_{31}^2\right) & \text{for } w(L,t)\dot{w}(L,t) \geq 0 \\ \text{(switch to high stiffness or open circuit)} & \\ E_p^{\text{low}} = E_p & \text{for } w(L,t)\dot{w}(L,t) < 0 \\ \text{(switch to low stiffness or short-circuited)} & \end{cases} \tag{9.127}$$

where $w(L,t)$ and $\dot{w}(L,t)$ are the respective beam tip displacement and velocity corresponding to respective y and $\dot{y}$ as in SDOF setting. The change in low stiffness and high stiffness configurations can be performed by changing the value of E_p in left-hand side of (8.65); that is, for low stiffness $E_p^{\text{low}} = E_p$ and for high stiffness $E_p^{\text{high}} = E_p/\left(1-\kappa_{31}^2\right)$. The control law given in (9.127) can be written in the following more compact form,

$$E_p = \bar{E}_1 + \bar{E}_2 \,\text{sgn}(w(L,t)\dot{w}(L,t)) \tag{9.128}$$

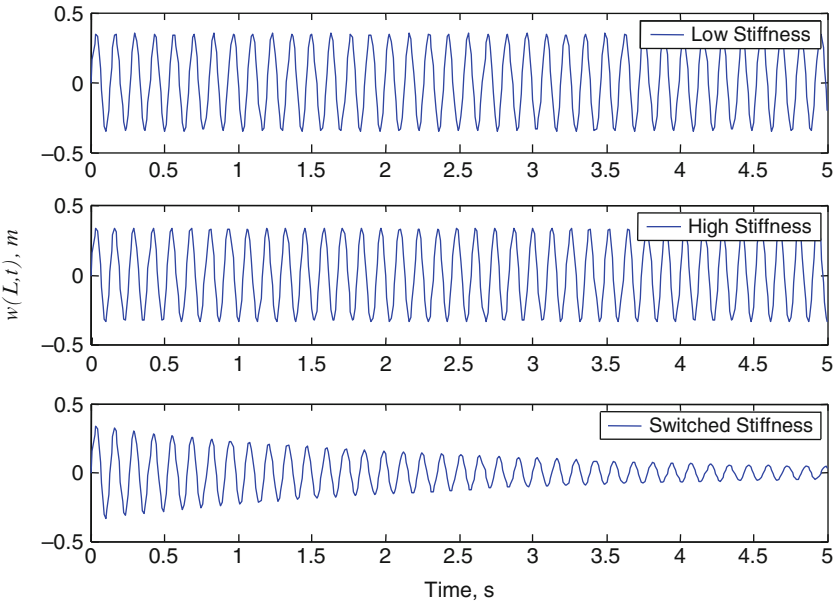

Fig. 9.41 Response of beam tip displacement in the case of fixed base configuration for different stiffness configurations of the piezoelectric material. (Ramaratnam, 2004)

where

$$\bar{E}_1 = \frac{\left(E_p/(1-\kappa_{31}^2)\right) + E_p}{2} \quad \text{and} \quad \bar{E}_2 = \frac{\left(E_p/(1-\kappa_{31}^2)\right) - E_p}{2}$$

Numerical Results for Switched-Stiffness Implementation: The flexible beam with piezoelectric laminar configuration of Fig. 9.21 (without base motion) is considered here for a set of simulations. The system parameters are listed in Table 9.3. The response of the system for different stiffness configurations is shown in Fig. 9.41. As seen, the switched stiffness configuration results in superior vibration suppression performance. The results shown in Fig. 9.41 are implemented using the simulated velocity to switch the stiffness. When the observer is used, due to the problem of discontinuity, it cannot track the actual velocity. The magnitude of observed velocity is very close to the simulated velocity, but there is a phase lag in the observed velocity when compared to the simulated velocity as seen in Fig. 9.42. The plot of sign of simulated velocity and sign of observed velocity, which is important to implement the control law (9.128), is shown in Fig. 9.43. The phase error, which is given by the difference in the sign of the simulated velocity and of the sign of observed velocity, is also plotted in Fig. 9.43 which indicates that the use of observed velocity in implementing the control law will lead to erroneous switching when there is a phase lag. The phase lag in the observed velocity causes ineffective switching, resulting in giving in energy to the system rather than taking out energy and hence may lead to instability.

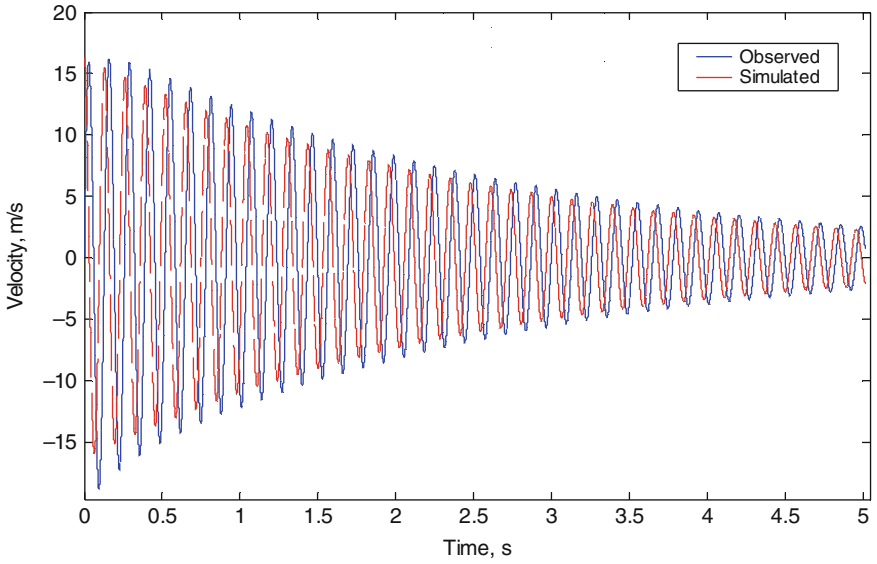

Fig. 9.42 Magnitude tracking by the observer (switched stiffness implemented using the simulated velocity). (Ramaratnam, 2004)

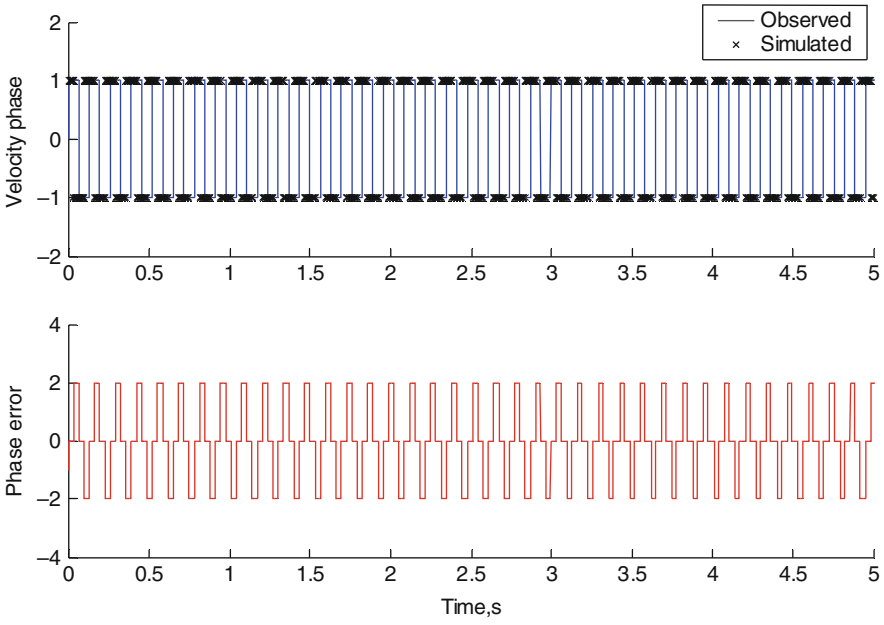

Fig. 9.43 Comparison between the sign of simulated and observed velocities for the performance of the observer shown in Fig. 9.42 (Ramaratnam, 2004)

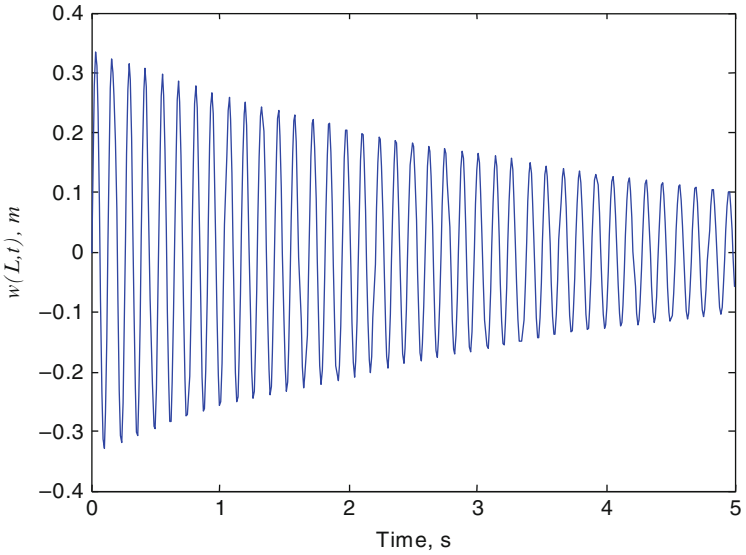

Fig. 9.44 Switched stiffness results using phase tracking observer. (Ramaratnam, 2004)

Although the observer estimated velocity does not exactly correspond to the simulated velocity, the phase can be made closer to the simulated velocity by optimizing the observer gains K_0 to K_2, and hence resulting in effective switching implementation as shown in Fig. 9.44. There might be an optimal set of gain values as a compromise between phase tracking and magnitude tracking. When the piezoelectric material is bonded to the beam and covers the entire length of the beam, the switched stiffness results are much better because of the satisfying differentiability condition of the velocity observer structure as shown in Fig. 9.45. However, the observed velocity still has some phase lag, though the problem of discontinuity is solved. This will not hold true for the general case and it might be due to the number of modes considered and the actual velocity does not necessarily correspond to the simulated modal velocity using three modes ($n = 3$). It is therefore necessary to utilize the velocity observer even with its suboptimum performance, as in real time the velocity obtained by numerical differentiation of the position signal is contaminated with signal noise.

9.4.4 Piezoelectric-Based Switched-Stiffness Experimentation

Experimental Setup: The experimental setup here consists of a flexible aluminum beam with one end fixed and the other end free as shown in Fig. 9.46. A piezoelectric actuator excites the beam, through a voltage given to the PZT actuator ranging from 30 to 150V. The beam vibrations are measured using laser displacement sensors. The

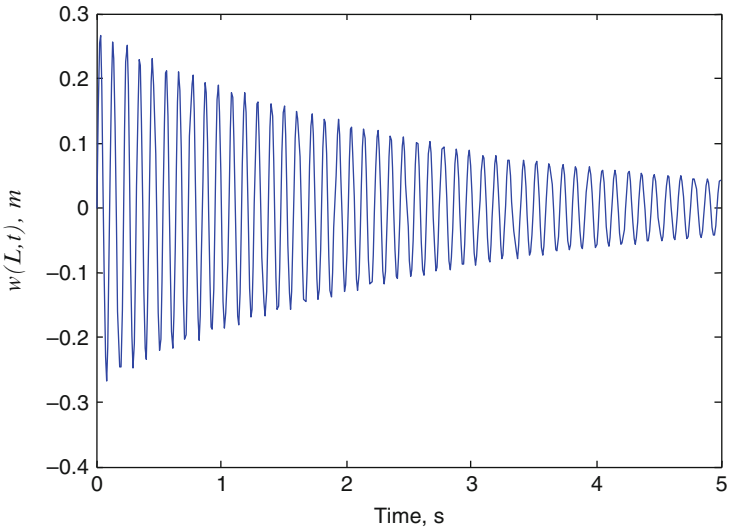

Fig. 9.45 Switched stiffness results using observer with piezoelectric material extending to cover the full length of the beam. (Ramaratnam, 2004)

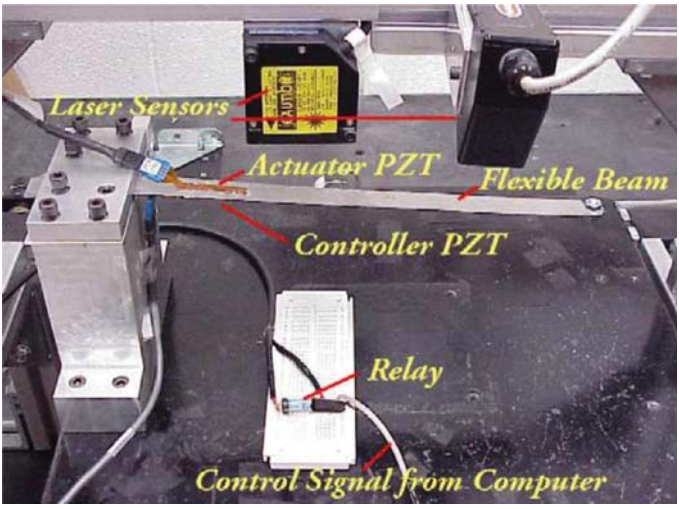

Fig. 9.46 Experimental setup of a piezoelectric-based switched-stiffness implementation. (Ramaratnam, 2004)

position feedback is obtained using the laser displacement sensors and the velocity feedback can be obtained by differentiating the position signal, but the resulting output is very noisy. In order to overcome this, the velocity observer (9.123–9.124) is used as explained earlier. The control law is implemented as given in (9.127). The position feedback obtained from the optical laser sensors is fed back to the host

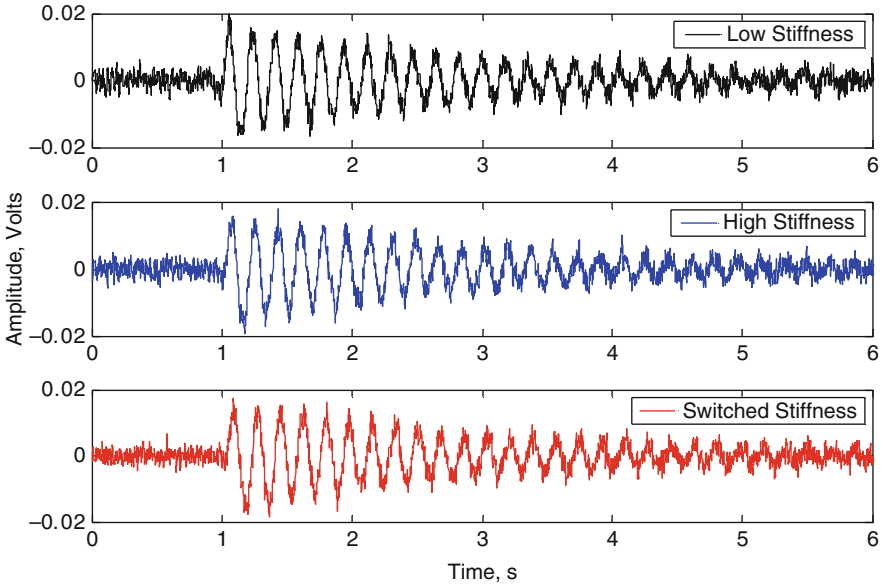

Fig. 9.47 Time domain response of the system with piezoelectric as switched stiffness controller. (Ramaratnam, 2004)

computer. According to the control law, a 0 or a 5V supply is given to the relay to open or short the piezoelectric materials. The relay has an operating time of 1 ms and a release time of 0.5 ms.

Switched-Stiffness Using Piezoelectric Actuator: An impulse function is given to the piezoelectric disturbance actuator with the response for different stiffness configurations shown in Figs. 9.47 and 9.48 for the piezoelectric controller. The low stiffness is implemented by shorting the PZT controller, the high stiffness by keeping the circuit open, and switched stiffness by switching the relay to ON and OFF states, according to control law given by (9.127). The time domain response of the results cannot be clearly interpreted, but the frequency domain results yield lower amplitudes for the switched stiffness case. Young's modulus of the beam was about 69 GPa and that of PZT controller was 60.98 GPa for low stiffness case and 72.59 Gpa for the high stiffness case, assuming k_{31} to be about 0.33.

The change in the equivalent stiffness for the total system can be found from (9.127). This proves the use of piezoelectric materials for semi-active vibration control using the concept of switched stiffness proposed here. The length of the PZT can be increased for more effective control, but this will lead to addition of weight to the structure. Figure 9.49 shows the velocity obtained by numerical differentiation of the position signal and using the observer. It is very clear that using numerical differentiation will not yield good switching results as it contains very noisy signals that cannot be interpreted. The observer seems to perform well in estimating the velocity. Figure 9.50 shows the tracking of actual position by the velocity observer.

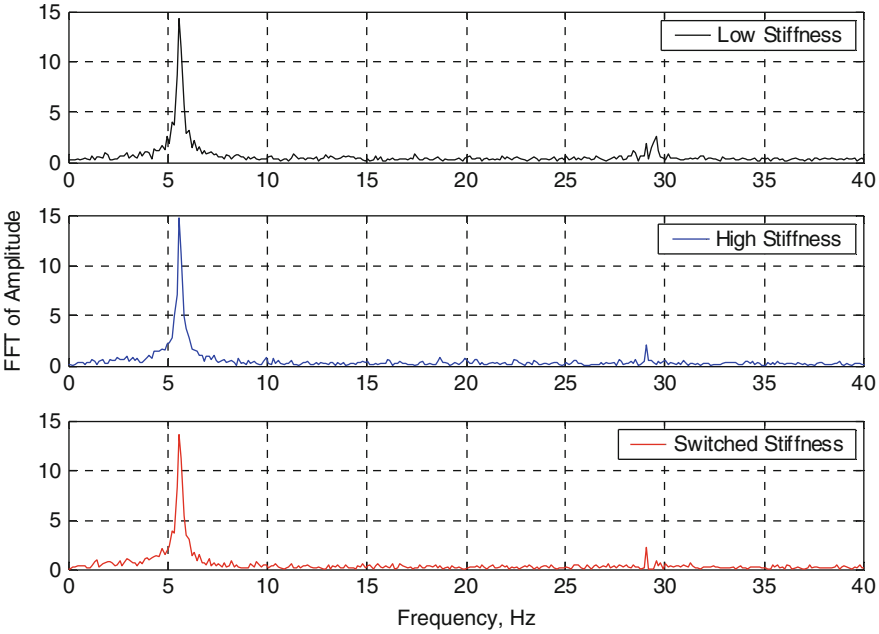

Fig. 9.48 Frequency domain responses of the piezoelectric as switched stiffness controller. (Ramaratnam, 2004)

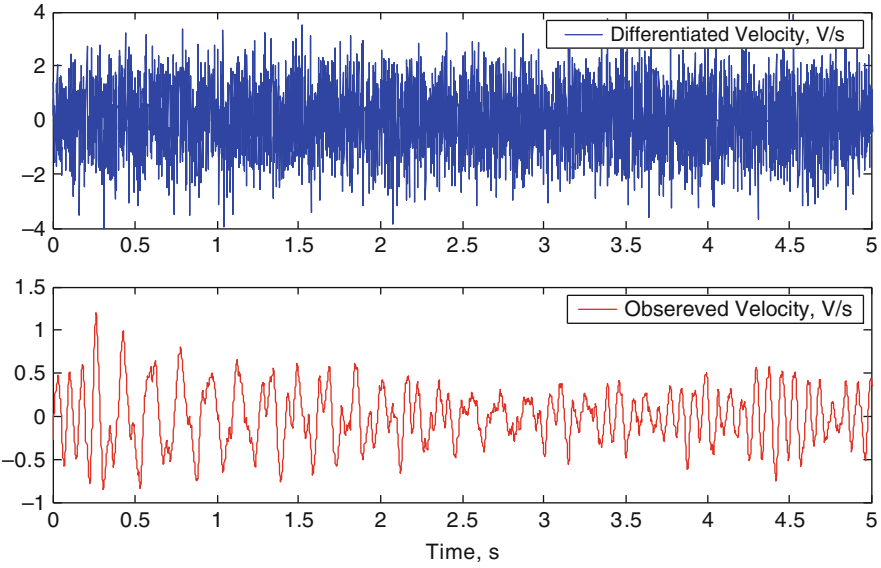

Fig. 9.49 Velocity obtained using numerical differentiation and observer. (Ramaratnam 2004)

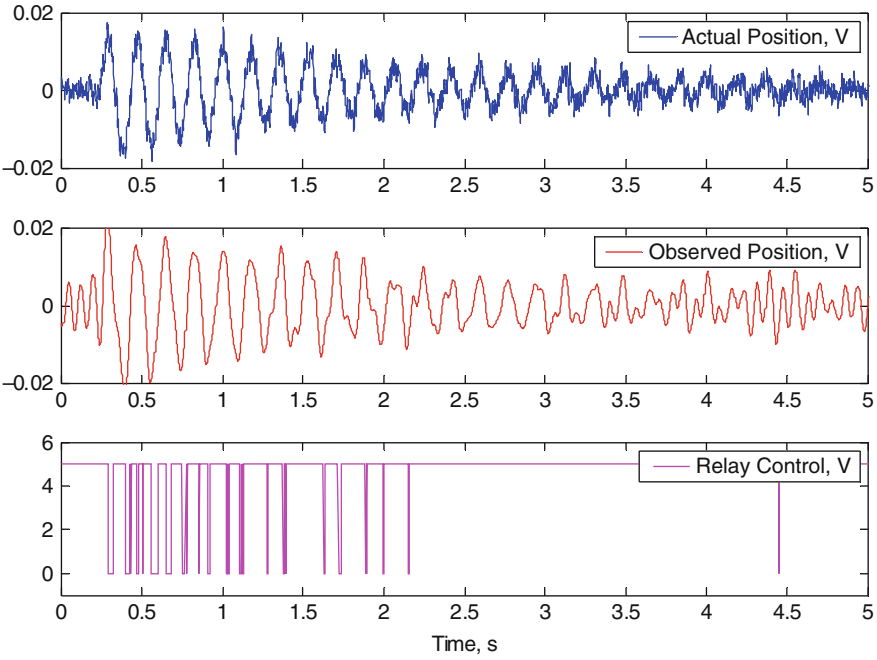

Fig. 9.50 Actual position (*top*), observed position (*middle*), and the control action (*bottom*). (Ramaratnam, 2004)

The switching control action is also shown in Fig. 9.49. The switching action may not be dense as the range of the control law was shifted (in the sense that it will check for the condition above or below a certain value and not referenced to zero) to avoid switching when there is just noise. Thus, the use of observer and the practical difficulties in implementing the control law with a noisy position feedback are to be noted. The system parameters used here are listed in Table 9.3.

9.5 Self-sensing Actuation using Piezoelectric Materials

9.5.1 Preliminaries and Background

As extensively disclosed so far in this book, the dual actuation and sensing attributes of piezoelectric materials make them an effective transducer that can be used for either actuation or sensing. A novel configuration is the simultaneous actuation and sensing using the same piezoelectric material, which is referred to as so-called self-sensing actuation. The underlying concept in self-sensing can be simply

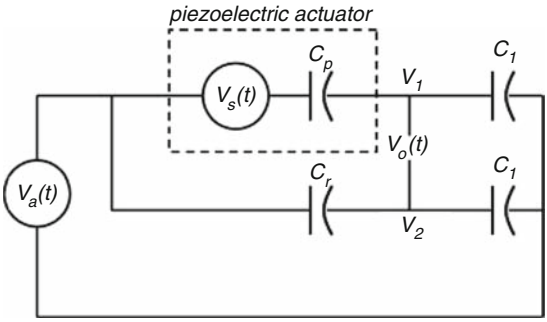

Fig. 9.51 Pure capacitance bridge self-sensing actuation

stated as: piezoelectric materials deform when subjected to external voltage, while simultaneously generating charges when subjected to mechanical deformations. Therefore, a piezoelectric actuator can also act as a sensor if augmented with a proper circuit. In the so-called self-sensing mode, a single piezoelectric patch can simultaneously actuate (inverse piezoelectric effect) and sense the beam vibrations (direct piezoelectric effect).

The simplest way to implement this mechanism is by using a capacitance bridge network to separate the actuation voltage from the self-induced voltage (Shen et al. 2006; Jones et al. 1994; Itoh et al. 1996; Zhou et al. 2003; Gurjar and Jalili 2007), see Fig. 9.51. As mentioned in Sect. 8.5.3, a piezoelectric actuator can be simply modeled as a capacitor, C_p, and a voltage source, V_s, in series (see the dotted lines in Fig. 9.51) (Moheimani and Fleming 2006; Dadfarnia et al. 2004b; Preumont 2002). The self-sensing mechanism can be implemented by using a capacitance bridge, for instance, to relate the actuation voltage $V_a(t)$ to the self-induced voltage $V_s(t)$ as:

$$V_0(t) = \left[\frac{C_p}{C_1 + C_p} - \frac{C_r}{C_1 + C_r}\right] V_a(t) + \frac{C_p}{C_1 + C_p} V_s(t) \tag{9.129}$$

where $C_p (= C^l_{\text{piezo}}$, see Sect. 8.5) represents the capacitance of the piezoelectric material, $V_s(t)$ is the induced voltage (see (8.137)), and C_1 and C_r represent the bridge capacitors (see Fig. 9.51).

From (9.129) it is clear that if $C_p = C_r$, then the bridge output voltage is proportional only to the self-induced voltage. This is said to be the *balanced* condition of the bridge. A balanced bridge output will yield the self-induced voltage $V_s(t)$, (Gurjar and Jalili 2007).

The inherent piezoelectric actuator capacitance (C_p) is, however, sensitive to changes in the ambient temperature. The success of self-sensing depends on the ability of the bridge capacitor to compensate for the piezoelectric capacitance dynamically. For this, an adaptive estimation strategy for piezoelectric capacitance value is utilized as discussed in detail next.

9.5.2 Adaptation Strategy for Piezoelectric Capacitance

It is clear from (9.129) that for the bridge to separate the actuation voltage from the sensing voltage, the introduced capacitance C_r needs to exactly match the effective capacitance of the piezoelectric material C_p. That is, if $C_p = C_r$, then the bridge output voltage, as seen from (9.129), is proportional only to the self-induced voltage, $V_s(t)$, and hence detectable. This is, however, very difficult to achieve in practice, because the piezoelectric capacitance cannot be accurately determined and is known to vary with temperature (Rogers et al. 2003). Obviously, a static capacitor connected in the bridge network cannot compensate for the variations in C_p. Hence, for the mechanism to work effectively, a capacitor element of the bridge needs to match the effective capacitance of the piezoelectric material (C_p).

A remedy to this is to use an adaptive estimation mechanism for automatic tuning of the capacitance bridge (Law et al. 2003). Along this line, we present, next, an improvement over a mechanism that is traditionally used for active vibration-control application. That is, a compensatory technique is presented to adaptively track changes in the piezoelectric capacitance in real time.

Adaptive Compensatory Self-sensing Mechanism: For practical implementation of self-sensing, the piezoelectric capacitance C_p must be compensated for in real time. The output voltage will reflect the sensing voltage only if the condition $C_p = C_r$ is satisfied. In an unbalanced bridge, a part of $V_a(t)$ is reflected in the output voltage. Since $V_a(t)$ is a few orders higher in magnitude than $V_s(t)$, even a fraction of $V_a(t)$ entering the bridge output voltage can mask $V_0(t)$. Hence, it is important to keep the bridge balanced at all times by compensating for the changes in piezoelectric capacitance dynamically.

The adaptive compensatory mechanism shown in Fig. 9.52 performs an online estimation of C_p and uses an adaptive algorithm to dynamically drive the error between the true value of the capacitance and its estimate to zero. For this, we first utilize a low power persistent excitation signal (t), see Fig. 9.52 in the absence of input excitation (i.e., $V_a = 0$). The low power ensures that the voltage signals do not induce a moment in the piezoelectric actuator and hence, do not set the beam into vibration (i.e., $V_s = 0$). This leads to

$$V_1(t) = \theta \Psi(t) \tag{9.130}$$

where

$$\theta = \frac{C_p}{C_1 + C_p} \tag{9.131}$$

represents the nondimensional piezoelectric capacitance parameter to be estimated. Considering this, and according to Fig. 9.52, the output voltage of the bridge can be written as:

$$V_0(t) = V_1(t) - \overline{V}_2(t) = (\theta - \hat{\theta})\Psi(t) = \tilde{\theta}\Psi(t) = e(t) \tag{9.132}$$

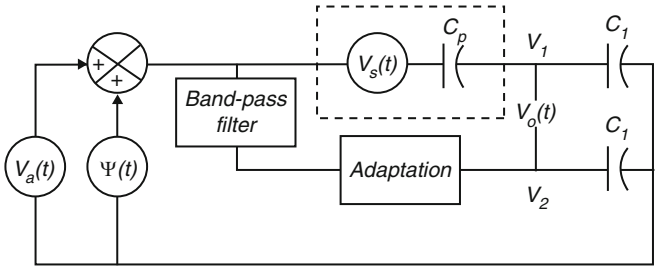

Fig. 9.52 Schematic of the adaptive self-sensing actuation strategy

where $\tilde{\theta} = \theta - \hat{\theta}$ represents the parameter estimation error. Utilizing a negative sense of the prediction error and the gradient of error square, the following update law for parameter θ is selected

$$\dot{\hat{\theta}}(t) = -ke(t) + G(t)\frac{\partial}{\partial\hat{\theta}}(e(t))^2 \tag{9.133}$$

where k is a constant gain and $G(t)$ is a time-dependant adaptation gain whose properties can be selected based on a least square strategy with constant exponential forgetting. This method has proven to be useful for the estimation of unknown time-varying parameters (Law et al. 2003). Proper tuning to parameters and/or structure of this adaptation can be performed for optimal operation. For instance, one can replace the time-varying adaptation gain $G(t)$ in (9.133) with a constant parameter to reduce numerical computations. This can be done by choosing a gradient estimation method instead of the least square with constant exponential forgetting.

Equation (9.133), on further simplification, yields:

$$\dot{\hat{\theta}} = -k_1\Psi\,\tilde{\theta} - P(t)\Psi^2\tilde{\theta} \tag{9.134}$$

where $P(t) = -2G(t)$. A cost function for least square with constant exponential forgetting can be defined as (Law et al. 2003; Slotine and Li 1990):

$$J_2 = \int_0^t \exp\left(-\alpha(t-\tau)\right)[e(\tau)]^2 \mathrm{d}\tau, \tag{9.135}$$

where α is a constant forgetting factor.

Modified Adaptive Compensatory Mechanism: The implementation of the adaptive law (9.134) is typically computationally intense and requires extensive iterations and complicated electronics. For cases where rapid changes in either the measurements or the environment do not occur, the adaptation law (9.154) can be modified by replacing the time-varying adaptation gain by a constant gain. In this case, the update law can be simplified and written as:

$$\dot{\hat{\theta}} = -k_1 \Psi \tilde{\theta} - P_0 \Psi^2 \tilde{\theta} \tag{9.136}$$

where P_0 ($P_0 > 0$) is a constant adaptation gain.

Theorem 9.6. *The update law presented in (9.136) is globally stable.*

Proof. We define the Lyapunov function:

$$V_L = P_0^{-1} \tilde{\theta}^2 > 0 \tag{9.137}$$

Leaving the intermediate steps to (Gurjar and Jalili 2007), the time derivative of the Lyapunov function (9.137) can be expressed as:

$$\dot{V}_L = -2 \left(k_1 P_0^{-1} \Psi + \Psi^2 \right) \tilde{\theta}^2 < 0, \tag{9.138}$$

which is negative definite and based on the Invariant Set theorem, this law is globally stable (Slotine and Li 1990), also see Appendix A, Sect. A.4. As this law does not require the adaptation gain to be recursively updated, it is computationally less intensive and very effective. After some manipulations, it can be shown that the estimate for θ can be expressed as:

$$\tilde{\theta}(t) = \exp \left[-\int_0^t k_1 \Psi(\tau) d\tau - \int_0^t P_0 \Psi^2(\tau) \mathrm{d}\tau \right] \tilde{\theta}(0) \tag{9.139}$$

It can be shown that the convergence of parametric error to zero is faster than the standard gradient estimation method (Slotine and Li 1990).

9.5.3 Application of Self-sensing Actuation for Mass Detection

Experimental Setup: In this section, the described self-sensing mechanism is implemented on a cantilever beam setup, as shown in Fig. 9.53, for mass detection applications. The experimental setup consists of a thin stainless steel beam of dimensions $0.52'' \times 5.2'' \times 0.01''$, with piezoelectric patch actuator from Smart Materials Inc. bonded on its surface using an epoxy adhesive (http://www.smart-material.com).

The voltage generated in the actuator is measured across an external capacitor mounted on a breadboard and fed back into an amplifier. A chirp signal ($V_a(t)$) with excitation frequency ranging from 4 to 20 Hz is mixed with low power white noise signal ($\Psi(t)$) and fed back into the dSPACE DS1104 digital signal processor through Real-Time Control software and Matlab/Simulink.

The controller needs $\Psi(t)$ and $V_a(t)$ to perform the adaptation. These signals can be fed from the source into the controller internally. However, this may create a delay and induce a phase shift between the input and the output signals. To minimize this effect, the signals are captured at the input side of the experiment and fed back

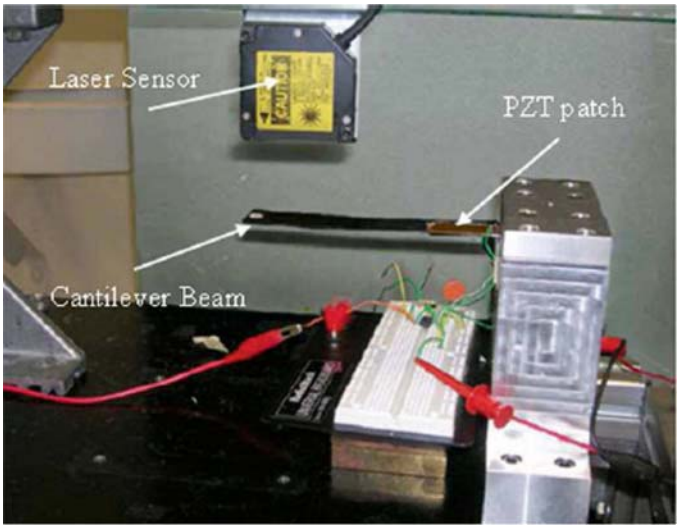

Fig. 9.53 Experimental setup used for self-sensing actuation for small mass detection at tip

into the computer. This also helps to minimize the phase shift between $\psi(t)$ and $\theta\psi(t)$, which were fed into the computer through two different band pass filters.

Adaptive Self-sensing Actuation Implementation: The experiment is carried out by sticking a small piece of paper ball on the beam. The Fast Fourier Transform (FFT) of the beam response before and after placement of the small tip mass is shown for both self-induced voltage and tip deflection (using an external laser-based measurement). In order to compensate for piezoelectric capacitance changes, several gain tuning trials were performed to optimally balance the bridge.

The first set of experiments is performed using the extended gradient estimation method (9.134) with and without a tip mass. The system is excited with a sinusoidal signal of $|V_a(t)| = 5\text{V}$. The adaptation gain is initialized at 6,000 and an error constant of $k_1 = 8$ is selected. A persistent excitation signal $\Psi(t)$ was chosen to be a white noise signal with a noise power 0.00001. The signals are sampled at 2 kHz. An FFT of the sensing voltage (Fig. 9.54, left) and the beam tip displacement (Fig. 9.54, right) was obtained in both cases. It can be seen from Fig. 9.54 (left) that the drop in frequency due to increase in mass is correctly reflected in the self-induced voltage when compared to external laser-based measurement shown in Fig. 9.54 (right). The adaptation gain $P(t)$ and estimates of θ are plotted in Figs. 9.55 (left and right, respectively).

The FFT of the signal for the beam with tip mass was obtained by increasing the chirp signal amplitude from 5 to 5.5V to obtain a better signal. In the second set of experiments, the modified form of gradient estimation stated in (9.136) was used. The adaptation gain $P(t)$ was replaced by a constant value of $P_0 = 2,000$ after noting the values of the gain from the previous experiment. The FFT of the self-induced voltage generated without the addition of tip mass is plotted in Fig. 9.56.

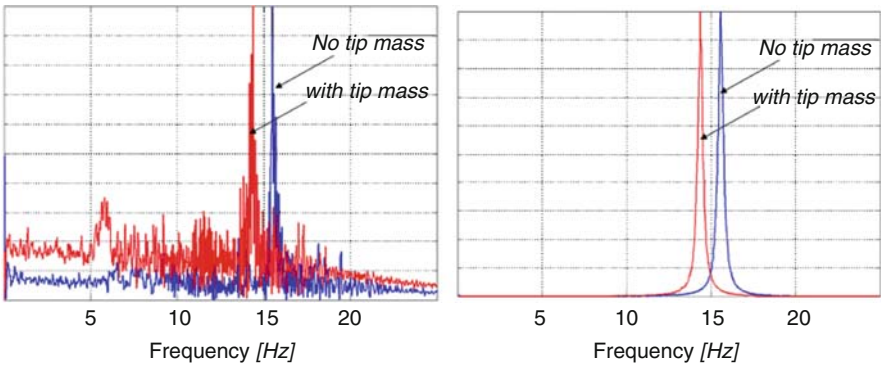

Fig. 9.54 FFT of cantilever beam response before and after placement of a small tip mass: (*left*) self-induced voltage and (*right*) laser-based noncontact measurements
Source: Gurjar and Jalili 2007), with permission

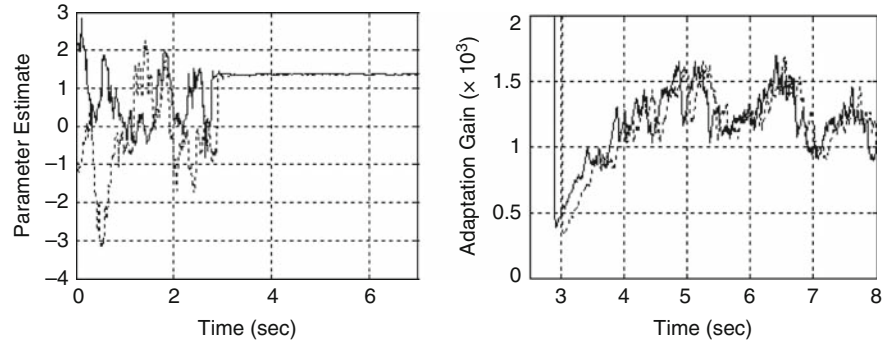

Fig. 9.55 Adaptive self-sensing actuation experiment: (*left*) estimation of θ and (*right*) adaptation gain
Source: Gurjar and Jalili (2007), with permission

Fig. 9.56 FFT of self-sensing voltage using modified form of gradient estimation method
Source: Gurjar and Jalili (2007), with permission

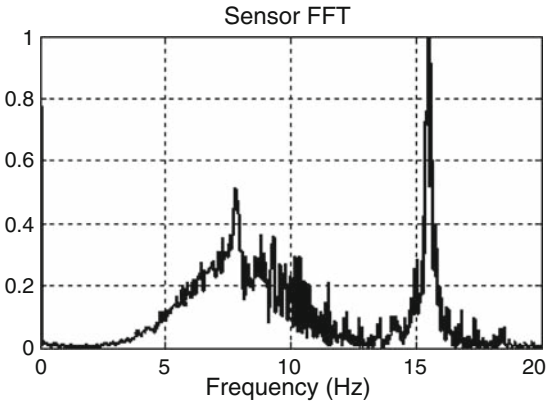

Discussion of the Results: It can be seen from Fig. 9.54 (both left and right) that the drop in frequency due to increase in the tip mass is correctly reflected in the self-induced voltage. However, Fig. 9.55 (left and right) does not reflect a correct reading in the first few seconds because of the specifics of using the real-time control software (Control Desk® from dSPACE) for capturing the experiment signals. Although the system is powered up, no signal is applied for the first few seconds of the experiment. As a result, both the adaptation gain and parameter estimate change erratically during this period. Typically, the drawback of using constant exponential forgetting factor can be seen with the explosion of adaptation gain in the absence of the persistent excitation signal during the first few seconds of the experiment. Experiments performed using the modified gradient estimation method also demonstrate the ability to measure the first natural frequency of the system accurately. In fact, the response is much cleaner than the previous method, suggesting that for controlled laboratory experiments this method may be more suitable.

The self-sensing platform developed in this section can be extended to a microcantilever-based mass sensing system. However, a number of challenges need to be addressed before this can be achieved. The current setup, which is a considerably simplistic representation of the microcantilever sensor, can be improved for the implementation of this self-sensing at this scale. Chapter 11 in Part III briefly reviews and presents the implementation and preliminary results for a microcantilever setup. We prefer not to include any additional materials here, and instead refer the interested readers to Chap. 11.

Summary

The fundamental principles of vibration-control systems were formulated here. Using the modeling developments and derivations in the preceding chapters, a comprehensive treatment was presented for active vibration absorption as well as vibration control using piezoelectric materials for a variety of systems. These included the application of piezoelectric actuators and/or sensors in both axial and transverse configurations as well as piezoelectric control design using lumped-parameters and distributed-parameters representations.

Part III
Piezoelectric-Based Micro/Nano Sensors and Actuators

Building based on the preceding two parts, the third part of the book presents advanced topics in piezoelectric-based micro/nano sensors and actuators with applications ranging from molecular manufacturing and precision mechatronics to molecular recognition and functional nanostructures. Chapter 10 gives an overview of piezoelectric-based micro- and nano-positioning systems with their widespread applications in scanning probe based microscopy and imaging. The preliminaries covered especially in Chaps. 7 and 8 are utilized here to help designing both feedforward and feedback control systems to achieve the ultrahigh positioning precision demanded in these applications. Starting from single-axis nano-positioning actuators to 3D positioning piezoactive actuators, this chapter provides the reader with a complete overview of the piezoelectric-based nano-positioning systems. As a totally different configuration for scanning probe based microscopy, Chapter 11 provides a relatively general overview of piezoelectric-based nanomechanical cantilever (NMC) sensors and actuators with their application in many NMC-based imaging and manipulation systems such as atomic force microscopy (AFM) and its varieties. This chapter also introduces some new concepts in modeling these systems and highlights the issues related to nonlinear effects at such small scale, the Poisson's effect and piezoelectric materials nonlinearity. More specifically, both linear and nonlinear models of piezoelectric NMC sensors and actuators are provided with their application in biological and ultrasmall mass sensing and detection. A relatively general comparison between modeling limitations for piezoelectric-based actuators and sensors at macroscale and microscale is also provided. The last chapter in this part provides recent advances in nanomaterials-based actuators and sensors utilizing either piezoelectric materials or possessing piezoelectric properties. More specifically, piezoelectric properties in nanotubes are disclosed and detailed, with a natural extension to nanotube-based piezoelectric sensors and actuators. As a byproduct of this arrangement, structural damping becomes possible using nanotubes-based composites. As a future pathway towards development of next-generation sensors and actuators comprised of nanomaterials, piezoelectric nanocomposites with tunable properties as well as electronic textiles comprised of functional nanomaterials are also briefly introduced and discussed.

Chapter 10
Piezoelectric-Based Micro- and Nano-Positioning Systems

Contents

10.1 Classification of Control and Manipulation at the Nanoscale 313
10.1.1 Scanning Probe Microscopy-Based Control and Manipulation 315
10.1.2 Nanorobotic Manipulation-Based Control and Manipulation 319
10.2 Piezoelectrically Driven Micro- and Nano-Positioning Systems 321
10.2.1 Piezoelectric Actuators Used in STM Systems 322
10.2.2 Modeling Piezoelectric Actuators Used in STM Systems 322
10.3 Control of Single-Axis Piezoelectric Nano-positioning Systems 328
10.3.1 Feedforward Control Strategies 330
10.3.2 Feedback Control Strategies 332
10.4 Control of Multiple-Axis Piezoelectric Nano-positioning Systems 336
10.4.1 Modeling and Control of Coupled Parallel Piezo-Flexural Nano-Positioning Stages 336
10.4.2 Modeling and Control of Three-Dimensional Nano-Positioning Systems 351

This chapter provides an overview of piezoelectric-based micro- and nano-positioning systems with their widespread applications in scanning probe-based microscopy and imaging. Starting from single-axis nano-positioning actuators to 3D positioning piezoactive systems, this chapter presents a complete overview of the piezoelectric-based nano-positioning systems.

10.1 Classification of Control and Manipulation at the Nanoscale

Advancement of emerging nanotechnological applications such as nanoelectromechanical systems (NEMS) requires precise modeling, control, and manipulation of objects, components and subsystems ranging in sizes from few nanometers to micrometers. One of the most challenging aspects of "nanoscale" manipulation and control design compared with "macroscale" control design is the added complexity of uncertainties and nonlinearities that are unique to nanoscale. This added complexity combined with the sub-nanometer precision requirement calls for the

N. Jalili, *Piezoelectric-Based Vibration Control*,
DOI 10.1007/978-1-4419-0070-8_10,

© Springer Science+Business Media LLC 2010

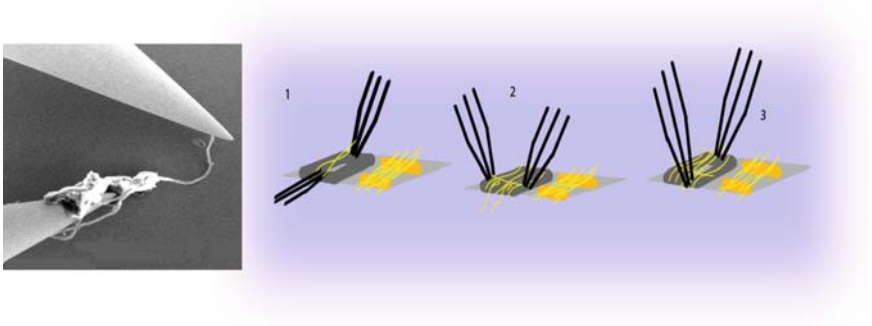

Fig. 10.1 (*left*) Manipulation of nanofiber using MM3A® Nanorobot from Kleindiek®, (right) schematic representation of automated weaving process; (**a**) placement of the fibers and folding in the warp direction, (**b**) fiber placement in the weft, and (**c**) unfolding of the warp

development of fundamentally new techniques and controllers for these applications.

This area of research has recently received widespread attention in different technologies such as fabricating electronic chipsets, testing and assembly of MEMS and NEMS, and microinjection and manipulation of chromosomes and genes (Kallio and Koivo 1995). For example, in nanofiber manipulation, the ultimate goal is to grasp, manipulate, and place nanofibers in certain predefined arrangement (see Fig. 10.1). Other applications could include defining materials properties, fabricating electronic chipsets, testing microelectronics circuits, assembly of MEMS and NEMS, teleoperated surgeries, microinjection, and manipulation of chromosomes and genes.

In general, nanoobject manipulation is defined as grasping, manipulating and placing nanoobjects in certain predefined arrangement. The strategies for control and manipulation at the nanoscale can be divided into the following two general categories:

1. Scanning Probe Microscopy (SPM)-based, and
2. NanoRobotic Manipulation (NRM)-based techniques.

Under the first category, the following platforms can be utilized: Scanning Tunneling Microscope (STM) and NanoMehcanical Cantilever (NMC)-based Systems (e.g., Atomic force microscopy – AFM), see Fig. 10.2. In order to maintain the focus of the book in this chapter, we only concentrate on the first category, that is, SPM-based techniques with special attention to piezoelectric-based micro- and nano-stages used in these systems. Chap. 11 is dedicated to NMC-based systems with their widespread applications in today's scanning and imaging needs.

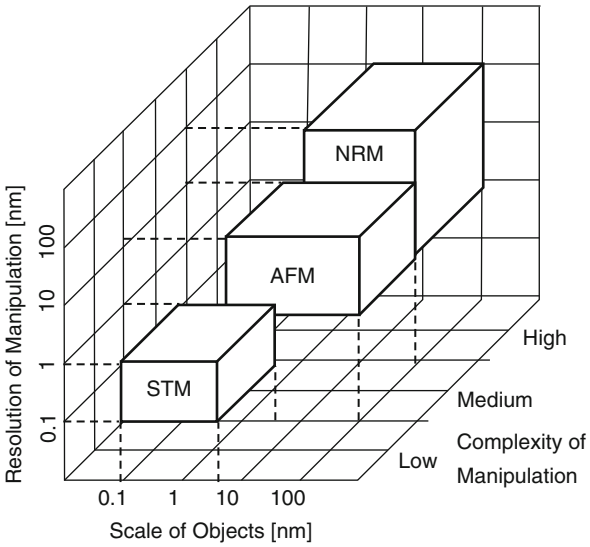

Fig. 10.2 A comparison of different nanomanipulation strategies
Source: Fukuda and Dong 2003, with permission

10.1.1 Scanning Probe Microscopy-Based Control and Manipulation

In SPM systems, a probe is scanned over the surface at a small distance, where an "interaction" between the probe and the surface is present. This interaction can be of various nature (e.g., electrical, magnetically, mechanical) and provides the measured signal (tunnel current, force, etc.), see Fig. 10.3. SPM systems have numerous applications in a variety of disciplines and fields such as materials science, biology, chemistry, and many more areas.

As mentioned earlier and depicted in Fig. 10.2, under SPM-based control and manipulation techniques, STM and AFM platforms are referred to as the two most widely accepted techniques. As a matter of fact, early efforts on nanomanipulation were initiated by both STM (Binnig et al. 1982) and AFM (Binnig et al. 1986) systems. Other techniques such as optical tweezers (Ashkin et al. 1986) and magnetic tweezers (Crick and Hughes 1950) have also been used for this purpose.

Scanning Tunneling Microscope, an Electrical SPM-based Control and Manipulation: The STM, invented in 1982 by Binnig and Rohrer (Binnig et al. 1982), was originally designed to perform real space atomic resolution imaging of a material's surface. The ability to obtain atomic resolution images with the STM arises from its unique operating principles. The microscope uses a sharp, metallic tip that is placed only a few Angstroms (10^{-10} m) from a conducting surface, see Fig. 10.4a–b. At this distance, the tip conducts tunneling electrons or "tunnel current" from the surface and probes the surface electron density at that point. The electron density is exponentially dependent on the tip–surface separation, which makes the tunnel

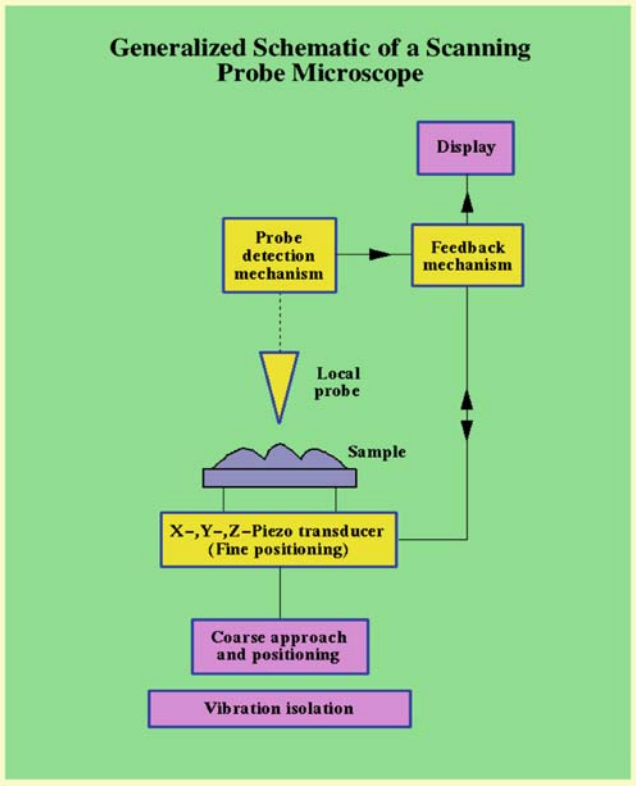

Fig. 10.3 Generalized schematic of scanning probe microscopy (SPM) system

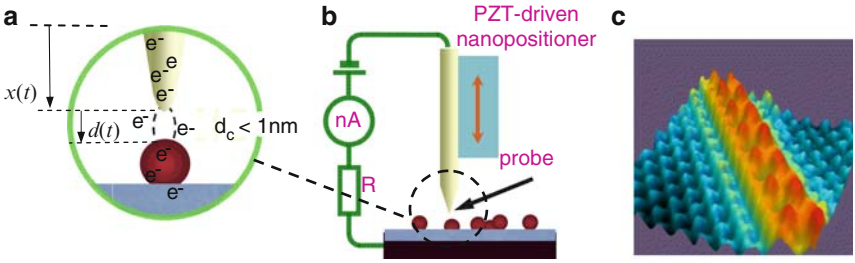

Fig. 10.4 (**a, b**) STM principle of operation and (**c**) STM image of GaAs(110) surface (http://physics.nist.gov)

current a highly sensitive measure of this relative distance. The image shown in Fig. 10.4c is formed by scanning the STM tip laterally across the GaAs(110) surface, monitoring the tunnel current, and varying the tip–sample separation to maintain that current at a constant value. Plotting the resulting tip height change at each point on the surface gives the depicted atomic-resolution image.

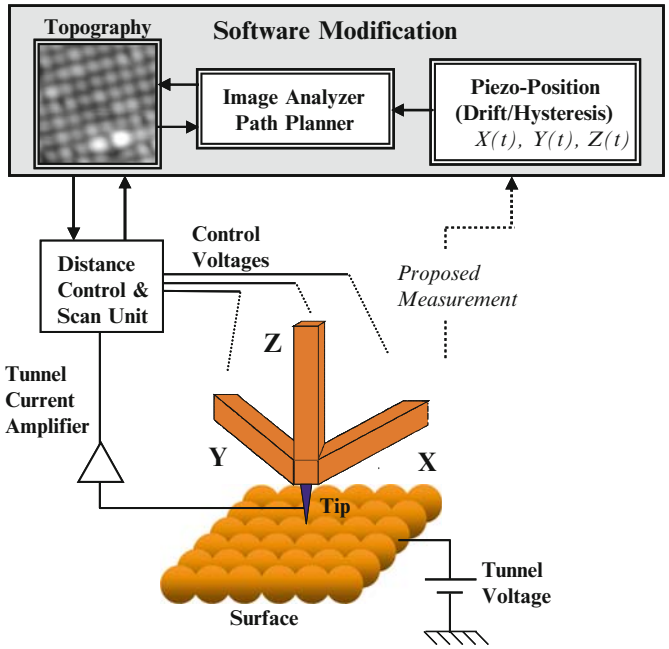

Fig. 10.5 Schematic of automated STM-based nanoscale manipulation and fabrication

The real space imaging capabilities of the STM have been utilized in basic surface science studies of metal and semiconductor surfaces to provide non-trivial structural information, see for example Stroscio and Kaiser (1993). Along with atomic-resolution imaging and high-resolution metrology, the STM also has the ability to modify or otherwise affect the surface. The strong interactions that can exist between a scanning tip and atoms/molecules at the surface can lead to alterations in surface chemical structure and, if controlled properly, can be used to move atoms or molecules and build nanoscale structures. It is this feature of the STM that forms the basic concept in nanomanipulation, that is, due to its ultrahigh imaging resolution, nanoparticles as small as atoms can be manipulated. As schematically depicted in Fig. 10.5, three piezoelectrically (PZT)-driven stages are utilized to control the position of the STM. At the software or algorithmic level, the influence of the PZT actuator nonlinearities (e.g., hysteresis and drift) can be systematically controlled (or compensated for).

More specifically, a tracking controller to measure the unknown distance between the STM tip and sample surface can be incorporated into the STM system. This will lead to controllable, high precision STM tip movements at the level required for atomic manipulation. It is this feature of STM that forms the main motivation for this chapter in presenting an overview of modeling and control of PZT-driven nanostages. Although we will provide, next, a brief overview of the other nanomanipulation techniques (i.e., AFM and NRM), we only provide detailed discussions

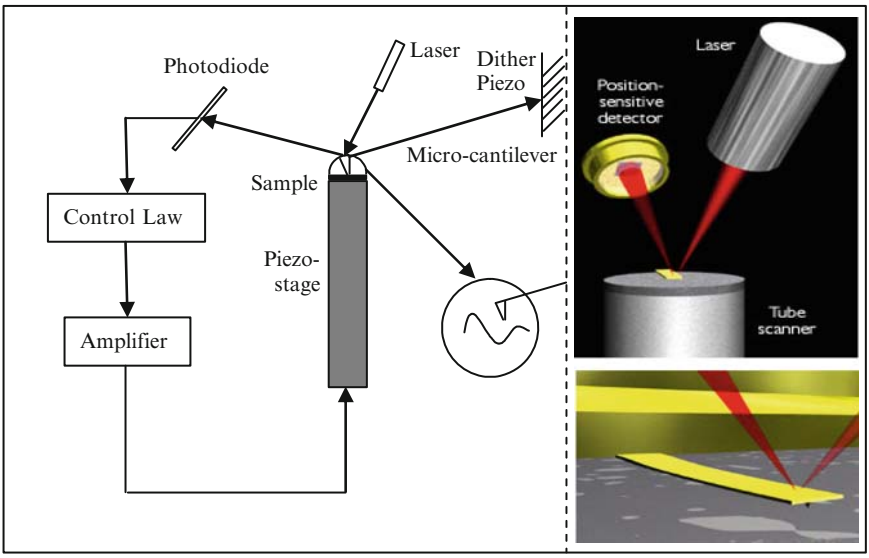

Fig. 10.6 (*Left*) Schematic depicting basic AFM operation and sub-components, and (*right*) real scale drawing

on STM-based manipulation and control, and especially PZT-actuated nanostages in this chapter. Chap. 11 provides some detailed information about NMC-based manipulation and sensing, the configuration that is utilized in AFM.

Atomic Force Microscope (AFM), an Electromechanical SPM-based Control and Manipulation: As mentioned earlier, AFM systems belong to the category of NanoMechanical Cantilever (NMC)-based systems, a subcategory of SPM systems. As depicted in Fig. 10.6, a typical AFM system consists of a micromachined cantilever probe with a sharp tip that is mounted to a piezoelectric actuator with a position sensitive photo detector that receives a laser beam reflected off the back of the AFM tip. Roughly speaking, AFM is operated by moving the sample under the AFM tip and then recording the vertical displacement of the tip as the samples moves. Piezoelectric actuators are usually utilized to maintain a constant force between the AFM tip and the sample surface. As the AFM tip rubs across the surface of the sample, the tip moves up and down with the contour of the surface. A laser beam, deflected off of the back of the AFM tip, is captured by a detector. This laser/detector configuration could provide displacement measurements that are utilized to generate topographical images and to control the piezoelectric actuators.

The AFM system has evolved into a useful tool for direct measurements of microstructural parameters and the intermolecular forces at the nanoscale level. The non-contact AFM offers unique advantages over other contemporary scanning probe techniques such as contact AFM and STM. Unlike STM and contact AFM, the absence of repulsive forces in non-contact AFM permits the imaging of "soft" samples, and hence, provides topography with little or no contact between the tip

and the sample. Since the samples are not contaminated or damaged through contact with the AFM tip, this mode of operation is especially preferred in many manufacturing processes such as non-destructive surface texture characterization, metrology for MEMS and 3D topography for nanoparticle manufacturing.

Similar to STM, AFM system can also be used for manipulation at the nanoscale as depicted in Fig. 10.2. Since nanomanipulation using STM is only feasible in a 2D working space, utilizing STM in complicated manipulation process is very difficult if not impossible. On the other hand, utilizing AFM in nanomanipulation is feasible in either contact or dynamic (i.e., non-contact and/or tapping) modes. In manipulation via AFM in non-contact mode, the image of nanoparticle is taken, the tip oscillation is removed and the tip is approached to particle while maintaining contact with the surface. In manipulation via AFM, larger forces can be applied to the nanoparticle and any object with arbitrary shape can be manipulated in 2D space. However, the manipulation of individual atoms or nanofibers with an AFM is sill a major challenge and practically difficult task (Fukuda and Dong 2003), see Fig. 10.2.

A relatively common manipulation configuration using AFM is to maintain a desired, mostly constant, at the cantilever tip. Hence, the control objective is to move the cantilever base in order to acquire this desired force at the tip. This is a highly demanding mission in nanomanipulation and imaging; for instance, in contact imaging in AFM, there is a need to keep the force at the cantilever's tip in a constant value (Abramovitch et al. 2007; Saeidpourazar and Jalili 2009). Moreover, in almost all of the non-destructive materials characterization and nanomanipulation tasks, there is a need to control the interaction force between the cantilever's tip and the surface or nanoparticle.

Figure 10.7 depicts the schematic of such nanoscale force tracking using a piezoresistive cantilever with a PZT-actuated base. The objective here is to sense the force acting on the piezoresistive cantilever's tip utilizing the output voltage of the piezoresistive beam and smoothly move its base to acquire the desired force on the piezoresistive cantilever's tip. The control objective is to obtain the desired force at the cantilever's tip, which is measured utilizing the output voltage of the piezoresistive layer, V_{out}. Acquiring the force acting on the tip, this force and the desired value for the force are fed back to the controller that generates the suitable control command and sends it to the nanostage as the input voltage V_{in}.

10.1.2 Nanorobotic Manipulation-Based Control and Manipulation

In manipulation via NRMs, much more degrees of freedom (DOFs) including rotation for orientation control of nanoparticle are feasible. For this reason, NRMs can be used for manipulations in 3D space. However, the relatively low resolution of electron microscope in manipulation with NRMs is a limiting factor in this nanomanipulation. A NRM system generally utilizes nanorobot as the manipulation device,

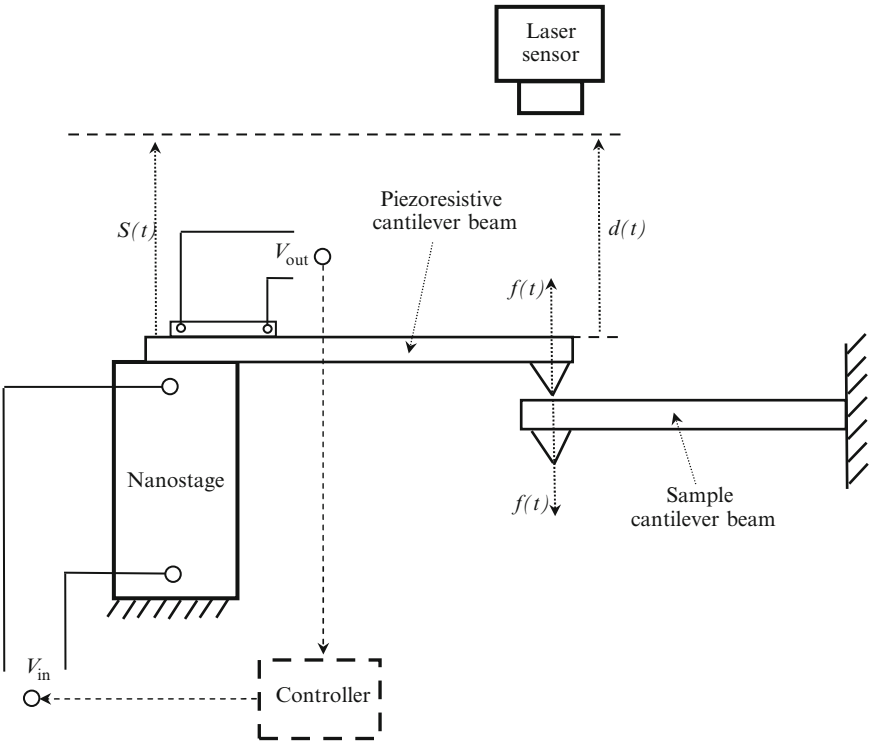

Fig. 10.7 Schematic of the NMC-based force sensing experimental setup
Source: Saeidpourazar and Jalili 2009, with permission

microscopes or CCD camera as visual feedback, end-effectors including cantilevers and tweezers or other type of SPM and some sensors (e.g., force, displacement, tactile and strain) to manipulate nanoparticles (Fukuda and Dong 2003).

Among the variety of available NRM-based configurations, an attractive platform is a 3-DOF nanomanipulator. This nanomanipulator, named as MM3A® and depicted in Fig. 10.8, consists of two rotational motors and one linear Nanomotor® (Kleindiek, Tech Report). The MM3A travels a distance of 1 cm within a second, with up to 1 nm step precision. Using a single drive system, it integrates both coarse and fine manipulations (Saeidpourazar and Jalili 2008a). It also offers a high degree of flexibility; that is, the nanomanipulator is capable of approaching a sample at any angle along the X, Y and Z-axes (Kleindiek, Tech Report; Saeidpourazar and Jalili 2008a).

As mentioned earlier and depicted in Fig. 10.2, one attractive application of NRMs is to manipulate nanofibers, weave and utilize them in a variety of textile-related applications (see Fig. 10.9). The MM3A nanomanipulator combined with a novel fused vision force feedback controller can be utilized to address such a critical need in nano-fabric production automation (Baumgarten 1971; Laxminarayana and Jalili 2005; Hiremath 2006; Hiremath and Jalili 2006).

Fig. 10.8 MM3A nanomanipulator (Kleindiek, Tech Report; Saeidpourazar et al. 2008b)

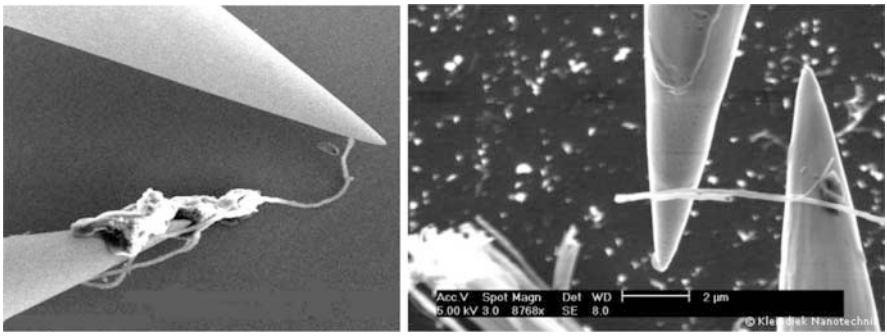

Fig. 10.9 MM3A manipulating nanofibers under Scanning Electron Microscope (SEM)
Source: Kleindiek, Tech Report, with permission

Now that a quick overview of available control and manipulation strategies at the nanoscale is given, the most related configuration to the scope of this book is now considered and discussed. For this, we will review, next, the STM-based control and manipulation platform with mostly covering materials related to their building block, that is, the piezoelectrically actuated nanostages.

10.2 Piezoelectrically Driven Micro- and Nano-Positioning Systems

Piezoelectric materials have become underlying components of variety of positioning and sensing instruments in micro- and nano-scale applications. Replacement of optical measurement devices in scanning probe microscopes with piezoelectric sensors (Takayuki et al. 2004), development of piezoelectric-based gyroscopes (Yang and Fang 2003; Kaqawa et al. 2006), robots and manipulators (Shaoze et al. 2006; Lopez et al. 2001), and other precise positioning and sensing applications demonstrate the significance of such advantageous technology. Although piezoelectrically driven systems benefit many applications with their ultra-fast response and ultrahigh

accuracy, their structural nonlinearities such as creep and hysteresis drastically degrade their performance. As mentioned in Chap. 7, hysteresis, in particular, can induce large positioning errors in the open-loop operation of piezoelectric actuators. Therefore, effective control and positioning methodologies need to overcome such drawbacks for today's industrial and scientific demands. Several examples of piezoelectrically driven micro- and nano-systems were briefly introduced and discussed earlier in Chap. 6.

10.2.1 Piezoelectric Actuators Used in STM Systems

As mentioned in the preceding subsection, one of the most promising precise positioning applications of piezoelectric actuators is in STM systems. A schematic of an in-house STM system is shown in Fig. 10.10, where PZT actuators and their input–output signals are integrated with an STM control system. The STM head movement is performed in three spatial directions. The movement in the Z direction directly affects the scanning precision, while the X and Y directions define the area scanned at the surface. In order to keep the focus here, we will only concentrate on the modeling and control of these actuators in one-, two- and three-dimensional configurations as the building blocks of these systems, and refer the interested reader to cited books and references for other modeling aspects of STM such as tunneling current model and sample–tip interactions (Bardeen 1961).

While the arrangement of PZT actuators could be in any form, the two configurations shown in Fig. 10.10 are common arrangements where both coarse and fine positioning requirements can be accomplished. That is, in Fig. 10.10-top, the STM tip is placed on a fine z-positioner (also shown in Fig. 10.11-left), and the entire z-positioner is placed on a combined x-y coarse positioner, while the sample is placed on a combined x-y fine positioner (also shown in Fig. 10.11-right) attached to a coarse z-positioner. Alternatively, the configuration shown in Fig. 10.10-bottom places the STM tip on a fine z-positioner (similar to the previous configuration), but the entire z-positioner is now placed on a combined x-y-z coarse positioner, while the sample is placed on a combined x-y fine positioner.

10.2.2 Modeling Piezoelectric Actuators Used in STM Systems

The piezoelectric actuators, described above (see Fig. 10.11) and reviewed earlier in Chap. 6, typically consist of a stack of many layers of electro-active solid-state materials, alternatively connected to the positive and negative terminals of a voltage source (see Fig. 10.12).

The dynamic of such system demonstrates the behavior of a distributed-parameters system, which is well described by partial differential equations (Aderiaens et al. 2000). In practice, however, the working frequency of piezoelectric actuators barley exceeds even their first natural frequency. Therefore, the

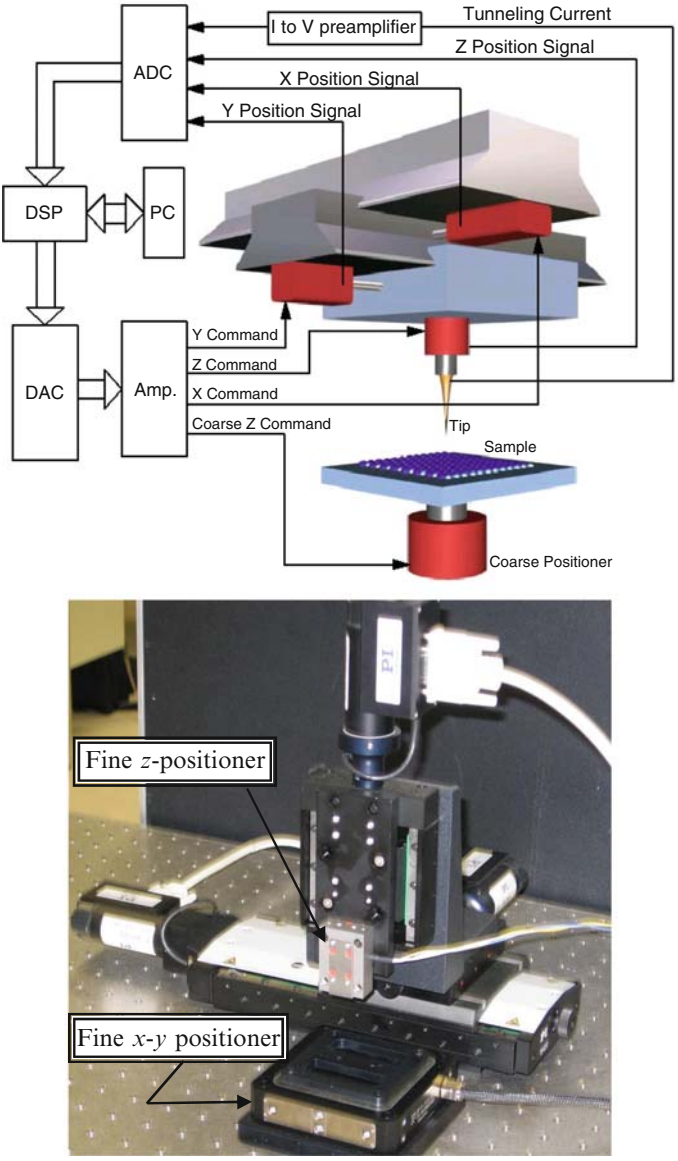

Fig. 10.10 (*top*) Schematic view of STM operation and control system, (*bottom*) experimental setup of the STM module micro/nano-positioner built at Clemson University Smart Structures and NEMS Laboratory

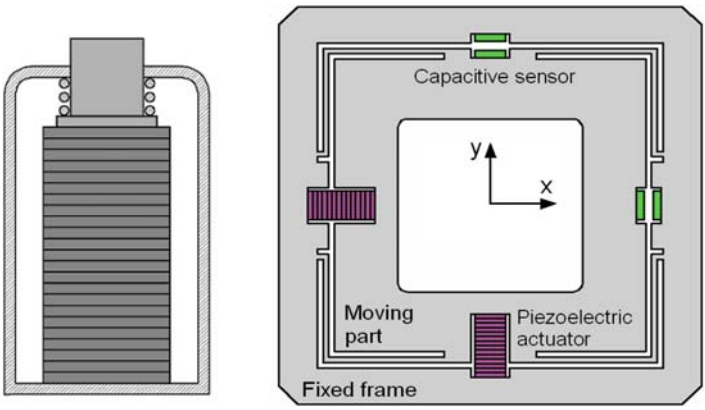

Fig. 10.11 Schematic of piezoelectrically driven fine positioners; (*left*) fine z-positioner and (*right*) combined x-y positioner

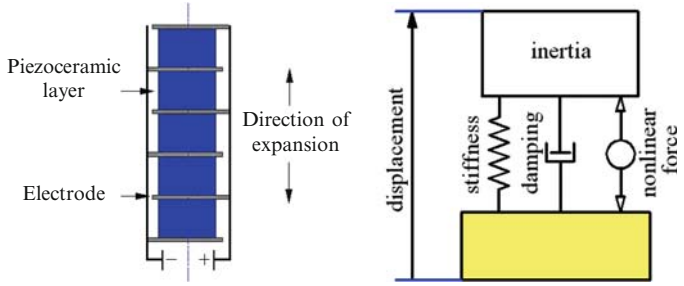

Fig. 10.12 (*left*) Schematic of a typical piezoelectric (linear) actuator, and (*right*) its equivalent dynamic model
Source: Bashash and Jalili 2007b, with permission

distribution of the actuator could be neglected, and the model could be reduced to a lumped-parameters system, typically a second-order model (Hwang et al. 2005; Tzen et al. 2003; Chen et al. 1999; Bashash and Jalili 2007a, b, 2008 and 2009). This is especially valid when they are integrated with flexural mechanical compartments. To capture both hysteretic and dynamic behaviors of these actuators, a second-order linear time-invariant model with a hysteresis operator appeared in the input excitation is proposed (Tzen et al. 2003; Bashash and Jalili 2007a). Hence, as shown in Fig. 10.13, the PZT actuator and STM tip are modeled as a simple mass-spring-damper trio with the governing equation of motion in the z-direction as

$$m_z\ddot{z}(t) + c_z\dot{z}(t) + k_z z(t) = f_z(t) \tag{10.1}$$

where m_z is the total moving mass in the z-direction including the PZT effective mass and STM tip mass (i.e., $m_{ePZT} + m_{tip}$, see Fig. 10.13), and $f_z(t)$ is the equivalent force exerted by the PZT $m_{ePZT} + m_{tip}$ actuator in the z-direction which includes hysteresis nonlinearity and is written as

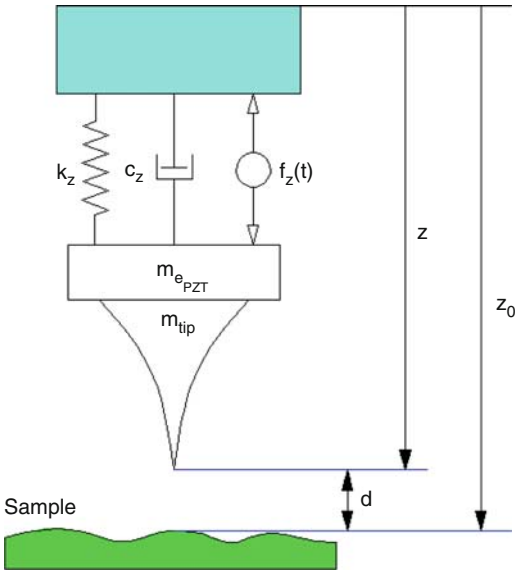

Fig. 10.13 Mathematical model of the STM tip and PZT actuator in the z-direction

$$f_z(t) = H\{V_a(t)\} \tag{10.2}$$

where H denotes the hysteresis nonlinearity (scaled) between the applied input voltage $V_a(t)$ and the generated output force $u_z(t)$ by the actuator.

The governing equation of motion (10.1) can be recast while also renaming the variables slightly, in the following standard second-order differential equation:

$$\ddot{x}(t) + 2\zeta\omega_n\dot{x}(t) + \omega_n^2 x(t) = H\{V_a(t)\} \tag{10.3}$$

where ζ and ω_n are the equivalent damping coefficient and natural frequency of the linear dynamic, respectively, and $x(t)$ is the actuator displacement output (i.e., z(t)).

Piezoelectric actuators have typically very high stiffness, and consequently possess very high natural frequency. In low-frequency operations, the effects of actuator damping and inertia could be safely neglected. Hence, one may reduce the governing equation of motion (10.3) to the following static hysteresis relation between the input voltage and actuator displacement:

$$\omega_n^2 x(t) = H\{V_a(t)\}, \quad \left(\omega_n^2 \gg 2\zeta\omega_n \gg 1\right) \tag{10.4}$$

Equation (10.4) facilitates the identification of the electromechanical hysteresis between the input voltage $V_a(t)$ and the excitation force by identifying the hysteresis between the input voltage and the actuator displacement and scaling it up with a factor of ω_n^2. Most inverse feedforward controllers perform based on the above approximation, which are suitable only for low-frequency operations. As extensively discussed in Chap. 7, proper hysteresis models schemes can be adopted

to identify this nonlinear, yet static relationship. Once this relationship is established, appropriate controllers, either in the form of feedback or feedforward, can be designed to achieve the desired positioning requirements.

Before we discuss the design and development of these controllers, it is worthy to individually evaluate the contribution of other (dynamic) terms in (10.3) that have been ignored in (10.4). For this, we consider the following four scenarios:

$$\ddot{x}(t) + 2\zeta\omega_n\dot{x}(t) + \omega_n^2 x(t) = H\{V_a(t)\} \tag{10.5}$$

$$\omega_n^2 x_1(t) = aV_a(t) \tag{10.6}$$

$$\omega_n^2 x_2(t) = H\{V_a(t)\} \tag{10.7}$$

$$\ddot{x}_3(t) + 2\zeta\omega_n\dot{x}_3(t) + \omega_n^2 x_3(t) = a\omega_n^2 V_a(t) \tag{10.8}$$

where $x(t)$, x_1,(t), $x_2(t)$ and $x_3(t)$ represent the responses to the given input voltage $V_a(t)$, respectively, with $x(t)$ in model (10.5) being the actual system response with both hysteretic and dynamic effects and other responses represent reduced and simplified models as follows. Model (10.6) resembles a linear relation between the input voltage and the actuator displacement (i.e., the effect of hysteresis is ignored); (10.7) proposes a pure static hysteretic relation between the input voltage and the stage displacement (i.e., ignoring the effects of dynamics similar to relationship 10.4); and finally model (10.8) represents a pure dynamic model for the stage without considering its hysteretic behavior.

As discussed earlier, due to the high stiffness, and thereby high natural frequency of these piezoelectric actuators, in low-rate and low-frequency operations where velocity $\dot{x}(t)$ and acceleration $\ddot{x}(t)$ are small, the effects of first two terms in (10.5), that is, inertia and damping terms, become negligible. Therefore, (10.5) can be safely reduced to that of (10.7), and model (10.8) can be safely reduced to (10.6). It is expected that for low-frequency operation, hysteresis model (10.7) can precisely predict the system response if the hysteresis nonlinearity is properly modeled and identified. In high-frequency operations, however, it is expected to see deviations from the actual system response when model (10.7) is utilized since the effects of system dynamics have been neglected.

To evaluate the effects of different assumptions and demonstrate the modeling accuracy for each of the proposed models of (10.5–10.8), two low ($\pm 10\,\mathrm{V/s}$)- and high ($\pm 1,000\,\mathrm{V/s}$)-rate triangular inputs with the same profiles are generated and implemented on an x-y nano-positioning system depicted in Fig. 10.11-right. The hysteresis model proposed in Sect. 7.3 is used and implemented here. Figure 10.14 depicts the low-rate experimental comparison of the system response for each of the models (10.5–10.8). From the similarity of the results seen in Figs. 10.14(a) with 10.14(c), as well as 10.14(b) with 10.14(d), it can be concluded that the effects of system dynamics are negligible for this low-rate operation as expected. Figure 10.15 demonstrates the high-rate responses of the models compared to that of the actual system. It can be clearly seen that only the combined hysteretic dynamic model (10.5) can precisely represent the actual system response. Other models lack accuracy because of ignoring either hysteresis or dynamics or both of them.

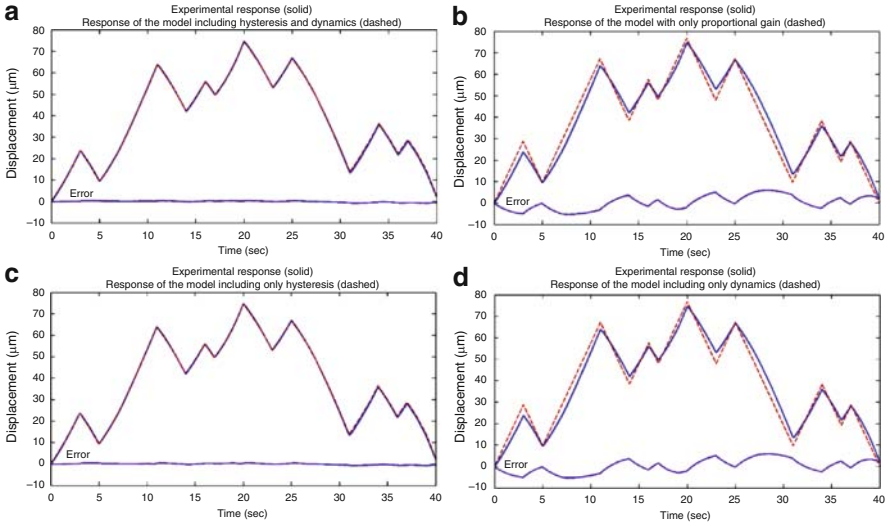

Fig. 10.14 Low-rate response of the x-y nano-positioning actuator compared to responses of (**a**) combined hysteretic and dynamics model, (**b**) proportional model, (**c**) pure hysteretic model, and (**d**) pure dynamic model (Bashash 2008)

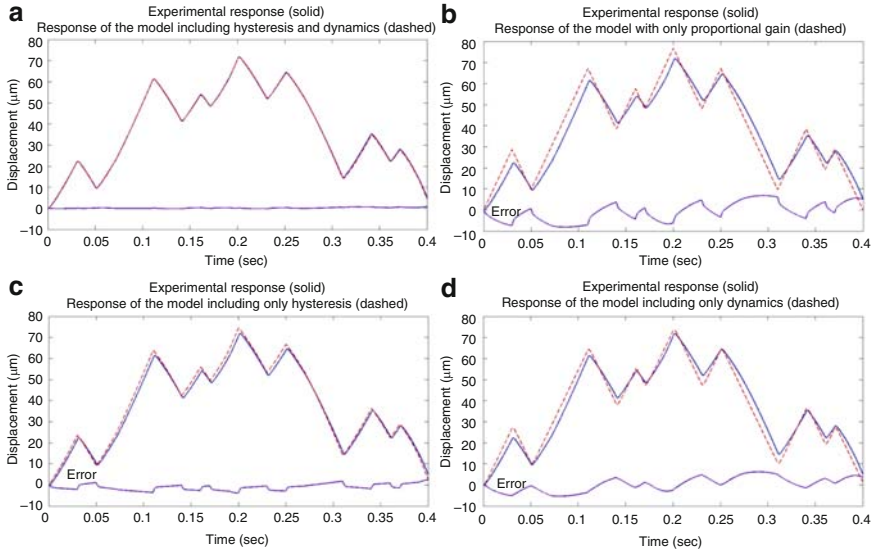

Fig. 10.15 High-rate response of x-y nano-positioning actuator versus responses of (**a**) combined hysteretic and dynamic, (**b**) proportional, (**c**) pure hysteretic and (**d**) pure dynamic models (Bashash 2008)

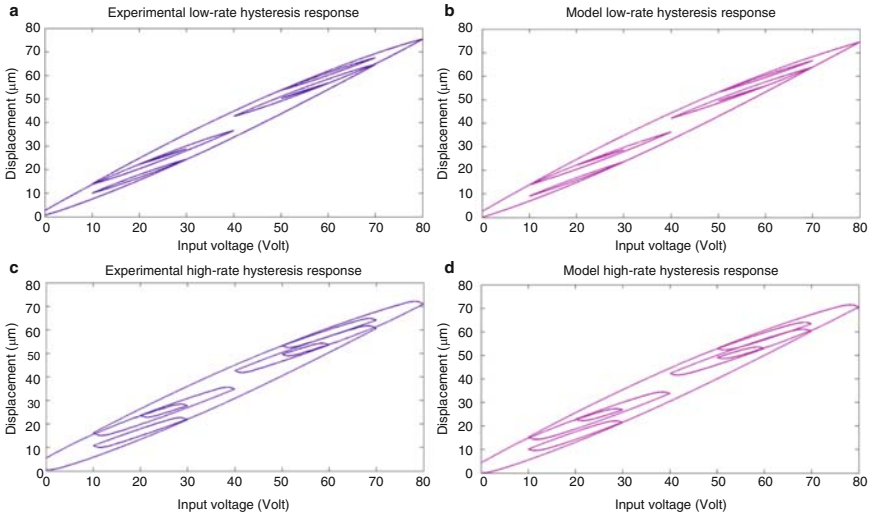

Fig. 10.16 (**a**) Low-rate experimental, (**b**) low-rate model, (**c**) high-rate experimental and (**d**) high-rate model hysteresis responses of the actual and simulated x-y nano-positioning actuator (Bashash 2008)

It is evident that for higher rate input excitation, the effect of system dynamics become more visible, while the effect of hysteresis nonlinearity remains the same. To demonstrate this, Fig. 10.16 demonstrates the input/output hysteresis responses of the actual system and model (10.5–10.8) for the given low- and high-rate inputs. As expected, the hysteresis loops are expanded as the input rate increases, due to the further induced hysteresis from the system damping. It is also realized that the combined model (10.5) not only precisely predicts the hysteresis response for the low-rate operations, but also effectively incorporates the effects of rate variation. Table 10.1 provides a more quantitative comparison of modeling errors among the different representative models.

10.3 Control of Single-Axis Piezoelectric Nano-positioning Systems[1]

As discussed in Sect. 7, hysteresis models typically have complicated structures due to the multi-branch and memory-dependent behavior of the phenomenon. One promising approach that briefly discussed in Sect. 7.3 is to use charge-driven circuits such that an input charge can be applied in a controlled way. However, the

[1] The materials for this section may have come, either directly or collectively, from our recent publication (Bashash and Jalili 2007b).

Table 10.1 Maximum and mean-square modeling error values for different models in low- and high-rate operations (Bashash 2008)

Model type	Low-rate input		High-rate input	
	Maximum error (%)	Mean-square error (μm)	Maximum error (%)	Mean-square error (μm)
Model including hysteresis and dynamics, (10.5)	1.24	0.26	1.04	0.21
Model with only a proportional gain, (10.6)	7.75	2.69	11.24	3.76
Model including only hysteresis nonlinearity, (10.7)	1.22	0.26	5.40	1.48
Model including only dynamics, (10.8)	7.73	2.68	8.60	2.84

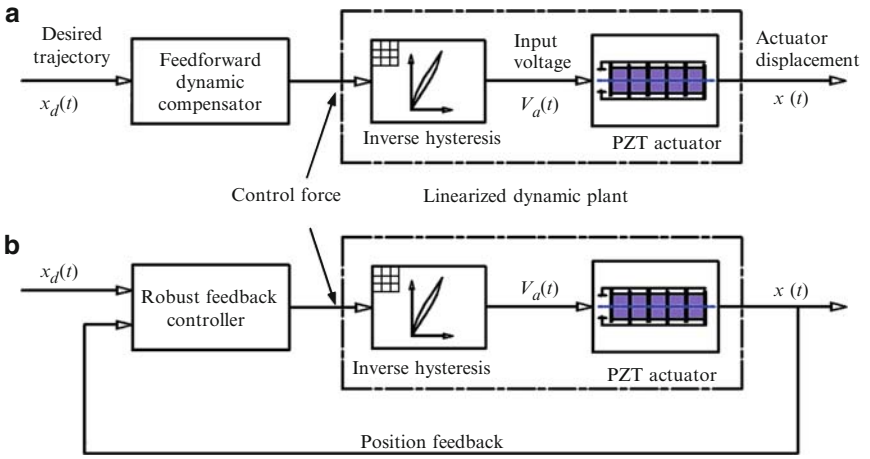

Fig. 10.17 Control schemes for position control of piezoelectric actuators; (**a**) inverse model-based feedforward, and (**b**) robust variable structure feedback controllers

need for expensive instrumentation, amplification of the measurement noise, and reduction in the system responsiveness are the main drawbacks of charge-driven strategy (Moheimani and Fleming 2006; Salah et al. 2007). Therefore, many applications prefer to utilize voltage-driven strategy and compensate hysteresis effect with inverse models through either feedforward (see Fig. 10.17a) or feedback (see Fig. 10.17b) controllers. These compensatory techniques are presented, next, for control of single-axis piezoelectric nanostages.

10.3.1 Feedforward Control Strategies

As mentioned earlier, feedforward schemes essentially employ an inverse hysteresis model to compensate for this nonlinearity as a dominant source of inaccuracy in low-frequency operations, see Fig. 10.17a (Bashash and Jalili 2007a, 2008; Lining et al. 2004; Changhai et al. 2004; Changhai and Lining 2005). However, to compensate for the effects of frequency-dependent dynamics, rate-dependent hysteresis model are proposed (Ang et al. 2003). Feedforward controllers are cost-effective, easy to implement and do not require deep knowledge of control theory. However, in many practical applications, this is the only control solution due to lack of feedback sensors and/or sophisticated control hardware.

To better demonstrate this technique, an inverse model-based feedforward controller is introduced and experimentally implemented on the piezoelectrically driven nano-positioning system of Fig. 7.7 for tracking control of multiple-frequency trajectories. Augmenting model (10.3) with an ever-present perturbation term to present a more realistic situation, the system dynamics can be represented as

$$\ddot{x}(t) + 2\zeta\omega_n\dot{x}(t) + \omega_n^2 x(t) = H\{V_a(t)\} + p(t) \tag{10.9}$$

where $p(t)$ is the influence of the parametric uncertainties, unknown terms and other ever-present unmodeled dynamics. For the system described by (10.9), a feedforward control law is proposed as

$$V_a(t) = H^{-1}\{\ddot{x}_d(t) + 2\zeta\omega_n\dot{x}_d(t) + \omega_n^2 x_d(t)\} \tag{10.10}$$

with $x_d(t)$ being the desired trajectory. Substituting the control law (10.10) into the system equation of motion results in the following error dynamics

$$\ddot{e}(t) + 2\zeta\omega_n\dot{e}(t) + \omega_n^2 e(t) = -p(t) \tag{10.11}$$

where $e(t) = x_d(t) - x(t)$ represents the tracking error. It can be interpreted from (10.11) that if the magnitude of the model perturbation $p(t)$ is bounded, the error signal is bounded and the feedforward controller leads to a uniformly stable tracking, since all coefficients of the system error and its first and second time derivatives are positive (see Appendix A, Sections A.4, for more details on the stability and boundedness of similar dynamic systems). However, the magnitude of the error depends on the model perturbations which appear as a forcing function to the second-order error dynamics. In low-frequency operation, such perturbation originates from the hysteresis model inaccuracy, and in high frequencies, the dynamic model inaccuracy adds to these perturbations as discussed in the preceding subsection (see Figs. 10.14 and 10.15).

Taking into account all the real-time implementation (e.g., measurements noise, digital signal processing delay), Figs. 10.18–10.20 depict the experimental and numerical tracking performance of controller (10.10) for low-, moderate- and high multiple-frequency trajectories, respectively (Bashash and Jalili 2007a). In order to

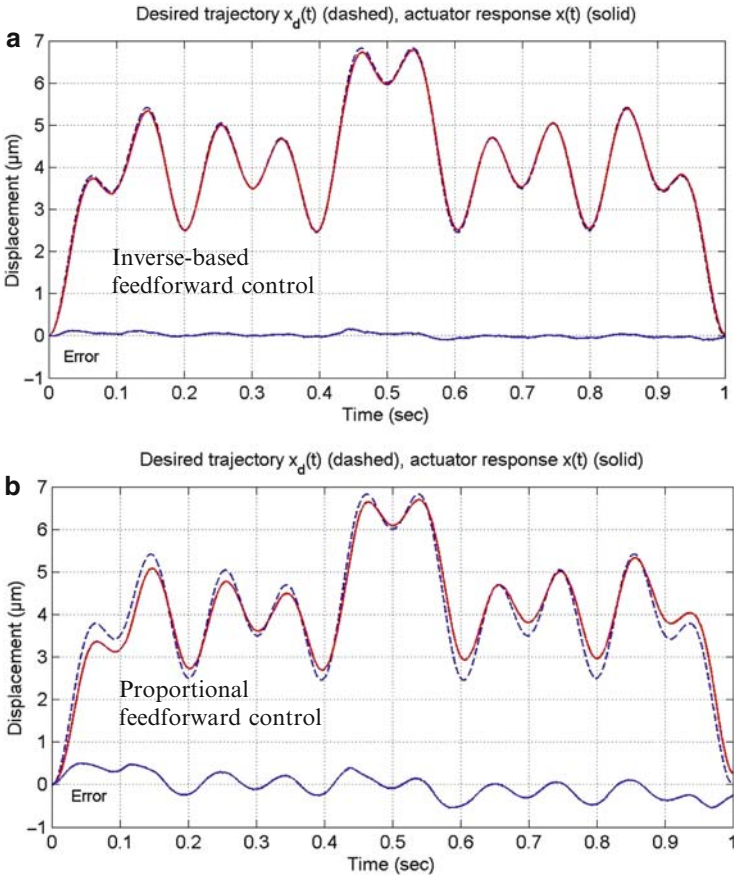

Fig. 10.18 Multiple-frequency trajectory tracking results for (**a**) inverse feedforward, and (**b**) proportional, in low-frequency (ranging from 1 to 10 Hz) operation
Source: Bashash and Jalili 2007b, with permission

evaluate the effectiveness of the controller, a proportional controller, which operates based on a single input/output conversion gain, is also tested and compared with the inverse feedforward controller for the given trajectories. The practical application of such trajectories could include SPM which is utilized for topography tracking of uniform and non-uniform surface profiles (Binnie et al. 1982; Bardeen 1961; Bashash 2005; Stroscio and Kaiser 1993). A summary of details of the desired trajectories as well as the maximum and mean-square values of the tracking error are all given in Table 10.2.

From the results given in Figs. 10.18–10.20, it is clear that the inverse feedforward controller is able to significantly suppress the tracking error originated form hysteresis nonlinearity and system dynamics in both low- and high-frequency operations. The results for the proportional controller demonstrate, however, that if the

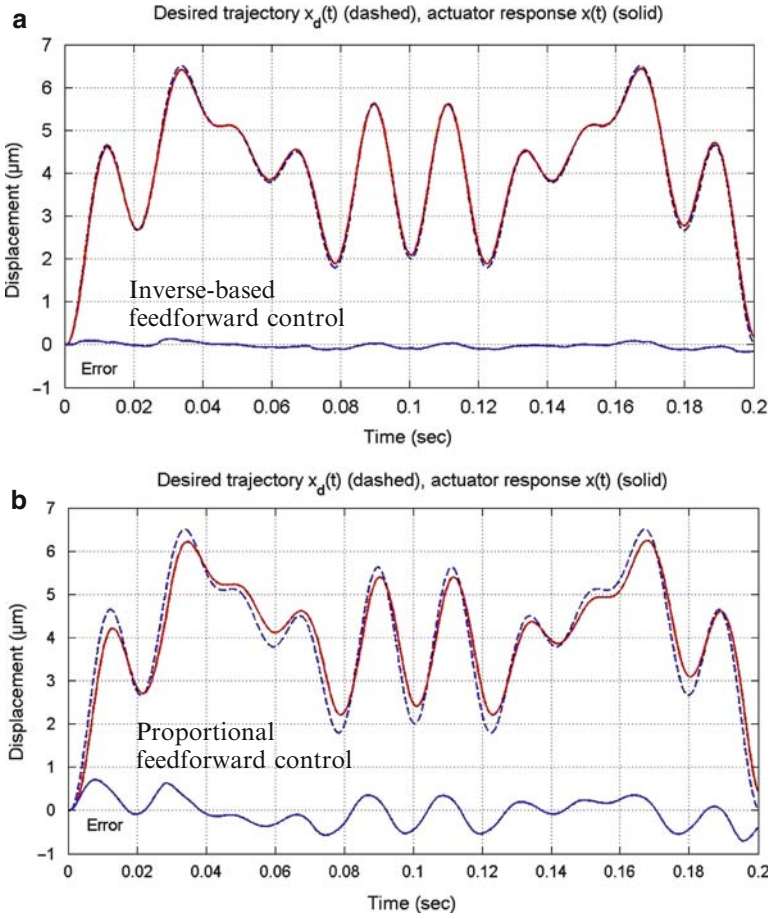

Fig. 10.19 Multiple-frequency trajectory tracking results for (**a**) inverse feedforward, and (**b**) proportional, in moderate-frequency (ranging from 10 to 50 Hz) operation
Source: Bashash and Jalili 2007b, with permission

frequency of operation increases, the tracking error increases as well, resulting in poor tracking performance. It must be noted that the proportional gain in the proportional feedforward is simply obtained through a least square optimization for the input/output data provided by a quasi-static loading.

10.3.2 Feedback Control Strategies

Integrating the feedforward hysteresis linearization with an additional feedback controller as depicted in Fig. 10.17b could significantly improve the trajectory tracking performance. Utilizing the sliding mode control strategy, adaptive control methods,

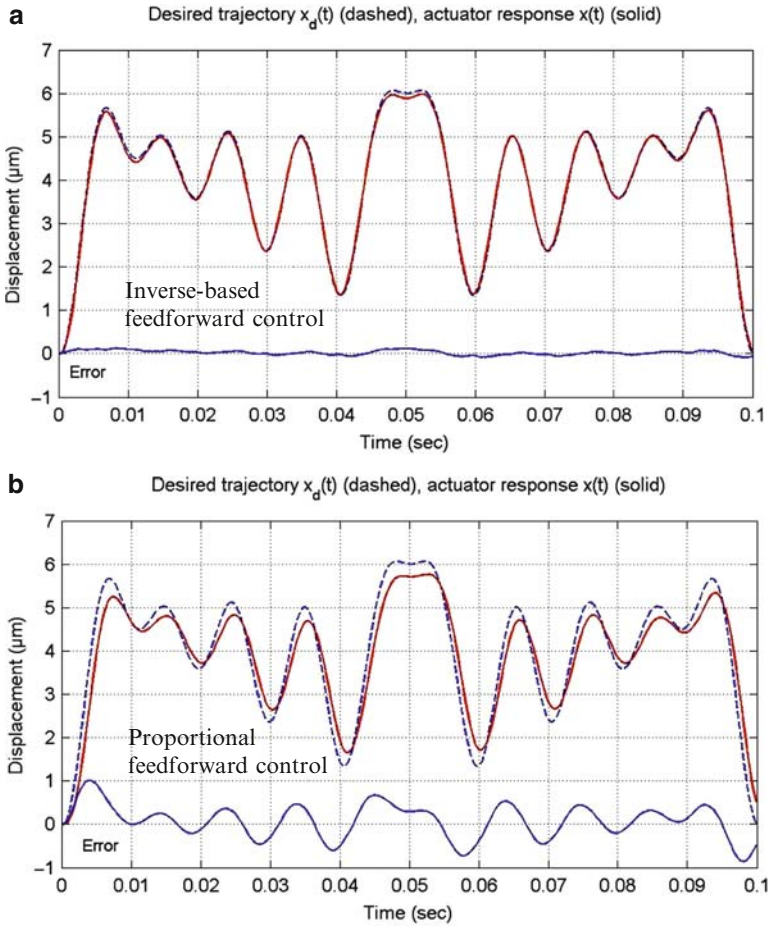

Fig. 10.20 Multiple-frequency trajectory tracking results for (**a**) inverse feedforward, and (**b**) proportional, in high-frequency (ranging from 30 to 100 Hz) operation
Source: Bashash and Jalili 2007b, with permission

Table 10.2 Trajectory profiles and tracking error values for feedforward control strategy

Desired trajectory profile (μm)	(Exp. run), controller	Maximum error (%)	Mean-square error (μm)
$4-[\cos(2\pi t)+\cos(6\pi t)$	(a) Inverse FF	2.34	0.04
$+\cos(10\pi t)+\cos(20\pi t)]$	(b) *Proportional FF*	*8.03*	*0.23*
$4-[\cos(20\pi t)+\cos(30\pi t)$	(c) Inverse FF	2.70	0.06
$+\cos(80\pi t)+\cos(100\pi t)]$	(d) *Proportional FF*	*10.92*	*0.27*
$4-[\cos(60\pi t)+\cos(100\pi t)$	(e) Inverse FF	2.12	0.05
$+\cos(140\pi t)+\cos(200\pi t)]$	(f) *Proportional FF*	*16.66*	*0.32*

the perturbation estimation technique for the real-time identification and compensation of the nonlinearities, and also employing charge measurement-based feedback controllers will be among the most commonly control frameworks toward achieving the precision trajectory requirement needed in the piezoelectrically driven nanopositioning systems utilized in STM- and other SPM-based systems.

The overall uncertainties of the feedforward methods and the presence of external disturbances necessitate the use of feedback control, particularly at higher frequencies (see Fig. 10.20b). Many feedback schemes utilize a PID (Proportional-Integral-Derivative) controller to overcome the drawbacks of feedforward compensators (Ping and Musa 1997; Changhai et al. 2004). Although significant improvements are achieved in low frequencies, a continuous increase in tracking error is observed as the frequency increases. On the other hand, robust and adaptive control schemes have also been developed, most of which require a representative hysteresis model (Bashash and Jalili 2007b, Hwang et al. 2005). There are also reported research works where no hysteresis model is required (Salapaka et al. 2002; Huang and Cheng 2004); although performance is improved compared to classical methods, parametric uncertainties are not effectively taken into account, thereby not compensated effectively. The fact that a robust controller loses its performance to compensate for disturbances originated from parametric uncertainties elucidates the need for robust adaptive methods where high-performance operations are demanded. Most asymptotic robust schemes such as sliding mode control are not practical due to the chatter phenomenon associated with their variable structure nature (Slotine and Sastry 1983). In turn, adaptive methods are capable of completely eliminating or otherwise significantly reducing the effects of uncertainties in system parameters (Sastry and Bodson 1989; Zhou et al. 2004; Su et al. 2000). The control problem becomes more involved when the system is subjected to other sources of uncertainties such as cross-coupling effect in multiple axes operation.

As a demonstrable example case study for hysteresis compensation using feedback, a Lyapunov-based robust variable structure controller is considered here. More specifically, a well-known subclass of variable structure control, known as the sliding mode control strategy, is used here (Slotine 1984). The objective of sliding mode control is to design asymptotically stable hyperplanes so that all system trajectories converge to these hyperplanes and slide along their path and ultimately approach their desired destinations (Slotine 1984). To simultaneously satisfy tracking control and robustness requirements, the sliding hyperplane is selected as both a function of tracking error and its first time derivative. It is expressed as

$$s(t) = \dot{e}(t) + \sigma\, e(t) \tag{10.12}$$

where $\sigma > 0$ is a control parameter and $e(t) = x_d(t) - x(t)$ represents the tracking error. Based on this equation, if through some control law, $s(t)$ is forced to move toward zero, $e(t)$ and $\dot{e}(t)$ also exponentially approach zero and stability of the system is attained (see Appendix A, Section A.4, for details and stability proof). To control the piezoelectric actuator displacement against the system perturbations, the

following controller for the system described by (10.9) is introduced (Bashash and Jalili 2007b).

$$V_a(t) = H^{-1}\left\{\ddot{x}_d(t) + 2\xi\omega_n\dot{x}(t) + \omega_n^2 x(t) + \sigma\dot{e}(t) + \gamma\text{sgn}\left(s(t)\right) + \lambda s(t)\right\} \tag{10.13}$$

where sgn(·) represents the signum function, and γ and λ are the positive scalar parameters. Selecting the positive definite Lyapunov function candidate $V = s^2/2$, taking its first derivative, using (10.9), (10.12), and (10.13) and after some manipulations, it yields

$$\dot{V} = -\lambda s^2 - \gamma\,\text{sgn}(s)s - p(t)s = -\lambda s^2 - \gamma\,|s| - p(t)s \tag{10.14}$$

If gain γ is selected so that the condition $\gamma > |p(t)|$ is satisfied, then $\dot{V} \leq -\lambda s^2$, and hence $s(t) \to 0$ as $t \to \infty$. Therefore, asymptotic task-space and subtask tracking of the system is guaranteed in the sense that the signal $e(t)$ is bounded. Therefore, $e(t)$ and $\dot{e}(t) \to 0$ as $t \to \infty$ (Slotine 1984; Bashash and Jalili 2007b).

Remark 10.1. The discontinuous response of the signum function used in the control law leads to the undesirable effect of the chattering phenomenon, which may lead to experimental instability. To avoid such problems in practice, the high-gain saturation function, $\text{sat}(s/\varepsilon)$, which is a refined continuous form of the signum function, is used. Although the system maintains stability, only a zone convergence is guaranteed. However, the steady-state error dynamics $|s|$ can be ensured to be always bounded by ε ($s < \varepsilon$). Parameter ε must be chosen in a tradeoff to keep the chattering and error magnitudes small.

Remark 10.2. Parameter γ is the robustizing feature of the controller that must satisfy stability condition $\gamma > |p(t)|$. Large perturbation amplitude requires selection of large values for γ, which may cause large chattering amplitude when using the signum function, and a large tracking error when using the high-gain saturation function. Therefore, precise hysteresis cancellation with the introduced inverse hysteresis model can significantly improve the stability of the closed-loop controller by reducing the amplitude of model perturbations, and subsequently increasing the control performance.

Leaving much of the details to Bashash and Jalili (2007b), the controller (10.13) can be augmented with a perturbation estimation term to estimate the model perturbations online as (Elamli and Olgac 1992, 1996)

$$v(t) = H^{-1}\{\ddot{x}_d(t) + 2\xi\omega_n\dot{x}(t) + \omega_n^2 x(t) + \sigma\dot{e}(t) + \gamma\text{sgn}(s) + \lambda s(t) - p_{\text{est}}(t)\} \tag{10.15}$$

where the perturbation estimation function used in this controller is obtained as

$$p_{\text{est}}(t) = \ddot{x}(t) + 2\xi\omega_n\dot{x}(t) + \omega_n^2 x(t) - H\{V_a(t-\tau)\} \tag{10.16}$$

with τ being a small sampling time.

Figure 10.21 depicts the block diagram of the control strategy considered here. Tracking performance of the controller is examined for different low- and high-speed single- and multiple-frequency trajectories as shown in Fig. 10.22. Using a gain approximation procedure and with the help of experimental results, the fine-tuned gain values for σ, λ, γ and ε are obtained as 4,000, 255,000, 50 and 0.002, respectively (Bashash and Jalili 2007b).

10.4 Control of Multiple-Axis Piezoelectric Nano-positioning Systems[2]

As mentioned earlier in Sect. 10.2 and schematically shown in Fig. 10.23, a double-axis piezoelectric nano-positioning system is utilized for scanning purposes, that is, either carrying the tip or moving the sample in x- and y- directions. In this section, a double-axis parallel piezo-flexural frictionless nano-positioning system capable of high precision scanning in two directions is first modeled and discussed extensively for variety of trajectory tracking applications used in SPM-based systems, especially STMs. Combining this nano-positioner with the single-axis actuator of Fig. 7.7 (see Sect. 7.3.1), a combined x-y-z nano-positioning system result that can be used for the combined tasks of tip motion in z-direction as well scanning in x-y directions.

10.4.1 Modeling and Control of Coupled Parallel Piezo-Flexural Nano-Positioning Stages

Parallel piezo-flexural stages are high precision frictionless nano-positioning systems providing multiple-axis displacements with nanometer resolution and micrometer travel ranges. They are utilized in many applications including SPM (Curtis et al. 1997; Gonda et al. 1999), micro-robotics and medical surgery (Hesselbach et al. 1998; Akahori et al. 2005), adaptive optics (Aoshima et al. 1992; Henke et al. 1999) and semiconductor fabrication (Kajiwara et al. 1997). However, the presence of hysteresis nonlinearity in the piezoelectric elements, the combined piezo-flexure dynamics, and the nonlinear interference of motions in different axes are some of the roadblocks for precision tracking control of time-varying desired trajectories.

In this section, a Lyapunov-based robust adaptive controller for simultaneous tracking of this double-axis nano-positioning stage is presented. In particular, two piezoelectric stack actuators move a single flexural stage in perpendicular directions, enabling precision scanning but causing undesirable motion interference.

[2] The materials for this section may have come, either directly or collectively, from our recent publication (Bashash and Jalili 2009).

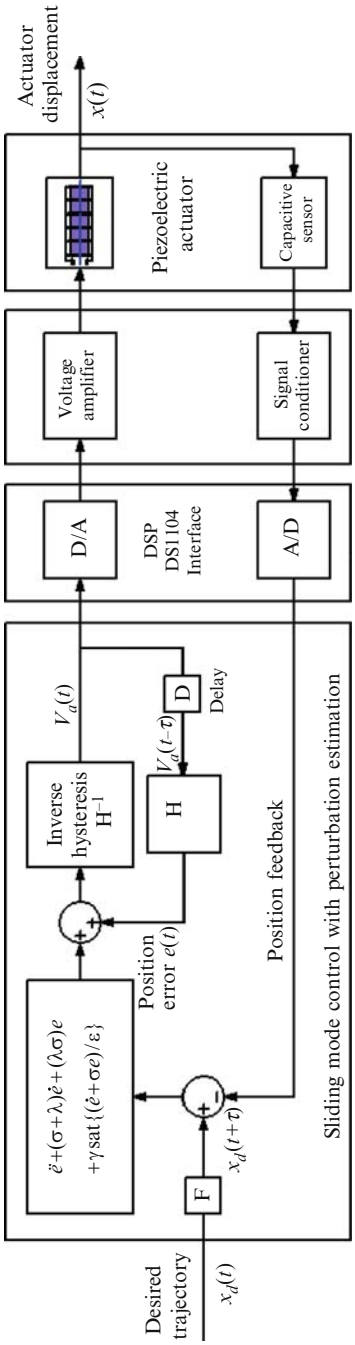

Fig. 10.21 Block diagram of real-time controller implementation
Source: Bashash and Jalili 2007b, with permission

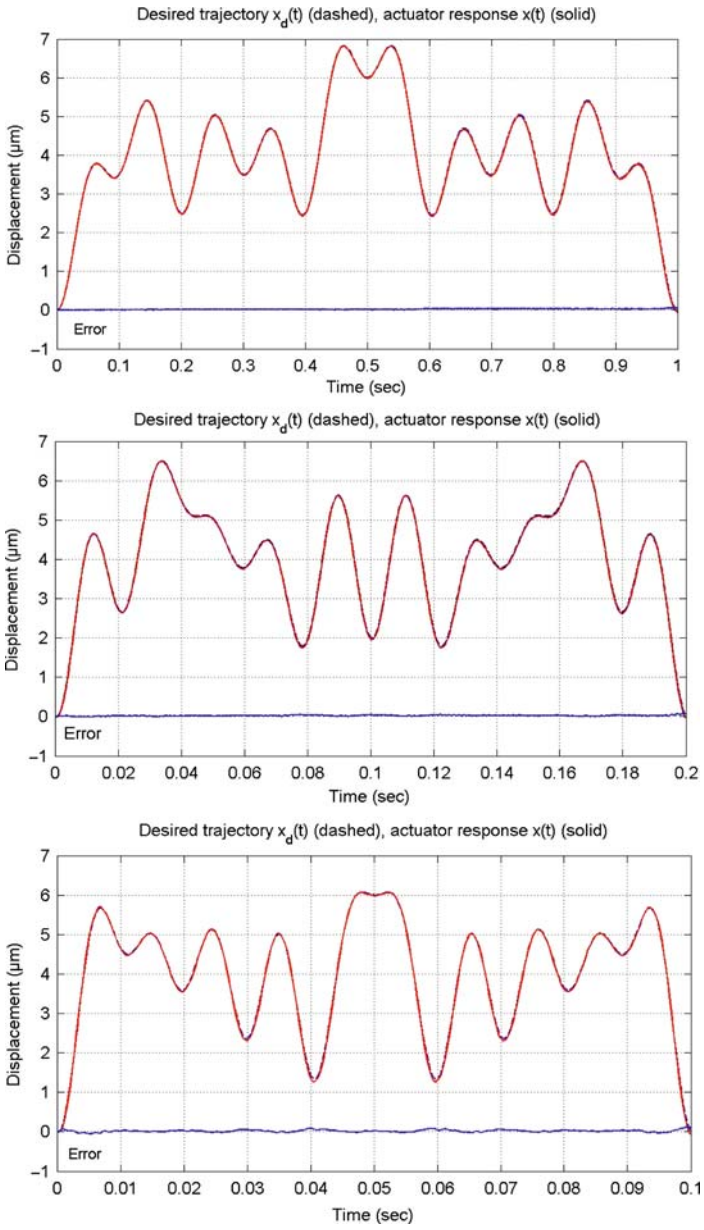

Fig. 10.22 Piezoelectric actuator displacement tracking trajectory results; (*top*) low-speed multi-frequency sinusoidal in the range of 1–10 Hz, (*middle*) moderate-speed multi-frequency sinusoidal in the range of 10–50 Hz, and (*bottom*) high-speed multi-frequency sinusoidal trajectories in the range of 30–100 Hz
Source: Bashash and Jalili 2007b, with permission

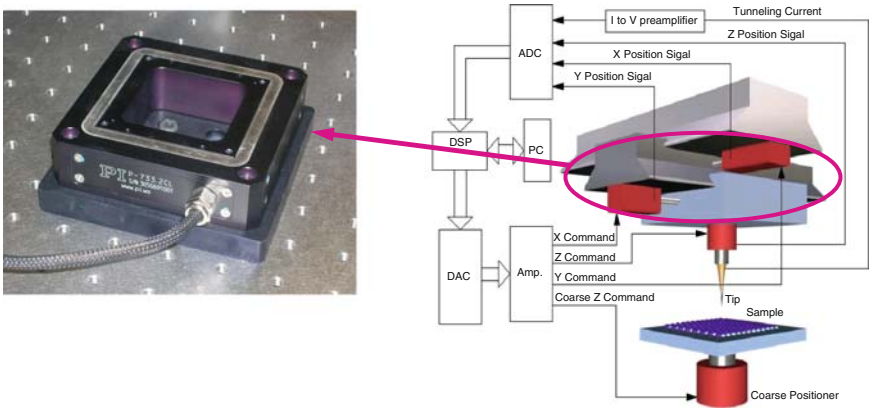

Fig. 10.23 Schematic of STM operation and parallel piezo-flexural nano-positioner utilization for sample/tip movement in x-y directions

System Configuration and Preliminary Observations: Piezo-flexural systems have been developed to respond to the demand for multiple-axis micro- and nano-scale motions for a wide range of displacements. They comprise of several piezoelectric stack actuators, usually made from PZT connected to a flexural mechanism to handle the multiple-axis motion for a single moving stage. A flexure is a frictionless mechanism which operates based on the elastic deformation of a solid part made from a stiff metal, providing maintenance-free and perfectly guided motion without any stick–slip effect.

A Physik Instrumente P-733.2CL double-axis parallel piezo-flexure stage with high-resolution capacitive position sensors is considered here for the experiments (see Fig. 10.24). Experimental data interfacing is carried out through a Physik Instrumente E-500 chassis for PZT amplifier along with DS1103 dSPACE® data acquisition and controller board. As shown in Fig. 10.24b, two piezoelectric stacks are preloaded by a wire-cut flexural stage with the ability to push in two perpendicular directions and generate a simultaneous double-axis motion. Since both actuators move a single stage, the system configuration is called *parallel-kinematics*. In addition to accurate positioning, system has the advantage of identical resonant frequencies and dynamic behavior in both directions.

Similar to single-axis PZT-driven nano-positioning system, piezo-flexural stages exhibit hysteretic response from their piezoelectric side, and dynamic behavior from their combined stack/flexure configuration, due to the flexibility, inertia and structural damping. The system dynamics for each of the axes are governed by the same model as in (10.3).

Using this piezo-flexural nano-positioner, several experiments are performed to observe the hysteresis behavior of each axis in different frequencies, when the other axis is not in action. Figure 10.25 demonstrates the hysteresis responses of the stage (x-axis) for two different sinusoidal inputs with 0.1 Hz and 20 Hz frequencies. The response of the system to 0.1 Hz input signal reflects only the hysteresis behavior

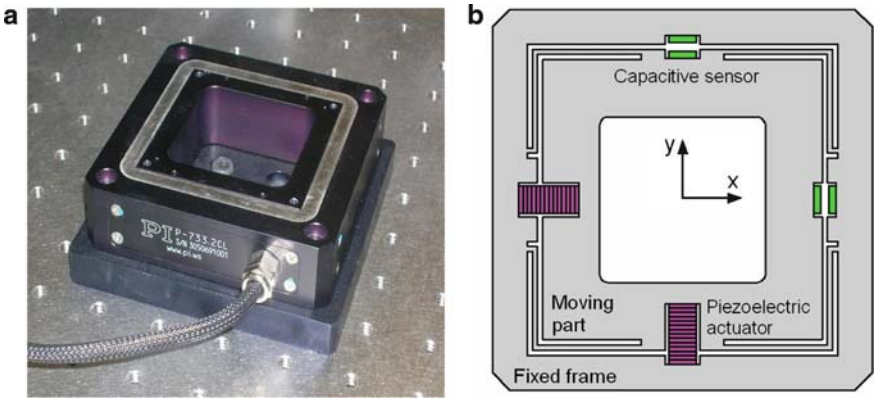

Fig. 10.24 Parallel piezo-flexural system configuration: (**a**) Physik Instrumente P-733.2CL double-axis parallel piezo-flexure stage for the experiments, and (**b**) its schematic representation
Source: Bashash and Jalili 2009, with permission

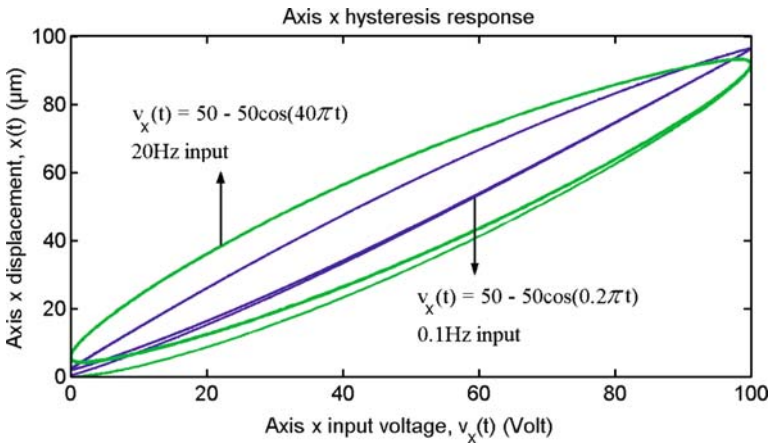

Fig. 10.25 Hysteresis response of x-axis of the piezo-flexural nano-positioner to 0.1 Hz and 20 Hz inputs (Similar responses are observed for y-axis)
Source: Bashash and Jalili 2009, with permission

of the material, since the loading can be considered as quasi-static; however, as the frequency increases to 20 Hz, the influence of the system dynamics merges into the hysteresis response, and the overall response becomes frequency dependent. It is remarked that similar responses are obtained for the other axis of the stage.

It is worthy to note that these systems typically suffer from a nonlinear cross-coupling phenomenon which originates from the asymmetrical arrangement of the actuators. That is, when the nano-positioner moves in one direction, the actuator in the other direction, which is tightly compressed between the moving surface and the stationary part, may rotate and deform due to the strong preload and the frictional

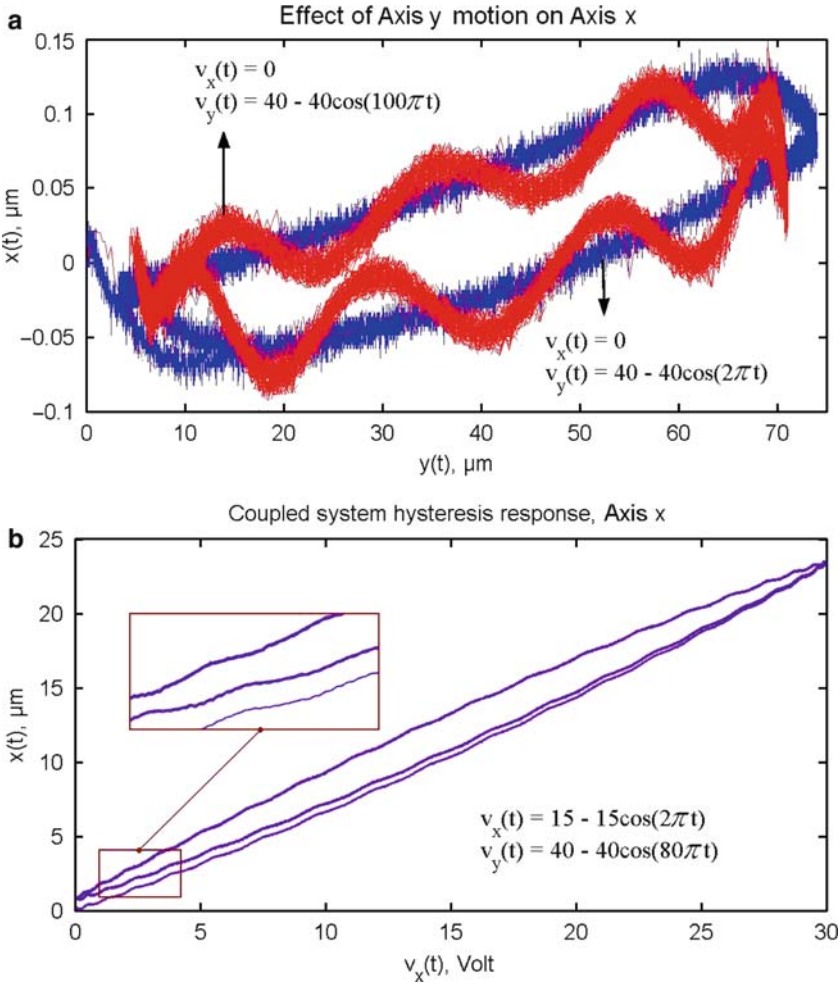

Fig. 10.26 Cross-coupling effect of y-axis motion on x-axis: (**a**) when x-axis is inactive while y-axis is excited by 1 Hz and 50 Hz inputs, and (**b**) coupled hysteresis response of x-axis in 1 Hz when y-axis is excited by 40 Hz input; (Similar responses are obtained for y-axis as a result of x-axis motion)
Source: Bashash and Jalili 2009, with permission

forces. The piezoelectric stacks, on the other hand, may slip on each other due to the generated shear force. The combined rotation, compression and slip effects influence the stage motion in the other direction. This cross-coupling becomes even more disruptive at high frequencies, particularly when it is close to the system natural frequency.

Figure 10.26a demonstrates the experimental coupling responses when one axis is neutral and the other axis is excited with 1 Hz and 50 Hz harmonic inputs. It is observed that the couplings in two directions are similar but demonstrate different

behavior in different frequencies. Comparing the coupling phenomenon with hysteresis, one can view their similar nature; however, the main difference can be in their input excitation sources; the input of hysteresis is the applied voltage, while coupling originates from the motion of other axis. Hence, the following model representing the coupling phenomenon for neutral axis when the other axis is under excitation is considered:

$$\ddot{x}(t) + 2\zeta\omega_n\dot{x}(t) + \omega_n^2 x(t) = \omega_n^2 C\{y(t)\} \tag{10.17}$$

where $x(t)$ is the neutral axis, $y(t)$ is the moving axis and $C\{y(t)\}$ is a nonlinear operator representing the coupling phenomenon. It is noticeable that about 0.3% of one axis motion is transferred into the other axis through this coupling. This may reduce the precision of open-loop and the stability of the closed-loop system if not effectively compensated.

When both axes are under simultaneous excitations, not only the hysteresis influences the response, but also the coupling phenomenon disturbs the performance. Figure 10.26b depicts hysteresis response of x-axis in 1 Hz when y-axis is excited by 40 Hz input. This shows that the motion of high-frequency axis induces a small-amplitude wave on the hysteresis response of the low-frequency axis.

The governing equations of motion can now be obtained through the superposition of the hysteretic excitation (10.3) and the coupling effect (10.17) for each of the axes. Hence, the following pair of equations represent the double-axis motion of the nano-positioner.

$$\begin{aligned}
\ddot{x}(t) + 2\zeta_x\omega_{nx}\dot{x}(t) + \omega_{nx}^2 x(t) &= \omega_{nx}^2\left(H_x\{V_{ax}(t)\} + C_{yx}\{y(t)\} + D_x(t)\right)\\
\ddot{y}(t) + 2\zeta_y\omega_{ny}\dot{y}(t) + \omega_{ny}^2 y(t) &= \omega_{ny}^2\left(H_y\left\{V_{ay}(t)\right\} + C_{xy}\{x(t)\} + D_y(t)\right)
\end{aligned} \tag{10.18}$$

where $D_{x/y}(t)$ represents the influence of the external disturbances on the system, with x and y subscripts specifying the parameters, operators and inputs for the corresponding axis.

Proportional-Integral (PI) Control of Piezo-flexure Nano-positioner: The use of conventional Proportional-Integral (PI) controller is a common practice for many positioning systems. Along this line, the PI controller is utilized here for trajectory tracking applications using the piezo-flexure nano-positioner. Using a trial-and-error exercise for the proportional and integral control gains, Fig. 10.27 depicts tracking results when both axes are forced to simultaneously track desired trajectories with different frequencies and nonzero initial values. The desired trajectories include 60 μm peak-to-peak sinusoids in 5 Hz and 50 Hz for x-axis and y-axis, respectively. The achieved maximum steady-state tracking error is 1% for x-axis and 20% for y-axis. With further increasing gains for a better performance, system tends to instability. Although results indicate excellent steady-state tracking for the low-frequency trajectory, its transient response includes large overshoot and undesired oscillations. On the other hand, improving overshoot by tuning the gains decreases

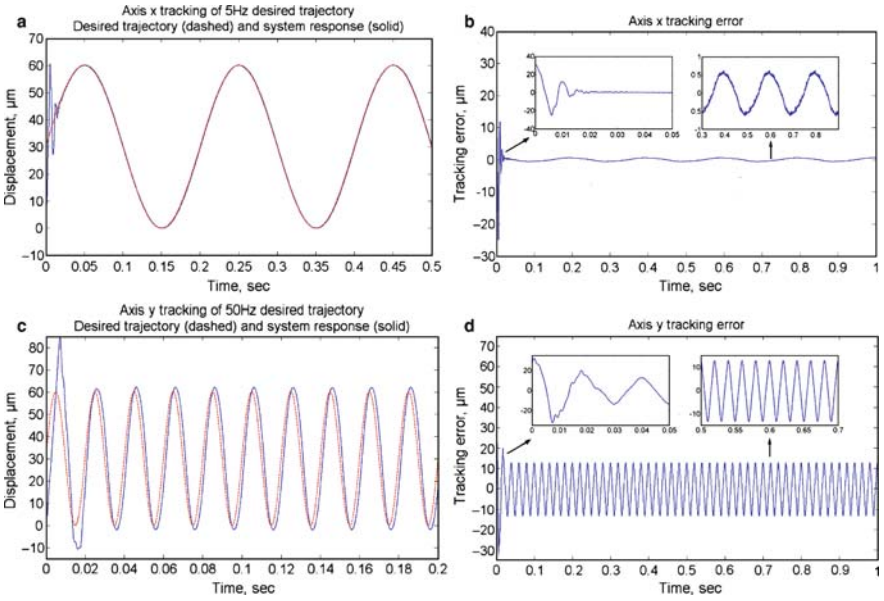

Fig. 10.27 PI controller results for simultaneous double-axis motion control: (**a**) x-axis 5 Hz tracking control, (**b**) x-axis tracking error, (**c**) y-axis 50 Hz tracking control, and (**d**) y-axis tracking error
Source: Bashash and Jalili 2009, with permission

the steady-state tracking performance. Hence, PI controller lacks a desirable transient response in tracking of time-varying trajectories and has low performance in high-frequency trajectory tracking.

Robust Adaptive Control of Piezo-flexure Nano-positioner: Precision tracking control of the double-axis piezo-flexural system in general encounters problems such as parametric uncertainties, external disturbances, and ever-present unmodeled dynamics including coupling and hysteresis modeling uncertainties. However, a properly designed closed-loop controller can offer a remedy for all these problems. Along this line, a Lyapunov-based robust adaptive control strategy for the precision tracking control of piezo-flexural nano-positioning systems is designed and implemented in this section. Since both axes present identical equations of motion, for the sake of simplicity, the controller is designed for only one axis, and, without loss of generality, is applied to the second axis as well. For this, we select x-axis and remove all the indices. The following definitions are considered first:

$$\begin{aligned} H\{V_a(t)\} &\triangleq a\left(V_a(t) + \hat{V}_h(t) + \tilde{V}_h(t)\right) \\ C\{y(t)\} &\triangleq b\left(y(t) + \hat{y}_c(t) + \tilde{y}_c(t)\right) \\ D(t) &\triangleq \hat{D}(t) + \tilde{D}(t) \end{aligned} \tag{10.19}$$

where operators $H\{V_a(t)\}$ and $C\{y(t)\}$ are assumed to be divided into linear segments with the respective slopes of a and b, known time-varying parts $\hat{V}_h(t)$ and $\hat{y}_c(t)$ (obtained from approximate models), and bounded uncertain parts $\tilde{V}_h(t)$ and $\tilde{y}_c(t)$, respectively. Similarly, the disturbance is divided into a known part $\hat{D}(t)$ and a bounded uncertain part $\tilde{D}(t)$. The validity of this assumption (separating the hysteresis into a linear and a bounded time-varying parts) has been shown in Su et al. (2000) for systems with backlash-like hysteresis including piezoelectric systems. Moreover, in Bashash and Jalili (2006a) it has been shown that hysteresis trajectories in piezo-flexural nano-positioners are bounded by reference curves, due to the hysteresis curve-alignment property.

Consequently, the equation of motion can then be written as

$$\begin{aligned} m\ddot{x}(t) + c\dot{x}(t) + kx(t) &= V_a(t) + \hat{V}_h(t) + r\,(y(t) + \hat{y}_c(t)) + \hat{D}(t) + p(t), \\ p(t) &= p_0 + \tilde{p}(t) = \tilde{V}_h(t) + r\tilde{y}_c(t) + \tilde{D}(t), \\ m &= \frac{1}{a\omega_n^2},\ c = \frac{2\zeta}{a\omega_n},\ k = \frac{1}{a},\ r = \frac{b}{a} \end{aligned} \tag{10.20}$$

with $p(t)$ being the overall system perturbations consisting of an average (static) term p_0 to be relaxed through an adaptation law, and a time-varying term $\tilde{p}(t)$ to be compensated through a robust control design. Parameters m, c, k and r are the system unknown parameters to be included in the adaptive strategy. It is remarked that one is free to take only the linear part of the operators and leave $\hat{V}_h(t)$ and $\hat{y}_c(t)$ completely in the uncertainty terms $\tilde{V}_h(t)$ and $\tilde{y}_c(t)$, respectively. However, the less the amplitude of system perturbation, the better the tracking performance will be in practice.

Controller Design: A Lyapunov-based adaptive sliding mode control strategy is developed for precise tracking control of the nano-positioner. The objective of the sliding mode control is to design asymptotically stable hyperplanes to which all system trajectories converge and slide along their path until approach the desired zones (Slotine and Sastry 1983; Slotine 1984; Jalili and Olgac 1998a). To simultaneously satisfy tracking control and robustness requirements, the sliding hyperplane is selected as

$$s(t) = \dot{e}(t) + \sigma\, e(t) = 0 \tag{10.21}$$

where $\sigma > 0$ is a control gain, and $e(t) = x_d(t) - x(t)$, with $x_d(t)$ being the two times continuously differentiable desired trajectory. Taking the time derivative of (10.21) and using (10.20) yields

$$\begin{aligned} \dot{s}(t) = \ddot{e}(t) + \sigma\,\dot{e}(t) = \ddot{x}_d(t) - \ddot{x}(t) + \sigma\,\dot{e}(t) \; = \ddot{x}_d(t) + \sigma\,\dot{e}(t) + \frac{1}{m}\times \\ \Big(c\dot{x}(t) + kx(t) - V_a(t) - \hat{V}_h(t) - r\,(y(t) + \hat{y}_c(t)) - \hat{D}_h(t) - p_0 - \tilde{p}(t)\Big) \end{aligned} \tag{10.22}$$

Theorem 10.1. *For the system described by (10.20), if the variable structure control is given by:*

$$V_a(t) = \hat{m}(t)\left(\ddot{x}_d(t) + \sigma\dot{e}(t)\right) + \hat{c}(t)\dot{x}(t) + \hat{k}(t)x(t) - \hat{r}(t)\left(y(t) + \hat{y}_c(t)\right)$$
$$-\hat{p}_0(t) - \hat{V}_h(t) - \hat{D}_h(t) + \eta_1 s(t) + \eta_2 \mathrm{sgn}\left(s(t)\right) \tag{10.23}$$

where η_1 and η_2 are positive control gains, $|\tilde{p}(t)| \leq \eta_2$ for $\forall t \in (0, \infty)$, the parameter adaptation laws given by

$$\hat{m}(t) = \hat{m}(0) + \frac{1}{k_1}\int_0^t s(\tau)(\ddot{x}_d(\tau) + \sigma\dot{e}(\tau))\,\mathrm{d}\tau$$

$$\hat{c}(t) = \hat{c}(0) + \frac{1}{k_2}\int_0^t s(\tau)\dot{x}(\tau)\,\mathrm{d}\tau$$

$$\hat{k}(t) = \hat{k}(0) + \frac{1}{k_3}\int_0^t s(\tau)\dot{x}(\tau)\,\mathrm{d}\tau \tag{10.24}$$

$$\hat{r}(t) = \hat{r}(0) - \frac{1}{k_4}\int_0^t s(\tau)\left(y(\tau) + \hat{y}_c(\tau)\right)\,\mathrm{d}\tau$$

$$\hat{p}_0(t) = \hat{p}_0(0) - \frac{1}{k_5}\int_0^t s\left(\tau\right)\,\mathrm{d}\tau$$

with k_1 to k_5 being adaptation gains, and $\hat{m}(0)$ to $\hat{p}(0)$ being approximate parameter values, then, asymptotic stability of the closed-loop system and tracking control of desired trajectory are guaranteed in the sense that $e(t)$ is bounded.

Proof. See Appendix B (Section B.4) for details.

Derivation and Analysis of Soft Switching Mode Control: Although the proposed adaptive sliding mode controller is robust and asymptotically stable, it cannot be effectively implemented in practice due to the chatter phenomenon (Slotine and Sastry 1983). That is, due to the hard switching of signum function in the control law, resonant modes of the system can be excited which may lead to large vibrations or even instability. A widely used remedy for this problem is to replace the hard switching term $sgn(s)$ with a softer switching method using the following saturation function:

$$\mathrm{sat}(s/\varepsilon) = \begin{cases} s/\varepsilon & |s| \leq \varepsilon \\ \mathrm{sgn}(s) & |s| > \varepsilon \end{cases} \tag{10.25}$$

with ε being a small positive parameter adjusting the rate of switching operation. The control law (10.23) is then modified to

$$V_a(t) = \hat{m}(t)\left(\ddot{x}_d(t) + \sigma\dot{e}(t)\right) + \hat{c}(t)\dot{x}(t) + \hat{k}(t)x(t) - \hat{r}(t)\left(y(t) + \hat{y}_c(t)\right)$$
$$-\hat{p}_0(t) - \hat{V}_h(t) - \hat{D}_h(t) + \eta_1 s(t) + \eta_2 \text{sat}\left(s(t)/\varepsilon\right) \tag{10.26}$$

It is remarked that the adaptation laws given by (10.24) are no longer applicable with the modified control law. The reason is that control law (10.26) can only guarantee the boundedness of the sliding trajectory, not its asymptotic convergence, that is, $s(t) \to \Omega$ as $t \to \infty$, where Ω is a bounded set. Hence, adaptation integrals in (10.24) can lead to unbounded values over time. To eliminate this problem, a projection operator is utilized as proposed in Sastry and Bodson (1989). This operator requires the lower and the upper bounds of parameters and is introduced as

$$\text{Proj}_\theta\left[\bullet\right] = \begin{cases} 0 & \text{if } \hat{\theta}(t) = \theta_{\max} \text{ and } \bullet > 0 \\ 0 & \text{if } \hat{\theta}(t) = \theta_{\min} \text{ and } \bullet < 0 \\ \bullet & \text{otherwise} \end{cases} \tag{10.27}$$

where $\hat{\theta}(t)$ represents the adaptation parameter (e.g., $\hat{m}(t)$ and $\hat{c}(t)$) with $\theta_{\min}$ and $\theta_{\max}$ being its lower and upper bounds, respectively. Accordingly, the adaptation laws are modified to

$$\hat{m}(t) = \hat{m}(0) + \frac{1}{k_1}\int_0^t \text{Proj}_m\left[s(\tau)\left(\ddot{x}_d(\tau) + \sigma\dot{e}(\tau)\right)\right]\mathrm{d}\tau$$
$$\hat{c}(t) = \hat{c}(0) + \frac{1}{k_2}\int_0^t \text{Proj}_c\left[s(\tau)\dot{x}(\tau)\right]\,\mathrm{d}\tau$$
$$\hat{k}(t) = \hat{k}(0) + \frac{1}{k_3}\int_0^t \text{Proj}_k\left[s(\tau)x(\tau)\right]\,\mathrm{d}\tau \tag{10.28}$$
$$\hat{r}(t) = \hat{r}(0) + \frac{1}{k_4}\tau\int_0^t \text{Proj}_r\left[-s(\tau)\left(y(\tau) + \hat{y}_c(\tau)\right)\right]\,\mathrm{d}\tau$$
$$\hat{p}_0(t) = \hat{p}_0(0) + \frac{1}{k_5}\int_0^t \text{Proj}_{p_0}\left[-s(\tau)\right]\,\mathrm{d}\tau$$

Hence, it is guaranteed that the adaptation parameters remain bounded by the lower and upper bounds, provided that they are initially selected within the bounds, that is, if $\theta_{\min} < \hat{\theta}(0) < \theta_{\max}$, then $\theta_{\min} < \hat{\theta}(t) < \theta_{\max}$, $\forall t \in (0, \infty)$. Furthermore, it can be shown that the following property holds for the projection operator:

$$\tilde{\theta}(t)\chi(t) \leq \tilde{\theta}(t)\,\text{Proj}_\theta\left[\chi(t)\right] \tag{10.29}$$

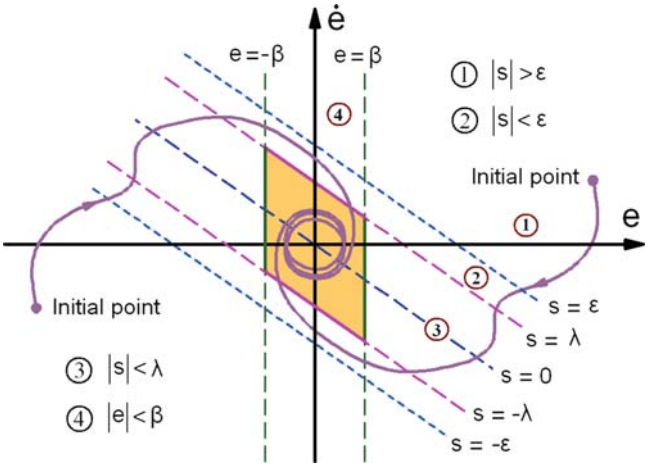

Fig. 10.28 Soft variable structure control graphical demonstration
Source: Bashash and Jalili 2009, with permission

Theorem 10.2. *For the system described by (10.20), if the soft variable structure control given by (10.26) and the adaptation laws given by (10.28) are applied, the closed-loop system becomes globally uniformly ultimately bounded, in the sense that the error signal $e(t)$ is bounded. Moreover, the bound of the steady-state error can be explicitly derived as:*

$$|e_{ss}(t)| \leq \frac{\eta_2 \varepsilon}{\sigma(\eta_1 \varepsilon + \eta_2)} \tag{10.30}$$

Proof. See Appendix B (Section B.5) for more details.

The intersection of regions $|s(t)| < \lambda$ and $|e(t)| < \beta$ forms a parallelogram in $e-\dot{e}$ plane to which the error phase trajectory converges. Figure 10.28 schematically demonstrates the function of the proposed soft variable structure controller. The $e - \dot{e}$ plane is divided into four regions: region 1, where $|s(t)| > \varepsilon$; region 2, the boundary layer where $|s(t)| < \varepsilon$; region 3, the convergence zone of $s(t)$ where $|s(t)| < \lambda$; and region 4, the convergence zone of $e(t)$ where $|e(t)| < \beta$. Starting from an initial point in region 1, the phase trajectory heads toward region 2, enters the region, and proceeds further inside into region 3. It is, however, possible that the trajectory inside region 3 escapes outside due to its initial momentum. In this case, the trajectory will be attracted back to region 3, since the Lyapunov function derivative is always negative outside this region (see Bashash and Jalili 2009). The trajectory will eventually enter region 4 and get entrapped inside the parallelogram of attraction, as depicted in the figure, representing a globally uniformly ultimately bounded response for the closed-loop system.

The appropriate selection of control parameters requires a number of trial–and-error experiments. With the help of explicit derivation of the system ultimate error

bound given by (10.30), the selected sets of control parameters can be initially checked for performance acceptability. The initially verified sets can then be implemented in the actual experiment for selecting the final set. It is remarked that if the constraints on the error bounds are too tight, the probability of chattering increases. Final set of control parameters is selected based on a trade-off and step-by-step squeezing of the ultimate error bound, while staying away from chatter. Equation (10.30) can also be helpful on performing such a trade-off, since it can present the sensitivity of the ultimate error with respect to the control parameters.

Closed-loop Control Experiments: The developed controller in the preceding subsection is experimentally implemented for tracking of the same sinusoidal trajectories given to PI controller in earlier section. Only the linear parts of the hysteresis and the coupling nonlinearities are taken into account, and no external disturbances affect the system, that is, $\hat{V}_h(t) = \hat{y}_c(t) = 0$ and $D(t) = 0$. The approximate values of the system parameters used for initialization of the adaptation integrals are given in Table 10.3. The selected control gains obtained from an experimental trial and error procedure are listed in Table 10.4.

Figures 10.29 and 10.30 depict the double-axis tracking control results for x-axis, and y-axis, respectively. Tracking of the desired trajectory, system error response, convergence of the sliding variable, $s(t)$, and the error phase portrait are given through sub-plots 10.29(a–d) for x-axis, and sub-plots 10.30(a–d) for y-axis. It is seen that the convergence of the error and the sliding trajectories to the prescribed zones are attained. Furthermore, the error phase trajectories converge to the predicted parallelogram formed by the control gains. The adaptations of parameters $\hat{k}(t)$ and $\hat{p}_0(t)$ are depicted in Fig. 10.31. For the other parameters, adaptation signals stay within their lower and upper bounds, similarly. However, the plots are not given here for brevity. It is remarked that the coefficients of the parameter adaptations are obtained experimentally to yield a sufficiently high adaptation rate while stay away from instability.

Maximum and average steady-state tracking error percentages are obtained as 1.67 and 0.83% for x-axis, and 1.71 and 0.82% for y-axis, respectively. It is seen

Table 10.3 The approximate values of the system parameters

System parameters	ω_n	ζ	A	B
Approximate values	2,700	3	10^{-6}	0.0025
Units	rad/s	–	m/V	–
System parameters	M	c	K	R
Approximate values	0.14	2,200	10^6	2,500
Units	Kg V/N	V s/m	V/m	V/m

Table 10.4 Control parameters values for the experiments

Control parameters	σ	ε	η_1	η_2	–
Values	500	0.01	300	20	–
Adaptation gains	k_1	k_2	k_3	k_4	k_5
Values	20	2×10^{-9}	5×10^{-14}	10^{-10}	2×10^{-6}

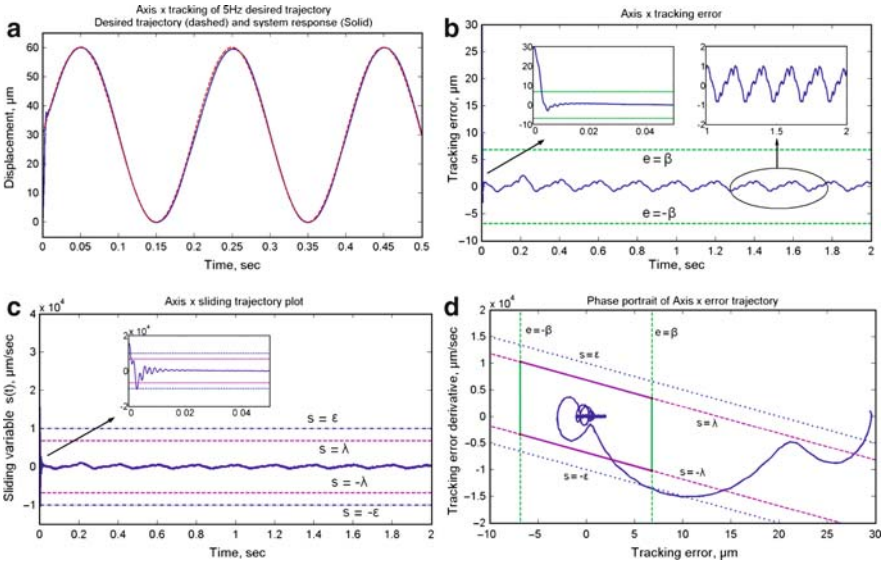

Fig. 10.29 *x*-axis tracking control results: (**a**) trajectory tracking, (**b**) tracking error, (**c**) sliding variable plot, and (**d**) phase portrait of error trajectory
Source: Bashash and Jalili 2009, with permission

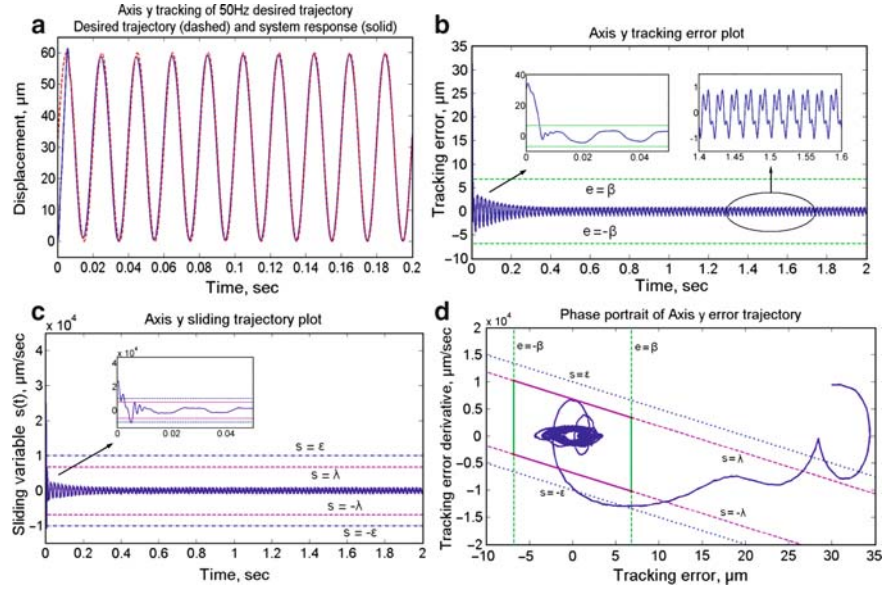

Fig. 10.30 *y*-axis tracking control results: (**a**) trajectory tracking, (**b**) tracking error, (**c**) sliding variable plot, and (**d**) phase portrait of error trajectory
Source: Bashash and Jalili 2009, with permission

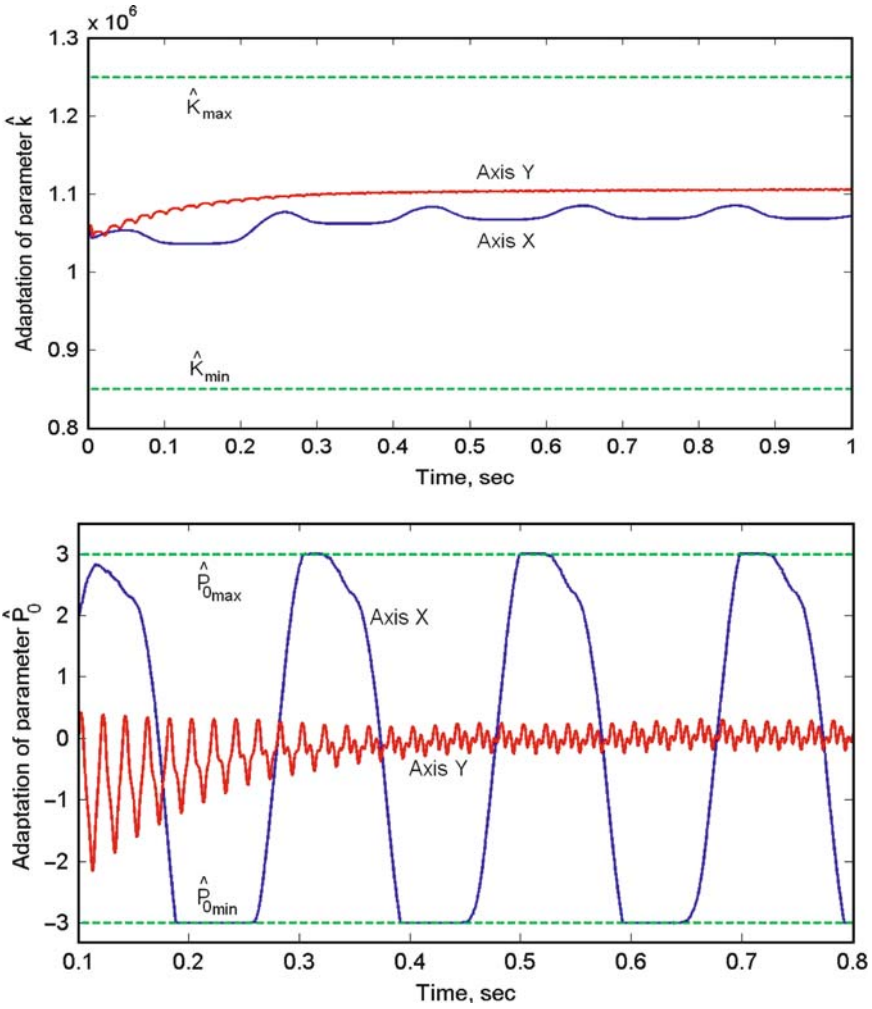

Fig. 10.31 Parameters adaptation results: adaptation of (**a**) $\hat{k}(t)$, and (**b**) $\hat{p}_0(t)$
Source: Bashash and Jalili 2009, with permission

that the controller yields similar tracking performance for both axes in different frequencies. However, it is remarked that some portion of performance drop is due to the simultaneous double-axis operation; experiments demonstrate that single axis tracking yields considerable improvement in performance (around 180% compared to the double-axis tracking) with the proposed control method.

Comparing with the PI controller, transient response in low-frequency tracking and the steady-state performance in high-frequency tracking have been significantly improved. Therefore, the proposed controller is preferred over the PI controller, especially at high frequencies. However, if low-frequency tracking with zero initial

value is desired or the transient properties are not the concern, PI controller is preferred due to its simple structure and straightforward implementation.

10.4.2 Modeling and Control of Three-Dimensional Nano-Positioning Systems

As mentioned in Sect. 10.2, the ultimate goal of the trajectory tracking control of PZT-driven nano-positioning systems is to perform surface topography. This section demonstrates this concept using a x-y-z nano-positioning system, depicted in Fig. 10.32, using the two configurations briefly mentioned in Sect.10.2.1 (see Fig. 10.10). The first configuration, shown in Fig. 10.32, utilizes the z-nano-positioner assembled on top of an x-y nano-positioner in order to track surface trajectories similar to those typically scanned by SPM. The second configuration, a laser-free AFM setup is using the z-nano-positioner for tip movement, while the x-y nano-positioner is used to move the sample beneath the tip.

Surface Topography Tracking using x-y-z Nano-positioning System: To demonstrate the surface topography tracking using x-y-z nano-positioner, a rectangular scan area is defined by combination of a ramp trajectory for x-axis, $x_d(t) = 5/6\,t$ [μm], and a sinusoidal trajectory for y-axis, $y_d(t) = 25 + 25\cos(2\pi t)$ [μm]. Trajectory for z-axis is then defined as a trigonometric function of x- and y-axes

Fig. 10.32 3D PZT-driven nano-positioning system comprising the Physik Instrumente P-753.11C z-nano-positioner on top of a PI P-733.2CL 2D x-y nano-positioner

positions, $z_d(t) = 0.3\ \cos(0.25x(t)) + \cos(0.30y(t))$, [μm]. For the given x- and y-axes trajectories, two memory units are required. However, determination of the minimum required number of memory units for the z-axis is impractical. Therefore, a relatively high memory capacity (with 5 memory units) is included in the controller for this axis. For further accuracy, the closed memory-allocation strategy is applied (Bashash and Jalili 2008).

Figures 10.33 and 10.34 depict the trajectory tracking results for every individual axis, as well as for the combined triple-axis of the stage. For x-axis with the ramp input, an increasing tracking error with the maximum value of 0.7% at the end of tracking is observed. Tracking performance for x-axis, which is demonstrated in Fig. 10.33(a), implies that the controller is able to effectively track a linear ramp trajectory. Tracking y- and z-axes are performed with respectively 1.4 and 4.3% tracking error values. Figure 10.33(b) demonstrates successful y-axis tracking response to a uniform sinusoidal input. However, Fig. 10.33(c) demonstrates the lack of accuracy for z-axis in tracking the non-uniform trigonometric trajectory. This is probably due to the large and sudden variations of desired trajectory which adds the unpredictable effects of dynamics to the system response. Combined together, the effective tracking control of the desired surface topography is attained through the 3D nano-positioner system as depicted in Fig. 10.34.

High-speed Laser-free Atomic Force Microscopy: In an effort to reduce the cost and improve the speed of AFM in molecular-scale imaging of materials, a laser-free AFM proposition augmented with an accurate control strategy for its scanning axes is presented here. To replace the bulky and expensive laser interferometer, a piezoresistive sensing device with an acceptable level of accuracy is employed. Change in the resistance of piezoelectric layer due to the deflection of micro-cantilever, caused by the variation of surface topography, is monitored through a Wheatstone bridge. Hence, the surface topography is captured without the use of laser and with nanometer-scale accuracy. To improve the speed of imaging, however, a Lyapunov-based robust adaptive control strategy is implemented using a x-y nano-positioner.

Figure 10.35 depicts the proposed laser-free AFM setup. The sample to be imaged is mounted on the double-axes parallel Physik Instrumente PI-733.2CL piezo-flexural stage, while a piezoresistive microcantilever is mounted on a Physik Instrumete P-753.11C z-stage for acquiring sample topography. The z-stage is used only for the initial adjustment, and to bring the cantilever into a desired contact with the sample. During the scanning, z-stage does not move; hence, the cantilever deflection corresponds to the surface topography (see Fig. 10.36 for the schematic view of laser-free AFM setup).

A self-sensing microcantilever, PRC-400, is utilized here for imaging purpose. Figure 10.37(a) depicts the piezoresistive cantilever image under a 100X magnification light microscopy consisting of a silicon microcantilever with a piezoresistive layer on its base, a sharpened tip, and a piezoresistive reference lever. The piezoresistive layers on cantilever and reference lever are utilized as the resistances in a

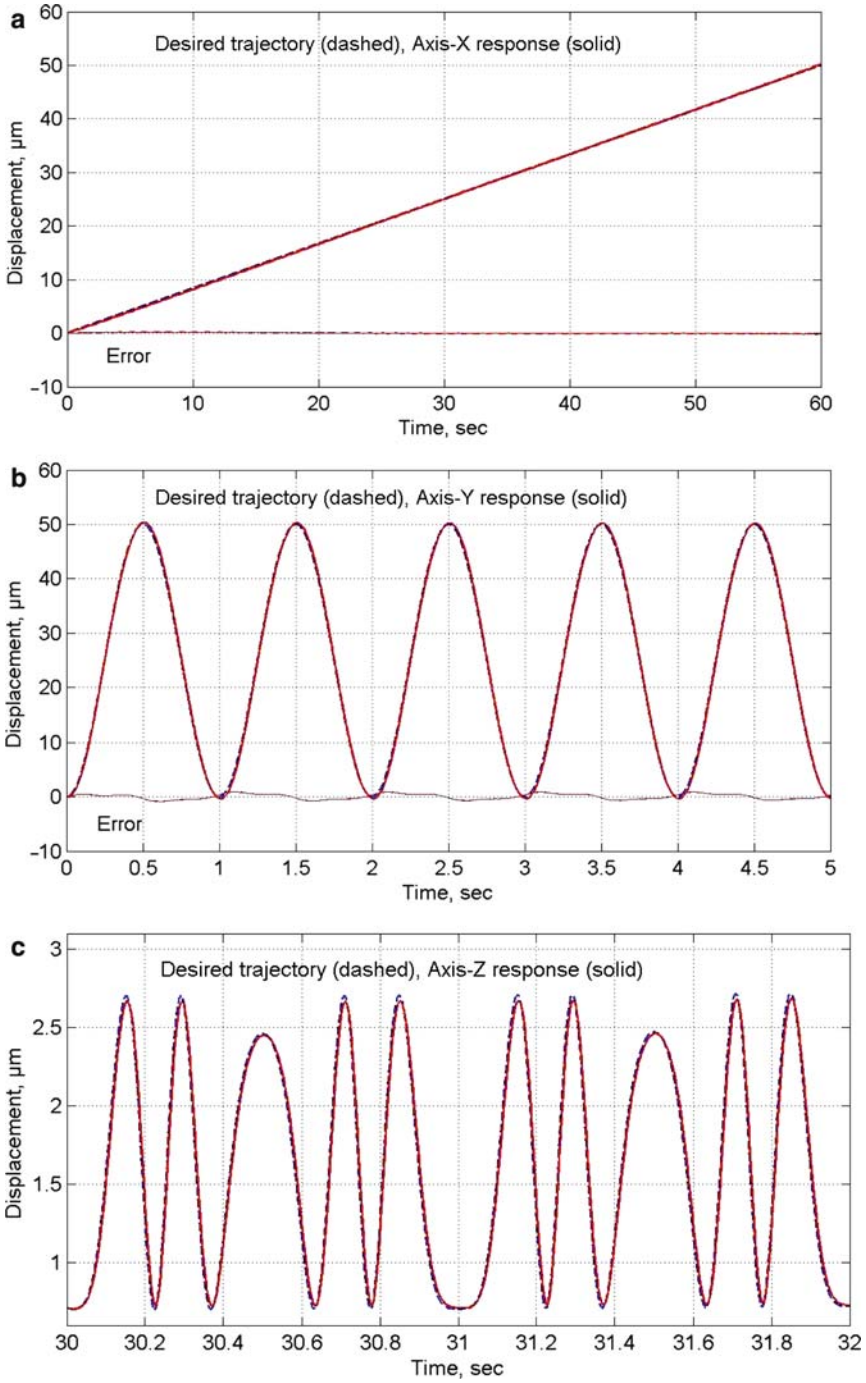

Fig. 10.33 Surface topography tracking with Physik Instrumente 753.11C z-nano-positioner mounted on top of P-733.2CL x-y nano-positioner: (**a**) x-axis tracking, (**b**) y-axis tracking, and (**c**) z-axis tracking
Source: Bashash 2008

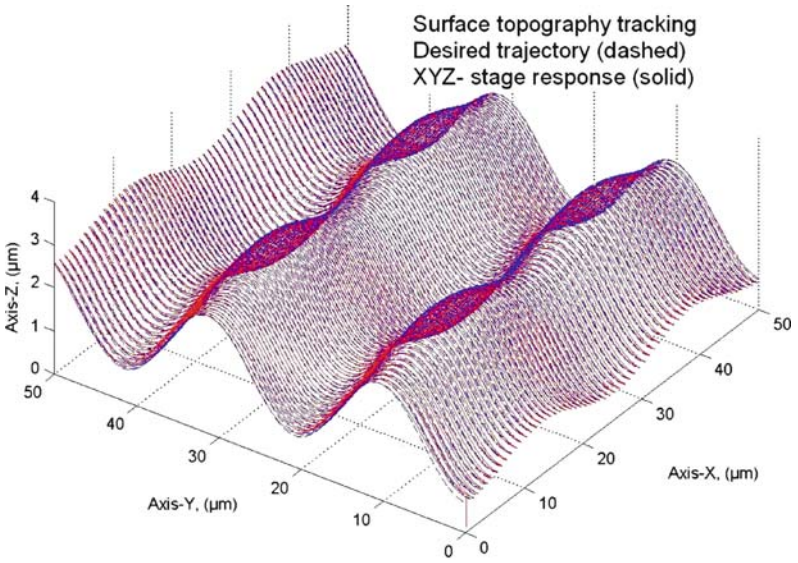

Fig. 10.34 Surface topography tracking with Physik Instrumente 753.11C *z*-nano-positioner mounted on top of P-733.2CL *x*-*y* nano-positioner
Source: Bashash 2008

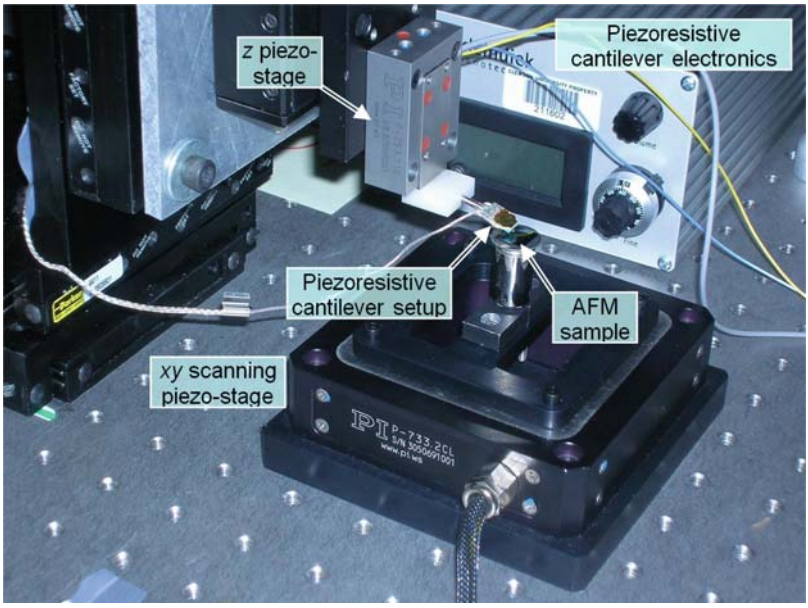

Fig. 10.35 Piezoresistive cantilever-based laser-free AFM setup

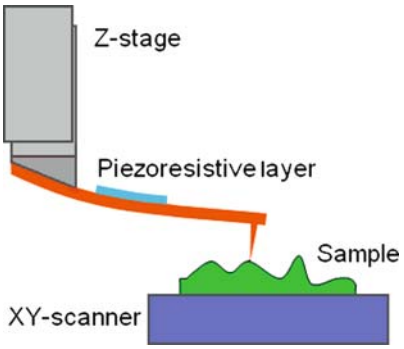

Fig. 10.36 Schematic representation of laser-free AFM setup

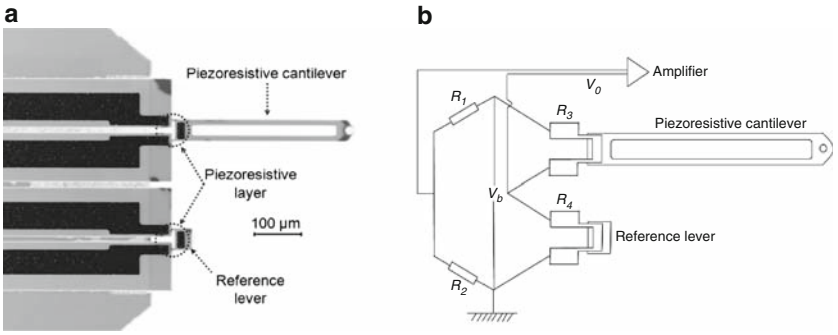

Fig. 10.37 Piezoresistive microcantilever with Weston bridge circuit
Source: Saeidpourazar and Jalili 2009, with permission

Wheatstone bridge. Due to the external force on the piezoresistive cantilever's tip, it bends and results in a change of resistance in the piezoresistive layer. This change of resistance can be monitored utilizing the output voltage of the Wheatstone bridge. Figure 10.37(b) depicts a schematic of the PRC-400 self-sensing cantilever, with external Wheatstone bridge and amplifier. Since the first resonant frequency of cantilever is in the order of several kHz, in low-frequency operations (e.g. below 100 Hz), the cantilever behaves similar to a lumped-parameters system. Hence, the relation between the cantilever deflection and output voltage of the Wheatstone bridge becomes linear (Saeidpourazar and Jalili 2009). Thus, the cantilever deflection can be estimated through the deflection-to-voltage gain of the piezoresistive cantilever.

At the tip/sample contact point, the magnitude of the force applied to the cantilever tip is equally the same as the magnitude of the force applied to the sample surface. Cantilever's dimensions are, however, extremely small, and it only undergoes bending. Hence, the high flexibility of the cantilever is realized compared to the sample that distributes the force around the contact point and resists against it. As a result, the vertical deformation of sample at the contact point becomes negligible compared to that of the cantilever. This assumption is valid unless ultra soft samples

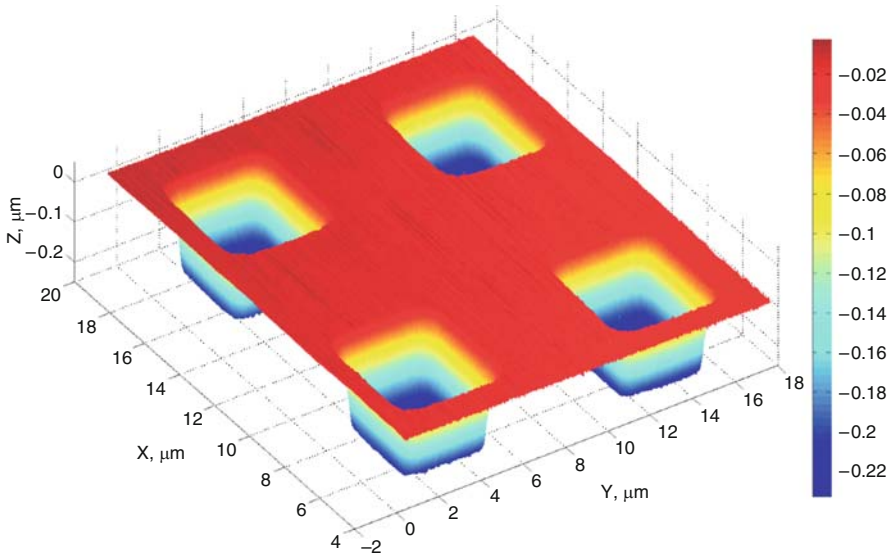

Fig. 10.38 3D image of an AFM calibration sample with 200 nm steps captured by the developed laser-free AFM setup at 10 Hz raster scanning

(e.g., liquids, soft biological species or ultrathin polymeric layers) are under study. Within the scope of this chapter, only stiff enough samples are addressed. Imaging ultra-soft samples requires further experiments to identify the local stiffness of the material, and is better done using non-contact or tapping AFM modes. On the other hand, the variation of surface topography in contact mode AFM should not exceed a certain value beyond which cantilever would experience plastic deformation or yield. Since the length of a typical AFM cantilever is in the order of several hundred micrometers, it can safely bend for few tens of microns. This flexibility is sufficient for most of the current AFM applications with micro- and nano-scale topographical variations.

Utilizing the developed robust adaptive controller in the preceding section for the x-y nano-positioner, an AFM calibration sample with $5 \times 5\,\mu m^2$ cubic pools with 200 nm depth, uniformly distributed on its surface, is considered for the experimental implementation of the proposed laser-free AFM setup. Figure 10.38 demonstrates the 3D image of the sample within a $16 \times 16\,\mu m^2$ scanning area at 10 Hz scanning frequency. It is particularly desired to observe the quality of images acquired in different scanning speeds (or in other words, scanning frequencies). Figure 10.39 demonstrates the top view of images at frequencies varying from 10 to 60 Hz with 10 Hz increments. It is seen that as the frequency increases, the quality drops and images become more blurry. This effect could have been originated from the increased transversal vibrations of microcantilever due to facing with the steeper steps in the surface at higher speeds, and/or the sensitivity reduction of piezoresistive

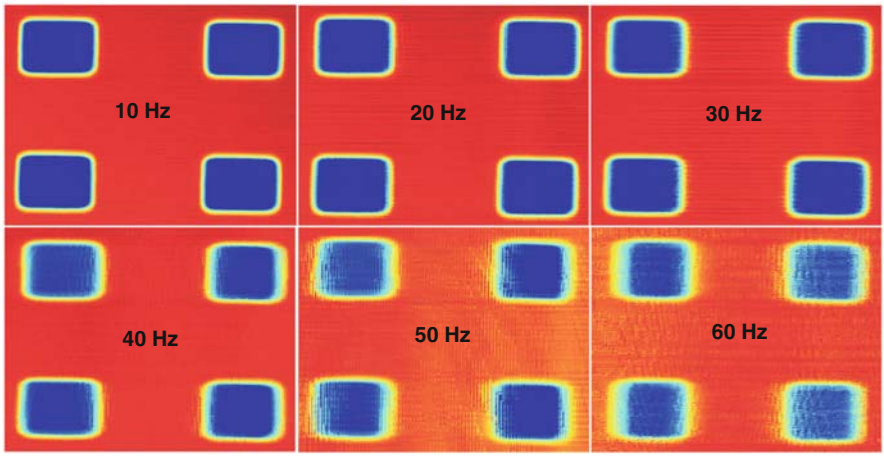

Fig. 10.39 Effects of raster scanning frequency on the image quality of laser-free AFM

layer due to the frequency increase. Further information such as cross-sectional view (line scan) of the surface could yield better judgment in this regard.

The cross-sectional views of the surface at different scanning frequencies are depicted in Figure 10.40. It reveals that at frequency of 30 Hz or less, the steep topographical steps are captured clearly by the cantilever and its piezoresistive sensor. However, when the frequency increases to 40 Hz and more, the stepped edges seem smoother and the image loses accuracy around the step areas. Moreover, at high frequencies, particularly at 60 Hz, the measured topography finds a negative slope which leads to further accuracy loss. Both of these effects cannot originate from the cantilever's vibrations, neither can they come from cantilever's irresponsiveness. This is due to the ultrahigh natural frequency of microcantilevers (in the order of several kHz) which significantly reduces their rise time and makes them extremely responsive. Hence, we may conclude that the degradation of image at high frequencies is due to the deficiency of the piezoresistive measurement at high frequencies which sets the limit to the proposed laser-free AFM device. Hence, one of the important future directions of piezoresistive-based AFMs would be improving the accuracy of piezoresistive sensors through their manufacturing process and electronics integration.

Nevertheless, acquiring high-quality images at frequencies up to 30 Hz could imply to the effectiveness of the proposed control framework in increasing the speeds of current AFMs which typically suffer from the low speed of their PID controllers.

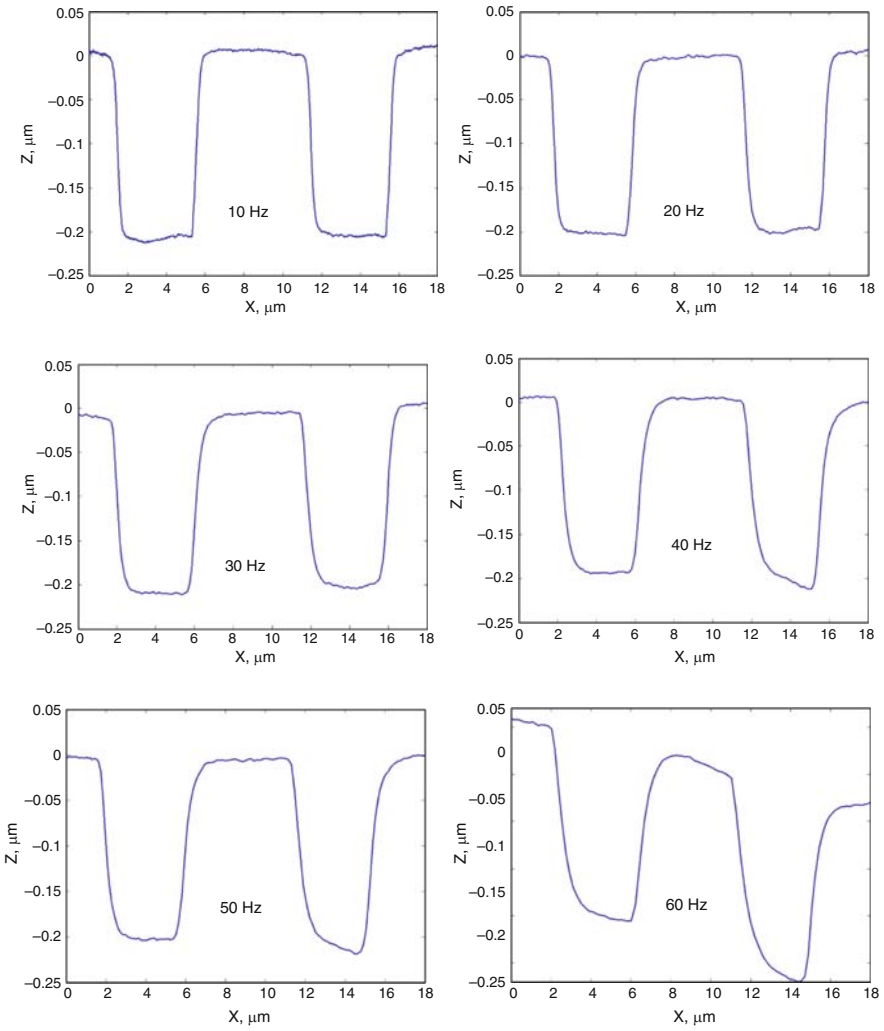

Fig. 10.40 Cross-sectional view of the effect of scanning frequency on the image quality of laser-free AFM

Summary

This chapter provided a comprehensive modeling treatment and control implementation of piezoelectric-based micro- and nano-positioning systems with their widespread applications in scanning probe-based microscopy and imaging. Starting from single-axis nano-positioning actuators to 3D positioning piezoactive systems, this chapter presented a complete overview of the piezoelectric-based nano-positioning systems.

Chapter 11
Piezoelectric-Based Nanomechanical Cantilever Sensors

Contents

11.1 Preliminaries and Overview 360
11.1.1 Fundamental Operation of Nanomechanical Cantilever Sensors 360
11.1.2 Linear vs. Nonlinear and Small-scale vs. Large-scale Vibrations 363
11.1.3 Common Methods of Signal Transduction in NMCS 363
11.1.4 Engineering Applications and Recent Developments 366
11.2 Modeling Frameworks for Nanomechanical Cantilever Sensors 368
11.2.1 Linear and Nonlinear Vibration Analyses of Piezoelectrically-driven NMCS ... 368
11.2.2 Coupled Flexural-Torsional Vibration Analysis of NMCS 388
11.3 Ultrasmall Mass Sensing and Materials Characterization using NMCS 399
11.3.1 Biological Species Detection using NMCS 401
11.3.2 Ultrasmall Mass Detection using Active Probes 411
Summary

This chapter provides a relatively general overview of piezoelectric-based nanomechanical cantilever sensors (NMCS) with their applications in many cantilever-based imaging and manipulation systems such as atomic force microscopy (AFM) and its varieties. Some new concepts in modeling these systems are also introduced along with highlighting the issues related to nonlinear effects at such small scale, the Poisson's effect, and piezoelectric materials nonlinearity. More specifically, both linear and nonlinear models of piezoelectric NMCS are presented with their applications in biological and ultrasmall mass sensing and detection.

It might be worth noting that a comprehensive modeling and treatment of these systems including both linear and nonlinear vibration analyses, system identification, as well as practical applications in ultrasmall mass sensing, laser-free imaging, and nanoscale manipulation and positioning, will appear in a new book by the author (Jalili in press). In order to avoid potential overlaps while also keeping this chapter focused, only a small part of the aforementioned book is presented here with a major emphasis on piezoelectric-based nanomechanical cantilever sensors.

N. Jalili, *Piezoelectric-Based Vibration Control*,
DOI 10.1007/978-1-4419-0070-8_11,

© Springer Science+Business Media LLC 2010

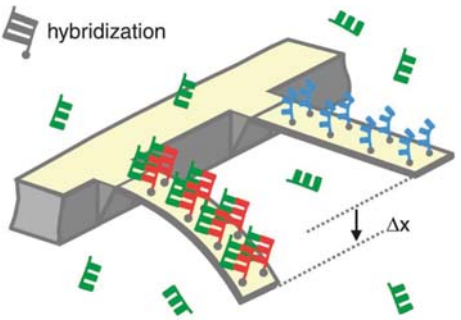

Fig. 11.1 Schematic of the DNA hybridization causing deflection (Δx) in the cantilevers
Source: Datskos and Sauers 1999, with permission

11.1 Preliminaries and Overview

Nanomechanical cantilever sensors (NMCS) have recently emerged as an effective means for label-free chemical and biological species detection. Selectivity, low cost, and easy mass production make them an enabling technology for micro- and nano scale mass and materials detection techniques. NMCS operate through the adsorption of species on the functionalized surface of cantilevers. Through this functionalization, molecular recognition is directly transduced into a micromechanical response. As schematically illustrated in Fig. 11.1, chemical reactions occurring on one side of the sensor result in surface stress changes that cause the cantilever to deflect and shift its resonance frequency (Gupta et al. 2004a,b; Yang et al. 2003). These chemically induced mechanical forces can be estimated by measuring the cantilever deflection (static mode) and/or its resonance-frequency shift (dynamic mode), (Chen et al. 1995; Daering and Thundat 2005).

11.1.1 Fundamental Operation of Nanomechanical Cantilever Sensors[1]

The aforementioned functionalization of NMCS can be performed on one or both sides of these microcantilevers. This means that for biosensing, for example, if only one surface shows high affinity for the targeted species and the other surface is relatively passivated, these targeted species will be adsorbed to one side of the microcantilever, and as a result, the adsorption-induced surface stress bends the microcantilever, as schematically depicted in Fig. 11.1.

NMCS operate in two different modes: (1) *static mode*, where the adsorption-induced deflection of the microcantilever is measured and (2) *dynamic mode*, where the adsorption-induced shift in the resonance frequency of microcantilever is

[1] The materials in this section may have come, directly or collectively, from our earlier publication (Afshari and Jalili, 2008).

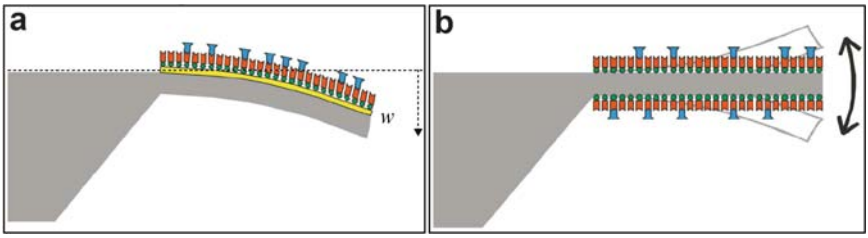

Fig. 11.2 Schematic of a microcantilever biosensor with (**a**) one functionalized surface (identified via static detection measurement), and (**b**) both surfaces functionalized (characterized via dynamic detection mode)
Source: Kirstein et al. 2005, with permission

measured. Shift in the resonance frequency may originate from either the change in the mass or stiffness (due to the differential stress between the two sides of the microcantilever) in the presence of the target molecules. In contrast, the deflection of microcantilever is solely due to the surface stress variation. That is, if only one side of the microcantilever is functionalized, as depicted in Fig. 11.2a, the adsorption-induced surface stress may be formulated by measuring either the deflection or the shift in the resonance frequency. However, if both sides of the microcantilever are functionalized, as shown in Fig. 11.2b, the static deflection measurement will not be a practical method for surface stress measurements. Hence, the measurements of shift in the microcantilevers resonance frequency should be utilized for the adsorption-induced surface stress measurements. In addition, when the target molecules are adsorbed on the functionalized surface of the microcantilever, its overall mass changes, and therefore, the natural frequency is altered by a small but detectable amount. This forms the basis of the dynamic mode of operation for the microcantilever sensors and the adsorbed mass measurements (Ibach 1997; Itoh et al. 1996).

Static Mode Deflection Detection Method: As mentioned earlier, if the target species are adsorbed only on one of the microcantilever surfaces, the beam undergoes bending because of adsorption-induced variations in the surface stress. As the surface stress changes occur only on one side of the sensor, the differential stress between the top and bottom surfaces results in microcantilever's bending. It must be emphasized that the static method only works when there exists a differential surface stress between two sides of the microcantilever.

While there are numerous methods and modeling frameworks to quantify the interaction in this mode, we only present the most commonly used technique, the so-called Stoney's formula, and refer the interested readers to Afshari and Jalili 2008 and references therein. On the basis of Stoney's formula (Stachowiak et al. 2006), the surface stress is calculated from the observed deformation of the rectangular plate, using the following simple equation (commonly referred to as Stoney's formula):

$$w = \frac{3\,(1-\upsilon)\,L^2}{t^2 E}\sigma \tag{11.1}$$

where w is the displacement of the cantilever; υ, L, t, and E are the Poisson's ratio, length, thickness, and modulus of elasticity of the cantilever, respectively; and $\boldsymbol{\sigma}$ is the adsorption-induced differential surface stress.

The Stoney's formula is applicable to thin plates of arbitrary plane view and uniform thickness exhibiting small deflections, where the effect of in-plane loading on the transverse (out-of-plane) deflections is negligible. Among the most important extensions to Stoney's formula, the following could be listed along with the cited references: Poisson's effect and thin-film coating on thick cantilevers (Jensenius et al. 2001), thick films and multilayer laminates theory (Ji et al. 2001), static deflection based on (Schell-Sorokin and Tromp 1990), and static deflection based on molecular interactions (Shuttleworth 1950; Chen et al. 1995).

Dynamic Mode Frequency Response Measurement: As mentioned before, NMCS in dynamic mode could be utilized to measure changes in system parameters, using frequency change. That is, changes in cantilever resonance frequency provide a direct measure of the mass of adsorbed species if the spring constant remains fixed. However, in many cases the spring constant changes as a result of the adsorption-induced surface stress. Therefore, the shift in frequency can be written as follows (Stoney 1909):

$$\mathrm{d}f(m,K) = \left(\frac{\partial f}{\partial m}\right)\mathrm{d}m + \left(\frac{\partial f}{\partial K}\right)\mathrm{d}K = \frac{f}{2}\left(\frac{\mathrm{d}K}{K} - \frac{\mathrm{d}m}{m}\right) \tag{11.2}$$

where $f(\mathrm{d}f)$ is the frequency (change), m ($\mathrm{d}m$) represent mass (change), and K ($\mathrm{d}K$) is the equivalent mass (change). Different beam models have been examined for analyzing a microcantilever and formulating its resonance frequency and spring constant. Some representative examples include taut string analogy in which the cantilever is simplified as a taut string (Rangelow et al. 2002), beam model with axial force in which the surface stress is expressed as the non-varying force with its induced bending moment applied at the free end of the microcantilever (Lee et al. 2000), and many more comprehensive and thorough methods (Afshari and Jalili 2008; Mahmoodi and Jalili 2007, 2008; Mahmoodi et al. 2008a,b). Without going into too much details, some of these modeling frameworks are discussed and detailed in next section.

The effect of surface stress on the resonance frequency shifts of microcantilevers has not received great attention in the literature and most of the reported works mainly assume a simple model for the vibrating microcantilever beam. A more recent modeling has been proposed to relate the adsorption-induced surface stress to the shift in the resonance frequency of the microcantilever, while considering a general, nonlinear behavior of the microcantilever (Lockhart and Winzeler 2000; Lu et al. 2001; Mahmoodi et al. 2008a, 2008b).

11.1.2 Linear vs. Nonlinear and Small-scale vs. Large-scale Vibrations

As mentioned briefly in Chap. 1, depending on the structures' dimensions and/or their materials level behavior, different levels of modeling complexity could be adopted. As clearly evident, when considering micro- and nano scale cantilevers, even small vibrations could easily lead to nonlinear behavior because of the relatively small dimensions of cantilever's size. In addition, other factors such as Poisson's effect could become more prominent especially for NMCS in which the width becomes more significant compared to the cantilever's length. Along this line, more comprehensive nonlinear modeling frameworks are required in order to take into account these effects. For this, Sect. 11.2 presents the modeling techniques that are adequate for such arrangement.

For instance, in a nonlinear modeling framework of piezoelectrically-actuated NMCS, the Lennard-Jones attraction/repulsion forces (Chen et al. 1995) in addition to nonlinear vibrations (Mahmoodi and Jalili 2008b) and/or piezoelectric materials level nonlinearities (Mahmoodi et al. 2008a), could result in a very complicated equation of motion. Sect. 11.2 provides a relatively brief introduction to the development and validation of this nonlinear-comprehensive modeling framework, while leaving the detailed derivations and analyses to the author's recent book on the subject (Jalili in press).

11.1.3 Common Methods of Signal Transduction in NMCS

As mentioned earlier, NMCS translate the molecular recognition of the adsorbed species into a nanomechanical response, which is coupled to one of the available readout mechanisms. Among the many readout or signal transduction methods, this section briefly reviews some of the most common methods such as optical (Datskos et al. 1996), piezoresistive (Onran et al. 2002), piezoelectric (Lu et al. 2001), and capacitive (Bizet et al. 1998), with special emphasis on piezoelectric-based NMCS, the subject of this book.

Optical Readout: Optical beam deflection is one of the most common methods of measuring the deflection or frequency response of microcantilever beams. In its simplest form, a laser beam is focused at the tip of the microcantilever, and the reflected beam is sensed by a position sensitive detector (Datskos et al. 1996; Townsend et al. 1987). AFM is the most common setup utilized in the laser (optical) detection mode (*see* Fig. 11.3). However, the frequency response of this system is sometimes disturbed by false signals. This results in double or even multiple maxima in the frequency response of the resonating microcantilever, which cannot be explained by the simple beam-vibration theory (Perazzo et al. 1999).

Another promising laser-based readout setup is the state-of-the-art Micro System Analyzer (MSA) 400, which is capable of the out-of-plane, in-plane, and topography

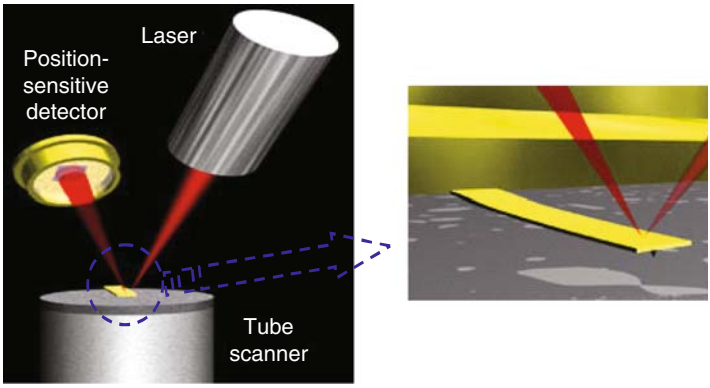

Fig. 11.3 Schematic depicting basic AFM operation and optical readout mechanism

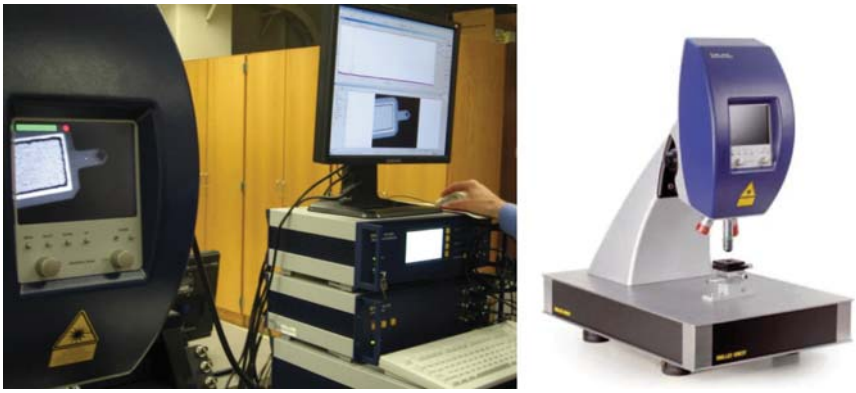

Fig. 11.4 Polytec Micro System Analyzer MSA 400 setup, (*left*) utilized in SSNEMS Laboratory (Mahmoodi et al. 2008b), and (*right*) listed in www.polytec.com

measurements, all in one setup (Zurn et al. 2001). Using the laser-Doppler vibrometry, instead of having the position sensitive detector and measuring the change in the voltage, MSA 400 results in much more accurate frequency responses of the resonating nanocantilevers (Zurn et al. 2001; Afshari and Jalili 2007). A schematic of the MSA 400 utilized in the SSNEMS Laboratory[2] is depicted in Fig. 11.4.

Piezoresistive Readout: Piezoresistive detection methods rely on the ability of piezoresistive materials such as doped silicon to change resistivity upon application of stress (*see* Fig. 11.5). The change in resistivity can then be measured using a sensitive Wheatstone's bridge (*see* Fig. 11.6). In one instance, the change in resistivity has simply been measured using sensitive precision multimeters (Onran et al. 2002). In another instance, the resistors have been integrated into the microcantilever

[2] Smart Structures and NanoElectroMechanical Systems Laboratory, Mechanical Engineering Department, Clemson University, Clemson, South Carolina, USA.

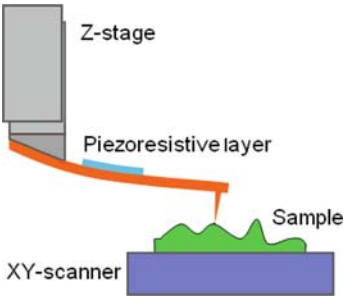

Fig. 11.5 Schematic representation of piezoresistive-based AFM setup

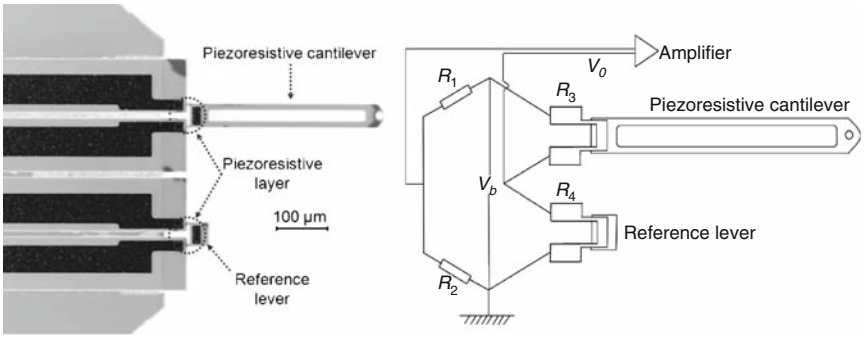

Fig. 11.6 Piezoresistive microcantilever with Weston bridge circuit

system, thereby making it possible to monitor the microcantilever deflection with significant reduction in background noise (Itoh et al. 1996). Some other piezoresistive detection methods are listed for reference (Rabe et al. 2007; Weigert et al. 1996).

Piezoelectric Readout: Piezoelectric techniques of detection rely on the ability of piezoelectric materials to induce electric charge when set into vibration. One such method consists of depositing a thin film of piezoelectric material such as ZnO on the microcantilever surface (Adams et al. 2003), *see* Fig. 11.7. Vibration of the beam induces charges in the ZnO layer which, in deed, are related to the frequency of vibration of the microcantilever. Other methods involve fabricating microcantilever beams of piezoelectric material such as PZT and using them in sensing applications (Ilic et al. 2001; Yang et al. 2003).

Capacitive Readout: Capacitive detection methods rely on the transduction principle of change in capacitance of a parallel plate capacitor as a function of the distance between the parallel plates. One of the two plates of the capacitor is kept fixed, while the microcantilever acts as the second plate (Bizet et al. 1998). Motion or change in motion can be easily sensed by incorporating the microcantilever-based capacitor in a sensitive bridge network.

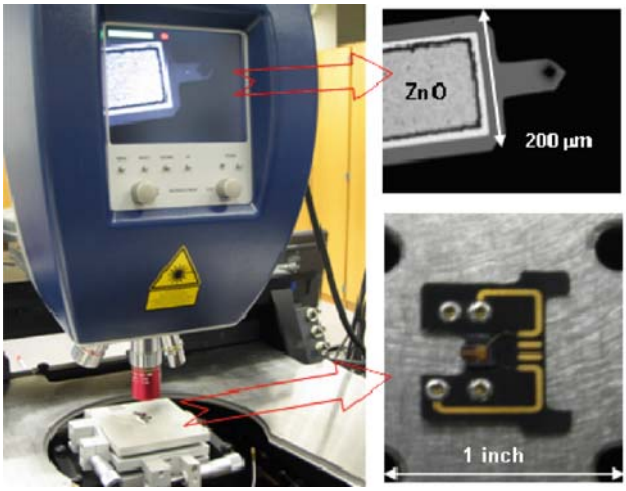

Fig. 11.7 (*Left*) MSA-400 Microsystems analyzer, (*right*) DMASP® microcantilever, and microscopic image of microcantilever.
Source: Mahmoodi et al. 2008a, b, with permission

11.1.4 Engineering Applications and Recent Developments

As mentioned earlier, with cost effective means for fabrication in place, microcantilevers are readily available for a plethora of applications transducing chemical and biological processes into micromechanical motion. Soon after realizing such potential about a decade ago, they were realized to be the ideal choice for detecting the most infinitesimal mechanical responses generated by molecular interactions.

Indeed, these types of measurements permit an investigation of the interactions between individual molecules in a host of various media at high sensitivity down to forces of a few pN (Su et al. 2003). It has been documented that NMCS are capable of detecting vapors (Lang et al. 1998), bacterial cells, proteins, and antibodies (Ilic et al. 2004; Zhang and Feng 2004; Savran et al. 2003), and can provide a mechanism for DNA hybridization (Hansen et al. 2001). NMCS have also impacted healthcare by providing a mechanism to measure blood glucose levels for diabetes diagnoses (Pei et al. 2004) as well as identifying important cardiac muscle proteins indicative of myocardial infarction (Arntz et al. 2003) and detecting antigens specifically used to monitor prostate cancer (Lee et al. 2005a).

With proven potential for label-free detection of complex biomolecular organisms and molecules, chemical applications for NMCS have also evolved. Using these sensors, dangerous chemical agents such as toxic vapors (Dareing and Thundat 2005) and chemical nerve weapons (Yang et al. 2003) have been precisely and accurately identified. Industrial utilization, such as swelling of polymer brushes (Bumbu et al. 2004) and pH changes (Zhang and Feng 2004), has also been demonstrated. Physical applications are also growing and may include, for example, thermal detection and measurement (Corbeil et al. 2002; Berger et al. 1996),

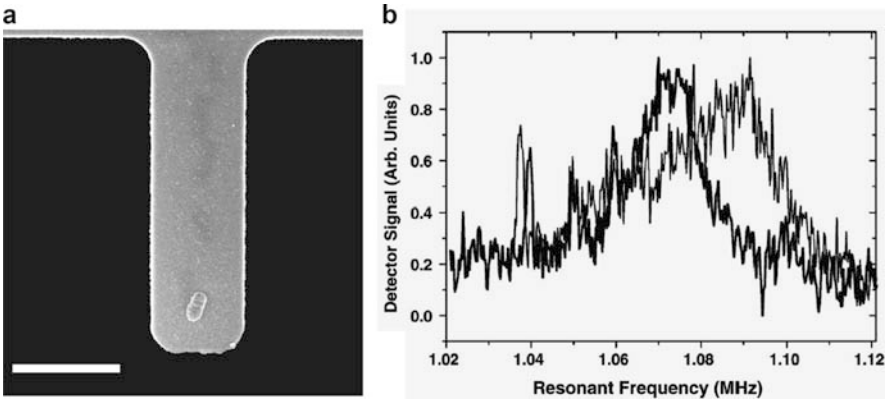

Fig. 11.8 (a) Scanning electron micrograph (SEM) of a single *E. coli* O157:H7 cell bound to the immobilized antibody layer on top of the microcantilever sensor, and (**b**) the corresponding transverse vibration spectra of the cantilever before and after single cell attachment.
Source: Ilic et al. 2001, with permission

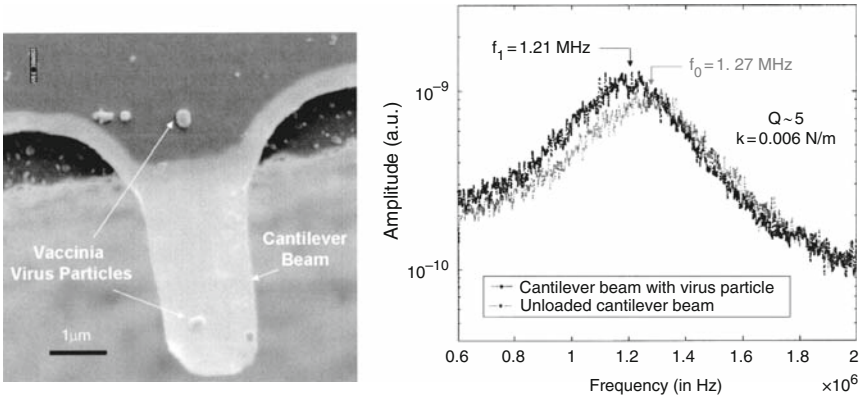

Fig. 11.9 (*Left*) SEM showing a microcantilever beam with an adsorbed single vaccine virus particle, and (*right*) Plot of the microcantilever's resonant frequency decrease for an amount of 60 kHz after the adsorption of the single virus particle
Source: Gupta et al. 2004, with permission

micro-scale investigations of solid electrode-electrolyte interfaces (Tian et al. 2004), phase transitions (Berger et al. 1996; Nagakawa et al. 1998), and detecting infrared radiation (Thundat et al. 1995).

Clinical applications of NMCS also include specific detection of proteins (Wachter and Thundat 1995), DNA (Álvarez et al. 2004; Datskos and Sauers 1999; Hagan et al. 2004; Ren and Zhao 2004), pesticides (Álvarez et al. 2003), and different pathogens such as single virus particles (Gimzewski et al. 1994; Grigorov et al. 2004; Ilic et al. 2000) and bacteria (Hansen et al. 2001). Some examples of the microcantilever biosensors with the detected virus particle on their surfaces, and their experimental results are depicted in Figs. 11.8 and 11.9.

11.2 Modeling Frameworks for Nanomechanical Cantilever Sensors

Despite the tremendous variety of experimental applications (such as those mentioned in Sect. 11.1.4), little attention has been paid to the theoretical modeling of NMCS. More specifically, very few research studies were directed towards understanding how electrical and chemical properties of the adsorbing agents culminate in NMCS detection by exerting tensile and compressive stresses on the cantilever surface. Developing a comprehensive model that captures the static and dynamic response of the sensor will undoubtedly provide a solid foundation for advancing their implementation into other areas especially nanorobotics where they can be used to control the important processes involved in protein folding, actuate microdevices using biological and chemical processes, or even facilitate our understanding of the molecular basis of friction and nanofluidics. Moreover, establishing a sound mathematical model will provide an insight into the effect of the design parameters on the response of the sensor, thereby allowing for their optimization in order to realize the desired response characteristics. This forms our main motivation for this section.

11.2.1 Linear and Nonlinear Vibration Analyses of Piezoelectrically-driven NMCS

The linear model for the NMCS along with the need for an effective parameters identification technique to be augmented with this linear model was discussed extensively earlier in Chap. 8 (*see* Sect. 8.3.2). Following this modeling exercise, we present a nonlinear model that takes into account both geometrical and material-level nonlinearities. To extend this model even further, a 3D nonlinear model for the NMCS is briefly introduced to show the effects of torsional vibrations and their coupling effect on the flexural vibrations. As mentioned before, we only consider piezoelectric NMCS for these modeling developments in an effort to keep this chapter focused. Also, we limit the materials to only overall derivations and refer interested reader to the companion book on the subject of the NMC sensors and actuators (Jalili in press).

Many experimental studies have already demonstrated the great impact of NMCS in a wide range of applications. However, further advances in detection methodologies are clearly dependent on the ability of available theoretical models to accurately capture the response of the sensor, thereby allowing for accurate estimation of the deflections and resonance frequency shifts emanating from chemical reactions occurring at its surface. Previous experimental investigations (McFarland et al. 2005; Zhang and Meng 2005) have demonstrated that simple modeling methodologies cannot be used to describe the behavior of NMCS, especially with the nonlinearly interacting energy fields that arise from the large sensor's

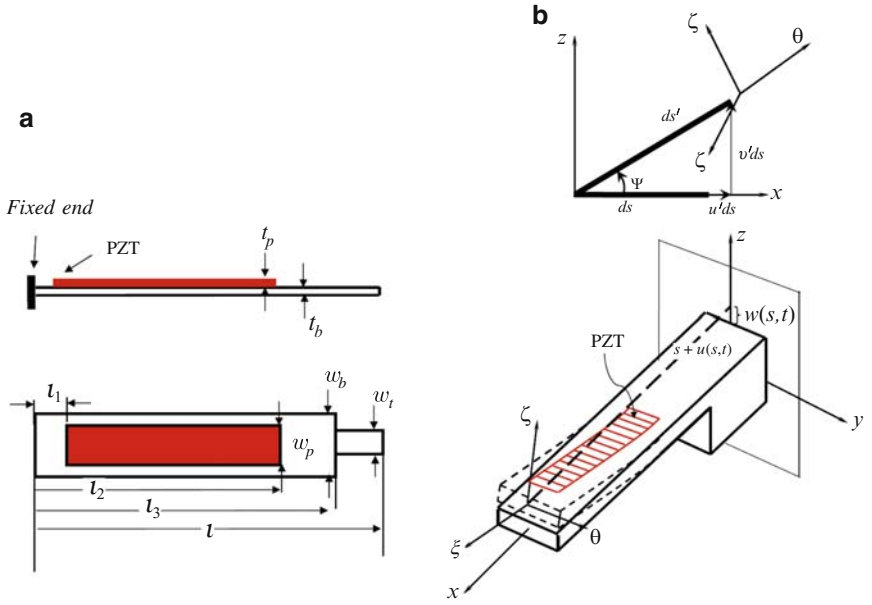

Fig. 11.10 (**a**) Schematic of the microcantilever sensor, and (**b**) the principal and inertial coordinate systems

deformation, surface adsorption of atoms, molecular interactions, and piezoelectric actuation. A comprehensive theoretical model will enable further development of new sensing methodologies and will create solid foundations for testing novel parameter estimation strategies and control techniques.

Along this line of reasoning, a nonlinear comprehensive model is developed in this section. In order to better follow the proposed modeling framework, a two-step approach is taken here; first the nonlinearity arising from NMCS deformation and geometry is discussed, followed by augmenting this nonlinearity with piezoelectric material-level nonlinearity. This framework allows the designer to conduct a qualitative analysis of the effect of the mechanical parameters on the sensor performance, thereby creating an efficient redesign approach that results in more effective NMCS in practice.

Nonlinearities Due to Geometry and Inextensibility: To develop the nonlinear model, a uniform flexible beam with a piezoelectric layer on its top surface is considered as shown in Fig. 11.10a (*see* Sect. 8.3.2 for a complete description of the setup). For simplicity and without loss of generality, it is assumed that the piezoelectric width is the same as the beam width. The beam is initially straight and it is clamped at one end and free at the other end. In addition, the beam follows the Euler-Bernoulli beam theory, where shear deformation and rotary inertia terms are negligible.

Figure 11.10b shows a beam segment of length ds with z–y and ξ–θ axes being the inertial and the principal axes of the beam cross section, respectively. The

bending angle between z-axis and ξ-axis is ψ. Using Fig. 11.10b, angle ψ for an element of length ds can be obtained as

$$\psi = \tan^{-1} \frac{w'}{1+u'}, \tag{11.3}$$

where over prime denotes derivative with respect to position s, and u and w are the respective longitudinal and transverse displacements. The transformation of the coordinates can be represented in the following matrix form:

$$\begin{Bmatrix} x \\ y \\ z \end{Bmatrix} = \begin{bmatrix} \cos(\psi) & 0 & -\sin(\psi) \\ 0 & 1 & 0 \\ \sin(\psi) & 0 & \cos(\psi) \end{bmatrix} \begin{Bmatrix} \xi \\ \theta \\ \zeta \end{Bmatrix}. \tag{11.4}$$

Using (11.3) and (11.4), and Taylor's series expansion, the curvature and angular velocity of the beam can be respectively obtained as

$$\kappa = w'' - w''u' - w'u'' - w''w'^2, \tag{11.5}$$

$$\dot{\psi} = \dot{w}' - \dot{w}'u' - w'\dot{u}' - \dot{w}'w'^2, \tag{11.6}$$

where over dot indicates the derivative with respect to time t. The Green's strain associated with the material located at neutral axis is given by (Hsieh et al. 1994)

$$S_0 = \sqrt{(1+u')^2 + w'^2} - 1, \tag{11.7}$$

which is utilized to relate longitudinal and bending vibrations through the inextensibility condition.

Similar to the case in Chap. 8, the piezoelectric layer is not attached to the entire length of the beam, and hence, the neutral surface changes for each section of the beam (*see* 8.51).

As mentioned before, the special configuration of microcantilever beam necessitates the use of the "plane strain" configuration. That is, for such microscale size beam, the thickness of the beam is typically much smaller than its width, and hence, the modulus of elasticity must be corrected in the form of (Ziegler 2004; Lam et al. 2003)

$$E = \frac{E^*}{(1-\nu^2)} \tag{11.8}$$

Governing Equations of Motion: An energy method is used here in order to derive the equations of motion. Using the obtained angular velocity, the total kinetic energy of the system can be expressed as

$$T = \frac{1}{2} \int_0^l \left\{ m(s)(\dot{u}^2 + \dot{w}^2) + J(s) \left(\dot{w}'^2 - 2\dot{w}'^2 u' - 2w'\dot{u}'\dot{w}' - 2\dot{w}'^2 w'^2 \right) \right\} \mathrm{d}s, \tag{11.9}$$

where

$$m(s) = W_b \left(\rho_b t_b + (H_{l1} - H_{l2})\, \rho_p t_p\right), \tag{11.10}$$

$$H_{l_1} = H(s - l_1),\ H_{l_2} = H(s - l_2), \tag{11.11}$$

and $H(s)$ is the Heaviside function defined earlier in Part II. For the microcantilever beam considered here, the electrical field is one dimensional; therefore, the electrical displacement vector has one non-zero component which is D_3. Hence, the electrical displacement vector can now be defined as

$$D_1 = D_2 = 0,\ D_3\,(s,t). \tag{11.12}$$

Therefore, the coupling of stress and electrical field for piezoelectric material (*see* 6.23) can be related as follows

$$\boldsymbol{\sigma}_1^{\,p} = c_p^D S_1^p - h_{31} D_3,\ \boldsymbol{\epsilon}_3 = -h_{31} S_1^p + \beta_{33}^S D_3 \tag{11.13}$$

with the stress–strain relation for the sections where piezoelectric materials are not attached expressed as

$$\boldsymbol{\sigma}_1^{\,b} = c_b^D S_1^b \tag{11.14}$$

The total potential energy of the system can now be written as (Dadfarnia et al. 2004a)

$$\begin{aligned} U = &\frac{1}{2}\int_0^{l_1}\iint_A \boldsymbol{\sigma}_1^b S_1^b \,\mathrm{d}A\,\mathrm{d}s + \frac{1}{2}\int_{l_1}^{l_2}\iint_A \boldsymbol{\sigma}_1^b S_1^b \,\mathrm{d}A\,\mathrm{d}s + \frac{1}{2}\int_{l_1}^{l_2}\iint_A \left(\boldsymbol{\sigma}_1^{\,p} S_1^p + \boldsymbol{\epsilon}_3 D_3\right)\mathrm{d}A\,\mathrm{d}s \\ &+ \frac{1}{2}\int_{l_2}^{l}\iint_A \boldsymbol{\sigma}_1^b S_1^b \,\mathrm{d}A\,\mathrm{d}s + \frac{1}{2}\int_0^l c_b^D A(s)\left(u'^2 + u'w'^2 + \frac{1}{4}w'^4\right)\mathrm{d}s \end{aligned} \tag{11.15}$$

Using (11.6–11.15), the Lagrangian of the system can be expressed as

$$\begin{aligned} L = \frac{1}{2}\int_0^l \Big\{ & m(s)(\dot{u}^2 + \dot{w}^2) + J(s)\left(\dot{w}'^2 - 2\dot{w}'^2 u' - 2w'\dot{u}'\dot{w}' - 2\dot{w}'^2 w'^2\right) \\ & - C_\zeta(s)\left(w''^2 - 2w''^2 w'^2 - 2w''^2 u' - 2w'w''u''\right) \\ & + c_b^D A(s)\left(u'^2 + u'w'^2 + \frac{1}{4}w'^4\right) - 2C_d(s) D_3\left(w'' - w''u' - w'u'' - w''w'^2\right) \\ & + C_\beta(s) D_3^2 \Big\}\,\mathrm{d}s \end{aligned} \tag{11.16}$$

[3] Note that for the beam material, which is a non-piezoelectric material we have $c_b^D = c_b^E$.

where

$$C_\zeta(s) = (H_0 - H_{l1})\, c_b^D I_b + (H_{l1} - H_{l2})\, c_b^D \left(I_b + b t_b z_n^2\right) + (H_{l1} - H_{l2})\, c_p^D I_p + (H_{l2} - H_l)\, c_b^D I_b \tag{11.17}$$

$$C_d(s) = (H_{l1} - H_{l2})\; h_{31} I_d, \tag{11.18}$$

$$C_\beta(s) = (H_{l1} - H_{l2})\; W_b t_b \beta_{33}^S, \tag{11.19}$$

$$I_b = \frac{W_b t_b^3}{12};\; I_d = \frac{W_b}{2}\left(t_b t_p + t_p^2 - 2 t_p z_n\right)$$

$$I_p = W_b \left(t_p z_n^2 + \left(t_p^2 + t_b t_p\right) z_n + \frac{1}{3}\left(t_p^3 + \frac{3}{2} t_b t_p + \frac{3}{4} t_b^2 t_p\right)\right) \tag{11.20}$$

$$z_n = \frac{c_p^D t_p \left(t_p + t_b\right)}{2\left(c_b^D t_b + c_p^D t_p\right)} \tag{11.21}$$

The beam is considered to be inextensible here, in which the inextensibility condition demands no relative elongation of the neutral axis (i.e., $S_0 = 0$). Therefore, using (11.7) it yields

$$\left(1 + u'\right)^2 + w'^2 = 1. \tag{11.22}$$

Using (11.22), variable u can now be coupled to w. This reduces the number of independent variables to two, i.e., w (the beam bending vibration) and D_3 (the non-zero component of dielectric displacement vector). Hence, the Lagrangian expression derived in (11.16) will lead to two equations, one for w and one for D_3. Considering the Euler-Bernoulli beam theory, ignoring the rotary inertia effect, while substituting (11.22) into (11.16), and considering it to be a constrained minimization problem (*see* Sect. 3.1.4), the governing equations of motion of the system using extended Hamilton principle can be obtained as

$$\frac{\partial}{\partial s}\left(w'\left(C_\zeta(s) w'' w'\right)' - w'\left(C_d(s) D_3 w'\right)'\right) - \frac{\partial^2}{\partial s^2}\left[C_\zeta(s)\left(w''\right) + C_d(s) D_3\left(1 - \frac{1}{2} w'^2\right)\right], - m(s)\ddot{w} - \frac{\partial}{\partial s}\left[w' \int_l^s m(s) \int_0^s \left(\ddot{w} w' + \dot{w}'^2\right) \mathrm{d}s \mathrm{d}s\right] = 0 \tag{11.23a}$$

$$C_d(s)\left(w'' + \frac{1}{2} w'' w'^2\right) + C_\beta(s) D_3 = W_b V_a(t), \tag{11.23b}$$

$$w(0,t) = w'(0,t) = w''(l,t) = w'''(l,t) = 0. \tag{11.23c}$$

where $V_a(t)$ is the input voltage applied to the piezoelectric layer. Equations (11.23a) and (11.23b) are coupled partial differential equations for w and D_3, respectively. One can combine (11.23a) and (11.23b) to eliminate variable D_3. Hence, the equation of motion of the system reduces to its final form as

$$\begin{aligned} m(s)\ddot{w} \; &+\frac{\partial^2}{\partial s^2}\left(C_\zeta(s)w''\right)+\frac{\partial}{\partial s}\left[w'\int_l^s m(s)\int_0^s\left(\ddot{w}w'+\dot{w}'^2\right)\mathrm{d}s\,\mathrm{d}s\right] \\ &+\left[w'\frac{\partial^2}{\partial s^2}\left(C_\zeta(s)w''w'\right)+w''\frac{\partial}{\partial s}\left(C_\zeta(s)w''w'\right)\right] \\ &+w'\frac{\partial}{\partial s}\left(\frac{C_d^2(s)}{C_\beta(s)}w''w'-\frac{bC_d(s)}{C_\beta(s)}V_a(t)w'\right) \\ &-\frac{\partial^2}{\partial s^2}\left[\frac{bC_d(s)}{C_\beta(s)}V_a(t)\left(1-\frac{1}{2}w'^2\right)+\frac{C_d^2(s)}{C_\beta(s)}\left(w''\right)\right]=0 \end{aligned} \tag{11.24}$$

with the boundary conditions (11.23c). As expected, the cubic nonlinear inertia and stiffness terms appear in the equations of motion, but because of coupling of electrical and mechanical fields there emerges quadratic and cubic nonlinear terms due to piezoelectric effect. The linear terms due to presence of piezoelectric layer have been obtained before (Dadfarnia et al. 2004a,b). It can be, however, observed that new nonlinearities due to piezoelectric terms appear in the equations of motion.

Modal Analysis and Nonlinear Natural Frequency Development: In order to solve the original partial differential equation and obtain the resonance frequency and beam mode shape, the time and position functions must be separated. Following the same procedure as in Chap. 4, the Galerkin method is utilized to discretize the system as

$$w(s,t)=\sum_{n=1}^{\infty}w_n(s,t)=\sum_{n=1}^{\infty}\phi_n(s)q_n(t), \tag{11.25}$$

where ϕ_n represents the comparison functions (i.e., only satisfying boundary conditions and not necessarily the equation of motion) of the microcantilever beam and q_n represents the generalized time-dependent coordinates. Substituting (11.25) into (11.24) and using Lagrangian approach, the equation of motion can be obtained as

$$\hat{g}_{1n}\ddot{q}_n+\hat{g}_{2n}q_n+\hat{g}_{3n}V_a(t)q_n^2+\hat{g}_{4n}q_n^3+\hat{g}_{5n}\left(q_n^2\ddot{q}_n+q_n\dot{q}_n^2\right)+\hat{g}_{6n}V_a(t)=0, \tag{11.26a}$$

where

$$\hat{g}_{1n}=\int_0^l m(s)[\phi_n(s)]^2\,\mathrm{d}s, \tag{11.26b}$$

$$\hat{g}_{2n} = \int_0^l C_\zeta(s)\phi_n''(s)\,\mathrm{d}s - \frac{h_{31}I_d\left(\phi_n'(l_2)-\phi_n'(l_1)\right)}{W_b t_p \beta_{33}^S (l_2-l_1)} \int_0^l C_d(s)\phi_n''(s)\,\mathrm{d}s, \quad (11.26c)$$

$$\hat{g}_{3n} = \frac{1}{t_p\beta_{33}^S}\int_0^l C_d(s)\phi_n''(s)[\phi_n'(s)]^2\,\mathrm{d}s, \quad (11.26d)$$

$$\begin{aligned}\hat{g}_{4n} = {} & 2\int_0^l C_\zeta(s)[\phi_n''(s)]^2[\phi_n(s)]^2\,\mathrm{d}s \\ & -\frac{h_{31}I_d\left([\phi_n'(l_2)]^3-[\phi_n'(l_1)]^3\right)}{2W_b t_p\beta_{33}^S(l_2-l_1)}\int_0^l C_d(s)\phi_n''(s)\,\mathrm{d}s, \\ & -\frac{h_{31}I_d\left(\phi_n'(l_2)-\phi_n'(l_1)\right)}{W_b t_p\beta_{33}^S(l_2-l_1)}\int_0^l C_d(s)\phi_n''(s)[\phi_n'(s)]^2\,\mathrm{d}s \end{aligned} \quad (11.26e)$$

$$\hat{g}_{5n} = 2\int_0^l \phi_n(s)\left[m(s)\phi_n'(s)\int_l^s\int_0^s 2[\phi_n'(s)]^2\,\mathrm{d}s\,\mathrm{d}s\right]'\mathrm{d}s, \quad (11.26f)$$

$$\hat{g}_{6n} = \frac{1}{t_p\beta_{33}^S}\int_0^l C_d(s)\phi_n''(s)\,\mathrm{d}s. \quad (11.26g)$$

As the boundary conditions are clamped-free here, the linear mode shapes of a clamped-free beam are considered as the comparison functions $\phi_n(x)$;

$$\begin{aligned}\phi_n(x) = A_n\Big\{ & \cosh(\gamma_n x)-\cos(\gamma_n x)+[\sin(\gamma_n x)-\sinh(\gamma_n x)] \\ & \times\frac{\cosh(\gamma_n)+\cos(\gamma_n)}{\sin(\gamma_n)+\sinh(\gamma_n)}\Big\},\end{aligned} \quad (11.27)$$

where γ_n represents the roots of the frequency equation

$$1+\cos(\gamma_n)\cosh(\gamma_n)=0 \quad (11.28)$$

Leaving much of the details of nonlinear natural frequency development and its stability to Mahmoodi and Jalili (2007), utilizing the method of multiple scales, and ultimately solving (11.26a), the amplitude and nonlinear natural frequency can be presented as (Mahmoodi and Jalili 2007)

$$\begin{cases} a_n = a_{n0} \\ \omega_{Nn} = \omega_n + \varepsilon\dfrac{3k_{2n}}{8\omega_n}a_{n0}^2 \end{cases} \quad (11.29)$$

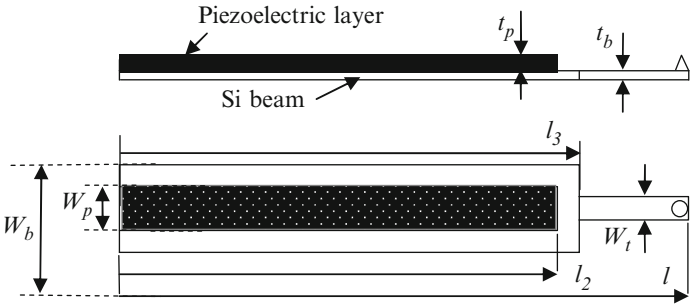

Fig. 11.11 Geometry of the microcantilever beam

where a_{n0} is a constant. Equation (11.29) indicates that the nonlinear natural frequency of the system is related to square of amplitude of vibration. The constant coefficients ε and k_n are dependent on beam and piezoelectric layer mechanical and electrical properties.

Experimental Setup and Methods: An experimental setup, similar to the arrangement and configuration presented in Sect. 8.3.2 (*see* Figs. 8.11 and 8.12), is utilized for nonlinear vibration analysis of the microcantilever beam. The objective of the experiment is to find the fundamental natural frequency of the microcantilever beam shown in Fig. 8.9 and subsequently compare the results with the resonance frequency derived from theoretical development. The same state-of-the-art microsystem analyzer, the MSA-400 manufactured by Polytec Inc. (www.polytec.com), is utilized as the testing device (*see* Fig. 8.11). The beam geometrical and the physical properties are provided in Fig. 11.11 and Table 11.1, respectively.

The microcantilever beam velocity is then measured in response to a 1 V AC voltage applied to the piezoelectric layer as the excitation source. The frequency response of the velocity signal is depicted in Fig. 11.12. First strip from left side in FFT plot of Fig. 11.12 locates the first resonance of the beam. The software provides the ability to identify the beam's first natural frequency which is 55,560 Hz in this case.

Numerical and Experimental Results Comparison: The nonlinear equations of motion for vibrations of a piezoelectrically-driven microcantilever beam were theoretically derived, and experimental frequency response was obtained in the preceding subsections. The frequency response of the experimental data for the microcantilever beam with properties listed in Table 11.1 is depicted in Fig. 11.13, which clearly presents the first natural frequency of the microcantilever beam.

The frequency response of model (11.26) is illustrated in Fig. 11.14. When comparing Figs. 11.13 and 11.14, it is observed that the resonance frequency of the system matches the experimental results very closely (i.e., 55,560 Hz in experiment vs. 55,579 Hz in theory).

In order to compare the results with linear methods, the method used in references (Lee et al. 2004, 2005) is utilized here to obtain the resonance frequency of

Table 11.1 Physical properties of the microcantilever

Microcantilever beam		ZnO piezoelectric layer	
Symbol	Value	Symbol	Value
c_b^D	185 GPa	c_p^D	133 GPa
l	500 μm	l_2	375 μm
W_b	250μm	β_{33}^S	45.5 Mm/F
W_t	55 μm	h_{31}	500 MV/m
ρ_b	2330 kg/m^3	ρ_p	6390 kg/m
t_b	4 μm	t_p	4 μm
ν_b	0.28	W_p	130 μm
d_{31}	11 pC/N	ν_p	0.25

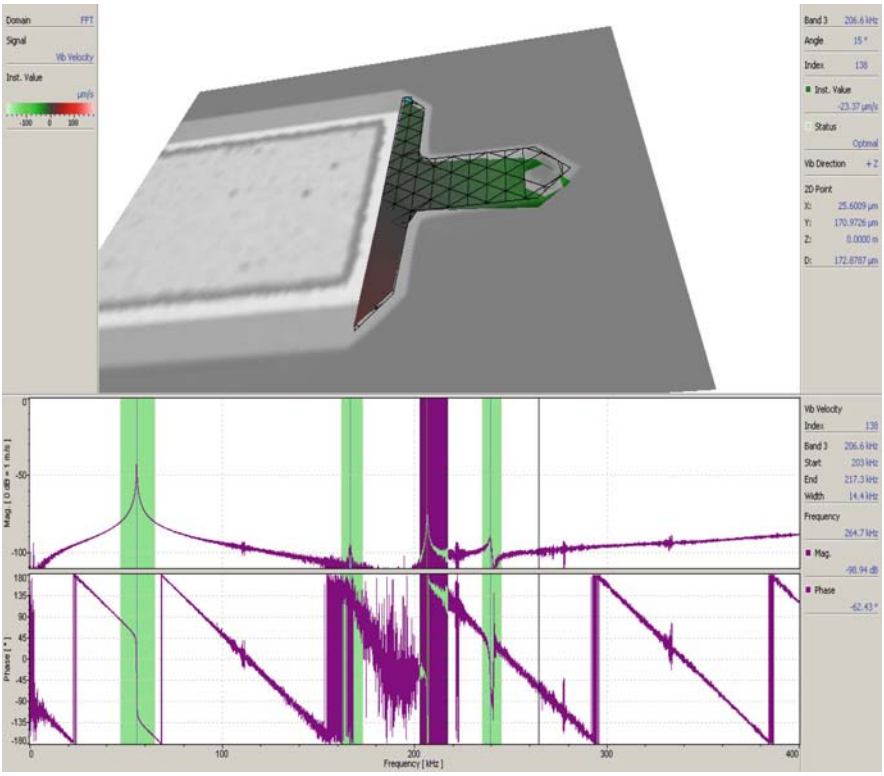

Fig. 11.12 Microcantilever fundamental frequency response for 1 V piezoelectric excitation
Source: Mahmoodi and Jalili 2007, with permission

the system. This is a linear method which uses the following formulations (Lee et al. 2004),

$$\omega_n = \frac{3.52}{2\pi l^2}\sqrt{\frac{\overline{EI}}{\rho_b t_b + \rho_p t_p}}, \tag{11.30}$$

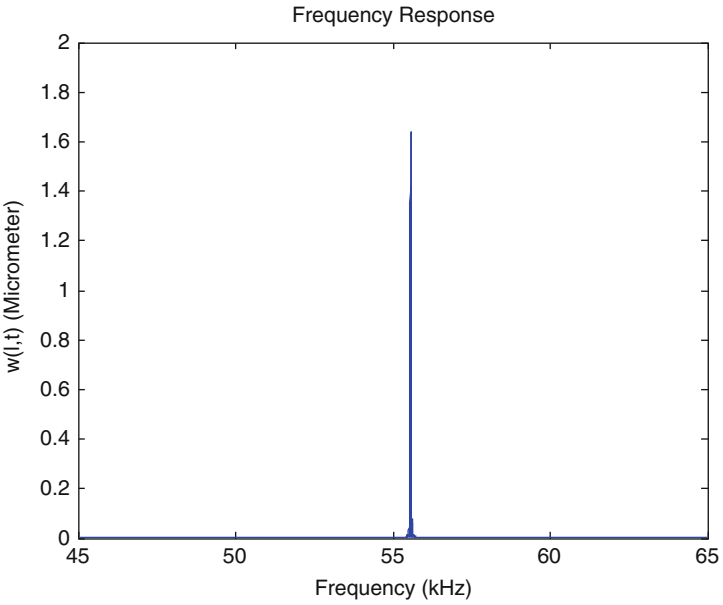

Fig. 11.13 Fast Fourier Transform of the microcantilever tip deflection, experimental
Source: Mahmoodi and Jalili 2007, with permission

where

$$\overline{EI} = \frac{W_b \left((c_p^D)^2 t_p^4 + (c_b^D)^2 t_b^4 + c_p^D t_p c_b^D t_b \left(4t_p^2 + 4t_b^2 + 6t_p t_b\right)\right)}{12(c_b^D t_b + c_p^D t_p)} \tag{11.31}$$

Equations (11.30) and (11.31) are the same expressions that appeared as (2) and (3) of Lee et al. (2004). In this case, there is a significant difference between experimental and linear analytical results. Using (11.30) and (11.31), the frequency is calculated to be 32,385 Hz, which indicates significant error compared to experimental results.

For investigating the influence of correction in modulus of elasticity presented in (11.8), the resonance frequency of the system has been obtained without considering the correction in (11.8). The obtained frequency is 53,598 Hz which shows a 3.55% error in result when compared with the frequency obtained with corrected modulus of elasticity as in (11.8). Therefore, it is concluded that the correction in modulus of elasticity must be considered.

One of the important results that can be concluded is the noticeable sensitivity of the amplitude of microcantilever vibration to input excitation. In Fig. 11.15, the excitation voltage is experimentally increased from 0.5 V in Fig. 11.15a to 1.5 V in Fig. 11.15b. This results in significant increase in vibration amplitude as shown in

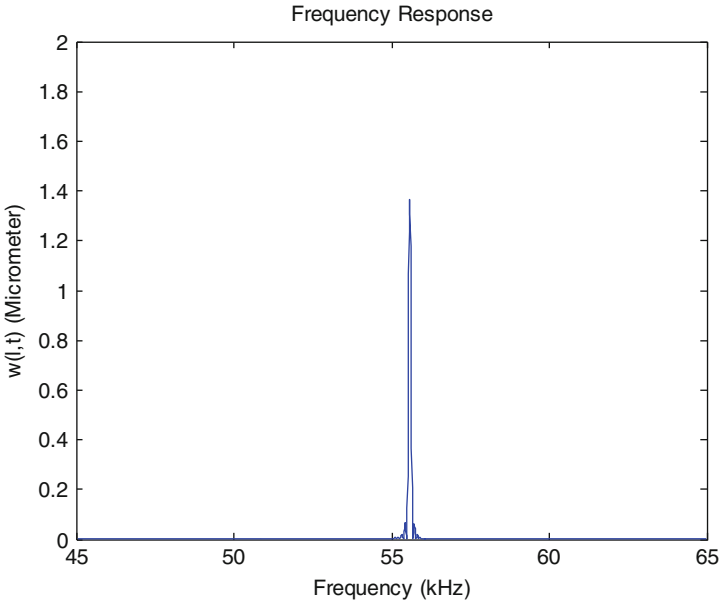

Fig. 11.14 Fast Fourier Transform of the microcantilever tip deflection, simulations
Source: Mahmoodi and Jalili 2007, with permission

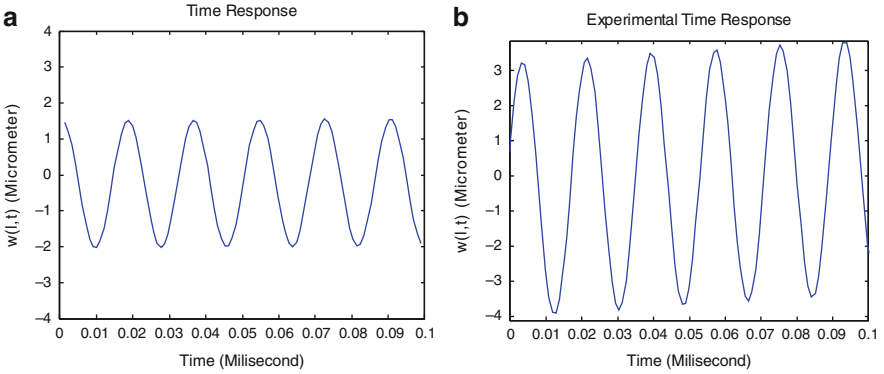

Fig. 11.15 Experimental results for amplitude of tip vibration; (**a**) 0.5 V excitation, and (**b**) 1.5 V excitation
Source: Mahmoodi and Jalili 2007, with permission

Fig. 11.15b. The nonlinear modeling proposed here can predict this phenomenon very closely as depicted in Fig. 11.16.

There are some small discrepancies between amplitude of experimental results and the numerical ones, which is expected since the numerical parameters (provided by the manufacturer) used in simulations may not exactly match the real parameters (microcantilever's parameters). These parameters are typically obtained and

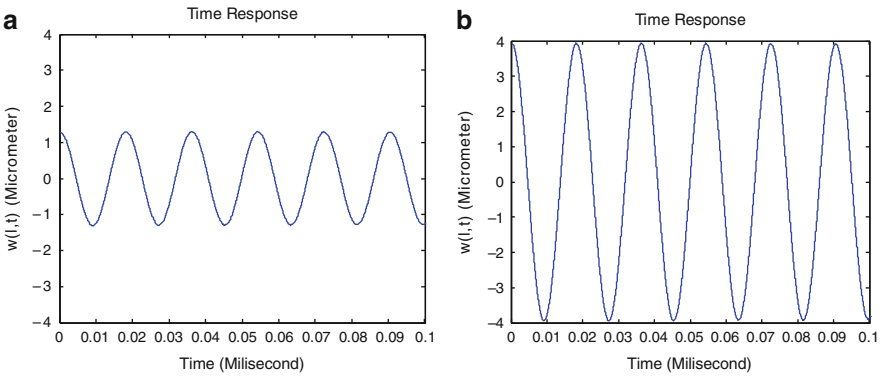

Fig. 11.16 Simulation results for amplitude of tip vibration; (**a**) 0.5 V excitation, and (**b**) 1.5 V excitation
Source: Mahmoodi and Jalili 2007, with permission

measured by manufacturer in a specific condition which may be different from the condition of the present laboratory experiment. These differences might also be due to the damping in real experiment which has not been modeled here.

At this stage, the nonlinear frequency response curves can be plotted for the two different piezoelectric excitation amplitudes of 0.5 and 1.5 V, as shown respectively in Figs. 11.17 and 11.18. It is clear from both Figs. 11.17 and 11.18 that the linear and nonlinear natural frequencies are different. The zero point on $\boldsymbol{\sigma}$ axis in Fig. 11.17 is the linear natural frequency point and the peak point of the curve shows the place of nonlinear natural frequency.

By studying (11.29) numerically, it is observed that the nonlinear frequency for a large amount of a_n (in this case larger that 10^{-9}) can become very significant. In addition, it is demonstrated in Fig. 11.17 that for forced vibration there is also a shift in frequency due to nonlinearity and applied excitation. As seen from Fig. 11.18, the response amplitude obviously increases when higher excitation voltage is applied compared to Fig. 11.17. In addition, increasing the voltage of excitation shifts the nonlinear natural frequency further more to the right side of the plot, which shows that nonlinear frequency increases with higher excitation voltages. While Fig. 11.17 shows a good match between numerical and analytical results, such agreement between analytical and numerical approaches begins to diminish in Fig. 11.18 as the excitation frequency passes the resonance. However, it can be argued that these discrepancies are still acceptable and a good match between analytical and simulation results is observed.

Addition of Piezoelectric Materials Nonlinearity: In this section, the governing equations of motion for the flexural vibrations of the piezoelectrically-actuated NMCS developed earlier are used to augment them with an additional nonlinearity, the piezoelectric material nonlinearity. Adopting the same procedure as in previous subsection for the microcantilever geometry, the constitutive equations of for the silicon (microcantilever beam) (*see* Chap. 4 as well as 11.14) are expressed as

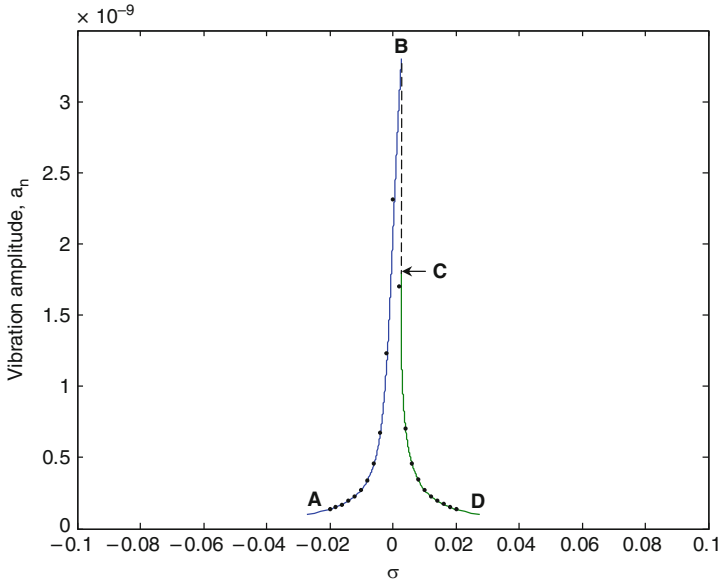

Fig. 11.17 Analytical and numerical results for frequency response of the system with 0.5 V excitation with points B and C representing the turning points (the "dots" represent the corresponding numerical results obtained by directly solving 11.26)
Source: Mahmoodi and Jalili 2007, with permission

$$\boldsymbol{\sigma}_1^b = c_b^D S_1^b \tag{11.32}$$

where $c_b^D = c_b^{D*}/\left(1-\nu_b^2\right)$; see (11.8). Here, c_b^{D*} is modulus of elasticity for silicon with ν_b its Poisson's ratio. Further, for the piezoelectric material the constitutive equations (11.13 and 11.14) are modified as (Crespo da Silva 1988)

$$\boldsymbol{\sigma}_1^p = c_p^D S_1^p - h_{31} D_3 + \frac{\alpha_1 \left(S_1^p\right)^2}{2} + \frac{\alpha_2 D_3^2}{2} - \alpha_3 D_3 S_1^p, \tag{11.33}$$

$$\boldsymbol{\epsilon}_3 = -h_{31} S_1^p + \beta_{33}^S D_3 + \frac{\alpha_3 \left(S_1^p\right)^2}{2} + \frac{\alpha_4 D_3^2}{2} - \alpha_2 D_3 S_1^p \tag{11.34}$$

where $c_p^D = {}^{c_p^{D*}}/_{(1-\nu_p^2)}$, c_p^{D*} is the modulus of elasticity for the piezoelectric material, ν_p is its Poisson's ratio, and α_i represents nonlinear piezoelectric coefficients.

As the sensor operates in air under very low electric fields, it is assumed that the nonlinearity in the electric field is very small and hence can be neglected. This implies that $\alpha_2 = \alpha_4 = 0$. Further, it is assumed that the piezoelectric material nonlinearities (the third term in 11.33) are at least one order of magnitude larger than the coupling nonlinearity; therefore, the effect of coupling term $\alpha_3 D_3 S_1^p$ is also neglected. Expressing the electric field in terms of the applied voltage, $V_a(t)$, and introducing the piezoelectric constant, d_{31} (*see* Table 6.2 and 8.18), (11.33) reduces

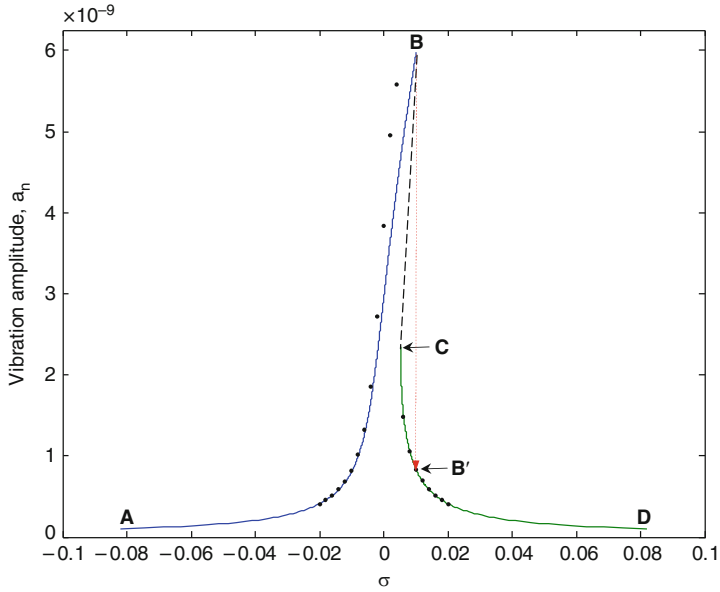

Fig. 11.18 Analytical and numerical results for frequency response of the system with 1.5 V excitation with points B and C representing the turning points (the "dots" represent the corresponding numerical results obtained by directly solving 11.26)
Source: Mahmoodi and Jalili 2007, with permission

as follows:

$$\boldsymbol{\sigma}_1^p = E_p S_1^p + \frac{\alpha_1}{2}\left(S_1^p\right)^2 - E_p d_{31}\frac{V_a(t)}{t_p}, \tag{11.35}$$

where $E_p \triangleq c_p^E = c_p^D\left(1-\boldsymbol{\kappa}_{31}^2\right)$ was defined earlier in Sect. 8.3, and t_p is the piezoelectric material thickness. Now, the total strain energy of the beam and piezoelectric layer can be written as (*see* Mahmoodi et al. 2006; Nayfeh et al. 1992 for the detailed derivations of the linear version of this piezoelectrically-driven system)

$$\begin{aligned} U = {} & \frac{1}{2}\int_0^{l_1}\iint_A \left(\boldsymbol{\sigma}_1^b S_1^b\right)\mathrm{d}A\,\mathrm{d}s + \frac{1}{2}\int_{l_1}^{l_2}\iint_A \left(\boldsymbol{\sigma}_1^b S_1^b\right)\mathrm{d}A\,\mathrm{d}s \\ & + \frac{1}{2}\int_{l_1}^{l_2}\iint_A \left(\boldsymbol{\sigma}_1^p S_1^p + \boldsymbol{\epsilon}_3 D_3\right)\mathrm{d}A\,\mathrm{d}s + \frac{1}{2}\int_{l_2}^{l_3}\iint_A \left(\boldsymbol{\sigma}_1^b S_1^b\right)\mathrm{d}A\,\mathrm{d}s \\ & + \frac{1}{2}\int_{l_3}^{l}\iint_A \left(\boldsymbol{\sigma}_1^b S_1^b\right)\mathrm{d}A\,\mathrm{d}s + \frac{1}{2}\int_0^l EA(s)\left(u'^2 + u'w'^2 + \frac{1}{4}w'^4\right)\mathrm{d}s \end{aligned} \tag{11.36}$$

where $\mathrm{d}A$ is the cross sectional area of a differential beam element and

$$EA(s) = \left(H_0 - H_{l_3}\right) c_b^D W_b t_b + \left(H_{l_1} - H_{l_2}\right) E_p W_p t_p + \left(H_{l_3} - H_l\right) c_b^D W_t t_b \tag{11.37}$$

where $H(s)$ is the Heaviside function, w denotes the width, t denotes the thickness, and the subscripts b, p and t indicate the silicon, piezoelectric material, and tip area of the beam, respectively; see Fig. 11.11 for these and other dimensions used.

Next, the kinetic energy of the system can be expressed as

$$T = \frac{1}{2} \int_0^l m(s)(\dot{u}^2 + \dot{w}^2)\, \mathrm{d}s, \tag{11.38}$$

where

$$m(s) = \left(\rho_b A_b + (H_{l1} - H_{l2})\, \rho_p A_p\right), \tag{11.39}$$

and ρ_b and ρ_p are the mass densities of silicon and the piezoelectric layer, respectively.

Using (11.36–11.38), the Lagrangian of the system, $L = T - U$ can be written as

$$\begin{aligned} L = \frac{1}{2} \int_0^l \Bigg\{ & m(s)(\dot{u}^2 + \dot{w}^2) - K(s)\left(w''^2 - 2w''^2 w'^2 - 2w''^2 u' - 2w' w'' u''\right) \\ & - \frac{\alpha_1}{2} I_{np}(s) w''^3 + K_p(s)\left(w'' - w'' u' - w' u'' - w'' w'^2\right) V_a(t) \\ & - EA(s)\left(u'^2 + u' w'^2 + \frac{1}{4} w'^4\right)\Bigg\}\, \mathrm{d}s, \end{aligned} \tag{11.40}$$

where

$$\begin{cases} K(s) = (H_0 - H_{l1})\, c_b^D I_b + (H_{l1} - H_{l2})\, c_b^D \left(I_b + W_b t_b z_n^2\right) \\ \qquad + (H_{l1} - H_{l2})\, E_p I_p + (H_{l2} - H_{l3})\, c_b^D I_b + (H_{l3} - H_l)\, c_b^D I_t \\ K_p(s) = (H_{l1} - H_{l2})\, \dfrac{W_p}{2} E_p d_{31} \left(t_p + t_b - 2z_n\right) \end{cases} \tag{11.41}$$

where z_n represents the neutral axis of the beam and given by (11.21).

In addition,

$$\begin{cases} I_b = \dfrac{W_b t_b^3}{12} \\ I_t = \dfrac{W_t t_t^3}{12} \\ I_{np}(s) = (H_{l1} - H_{l2})\, \frac{W_p}{4} \left[\left(\frac{t_b}{2} + t_p - z_n\right)^4 - \left(\frac{t_b}{2} - z_n\right)^4\right] \\ I_p = W_p\left(t_p z_n^2 + \left(t_p^2 + t_b t_p\right) z_n + \frac{1}{3}\left(t_p^3 + \frac{3}{2} t_b t_p^2 + \frac{3}{4} t_b^2 t_p\right)\right) \end{cases} \tag{11.42}$$

Using the same inextensibility condition (11.22) to relate the flexural and the longitudinal vibrations of the beam and substituting (11.36–11.42) into the extended Hamilton's principle results in the following equations of motion and the associated boundary conditions

$$m(s)\ddot{w} + \left(K(s)w''\right)'' + \left(\frac{3\alpha_1}{2} I_{np}(s) w'^2\right)'' + \left[w'\left(K(s)w'w''\right)'\right]' + \left[w' \int_l^s m(s) \int_0^s \left(\ddot{w}'w' + \dot{w}'^2\right) \mathrm{d}s\, \mathrm{d}s\right]' - \left[\frac{1}{2} w' \left[K_p(s)w'V_a(t)\right]'\right]' + \left[\frac{1}{4} K_p(s)w'^2 V_a(t)\right]'' = \left[\frac{1}{2} K_p(s)V_a(t)\right]'' \tag{11.43}$$

$$w = w' = 0 \text{ at } s = 0;\ w'' = w''' = 0 \text{ at } s = l \tag{11.44}$$

By examining (11.43), two types of nonlinearities are observed: first quadratic nonlinearities that are manifested in the third term and results from the material nonlinearities in the piezoelectric layer; second cubic nonlinearities that are due to the geometry of the beam and appear as nonlinear inertia and stiffness terms (fourth and fifth terms in (11.43)). In addition, the sixth and seventh terms in (11.43) represent nonlinear parametric excitations emanating from the nature of the piezoelectric excitation. The last term in the equation represents a direct excitation term.

Reduced-order Modeling: Similar to the preceding subsection, a reduced-order model of (11.43) can be obtained by utilizing a Galerkin procedure in which the deflection *w(s,t)* is discretized as (11.25). Taking the same orthogonal set of basis functions $\phi_n(s)$ as in (11.27), and substituting Galerkin approximation (11.25) into (11.43), multiplying the result by the mode shapes, ϕ_n, integrating the outcome over the length of the beam and using the orthonormality properties of the linear mode shapes, the following set of ordinary differential equations can be obtained:

$$\ddot{q}_n(t) + \hat{\mu}_n \dot{q}_n(t) + \boldsymbol{\omega}_n^2 q_n(t) + \hat{g}_{n1} q_n^2(t) V_a(t) + \hat{g}_{n2} q_n^3(t) + \hat{g}_{n3}\left(q_n^2(t)\ddot{q}_n(t) + q_n(t)\dot{q}_n^2(t)\right) + \hat{g}_{n5} q_n^2(t) = \hat{g}_{n4} V_a(t) \tag{11.45}$$

where $\hat{g}_{ni}$ are modal time-independent coefficients defined as

$$\boldsymbol{\omega}_n^2 = \int_0^l \phi_n(s)\left(K(s)\phi_n''(s)\right)'' \mathrm{d}s \tag{11.46a}$$

$$\hat{g}_{n1} = \frac{1}{4}\int_0^l \phi_n(s)\left(K_p(s)\phi_n'^2(s)\right)'' \mathrm{d}s - \frac{1}{2}\int_0^l \phi_n(s)\left[\phi_n'\left(K_p(s)\phi_n'(s)\right)'\right]' \mathrm{d}s \tag{11.46b}$$

$$\hat{g}_{n2} = \int_0^l \phi_n(s) \left[\phi_n'(s) \left(K(s) \phi_n'(s) \phi_n''(s) \right)' \right]' \, \mathrm{d}s \tag{11.46c}$$

$$\hat{g}_{n3} = \int_0^l \phi_n(s) \left[\phi_n'(s) \int_l^s m(s) \int_0^s 2\phi_n'^2(s) \, \mathrm{d}s \, \mathrm{d}s \right]' \mathrm{d}s \tag{11.46d}$$

$$\hat{g}_{n4} = \frac{1}{2} \int_0^l \phi_n(s) K_p''(s) \, \mathrm{d}s \tag{11.46e}$$

$$\hat{g}_{n5} = \frac{3}{2} \alpha_1 \int_0^l \phi_n(s) \left(I_{np}(s) \phi'^2(s) \right)'' \mathrm{d}s \tag{11.46f}$$

and $\hat{\mu}_n$ represents modal damping coefficients introduced to represent linear damping effects.

Similar to preceding subsection, the details of the nonlinear frequency equation development and its stability are left to Mahmoodi et al. (2008a,b) for interested readers because of their lengthy expressions. Utilizing the method of multiple scales (Nayfeh 1973) and seeking a uniform second-order nonlinear approximate solution of (11.45) near ω_n, after some derivations and manipulations the nonlinear frequency-response equation for the piezoelectrically-actuated NMCS can be represented as

$$(\hat{\mu}_n \omega_n a_n)^2 + \left[\frac{N_{\text{eff}} a_n^3 - 8\omega_n^2 \sigma a_n}{4\hat{g}_{n4} - 2\hat{g}_{n1} a_n^2} \hat{g}_{n4} \right]^2 = (\hat{g}_{n4} f)^2 \tag{11.47}$$

where N_{eff} is a measure of the effective nonlinearity of the system given by

$$N_{\text{eff}} = \frac{3\hat{g}_{n2} - \frac{10}{3}\hat{g}_{n5}^2 - 2\hat{g}_{n3}\omega_n^2}{8} \tag{11.48}$$

For a given level of voltage excitation f, (11.47) can be solved numerically for the associated response amplitude, a_n. Using this equation, a family of frequency-response curves is generated as shown in Fig. 11.19 for the fundamental vibration mode and different values of $\hat{g}_{15}$.

The coefficient of effective nonlinearity plays an essential role in characterizing the nonlinear behavior of the sensor response. For instance, when the coefficient of effective nonlinearity is positive, the system has a hardening-type behavior meaning that large amplitudes responses occur at excitation frequencies that are larger than $\boldsymbol{\omega}_1$, Fig. 11.19. On the other hand, when this coefficient is negative, the nonlinearity is said to be of the softening-type meaning that large amplitude motions occur at excitation frequencies that are lower than the natural frequency of the system.

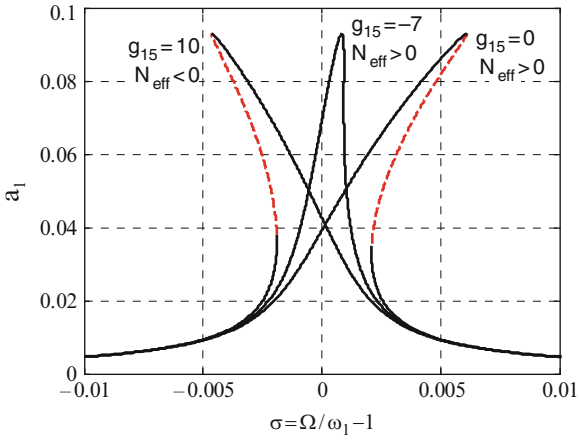

Fig. 11.19 A family of nonlinear frequency response curves obtained for $f = 9\,\mathrm{V}$, $\hat{\mu} = 0.0005$, and different values of $\hat{g}_{15}$. Dashed lines represent unstable solutions
Source: Mahmoodi et al. 2008b, with permission

The effect of the material nonlinearities in the piezoelectric layer on the fundamental vibration mode are lumped into coefficient $\hat{g}_{15}$, when these nonlinearities are neglected; in other words, $\hat{g}_{15} = 0$, and the first mode of a cantilever beam is known to exhibit a hardening-type behavior; see also the works of (Arafat et al. 1998; Malatkar and Nayfeh 2002). Since $\hat{g}_{15}$ appears as a negative and squared term in the effective nonlinearity expression, including the material nonlinearities would certainly decrease the magnitude of the effective nonlinearity of the sensor, making the frequency response less and less hardening; see Fig. 11.19. For a sensor of known geometry and linear material properties, the coefficients $\hat{g}_{n2}$ and $\hat{g}_{n3}$ are well-defined, see Table 11.1. On the other hand, the coefficient $\hat{g}_{15}$, which depends on the nonlinear material properties of the piezoelectric layer, cannot be theoretically computed because the experimental value of α_1 is not available in the literature. As such, this coefficient will be obtained experimentally by examining the nonlinear response characteristics of the sensor as illustrated next.

Experimental Validation: Similar to the previous two subsections, the same experimental setup of Figs. 8.11 and 8.12 is utilized to validate the nonlinear theoretical model and to identify the unknown linear and nonlinear parameters.

Figure 11.20 displays a family of frequency-response curves obtained experimentally for the fundamental vibration mode of the sensor. Increasing values of the magnitude of voltage are utilized which clearly demonstrates that the sensor exhibits a softening-type behavior with large amplitude responses occurring at frequencies that are smaller than the first modal frequency. In fact, these results are contrary to the common understanding that the fundamental vibration mode of a cantilever beam has a hardening-type behavior. The reason for these differences can be attributed to the fact that, at the microscale, material nonlinearities in the piezoelectric layer (quadratic) overcome the geometric (cubic) nonlinearities, thereby producing a softening-type response.

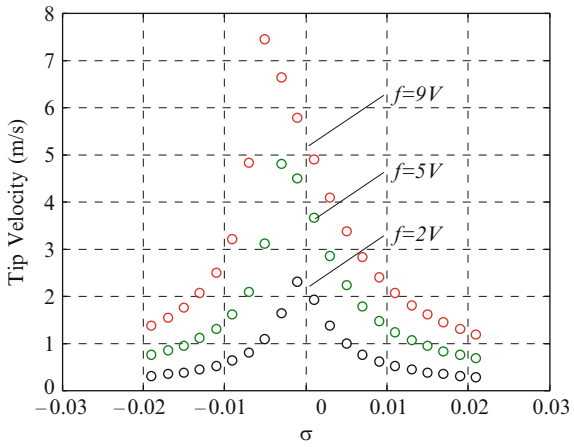

Fig. 11.20 Experimental frequency-response curves of a piezoelectrically-actuated microsensor *Source*: Mahmoodi et al. 2008b, with permission

To validate the theoretical model, we compare the frequency-response curves obtained experimentally to those obtained theoretically via (11.47). To that end, two unknown parameters are obtained experimentally. First, the linear damping coefficient $\hat{\mu} = \zeta_{\text{exp}}/(2\omega_1)$, where ζ_{exp} represents the experimental damping ratio, is obtained using the half-power points approach (Meirovitch 1997). For the sensor under consideration, we found that the damping ratio varies between $\zeta_{\text{exp}} = 0.0025$ and 0.0034 (air and structural dampings). As such, we utilized an average value of $\zeta_{\text{exp}} = 0.00295$.

Second, the coefficient of material nonlinearity in the piezoelectric layer is obtained using the frequency-response curves displayed in Fig. 11.20. More specifically, by utilizing the loci of the peaks of the experimental response for different voltages, we curve fit the best quadratic polynomial relating the response peaks to the frequency-detuning parameter. The generated polynomial, known also as the *backbone* curve, is compared to that obtained analytically by finding the extrema of (11.47). These correspond to the solution of

$$\frac{\mathrm{d}a_1}{\mathrm{d}\sigma} = 0 \tag{11.49}$$

or

$$a_{1\,\max} = \sqrt{8\omega_1^2\sigma \,/\, \left(3\hat{g}_{12} - \frac{10}{3}\hat{g}_{15}^2 - 2\hat{g}_{13}\omega_1^2\right)} \tag{11.50}$$

The only unknown in (11.50) is the coefficient $\hat{g}_{15}$. By comparing (11.50) to the best polynomial fit shown in Fig. 11.21, we find that $\hat{g}_{15}$ is equal to 60 and, hence, by virtue of (11.46f), the material nonlinearity coefficient of the piezoelectric layer can be found to be $\alpha_1 = 4645.23\,\text{GPa}$. Using the experimental values of the linear

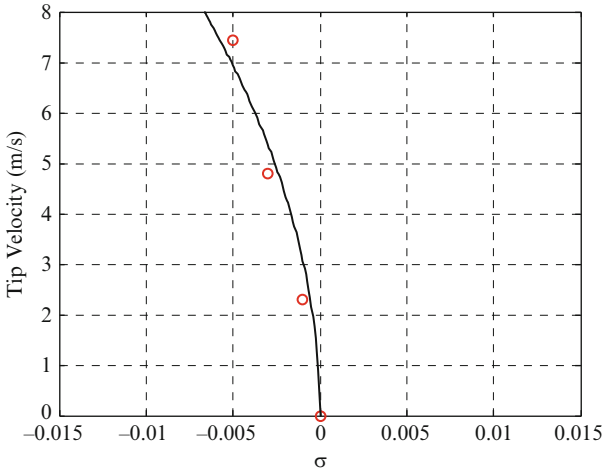

Fig. 11.21 Backbone curve of the frequency response. Circles represent the peaks of the experimentally-obtained frequency response curves and the solid line represents their best quadratic curve fit
Source: Mahmoodi et al. 2008b, with permission

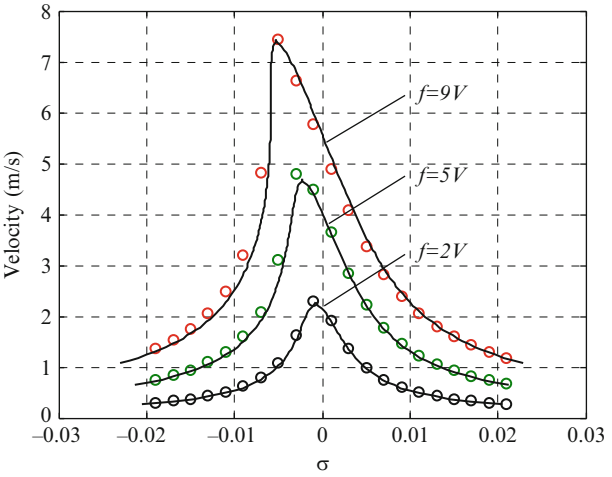

Fig. 11.22 Analytical and experimental frequency response curves. Circles represent experimental data and solid lines represent analytical results
Source: Mahmoodi et al. 2008b, with permission

damping and material nonlinearity coefficient, the frequency-response curves can be generated. These curves are compared to the experimental data in Fig. 11.22 demonstrating excellent agreement everywhere in the frequency range and not only at the peak frequencies (Mahmoodi et al. 2008b).

11.2.2 Coupled Flexural-Torsional Vibration Analysis of NMCS

The coupled flexural-torsion vibrations in beams may mostly occur because of the following three conditions: (1) shear center of the beam being offset from the neutral axis, (2) gyroscopic effect, and (3) geometrical asymmetry of the beam. The presence of an offset between center of gravity and shear center can lead to a coupling between flexural and torsional vibrations in mechanical structures (Takaway et al. 1997). Research results show for such beam systems, there is a significant effect in natural frequencies, mode shapes, and response because of flexure-torsion coupling (Eslimy-Isfahany and Banerjee 2000). This effect appears in linear form, i.e., the coupling of flexural-torsional vibrations leads to linear coupled differential equations of motion. A gyroscopic effect caused by rotation of beam base can also produce a coupled flexural-torsional vibration in the system (Bhadbhade et al. 2008). In this case, the coupling is due to the angular velocity at the base of the beam.

In this subsection, the flexural-torsion coupling due to geometry and the nonlinearity appearing in NMCS is investigated. More importantly, the presence of a piezoelectric layer on the beam for the purpose of actuation and sensing introduces new nonlinear terms in the equations of motion of the NMCS. Considering the higher order terms of vibration in motion of NMCS will result also in coupling between torsional and flexural motions. These higher order terms are due to geometry of the system, which can be attributed due to either large amplitude vibration of the NMCS or considering the inextensibility of the beam. By considering the inextensibility condition, the effect of longitudinal vibration can be imposed into flexural vibration which brings added nonlinearity into equations of motion (Esmailzadeh and Jalili 1998b). The reason that such geometrical nonlinearity is considered here is because of the small scale nature of microcantilevers, i.e., they may vibrate with large amplitude in response to a small applied force (Xie et al. 2003).

Dynamic System Modeling: The same uniform and initially straight metallic NMCS of Fig. 11.10 or Fig. 11.11 is revisited here with the same materials and geometrical properties mentioned earlier. In an effort to expand our vibration analysis, we consider the general 3D beam theory and include torsional vibration in addition to longitudinal and flexural vibrations. For this, the (x, y, z) axes in Figs. 11.10 and 11.23 are considered again here to be inertial, while the (ξ, θ, ζ) axes are assumed to be principal coordinates of the beam cross section at the arbitrary position s.

Here, $u(s,t)$ and $w(s,t)$ are components of displacement vector s along the axes x and z, respectively; and t is the time. The relationship between principal axes and the inertial axes are described by two Euler angle rotations. As depicted in Figs. 11.10 and 11.23, $\varphi(s,t)$ and $\psi(s,t)$ are rotation angles to take x and y to ξ and θ, respectively.

Three variables u, w, and φ are introduced to measure longitudinal, flexural, and torsional vibrations, respectively. The flexural angle between x and ξ axis is defined as ψ (*see* 11.3). The angular velocity, ω, of the beam can be obtained as (Crespo da Silva and Glynn, 1978; Arafat et al. 1998)

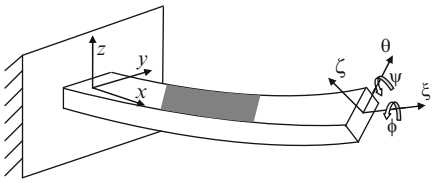

Fig. 11.23 Schematic of the microcantilever beam
Source: Mahmoodi and Jalili 2008, with permission

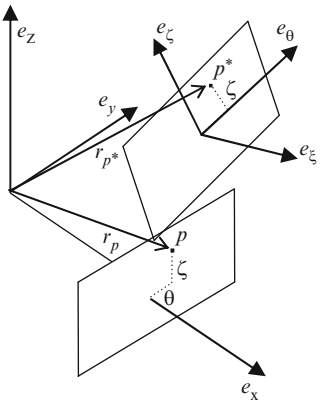

Fig. 11.24 Straight and deformed positions of an arbitrary point
Source: Mahmoodi and Jalili 2008, with permission

$$\vec{\omega} = \dot{\varphi}\vec{e}_\xi + \dot{\psi}\cos(\varphi)\vec{e}_\theta - \dot{\psi}\sin(\varphi)\vec{e}_\zeta$$
$$= \dot{\varphi}\vec{e}_\xi + \left(\dot{w}' - \dot{w}'u' - w'\dot{u}' - \dot{w}'w'^2\right)\left(-\varphi\vec{e}_\zeta + \left(1 - \frac{1}{2}\varphi^2\right)\vec{e}_\theta\right) \quad (11.51)$$

where $\vec{e}_i$ is a unit vector and $i = x, y, z, \xi, \theta, \zeta$ indicates the direction of the unit vector. The over dot and prime denote a partial derivative with respect to time and position, respectively. Similarly, the curvature vector $\vec{\rho}$ of the beam can be written as

$$\vec{\rho} = \varphi'\vec{e}_\xi + \psi'\left(\cos(\varphi)\vec{e}_\theta - \sin(\varphi)\vec{e}_\zeta\right)$$
$$= \varphi'\vec{e}_\xi + \left(w'' - w''u' - w'u'' - w''v'^2\right)\left(-\varphi\vec{e}_\zeta + \left(1 - \frac{1}{2}\varphi^2\right)\vec{e}_\theta\right) \quad (11.52)$$

The beam is assumed to possess uniform cross-sectional area. If it is considered that the cross-section of the beam is at an arbitrary position s as shown in Fig. 11.24 and p is a point on the cross-section located at (θ, ζ) relative to the neutral axis, then after deformation, point p with the displacement components u, v, and w moves to p^*. The coordinates of p^* are θ and ζ because of the assumption that the shape of the cross-section remains uniform after deformation.

The position vectors for both p and p^* can be written as

$$\vec{r}_p = s\vec{e}_x + \theta\vec{e}_y + \zeta\vec{e}_z \tag{11.53}$$

$$\vec{r}_{p^*} = (s+u)\vec{e}_x + w\vec{e}_z + \theta\vec{e}_\theta + \zeta\vec{e}_\zeta \tag{11.54}$$

Using the displacement vectors and definition of strain tensor S_p (*see* Chap. 4), one can write

$$S_1 = \zeta\rho_\theta - \theta\rho_\xi, S_2 = S_3 = S_4 = 0, S_5 = \theta\rho_\xi, \text{ and } S_6 = -\zeta\rho_\xi \tag{11.55}$$

Considering the plain strain in the beam and the fact that the ratio of beam width to thickness is very high for such microscale size beam configuration, the modulus of elasticity, like plates, must be corrected in the form of 11.8 (Ziegler 2004).

Similar to the preliminaries provided in Sect. 11.2.1, i.e., the constitutive equations of piezoelectric (11.13, 11.14) and stress–strain relationships (11.55), the governing equations of motion can be obtained using the energy method similar to the previous cases. Using the assumptions and preliminary derivations obtained in the previous subsection, the total kinetic energy of the system can be presented as

$$T = \frac{1}{2}\int_0^l \Big\{ m(s)(\dot{u}^2 + \dot{w}^2) + J_\xi\dot{\varphi}^2 + J_\theta\varphi^2\dot{w}'^2 + J_\zeta\left(\dot{w}'^2 - 2\dot{w}'^2u'\right. \\ \left. -2w'\dot{u}'\dot{w}' - 2\dot{w}'^2w'^2\right)\Big\}\,\mathrm{d}s \tag{11.56}$$

where

$$\begin{cases} m(s) = W_b\left(\rho_b t_b + (H_{l1} - H_{l2})\,\rho_p t_p\right) \\ J_\xi(s) = \frac{1}{12}m(s)\left[W_b^2 + \left(t_b + (H_{l1} - H_{l2})\,t_p\right)^2\right], \\ J_\theta(s) = \frac{1}{12}m(s)W_b^2 \\ J_\zeta(s) = \frac{1}{12}m(s)\left(t_b + (H_{l1} - H_{l2})\,t_p\right)^2 \end{cases} \tag{11.57}$$

and

$$H_{l_1} = H(s - l_1), \tag{11.58}$$

$$H_{l_2} = H(s - l_2) \tag{11.59}$$

$H(s)$ is the Heaviside function, ρ is the linear mass density, and J_i is mass moment of inertia with respected to axis $i = \xi, \theta, \zeta$.

The total potential energy of the beam and piezoelectric layer can now be written as

$$
\begin{aligned}
U = & \frac{1}{2}\int_0^{l_1}\iint_A \left(\sigma_1^b S_1^b + \sigma_6^b S_6^b + \sigma_5^b S_5^b\right) \mathrm{d}A\,\mathrm{d}s + \frac{1}{2}\int_{l_1}^{l_2}\iint_A \left(\sigma_1^b S_1^b + \sigma_6^b S_6^b + \sigma_5^b S_5^b\right) \mathrm{d}A\,\mathrm{d}s \\
& + \frac{1}{2}\int_{l_1}^{l_2}\iint_A \left(\sigma_1^p S_1^p + \epsilon_3 D_3\right) \mathrm{d}A\,\mathrm{d}s + \frac{1}{2}\int_{l_2}^{l}\iint_A \left(\sigma_1^b S_1^b + \sigma_6^b S_6^b + \sigma_5^b S_5^b\right) \mathrm{d}A\,\mathrm{d}s \\
& + \frac{1}{2}\int_0^l EA(s)\left(u'^2 + u'w'^2 + \frac{1}{4}w'^4\right) \mathrm{d}s
\end{aligned} \tag{11.60}
$$

where

$$
EA(s) = (H_0 - H_{l1})\, c_b^D W_b t_b + (H_{l1} - H_{l2})\, E_p W_p t_p \tag{11.61}
$$

Using (11.52–11.56), the Lagrangian of the system can be expressed as

$$
\begin{aligned}
L = & \frac{1}{2}\int_0^l \Big\{ m(s)(\dot{u}^2 + \dot{w}^2) + J_\xi \dot{\varphi}^2 + J_\theta \varphi^2 \dot{w}'^2 \\
& + J_\xi \left(\dot{w}'^2 - 2\dot{w}'^2 u' - \varphi^2 \dot{w}'^2 - 2w'\dot{w}'\dot{u}' - 2\dot{w}'^2 w'^2\right) - C_\xi(s)\varphi'^2 - C_\theta(s)\varphi^2 w''^2 \\
& - C_\zeta(s)\left(w''^2 - 2w''^2 w'^2 - \varphi^2 w''^2 - 2w''^2 u' - 2w'w''u''\right) \\
& + C_c(s)\left(w'' - w''u' - w'u'' - w''w'^2 - \frac{1}{2}w''\varphi^2\right) V_a(t) \\
& - EA(s)\left(u'^2 + u'w'^2 + \frac{1}{4}w'^4\right) \Big\}\, \mathrm{d}s,
\end{aligned} \tag{11.62}
$$

where

$$
\begin{cases}
C_\xi(s) = (H_0 - H_{l1})\, G_b I_\xi^b + (H_{l1} - H_{l2})\, G_b \left(I_\xi^b + W_b t_b z_n^2\right) \\
\qquad\quad + (H_{l1} - H_{l2})\, G_p I_\xi^p + (H_{l2} - H_l)\, G_b I_\xi^b \\
C_\theta(s) = (H_0 - H_{l1})\, c_b^D I_\theta^b + (H_{l1} - H_{l2})\, c_b^D I_\theta^b + (H_{l1} - H_{l2})\, E_p I_\theta^p \\
\qquad\quad + (H_{l2} - H_l)\, c_b^D I_\theta^b \\
C_\zeta(s) = (H_0 - H_{l1})\, c_b^D I_\zeta^b + (H_{l1} - H_{l2})\, c_b^D \left(I_\zeta^b + W_b t_b z_n^2\right) \\
\qquad\quad + (H_{l1} - H_{l2})\, E_p I_\zeta^p + (H_{l2} - H_l)\, c_b^D I_\zeta^b \\
C_c(s) = (H_{l1} - H_{l2})\, \frac{W_p}{2} E_p d_{31}\left(t_p + t_b - 2z_n\right),
\end{cases} \tag{11.63}
$$

and

$$\begin{cases} I_{\xi}^{b} = W_b t_b^3 k_{\xi}^{b},\ k_{\xi}^{b} = \dfrac{1}{3}\left[1 - \left(\dfrac{192 t_b}{\pi^5 W_b}\right) \sum\limits_{n=1,3,\ldots}^{\infty} \dfrac{1}{n^5} \tanh\left(\dfrac{n\pi W_b}{2t_b}\right)\right] \\ I_{\theta}^{b} = \dfrac{W_b^3 t_b}{12} \\ I_{\zeta}^{b} = \dfrac{W_b t_b^3}{12} \\ I_{\xi}^{p} = W_p t_p^3 k_{\xi}^{p},\ k_{\xi}^{p} = \dfrac{1}{3}\left[1 - \left(\dfrac{192 t_p}{\pi^5 W_p}\right) \sum\limits_{n=1,3,\ldots}^{\infty} \dfrac{1}{n^5} \tanh\left(\dfrac{n\pi W_p}{2t_p}\right)\right] \\ I_{\theta}^{p} = \dfrac{W_p^3 t_p}{12} \\ I_{\zeta}^{p} = W_p \left(t_p z_n^2 - \left(t_p^2 + t_b t_p\right) z_n + \dfrac{1}{3}\left(t_p^3 + \dfrac{3}{2} t_b t_p^2 + \dfrac{3}{4} t_b^2 t_p\right)\right) \end{cases} \tag{11.64}$$

Utilizing the Lagrangian expression presented in (11.62), the equations of motion of the system with respect to three variables u, ϕ and w can be obtained as

$$\left(J_{\theta} - J_{\zeta}\right)\varphi \dot{w}'^2 - \left(C_{\theta} - C_{\zeta}\right)\varphi w''^2 + \left(C_{\xi}\varphi'\right)' - \frac{1}{2} C_c w'' \varphi V_a(t) = J_{\xi}\ddot{\varphi}, \tag{11.65a}$$

$$\varphi = 0 \text{ at } s = 0; \quad \varphi' = 0 \text{ at } s = l, \tag{11.65b}$$

$$\left[\frac{1}{2} C_c w'' V_a(t) + J_{\zeta}\dot{w}'^2 + EA\left(u' + \frac{1}{2} w'^2\right) - C_{\zeta} w''^2\right]' + \left(C_{\zeta} w' w'' - \frac{1}{2} C_c w' V_a(t)\right)'' = m\ddot{u}, \tag{11.65c}$$

$$u = 0 \text{ at } s = 0; \quad u' = 0 \text{ at } s = l, \tag{11.65d}$$

$$\begin{aligned} &\left[J_{\zeta}\left(\dot{u}'\dot{w}' + 2w'\dot{w}'^2\right) - C_{\zeta}\left(u''w'' + 2w'w''^2\right) + EA\left(u'w' + \frac{1}{2} w'^3\right)\right. \\ &\left. + C_c\left(\frac{1}{2} u'' + w''w'\right) V_a(t)\right]' \\ &- \left[C_{\theta} w'' \varphi^2 + C_{\zeta}\left(w'' - w''\varphi^2 - 2w''w'^2 - 2w''u' - w'u''\right)\right. \\ &\left. - \frac{1}{2} C_c\left(1 - u' - w'^2 - \frac{\varphi^2}{2}\right) V_a(t)\right]'' \\ &+ \frac{\partial}{\partial t}\left[J_{\theta}\dot{w}'\varphi^2 + J_{\zeta}\left(\dot{w}' - \dot{w}'\varphi^2 - 2u'\dot{w}' - \dot{u}'w' - 2\dot{w}'w'^2\right)\right]' = m\ddot{w} \end{aligned} \tag{11.65e}$$

$$w = w' = 0 \text{ at } s = 0; \quad w'' = w''' = 0 \text{ at } s = l \tag{11.65f}$$

As seen from (11.65), there exist nonlinear terms in the equations from order two to three. However, the nonlinearities of the second order are due to presence

of piezoelectric layer. Considering (11.65a) and (11.65e), it is observed that the torsional and flexural vibrations are coupled in two ways; one is a third order nonlinearity coupling due to beam geometry and the other one is a second order nonlinearity due to both geometry and electromechanical coupling of piezoelectric layer. The former nonlinear terms have been obtained in previous studies, while the latter is a new observation which is disclosed (Mahmoodi and Jalili 2008). Having the equations of motion, a number of case studies are considered next to study the coupling of flexural and torsional vibration in presence of piezoelectric actuator patch and effect of nonlinearity due to beam geometry.

Flexural-torsional Vibration: If the longitudinal vibration is ignored, then the equations of motion reduce to the following form:

$$\left(J_\theta - J_\zeta\right)\varphi\dot{w}'^2 - \left(C_\theta - C_\zeta\right)\varphi w''^2 + \left(C_\xi\varphi'\right)' - \frac{1}{2}C_c w''\varphi V_a(t) = J_\xi\ddot{\varphi}, \quad (11.66a)$$

$$\varphi = 0 \text{ at } s = 0, \quad \varphi' = 0 \text{ at } s = l, \quad (11.66b)$$

$$\left[2J_\zeta w'\dot{w}'^2 - 2C_\zeta w'w''^2 + \frac{1}{2}EAw'^3 + C_c w''w'V_a(t)\right]' + \frac{\partial}{\partial t}\left[J_\theta\dot{w}'\varphi^2 + J_\zeta\left(\dot{w}' - \dot{w}'\varphi^2 - 2\dot{w}'w'^2\right)\right]' \quad (11.66c)$$

$$-\left[C_\theta w''\varphi^2 + C_\zeta\left(w'' - w''\varphi^2 - 2w''w'^2\right) - \frac{1}{2}C_c\left(1 - w'^2 - \frac{\varphi^2}{2}\right)V_a(t)\right]'' = m\ddot{w}$$

$$w = w' = 0 \text{ at } s = 0; \quad w'' = w''' = 0 \text{ at } s = l \quad (11.66d)$$

As seen, there still exists the same coupling between bending and torsion in the system. A closer look at (11.65a, b) and (11.66a, b) reveals that there is no effect of longitudinal vibrations in the equation of the torsional vibrations. This shows that even consideration of higher order terms in the geometry does not result in coupling between the torsion and longitudinal vibrations. However, the flexural and longitudinal vibrations are coupled and ignoring of longitudinal vibrations leads to omission of coupled nonlinear terms in (11.65e) which leads to (11.66c).

Fully Symmetric Uniform Beam: If the beam is considered to be completely symmetric in the sense that $J_\theta = J_\zeta$ and $C_\theta = C_\zeta$ (this corresponds, for example, to square or circular cross-sectional areas), then the nonlinear terms in (11.65a) are removed and torsional vibration is not only linear but also decoupled from flexural vibration. This concludes that even for large deformations, the nonlinear terms in torsional vibrations will not appear if the beam cross-section is square or circular shape. However, even for such beams, the presence of piezoelectric layer still couples the flexural and torsional vibrations. In this case, the equations of motion in (11.65) reduce to the following form:

$$\left(C_\xi\varphi'\right)' - \frac{1}{2}C_c w''\varphi V_a(t) = J_\xi\ddot{\varphi}, \quad (11.67a)$$

$$\varphi = 0 \text{ at } s = 0, \quad \varphi' = 0 \text{ at } s = l, \quad (11.67b)$$

$$\left[\frac{1}{2}C_c w'' V_a(t) + J_\xi \dot{w}'^2 + EA\left(u' + \frac{1}{2}w'^2\right) - C_\xi w''^2\right]' + \left(C_\xi w' w'' - \frac{1}{2}C_c w' V_a(t)\right)'' = m\ddot{u}, \tag{11.67c}$$

$$u = 0 \text{ at } s = 0, \quad u' = 0 \text{ at } s = l, \tag{11.67d}$$

$$\left[J_\xi\left(\dot{u}'\dot{w}' + 2w'\dot{w}'^2\right) - C_\xi\left(u''w'' + 2w'w''^2\right) + EA\left(u'w' + \frac{1}{2}w'^3\right) + C_c\left(\frac{1}{2}u'' + w''w'\right)V_a(t)\right]' - \left[C_\xi\left(w'' - 2w''w'^2 - 2w''u' - w'u''\right) - \frac{1}{2}C_c\left(1 - u' - w'^2 - \frac{\varphi^2}{2}\right)V_a(t)\right]'' + \frac{\partial}{\partial t}\left[J_\xi\left(\dot{w}' - 2u'\dot{w}' - \dot{u}'w' - 2\dot{w}'w'^2\right)\right]' = m\ddot{w} \tag{11.67e}$$

$$w = w' = 0 \text{ at } s = 0, \quad w'' = w''' = 0 \text{ at } s = l \tag{11.67f}$$

Although there still exist some nonlinear terms in the equations, the only term which couples the flexure and torsion is the second order nonlinear term in (11.67a) and the one in (11.67e), which are due to presence of piezoelectric actuator layer (i.e., C_c in 11.63). Equation (11.67a) has no longer the third order nonlinearity when compared with (11.65a).

Inextensible Beam: The inextensibility condition expresses that the elongation of the neutral axis during the vibration is ignorable. Considering the inextensibility condition and using (11.22), (11.65c) and (11.65e) can be reduced into one equation consequently. Then, the equations of motion of the system can be presented in the following form:

$$\left(J_\theta - J_\xi\right)\varphi\dot{w}'^2 - \left(C_\theta - C_\xi\right)\varphi w''2 + \left(C_\xi\varphi'\right)' - \frac{1}{2}C_c w''\varphi V_a(t) = J_\xi\ddot{\varphi}, \tag{11.68a}$$

$$\varphi = 0 \text{ at } s = 0, \varphi' = 0 \text{ at s} = l, \tag{11.68b}$$

$$\left[\frac{1}{2}w'\left[C_c w' V_a(t)\right]' - w'\left(C_\xi w' w''\right)' - mw'\int_l^s\int_0^s\left(\ddot{w}'w' + \dot{w}'^2\right)\mathrm{d}s\,\mathrm{d}s\right]' - \left[C_\theta w''\phi^2 + C_\xi\left(w'' - w''\phi^2\right) - \frac{1}{2}C_c\left(1 - \frac{w'^2}{2} - \frac{\phi^2}{2}\right)V_a(t)\right]'' + \frac{\partial}{\partial t}\left[J_\theta\dot{w}'\phi^2 + J_\xi\left(\dot{w}' - \dot{w}'\phi^2\right)\right]' = m\ddot{w} \tag{11.69a}$$

$$w = w' = 0 \text{ at } s = 0, \quad w'' = w''' = 0 \text{ at } s = l \tag{11.69b}$$

Using the coupling of stretching and flexure to the inextensibility condition, the two nonlinear equations for longitudinal and flexure vibrations are combined into one. There are now two orders of nonlinearities, the second order nonlinearity is due to presence of piezoelectric layer and the third order nonlinear terms are due to geometry and appear as nonlinear inertia and stiffness terms.

Assumed Mode Model Expansion: Similar to the previous two cases, the equations of motion of system (11.68–11.69) can be reduced to (for the sake of simplicity, the effect of rotary inertia (J_θ, J_ξ) terms is ignored here) the following:

$$J_\xi \ddot{\varphi} - \left(C_\xi \varphi'\right)' + \left(C_\theta - C_\xi\right)\varphi w''^2 + \frac{1}{2} C_c w'' \varphi V_a(t) = 0, \tag{11.70a}$$

$$\varphi = 0 \text{ at s} = 0, \quad \varphi' = 0 \text{ at s} = l, \tag{11.70b}$$

$$\begin{aligned} m\ddot{w} + \left(C_\xi w''\right)'' + \left[w' \int_l^s m \int_0^s \left(\ddot{w}' w' + \dot{w}'^2\right) \mathrm{d}s \, \mathrm{d}s \right]' \\ + \left[w' \left(C_\xi w' w''\right)' \right]' + \left[\left(C_\theta - C_\xi\right) w'' \varphi^2 \right]'' \\ + \frac{1}{2} \left\{ \left[C_c \left(\frac{w'^2}{2} + \frac{\varphi^2}{2} \right) \right]'' - \left[w' \left[C_c w' \right]' \right]' \right\} V_a(t) = \frac{1}{2} C_c'' V_a(t) \end{aligned} \tag{11.70c}$$

$$w = w' = 0 \text{ at } s = 0, \quad w'' = w''' = 0 \text{ at } s = l \tag{11.70d}$$

In order to produce the ordinary differential equations governing the time functions of equations of motion, these equations are separated into position and time components using Galerkin approximation as

$$\varphi(s,t) = \sum_{m=1}^{\infty} \varphi_m(s,t) = \sum_{m=1}^{\infty} \alpha_m(s) q_m(t), \tag{11.71}$$

$$w(s,t) = \sum_{n=1}^{\infty} w_n(s,t) = \sum_{n=1}^{\infty} \beta_n(s) r_n(t), \tag{11.72}$$

where α_m and β_n are the comparison functions satisfying only beam boundary conditions and not necessarily the equations of motion (11.70a) and (11.70c) for bending and torsion of the microcantilever beam, respectively, and q_m and r_n are the generalized time-dependent coordinates. Since the boundary conditions of the beam are clamped-free, the linear mode shapes for torsion and flexure are considered as the following comparison functions;

$$\alpha_m(s) = A_m \sin(\gamma_m s), \tag{11.73}$$

$$\beta_n(s) = B_n \left\{ \cosh(\lambda_n s) - \cos(\lambda_n s) + [\sin(\lambda_n s) - \sinh(\lambda_n s)] \frac{\cosh(\lambda_n l) + \cos(\lambda_n l)}{\sin(\lambda_n l) + \sinh(\lambda_n l)} \right\}, \tag{11.74}$$

where

$$\gamma_m = (2m-1)\,\frac{ß}{2l}, \tag{11.75a}$$

and λ_n represents the roots of the frequency equation,

$$1 + \cos(\lambda_n l)\cosh(\lambda_n l) = 0 \tag{11.75b}$$

Constants A_n and B_n can be obtained using the orthogonality conditions. Substituting (11.71) and (11.72) into (11.70) and taking into account the orthogonality conditions between $\alpha_n(s)$ and $\beta_n(s)$, we get

$$k_{1mn}\ddot{q}_m(t) + k_{2mn}q_m(t) + k_{3mn}q_m(t)r_n^2(t) + k_{4mn}q_m(t)r_n(t)V_a(t) = 0, \tag{11.76a}$$

$$k_{5mn}\ddot{r}_n(t) + k_{6mn}r_n(t) + k_{7mn}r_n^2(t)V_a(t) + k_{8mn}r_n^3(t) + k_{9mn}\left(r_n^2(t)\ddot{r}_n(t) + r_n(t)\dot{r}_n^2(t)\right) + k_{10mn}r_n(t)q_m^2(t) + k_{11mn}q_m^2(t)V_a(t) = k_{12mn}V_a(t) \tag{11.76b}$$

where

$$k_{1mn} = \int_0^l J_\xi(s)\alpha_m^2(s)\,\mathrm{d}s \tag{11.77a}$$

$$k_{2mn} = \int_0^l \left(-C_\xi(s)\alpha_m'(s)\right)'\alpha_m(s)\,\mathrm{d}s \tag{11.77b}$$

$$k_{3mn} = \int_0^l \left(C_\theta(s) - C_\zeta(s)\right)\alpha_m^2(s)\beta_n''^2(s)\,\mathrm{d}s \tag{11.77c}$$

$$k_{4mn} = \frac{1}{2}\int_0^l C_c(s)\alpha_m^2(s)\beta_n''(s)\,\mathrm{d}s \tag{11.77d}$$

$$k_{5mn} = \int_0^l m(s)\beta_n^2(s)\,\mathrm{d}s \tag{11.77e}$$

$$k_{6mn} = \int_0^l \beta_n(s)\left(C_\zeta(s)\beta_n''(s)\right)''\,\mathrm{d}s \tag{11.77f}$$

$$k_{7mn} = \frac{1}{4}\int_0^l \beta_n(s)\left(C_c(s)\beta_n'^2(s)\right)'' \,\mathrm{d}s - \frac{1}{2}\int_0^l \beta_n(s)\left[\beta_n'\left(C_c(s)\beta_n'(s)\right)'\right]' \,\mathrm{d}s \tag{11.77g}$$

$$k_{8mn} = \int_0^l \beta_n(s)\left[\beta_n'(s)\left(C_\zeta(s)\beta_n'(s)\beta_n''(s)\right)'\right]' \,\mathrm{d}s \tag{11.77h}$$

$$k_{9mn} = \int_0^l \beta_n(s)\left[\beta_n'(s)\int_l^s m(s)\int_0^s 2\beta_n'^2(s)\,\mathrm{d}s\,\mathrm{d}s\right]' \,\mathrm{d}s \tag{11.77i}$$

$$k_{10mn} = \int_0^l \beta_n(s)\left[\left(C_\theta(s) - C_\zeta(s)\right)\beta_n''(s)\alpha_m^2\right]'' \,\mathrm{d}s \tag{11.77j}$$

$$k_{11mn} = \frac{1}{4}\int_0^l \beta_n(s)\left(C_c(s)\alpha_m^2(s)\right)'' \,\mathrm{d}s \tag{11.77k}$$

$$k_{12mn} = \frac{1}{2}\int_0^l \beta_n(s)C_c''(s)\,\mathrm{d}s \tag{11.77l}$$

Using (11.77), the nonlinear coupled equations (11.76) can be simulated with Matlab®/Simulink® and the results are presented, and compared with experiments as discussed next.

Numerical Simulations and Experimental Results: In order to compare the numerical results with experiments, the coefficients introduced in (11.70) are calculated for different mode shapes of flexure and torsion. Having these values, the nonlinear equations of motion (11.68,11.69) can be numerically simulated. Some of the values for k_{imn} have very large quantities because of microscale nature of the beam with its small dimensions. This can behave highly nonlinear when large deformation is applied to the microcantilever because of the actuation of piezoelectric layer. This actuation depends primarily on the applied voltage to piezoelectric material. Hence, even small voltage can move the vibration of the microscale beam into nonlinear regime.

In order to compare the experimental and numerical results, the beam is experimentally actuated. The results for first flexural natural frequency depicted in Fig. 11.25a show that the first natural frequency of the beam is 55,561 Hz. In addition, the time response is illustrated with 1 V actuation applied to the beam through the piezoelectric layer. The properties listed in Table 11.1 have been utilized to perform a numerical simulation to find the frequency response. As seen, the obtained results match the experimental results very closely. The logarithmic numerical results for the first flexural mode are depicted in Fig. 11.25b. It should

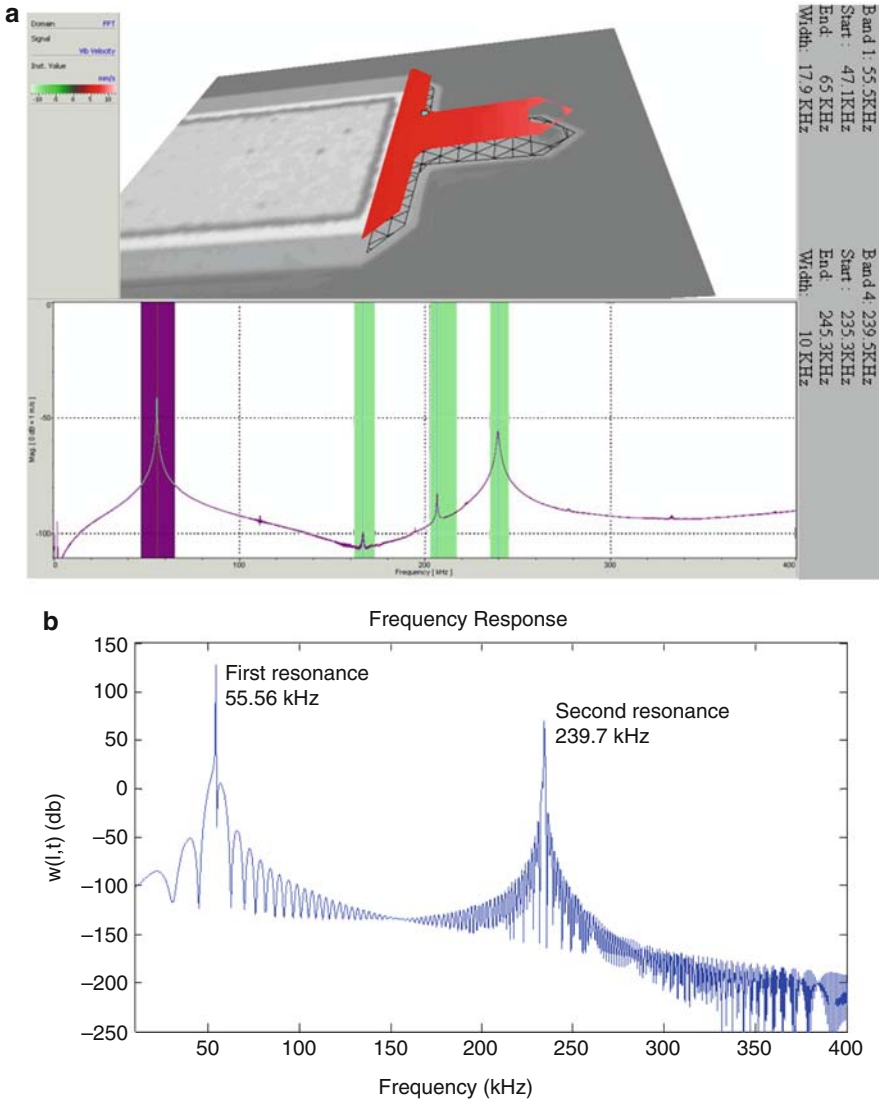

Fig. 11.25 (**a**) Experimental result, and (**b**) logarithmic simulation results for 1 V chirp excitation signal with first flexural natural frequency highlighted
Source: Mahmoodi and Jalili 2008, with permission

be noticed that experimental results are for the tip velocity, while the numerical ones are for tip displacement responses. The focus of comparison here is only on frequencies and not the amplitude at this stage.

The numerical simulations for frequency response of the system with the second flexural natural frequency highlighted as fourth band is depicted in Fig. 11.25b. There are two small peaks in experimental results (Fig. 11.25a). These peaks are due

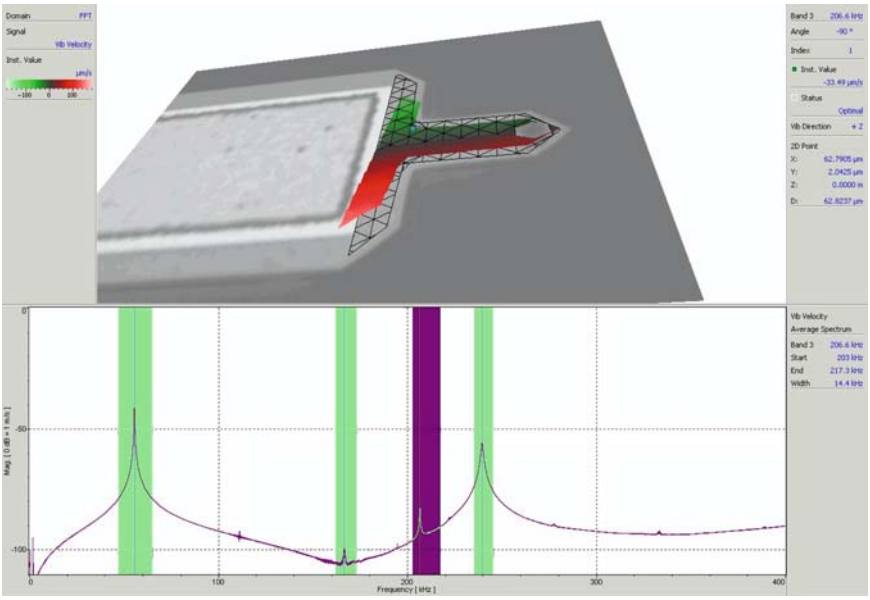

Fig. 11.26 (**a**) Experimental result for 1 V chirp excitation signal with flexural-torsional frequency of about 206 kHz highlighted
Source: Mahmoodi and Jalili 2008, with permission

to subharmonic resonance in the system. They actually exist in numerical results, but they are very small compared to resonance frequencies and also their amplitude changes because of initial conditions. In order to better realize the coupling between flexural and torsional vibrations, Fig. 11.26 shows the experimental result of the same experiment reported in Fig. 11.25a with the difference being the highlighted frequency of about 206 kHz. As clearly seen from this figure, there is a pronounced coupling between flexural and torsional vibrations at this frequency. Figure 11.27 also shows the first three nonlinear natural frequencies of the torsional vibrations of the microcantilever beam obtained by simulation in presence of nonlinear coupled geometry and piezoelectric terms.

11.3 Ultrasmall Mass Sensing and Materials Characterization using NMCS

As mentioned earlier, NMCS were first utilized in scanning force microscopy (SFM), (Thundat et al. 1994), and soon after their discovery they were mainly used as chemical (Wachter and Thundat 1995; Lang et al. 1998), thermal (Chen et al. 1995; Berger et al. 1996), and physical (Oden et al. 1999) sensors. NMCS were generally considered to be performing in air or in vacuum, resulting in the

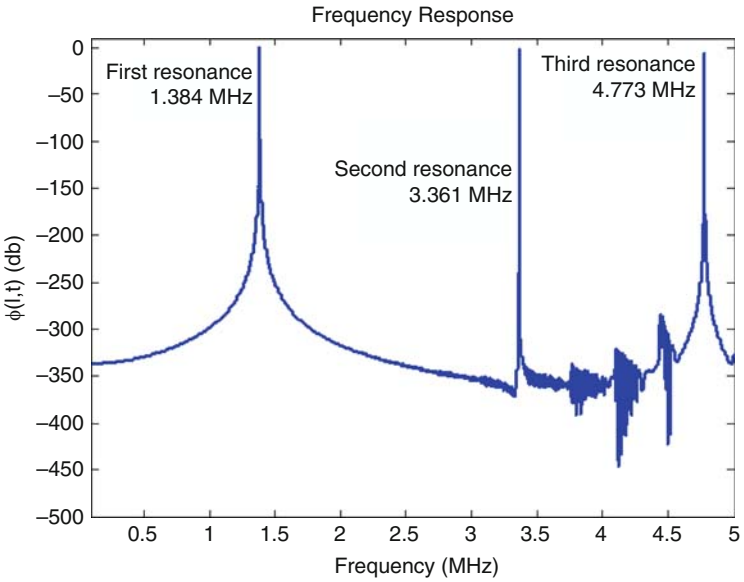

Fig. 11.27 Simulation results for the first three torsional natural frequencies for 1 V chirp excitation signal
Source: Mahmoodi and Jalili 2008, with permission

elimination of the environmental damping effect on the resonance frequency of microcantilevers. Utilizing microcantilever sensors for studying biological systems under native conditions[3] and investigating processes at liquid-solid interface brought the idea of considering the damping effect of the surrounding media on the resonance frequency of microcantilevers (Weigert et al. 1996). It was by 1996 that the applicability and potential of microcantilevers as biosensors attracted attention (Baselt et al. 1996; Berger et al. 1997).

Generally speaking, it seems more reasonable to utilize the static detection mode of NMCS for surface stress measurements (McKendry et al. 2002; Yue et al. 2004; Huber et al. 2006) and dynamic detection mode for the measurements of the added mass on microcantilever biosensors (Gupta et al. 2004a,b; Braun et al. 2005; Gfeller et al. 2005). Moreover, NMCS may also be used as sensors for detection of only the presence of biological species in an environment (Liu et al. 2003). Along this line and in order to demonstrate the great potential of NMCS as mass sensors, this subsection briefly reviews the modeling development and applications of NMCS for biological species detection as well as ultrasmall mass sensing and materials characterization.

[3] The "native conditions" of the biological systems refer to the fluidal environment in which almost all biological species would survive.

11.3.1 Biological Species Detection using NMCS

In this subsection, nonlinear vibrations of a piezoelectrically-driven NMCS in presence of a biological monolayer are investigated and the corresponding equations of motion are derived and simulated. The adsorbed biological layer is considered to be a monolayer and its adsorption induced surface stress is formulated from the molecular viewpoint. Similar to previous sections, the nonlinear terms in the governing equations of motion of the beam appear in the form of a quadratic because of the presence of piezoelectric layer, and cubic because of geometry of the beam and the adsorbed biological layer. Through extensive numerical simulations, it is demonstrated that the nonlinear effect of piezoelectric layer is significant in the microcantilever resonance sensing range. It is also shown that the effect of intermolecular attraction/repulsion on the surface stress is less dominant than other sources of surface stress (e.g., the electrostatic forces). Through this exercise, it is observed that piezoelectrically-actuated NMCS provides the ability of indirect measurement of vibrations and frequency response characteristics, instead of using bulky laser sensor.

Mathematical Modeling: A uniform and initially straight metallic microcantilever with a biological layer and a piezoelectric layer on top of the surface is considered as depicted in Fig. 11.28. It is assumed that both layers have the same width equal to the beam width. In addition, the beam follows the Euler-Bernoulli beam theory, in which shear deformation and rotary inertia terms are negligible.

The position of each layer on the microcantilever is located in Fig. 11.29(a). A beam segment of length s with initial axes of $y - z$ and principal axes of $\xi - \theta$ is depicted in Fig. 11.29(b). The bending angle between x-axis and ξ-axis is defined as ψ as seen before.

Similar to the procedure used in the preceding two subsections, the same angle ψ for an element of length ds can be obtained as a function of longitudinal deformation

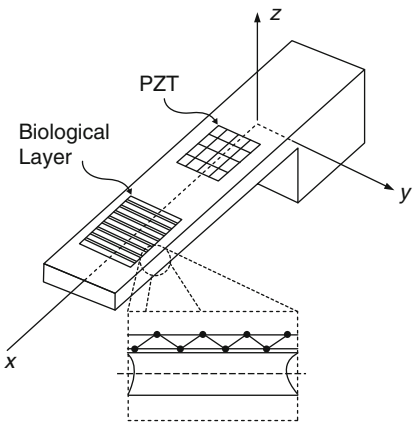

Fig. 11.28 Schematic of the microcantilever beam *Source*: Mahmoodi et al. 2008a,b, with permission

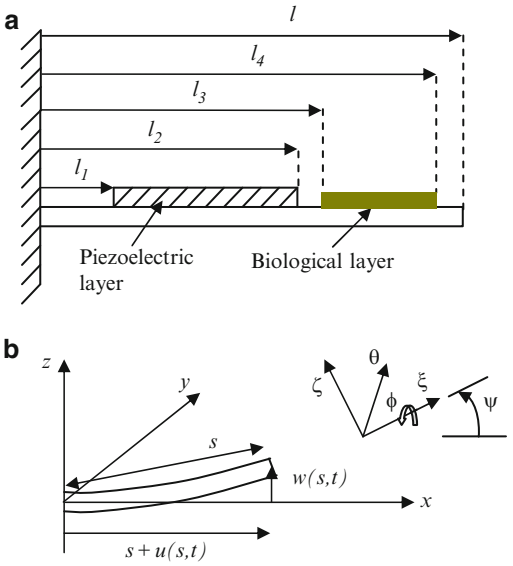

Fig. 11.29 (**a**) Position of layers, (**b**) Coordinate systems of an element of the microcantilever
Source: Mahmoodi et al. 2008a, with permission

$u(s,t)$ and bending deformation $w(s,t)$ (*see* 11.3). Using the inextensibility condition that demands no relative elongation of the neutral axis, the longitudinal deformation can be related to bending deformation as per (11.22). Using these relationships, the different energies for this problem can be formulated as described next.

The total kinetic energy of the system can be expressed as

$$T = \frac{1}{2}\int_0^l \left\{ m(s)\left[\left(-\frac{1}{2}\frac{\mathrm{d}}{\mathrm{d}t}\int w'^2 \mathrm{d}s\right)^2 + \dot{w}^2\right]\right\} \mathrm{d}s \tag{11.78}$$

where

$$m(s) = W_b\left(\rho_b t_b + (H_{l1} - H_{l2})\,\rho_p t_p + (H_{l3} - H_{l4})\,\rho_s t_s\right) \tag{11.79}$$

$$H_{l_i} = H(s - l_i), \quad i = 1, 2, 3 \text{ and } 4 \tag{11.80}$$

and $H(s)$ is the Heaviside function; ρ and W are the volumetric mass density and width of the beam, respectively. For all the parameters used in this section, subscripts b, p, and s denote the beam material, piezoelectric layer, and biological species layer, respectively.

For the potential energy of the piezoelectric layer, similar to previous subsection utilizing the coupling relation between the stress and the electrical field for piezoelectric layer (Preumont 2002), the potential energy of the piezoelectric layer can be written as

$$U_p = \frac{1}{2}\int_0^l \left\{ (H_{l1} - H_{l2}) \frac{E_p}{1-\nu_p^2} I_p \left(w''^2 + w''^2 w'^2\right) - C_c(s)\left(w'' + \frac{1}{2}w''w'^2\right) V_a(t) \right\} \mathrm{d}s \tag{11.81}$$

where

$$C_c(s) = (H_{l1} - H_{l2}) \frac{W_p}{t_p} \frac{E^{\text{piezo}}}{1-\nu_p^2} d_{31} \left[\frac{t_p^2}{2} - \frac{t_b^2}{8} + z_n \left(\frac{t_b}{2} - t_p \right) \right] \tag{11.82}$$

$$I_p = W_b \left(t_p z_n^2 + \left(t_p^2 + t_b t_p\right) z_n + \frac{1}{3}\left(t_p^3 + \frac{3}{2} t_b t_p + \frac{3}{4} t_b^2 t_p \right) \right) \tag{11.83}$$

with d_{31} being the dielectric constant of the piezoelectric.

For the potential energy due to surface stress, the intermolecular adhesion forces of molecules of the adsorbed biological species on the surface of microcantilever to their neighboring molecule are considered. These adhesion forces are mainly the attraction/repulsion and the electrostatic forces. For the sake of brevity here, only the attraction/repulsion force is considered. A model for the electrostatic forces is desirable for general cases; however, this is beyond the scope of this chapter. For this, the Lennard–Jones potential formulation is utilized as it is better compared to the van der Waals, since it considers both attraction and repulsion effects. It is formulated as (Dareing and Thundat 2005)

$$U_s(r) = \frac{-A}{r^6} + \frac{B}{r^{12}} \tag{11.84}$$

where r is the spacing between molecules and A and B are the Lennard–Jones constants depending on the types of molecules. These constants are available for individual atoms and simple molecules. However, it is not an easy and straightforward procedure to obtain the Lennard-Jones constants for complex molecules and biological species such as protein.

We are interested in finding the effect of the surface stress of a monolayer of biological species adsorbed to a microcantilever ultimately on its resonance frequency changes. In order to have the pure effect of surface stress on resonance frequency and isolate other effects, we assume that the monolayer thickness is much smaller than the thickness of the beam; hence it does not affect the beam's overall flexural rigidity. Having a monolayer, we consider a simple molecular structure for the adsorbed biological species, as depicted in Fig. 11.30.

Parameter b (distance between two neighboring molecules) depends on how packed the biological species monolayer has been adsorbed on microcantilever's surface. Considering this fact and applying (11.84) for the deflected microcantilever shown in Fig. 11.30b, the potential field can be found as

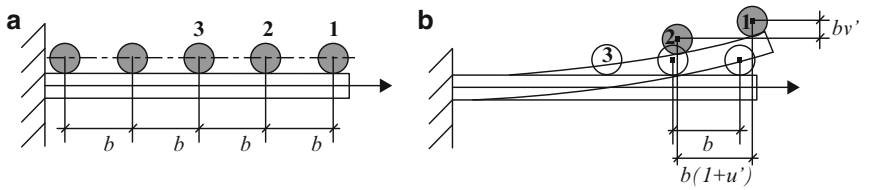

Fig. 11.30 Arrangement of a monolayer of biological species (e.g., protein) on microcantilever surface; (**a**) before the deflection, (**b**) after the deflection of microcantilever
Source: Mahmoodi et al. 2008a, with permission

$$U_s(s) = 2\int_{l_3}^{l_4} \left\{ \left[\frac{-A}{b^6\left[(1+u')^2 + w'^2\right]^3} + \frac{B}{b^{12}\left[(1+u')^2 + w'^2\right]^6} \right] \frac{1}{b(1+u')} \right\} \mathrm{d}s \tag{11.85}$$

Using Taylor's series expansion and applying the inextensibility condition (11.22) to (11.85), the potential energy (11.85) reduces to

$$U_s(s) = \int_0^l \left(-K_1(s)w'^2 + K_2(s)w'^4 - 2K_1(s)\right) \mathrm{d}s \tag{11.86}$$

where

$$K_1(s) = (H_{l_3} - H_{l_4})\left(\frac{A}{b^7} - \frac{B}{b^{13}}\right), \quad K_2(s) = (H_{l_3} - H_{l_4})\left(\frac{21A}{b^7} - \frac{78B}{b^{13}}\right) \tag{11.87}$$

Since the biological layer has a nanoscale thickness, it does not change the moment of inertia and neutral axis of the beam. However, the mass of this layer has been considered in the kinetic energy of the microcantilever.

Having the potential energy of the microcantilever expressed as

$$U_b = \frac{1}{2}\int_0^l \left\{ (H_0 - H_{l1})\frac{c_b^D}{1-\nu_b^2} I_b + (H_{l1} - H_{l2})\frac{c_b^D}{1-\nu_b^2}\left(I_b + W_b t_b z_n^2\right) + (H_{l2} - H_l)\frac{c_b^D}{1-\nu_b^2} I_b \right\} \left(w''^2 + w''^2 w'^2\right) \mathrm{d}s, \tag{11.88}$$

with

$$I_b = \frac{W_b t_b^3}{12} \tag{11.89}$$

and considering the other two potential fields derived in (11.81) and (11.86), the total potential energy of the microcantilever beam can now be written as

$$U = \frac{1}{2}\int_0^l \left\{ C_\xi(s)\left(w''^2 + w''^2 w'^2\right) - C_c(s)\left(w'' + \frac{1}{2}w''w'^2\right)V_a(t) - K_1(s)w'^2 + K_2(s)w'^4 - 2K_1(s)\right\} \mathrm{d}s \tag{11.90}$$

where

$$C_\xi(s) = (H_0 - H_{l1})\frac{c_b^D}{1-\nu_b^2}I^b + (H_{l1} - H_{l2})\frac{c_b^D}{1-\nu_b^2}\left(I^b + W_b t_b z_n^2\right) + (H_{l1} - H_{l2})\frac{E_p}{1-\nu_p^2}I^b + (H_{l2} - H_l)\frac{c_b^D}{1-\nu_b^2}I^b \tag{11.91}$$

Using the obtained kinetic and total potential energies in (11.78) and (11.90), respectively, the equations of motion of the system can be derived as described next.

Governing Equation of Motion: Utilizing the extended Hamilton's principle, equations of motion of the system and the corresponding boundary conditions with respect to variable v can be obtained as

$$\left[C_\xi(s)w'w''^2 - \frac{1}{2}C_c(s)w'w''V_a(t)\right]' - \left[mw'\int_l^s\int_0^z\left(\ddot{w}'w' + \dot{w}'^2\right)\mathrm{d}x\,\mathrm{d}z\right]' - \left[C_\xi(s)\left(w'' + w''w'^2\right) - \frac{1}{2}C_c(s)\left(1 + \frac{1}{2}w'^2\right)V_a(t)\right]'' + \left(2K_1(s)w'\right)' - \left(4K_2(s)w'^3\right)' = m\ddot{w} \tag{11.92}$$

$$w = w' = 0 \text{ at } s = 0, \quad w'' = w''' = 0 \text{ at } s = l \tag{11.93}$$

The cubic nonlinear terms of inertia and stiffness, resulting from the geometry of the vibrating beam, appear in the equations of motion as expected. Surface stress also adds linear and cubic nonlinear terms to the equations. Its linear term was expected, as most of the previous works have considered (Ren and Zhao 2004; Lu et al. 2001). However, the nonlinear term originating from the geometry of the vibrating beam is introduced for the first time (Mahmoodi et al. 2008a,b). In addition, coupling of electrical and mechanical fields, originating from the piezoelectric effects, introduces quadratic and cubic nonlinearities. It is observed that the piezoelectric actuation appears in both forms of *parametric* and direct excitations to the

system where the quadratic nonlinearity of the piezoelectric layer is also combined with this excitation.

In order to numerically investigate the obtained equations of motion, Galerkin approximation (11.25) is used again here to discretize the original partial differential equation into the ordinary differential equations with the same comparison function $\phi_n(s)$ as in (11.27). Consequently and similar to previous subsection, the ordinary differential equation governing generalized time-dependent $q_n(t)$ is expressed as follows:

$$\hat{g}_{1n}\ddot{q}_n + \hat{g}_{2n}q_n + \hat{g}_{3n}q_n^3 + \hat{g}_{4n}\left(q_n^2\ddot{q}_n + q_n\dot{q}_n^2\right) - \hat{g}_{5n}q_n^2V_a(t) = \hat{g}_{6n}V_a(t) \tag{11.94}$$

where

$$\hat{g}_{1n} = \int_0^l m(s)\varphi_n^2(s)\,\mathrm{d}s \tag{11.95a}$$

$$\hat{g}_{2n} = \int_0^l \left[\varphi_n(s)\left(C_\zeta(s)\varphi_n''(s)\right)'' - \left(2K_1(s)\varphi_n'(s)\right)'\right]\mathrm{d}s \tag{11.95b}$$

$$\hat{g}_{3n} = \int_0^l \phi_n(s)\left(C_\zeta(s)\phi_n'(s)\phi_n''^2(s)\right)'\,\mathrm{d}s + \int_0^l \phi_n(s)\left(C_\zeta(s)\phi_n'^2(s)\phi_n''(s)\right)''\,\mathrm{d}s + \int_0^l 4\phi_n(s)\left(K_2(s)\phi_n'^3(s)\right)'\,\mathrm{d}s \tag{11.95c}$$

$$\hat{g}_{4n} = \int_0^l \phi_n(s)\left[m(s)\phi_n'(s)\int_l^s\int_0^z 2\phi_n'^2(x)\,\mathrm{d}x\,\mathrm{d}z\right]'\mathrm{d}s \tag{11.95d}$$

$$\hat{g}_{5n} = \int_0^l \varphi_n(s)\left(C_c(s)\varphi_n'(s)\varphi_n''(s)\right)'\,\mathrm{d}s + \frac{1}{2}\int_0^l \varphi_n(s)\left(C_c(s)\varphi_n'^2(s)\right)''\,\mathrm{d}s \tag{11.95e}$$

$$\hat{g}_{6n} = \frac{1}{2}\int_0^l \varphi_n(s)C_c''(s)\,\mathrm{d}s \tag{11.95f}$$

Using (11.95), the nonlinear equation (11.94) can be simulated with Matlab®/Simulink® with the results presented and discussed next.

Numerical Simulations and Discussions: Now that the governing equations of motion have been derived, the effects of both biological and piezoelectric layers on the resonance frequency of microcantilever beam can be investigated. The nonlinear terms and their influence on the frequency response of the system are first studied

for each of the mentioned layers separately and then for the case where both layers are present on the surface of microcantilever.

In order to study the influence of the surface stress on the frequency response of the microcantilever, the Lennard–Jones constants of the adsorbed biological species are required. The Lennard-Jones constants for different molecular structures vary in the range of $A = 2\times10^{-79}$ to $1\times10^{-76}\,\mathrm{J\,m^6}$ and $B = 2\times10^{-136}$ to $4\times10^{-134}\,\mathrm{J\,m^{12}}$ (Britton et al. 2000; Rappe et al. 1992). For biological species, however, the values of A and B are not available as they are found empirically for each biological species in the desired conditions. The experimental results of McFarland et al. (McFarland et al. 2005) are used to perform an inverse engineering in order to obtain approximate values of A and B for the specific biological species of (McFarland et al. 2005) (i.e., a monolayer of thiol molecules on the surface of microcantilever). This is done in order to obtain the resonance frequency shifts as measured in McFarland and coworkers experiment. Considering a silicon microcantilever without any other layers on it, with the modulus of elasticity of 170 GPa, length, width, and thickness of 500 μm, 100 μm, and 0.8–1 μm, respectively (as listed in McFarland et al. 2005), its frequency response can be obtained using numerical simulation and depicted in Fig. 11.31.

Unlike the biological layer with its thickness and rigidity being negligible, the piezoelectric layer is thick enough to change the rigidity of the system. Considering the microcantilever studied before, a piezoelectric layer of ZnO with the same length, width, and half the thickness of silicon microcantilever is added on its surface. The modulus of elasticity of the piezoelectric layer is 133 GPa. Practically, this layer can not stand alone on the microcantilever; therefore two layers

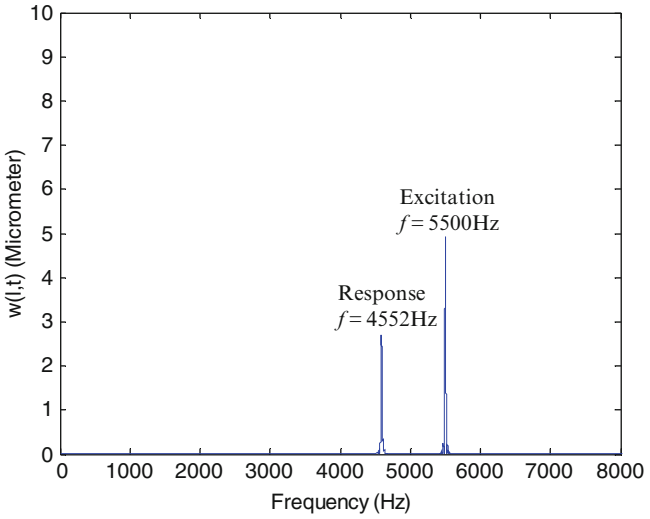

Fig. 11.31 Frequency response of a plain silicon microcantilever ($E_b = 170$ GPa, $L = 500$ μm, $w_b = 100$ μm and $h_b = 1$ μm)
Source: Mahmoodi et al. 2008a, with permission

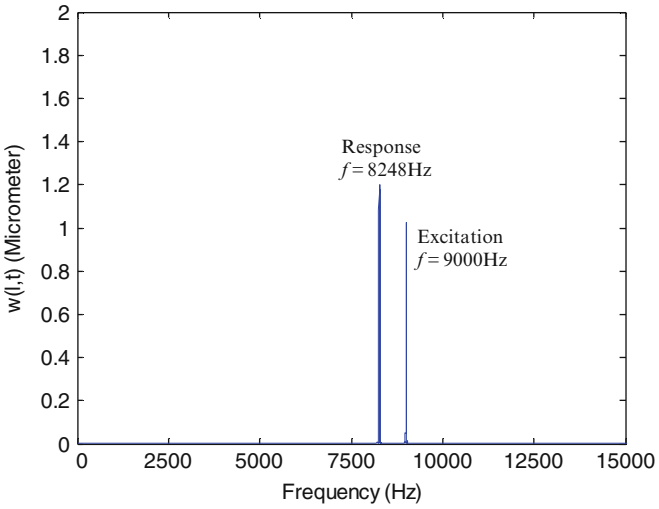

Fig. 11.32 Linear frequency response of silicon microcantilever covered by a piezoelectric layer
Source: Mahmoodi et al. 2008a, with permission

of 0.1 μm Ti/Au on top and beneath the ZnO are deposited. These layers together with the silicon cantilever act as a bimorph configuration for controlling the vertical displacement of the tip. It was observed from the equations of motion (11.92) that the piezoelectric actuation produces both parametrically- and directly-excited vibrations in the microcantilever.

In the first step, we will only consider the effect of linear terms on frequency response of the system; therefore, the coefficients of nonlinear terms are considered to be zero. A voltage of 1 V with frequency of excitation of 9 kHz is applied to the piezoelectric actuator to obtain the linear frequency. Figure 11.32 shows the response of the system with the added piezoelectric layer. It is indicated that its resonance appears at the frequency of 8,248 Hz (which is much higher than the resonance frequency of the microcantilever without the piezoelectric layer).

The nonlinear terms are now considered in the simulations and the numerical frequency response is calculated again. The values of the exciting voltage are considered to be the same as the excitation for linear frequency response. The obtained nonlinear frequency response is depicted in Fig. 11.33.

When linear and nonlinear frequency responses are compared (Figs. 11.32 and 11.33), it is observed that there exists roughly 14 Hz of shift in the frequency responses. Although this amount is small compared to the high value of the microcantilever resonance frequency, the important point is that this difference is in the measurable range of the microcantilever sensors, and hence, crucial for accurate measurement. This demonstrates that it is extremely important to consider the nonlinearity of the system in resonance response calculations. The importance of considering the nonlinear model, instead of the linear one, can be clearly observed

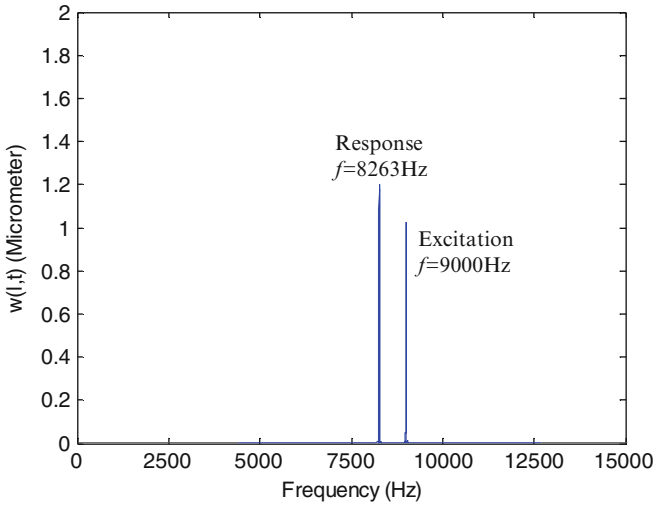

Fig. 11.33 Nonlinear frequency response of silicon microcantilever covered by a piezoelectric layer
Source: Mahmoodi et al. 2008a, with permission

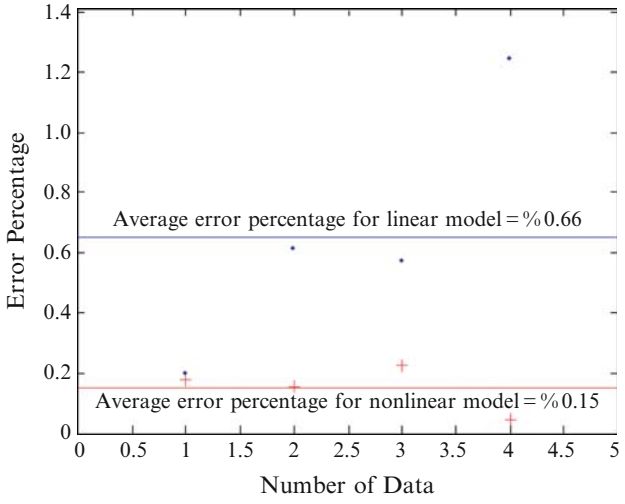

Fig. 11.34 Comparison of error percentage for linear (.) and nonlinear (+). The error is with respect to the experimental results
Source: Mahmoodi et al. 2008a, with permission

from Fig. 11.34, in which the error percentages of the linear and the nonlinear models from the experimental results are compared.

In the simulations so-far, it was observed that considering the biological layer, the effect on the resonance frequency shift in the presence of piezoelectric layer highly

Table 11.2 Simulation results for constants A and B and the corresponding frequencies for piezoelectrically-actuated microcantilever Source: Mahmoodi et al. 2008a, with permission)

$A[\mathrm{J\,m^6}]$	$B[\mathrm{J\,m^{12}}]$	f [Hz]	δ[Hz]
0	0	8,262	0
0.7×10^{-72}	0.3×10^{-135}	8,265	3
1×10^{-72}	0.4×10^{-135}	8,267	5
1.3×10^{-72}	0.4×10^{-135}	8,268	6

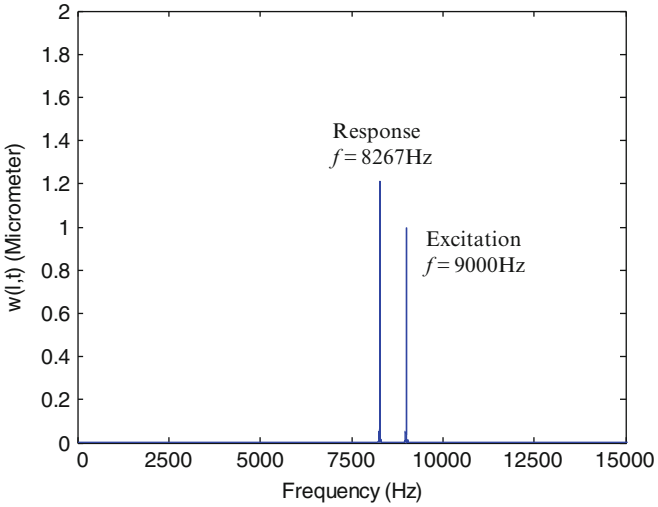

Fig. 11.35 Nonlinear frequency response of piezoelectrically-actuated microcantilever covered by a biological layer with $A = 1 \times 10^{-72}\,\mathrm{J\,m^6}$ and $B = 0.4 \times 10^{-135}\,\mathrm{J\,m^{12}}$
Source: Mahmoodi et al. 2008a, with permission

depends on the geometry of the system. For the original microcantilever with length, width, and thickness of 500 μm, 100 μm, and 1 μm, respectively, and with no piezoelectric layer, a shift in the range of 11–34 Hz was induced, depending on the Lennard-Jones constants (*see* Table 11.2). However, this shift is further decreased if the piezoelectric layer is added to the microcantilever, as listed in Table 11.2 and depicted in Fig. 11.35 for $A = 1 \times 10^{-72}\,\mathrm{J\,m^6}$ and $B = 0.4 \times 10^{-135}\,\mathrm{J\,m^{12}}$.

This demonstrates that adding a piezoelectric layer with half the thickness of the microcantilever results in a thicker beam, and hence the molecular surface stress of the adsorbed biological species will have less effect on the frequency response of the system. This indicates that there exist limitations on the structural geometry of the microcantilever in order to be applicable for biosensing.

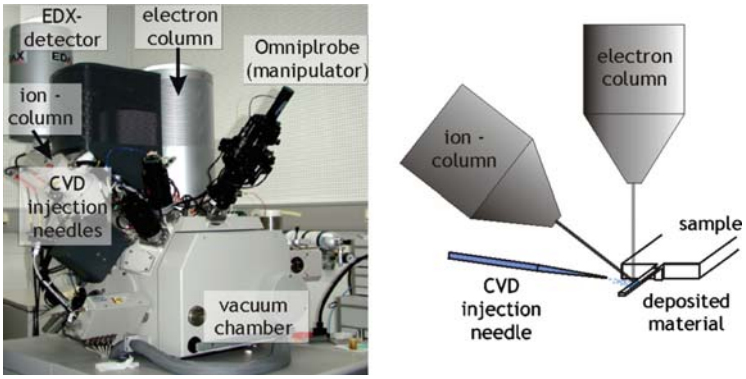

Fig. 11.36 Combination of focused ion beam and scanning electron microscopy for the deposition of defined mass on nanomechanical cantilever samples
Source: Salehi-Khojin et al. 2009b, with permission

11.3.2 Ultrasmall Mass Detection using Active Probes

One of the most important applications of piezoelectrically-driven NMCS is in ultrasmall detection. The idea originates from utilizing the unique configuration and the embedded piezoelectricity of NMCS for high amplitude vibration, the attribute that is essential for precise measurement of ultrasmall mass by cantilever-based vibratory sensors. To validate this concept, using focused ion beam (FIB) technique, a small mass in the order of pico-gram is added at tip of NMCS. To detect the added mass, the precise model for modal characterization of NMCS presented in Chap. 8 is utilized along with a parameter estimation technique. Using the shifts in the resonant frequencies of the identified system, the amount of added tip mass is estimated at the most sensitive mode of operation. Results indicate that system identification procedure proposed in this work is an inevitable step towards achieving precise measurement of ultrasmall masses using NMCS with great potential in bio- and chemo-mass detection applications.

Experimental Setup and Procedure: The same commercially available piezoelectrically-actuated NMCS (Active Probe®), the DMASP manufactured by Veeco Instruments Inc. and shown in Fig. 11.7, is used for mass detection purpose. For this, a small amount of material at defined position and geometry can be deposited by means of focused ion beam (*see* Fig. 11.36), (Volkert and Minor 2007). Here, we used a FIB (FEI Nova 600, Netherlands) that allows imaging the deposited structures by scanning electron microscopy. Furthermore, the deposited material can be analyzed by energy-dispersive x-ray spectroscopy (EDX).

NMCS were mounted onto a FIB holder and were grounded by conductive tape to prevent charging of the cantilever during focused ion beam deposition. The FIB chamber was evacuated to a pressure of 10^{-5} mbar. For the deposition of material on the microcantilever, the chemical vapor gas injection needle was placed close to the desired area (CVD injection needle). Then, the precursor gas

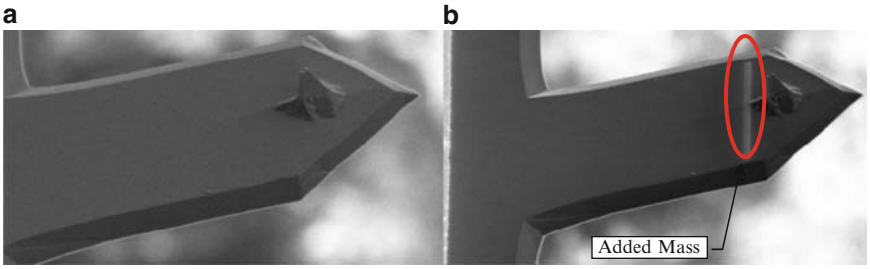

Fig. 11.37 SEM images of active probe cantilevers before (**a**) and after (**b**) tip mass deposition
Source: Salehi-Khojin et al. 2009b, with permission

(Methylcyclopentadienyl[Trimethyl]Platinum) was released into the chamber. The precursor gas is decomposed under the Ga^{+}-ion beam (30 kV, 0.5 nA) on the surface leading to the formation of a material mainly composed of Pt and C (highlighted area in Fig. 11.37b). EDX revealed a content of 69% Pt, 15% C, 10% Ga, and 6% Si. The deposition area of 50 μm by 2 μm was selected. By controlling the ion exposure time (310 s), 500 nm thick elements were fabricated on the nanomechanical cantilever. Afterwards, the deposited elements were imaged by the integrated SEM (Fig. 11.37).

In order to obtain resonant frequencies and mode shapes of the probe before and after mass deposition, the MSA-400 microsystem analyzer setup is utilized again here for out-of-plane motion measurement (*see* Fig. 8.11). As voltage is applied to the piezoelectric layer, the velocity and displacement of probe are measured on the basis of processing the backscattered laser light from the surface of cantilever. In this study, a 10 V AC chirp signal with 500 kHz bandwidth is applied to the piezoelectric layer for the excitation.

Figure 11.38 depicts the first three resonant frequencies of the Active Probe before and after mass deposition. It is seen that these frequencies before mass deposition are respectively 54.257, 222.812, and 380.742 kHz; while after mass deposition they change to 54.218, 220.781, and 380.078 kHz with the maximum shift of 2.031 kHz at the second resonant frequency. Moreover, the sharp peaks in Fig. 11.38 indicate that the system is lightly damped, and hence the natural frequencies of the system can be safely considered as its resonant frequencies. Considering these outcomes and the precise modeling framework developed in Chap. 8 for frequency and modal analyses of the Active Probe, the modal displacements of the probe obtained from experiment and theory can be compared.

Identification Algorithm and Sensitivity Study: From the equation of motion and boundary conditions obtained in Chap. 8, the independent parameters to be identified include both cantilever parameters and added tip mass which form the independent parameters' vector:

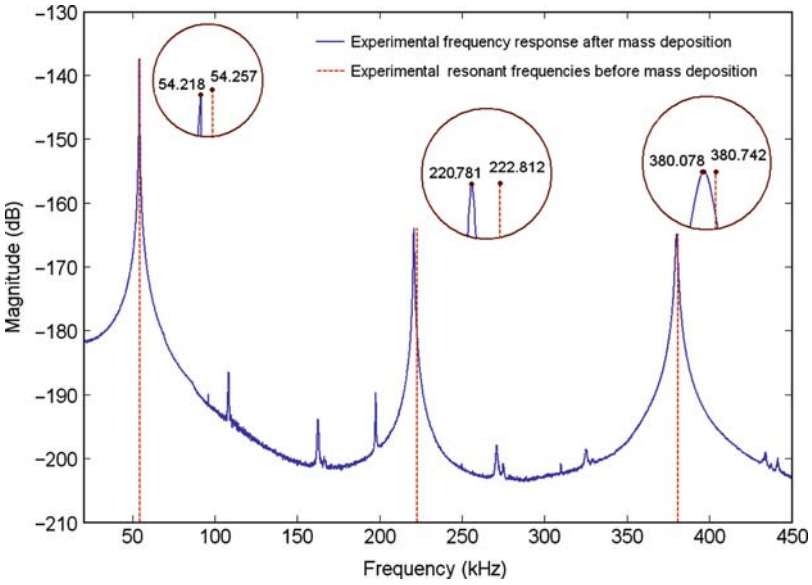

Fig. 11.38 Experimental resonant frequency of Active Probes before and after mass deposition
Source: Salehi-Khojin et al. 2009b, with permission

$$\mathbf{P} = \left[\frac{m_1}{(EI)_1}, \frac{m_2}{(EI)_2}, \frac{m_3}{(EI)_3}, \frac{(EI)_2}{(EI)_1}, \frac{(EI)_3}{(EI)_2}, \frac{m_e}{(EI)_3}, l_1, l_2, l \right] \quad (11.96)$$

As seen from (11.96), the tip mass does not appear as a single parameter. Hence, at least one of the parameters m_1, m_2, m_3, $(EI)_1$, $(EI)_2$, or $(EI)_3$ must be primarily known or measured in order to independently estimate the tip mass after system identification. This becomes important for detection of ultrasmall mass in view of the fact that the presence of the uncertainty associated with parameters may drastically degrade model accuracy.

For the identification purpose, two approaches, namely, forward and backward can be employed. In the forward approach, the entire set of parameters can be identified on the basis of simultaneously minimizing a constructed error function between modal displacement and resonant frequencies of the model and actual system before mass deposition. Having the system with the identified parameters, the shift in the resonant frequencies obtained from theory and experiment can then be utilized to detect the amount of deposit mass. In this respect, the added tip mass can be stated by the gradual increase of the tip mass in the identification procedure such that the theoretical shifts in the resonant frequencies could meet those of experiment. In the backward approach, the aforementioned system parameters including an unstated tip mass plus added mass are identified after mass deposition. The added tip mass can then be detected by the gradual decrease of the unstated mass in the identification procedure such that the theoretical shifts in the resonant frequencies could

match those of experiment. In this approach, the amount of deposited mass at the end of probe is equal to mass removed in the identification procedure.

Here, we aim at employing the second approach for tip mass detection which can be a promising alternative for the first one. In this regard and in order to identify the system, a number of points are selected along the length of cantilever with attached mass for comparison of the modal displacements and resonant frequencies of experiment and theory. The error function utilized for the system identification calculates the percentage of the average weighted error between the measured and evaluated resonant frequencies and modal displacement at each selected point for a finite number of modes as follows:

$$PI = \frac{1}{K}\left\{ W \sum_{r=1}^{K} \left(\frac{1}{Pt} \sum_{j=1}^{Pt} \left| \frac{\mu_r w_{\max}^{(r)E}(x_j) - \varphi^{(r)T}(x_j)}{\mu_r w_{\max}^{(r)E}(x_j)} \right| \right) + (1-W) \sum_{r=1}^{K} \left| \frac{\omega_r^E - \omega_r^T}{\omega_r^E} \right| \right\} \times 100 \tag{11.97}$$

where K is the number of modes, Pt represents the number of selected points on the probe length, $0 < W < 1$ is a parameter scaling the importance of natural frequencies vs. mode shapes, $\phi^{(r)T}(x_j)$ stands for the rth theoretical modal displacement evaluated at point x_j, $w_{\max}^{(r)E}(x_j)$ indicates the experimental amplitude of point x_j at rth resonant frequency, and μ_r is a scaling optimization variable used to match rth experimental resonant amplitude with the corresponding theoretical modal displacement. Other optimization variables including parameters associated with system property and geometry (as listed in Table 8.2) are constrained within a limited range around their approximate values. To estimate the parameters independently, we have calculated the value of parameter m_3 from the data provided by the manufacturer's data sheet, and identified the rest of parameters on the basis of this value.

Figure 8.13 in Chap. 8 depicted the first three modal displacements of the actual system as well as those of the theory. Results indicate that the resonance deflection of the proposed model match with the experimental data very well. For the identified system, the amount of added mass can be accurately estimated from the resonance shift at the most sensitive mode of the probe. Table 11.3 lists the resonant frequencies obtained from experiments before and after mass deposition, as well as the corresponding frequency shifts. It is seen that the shift in the resonant frequencies of the first and third modes are fairly smaller than that of the second. This implies that the second mode displays more sensitive response against corresponding added mass compared to the other modes.

In order to validate this observation for a broad range of added masses, we have numerically studied the sensitivity of the first three modes to the added mass. Figure 11.39 depicts the change in the resonant frequency of each mode with respect to the added mass. Results indicate that the second mode, as expected, demonstrates the most sensitive response, while the first mode shows the least sensitivity in this

Table 11.3 Resonant frequencies before and after mass deposition

Mode number	Resonance before mass deposition (kHz)	Resonance after mass deposition (kHz)	Frequency shift
Mode 1	54.257	54.218	0.039 (kHz), 0.07%
Mode 2	222.812	220.781	2.031 (kHz), 0.92%
Mode 3	380.742	380.078	0.664 (kHz), 0.17%

Source: Salehi-Khojin et al. 2009b, with permission

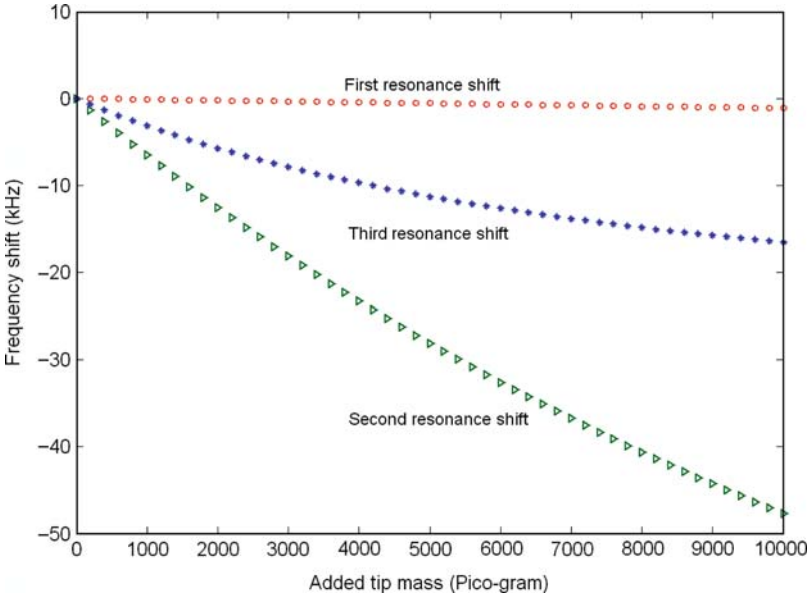

Fig. 11.39 Sensitivity of each mode to the added mass
Source: Salehi-Khojin et al. 2009b, with permission

regard. This trend can be explained by resonance deflections of the probe depicted in Fig. 8.13. It is seen that in the second mode, free end of the probe displays more sensitive motion compared to its main body. However, in the first and third modes, this sensitivity decreases. In conclusion, the shift in the resonant frequency of the second mode can be more reliably utilized for estimating the amount of added mass. By means of these considerations and on the basis of the aforementioned procedure, for the 2.031 kHz shift in the second resonant frequency, the amount of added tip mass is estimated to be 310 pg.

Because of the fact that the physical and geometrical parameters provided by the manufacturer have deviation from one cantilever to another because of manufacturing tolerances, care must be taken when using these parameters as they may result in inaccuracy of estimation. Here, we aim to demonstrate how parametric uncertainties can affect the mass measurement precision.

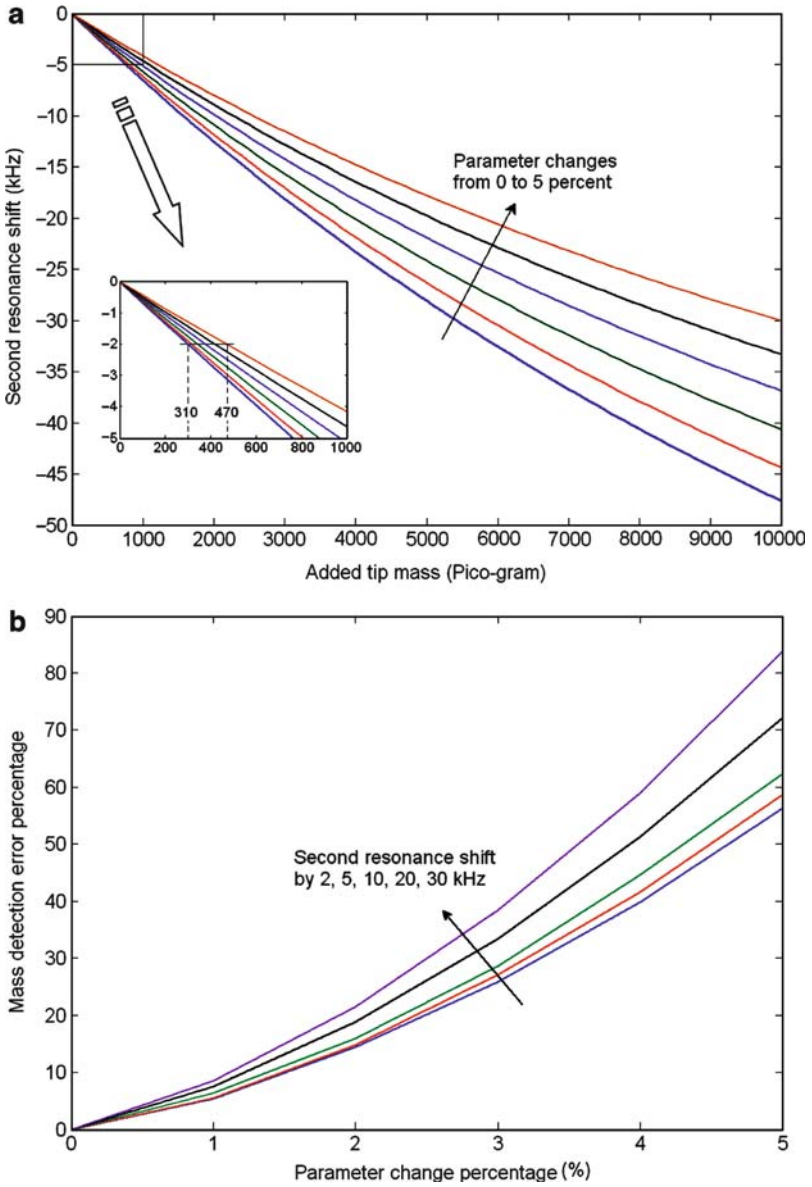

Fig. 11.40 (**a**) Effects of parametric uncertainties on the frequency shifts, and (**b**) the resultant mass measurement error percentage
Source: Salehi-Khojin et al. 2009b, with permission

Figure 11.40a depicts the frequency shift of the second mode with respect to added mass at different levels of parametric uncertainties ranging from 0 to 5%. It is seen that even small uncertainties can produce large mass detection errors. For example, if the parameters of the investigated probe are deviated by 5%, the added mass estimation changes from 310 to 470 pg which corresponds to 52% detection error. Moreover, Fig. 11.40b shows the mass measurement error percentage vs. the percentage of parametric uncertainties for different levels of shift in the second resonance. Results indicate that at higher frequency shifts (corresponding to larger added masses), higher measurement errors are observed. Hence, system identification proposed in the previous section is an inevitable step towards achieving precise mass detection.

Summary

This chapter provided a relatively general overview of modeling frameworks and vibration analysis of piezoelectric-based microcantilever sensors with their applications in many cantilever-based imaging and manipulation systems such as atomic force microscopy (AFM) and its varieties. It specifically presented some new concepts in modeling these systems and highlighted the issues related to nonlinear effects at such small scale, the Poisson's effect and piezoelectric materials nonlinearity. Both linear and nonlinear models were discussed with their applications in biological and ultrasmall mass sensing and detection.

Chapter 12
Nanomaterial-Based Piezoelectric Actuators and Sensors

Contents

12.1 Piezoelectric Properties of Nanotubes (CNT and BNNT) 420
12.1.1 A Brief Overview of Nanotubes 420
12.1.2 Piezoelectricity in Nanotubes and Nanotube-Based Materials 421
12.2 Nanotube-Based Piezoelectric Sensors and Actuators 423
12.2.1 Actuation and Sensing Mechanism in Multifunctional Nanomaterials 423
12.2.2 Fabrication of Nanotube-Based Piezoelectric Film Sensors 426
12.2.3 Piezoelectric Properties Measurement of Nanotube-Based Sensors 432
12.3 Structural Damping and Vibration Control Using Nanotubes-Based Composites 434
12.3.1 Fabrication of Nanotube-Based Composites for Vibration Damping and Control 434
12.3.2 Free Vibration Characterization of Nanotube-Based Composites 436
12.3.3 Forced Vibration Characterization of Nanotube-Based Composites 441
12.4 Piezoelectric Nanocomposites with Tunable Properties 446
12.4.1 A Brief Overview of Interphase Zone Control 446
12.4.2 Molecular Dynamic Simulations for Nanotube-Based Composites 448
12.4.3 Continuum Level Elasticity Model of Nanotube-Based Composites 451
12.4.4 Numerical Results and Discussions of Nanotube-Based Composites 451
12.5 Electronic Textiles Comprised of Functional Nanomaterials 455
12.5.1 The Concept of Electronic Textiles 455
12.5.2 Fabrication of Nonwoven CNT-based Composite Fabrics 455
12.5.3 Experimental Characterization of CNT-based Fabric Sensors 459
Summary

Due to the unique structure of nanomaterials, improved material properties can be achieved in addition to the added multifunctionality of these materials. Such unique feature is a key factor in the design and development of sensors and actuators comprised of functional nanomaterials. Along this line of reasoning, this chapter presents an overview of advances in nanomaterial-based actuators and sensors utilizing either piezoelectric materials or possessing piezoelectric properties. More specifically, piezoelectric properties of nanotubes are disclosed and detailed, with a natural extension to nanotube-based piezoelectric sensors and actuators. As a byproduct of this arrangement, structural damping becomes possible using nanotube-based composites. As a future pathway toward the development of next-generation sensors and actuators comprised of nanomaterials, piezoelectric

N. Jalili, *Piezoelectric-Based Vibration Control*,
DOI 10.1007/978-1-4419-0070-8_12,

© Springer Science+Business Media LLC 2010

nanocomposites with tunable properties, as well as electronic textiles consisting of functional nanomaterials, are also briefly introduced and discussed.

12.1 Piezoelectric Properties of Nanotubes (CNT and BNNT)

12.1.1 A Brief Overview of Nanotubes

Carbon nanotubes (CNTs) are one of the most promising nanosize materials, which have attracted widespread attention since their discovery in 1991 (Iijima 1991; Tans et al. 1998; Dai et al. 1996; Pancharal et al. 1999; Kong et al. 2000; Collins et al. 2000; Dillon et al. 1997; Wang et al. 1998; Fan et al. 1999; Lee et al. 1999; Kim and Lieber 1999). It has been proved that CNTs possess extraordinary properties such as outstanding mechanical, thermal, electrical, and physical properties. This is due to the special nature of carbon combined with the molecular perfection of nanotubes, which endows them with these exceptional properties. No other element in the periodic table bonds to itself in an extended network with the strength of the carbon–carbon bond. The delocalized pi-electron donated by each atom is free to move about the entire structure, rather than stay home with its donor atom, giving rise to the first molecule with metallic-type electrical conductivity.

Subsequent to the discovery of CNTs, nanotubes with other compositions such as MoS2 (Feldman et al. 1995) and boron nitride nanotubes (BNNT) (Chopra and Zettl 1998; Han et al. 1998) have been synthesized. In particular, BNNTs can be synthesized by a variety of methods including arc discharge (Cummings and Zettl 2000), ball milling (Chopra and Zettl 1998), and plasma methods (Shimizu et al. 1999).

The exceptional electrical and mechanical properties of nanotubes facilitate the synthesis of lightweight, strong, multifunctional composite actuators that can change shape for use in many applications such as interfacial force microscope for polymer matrix composite characterization, miniature actuators, and adaptive structural materials for automobiles. Due to their high electrical conductivity and the unbeatable sharpness of their tip, nanotubes are the best known field emitters of any material – this is the same reason as why lightning rods are sharp (see Fig. 12.1). The sharpness of the tip also means that they emit at especially low voltage, an important fact for building electrical devices that utilize this feature (next-generation LCDs and TVs).

Another application of nanotubes is conductive plastic. For structural applications, plastics have made tremendous headway, but not where electrical conductivity is required, plastics being famously good electrical insulators. This deficiency is overcome by loading plastics up with conductive fillers, such as carbon black and graphite fibers; however, the loading required to provide the necessary conductivity is typically high. The natural tendency for nanotubes to form ropes provides inherently very long conductive pathways even at ultralow loadings. Applications

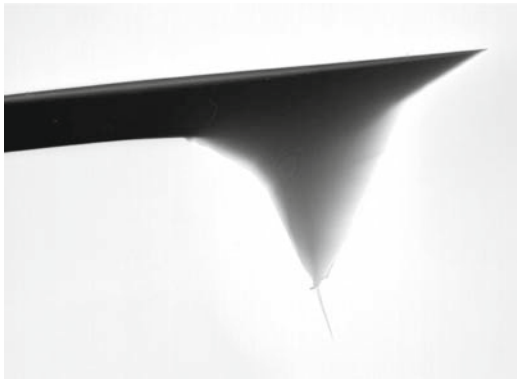

Fig. 12.1 TEM images of a CNT probe mounted at the end of a conventional AFM tip (with permission)

that exploit this behavior of nanotubes include EMI/RFI shielding composites and coatings for enclosures, gaskets, and other uses; electrostatic dissipation (ESD), and anti-static materials and (even transparent) coatings; and radar-absorbing materials.

Nanotubes in general can be classified into several categories on the basis of their twist (or chirality) or the number of walls. They can be defined by their diameter, length, and chirality, or twist. They can be classified as either single-walled nanotubes (SWNTs) or multiwalled nanotubes (MWNTs). Nanotubes, and especially CNTs, can be fabricated using different methods, including the following most common techniques.

Arc Discharge: This method involves the evaporation of carbon atoms by a plasma of Helium gas that is ignited by high currents passed through opposing carbon anode and cathode.

Laser Ablation: This technique involves scanning of a laser beam onto a metal graphite composite target surface under computer control.

Chemical Vapor Deposition (CVD): A catalytic process involving the deposition of hydrocarbons (methane, ethylene, acetylene) over certain supported catalyst materials (Co, Cu, or Fe on silica or zeolite surfaces). The principle of operation is the "dissociation of hydrocarbon molecules catalyzed by the transition metal followed by the dissolution and saturation of carbon atoms in the metal nanoparticle".

12.1.2 Piezoelectricity in Nanotubes and Nanotube-Based Materials

As mentioned earlier, with the widespread application of mechatronic concepts to dynamic systems in recent years, interest has been focused on the substitution of piezoelectric ceramic (PZT) fibers for conventional electrical motors and actuators. Piezoelectricity effects in elongated and poled polyvinylidene fluoride (PVDF) as well as the ferroelectric properties have been observed for a number of decades. Although PVDF copolymers have found diverse uses in industrial applications, such as ultrasonic transducers and vibration damping (Fukada 2000; Baz

and Ro 1996), their low stiffness and electromechanical coupling coefficients have limited their use.

To improve the performance and capability of future intelligent systems, the development of next-generation actuator/sensor subsystems utilizing nanotubes has been exercised. Specifically, the actuation mechanism associated with CNTs or BNNTs, and ultimately manufacturing macrolevel actuators and sensors compromised of these nanotubes have received great attention (Mele and Kral 2001,2002; Laxminarayana and Jalili 2005; Ramaratnam and Jalili 2006b; Salehi-Khojin et al. 2008a, b). This exciting area of research is motivated by discovery of bond extension in charged nanotubes (Baughman 2000). Termed "artificial muscles", such actuators provide wonderful opportunities in MEMS because of their incredible strength and stiffness, with relatively low ($\sim$10 V) driving voltage. The proposed nanotube-based actuator configuration could be utilized for many applications such as miniature motors, vibration control of flexible structures, micro scale robotic systems, and biomedical (drug delivery and tumor removal) and power generation applications.

The electrical properties of the CNTs are strongly affected by the rolling angle of the nanotube lattice molecular structure known as chirality which has limited the applications of CNTs in electrical components, especially in nanoeclectrical devices (Wilder et al. 1998). In contrast to CNTs, BNNTs are purely wide band gap semiconducting nanotubes. As depicted in Fig. 12.2, similar to the structure of graphite, BNNTs possess a hexagonal lattice molecular structure which is composed of alternating atoms of boron and nitrogen in its lattice structure. BNNTs have shown to possess strong piezoelectricity even for low operating voltages (Mele and Kral 2002). This property makes BNNTs promising candidate materials in a

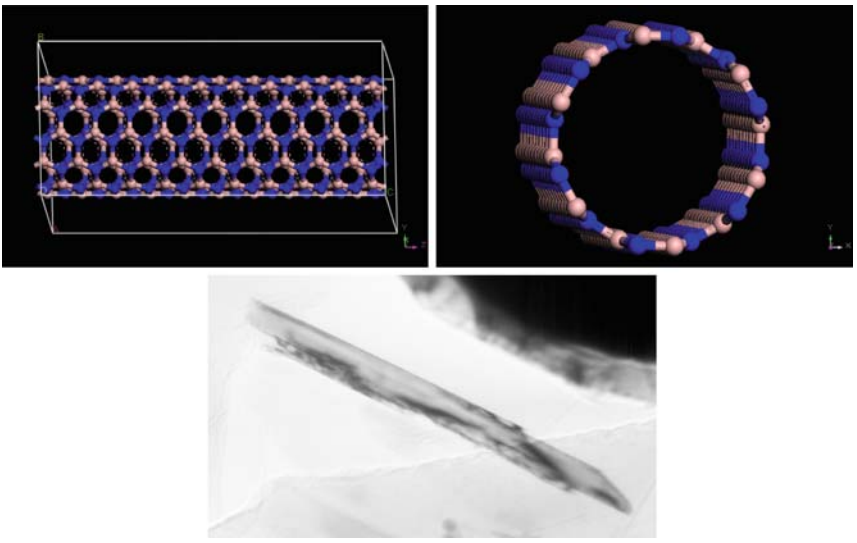

Fig. 12.2 (*top*) BNNTs molecular structure with (6,6) chirality and 8.14 Angstrom diameter *Source:* Salehi-Khojin et al. 2009a, with permission, and (*bottom*) TEM image of a Clemson BNNT *Source:* Jalili et al. 2002a, Jalili 2003 with permission

large variety of nanosized electronic and photonic devices. Compared to CNTs, BNNTs are more suitable reinforcement candidate materials in composite structures because of their high resistance to oxidation at elevated temperatures, outstanding mechanical properties, and high thermal conductivity (Zhi et al. 2005).

12.2 Nanotube-Based Piezoelectric Sensors and Actuators

The process of assembling macroscopic structures from functional nanoscopic materials (whose integrity is preserved) is a promising method for improving performance and capability of future automated systems. Along this line, this section presents a brief overview of next-generation macroscopic structures composed of functional nanotube materials which are capable of actuation and sensing. The feasibility of the proposed nanotube-functional composites is demonstrated through fabricating thin film polyvinylidene fluoride (PVDF) embedded with SWNTs or MWNTs to result in a composite matrix. The preliminary research results clearly demonstrate the role of the nanotube in improving the actuation and sensing characteristics.

12.2.1 Actuation and Sensing Mechanism in Multifunctional Nanomaterials

BNNT theory predicts that spontaneous electric polarization arises as the result of changes in the tube geometry (Adourian 1998). Unlike conventional ferroelectric actuators, low operating voltages can be applied to the nanotube-based actuators to generate large enough strains for effective actuation. In order to keep these high stiffness nanotubes together and create practical actuator and sensor subsystems, the individual nanotube can be joined by mechanical entanglement and van der Waals forces and reinforced using appropriate polymer composites (e.g. PVDF). For this, the thin film (e.g., about 20 μm) of PVDF is cured with nanotube/PVDF composite matrix. The composite layer is then sandwiched between two vapor deposited Ag electrodes. Like natural muscle, the nanotube sheet actuators will form arrays of nanofiber actuators. A schematic diagram of the thin film composite actuator along with a typical deflection configuration in response to a modulated input voltage is shown in Fig. 12.3 (Jalili et al. 2002a; Jalili 2003).

This configuration results in a novel type of actuation/sensing mechanism because the nanotubes add high surface area with exceptional stiffness to the mechanical properties of actuator/sensor subsystems (Chopra and Zettl 1998; Vaccarini et al. 2000). The functional nanotube/PVDF composite layers can then be utilized to generate muscle type macroscopic motion. When the actuator is energized, each layer deflects, and hence, results in a linear motion proportional to the applied voltage (converse piezoelectric effect or actuation property). Conversely, when

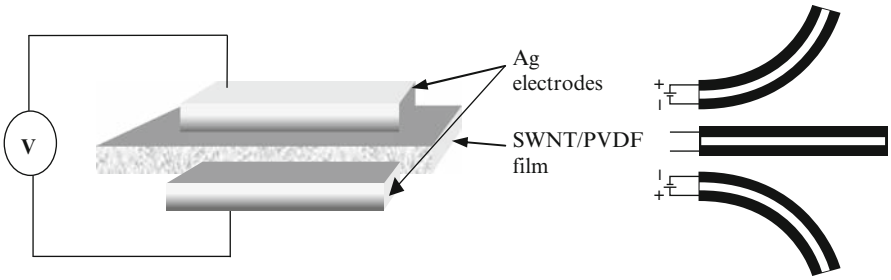

Fig. 12.3 Schematic of PVDF/SWNT thin film actuator/sensor (Jalili et al. 2002a; Jalili 2003)

stress is applied, an electrical charge is generated in proportion to the applied stress (piezoelectric effect or sensing property). The displacement generated by the proposed actuator might be relatively small with maximum free strains on the order of 0.1% (Spinks 2001; Ahuwalia 2001). However, the nanotube has a high modulus of elasticity (Hernandez et al. 1999; Falvo et al. 1997; Vaccarini et al. 2000) such that the force generated by the actuator will be extremely large. In order to preserve the axial force generation function, several motion amplifiers and compliant mechanisms can be utilized (see Sect. 6.5.2, and Jalili et al. 2002a, b, 2003; Millar et al. 1996).

Macroscopic Actuator/Sensor Subsystem Configurations: The actuator/sensor technology proposed here is aimed at providing building blocks for next-generation nanotube-based nano-motors with incredible strength and stiffness and relatively low ($\sim$10 V) driving voltages. This novel concept is originated from the observation of the piezoelectricity effect in nanotubes, especially BNNTs. As mentioned earlier, BNNT theory predicts that electric polarization arises as an intrinsic effect of the tube geometry in a single nanotube (Mele and Kral 2001). This leads to an electric polarization along the nanotube axis which is controlled by the quantum mechanical boundary conditions on its electronic states around the tube circumference. Thus, the macroscopic dipole moment has an *intrinsically* mechanical origin from the wrapped dimensions. Preliminary experimental testing has shown that the strain due to quantum mechanical effects (change in orbital occupation and band structure) changes sign from an expansion for electron injection to a contraction for hole injection (Mele and Kral 2002).

For the macroscopic actuator/sensor subsystems, we consider two configurations; namely, *laminar* and *axial* configurations. In *laminar* actuator/sensor configuration, thin film (e.g., about 20 μm) of PVDF is cured with a BNNT/PVDF composite matrix. The composite layer is then sandwiched between two vapor deposited Ag electrodes. In *axial* configuration and in order to generate muscle type linear motion through the laminar configuration, two BNNT/PVDF composite layers are utilized which are coupled through a rigid link and then clamped at the center (see Fig. 12.4). When the actuator is energized, each layer deflects, and hence, results in a linear motion proportional to the applied voltage.

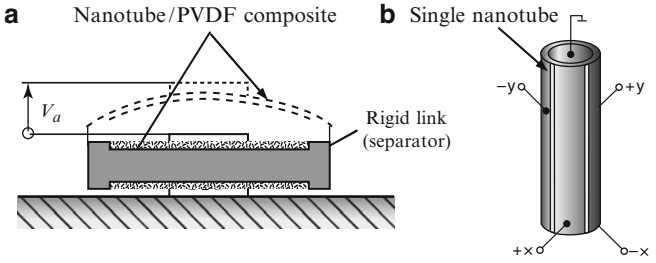

Fig. 12.4 (**a**) Laminar configuration made from nanotube/PVDF composites, and (**b**) axial configuration using single nanotube

In order to demonstrate the effectiveness of this technology, PVDF polymer is blended with CNTs to form a composite material for use as a transducer. Recent developments in the copolymers of PVDF with increased piezoelectric properties are notable. Poly(vinylidene fluoride-trifluoroethylene), referred to as P(VDF-TrFE) hereafter and a copolymer of PVDF, is used for blending with nanotubes. Both types of nanotubes (i.e., SWNTs and MWNTs) are used here for blending with P(VDF-TrFE). The feasibility of these nanotube-reinforced polymers has been studied (Ramaratnam and Jalili 2006b) and the initial results were promising (Iyer 2001; Xing 2002; Courty et al. 2003; Ramaratnam 2004; Ramaratnam and Jalili 2004a). Addition of nanotubes increases the stiffness of the composite material, thereby increasing the effects of actuation.

One needs to note that, however, with an increase in the concentration of CNTs in PVDF polymer or its copolymers, the glass transition temperature may change dramatically. Even in some cases, the composite may also develop cluster of cracks, thereby reducing its stiffness and strength. Such practical aspects must be considered when utilizing these nanotubes for increasing stiffness and strength of the host material.

Materials and Methods: SWNTs are reported to have better bending properties than MWNTs because of their thinner structure. The strength and weakness of adding SWNTs to polymer composites have been studied (Ajayan et al. 2000). Some types of SWNTs with high intrinsic conductivity and aspect ratios of about 1,000–10,000 are ideal materials to impart conductivity to composites. However, in the case of piezoelectric materials, it would be preferred to have dielectric nanotubes rather than conducting ones so that the dielectric anisotropy could increase the actuation and sensing properties of the polymers. On the other hand, MWNTs are brittle and are reported to have many defects due to their concentric walls. The inner walls are not accessible, and hence, it is difficult to quantify their properties.

Owing to the different properties of each type of nanotube (i.e., SWNTs or MWNTs), both types of nanotubes are used here to fabricate the transducers proposed here. SWNTs purchased from Nanostructured and Amorphous Materials Inc., were blended with the P(VDF-TrFE) polymer. The nanotubes were reported to be of 90% purity and of 1–2 nm outer diameters. P(VDF-TrFE) copolymer

pellets of 65/35-weight percent were obtained from Ktech Corp. MWNTs were purchased from Catalytic Materials Ltd., with 99.9% purity and approximately 10 nm diameters.

The important issues that affect the response of these nanotube-based piezoelectric polymers are the percentage weight ratio of nanotubes in the polymer, their type, diameter, length, and their alignment, seemingly the most important of all. Some of these factors have not been considered in the performance characteristics of the sensors and need to be treated significantly in the future. Alignment of CNTs has been done in the past (Jin et al. 1998; Ajayan et al. 2000; Sennett et al. 2003). Stretching the polymer composites after sonication and film casting also yields well-dispersed and aligned nanotubes; however, sonication for a long time could cause damage to the nanotubes (Lu et al. 1996). The following subsections discuss the preparation of nanotubes, polymers preprocessing, and finally fabrication of nanotube-based films.

12.2.2 Fabrication of Nanotube-Based Piezoelectric Film Sensors[1]

This section gives a brief overview of fabricating nanotube-based piezoelectric film sensors described in the preceding section. For this, 20% by weight of plain polymer P(VDF-TrFE) pellets are dissolved into an organic solvent, N,N-Dimethylacetamide. The pellets are fully dissolved in the solvent in about 5–6 h. The highly viscous solution is poured on an aluminum plate and a wet film applicator is used to draw a thin film of required thickness on the aluminum base. Mould release is used for easy removal of the film. Achieving desired thickness is relatively difficult and dependent on the viscosity. The thin film is then heated on a hot plate with the aluminum base to evaporate the solvent. The thickness of the films is further reduced after evaporating the solvent. Next, the thin films are carefully removed from the aluminum base. Thin films preparation is tedious and has to be repeated many times in order to produce a proper film. The viscosity of the wet film, which is proportional to the polymer addition in the solvent, affects the film formation to a very large extent. The thickness of the films was measured to be about 130 μm.

For the nanotube-added films, the process involves the preparation of two mixtures. First, 0.5% by weight of nanotubes with respect to the polymer pellets is added to the organic solvent (N,N-dimethylacetamide). The nanotube percentage is chosen on the basis of inferences from past research (Ramaratnam 2004). Addition of more nanotubes may cause the films to be conductive. The solvent-nanotube mixture is then sonicated for about 10 min at about 240 Watts, using a Branson Sonifier. Second, 20% by weight of the polymer is dissolved in the solvent separately and allowed to dissolve. The polymer is sonicated at about 200 Watts for 7 min for homogenization of the mixture. The sonicated mixture of nanotubes and

[1] The materials in this section may have come, directly or collectively, from our earlier publication (Ramaratnam and Jalili 2006b).

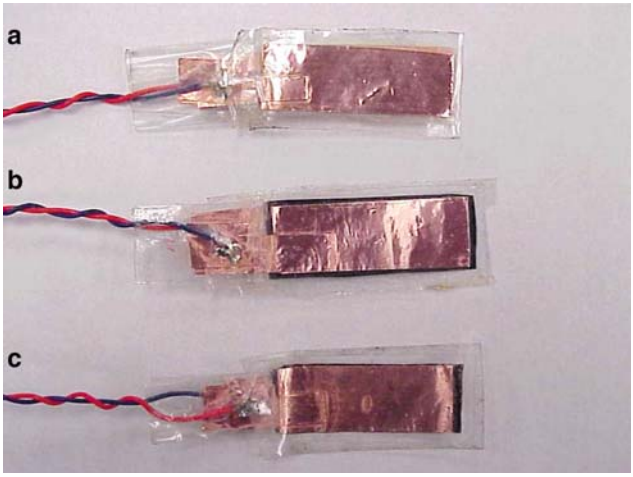

Fig. 12.5 Fabricated sensors, (**a**) Plain P(VDF-TrFE), (**b**) MWNT-based P(VDF-TrFE), and (**c**) SWNT-based P(VDF-TrFE)
Source: Ramaratnam and Jalili 2006b, with permission

the polymer solution are mixed together and sonicated again for about 4 min at 240 Watts. The nanotube-based mixture has a very high viscosity when compared to the mixture prepared for preparing pure P(VDF-TrFE) films (if the solvent amounts are equal in both the cases). The mixture is then cast into films using the applicator and the solvent is evaporated. Mould release is applied as a layer between the polymer mixture and the aluminum base to ease removing the films. A constant low temperature evaporation of the solvent would be of help to prevent excess adhesion of the polymer film to the base. Same procedure is done for fabricating SWNT-based and MWNT-based polymer films. The thickness of the SWNT-based films was about 60.5 μm, while it was approximately 50 μm for MWNT-based films.

The nanotube-based films prepared in the previous step, are annealed at about 90°C for about 4–5 h. Then, copper foils with conductive adhesives are attached to the film on both sides. Care must be taken to separate the electrodes from touching each other after adhesion to prevent shorting of electrodes. Wires are attached to these copper foils by soldered connections as shown in Fig. 12.5. An insulating layer (a rigid thin sheet of an insulating polymer) is used to separate the copper foils at the location of these wire connections. The films are then poled using a high voltage DC source at 2000VDC for about 5 h at room temperature. Insulation tapes are also applied to the films for preventing leakage of the charges. The films have to be carefully poled, as the dielectric breaks down easily in thin films. The piezoelectric materials are generally represented as voltage sources with some capacitance in combination. The capacitance of the pure P(VDF-TrFE) was 0.13 nF; 0.56 nF for the SWNT-based films; and 0.51 nF for the MWNT-based films. The fabricated sensors are shown in Fig. 12.5, with the nanotube added films seen to be partially black. Previous experiments with 2% SWNTs yielded a completely black film (Ramaratnam 2004).

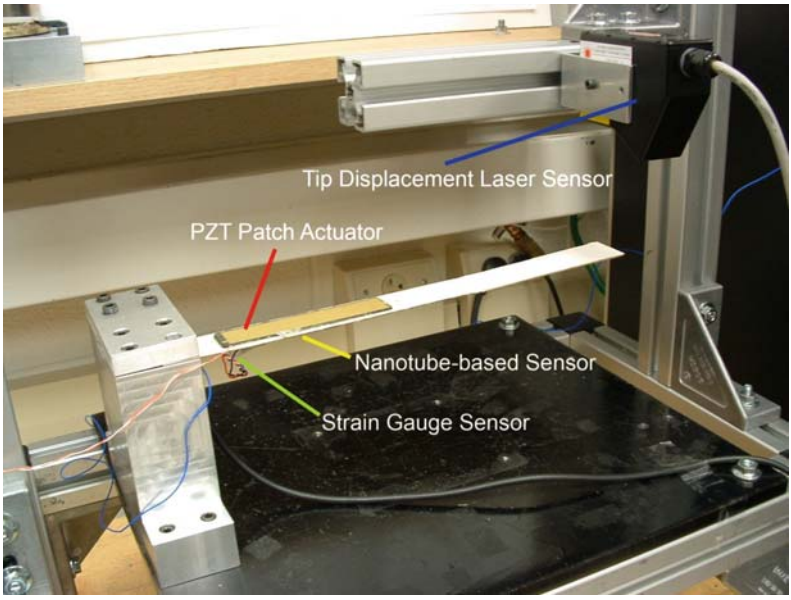

Fig. 12.6 Experimental setup for testing the proposed nanotube-based sensors
Source: Ramaratnam and Jalili 2006b, with permission

Experimental Setup, Procedures, and Results: In order to fully realize the potential of the nanotube-based sensors developed in the preceding section, an experimental setup is proposed here to investigate the improved sensing performance of these sensors.

The experimental setup consists of a thin cantilever beam, made of a nonconducting wooden material, a PZT patch actuator to actuate the beam, a strain gauge to detect the base strain, and a laser displacement sensor to measure the tip displacement (see Fig. 12.6). A detailed drawing for the beam dimensions, the position of the PZT actuator, strain gauge sensor, and nanotube-based sensors is given in Fig. 12.7. The laser sensor beam is located at about middle of the beam width and 6.35 mm from the tip end of the beam. A wooden beam is selected so that the beam remains nonconductive in order to prevent problems with the bare electrodes of the piezoelectric sensor. The experiments conducted here are focused on the sensing properties of the novel films. The PZT actuator actuates the beam with the input voltage ranging from 30 to 150 V. Due to the flexibility of the beam, the beam undergoes vibrations when the PZT actuator is excited. These vibrations are measured using piezoelectric strain sensors, and cross-verified with the strain gauge and noncontact laser measurements.

Different strain sensors, namely fabricated plain P(VDF-TrFE), SWNT-based, and MWNT-based P(VDF-TRFE) sensors are attached to the beam and their response to similar excitation conditions are measured for comparison. The same beam is used for all the three cases of sensors with the strain gauge and the PZT actuator attached in permanent locations (see Fig. 12.7). For different sensor application,

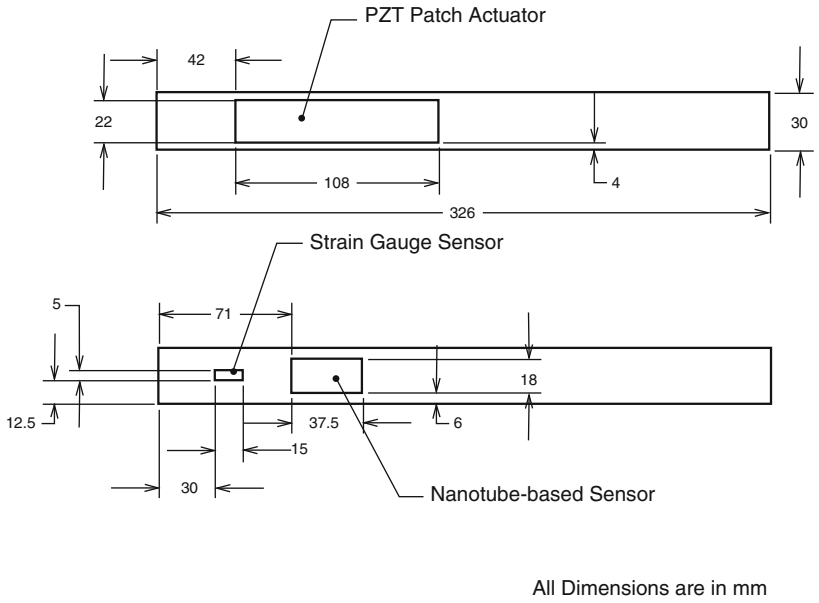

Fig. 12.7 Detailed drawing of the cantilever beam under experimentation; top (*top view*) and bottom (*bottom view*) corresponding to the arrangement shown in Fig. 12.6
Source: Ramaratnam and Jalili 2006b, with permission

it was tried to keep the bonding conditions of the sensors unchanged for each experiment. The strain gauge and laser sensor give voltage outputs proportional to their sensitivity. That is, the sensitivity of the strain gauge was $58.5\,\mathrm{mV}/\mu\varepsilon$ and that of laser sensor $-6.20\,\mathrm{mV/mm}$. Consequently, the sensitivity of the fabricated nanotube-based sensor can be calculated from the strain gauge and laser sensor measurements as will be discussed in detail later. All of these signals are acquired by the host computer using a digital signal processing board (dSPACE 1104 from dSPACE®).

The poling voltages are significantly lower than their nominal values for the copolymer films. Commercial PVDF sensors are fabricated as very thin films and their poling voltages are very high and in the order of 50–100 KV/mm of thickness (Piezo Film Sensors). The resonance condition of the beam is approximately about 10 Hz, so a filter is used to remove the higher frequencies, specifically noise and the electromagnetically induced voltage due to the AC power lines at a frequency of 60 Hz.

The piezoelectric actuator is actuated at 150 V and 10 Hz, with the results obtained for different sensors shown in Figs. 12.8–12.10. Figure 12.8 corresponds to fabricated sensors voltage, Fig. 12.9 depicts the strain gauge outputs, and Fig. 12.10 shows the laser sensor outputs measured at the tip. To better compare the results, Table 12.1 lists the maximum FFT values of nanotube-based sensor, strain gauge, and laser output for the three fabricated sensors. It is clearly visible, from Fig. 12.8,

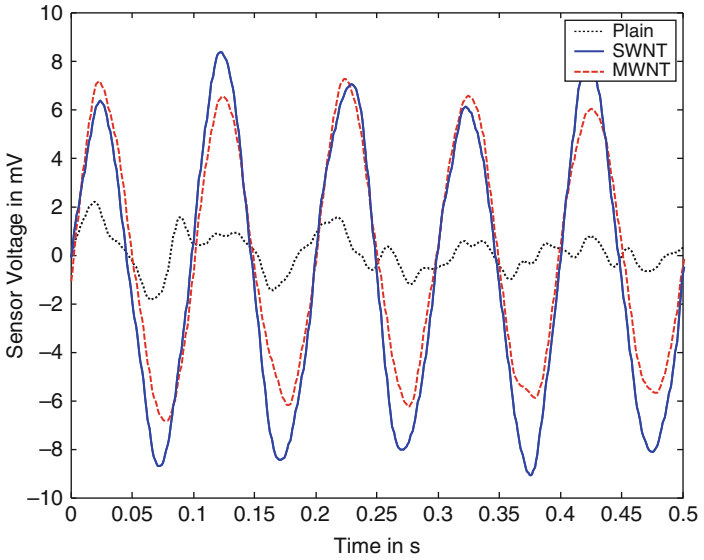

Fig. 12.8 Comparison between time domain responses (*sensor ouput*) of different sensors; dotted lines: plain P(VDF-TrFE), solid lines: SWNT-based P(VDF-TrFE) and dashed lines: MWNT-based P(VDF-TrFE) sensor
Source: Ramaratnam and Jalili 2006b, with permission

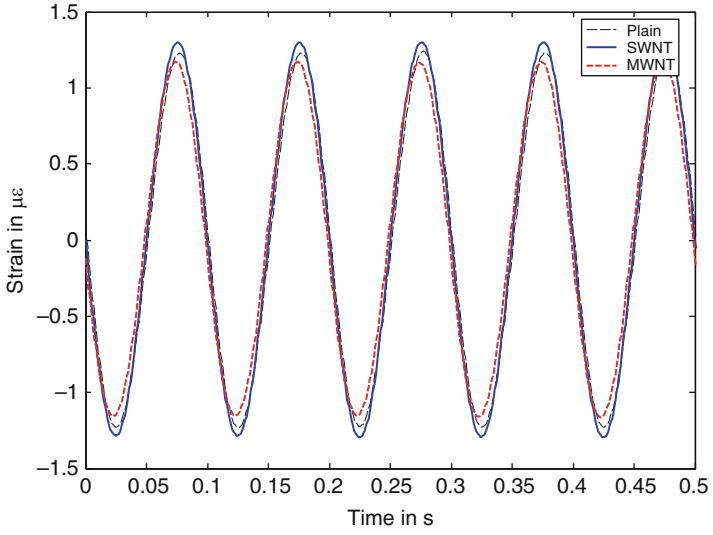

Fig. 12.9 Comparison between time domain responses (*strain gauge ouput*) for the different test cases; dotted lines: plain P(VDF-TrFE), solid lines: SWNT-based P(VDF-TrFE) and dashed lines: MWNT-based P(VDF-TrFE) sensor
Source: Ramaratnam and Jalili 2006b, with permission

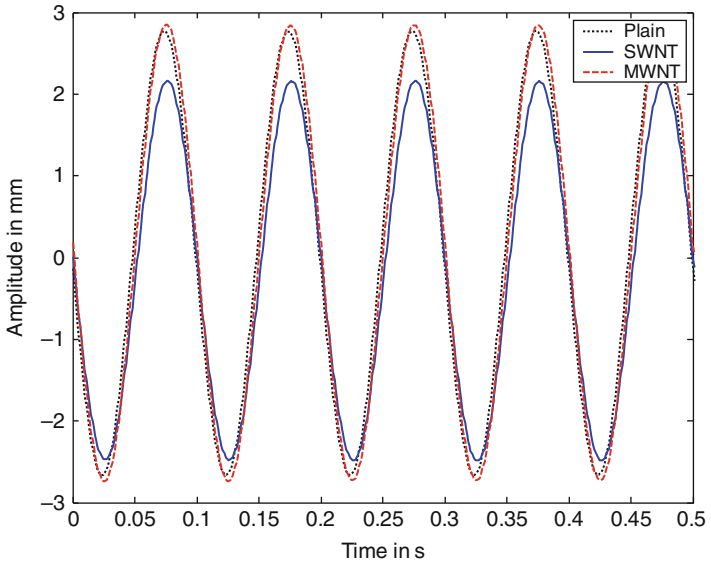

Fig. 12.10 Comparison between time domain responses (*laser sensor ouput*) for the different test cases; dotted lines: plain P(VDF-TrFE), solid lines: SWNT-based P(VDF-TrFE) and dashed lines: MWNT-based P(VDF-TrFE) sensor
Source: Ramaratnam and Jalili 2006b, with permission

Table 12.1 Comparison between different sensor outputs for the three fabricated sensors

Type of Sensor → Sensor output ↓	Plain P(VDF-TrFE)	MWNT-based P(VDF-TrFE)	SWNT-based P(VDF-TrFE)
Fabricated sensor output (mV)	0.8368	6.4506	7.8015
Strain gauge output, $\mu\varepsilon$	1.2320	1.1678	1.2915
Laser output (tip displacement) mm	2.7092	2.7865	2.3161

Source: Ramaratnam and Jalili 2006b, with permission

that nanotube-based sensors (both SWNT and MWNT) outperform the fabricated plain P(VDF-TrFE) sensor. Such notable improvement needs to be studied in detail in order to understand the factors and mechanisms contributing to this improvement. The increased magnitude of the electromechanical response of these nanotube-based copolymer sensors, when compared to those of plain copolymer sensors, promises the nanotube-based transducers a better future.

Proper methods of attaching electrodes, fabricating films, and higher poling voltages could yield better performance. Although different film parameters are not exactly the same for proper comparison (like that of different thickness of films, different response of the PZT actuator for the same input voltage and frequency, and fabrication differences), they closely resemble each other.

The areas under the curves in Fig. 12.8 are 1.3 mV.sec for the plain sensors, 8.2 mV s for MWNT-based, and 9.8 mV s for SWNT-based sensors, indicating better response for the nanotube-added films. The areas under the curve are for duration of 2 s.

12.2.3 Piezoelectric Properties Measurement of Nanotube-Based Sensors[2]

As discussed in the preceding section, a significant improvement in nanotube-based sensing capability has been achieved. In order to explain such improvements and further characterize the influence and role of CNTs in the polymer, measurements of some of the key properties are discussed in this section which can be used to analytically study the effect of nanotube addition in sensing improvement.

Young's Modulus: The Young's modulus was measured using the Instron 5582. The experiment directly gives the Young's modulus values by calibrating the stress vs. strain curve, which is obtained by testing the tensile strength of the samples placed between two jaws at a known force level. A total of about 8–10 samples were used for each type of sensors (i.e., plain polymer, SWNT-based, and MWNT-based), with the results shown in Table 12.2. As seen from the mean values in this table, SWNT-based sensors have the highest modulus ($\sim$390 kgf/mm^2), followed by MWNT-based ($\sim$330 kgf/mm^2), and plain PVDF ($\sim$300 kgf/mm^2) sensors.

d_{31} *Measurements:* Although the direct piezoelectric coefficient is defined as the reversible changes in polarization of a material with a change in stress, in practice the macroscopic coefficient is usually determined from the charge Q induced on a sample electrodes of area A upon a stress change (Garn 1982a, b). For this, d_{31} measurements were carried down with a quasi-static charge-integration technique as shown schematically in Fig. 12.11 (Kunstler et al. 2001).

The experimental arrangement shown in Fig. 12.11 consists of a piezoelectric sensor held firmly using a fixture. The top part of the fixture, which is fixed, holds the piezoelectric film and the positive electrode. The bottom part of the fixture holds the piezoelectric film and the negative electrode. By this arrangement, a known force F can be used to pull the piezoelectric film and simultaneously collect the voltage induced by the force. The capacitor C_m is used to collect the charge Q_3 accumulated on the electrodes upon loading the piezoelectric sensor. The voltage V measured

Table 12.2 Comparison of Young's Modulus between different polymer films

Young's Modulus → Type of film ↓	Min-max range [kgf/mm^2]	Mean values [kgf/mm^2]
Plain P(VDF-TrFE)	183–385	303.67
MWNT-based P(VDF-TrFE)	263–443	332.88
SWNT-based P(VDF-TrFE)	325–500	388.16

Source: Ramaratnam and Jalili 2006b, with permission

[2] The materials in this section may have come, directly or collectively, from our earlier publication (Ramaratnam and Jalili 2006b).

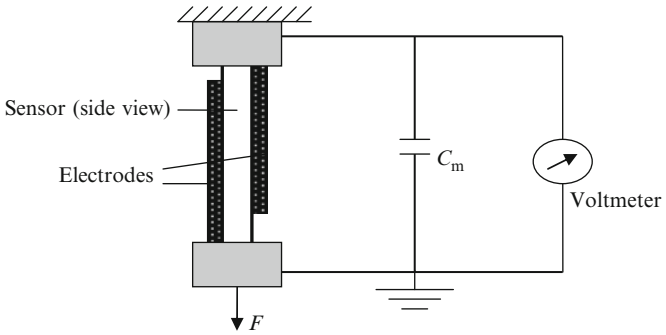

Fig. 12.11 Experimental setup for quasi-static piezoelectric d_{31} measurements (Kunstler et al. 2001)
Source: Ramaratnam and Jalili 2006b, with permission

using the voltmeter is a measure of the charge Q_3 given by $Q_3 = C_m V$. Hence, the piezoelectric constant can be calculated using the equation,

$$d_{31} = Q_3/F \tag{12.1}$$

The applied force exerted on the piezoelectric sensor is due to a known mass suspended under the influence of gravity, so the force can be calculated as $F = mg$. The mass m used here was 31.655 g. The value of C_m used was 11.7 nF. All the three piezoelectric sensors gave an output voltage of 1.2 mV, questioning the reliability of the results obtained using the experimental setup arranged in the laboratory. The calculated d_{31} value was about $9 \times 10^{-12} C/N$, which matches the value of d_{31} available in the literature (see for examples; Piezo Film Sensors 1999; Kunstler et al. 2001), justifying the results obtained here.

Other Measurements: The capacitance of the various films was measured using a multimeter with values shown in Table 12.3.

The thickness of the films was measured using Nikon Digimicro Stand with a resolution of 0.1 μm. The best comparison of different sensors could be obtained only when the thickness of the various films is the same. This is difficult at this point because of the use of wet film casting method to cast the films. This difficulty can be overcome only when a sophisticated method for dispersing and aligning nanotubes into polymers is devised. Other measurements such as the size of electrodes used for calculation of d_{31} and the dimensions of the different transducers measured using a screw gauge are also reported in Table 12.3.

Table 12.3 Various other measurements used to characterize the films

Inherent Capacitance of the Sensor	
Plain P(VDF-TrFE)	0.13 nF
MWNT-based P(VDF-TrFE)	0.51 nF
SWNT-based P(VDF-TrFE)	0.56 nF
Thickness	
Plain P(VDF-TrFE) film	130.9 μm
MWNT-based P(VDF-TrFE) film	50.6 μm
SWNT-based P(VDF-TrFE) film	60.5 μm
PZT Actuator	1.58 mm
Beam	1.15 mm
Polymer Sensor thickness (generalized)	0.38 mm
Area of Electrode	
Used for Sensing Experiments	37 mm × 16mm
Used for d_{31} measurement	30 mm × 16 mm

Source: Ramaratnam and Jalili 2006b, with permission

12.3 Structural Damping and Vibration Control Using Nanotubes-Based Composites[3]

The stiffness and damping properties of nanotube-based composites can be used to engineer novel composites at macroscale with tunable mechanical properties ranging from stiffer structure to better damper, the attributes that are essential for structural vibration control. Along this line, this section presents a brief overview of vibration damping and control using these nano-composites. For this, both single-walled and multiwalled nanotube-epoxy composites with different proportion of nanotubes are considered. Free and forced vibration tests are conducted on these samples (in the form of cantilevered beams) to extract natural frequency and damping ratio from the acquired responses.

One could relate the macroscopic piezoelectric properties (e.g., d_{31} obtained in the preceding section) to the nanoscopic interaction between host and nanotube materials (e.g., the interface zone), (Anand and Mahapatra 2009; Anand and Roy 2009). A pathway towards this concept is laid out next.

12.3.1 Fabrication of Nanotube-Based Composites for Vibration Damping and Control

This section describes various samples that were prepared to analyze the effect of several parameters such as CNT proportion, CNT type, and frequency dependence.

[3] The materials presented here may have come from, either directly or collectively, from our earlier publication (Rajoria and Jalili 2005).

MWNTs (with purity of 99.9% and diameter of 10 nm) were obtained from *Catalytic Materials* (http://www.catalyticmaterials.com) and SWNTs (with purity of 90% and diameter of 1–2 nm) were obtained from *Nanostructured & Amorphous Materials Inc* (http://www.nanoamor.com). Carbon fibers (CFs) (ACF-15) were obtained from $Kynol^{TM}Inc$ (http://www.kynol.com). Samples of plain epoxy and CF-epoxy were prepared for comparisons with the ones reinforced with CNTs. Figure 12.12 depicts the scanning electron microscope (SEM) images of MWNTs, SWNTs, and CFs utilized in this study.

A two-part epoxy consisting of an epoxy resin and an amine hardener was used for the experiments. First, 1g epoxy resin and 1g hardener were mixed together. The desired amount of CNTs was then added to the mixed resin. Following this, the mixture was manually mixed for about 4 min. The CNTs were dispersed in epoxy to a good extent by the manual mixing method at macroscopic level. The composites were made in the form of sandwiched laminated beams. The CNT-epoxy mixture was applied on one side of two thin steel beams ($12'' \times 0.25'' \times 0.01''$) and the beams were made to adhere together. The composite beam was then cured at

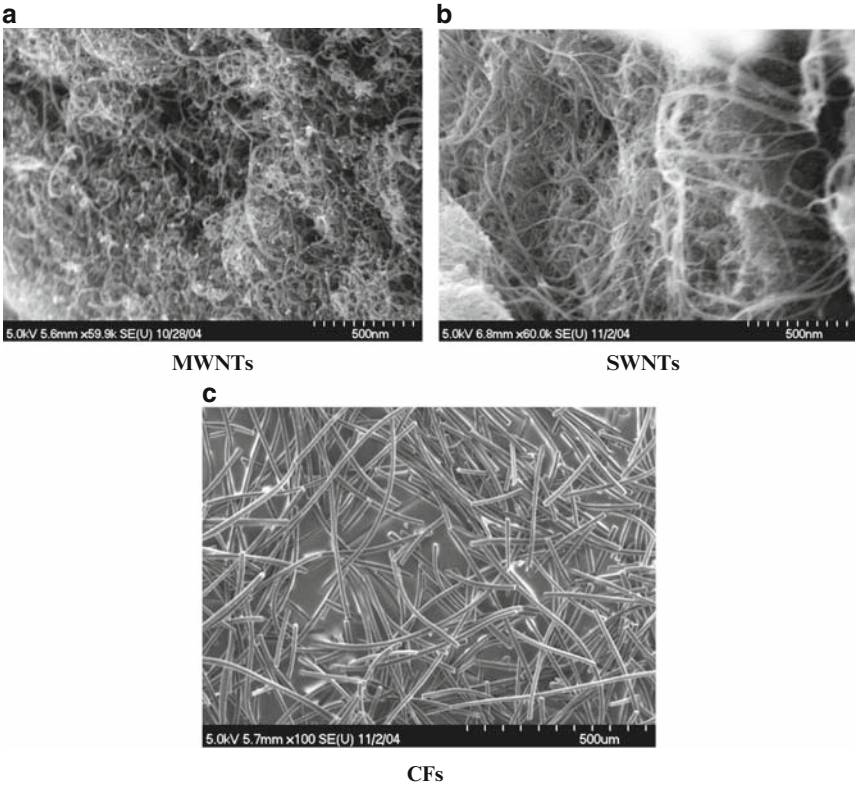

Fig. 12.12 SEM images of various reinforcing fibers; (**a**) MWNTs, (**b**) SWNTs, and (**c**) CFs
Source: Rajoria and Jalili 2005, with permission

room temperature for about 4.5 h under a load of 20 N. Following this, the samples were cured at 50°C for about 5 h under no load. Finally, the temperature was brought down to room temperature with further curing of the samples for about 10 h. The extra epoxy coming out of the edges was trimmed and the beams were cleaned. The composite samples, thus prepared, were ready for vibration testing. Eight composite beam samples comprising of different weight ratio (%) and the reinforcing fiber were prepared. They are designated as plain epoxy, 2.5% MWNT-epoxy, 5.0% MWNT-epoxy, 7.5% MWNT-epoxy, 2.5% SWNT-epoxy, 5.0% SWNT-epoxy, 7.5% SWNT-epoxy, and 5.0% CF-epoxy beams.

12.3.2 Free Vibration Characterization of Nanotube-Based Composites

Free vibration tests were performed on the composite beam samples to determine the effect of various parameters on elastic modulus and damping ratio of the composites. The composite beam samples were used as cantilever beams (see Fig. 12.13). An initial tip displacement was given and the resulting free vibration response acquired using dSPACE® DS 1104 real-time DSP board. FFT of the response gave the damped natural frequency and the damping ratio was found using logarithmic decrement method. The results demonstrate that the first vibration mode was the dominant mode during the excitation with higher modes being of significantly small amplitudes. To determine the frequency dependence of elastic modulus and damping ratio, the samples were excited at different frequencies by varying the beam length. Figures 12.14 and 12.15 show the variation of fundamental damped natural frequency (ω_d) and fundamental damping ratio (ξ) as a function of beam length (l) for all the beams.

It can be seen that the damped natural frequency (ω_d) has its highest value for 5.0% MWNT-epoxy beam as compared to other beam samples. For larger values of beam lengths, there is not much difference between various samples, while at

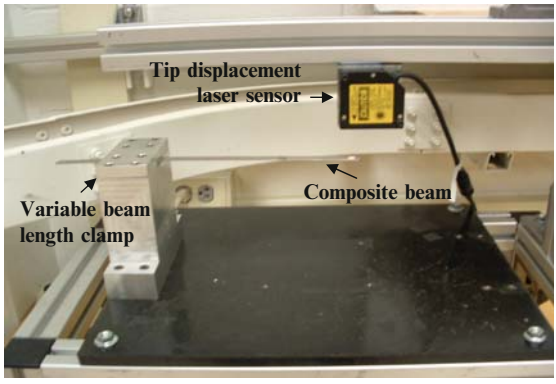

Fig. 12.13 Experimental setup for free vibration tests

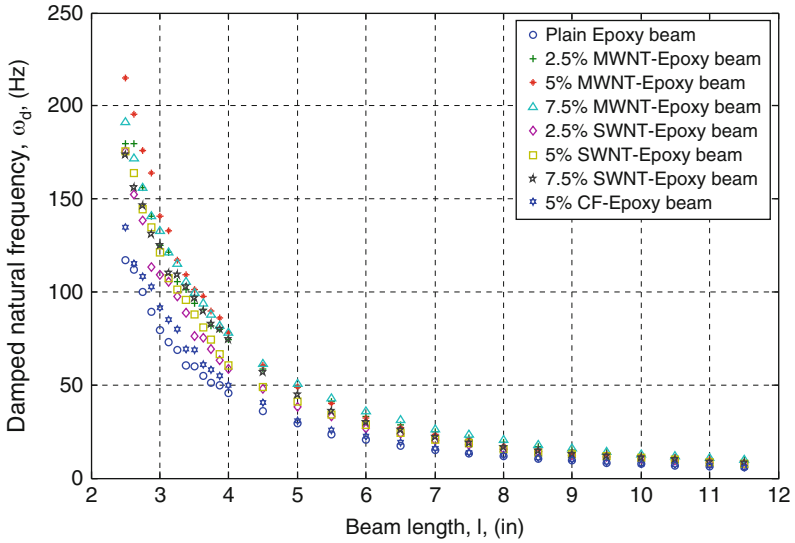

Fig. 12.14 Variation of fundamental damped natural frequency (ω_d) vs. beam length (l)
Source: Rajoria and Jalili 2005, with permission

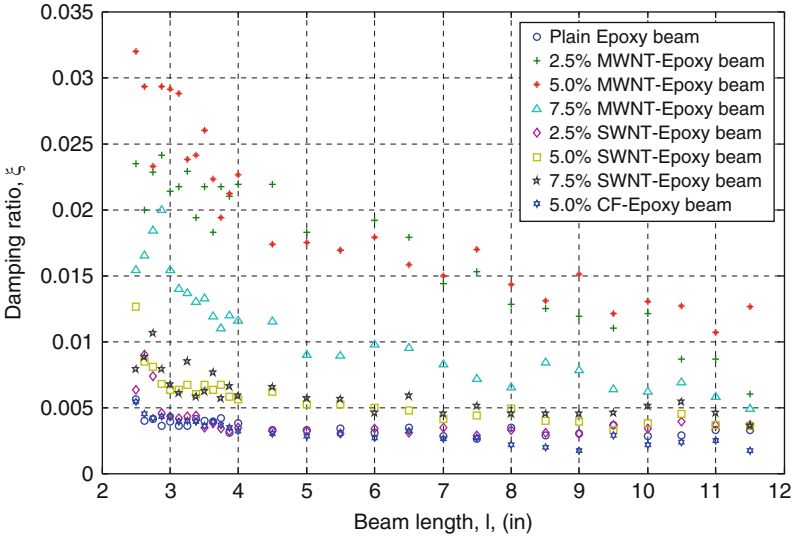

Fig. 12.15 Variation of fundamental damping ratio (ξ) vs. beam length *(l)*
Source: Rajoria and Jalili 2005, with permission

small beam lengths, the difference is clear. However, this difference is small and may not be due to changes in elastic modulus only. It is also seen that the maximum value of ω_d is for 5.0% MWNT case and neither for 2.5% nor for 7.5% MWNT cases, indicating a maximum occurring in ω_d vs. wt % curve. Elastic moduli need

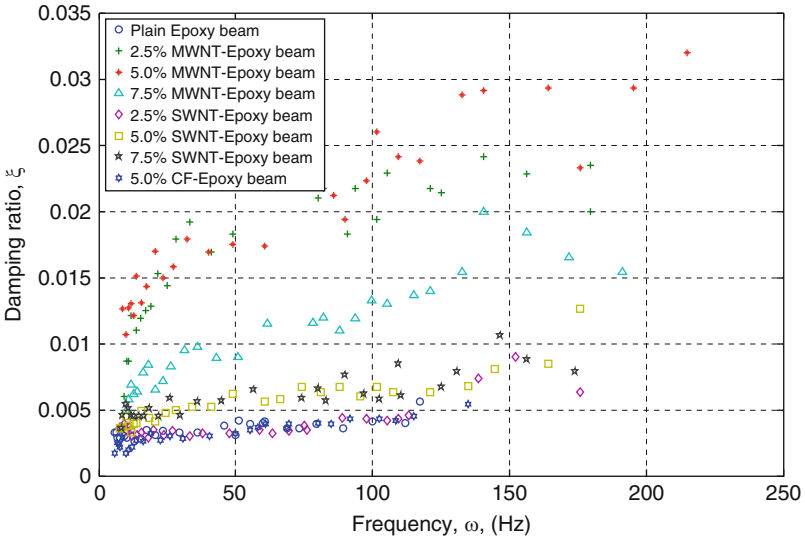

Fig. 12.16 Frequency dependence of fundamental damping ratio
Source: Rajoria and Jalili 2005, with permission

to be calculated to compare various beams. Figure 12.15 depicts the variation in fundamental damping ratio, ξ, as a function of beam length, l. The difference in damping ratio for various beams is quite clear at all beam lengths. It is seen for all the samples that as beam length increases, damping ratio decreases. More importantly, damping ratio is significantly higher for 5.0% MWNT-epoxy beam as compared to other samples. It is clearly observed that addition of CNTs (both SWNTs and MWNTs) enhances damping of composites. The damping enhancement was more pronounced for MWNT case. The damping ratios of plain epoxy, 2.5% SWNT-epoxy, and 5.0% CF-epoxy beams are similar.

The variable beam length, l, can be eliminated from the graphs in Figs. 12.14 and 12.15 to obtain the frequency dependence of damping ratio, ξ, vs. excitation frequency, ω (see Fig. 12.16 for this dependence), which is the same as the damped natural frequency, ω_d. As seen from Fig. 12.16, the damping ratio is higher for higher frequency for all the samples up to a frequency range of about 200 Hz. To quantitatively compare the enhancements in damping ratio, the percent increase in ξ as compared to plain epoxy beam as a function of beam length, l, has been calculated for all the beams and shown in Fig. 12.17. It can be seen that up to 700% increase in damping ratio has been obtained by using MWNTs. For other cases of CNT reinforcements also, there is significant damping enhancement (Rajoria and Jalili 2005).

To consolidate the effects of composition and fiber type, bar graphs have been plotted for a beam length of 2.5″. Figures 12.18 and 12.19 show the result of ω_d and ξ for all the beams at this beam length. Note that plain epoxy case is the same as 0% fiber reinforced in epoxy.

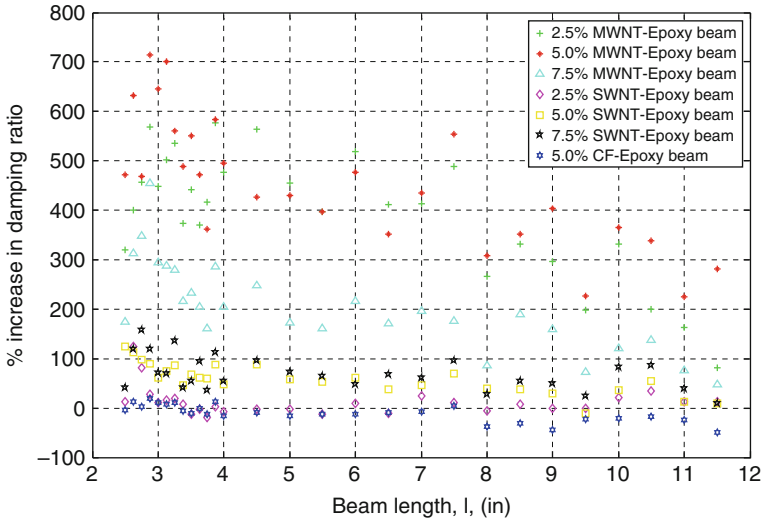

Fig. 12.17 The percent (%) increase in fundamental damping ratio with beam length, l, for different samples
Source: Rajoria and Jalili 2005, with permission

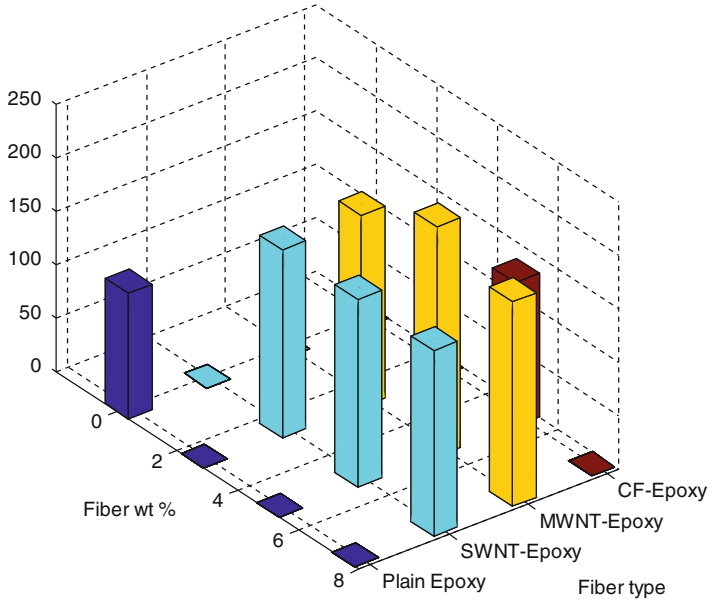

Fig. 12.18 Bar graph for fundamental damped natural frequency ω_d (Hz) vs. fiber weight % and fiber type for beam length $l = 2.5''$
Source: Rajoria and Jalili 2005, with permission

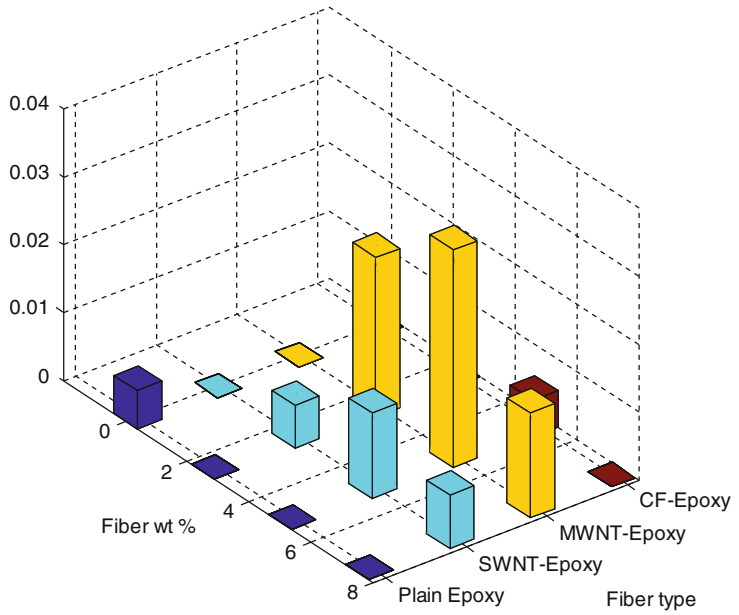

Fig. 12.19 Bar graph for fundamental damping ratio ξ vs. fiber weight % and fiber type for beam length $l = 2.5''$
Source: Rajoria and Jalili 2005, with permission

From these figures, the significant enhancement in fundamental damping ratio is clear. As a result, a reduction in fundamental damped natural frequency, ω_d, is expected on the basis of the formula, $\omega_d = \omega_n\sqrt{1-\xi^2}$, where ω_n is the fundamental undamped natural frequency which is dependent on beam flexural stiffness, $E_c' I_c$. Despite this, an increase in ω_d is observed. This is an indication of an increase in ω_n, and hence, in $E_c' I_c$. The decrease in ω_d caused by the increase in ξ is overcome by the increase in $E_c' I_c$. It can also be seen from Fig. 12.19 that MWNTs were much more effective in increasing damping properties of the composite than other fillers (SWNTs and CFs). The dependence on fiber wt% can also be seen. It is observed that there occurs a maximum in the damping ratio for both SWNT and MWNT reinforcements as the wt % is increased, which is at 5% here for both SWNTs and MWNTs. This implies the existence of an optimum wt% for maximum damping. Similar trend is observed for fundamental damped natural frequency. Such trends can be observed at other beam lengths also, as evidenced from Fig. 12.15 (the plot of ξ vs. l).

The characteristic storage modulus and loss modulus of the composite beams can also be calculated using the results of free vibration tests. Storage modulus is determined by equating the fundamental natural frequency of the beam to the theoretical value given by Euler-Bernoulli beam theory.

$$\omega_1 = \frac{1.875^2}{2\pi l^2}\sqrt{\frac{(E'I)_c}{\rho A}} \Rightarrow E_c' = \left(\frac{2\pi l^2 \omega_1}{1.875^2}\right)\frac{\rho A}{I_c} \tag{12.2}$$

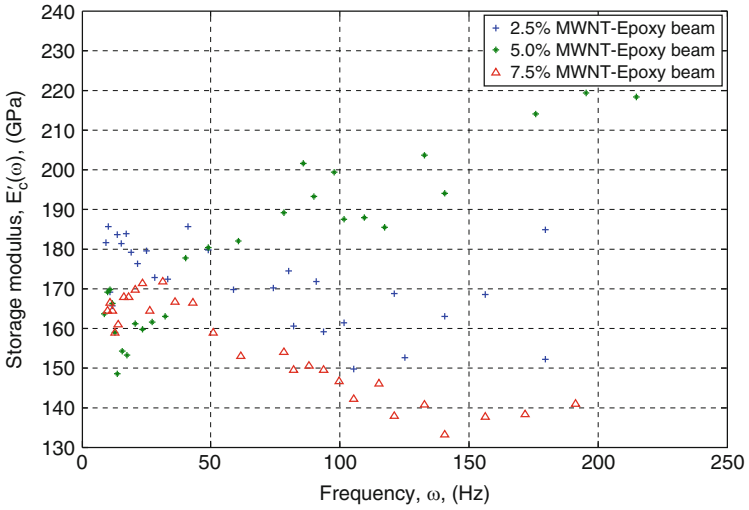

Fig. 12.20 Storage moduli of MWNT-epoxy beams vs. frequency
Source: Rajoria and Jalili 2005, with permission

where ω_1 is fundamental natural frequency (Hz), E_c' is storage modulus of the composite beam (which is frequency dependent here), l is beam length, ρ is the mass density of the beam, A is the cross sectional area of the beam, and I_c is the cross sectional moment of inertia of the beam about the axis of bending. All the parameters in (12.2) are known, and thus, E_c' can be calculated as shown in Fig. 12.20 for MWNT-epoxy beams (as just representative results among other materials). To calculate the loss modulus, E_c'', following equation can be utilized.

$$E_c''(\omega) = E_c'(\omega)\tan\delta = 2E_c'(\omega)\xi(\omega) \tag{12.3}$$

where $\tan\delta$ is the loss factor of the composite beam. Knowing $E_c'(\omega)$ and $\xi(\omega)$, $E_c''(\omega)$ can be calculated which is shown, again only for MWNT-epoxy beams, in Fig. 12.21.

12.3.3 Forced Vibration Characterization of Nanotube-Based Composites

The previous section described the free vibration tests that were done on the eight composite beam samples. The first vibration mode was the dominant mode during these tests. This section describes the forced vibration tests that are performed on the same samples to determine the modal dependence of various vibration characteristics by exciting the beams at multiple modes.

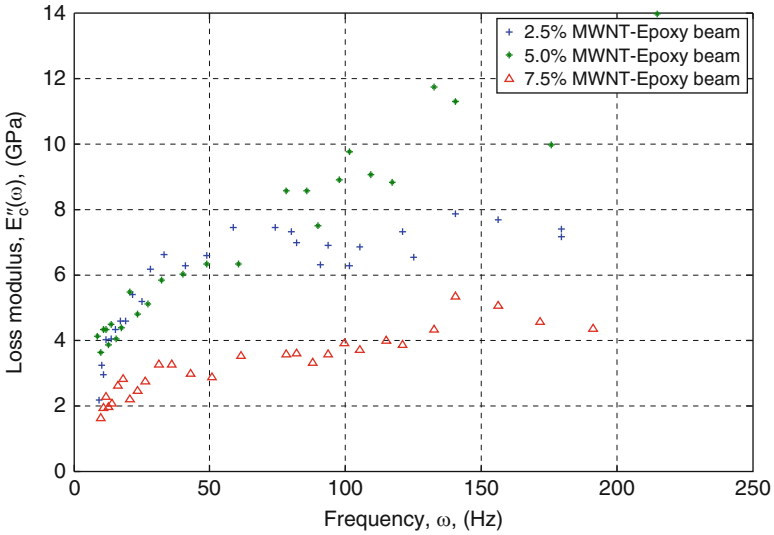

Fig. 12.21 Loss moduli of MWNT-epoxy beams vs. frequency
Source: Rajoria and Jalili 2005, with permission

Two forced vibration tests were done; impact testing and sinusoidal sweep testing. Impact testing was done to identify the modal frequencies of the beams around which the refined sinusoidal sweeps were done.

Impact Test: An HP 35670A Dynamic Signal Analyzer (DSA) was used to analyze all the signals (force and displacement) that were acquired. The composite beam was held vertically as a cantilever beam. An impact hammer (equipped with a force sensing transducer) was used to provide the force impulse to the beam. The force and tip displacement (acquired using a laser sensor) were fed into two channels of the DSA. Power spectra and frequency response functions of the DSA were used for the analysis. Three impact responses were acquired and averaged. The beam length was kept unchanged (11.5″) for all the tests.

The beam was hit at the base so as to excite multiple vibration modes. However, the data was captured only up to frequencies of 100 Hz. This frequency range mostly included two vibration modes. Frequency response (fft{tip displacement}/fft{base force}) and displacement power spectrum were obtained for all the eight composite beam samples. First two modal frequencies were then identified for all the samples. Higher modal frequencies were observed for CNT-reinforced beams. MWNT-epoxy beams showed higher modal frequencies compared to SWNT-epoxy beams. Sinusoidal sweep tests were done with refined frequency increment around the modal frequencies, which is described next.

Sinusoidal Sweep Test: The ECP rectilinear plant (model # 210) was used to perform the sinusoidal sweep tests (http://www.ecpsystems.com). The beams were clamped vertically as cantilever beams with a beam length of 11.5″. The base was given

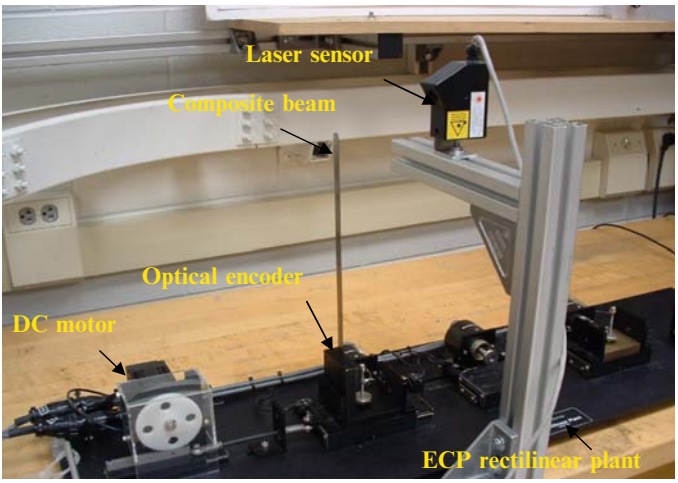

Fig. 12.22 Experimental setup for sinusoidal sweep tests
Source: Rajoria and Jalili 2005, with permission

a sinusoidal excitation using a DC brushless motor. An optical encoder was used to monitor the base displacement and a laser sensor was used to monitor the tip displacement (see Fig. 12.22). The frequency increment near the modal frequencies was 0.05 Hz, while at distant frequencies the increment was selected to be 2.5 Hz. The excitation frequency was kept up to 70 Hz (which included first two vibration modes for all the beams). The data was acquired using the same DSP platform as in free vibration tests. Amplitudes of tip displacement and base motion were found from the acquired data at each frequency and the frequency response function (FRF) was determined by taking their ratio. The FRFs for various beams are shown in Figs. 12.23–12.26.

Results and Discussion: The damping ratio at the modal frequencies is calculated using half power method which is shown in Table 12.4. Using half-power method, the damping ratio of interest (fundamental damping ratio here) can be calculated as:

$$\xi = \frac{\Delta\omega}{\omega_d} \tag{12.4}$$

where $\Delta\omega$ is the difference between frequencies (ω_{d1} and ω_{d2}) corresponding to half power points around the fundamental damped natural frequency, ω_d. The results of the sinusoidal sweep tests (Table 12.4) indicate higher vibration damping for second vibration mode for CNT-reinforced beams, in general. For the plain epoxy and CF-epoxy beams, the first mode is more dampened than the second mode. FRFs are wider (at both first and second modes) for MWNT-epoxy beams compared to other beams indicating enhanced vibration damping by MWNT reinforcement.

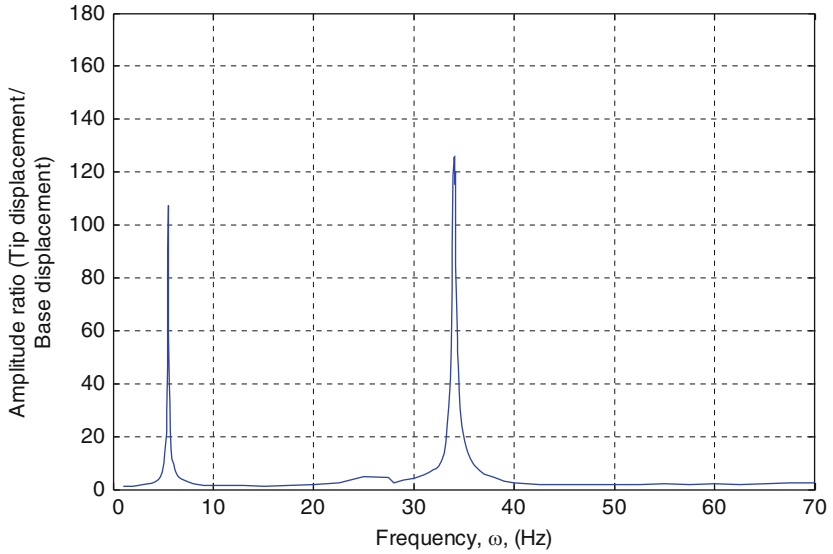

Fig. 12.23 Frequency response functions for *plain epoxy* beam
Source: Rajoria and Jalili 2005, with permission

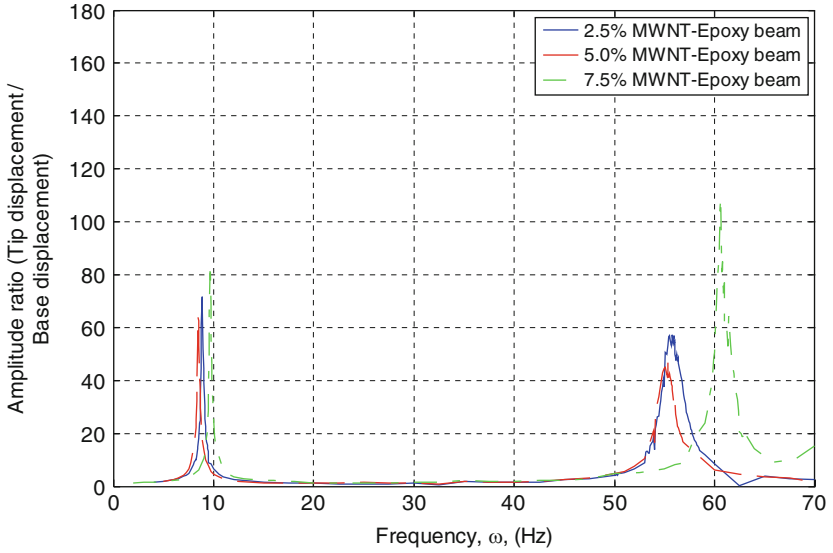

Fig. 12.24 Frequency response functions for *MWNT-epoxy* beams
Source: Rajoria and Jalili 2005, with permission

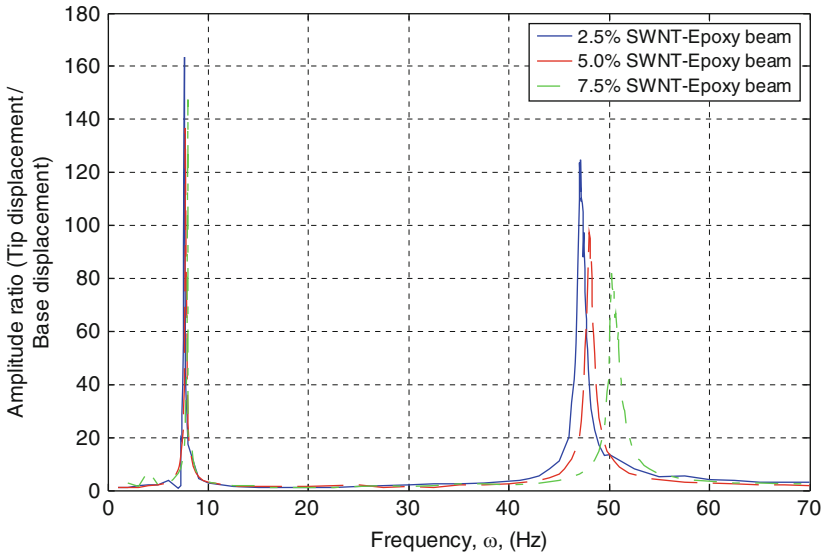

Fig. 12.25 Frequency response functions for *SWNT-epoxy* beams
Source: Rajoria and Jalili 2005, with permission

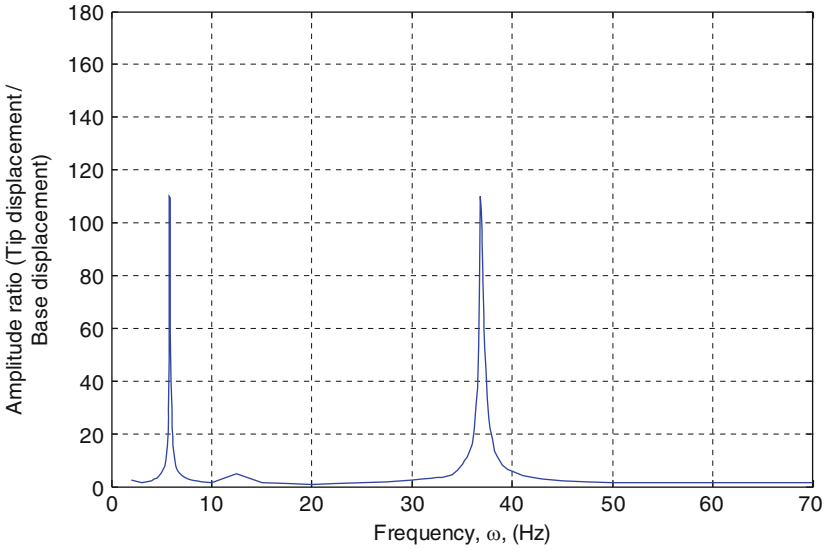

Fig. 12.26 Frequency response function for 5.0% *CF-epoxy* beam
Source: Rajoria and Jalili 2005, with permission

Table 12.4 Damped natural frequencies and corresponding damping ratios for different samples

Beam type	ω_{d1}(Hz)	ω_{d2} (Hz)	ζ_1	ζ_2
Plain epoxy	5.50	34.05	0.0164	0.0104
2.5% MWNT-epoxy	8.85	55.80	0.0216	0.0296
5.0% MWNT-epoxy	8.45	55.30	0.0257	0.0264
7.5% MWNT-epoxy	9.65	60.63	0.0160	0.0085
2.5% SWNT-epoxy	7.60	47.15	0.0108	0.0130
5.0% SWNT-epoxy	7.75	48.00	0.0109	0.0120
7.5% SWNT-epoxy	7.95	50.25	0.0062	0.0173
5.0% CF-epoxy	5.80	36.85	0.0184	0.0107

Source: Rajoria and Jalili 2005, with permission

12.4 Piezoelectric Nanocomposites with Tunable Properties[4]

This section briefly presents the development of a new class of nanotube-based piezoelectric polymeric composites with controllable bond expansion and contraction in the interface of nanotube and matrix for use in next-generation structural vibration-control systems. The application of external electrical field results in imparting the quality of adhesion between nanotube and the matrix at nanoscale to create novel engineered composites at macroscale with tunable mechanical properties ranging from stiffer structure to better damper. For demonstration purposes, both CNTs and BNNTs are investigated in this section to show the effect of change in parameters.

12.4.1 A Brief Overview of Interphase Zone Control

The interphase zone is a region formed as a result of the interaction between nanomaterials and the host matrix. It has heterogeneous properties that are different from those of nanotube and bulk matrix, and hence plays an important role in load transferring between them. Appropriate control of interphase zone is a major step towards obtaining composites with desired properties. While the strong interaction between nanotube and polymer in this zone is required to take advantage of very high Young's modulus and strength of nanotube, the weak bonding between them results in interfacial slippage at the interface of nanotube and polymer which is beneficial in terms of structural damping. In order to obtain a composite structure with tunable mechanical properties ranging from stiffer structure to better damper, the quality of adhesion between nanotube and matrix can be controlled through altering the interatomic force between them.

[4] The materials in this section may have come from, either directly or collectively, from our earlier publication (Salehi-Khojin et al. 2009a).

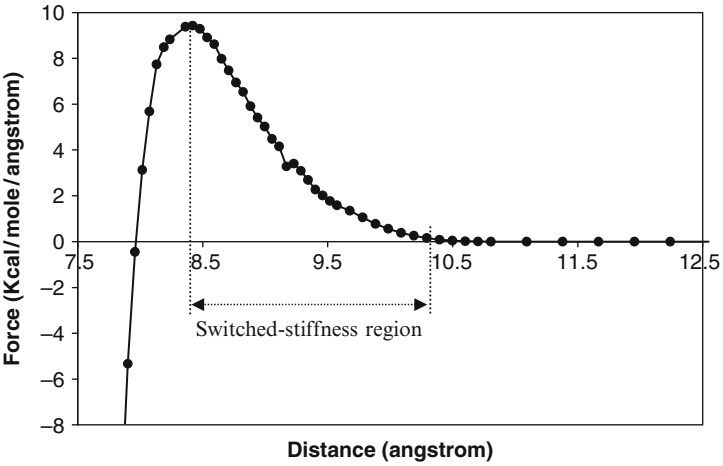

Fig. 12.27 Schematic of interatomic force between two atoms and proposed switched-stiffness region for BNNT-PVDF combination
Source: Salehi-Khojin et al. 2009a, with permission

The interatomic force between two atoms is schematically shown in Fig. 12.27 from which two characteristic regions on interatomic force curve with respect to distance can be observed. The first region, called "contact mode", is characterized by a sharp slope in which the interatomic force increases very rapidly. In the "noncontact region", the interatomic force decreases with the increase of separation distance between two atoms such that after a certain level of separation, interatomic force merges to zero. It is obvious that by altering the separation distance between two molecules in the region of maximum interatomic force level, indicated by "switched-stiffness region", the role of nanomaterials on the overall properties of composite structure can be tuned. This phenomenon can be described by the restriction effect of nanomaterials on the bulk polymeric matrix. The farther the polymeric segments from nanomaterials, the faster relaxation those segments display which leads to less immobilization of polymeric segments (Salehi-Khojin and Zhong, 2007a, b). Thus, smaller interphase zone is formed. However, smaller gap between nanomaterial and matrix results in greater immobilization of polymer, and consequently larger interphase zone between them.

To control interphase zone between two arbitrary levels, piezoelectric polymeric matrix such as polyvinylidene fluoride (PVDF) reinforced with nanotubes can be used. In the presence of electrical field, depending on the magnitude and direction, PVDF can be poled in the radial direction to align the electro-negative and electro-positive parts of molecular unit. In our previous work (Salehi-Khojin and Jalili 2008a), PVDF matrix was considered as a circular piezoelectric tube subjected to electrical loading, and an analytical solution was obtained to relate radial displacement of matrix to applied electrical field. This facilitates theoretical control of the interatomic distance between nanotube and matrix through applying corresponding electrical field. The schematic of this concept is shown in Fig. 12.28. It is

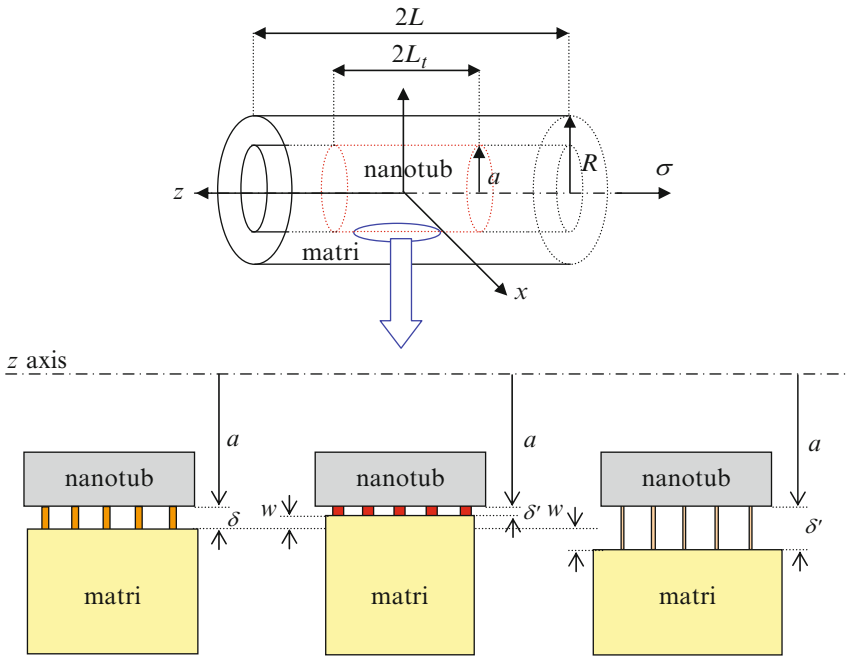

Fig. 12.28 (*top*) Schematic of representative volume element (RVE) of nanotube-based composite, and (*bottom*) radial displacement of polymeric matrix
Source: Salehi-Khojin et al. 2009a, with permission

assumed that there is an initial gap of δ between nanotube and PVDF. Through applying electrical field, depending on the direction, the distance between nanotube and matrix can be increased or decreased compared to initial gap. Thus, the interatomic force between adjacent layers of nanotube and PVDF can be tuned in the switched-stiffness region through applying corresponding electric field and the magnitude of load transferred to the nanotube can be controlled through separation distance.

12.4.2 Molecular Dynamic Simulations for Nanotube-Based Composites

Molecular dynamic (MD) simulation technique is utilized here to investigate the change in molecular energy level created between PVDF polymer and SWCNT or BNNT layer and ultimately the effect of spacing distance between the two simulated layers. In MD simulation series, both SWCNT and BNNT are assumed to possess symmetrical (6,6) chirality. However, it is possible to extend the study to investigate the created energy between SWCNT and MWCNT with different chiralities and PVDF layer as well. For this purpose, a layer of already constructed SWCNT or BNNT is placed at a specific fixed distance from a PVDF strand. The two layers are

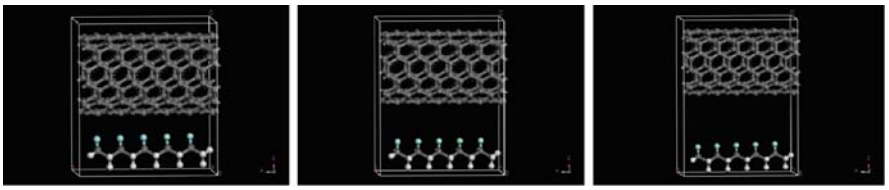

Fig. 12.29 SWCNT-PVDF molecular level layer with 8.14 Å (*left*), 10.14 Å (*middle*), 12.14 Å (*right*) axis to axis spacing
Source: Salehi-Khojin et al. 2009a, with permission

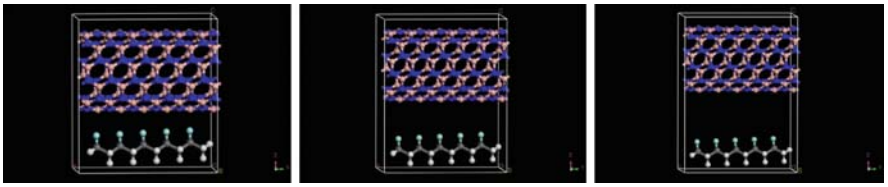

Fig. 12.30 BNNT-PVDF molecular level layer with 8.14 Å (*left*), 10.14 Å (*middle*), 12.14 Å (*right*) axis to axis spacing
Source: Salehi-Khojin et al. 2009a, with permission

placed parallel to each other so that the directional axis of both molecular structures is in the same direction. Several simulation cells are constructed by varying spacing distance between SWNT or BNNT layer and PVDF strand while the configuration of each molecular structure is kept unchanged. Figure 12.29 shows the constructed molecular level cells containing SWCNT and PVDF layers with different spacing distances, and similarly Fig. 12.30 depicts the BNN–PVDF layer simulation cells (Salehi-Khojin et al. 2009a).

The lengths of PVDF and nanotube strands are considered to be equal (13.542 Å here). It is also considered that the periodic boundary condition is in effect on each side of the cell. Therefore, it can be assumed that the model includes extended CNTs or BNNTs strands placed near PVDF layers. All the simulations are conducted for the normal temperature condition (i.e., $298.15° K$).

The potential energy calculations of the system were performed on the basis of the potential energy relation (Dauber-Osguthorpe et al. 1988) and can be defined in the following general form:

$$E_{\text{total}} = E_{\text{valence}} + E_{\text{crossterm}} + E_{\text{nonbond}} \tag{12.5}$$

which is the sum of the valence (or bond), cross-term, and nonbond interaction energy terms. The valance energy can be described as sum of bond stretching, bond angle, dihedral bond-torsion, inversion (or out of plane interaction), and Urey-Bradley terms as follows:

$$E_{\text{valence}} = E_{\text{bond}} + E_{\text{angle}} + E_{\text{torsion}} + E_{\text{oop}} + E_{\text{UB}} \tag{12.6}$$

The cross-term interacting energy involves bond lengths and angle change effects caused by the surrounding atoms and can be defined as

$$E_{\text{crossterm}} = E_{\text{bond-bond}} + E_{\text{bond-angle}} + E_{\text{angle-angle}} + E_{\text{end_bond-torsion}} + E_{\text{middle_bond-torsion}} + E_{\text{angle-torsion}} + E_{\text{angle-angle-torsion}} \quad (12.7)$$

In Eq. (12.7), $E_{\text{bond-bond}}$ relates the stretch-stretch interactions between two adjacent bonds, $E_{\text{bond-angle}}$ indicates the stretch-bend interactions between a two-bond angle and one of its bonds, $E_{\text{angle-angle}}$ represents bend-bend interactions between two valence angles associated with a common vertex atom, $E_{\text{end_bond-torsion}}$ relates the stretch-torsion interactions between a dihedral angle and one of its end bonds, $E_{\text{middle_bond-torsion}}$ represents the stretch-torsion interactions between a dihedral angle and its middle bond, $E_{\text{angle-torsion}}$ indicates the bend-torsion interactions between a dihedral angle and one of its valence angles, and $E_{\text{angle-angle-torsion}}$ represents the bend-bend-torsion interactions between a dihedral angle and its two valence angles (Salehi-Khojin et al. 2009a).

The interactions between nonbonded atoms can be categorized into the van der Waals energy and Coulomb electrostatic energy interactions as

$$E_{\text{nonbond}} = E_{\text{vdW}} + E_{\text{Columb}} \quad (12.8)$$

The detailed equations for each of the described energy terms can be found in (Salehi-Khojin et al. 2009a).

Using constructed molecular level cells, numerous energy calculations were performed for different PVDF-nanotubes axis to axis distances. It should be mentioned that the temperature variation and the created energy between nonbonded atoms can affect existing bonded atoms in each molecular structure resulting in a slight deformation in each strand. Therefore, in order to include these small effects in the simulations, it was allowed that the bonded atoms participating in the PVDF or nanotubes structures have limited movements, while the spacing between the two molecular structures was kept stationary. This causes a limited expansion or contraction of each molecular structure and results in a more realistic energy prediction.

The force function is the negative of the gradient of the energy potential. Therefore, by using the energy equations corresponding plots, it is possible to calculate the force created between nanotubes and PVDF layer at each axis to axis distance on the basis of the following relationship:

$$F(r) = -\sum_i \sum_{j>i} \nabla E_{ij} = -\sum_i \sum_{j>i} \frac{d}{dr} E_{ij} r \quad (12.9)$$

where $F(r)$ is the force created by the potential energy, and r is the distance vector between atoms. The obtained information can be used to investigate the stiffness of the composite materials containing SWCNT or BNNT and PVDF layers in their structure based on the nanotubes-PVDF distance.

12.4.3 Continuum Level Elasticity Model of Nanotube-Based Composites

A 3D solid elasticity solid model has been applied here for the analysis of nanocomposite RVE configuration shown in Fig. 12.28 (Salehi-Khojin et al. 2009a). Leaving the details of the modeling to Salehi-Khojin et al. (2009a), we only present the final results on this continuum model that will be augmented with the MD model of preceding section to arrive at the combined model.

We define $g(\delta')$ as displacement ratio of outer layer of nanotube to inner layer of matrix (non-iso-strain condition in the interphase zone) where δ' is the radial displacement of matrix as a result of applied thermal and electrical fields (see Fig. 12.28). In order to obtain an appropriate expression for $g(\delta')$, nanotube and matrix can be modeled as a set of concentric cylindrical shells with vdW interaction between adjacent layers. It is obvious that stronger interaction results in higher $g(\delta')$, and weaker interaction leads to smaller $g(\delta')$. Comparing the trend of $g(\delta')$ and interatomic force at noncontact mode (see Figs. 12.27 and 12.28) as a function of separation distance, the following formulation is suggested:

$$g(\delta') \propto \frac{F_{in}(r)_{r \geq r_{F_{\max}}}}{F_{in}(r)_{r=r_{F_{\max}}}} \tag{12.10}$$

where F_{in} is an interatomic force between nanotube and matrix obtained from MD simulations. As the attraction force between two atoms has the highest value at $r = r_{F_{\max}}$, the maximum relative displacement between two atoms can be obtained at this point. As distance between two atoms increases, the attraction force, and consequently, the relative displacement between them decrease accordingly, such that they merge to zero at higher distances.

So far, we have shown that the effect of applied electrical field and separation distance on the displacement ratio of outer layer of nanotube and inner layer of matrix can be obtained from MD simulations. Also, it was indicated that results from MD simulations should be applied into continuum level elastic model to quantify the load transferred from matrix to nanotube. We will implement, next, this interaction on two classes of nanotubes to demonstrate the feasibility of the proposed approach in manipulating interphase zone for arriving at next-generation nanocomposites with tunable parameters.

12.4.4 Numerical Results and Discussions of Nanotube-Based Composites

Figure 12.31 depicts the results of MD simulations for BNNT-PVDF and CNT-PVDF interactions. As seen, in smaller gaps in the "noncontact zone", BNNT and PVDF make a stronger bonding compared to that of PVDF and CNT. For instance,

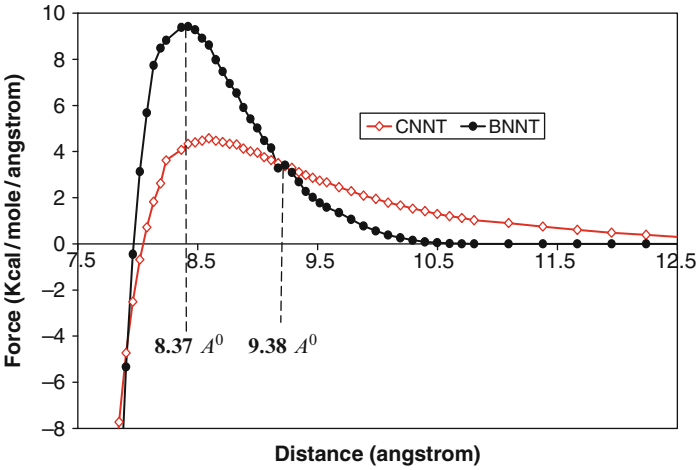

Fig. 12.31 Interatomic force diagrams of SWCNT-PVDF and BNNT-PVDF composites
Source: Salehi-Khojin et al. 2009a, with permission

in separation distance of 8.37 Å, the interatomic force between BNNT and PVDF is 9.38 (Kcal/mole/angstrom) which is almost twice than that of CNT-PVDF. As the separation distance increases, the interatomic force between two molecules decreases such that the rate of reduction in the force curve for BNNT-PVDF combination is much higher compared to that of CNT and PVDF. However, after a critical point of 9.22 Å, BNNT and PVDF combination shows weaker interaction than PVDF-CNT. It is seen that at separation distance of 10.3 Å, the interatomic force between CNT-PVDF is 1.5 (Kcal/mole/angstrom) while for BNNT-PVDF it is 0.085 (Kcal/mole/angstrom). Results indicate that adhesion strength of PVDF matrix reinforced with BNNT is more sensitive to separation distance when compared with CNT-PVDF combination.

On the basis of the continuum level model (see Salehi-Khojin et al. 2009a) and obtained MD simulations, the numerical results for axial and shear stresses can be obtained for a nanotube-reinforced PVDF composite subjected to electrical loading. As applying the electrical field in the radial direction is more practical and beneficial, the results given here are based on radial electrical field, and the axial electrical loading is not considered in this study. Furthermore, the effect of thermal loading is not considered in the numerical simulations. The physical properties of nanotubes considered in this study are $L_t = 135\,\text{nm}$, $a = 12.3\,\text{nm}$, $C_{55} = 2.64\,\text{GPa}$, $C_{33} = 1\,\text{TPa}$, and $\upsilon = 0.34$. The PVDF matrix properties are $C_{11} = C_{22} = C_{33} = 8\,\text{GPa}$, $C_{12} = C_{13} = C_{23} = 4.4\,\text{GPa}$, $C_{55} = 1.8\,\text{GPa}$ (C_{ij} refers to elements of material stiffness matrix), and $d_{13} = 23 \times 10^{-12}\,\text{m/V}$.

Figure 12.32 depicts the distribution of average axial normal stress in the nanotube along the nanotube length at different separation distances for CNT-PVDF and BNNT-PVDF. Results indicate that the axial normal stress has maximum values in the middle of nanotubes, whereas the minimum values are at its two ends.

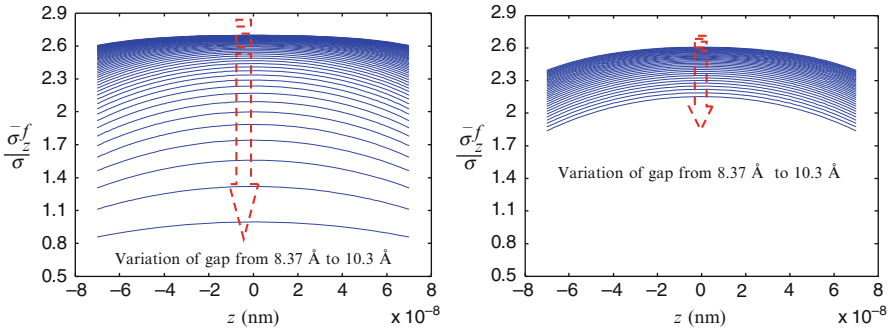

Fig. 12.32 Average axial normal stress in the nanotube along the nanotube length for different separation distances for (*left*) BNNT-PVDF, and (*right*) CNT-PVDF
Source: Salehi-Khojin et al. 2009a, with permission

As the distance between nanotubes and matrix increases, the normal stress in the nanotubes decreases accordingly. This means that at higher gaps, nanotubes has less contribution on the overall properties of the composite.

Comparison of the axial normal stress in BNNT- and CNT-based composite reveals that for the similar applied external load (electrical field), BNNT can carry much higher range of axial normal stress compared to CNT. As interfacial adhesion at smaller gaps is strong enough for both combinations, the load transferred from matrix to nanotube shows similar magnitude and trend at smaller gaps. However, at higher gaps, the interatomic force between BNNT and PVDF merges to zero faster than that between CNT and PVDF does. For example, at separation distance of 10.3 Å, the interatomic force in CNT-PVDF is about 18 times stronger than in BNNT-PVDF. As a result, at higher gaps in the interphase zone the slippage in BNNT-based composite would occur faster compared to CNT-reinforced matrix. The opposite trends are seen for the average axial normal stress of the matrix (Fig. 12.33). As the separation distance increases, the axial stress of matrix increases as well.

The variations of shear stress in the outer layer of nanotube are shown in Fig. 12.34. The shear stress shows the maximum values are at nanotube ends, while the middle of nanotube is shear stress free. With the increase in the separation distance, the shear stress along the length of nanotube decreases, while the shear stress in the inner layer of matrix shows the opposite trends. As seen in Fig. 12.35, the range of variation for shear stress in BNNT-based composite is much higher than that in CNT. This property results in a higher range of friction between BNNT and matrix that could be beneficial in terms of stick-slip mechanism. Therefore, it is concluded that BNNT-reinforced composite structures are more sensitive to properties of interphase zone through applying external fields. Hence, they possess better tuning properties ranging from stiffer structure to better damper compared to CNTs.

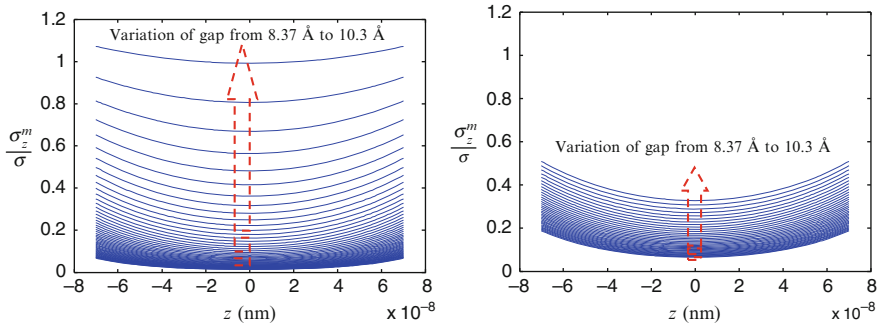

Fig. 12.33 Average axial normal stress in the matrix along the nanotube length for different separation distances for (*left*) BNNT-PVDF, and (*right*) CNT-PVDF
Source: Salehi-Khojin et al. 2009a, with permission

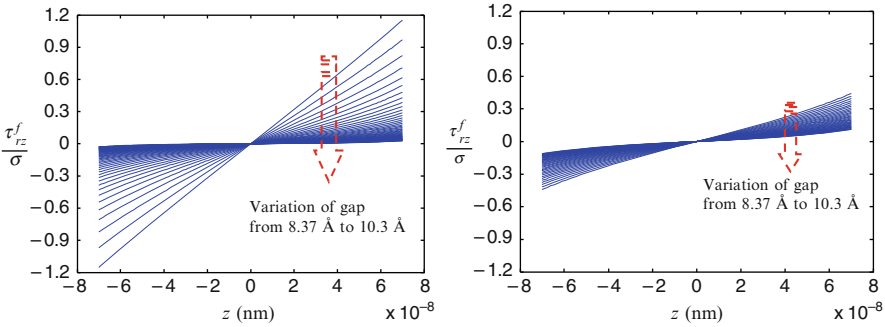

Fig. 12.34 Variations of shear stress in the outer layer of nanotube for different separation distances for (*left*) BNNT-PVDF, and (*right*) CNT-PVDF
Source: Salehi-Khojin et al. 2009a, with permission

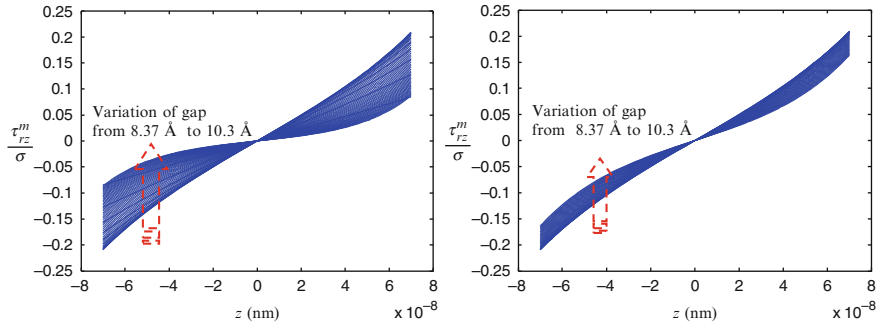

Fig. 12.35 Variations of shear stress in the inner layer of matrix for different separation distances for (*left*) BNNT-PVDF, and (*right*) CNT-PVDF
Source: Salehi-Khojin et al. 2009a, with permission

12.5 Electronic Textiles Comprised of Functional Nanomaterials

With daily improvement in technological advancements and the needs of diverse groups such as consumers, military and navy, the textile industry is shifting its focus to fabrication of next-generation textiles that not only meet the basic conventional requirements, but also serve a host of other functions. Along this line of reasoning, this section presents a brief overview of development of functional fabrics (named here *electronic textile* or *e-textile*) utilizing carbon nanotube (CNT) composites.

12.5.1 The Concept of Electronic Textiles

The groundbreaking discovery of CNTs in 1989–1991 followed by the realization of their amazing properties led scientists all over the world to focus their research efforts on these fascinating nanostructures. The proposed area of research in e-textile is primarily motivated by the discovery of bond extension in charged nanotubes (i.e., piezoelectric effect in nanotubes). On the other hand, the textile industry has already demonstrated a remarkable capability to incorporate both natural and manmade filaments into yarns and fabrics to satisfy a wide range of physical parameters that survive the manufacturing processes and are tailored to specific application environments. Hence, nanotube-based fabrics could become an enabling technology for a variety of macroscopic textile related applications such as energy harvesting, vibration dampening, pressure sensors, and shape modification of membrane structures.

As seen in different applications in preceding sections, the addition of CNTs in the polymer solution leads to a significant enhancement in the strain-sensing capability of the sensors (Laxminarayana and Jalili 2005). Such direct and reverse conversion of electrical energy into mechanical energy can create a platform for developing next-generation smart fabric with applications in membrane structures, distributed shape modulation, and energy harvesting. More recently, an automated electrospinning process has been developed to fabricate functional fabrics (or e-textiles) composed of CNT composites (Hiremath and Jalili 2006). In order to understand the fundamental properties and the physics of reinforcing mechanism of the CNT-based fabrics, there is a need for more reliable manipulation and characterization tools.

12.5.2 Fabrication of Nonwoven CNT-based Composite Fabrics[5]

The complete process of fabricating nano-sized composite fibers using the electrospinning technique can be divided into the following two major steps:

[5] The materials in this section may have come from our earlier publication (Laxminarayana and Jalili 2005).

(1) preparation of polymer/CNT melt and (2) electrospinning of the polymer melt to generate nano-sized fibers.

Preparation of Polymer/Nanotube Melt: In all the experiments, the copolymer of vinyldifluoride with trifluoroethylene (P(VDF-TrFE)) was used to fabricate piezoelectric sensors using the wet film casting method. The primary reasons behind choosing such a polymer for making these novel sensors are its high thermal stability and the fact that it possesses piezoelectric properties, which is ideal for strain-sensing applications. The process of preparing a composite solution containing CNTs dispersed in a polymer that would be later electrospun into a nonwoven fabric, can be further sub-divided into the following three processes.

Dispersion of Nanotubes: This phase involves the dissolution/dispersion of CNTs in a solvent (in this case, N,N-dimethylformamide (DMF)) in order to disentangle the nanotubes that typically tend to cling together and form lumps. This solution is further sonicated using a mechanical probe sonicator (Branson sonifier), capable of vibrating at ultrasonic frequencies to induce an efficient dispersion of nanotubes. For our experiments, different CNT solutions were prepared (containing CNTs in various weight ratios): (1) 0.01 wt% CNTs, (2) 0.02 wt% CNTs, (3) 0.035 wt% CNTs, and (4) 0.05 wt% CNTs.

Dissolution of the Polymer: This stage involves the dissolution of the polymer in a suitable organic solvent (i.e., DMF). A specific amount of polymer (in this case 2 g) weighed using a balance is added to a certain quantity of organic solvent (6 ml of DMF) thereby maintaining a desired polymer weight ratio. This mixture is stirred and kept in an air-tight bottle (to prevent evaporation of DMF) for a certain duration of time until the polymer gets uniformly dissolved in the solvent.

Mixing of Polymer and Nanotube Solutions: This is the final step in the melt preparation process and basically involves thorough mixing of the solutions prepared in the first and second stages, resulting in a solution that consists of a good blend of nanotubes in the polymer.

Electrospinning of the Polymer Melt: Electrospinning, invented in the 1930s, is an electrostatic process that has widely been used for drawing out nano-sized fibers from numerous polymers. Due to its ability to generate fibers of unusually small diameters, it has been considered as a potential candidate for effectively blending CNTs with polymers (Seoul et al. 2003; Ko et al. 2003). In the current work, the prepared polymer/CNT melt is processed to form nano-sized fibers using the technique of electrospinning. For this, the prepared polymer melt is inserted into a syringe consisting of a thin needle mounted to its end (see Figure 12.36-top). The assembly is now placed in a syringe pump (Harvard PHD 22/2000) that is used to pump the polymer/CNT melt to the edge of the needle forming a hemi-spherical shape. The entire pump assembly is positioned on a stager that experiences displacement in x and z directions (i.e., along the axis of fluid jet, z, and normal to it, x). The stager is driven by a stepper motor of very small step size and has a motion range of about 15 cm along both axes (see Figure 12.36-bottom). This stager is used to control the distance of separation between the nozzle tip and the collector surface along the z-direction

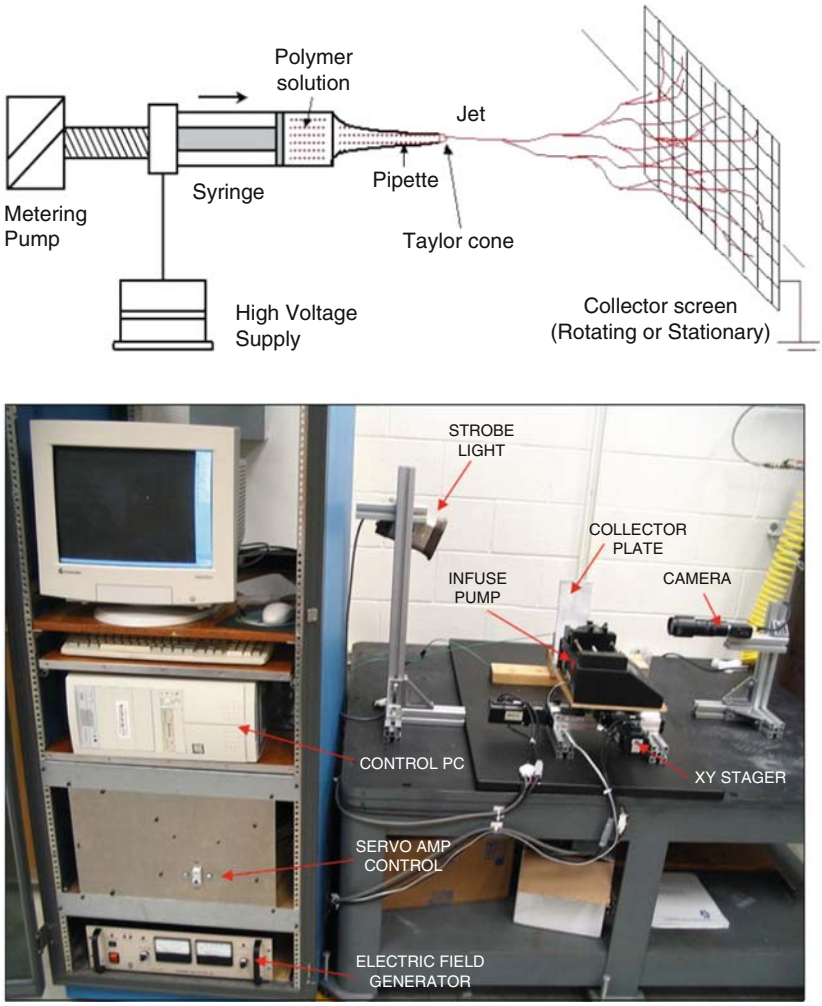

Fig. 12.36 (*top*) Working principle of the e-spinning, and (*bottom*) automated e-spinning setup and interface system
Source: Laxminarayana and Jalili 2005, with permission

and the uniformity of the fiber collection is controlled by moving the stager along x-direction. At this point, a strong DC voltage is applied to the polymer solution using a high-voltage DC power supply (Glassman High Voltage with capability of generating up to 85 kV at 3.5 mA, see Figure 12.36-bottom) with a grounded collector plate kept at a certain distance from the edge of the needle. According to the principle of the electrospinning process, fibers of the polymer/CNT solution get drawn out which eventually deposit on the grounded plate to form a nonwoven mat of nanotube-based composite.

The images of jet formation are captured using a CCD camera, whose line of focus is perpendicular to the axial length of the jet. The jet formation images obtained from this CCD camera appear as multiple segmented jets in the whipping jet section, but the linear part of the jet appears continuous. Hence, the simple CCD camera suffices the need. The camera is fixed on to the stager as its view has to be stationary relative to the pipette tip. These images obtained are transferred to a computer with a frame grabber board for processing and analysis.

Various nonwoven composite fabrics were made by electrospinning pure polymer solution as well as by incorporating nanotubes in them. The distance between the needle tip and the ground electrode was kept at 7 cm and a high voltage of 20 kV was applied between the needle and the ground plate. The process of electrospinning is continued for a certain duration until a desired thickness of the nonwoven fabric is obtained. In all the experiments, the electrospun films had a thickness of 5 microns. Figure 12.37a and b demonstrate the SEM images of the fibers spun under the conditions outlined here, while Figure 12.37c and d depict the images taken form the optical camera showing how the nanofiber is layered with time.

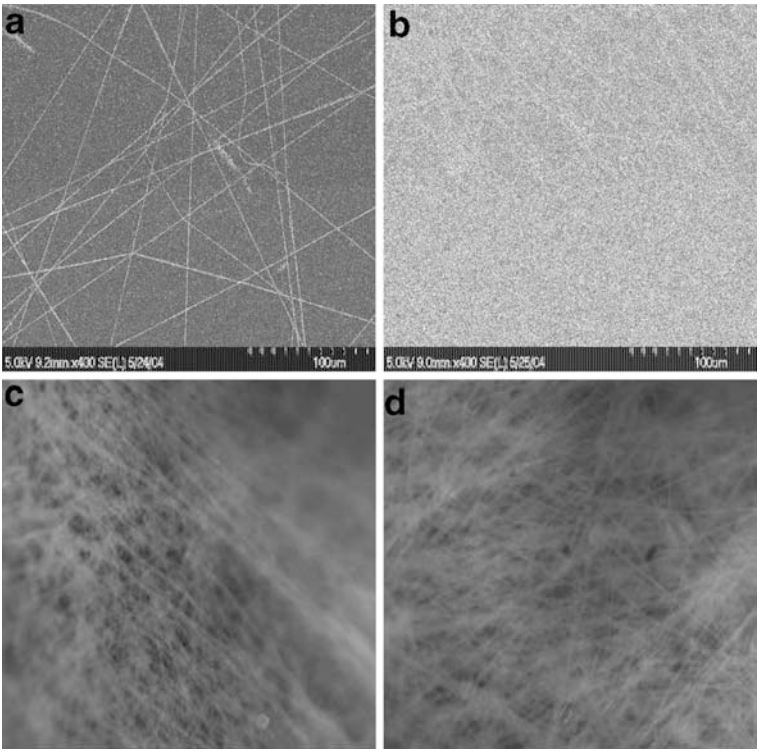

Fig. 12.37 (**a** and **b**) SEM images of electrospun fibers from plain copolymer melt, and (**c** and **d**) images taken form the optical camera demonstrating the thickening fabric with time
Source: Laxminarayana and Jalili 2005, with permission

12.5.3 Experimental Characterization of CNT-based Fabric Sensors

As mentioned earlier, the polymer that was electrospun into a thin fabric demonstrated piezoelectric properties and therefore needed further processing before being used for strain sensing. This characterization will consist of three components: processing of the nonwoven fabric, characterization of the nonwoven fabric, and experimental results as described next.

Processing of the Nonwoven Fabric obtained from Electrospinning: As discussed in Chap. 6, piezoelectric materials are subjected to a process called poling which involves the application of high voltage across electroded faces. The application of high voltages essentially leads to the alignment of the dipoles present in the material, with the degree of alignment being proportional to the magnitude of the applied electric field. Removal of the electric field at the end of the poling process would cause a nominal loss in the alignment of the dipoles. However, the dipoles remain aligned to a considerable extent, thus retaining the piezoelectric properties induced into the material. These piezoelectric properties of the fabric will result in the generation of voltage across the electroded faces when subjected to mechanical strain.

In order to pole the thin films obtained from the electrospinning process, the opposite faces are electroded by attaching thin copper tapes, with wires soldered to them. The output of a high voltage power supply (EMCO), capable of generating up to 2 kV is now applied across the terminals coming off the electroded faces. This process of poling is carried out for about 4–5 h after which the films develop the ability to respond to mechanical strain by generating a potential difference across its electroded faces (Laxminarayana and Jalili 2005). Some recently fabricated sensors through this method are shown in Fig. 12.38.

Characterization of the Nonwoven Fabric Obtained from Electrospinning: The fabricated sensors are now subjected to a testing process in order to characterize and study the effect of addition of CNTs on the strain sensing performance. Figure 12.39

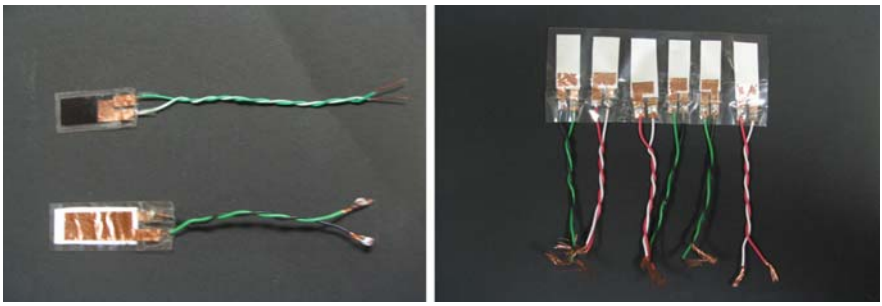

Fig. 12.38 (*left*) samples of electrospun sensors fabricated from plain copolymer (*bottom left*) and MWNTs sensors (*top left*); and (*right*) array of fabric sensors used for distributed sensing and actuation applications
Source: Laxminarayana and Jalili 2005, with permission

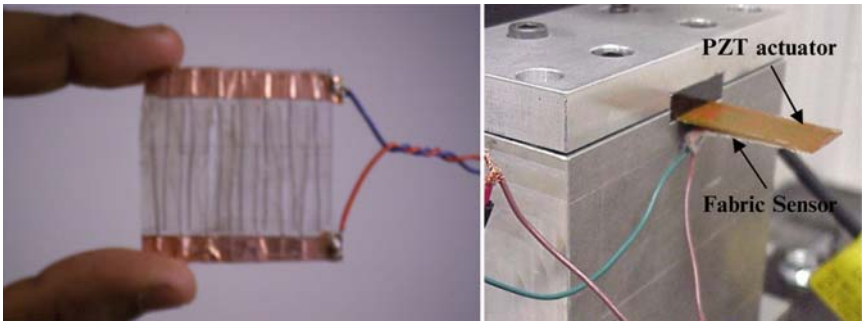

Fig. 12.39 Prototype of the fabric sensor (*left*), and experimental setup for CNT-based fabric characterization (*right*)
Source: Laxminarayana and Jalili 2005, with permission

shows a proptotype of the fabric-based sensor with the accompanying experimental setup used for the vibration testing process (Laxminarayana and Jalili 2005; Jalili et al. 2005). It consists of a PZT actuator utilized as a cantilever beam. The electrospun films were attached firmly to the PZT actuator by applying a very thin layer of epoxy followed by a curing and setting process of the resin which lasts for up to 2 h. The experimental setup was interfaced to a PC using a DSP board (DS1104) from dSPACE® Inc. Matlab/Simulink in conjunction with ControlDesk® (a software used to drive the DSP board) was used to communicate with the experimental setup. ControlDesk® is equipped with an interactive virtual instrument panel that simulates the feel of controlling real hardware and also provides transparent data acquisition. A power amplifier with a gain of 30 Volt/Volt was used to actuate the PZT, since the DSP board is limited to send/receive a maximum of ± 10 V.

The experiments involve actuating the PZT beam by applying sinusoidal voltages of specific amplitude and frequency. The deflection of the beam is transferred to the electrospun piezoelectric sensor that is attached firmly to it. The resulting strain induced in the sensor generates a voltage across its electroded faces due to piezoelectric effect, which is read using the A/D channel of the DSP board. This experiment is repeated on various types of sensors (without nanotubes as well as containing nanotubes with various weight ratios) that were fabricated using the electrospinning process.

Experimental Results: Figure 12.40 compares the results obtained from the sensors made with and without nanotubes. In this figure, the PZT film was actuated by a 160 V supply at a frequency of 175 rad/s, (Laxminarayana and Jalili 2005). The corresponding voltage generated by the plain copolymer sensor was 2.4 mV, whereas the voltage obtained using the composite sensor containing 0.01 wt% NTs was almost twice the response obtained using the plain copolymer sensor. This enhancement in the strain-sensing ability has been observed to increase with an increase in the amount of CNTs added to the polymer solution. When the proportion of CNTs in the composite was increased (to 0.05 wt%), the response generated by the sensor also increased drastically to as much as 35 times the response obtained from the

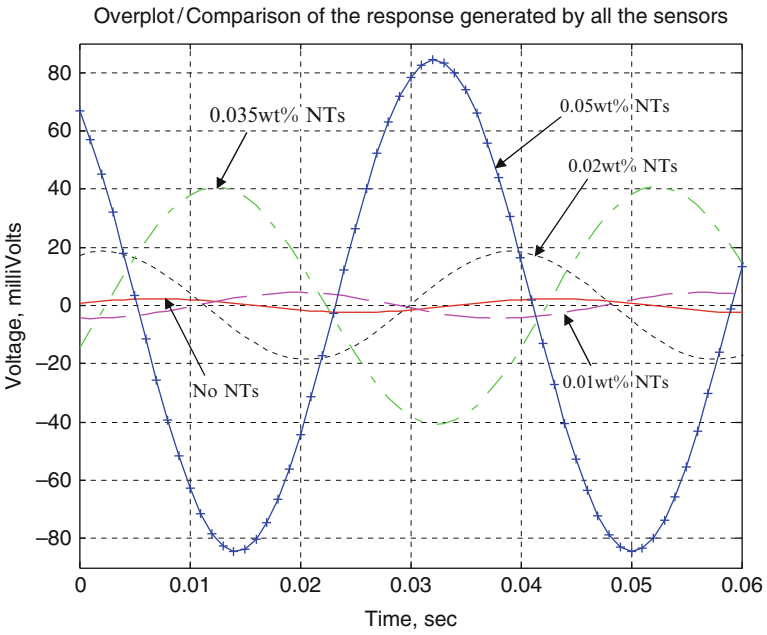

Fig. 12.40 Response of the plain polymer sensors and CNT-based composite sensors containing CNTs in different weight ratios by exciting the PZT at a frequency of 175 rad/s and amplitude of 160 V
Source: Laxminarayana and Jalili 2005, with permission

plain sensor. It can be seen that the addition of CNTs in the polymer solution leads to a significant enhancement in the strain-sensing capability of the sensors (Jalili et al. 2005).

Summary

This chapter presented a brief overview of advances in nanomaterials-based actuators and sensors. More specifically, piezoelectric properties in nanotubes were described, with a natural extension to nanotube-based piezoelectric sensors and actuators. As a byproduct of this arrangement, structural damping became possible using nanotube-based composites. As a future pathway towards development of next-generation sensors and actuators composed of nanomaterials, piezoelectric nanocomposites with tunable properties were discussed. It was demonstrated that by controlling the interphase zone between nanotubes and host matrix through applying external voltage, the inter atomic forces can be selectively varied. This resulted in a nanocomposite arrangement with tunable properties ranging from softer dampers to stiffer stiffness. As the last application of nanomaterials-based sensors and actuators, the concept of electronic textiles composed of functional nanomaterials was briefly introduced and discussed.

Appendix A
Mathematical Preliminaries

Contents

A.1 Preliminaries and Definitions 463
A.2 Indicial Notation and Summation Convention 466
A.2.1 Indicial Notation Convention 466
A.2.2 The Kronecker Delta 467
A.3 Equilibrium States and Stability 468
A.3.1 Equilibrium Points or States 468
A.3.2 Concept of Stability 469
A.4 A Brief Overview of Fundamental Stability Theorems 471
A.4.1 Lyapunov Local and Global Stability Theorems 471
A.4.2 Local and Global Invariant Set Theorems 474

A.1 Preliminaries and Definitions

2-norm and ∞–norm of a Function: The 2-norm of function $f(t) \in \mathbb{R}$, operated on interval $[0, \infty)$, is defined as

$$\|f(t)\|_2 = \sqrt{\int_0^\infty (f^2(\tau)\mathrm{d}\tau)}, \tag{A.1}$$

while its ∞–norm is defined as

$$\|f(t)\|_\infty = \sup_t |f(t)| \tag{A.2}$$

If the 2-norm is bounded, that is, $\|f(t)\|_2 < \infty$, then function $f(t)$ belongs to the subspace L_2 of the space of all possible functions. This is denoted as $f(t) \in L_2$. Similarly, if the ∞–norm is bounded, that is, $\|f(t)\|_\infty < \infty$, then function $f(t)$ belongs to the subspace L_∞ of the space of all possible functions. This is represented as $f(t) \in L_\infty$.

Local Positive Definite Function: A scalar function $V(\mathbf{x})$ is said to be locally positive definite if $V(\mathbf{0}) = 0$ and $V(\mathbf{x}) > 0$ for all $\mathbf{x} \neq \mathbf{0}$.

Global Positive Definite Function: A scalar function $V(\mathbf{x})$ is said to be globally positive definite if $V(\mathbf{0}) = 0$ and $V(\mathbf{x}) > 0$ over the entire state-space.

Lyapunov Function: If $V(\mathbf{x})$ is, at least, locally positive definite and in addition $\dot{V}(\mathbf{x}) \leq 0$[1] along any state trajectory of $\dot{\mathbf{x}} = \mathbf{f}(\mathbf{x})$, then $V(\mathbf{x})$ is said to be a *Lyapunov function* of dynamic system $\dot{\mathbf{x}} = \mathbf{f}(\mathbf{x})$.

Radially Unbounded Function: A scalar function $V(\mathbf{x})$ is said to be radially unbounded if $V(\mathbf{x}) \to \infty$ as $\|\mathbf{x}\| \to \infty$, where $\| \ \|$ represents the standard Euclidean norm of $\mathbf{x}$ defined as $\|\mathbf{x}\| = \sqrt{x_1^2 + x_2^2 + \ldots + x_n^2}$.

Invariant Set: A set G is an invariant set for the dynamic system $\dot{\mathbf{x}} = \mathbf{f}(\mathbf{x})$ if every system trajectory that starts from a point in G remains in G for all the future time.

Autonomous and Nonautonomous Systems: An autonomous function or system is a system where the time variable t is not explicitly present in the governing equations of motion, that is, $\dot{\mathbf{x}} = \mathbf{f}(\mathbf{x})$ is an autonomous system while $\dot{\mathbf{x}} = \mathbf{f}(\mathbf{x}, t)$ is a nonautonomous system.

Integration by Part: If $u(x)$ and $v(x)$ are continuously differentiable functions of scalar variable x, then the following relationship holds.

$$\int_{x_1}^{x_2} u(x) \frac{\mathrm{d}}{\mathrm{d}x}(v(x))\,\mathrm{d}x = u(x)v(x)|_{x_1}^{x_2} - \int_{x_1}^{x_2} v(x) \frac{\mathrm{d}}{\mathrm{d}x}(u(x))\,\mathrm{d}x \tag{A.3}$$

Total Differential: Let $f = f(x, y, z)$ be a function of three independent variables x, y and z, then, the total differential of f is defined as

$$\mathrm{d}f = \frac{\partial f}{\partial x}\mathrm{d}x + \frac{\partial f}{\partial y}\mathrm{d}y + \frac{\partial f}{\partial z}\mathrm{d}z \tag{A.4}$$

The Gradient: The gradient operator in Cartesian coordinate is defined as

$$\vec{\nabla} = \vec{i}\frac{\partial}{\partial x} + \vec{j}\frac{\partial}{\partial y} + \vec{k}\frac{\partial}{\partial z} \tag{A.5}$$

For instance, operating the gradient on scalar function f can be expressed as

$$\vec{\nabla} f \triangleq \mathrm{grad}(f) = \left(\frac{\mathrm{d}f}{\mathrm{d}n}\right)\vec{n} \tag{A.6}$$

where $\vec{n}$ is the unit normal vector to (surface) function f in the state-space, see Fig. A.1. Hence, the total differential d efined in (A.4) using gradient operator can be rewritten as

$$\mathrm{d}f = \vec{\nabla} f \cdot \mathrm{d}\vec{r} \tag{A.7}$$

where "$\cdot$" represents the inner product of vectors and $\mathrm{d}n = \vec{n} \cdot \mathrm{d}\vec{r}$.

[1] The time derivative of function $V(\mathbf{x})$ can be calculated as $\dot{V} = \frac{\mathrm{d}V}{\mathrm{d}t} = \frac{\partial V}{\partial \mathbf{x}}\frac{\mathrm{d}\mathbf{x}}{\mathrm{d}t} = \frac{\partial V}{\partial \mathbf{x}}\dot{\mathbf{x}} = \frac{\partial V}{\partial \mathbf{x}} \cdot \mathbf{f}(\mathbf{x})$.

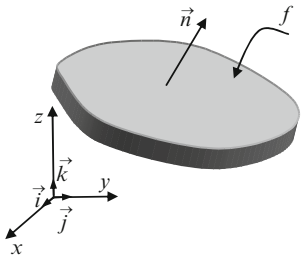

Fig. A.1 Gradient of function f

Divergence Theorem: If $\vec{\mathbf{F}}$ is a continuously differentiable vector field defined in a compact volume $V \in \mathbb{R}^3$ with smooth and closed boundary volume ∂V, then

$$\int_V \left(\vec{\nabla} \cdot \vec{\mathbf{F}}\right) \mathrm{d}V = \oint_{\partial V} \vec{\mathbf{F}} \cdot \vec{\mathbf{n}} \mathrm{d}S \tag{A.8}$$

where $\vec{\mathbf{n}}$ is the outward pointing unit normal to boundary volume ∂V.

Linearization: As mentioned in Chap. 1, a nonlinear dynamic system is governed by a set of nonlinear PDEs or ODEs. Without undue complication and for the sake of demonstrating the linearization technique, a nonlinear discrete and autonomous system is considered whose governing equation can be expressed as

$$\dot{\mathbf{x}}(t) = \mathbf{f}\left(\mathbf{x}(t)\right) \tag{A.9}$$

where $\mathbf{x} \in \mathbb{R}^n$. Using Taylor's series expansion, (A.9) can be expanded into

$$\dot{\mathbf{x}} = \left(\frac{\partial \mathbf{f}}{\partial \mathbf{x}}\right)\Big|_{x=\mathbf{0}} \mathbf{x} + \mathrm{HOT}^2 \tag{A.10}$$

where $\left(\frac{\partial \mathbf{f}}{\partial \mathbf{x}}\right)$ represents the Jacobian matrix defined by $\left(\frac{\partial \mathbf{f}}{\partial \mathbf{x}}\right) = \left\{a_{ij}\right\}$, $a_{ij} = \frac{\partial f_i}{\partial x_j}$. Then, the linearized model of system dynamic (A.9) can be expressed as

$$\dot{\mathbf{x}} = \mathbf{A}\mathbf{x} \tag{A.11}$$

where $\mathbf{A} = \left(\frac{\partial \mathbf{f}}{\partial \mathbf{x}}\right)\Big|_{\mathbf{x}=\mathbf{0}}$.

If the nonlinear system (A.9) is augmented with some controllers $\mathbf{u} \in \mathbb{R}^m$ (this is a common scenario for most active vibration-control systems in this book) and has the general form

$$\dot{\mathbf{x}}(t) = \mathbf{f}\left(\mathbf{x}(t), \mathbf{u}(t)\right), \tag{A.12}$$

[2] Higher order terms.

then the Taylor's series can be used to expand (A.12) to

$$\dot{\mathbf{x}} = \left(\frac{\partial \mathbf{f}}{\partial \mathbf{x}}\right)\Big|_{x=\mathbf{0},u=\mathbf{0}} \mathbf{x} + \left(\frac{\partial \mathbf{f}}{\partial \mathbf{u}}\right)\Big|_{x=\mathbf{0},u=\mathbf{0}} \mathbf{u} + \text{HOT} \tag{A.13}$$

Similar to system dynamic (A.9), the linearized model of (A.12) can be finally expressed as

$$\dot{\mathbf{x}} = \mathbf{A}\mathbf{x} + \mathbf{B}\mathbf{u} \tag{A.14}$$

where Jacobian matrices $\mathbf{A}$ and $\mathbf{B}$ are defined as $\mathbf{A} = \left(\frac{\partial \mathbf{f}}{\partial \mathbf{x}}\right)\Big|_{\mathbf{x}=\mathbf{0},\mathbf{u}=\mathbf{0}}$ and $\mathbf{B} = \left(\frac{\partial \mathbf{f}}{\partial \mathbf{u}}\right)\Big|_{\mathbf{x}=\mathbf{0},\mathbf{u}=\mathbf{0}}$.

A.2 Indicial Notation and Summation Convention

As discussed in Sect. 1.1., smart structures typically comprise one or more active materials that couple at least two different physical fields. These coupled fields require an appropriate system or coordinates to describe and relate the quantities that are used in the constitutive models of these structures. On the other hand, the physical parameters of smart structures need to be independent of any coordinate system or frame of reference. To remedy such conflicting requirements, these quantities can be represented by *tensors*. Once the components of a tensor in one coordinate system are quantified or measured, they can be conveniently described in any other coordinate using transformations. Hence, if quantities are described using tensors, they will have coordinate information in addition to be invariant with respect to the frame of reference in which they are measured. For instance, E_3 means the component of electrical field $\mathbf{E}$ in third direction. It is worthy to note that scalars are zero-order tensors, vectors are first-order tensors, and matrices are second-order tensors. The best way to describe tensors is to use "indicial notation" convention as briefly described next.

A.2.1 Indicial Notation Convention

In this notation, two types of indices are introduced; namely, range (or free) indices and summation (dummy) indices. Range indices appear only once and in each side of the equations, while summation indices appear twice (but not repeated more than two) and represent summation over the index from 1 to n. There is no limit on the number of different summation in an expression. An expression with two dummy indices has a total of n^2 terms, with three dummy indices has a total of n^3 terms, and with p dummy indices has a total of n^p terms.

Example A.1. Expansion using summation convention.

Expand the following expression represented in indicial notation:

$$A = C_{rs}x_r x_s, \quad r, s = 1,\ 2,\ \text{and}\ 3$$

Solution. Since there are only two dummy indices, we expect to have $3^2 = 9$ terms as detailed below.

$$\begin{aligned} A &= C_{r1}x_r x_1 + C_{r2}x_r x_2 + C_{r3}x_r x_3 \\ &= C_{11}x_1 x_1 + C_{21}x_2 x_1 + C_{31}x_3 x_1 + C_{12}x_1 x_2 + C_{22}x_2 x_2 \\ &\quad + C_{32}x_3 x_2 + C_{13}x_1 x_3 + C_{23}x_2 x_3 + C_{33}x_3 x_3 \end{aligned}$$

□

In order to emphasize the importance of proper handling of dummy and free indices, the following example is considered.

Example A.2. Proper handling of dummy indices in indicial notation.

Substitute $y_i = C_{ij}x_j$ into $A = D_{ij}y_i x_j$.

Solution. If one would just simply substitute y_i into A without observing the rules governing the dummy indices, it yields $A = D_{ij}C_{ij}x_j x_j$. This results in an improper use of indicial notation convention since the dummy index j appears more than twice. The proper way to handle this substitution is to change the dummy index j to a new one, say k. Since this is a dummy index and will be repeated in the expression, this change of index will not affect the results. Hence, we shall first change $y_i = C_{ij}x_j$ to $y_i = C_{ik}x_k$ and then substitute it to arrive at the final expression $A = D_{ij}C_{ik}x_k x_j$. As seen, the dummy indices in this expression are not repeated more than two times.

□

A.2.2 The Kronecker Delta

The Kronecker delta δ_{ij} is defined as

$$\delta_{ij} = 1 \quad \text{if} \quad i = j, \quad \text{and} \quad \delta_{ij} = 0 \ \text{otherwise} \tag{A.15}$$

The Kronecker delta is extensively used in the derivation of equations of motions of elastic bodies, especially in the orthogonality relationships between eigenfunctions in continuous systems as shown later in Chaps. 4 and 8. The following example demonstrates the effect of annihilating the "off-diagonal" terms in indicial notation expressions.

Example A.3. Proper handling of Kronecker delta in indicial notation expressions. Simplify $A = \frac{\partial U_i}{\partial u_j}\delta_{ij}$ where $\mathbf{U} = \mathbf{U}(u_1, u_2, u_3), \mathbf{U} = \begin{bmatrix} U_1 & U_2 & U_3 \end{bmatrix}$ and $i, j = 1, 2, 3$:

Solution.

$$\begin{aligned} A = \frac{\partial U_i}{\partial u_j}\delta_{ij} &= \frac{\partial U_i}{\partial u_1}\delta_{i1} + \frac{\partial U_i}{\partial u_2}\delta_{i2} + \frac{\partial U_i}{\partial u_3}\delta_{i3} \\ &= \frac{\partial U_1}{\partial u_1}\delta_{11} + \frac{\partial U_2}{\partial u_1}\delta_{21} + \frac{\partial U_3}{\partial u_1}\delta_{31} \\ &\quad + \frac{\partial U_1}{\partial u_2}\delta_{12} + \frac{\partial U_2}{\partial u_2}\delta_{22} + \frac{\partial U_3}{\partial u_2}\delta_{32} \\ &\quad + \frac{\partial U_1}{\partial u_3}\delta_{13} + \frac{\partial U_2}{\partial u_3}\delta_{23} + \frac{\partial U_3}{\partial u_3}\delta_{33} \end{aligned}$$

Since $\delta_{ij} = 0$ when $i \neq j$, the above expression reduces to

$$A = \frac{\partial U_1}{\partial u_1}\delta_{11} + \frac{\partial U_2}{\partial u_2}\delta_{22} + \frac{\partial U_3}{\partial u_3}\delta_{33} = \frac{\partial U_i}{\partial u_i}\delta_{ii} = \frac{\partial U_i}{\partial u_i} \text{ or } A = \frac{\partial U_j}{\partial u_j}\delta_{jj} = \frac{\partial U_j}{\partial u_j}$$

This reveals an important conclusion that wherever the Kronecker delta is used in an indicial notation expression, its indices (in the above example, i and j) used in the variables appearing in the same terms as the Kronecker delta, become identical (i.e., in this example, $i = j$). Hence, using this observation, one can quickly simplify the expression $A = \frac{\partial U_i}{\partial u_j}\delta_{ij}$ as $A = \frac{\partial U_i}{\partial u_i}$ by simply substituting $i = j$ in all the terms where δ_{ij} is used.

□

A.3 Equilibrium States and Stability

A.3.1 Equilibrium Points or States

A system is said to be in "equilibrium state" when it remains in one state in the absence of any external inputs for all the future times. Mathematically, if we consider the following autonomous dynamic system

$$\dot{\mathbf{x}} = \mathbf{f}(\mathbf{x}) \tag{A.16}$$

where $\mathbf{x} \in \mathbb{R}^n$ is a vector of system states and $\mathbf{f} \in \mathbb{R}^n$ is a nonlinear function of system states (the overdot represents the derivative with respect to time variable t), then $\mathbf{x}_e$ is an equilibrium state if

$$\mathbf{f}(\mathbf{x}_e) = \mathbf{0} \tag{A.17}$$

Example A.4. Equilibrium states of a linear system.

Consider a linear system whose dynamics can be represented as

$$\dot{\mathbf{x}} = \mathbf{f}(\mathbf{x}) = \mathbf{A}\mathbf{x} \tag{A.18}$$

where $\mathbf{A} \in \mathbb{R}^{n \times n}$ is the system parameters matrix. According to the definition of the equilibrium state, the solution to

$$\mathbf{A}\mathbf{x}_e = \mathbf{0} \tag{A.19}$$

will determine all the equilibrium states. Depending on the nature of $\mathbf{A}$, several scenarios may be encountered:

a. If $\mathbf{A}$ is nonsingular (i.e., it is full rank or $\det(\mathbf{A}) \neq 0$), then the origin is the "only" equilibrium state for this system.
b. If $\mathbf{A}$ is singular, then the linear subspace defined by $\mathbf{A}\mathbf{x}_e = \mathbf{0}$ is an equilibrium region for this system. □

Example A.5. Equilibrium states of a nonlinear system.

Consider the following nonlinear system

$$\dot{x} = x^2 + r$$

where $x \in \mathbb{R}$ and r is a time-invariant parameter. Based on the sign of r, we consider the following three cases:

Case I: $r < 0$: In this case, the solution to $\dot{x} = 0$ reveals two equilibrium points $x_e = \pm\sqrt{-r}$ (i.e., $x_e^1 = +\sqrt{-r}$ and $x_e^2 = -\sqrt{-r}$).

Case II: $r = 0$: In this case, the solution to $\dot{x} = 0$ reveals repeated equilibrium points at the origin, that is, $x_e^1 = 0$ and $x_e^2 = 0$.

Case III: $r > 0$: In this case, no equilibrium points exist.

A.3.2 Concept of Stability

There are two different viewpoints on dynamic stability; namely, internal and external. Internal behavior includes the effect of all characteristic roots and equilibrium states, and hence, is an inherent property of the dynamic systems, while external behavior may be affected by the types of inputs (e.g., pole-zero cancellation). A system has internal or asymptotic stability if the zero-input response (i.e., the response to initial conditions or perturbations) decays to zero as $t \to \infty$ for all possible initial conditions. This type of stability is concerned with the fact that system will return to its equilibrium states after a disturbance has been removed. On the other hand, a system has external or bounded-input-bounded-output (BIBO) stability if the zero-state response (i.e., the response to external inputs) is bounded as $t \to \infty$ for all bounded inputs. This form of stability is concerned with the question whether certain types

of inputs produce a bounded output. If the characteristic roots of a dynamic system are all on the left-half-plane of the complex plane, then the system is stable from both viewpoints.

Example A.6. Dynamic stability from different viewpoints.

Consider the following three system transfer functions:

$$T_1(s) = \frac{s+2}{(s+4)(s+6)}, \quad T_2(s) = \frac{s-5}{(s-1)(s+3)}, \quad \text{and}$$
$$T_3(s) = \frac{3(s-3)}{(s+1)(s-3)}$$

For each system, identify whether they are internally or externally stable or unstable.

Solution. System T_1 has two stable poles ($s_1 = -4$, $s_2 = -6$) and there is no pole-zero cancellation; hence, it is both asymptotically and BIBO stable. System T_2 has one unstable pole ($s_1 = 1$) which is not cancelled by any zero; hence, it is both asymptotically and BIBO unstable. System T_3 has one unstable pole ($s_1 = 3$) which can be cancelled by a zero ($z_1 = 3$); hence, it is asymptotically unstable, but BIBO stable. □

Since BIBO stability predominately depends on the types of inputs, the stability analysis and assurance conditions vary for different inputs. On the other hand, the internal stability is an inherent property of a dynamic system, and therefore, a more structured and systematic analysis can be utilized. Along this line of reasoning and due to the fact that if a dynamic system is internally stable, it is more likely to be also BIBO stable; we will present, next, some of the fundamental definitions and mathematical preliminaries for this type of stability. These will serve, for all practical purposes, as *the* definitions and properties of system stability.

Definition of Stability: The equilibrium state $x_e = 0$ is said to be stable[3] if

$$\forall\, R > 0, \exists\, r > 0, \|x(0)\| < r \Rightarrow \forall\, t \geq 0, \|x(t)\| < R \tag{A.20}$$

A marginally stable point (e.g., a linear system having its right-most characteristic roots on the imaginary axis in the complex plane) is, therefore, stable from Lyapunov stability viewpoint.

Asymptotic Stability: An equilibrium point is said to be asymptotically stable if it is stable (see definition (A.20)) and

$$\exists\, r > 0, \|x(0)\| < r \Rightarrow \lim_{t\to\infty} x(t) \to 0 \tag{A.21}$$

Exponential Stability: An equilibrium point is exponentially stable if

$$\exists\, \alpha, \beta > 0 \Rightarrow \forall\, t > 0, \|x(t)\| < \alpha \|x(0)\| \, \mathrm{e}^{-\beta t} \tag{A.22}$$

[3] This definition of internal stability is sometime referred to as *Lyapunov* stability.

where β is called the rate of exponential convergence. It is clear that exponential stability implies asymptotic stability but not the other way around.

Structural Stability: For a general (nonlinear) dynamic system, both stability properties and number of equilibrium points may change as a result of either variation in the system parameters or types of disturbance. A dynamic system is said to be "structurally stable" if it has the desirable property that small change in the disturbance yields only small change in the system's performance. If there are points in the system parameters where system is not structurally stable, such points are called "bifurcation points" since the system performance bifurcates (Marquez 2003).

The materials on the concept of stability and equilibrium points presented briefly here will be used in the following section to establish some of the very important and useful stability analysis tools. We will show later in Chaps. 8–10 that how a thorough stability analysis in general can be helpful in the design and development of effective control laws for the piezoelectric actuation used in a variety of active vibration-control systems.

A.4 A Brief Overview of Fundamental Stability Theorems

It is evident that the stability analysis of the combined systems (i.e., collection of plant, controllers, actuator and sensor dynamics) considered in this book, which could be in general nonlinear (due to, for instance, utilization of active controllers), plays an important role in the controller design development. Along this line of reasoning, a number of useful stability theorems are briefly presented in this section that aid in the development of the control designs and closed-loop stability analyses of many vibration-control systems throughout the book (e.g., Chaps. 8–10). The proofs for most of the lemmas and theorems are omitted for the sake of brevity, but can be found in the cited references.

A.4.1 Lyapunov Local and Global Stability Theorems

When dealing with stability analysis of (nonlinear) systems, the Lyapunov stability criteria would single out as one of the most attractive stability tool. Before we proceed with these criteria, it is worth clarifying the stability definition from *local* and *global* viewpoints. When the stability criteria or properties hold for any initial condition or equilibrium point for a dynamic system, the stability is considered to be *in the large* or global. Otherwise, the stability is a local stability.

Lyapunov's Linear Stability: This stability is concerned with local stability and originates from the fact that a nonlinear system shall behave similarly to its linearized model if the small range of motion is considered (Slotine and Li 1991). Based on this theory, three possibilities exist:

(a) If the linearized model is strictly stable, then the equilibrium points of the original nonlinear system are asymptotically stable.
(b) If the linearized model is unstable, then the equilibrium points of the original nonlinear system are also unstable.
(c) If the linearized model is marginally stable, then nothing can be said about the stability of the equilibrium points of the original nonlinear system.

Example A.7. Lyapunov's linear stability analysis for the van der Pol oscillator.
Implement the Lyapunov's linear stability for the van der Pol oscillator

$$\ddot{y}(t) - \mu(1 - y^2(t))\dot{y}(t) + y(t) = 0, \mu \neq 1 = \text{constant} > 0$$

Solution. Taking $x_1 = y$ and $x_2 = \dot{y}$, the state-transition representation of the system can be expressed as

$$\begin{aligned}\dot{x}_1 &= x_2\\ \dot{x}_2 &= -x_1 + \mu(1 - x_1^2)x_2\end{aligned}$$

It is easy to see that the equilibrium point of this system is at the origin (setting simultaneously $\dot{x}_1 = 0$ and $\dot{x}_2 = 0$), that is,

$$(x_{1e}, x_{2e}) = (0, 0)$$

Consequently, the linearized model of this system around this equilibrium point can be obtained using Taylor's series expansion as detailed in Sect. A.1. This yields

$$\begin{aligned}\dot{z}_1 &= z_2\\ \dot{z}_2 &= -z_1 + \mu z_2\end{aligned}$$

Or in matrix form,

$$\dot{\mathbf{z}} = \mathbf{A}\mathbf{z},$$

where

$$\mathbf{A} = \begin{pmatrix} 0 & 1 \\ -1 & \mu \end{pmatrix}$$

The characteristic equation of this linear system can then be obtained as

$$\det(s\mathbf{I} - \mathbf{A}) = 0 \Rightarrow s^2 - \mu s + 1 = 0$$

Without knowing the values of parameter μ, one can determine the system stability properties. Since $\mu > 0$, it is not difficult to see the characteristic roots have positive real values. Hence, the linearized model of the system is unstable at this equilibrium point (i.e., origin). Accordingly and based on the Lyapunov's linear stability criteria, the original nonlinear system is unstable at the origin. However, we will see later in

this section that the original nonlinear system is stable for all the initial conditions except for those which start at the origin. This demonstrates some of the serious limitations of the Lyapunov's linear stability.

Lyapunov's Direct Methods: The Lyapunov's direct method of stability analysis is based on the total energy of the dynamic system of concern. It directly relates to energy dissipation and/or generation. It is evident by our intuition that if the energy of a dynamic system is dissipating, then it is naturally stable. If there is a growth of mechanical energy, then the amplitude of oscillation or motion will accordingly increase which leads to system instability. Moreover, the zero energy corresponds to the equilibrium points. Consequently, the stability of a dynamic system may be found by examining the variation of a single scalar function. This forms the basis for all Lyapunov-based stability criteria as discussed next.

Lyapunov's Local Stability: Let's assume that $V(\mathbf{x})$ is a continuously differentiable function representing the total energy or an energy-like expression of the dynamic system $\dot{\mathbf{x}} = \mathbf{f}(\mathbf{x})$. If $V(\mathbf{x})$ is locally positive definite (see Sect. A.1), that is,

$$(1)\, V(\mathbf{0}) = 0, \quad (2) V(\mathbf{x}) > 0 \text{ in } D - \{\mathbf{0}\}, \tag{A.23}$$

then if $\dot{V}(\mathbf{x}) \leq 0$ on $\mathbf{x} \in D - \{\mathbf{0}\}$, the equilibrium point $\mathbf{x} = \mathbf{0}$ is locally stable, and if $\dot{V}(\mathbf{x}) < 0$ on $\mathbf{x} \in D - \{\mathbf{0}\}$, the equilibrium point $\mathbf{x} = \mathbf{0}$ is locally asymptotically stable.

Lyapunov's Global Stability: Under Lyapunov's local stability conditions, if $V(\mathbf{x})$ is radially unbounded (see also Sect. A.1 for the definition of unboundedness of a function), then the equilibrium point $\mathbf{x} = \mathbf{0}$ is globally (asymptotically if $\dot{V}(\mathbf{x}) < 0$) stable.

Remark A.1. The equilibrium points in the theorems given in this section are usually taken to be the origin. However, this does not cause any oversimplification or restrictions on the results. Given any other equilibrium point, a simple change of variables can be performed to define a new system with an equilibrium point at the origin. For instance, if $\mathbf{x}_e \neq \mathbf{0}$ is an equilibrium point of system $\dot{\mathbf{x}} = \mathbf{f}(\mathbf{x})$, then a change of variable $\mathbf{y} = \mathbf{x} - \mathbf{x}_e$ results in a new system $\mathbf{f}(\mathbf{x}) = \mathbf{f}(\mathbf{y} + \mathbf{x}_e) \triangleq \mathbf{g}(\mathbf{y})$. Thus, the equilibrium $\mathbf{y}_e$ of the new dynamic system $\dot{\mathbf{y}} = \mathbf{g}(\mathbf{y})$ is $\mathbf{y}_e = \mathbf{0}$ since $\mathbf{g}(\mathbf{0}) = \mathbf{f}(\mathbf{0} + \mathbf{x}_e) = \mathbf{f}(\mathbf{x}_e) = \mathbf{0}$.

Example A.8. Stability analysis of a nonlinear mechanical oscillator.

Consider the mechanical oscillator of Fig. A.2 with an additional nonlinear Coulomb friction force f_c as shown. Discuss the stability properties of the equilibrium points using Lyapunov's direct method.

Solution. The governing equation of motion can be readily found to be in the form

$$m\ddot{x} + kx - f_c = 0$$

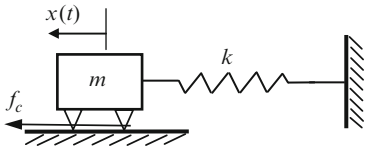

Fig. A.2 Nonlinear mechanical oscillator Example A.8 with Coulomb friction force f_c

Assigning $x_1 = x$ and $x_2 = \dot{x}$, the system state-transition representation can be written as:

$$\dot{x}_1 = x_2, \dot{x}_2 = (-kx_1 + f_c)/m$$

Using the general relationship between total system energy and Lyapunov's function, one could select the following Lyapunov candidate function that represents the total (kinetic and potential) energy of the system.

$$V = \frac{1}{2}mx_2^2 + \frac{1}{2}kx_1^2$$

It is easy to see that this function is a positive definite function satisfying the first two properties of Lyapunov's direct method (A.23). The time derivative of $V(\mathbf{x})$, $\mathbf{x} = \{x_1, x_2\}^{\mathrm{T}}$, can be then determined as

$$\dot{V}(\mathbf{x}) = \begin{pmatrix} kx_1 & mx_2 \end{pmatrix} \begin{pmatrix} \dot{x}_1 \\ \dot{x}_2 \end{pmatrix} = \begin{pmatrix} kx_1 & mx_2 \end{pmatrix} \begin{pmatrix} x_2 \\ (-kx_1 + f_c)/m \end{pmatrix} = f_c x_2$$

Since the Coulomb friction f_c is always in the opposite direction of motion (i.e., relative velocity of mass with respect to the ground), $f_c x_2$ is always negative (zero if $x_2 = 0$). Hence, $\dot{V}(\mathbf{x}) \leq 0$, which shows that the equilibrium point associated with this system is stable. In addition, since $V(\mathbf{x})$ is radially unbounded, the stability is global. It is clear that, however, based on the stated conditions, the asymptotic stability cannot be concluded despite the dissipating nature of the Coulomb friction. This example reveals some of the limitations of the Lyapunov's direct method where true stability properties cannot be disclosed. We will show, next, how this situation can be addressed to unravel the true stability features of the system. □

A.4.2 Local and Global Invariant Set Theorems

For all the above conditions, the positive definiteness of function $V(\mathbf{x})$ was required (see (A.23)), and in addition, we must have $\dot{V}(\mathbf{x}) < 0$ for assurance of asymptotic stability. It can be shown that these conditions overcomplicate some of the control design steps and most desirably must be eliminated or relaxed otherwise. To remedy this, we present the following theorems.

Local Invariant Set Theorem (LaSalle's Theorem): Assume that $V(\mathbf{x})$ is a scalar continuous function and,

(a) For some $\ell > 0$, the region defined by $\mathbf{\Omega}_\ell = \{\mathbf{x}, V(\mathbf{x}) < \ell\}$ is bounded,
(b) $\dot{V}(\mathbf{x}) \leq 0$ for all $\mathbf{x} \in \mathbf{\Omega}_\ell$ (this makes $\mathbf{\Omega}_\ell$ an invariant set),
(c) $M = \left\{\mathbf{x}, \mathbf{x} \in \mathbf{\Omega}_\ell, \dot{V}(\mathbf{x}) = 0\right\}$, and
(d) N is the largest invariant set in M

then, every solution originally from $\mathbf{\Omega}_\ell$ tends to go asymptotically to N as $t \to \infty$.

Global Invariant Set Theorem: Assume that $V(\mathbf{x})$ is a scalar continuous function and,

(a) $V(\mathbf{x})$ is radially unbounded (i.e., $V(\mathbf{x}) \to \infty$ as $\|\mathbf{x}\| \to \infty$),
(b) $\dot{V}(\mathbf{x}) \leq 0$ over the entire state-space,
(c) $M = \left\{\mathbf{x}, \mathbf{x} \in \mathbf{\Omega}_\ell, \dot{V}(\mathbf{x}) = 0\right\}$, and
(d) N is the largest invariant set in M

then, all solutions globally asymptotically converge to N as $t \to \infty$.

As seen from these two theorems, the positive definiteness conditions of Lyapunov's methods have been relaxed to allow using one single Lyapunov-like function to describe systems with multiple equilibrium points.

Example A.9. Stability analysis of nonlinear mechanical oscillator.

Let us revisit the nonlinear mechanical oscillator of Example A.2 and reassess the system stability at equilibrium point.

Solution. As declared in Example A.2, we could not prove system asymptotic stability and only stability properties were proven despite the dissipating nature of Coulomb friction. We obtained $\dot{V}(\mathbf{x}) = f_c x_2$, hence by setting $\dot{V}(\mathbf{x}) = 0$, one could obtain set M which is defined by $x_2 = \dot{y} = 0$ (since $f_c \neq 0$). That is, M is the entire horizontal axis in phase-plane. To prove asymptotic stability of the equilibrium point, we need to show that the largest invariant set N in M is the origin in order to use the results of LaSalle's theorem to show that $x(t) \to M$ (or 0 here) as $t \to \infty$. To do this, we contradictorily assume that set M contains points other than origin on the x-axis, that is, nonzero positions $x(x \neq 0)$. On the other hand, based on the governing equation of motion,

$$\ddot{x} = -(k/m)x + f_c,$$

a nonzero state x results in a nonzero acceleration $\ddot{x}$, which implies that the trajectory will move out of M. This is an obvious contradiction to the fact that set M is an invariant set and the trajectory which starts from a point in this set must remain in the set for all future time. Hence, the largest invariant set in M is $N = \{0\}$ and every trajectory converge to 0 as $t \to \infty$, that is, the system is asymptotically stable. Since $V(\mathbf{x})$ is also radially unbounded, the equilibrium point is globally asymptotically stable. As clearly seen, this is the result that we would have expected from such dissipating system. □

Appendix B
Proofs of Selected Theorems

Contents

B.1 Proof of Theorem 9.1 (Dadfarnia et al. 2004a) 477
B.2 Proof of Theorem 9.2 (Dadfarnia et al. 2004b) 480
B.3 Proof of Theorem 9.3 (Ramaratnam and Jalili 2006a) 482
B.4 Proof of Theorem 10.1 (Bashash and Jalili 2009) 483
B.5 Proof of Theorem 10.2 (Bashash and Jalili 2009) 484

B.1 Proof of Theorem 9.1 (Dadfarnia et al. 2004a)

Selecting the following Lyapunov candidate function

$$V = \frac{1}{2}\dot{\mathbf{\Delta}}^T \mathbf{M}\dot{\mathbf{\Delta}} + \frac{1}{2}\mathbf{\Delta}^T \mathbf{K}\mathbf{\Delta} + \frac{1}{2}k_p \Delta s^2, \tag{B.1}$$

taking its time derivative, and taking into account the symmetricity of matrices **M** and **K**, it yields

$$\dot{V} = \dot{\mathbf{\Delta}}^T \left(\mathbf{M}\ddot{\mathbf{\Delta}} + \mathbf{K}\mathbf{\Delta}\right) + k_p \dot{s}(t)\Delta s \tag{B.2}$$

Substituting (9.64) into (B.2) yields

$$\dot{V} = f(t)\dot{s}(t) + \left(\tau_1 \dot{q}_1(t) + \tau_2 \dot{q}_2(t)\right) V_a(t) + k_p \dot{s}(t)\Delta s \tag{B.3}$$

by substituting the piezoelectric input voltage control (9.68) and arm base force law (9.67 into (B.3)), the derivative of the Lyapunov function reduces to

$$\dot{V} = -k_d \dot{s}^2(t) - k_v \left(\tau_1 \dot{q}_1(t) + \tau_2 \dot{q}_2(t)\right)^2 \tag{B.4}$$

It is clear that $\dot{V}(t) \leq 0$, then $V(t) \in L_\infty$. From (B.1), we can conclude that $\dot{s}(t)$, $\dot{q}_1(t)$, $\dot{q}_2(t)$, $q_1(t)$, $q_2(t)$, Δs, $f(t)$, and $v(t) \in L_\infty$. Then, (9.64) can be used to show that $\ddot{s}(t)$, $\ddot{q}_1(t)$, $\ddot{q}_2(t) \in L_\infty$, and therefore, all signals in the system are bounded. Applying the extended Barbalat's Lemma (Slotine and Li 1991), see also

Appendix A, to (B.4) yields

$$\lim_{t\to\infty} \dot{s}(t) = 0, \quad \text{and} \quad \lim_{t\to\infty} \left(\tau_1 \dot{q}_1(t) + \tau_2 \dot{q}_2(t)\right) = 0 \tag{B.5}$$

Solving (9.63) for $\ddot{s}(t)$, $\ddot{q}_1(t)$, $\ddot{q}_2(t)$ and substituting the control laws (9.67) and (9.68) yields

$$\begin{aligned}\ddot{s}(t) = {} & \frac{1}{\psi_1}\left(\frac{k_{11}m_1}{m_{d1}} + \frac{k_{12}m_2}{m_{d2}}\right) q_1(t) + \frac{1}{\psi_1}\left(\frac{k_{12}m_1}{m_{d1}} + \frac{k_{22}m_2}{m_{d2}}\right) q_2(t) \\ & + \frac{\psi_2}{\psi_1} k_v \left(\tau_1 \dot{q}_1(t) + \tau_2 \dot{q}_2(t)\right) - \frac{1}{\psi_1}\left(k_p \Delta s + k_d \dot{s}(t)\right)\end{aligned} \tag{B.6a}$$

$$\ddot{q}_1(t) = -k_v \frac{\tau_1}{m_{d1}} \left(\tau_1 \dot{q}_1(t) + \tau_2 \dot{q}_2(t)\right) - \frac{k_{11}}{m_{d1}} q_1(t) - \frac{k_{12}}{m_{d1}} q_2(t) - \frac{m_1}{m_{d1}} \ddot{s}(t) \tag{B.6b}$$

$$\ddot{q}_2(t) = -k_v \frac{\tau_2}{m_{d2}} \left(\tau_1 \dot{q}_1(t) + \tau_2 \dot{q}_2(t)\right) - \frac{k_{12}}{m_{d2}} q_1(t) - \frac{k_{22}}{m_{d2}} q_2(t) - \frac{m_2}{m_{d2}} \ddot{s}(t) \tag{B.6c}$$

where

$$\psi_1 = \psi - \frac{m_1^2}{m_{d1}} - \frac{m_2^2}{m_{d2}}, \quad \psi_2 = \frac{m_1 \tau_1}{m_{d1}} + \frac{m_2 \tau_2}{m_{d2}} \tag{B.7}$$

Taking the time derivative of (B.6) results in

$$\begin{aligned}\dddot{s}(t) = {} & \frac{1}{\psi_1}\left(\frac{k_{11}m_1}{m_{d1}} + \frac{k_{12}m_2}{m_{d2}}\right) \dot{q}_1(t) + \frac{1}{\psi_1}\left(\frac{k_{12}m_1}{m_{d1}} + \frac{k_{22}m_2}{m_{d2}}\right) \dot{q}_2(t) \\ & + \frac{\psi_2}{\psi_1} k_v \left(\tau_1 \ddot{q}_1(t) + \tau_2 \ddot{q}_2(t)\right) - \frac{1}{\psi_1}\left(k_p \dot{s}(t) + k_d \ddot{s}(t)\right)\end{aligned} \tag{B.8a}$$

$$\dddot{q}_1(t) = -k_v \frac{\tau_1}{m_{d1}} \left(\tau_1 \ddot{q}_1(t) + \tau_2 \ddot{q}_2(t)\right) - \frac{k_{11}}{m_{d1}} \dot{q}_1(t) - \frac{k_{12}}{m_{d1}} \dot{q}_2(t) - \frac{m_1}{m_{d1}} \dddot{s}(t) \tag{B.8b}$$

$$\dddot{q}_2(t) = -k_v \frac{\tau_2}{m_{d2}} \left(\tau_1 \ddot{q}_1(t) + \tau_2 \ddot{q}_2(t)\right) - \frac{k_{12}}{m_{d2}} \dot{q}_1(t) - \frac{k_{22}}{m_{d2}} \dot{q}_2(t) - \frac{m_2}{m_{d2}} \dddot{s}(t) \tag{B.8c}$$

The expressions in (B.8) show that $\dddot{s}(t)$, $\dddot{q}_1(t)$, $\dddot{q}_2(t) \in L_\infty$. Taking the time derivative of the equations in (B.8), it can be further shown that $s^{(4)}(t)$, $q_1^{(4)}(t)$, $q_2^{(4)}(t) \in L_\infty$. Now letting

$$h = \tau_1 \dot{q}_1(t) + \tau_2 \dot{q}_2(t) \tag{B.9}$$

and taking the time derivative of (B.9) and substituting (B.6a–c) into the resulting expression, it yields

$$\dot{h} = g_1 + g_2$$

where

$$\begin{aligned} g_1 &= -\left(\frac{m_1\tau_1}{m_{d1}} + \frac{m_2\tau_2}{m_{d2}}\right)\ddot{s}(t) - \left(\frac{k_{11}\tau_1}{m_{d1}} + \frac{k_{12}\tau_2}{m_{d2}}\right)q_1(t) - \left(\frac{k_{12}\tau_1}{m_{d1}} + \frac{k_{22}\tau_2}{m_{d2}}\right)q_2(t) \\ g_2 &= -k_v\left(\frac{\tau_1^2}{m_{d1}} + \frac{\tau_2^2}{m_{d2}}\right)(\tau_1\dot{q}_1(t) + \tau_2\dot{q}_2(t)) \end{aligned} \tag{B.10}$$

From (B.5), (B.8a), and (B.10), it can be seen that $\lim_{t\to\infty} g_2 = 0$ and $\dot{g}_1 \in L_\infty$. Then, using the extended Barbalat's Lemma (Slotine and Li 1991), see also Appendix A, yields

$$\lim_{t\to\infty} \{\tau_1\ddot{q}_1(t) + \tau_2\ddot{q}_2(t)\} = 0 \tag{B.11}$$

$$\lim_{t\to\infty} g_1 = 0 \tag{B.12}$$

Similarly, applying the extended Barbalat's Lemma to (B.6a), it yields

$$\lim_{t\to\infty} \ddot{s}(t) = 0 \tag{B.13}$$

Using (B.12) and (B.13) in (B.10), it yields

$$\lim_{t\to\infty}\left\{\left(\frac{k_{11}\tau_1}{m_{d1}} + \frac{k_{12}\tau_2}{m_{d2}}\right)q_1(t) + \left(\frac{k_{12}\tau_1}{m_{d1}} + \frac{k_{22}\tau_2}{m_{d2}}\right)q_2(t)\right\} = 0 \tag{B.14}$$

Multiplying (B.8b) by τ_1, multiplying (B.8c) by τ_2 and adding them up, will result in

$$\begin{aligned} &\left(\frac{k_{11}\tau_1}{m_{d1}} + \frac{k_{12}\tau_2}{m_{d2}}\right)\dot{q}_1(t) + \left(\frac{k_{12}\tau_1}{m_{d1}} + \frac{k_{22}\tau_2}{m_{d2}}\right)\dot{q}_2(t) = g_3 + g_4 \\ &g_3 = -k_v\left(\frac{\tau_1^2}{m_{d1}} + \frac{\tau_2^2}{m_{d2}}\right)(\tau_1\ddot{q}_1(t) + \tau_2\ddot{q}_2(t)) \\ &g_4 = \left\{-\left(\frac{m_1\tau_1}{m_{d1}} + \frac{m_2\tau_2}{m_{d2}}\right)\dddot{s}(t) - \tau_1\dddot{q}_1(t) - \tau_2\dddot{q}_2(t)\right\} \end{aligned} \tag{B.15}$$

Since $s^{(4)}(t), q_1^{(4)}(t), q_2^{(4)}(t) \in L_\infty$, then $\dot{g}_4 \in L_\infty$. Using (B.11) and (B.14) along with applying the extended Barbalat's Lemma to (B.15), it can be shown that

$$\lim_{t\to\infty} \left\{ \left(\frac{k_{11}\tau_1}{m_{d1}} + \frac{k_{12}\tau_2}{m_{d2}} \right) \dot{q}_1(t) + \left(\frac{k_{12}\tau_1}{m_{d1}} + \frac{k_{22}\tau_2}{m_{d2}} \right) \dot{q}_2(t) \right\} = 0 \tag{B.16}$$

and comparing (B.5) and (B.16), it yields

$$\lim_{t\to\infty} \{\dot{q}_1(t), \dot{q}_2(t)\} = 0 \tag{B.17}$$

Similarly, applying extended Barbalat's Lemma to (9.63a), it can be shown that

$$\lim_{t\to\infty} \{\ddot{q}_1(t), \ddot{q}_2(t)\} = 0 \tag{B.18}$$

Finally, from (B.6), (B.13), (B.17), and (B.18), it can be concluded that

$$\lim_{t\to\infty} \{ q_1(t), q_2(t), \Delta s\} = 0 \tag{B.19}$$

□

B.2 Proof of Theorem 9.2 (Dadfarnia et al. 2004b)

We choose the following Lyapunov function candidate

$$V_L(t) = V_3(t) + V_4(t) + V_5(t) \tag{B.20}$$

where $V_3(t)$ is defined in (9.99) and

$$V_4(t) = \frac{1}{2} K_p u^2(0,t) + \frac{1}{2} m_b \gamma_0^2(t) \tag{B.21}$$

$$V_5(t) = \frac{1}{2} m_t \gamma_L^2(t) \tag{B.22}$$

If the design constant β_0 is selected to be sufficiently small, we can formulate the following upper and lower bounds on $V_3(t)$ given in (9.99)

$$V_3(t) \leq \lambda_1 \left[u^2(0,t) + \int_0^L \dot{u}^2(x,t)\mathrm{d}x + \int_0^L u''^2(x,t)\mathrm{d}x \right] \tag{B.23}$$

$$V_3(t) \geq \lambda_2 \left[\int_0^L \dot{u}^2(x,t)dx + \int_0^L u^2(x,t)dx + \int_0^L u''^2(x,t)dx \right] \tag{B.24}$$

where λ_1 and λ_2 are some selective positive constants (see Lemma A.3 given in Dadfarnia et al. 2004b for details). Utilizing (B.21–B.24), we can now find the upper and lower bounds for $V_L(t)$ as

$$V_L(t) \leq \lambda_3 \left[\int_0^L \dot{u}^2(x,t)\mathrm{d}x + u^2(0,t) + \gamma_0^2(t) + \dot{u}^2(L,t) + \int_0^L u''^2(x,t)\mathrm{d}x \right] \tag{B.25}$$

$$V_L(t) \geq \lambda_4 \int_0^L u''^2(x,t)\mathrm{d}x + \frac{1}{2}K_p u^2(0,t) \tag{B.26}$$

where λ_3 and λ_4 are some selective positive constants. After differentiating (B.20) with respect to the time variable and using (9.100), (9.107), and the boundary conditions (9.85), we can obtain the following upper bound for the time derivative of $V_L(t)$

$$\dot{V}_L(t) \leq -\lambda_5 \left[\int_0^L \dot{u}^2(x,t)\mathrm{d}x + u^2(0,t) + \gamma_0^2(t) + \dot{u}^2(L,t) + \int_0^L u''^2(x,t)\mathrm{d}x \right] \tag{B.27}$$

where λ_5 is a positive constant. Using inequality (B.25), the upper bound (B.27) can be rewritten as

$$\dot{V}_L(t) \leq -\frac{\lambda_5}{\lambda_3} V_L(t) \tag{B.28}$$

whose solution yields (de Querioz et al. 2000)

$$\begin{aligned} V_L(t) &\leq V_L(0) \exp\left(-\frac{\lambda_5}{\lambda_3}t\right) \\ &\leq \lambda_3 \left[\int_0^L \dot{u}^2(x,0)\mathrm{d}x + u^2(0,0) + \gamma_0^2(0) + \dot{u}^2(L,0) \right. \\ &\quad \left. + \int_0^L u''^2(x,0)\mathrm{d}x \right] \exp\left(-\frac{\lambda_5}{\lambda_3}t\right) \end{aligned} \tag{B.29}$$

Since $u''(x,t) = w''(x,t)$, we can use (9.87) and (9.81) into (B.26) to obtain

$$V_L(t) \geq \frac{\lambda_4}{L^3} w^2(x,t) + \frac{K_p}{2} {s_1}^2(t) \tag{B.30}$$

The result of Theorem 9.2 now directly follows by combing inequalities (B.29) and (B.30). □

B.3 Proof of Theorem 9.3 (Ramaratnam and Jalili 2006a)

We observe that (9.123) and (9.124) give the configuration of the observer and can be rewritten as

$$\dot{\hat{y}} = p + K_{01}\tilde{y} \tag{B.31}$$

$$\dot{p} = V_0 + K_{02}\tilde{y} \tag{B.32}$$

where

$$V_0 = -\frac{2\overline{K}_2}{m} y \,\mathrm{sgn}(y\dot{\hat{y}}) - \frac{\overline{K}_1}{m} y \tag{B.33}$$

Differentiating (B.31) and with the help of (B.32), we get,

$$\ddot{\hat{y}} = V_0 + K_{02}\tilde{y} + K_{01}\dot{\tilde{y}} \tag{B.34}$$

Considering $\ddot{\tilde{y}} = \ddot{y} - \ddot{\hat{y}}$ and the homogenous version of (9.116), (B.34) can be written as,

$$\ddot{\tilde{y}} = -\frac{1}{m}k(t) - V_0 - K_{02}\tilde{y} - K_{01}\dot{\tilde{y}} \tag{B.35}$$

To prove the stability, we select a Lyapunov candidate as

$$V_L = \frac{1}{2}\dot{y}^2 + \frac{1}{2}\frac{\bar{K}_1}{m}y^2 + \frac{1}{2}\dot{\tilde{y}}^2 + \frac{1}{2}K_{02}\tilde{y}^2 \tag{B.36}$$

Differentiating (B.36) and substituting (B.35) yields,

$$\dot{V}_L = -\frac{2\bar{K}_2}{m} y\dot{\tilde{y}}\,\mathrm{sgn}(y\dot{\hat{y}}) - \frac{\bar{K}_2}{m} y\dot{\hat{y}}\,\mathrm{sgn}(y\dot{\hat{y}}) - K_{01}\dot{\tilde{y}}^2 - \frac{\bar{K}_1}{m} y\dot{\tilde{y}} - V_0\dot{\tilde{y}} \tag{B.37}$$

$$\Rightarrow \quad \dot{V}_L = -\frac{\bar{K}_2}{m} y\dot{\hat{y}}\,\mathrm{sgn}(y\dot{\hat{y}}) - K_{01}\dot{\tilde{y}}^2 \tag{B.38}$$

As seen, $\dot{V}_L(y)$ is negative semi-definite, $V_L(y)$ is radially unbounded, that is, $V_L(y) \to \infty$, as $\|y\| \to \infty$ and

$$\ddot{y} = -\frac{1}{m} y \left\{\bar{K}_1 + \bar{K}_2\,\mathrm{sgn}(y\dot{\hat{y}})\right\} \tag{B.39}$$

Then, using the Invariant Set Theorem (Slotine and Li 1991, see also Appendix A), it can be proven that the system (9.116) with controller (9.118) and velocity observer system (9.123) and (9.124) is globally asymptotically stable. □

B.4 Proof of Theorem 10.1 (Bashash and Jalili 2009)

Let us define the parametric error signals as follows and take their time derivatives to obtain:

$$\begin{aligned}
&\tilde{m}(t) = m - \hat{m}(t);\ \dot{\tilde{m}}(t) = -\dot{\hat{m}}(t)\\
&\tilde{c}(t) = c - \hat{c}(t);\ \dot{\tilde{c}}(t) = -\dot{\hat{c}}(t)\\
&\tilde{k}(t) = k - \hat{k}(t);\ \dot{\tilde{k}}(t) = -\dot{\hat{k}}(t)\\
&\tilde{r}(t) = r - \hat{r}(t);\ \dot{\tilde{r}}(t) = -\dot{\hat{r}}(t)\\
&\tilde{p}_0(t) = p_0 - \hat{p}_0(t);\ \dot{\tilde{p}}_0(t) = -\dot{\hat{p}}_0(t)
\end{aligned} \tag{B.40}$$

Now, select the following positive definite Lyapunov candidate function:

$$V_L(t) = \frac{1}{2}\left(ms^2(t) + k_1\tilde{m}^2(t) + k_2\tilde{c}^2(t) + k_3\tilde{k}^2(t) + k_4\tilde{r}^2(t) + k_5\tilde{p}_0^2(t)\right) \tag{B.41}$$

Taking its time derivative yields

$$\begin{aligned}
\dot{V}_L(t) = {} & ms(t)\dot{s}(t) + k_1\tilde{m}(t)\dot{\tilde{m}}(t) + k_2\tilde{c}(t)\dot{\tilde{c}}(t)\\
& + k_3\tilde{k}(t)\dot{\tilde{k}}(t) + k_4\tilde{r}(t)\dot{\tilde{r}}(t) + k_5\tilde{p}_0(t)\dot{\tilde{p}}_0(t)
\end{aligned} \tag{B.42}$$

Substituting (10.22), (10.23) and (B.40) into (B.42) results in

$$\begin{aligned}
\dot{V}_L(t) = {} & \tilde{m}(t)\left[s(t)\left(\ddot{x}_d(t) + \sigma\,\dot{e}(t)\right) - k_1\dot{\hat{m}}(t)\right]\\
& + \tilde{c}(t)\left[s(t)\dot{x}(t) - k_2\dot{\hat{c}}(t)\right] + \tilde{k}(t)\left[s(t)x(t) - k_3\dot{\hat{k}}(t)\right]\\
& - \tilde{r}(t)\left[s(t)\left(y(t) + \hat{y}_c(t)\right) + k_4\dot{\hat{r}}(t)\right] - \tilde{p}_0(t)\left[s(t) + k_5\dot{\hat{p}}(t)\right]\\
& - \eta_1 s(t)^2 - \eta_2 s(t)\mathrm{sgn}\left(s(t)\right) + \tilde{p}(t)s(t)
\end{aligned} \tag{B.43}$$

Taking the time derivatives from the adaptation laws given by (10.24) and substituting into (B.43) makes the coefficients of the parametric error signals (the terms inside the squared brackets) zero. Hence, the time derivative of the Lyapunov function is reduced to

$$\begin{aligned}
\dot{V}_L(t) &= -\eta_1 s^2(t) - \eta_2 s(t)\mathrm{sgn}\left(s(t)\right) + \tilde{p}(t)s(t)\\
&= -\eta_1 s^2(t) - \eta_2\left|s(t)\right| + \tilde{p}(t)s(t)
\end{aligned} \tag{B.44}$$

If the condition $|\tilde{p}(t)| \le \eta_2$ is applied for all $t > 0$ then,

$$-\eta_2\left|s(t)\right| \le \tilde{p}(t)s(t) \text{ or } \dot{V}_L(t) \le -\eta_1 s^2(t) \le 0 \tag{B.45}$$

Equation (B.45) states that the time derivative of proposed positive definite Lyapunov function is negative, and hence asymptotic convergence of the sliding variable $s(t)$ is achieved, that is, $s(t) \to 0$ as $t \to \infty$ according to Su and Stepanenko (2000). Since all the adaptation signals are bounded, error signal $e(t)$ and its time derivative $\dot{e}(t)$ converge to zero, as a conclusion from (10.21). □

B.5 Proof of Theorem 10.2 (Bashash and Jalili 2009)

The time derivative of the Lyapunov function given in (B.41), after applying modified control law (10.26), adaptation laws (10.28), and property (10.29) leads to

$$\dot{V}_L(t) \leq -\eta_1 s(t)^2 - \eta_2 s(t)\text{sat}\left(s(t)/\varepsilon\right) + \tilde{p}(t)s(t) \tag{B.46}$$

Assume that the sliding variable starts from outside the boundary layer defined by ε, such that its initial value satisfies $|s(0)| > \varepsilon$. From (10.25) it follows that the Lyapunov derivative of the modified controller, (B.46) becomes identical to that of the primary controller, (B.44). Hence, $s(t)$ will be stirred toward zero through the controller as proved by Theorem 10.1. However, before arriving at the origin, it enters the boundary layer where $|s(t)| \leq \varepsilon$. Inside the boundary layer, the structure of the control input changes due to the change in the saturation output. For the trajectory $s(t)$ inside the boundary layer, the derivative of the Lyapunov function becomes

$$\begin{aligned}\dot{V}_L(t) &\leq -\eta_1 s^2(t) - \eta_2 s(t)\text{sat}\left(s(t)/\varepsilon\right) + \tilde{p}(t)s(t) \\ &= -\eta_1 s^2(t) - \eta_2 s^2(t)/\varepsilon + \tilde{p}(t)s(t) \\ &= s(t)\left(\tilde{p}(t) - \left[\eta_1 + \eta_2/\varepsilon\right]s(t)\right), \quad |s(t)| \leq \varepsilon\end{aligned} \tag{B.47}$$

If $s(t)$ stays inside a particular range in the boundary layer such that it satisfies $(|\tilde{p}(t)|\,\varepsilon)/(\eta_1\varepsilon + \eta_2) \leq |s(t)| \leq \varepsilon$, then it follows that $\dot{V}_L(t) \leq 0$. Therefore, $s(t)$ is further forced to move toward the origin. Once it enters the region where the inequality $|s(t)| < (|\tilde{p}(t)|\,\varepsilon)/(\eta_1\varepsilon + \eta_2) < \varepsilon$ holds, then the derivative of the Lyapunov candidate function becomes positive, that is, $\dot{V}_L(t) > 0$. This may force the trajectory $s(t)$ to move outside the region, where it will be forced back inside the region again. Eventually, $s(t)$ will be entrapped inside the region where $|s(t)| < (|\tilde{p}(t)|\,\varepsilon)/(\eta_1\varepsilon + \eta_2) \leq \lambda < \varepsilon$, where $\lambda = \eta_2\varepsilon/(\eta_1\varepsilon + \eta_2)$ after a finite time τ_λ, $\forall t \in [\tau_\lambda, \infty)$. Therefore, the region $|s(t)| < \lambda < \varepsilon$ is the zone of convergence or the region of attraction for any trajectory starting from outside the zone.

Assume that $s(t)$ enters the zone of convergence at $t = \tau_\lambda$ and the inequality $|s(t)| < \lambda$ holds for $\forall t \in [\tau_\lambda, \infty)$.Consequently, a time-varying positive function $l_1(t) > 0$ can be found such that

$$s(t) = \dot{e}(t) + \sigma e(t) = \lambda - l_1(t) \tag{B.48}$$

Solving the differential equation (B.48) yields

$$\begin{aligned} e(t) &= \frac{\lambda}{\sigma} + \left\{ e(\tau_\lambda) - \frac{\lambda}{\sigma} \right\} \exp\left(-\sigma(t-\tau_\lambda)\right) \\ &\quad - \exp\left(-\sigma t\right) \int_{\tau_\lambda}^{t} l_1(\tau) \exp\left(\sigma\tau\right) \mathrm{d}\tau \\ &< \frac{\lambda}{\sigma} + \left\{ e(\tau_\lambda) - \frac{\lambda}{\sigma} \right\} \exp\left(-\sigma(t-\tau_\lambda)\right) \;\; \forall t \in [\tau_\lambda, \infty) \end{aligned} \tag{B.49}$$

Therefore,

$$e_{ss}(t) < \frac{\lambda}{\sigma} \tag{B.50}$$

Similarly, there exists a time-varying function $l_2(t) > 0$, $\forall t \in [\tau_\lambda, \infty)$, for $|s(t)| < \lambda$ such that

$$s(t) = \dot{e}(t) + \sigma e(t) = -\lambda + l_2(t) \tag{B.51}$$

which similarly follows that

$$e(t) > -\frac{\lambda}{\sigma} + \left\{ e(\tau_\lambda) + \frac{\lambda}{\sigma} \right\} \exp\left(-\sigma(t-\tau_\lambda)\right); \;\; \forall t \in [\tau_\lambda, \infty) \tag{B.52}$$

And consequently,

$$e_{ss}(t) > -\frac{\lambda}{\sigma} \tag{B.53}$$

Form expressions (B.52) and (B.53), one can simply conclude:

$$|e_{ss}(t)| \leq \beta \quad \text{where} \quad \beta = \frac{\lambda}{\sigma} = \frac{\eta_2 \varepsilon}{\sigma(\eta_1 \varepsilon + \eta_2)} \tag{B.54}$$

References

Abramovitch DY, Anderson AB, Pao LY, Schitter G (2007) A tutorial on the mechanics dynamics and control of atomic force microscopes. Proceedings of the 2007 American control conference, New York, 11–13 July

Abu-Hilal M (2003) Forced vibration of Euler-Bernoulli beams by means of dynamic Green functions. J Sound Vib 267:191–207

Active Vibration Control Instrumentation, A Division of PCB Piezotronics, Inc., www.pcb.com

Adams JD, Parrott G, Bauer C, Sant T, Manning L, Jones M, Rogers B, McCorkle D, Ferrell TL (2003) Nanowatt chemical vapor detection with a self-sensing piezoelectric microcantilever array. Appl Phys Lett 83(16):3428–3430

Aderiaens H, Koning W, Baning R (2000) Modeling piezoelectric actuators. IEEE/ASME Trans Mechatron 5:331–341

Adourian S, Yang S, Westervelt RM, Campman KL, Gossard AC (1998) Josephson junction oscillators as probes of electronic nanostructures. J Appl Phys 84(5808):120–126

Afshari M, Jalili N (2007a) Towards nonlinear modeling of molecular interactions arising from adsorbed biological species on the microcantilever surface. Int J Non-Linear Mech. 42(4): 588–595

Afshari M, Jalili N (2007b) A sensitivity study on the static and dynamic detection modes of adsorption-induced surface stress in microcantilever biosensors. Proceedings of the ASME 2007 international design engineering technical conferences and computers and information in engineering conference IDETC/CIE 2007, Las Vegas, NV

Afshari M, Jalili N (2008) Nanomechanical cantilever biosensors: Conceptual design, recent developments and practical implementation, chapter 13 of biomedical applications of vibration and acoustics for imaging and characterization. ASME Press 13:353–374

Ahuwalia A, Baughman R, Rossi DD, Mazzoldi A, Tesconi M, Tognetti A, Vozzi G (2001) Microfabricated electroactive carbon nanotube actuators. Proc SPIE 4329:209–215

Ajayan PM, Schadler LS, Giannaris C, A Rubio (2000) Single-walled nanotubes – polymer composites: Strength and weakness. Adv Mater 12(10):750–753

Akahori H, Haga Y, Matsunaga T, Totsu K, Iseki H, Esashi M, Wada H (2005) Piezoelectric 2D microscanner for precise laser treatment in the human body. Third IEEE/EMBS special topic conference on microtechnology in medicine and biology, Oahu, Hawaii, pp 166–169

Álvarez M, Calle A, Tamayo J, Lechuga L, Abad A, Montoya A (2003) Development of nanomechanical biosensors for detection of the pesticide DDT. Biosens Bioelectron 18:649–653

Álvarez M, Carrascosa LG, Moreno M, Calle A, Zaballos A, Lechuga LM, Martinez AC, Tamayo J (2004) Nanomechanics of the formation of DNA self-assembled monolayers and hybridization on microcantilevers. Langmuir 20:9663–9668

Anand SV, Mahapatra DR (2009) The dynamics of polymerized carbon nanotubes in semiconductor polymer electronics and electro-mechanical sensing. Nanotechnology 20(14):145707

Anand SV, Roy D (2009) Quasi-static and dynamic strain sensing using carbon nanotube/epoxy nanocomposite thin films. Smart Mater Struct 18(4):045013

Ang WT, Garmon FA, Khosla PK, Riviere CN (2003) Rate-dependent hysteresis in piezoelectric actuators. Proceedings of IEEE international conference on intelligent robots and systems, vol 2. 1975–1980, Las Vegas, NV

Aoshima S, Yoshizawa N, Yabuta T (1992) Compact mass axis alignment device with piezoelements for optical fibers. IEEE Photon Technol Lett 4:462–464

Arafat HN, Nayfeh AH, Chin C (1998) Nonlinear nonplanar dynamics of parametrically excited cantilever beams. Nonlinear Dyn 15:31–61

Arntz Y, Seelig JD, Lang HP, Zhang J, Hunzicker P, Ramseyer JP, Meyer E, Hegener M, Gerber Ch (2003) Label-free protein assay based on a nanomechanical cantilever array. Nanotechnology 14(1):86

Ashkin A, Dziedzic JM, Bjorkholm JE, Chu S (1986) Observation of a single-beam gradient force optical trap for dielectric particles. Optics Lett 11:288–290

Audigier D et al (1994) Typical characteristics of a piezoelectric ceramic material for squeeze igniters. IEEE Int Symp Appl Ferroelectr 383–386

Austin SA (1993) The vibration damping effect of an electrorheological fluid. ASME J Vib Acoust 115(1):136–140

Balachandran B, Magrab EB (2009) Vibrations, 2nd ed. Cengage learning, Toronto, ON, Canada

Ballas RG (2007) Piezoelectric multilayer beam bending actuators: Static and dynamic behavior and aspects of sensor integration, Springer

Baller M, Lang HP, Fritz J, Gerber Ch, Gimzewski JK, Drechsler U, Rothuizen H, Despont M, Vettiger P, Battiston FM, Ramseyer JP, Fornaro P, Meyer E, Guntherodt H-J (2000) Cantilever array-based artificial nose. Ultramicroscopy 82(1):1–9

Banks HT, Ito K (1988) A unified framework for approximation in inverse problems for distributed parameter systems. Control Theory Adv Technol 4(1):73–90

Banks HT, Kunisch K (1989) Estimation techniques for distributed parameter systems. Birkhauser, Boston, MA

Banks, Smith, Wang (1996) Smart materials and structures: modeling, estimation and control, Wiley, New York

Bar-Cohen Y, Sherrit S, Lih SS (2001) Characterization of the electromechanical properties of EAP materials. SPIE's eighth annual international symposium on smart structures and materials, pp 4329–4343

Bardeen J (1961) Tunneling from a many-particle point of view. Phys Rev Lett 6:57–59

Barta RC (2004) Lecture notes for short-course: Engineering and designing smart structures. Virginia Tech, Blacksburg, VA

Baruh H (1999) Analytical dynamics. McGraw-Hill Companies

Baselt DR, Lee GU, Colton RJ (1996) Biosensor based on force microscope technology. J Vac Sci Technol B, 14(2):789–793

Bashash S (2005) Nonlinear modeling and control of piezoelectrically-driven nanostagers with application to scanning tunneling microscopy. M.Sc. Thesis. Clemson University, Clemson, SC

Bashash S (2008) Modeling and control of piezoactive micro and nano systems. PhD Dissertation, Department of Mechanical Engineering, Clemson University, Clemson, SC

Bashash S, Jalili N (2005) Trajectory control of piezoelectric actuators using nonlinear variable structure control. Proceedings of international symposium on collaborative research in applied science (ISOCRIAS). Vancouver, BC, Canada

Bashash S, Jalili N (2006a) Underlying memory-dominant nature of hysteresis in piezoelectric materials. J Appl Phys 100:014103

Bashash S, Jalili N (2006b) On the nonlinear modeling, System identification, and control of piezoelectrically-driven nanostagers. Proceedings of the 10th international conference on new actuators, Bremen, Germany

Bashash S, Jalili N (2007a) Intelligent rules of hysteresis in feedforward trajectory control of piezoelectrically-driven nanostages. J Micromech Microeng 17:342–349

Bashash S, Jalili N (2007b) Robust multiple-frequency trajectory tracking control of piezoelectrically-driven micro/nano positioning systems. IEEE Trans Control Syst Technol 15:867–878

Bashash S, Jalili N (2008) A polynomial-based linear mapping strategy for compensation of hysteresis in piezoelectric actuators. ASME Trans J Dyn Syst Measur Control 130:031008(1–10)

Bashash S, Jalili N (2009) Robust adaptive control of coupled parallel piezo-flexural nanopositioning stages. IEEE/ASME Trans Mechatron 14(1):11–20

Bashash S, Salehi-Khojin A, Jalili N (2008a) Forced vibration analysis of flexible Euler-Bernoulli beams with geometrical discontinuities. Proceedings of the 2008 American control conference, Seattle, WA, (June 2008)

Bashash S, Vora K, Jalili N (2008b) Distributed-parameters modeling and control of rod-like solid-state actuators. J Vibration and Control, submitted for publication

Bashash S, Vora K, Jalili N, Evans PG, Dapino MJ, Slaughter J (2008c) Modeling major and minor hysteresis loops in Galfenol-driven micro-positioning actuators using a memory-based hysteresis framework. 2008 ASME Dynamic Systems and Control Conference (DSCC'08). Ann Arbor, MI, October 20–22

Bashash S, Salehi-Khojin A, Jalili N, Thompson GL, Vertegel A, Müller M, Berger R (2009) Mass detection of elastically-distributed ultrathin layers using piezoresponse force microscopy. J Micromech Microeng 19, 025016:1–9

Batt RJ (1981) Application of pyroelectric devices for power and reflectance measurements. Ferroelectrics 34:11–14, Gordon and Breach, New York

Baughman RH (2000) Putting a new spin on carbon nanotubes. Science 290:1310

Baumgarten PK (1971) Electrostatic spinning of acrylic microfibers. J Colloid Interface Sci 36:71

Bayo E (1987) A finite-element approach to control the end-point motion of a single-link flexible robot. J Robotic Sys 4:63–75

Baz A, Ro J (1996) Vibration control of plates with active constrained layer damping. Smart Mater Struct 5:272

Beer FP, Johnson ER (1981) Mechanics of materials, McGraw-Hill Company

Benaroya H (1998) Mechanical vibration: Analysis, uncertainties, and control. Prentice Hall, Inc., NJ

Bent AA, Hagood NW (1993) Development of piezoelectric fiber composites for structural actuation. Proceedings of AIAA/ASME/ASCE/AHS/ASC structures, structural dynamics and materials conference, AIAA Paper No. 93–1717, La Jolla, CA

Berger R, Gerber Ch, Gimzewski JK (1996) Thermal analysis using micromechanical calorimeter. Appl Phys Lett 69(1):40–42

Berger R, Delamarche E, Lang HP, Gerber C, Gimzewski JK, Meyer E, Guntherodt H-J (1997) Surface stress in the self-assembly of alkanethiols on gold. Science 276:2021–2023

Berlincourt D (1981) Piezoelectric ceramics: Characteristics and applications. J Acoust Soc Am. 70:1586–1595

Berlincourt DA, Curran DR, Jaffe H (1964) Piezoelectric and piezomagnetic materials and their function as transducers. In: Mason WP (ed) Physical acoustics, 1A, Academic Press, New York

Bhadbhade V, Jalili N, Mahmoodi SN (2008) A novel piezoelectrically actuated flexural/torsional vibrating beam gyroscope. J Sound Vib 311:1305–1324

Billson D, Hutchins D (1993) Development of novel piezoelectric ultrasonic transducers for couplant-free non-destructive testing. Br J Non-Destructive Test 35:705–709

Binnie G, Rohrer H, Gerber CH, Weibel E (1982) Surface studies by scanning tunneling microscopy. Phys Rev Lett 49:57–61

Binnig G, Quate CF, Gerber C (1986) Atomic force microscope. Phys Rev Lett 56:93–96

Binnig G, Rohrer H, Gerber C, Weibel E (1982) Surface studies by scanning tunneling microscopy. Phys Rev Lett 49:57–61

Bizet K, Gabrielli C, Perrot H, Therasse J (1998) Validation of antibody-based recognition by piezoelectric transducers through electroacoustic admittance analysis. Biosens Bioelectron 13(3–4):259–269

Bobbio S, Miano G, Serpico C, Visone C (1997) Models of magnetic hysteresis based on play and stop hysterons. IEEE Trans Magn33:4417–4426

Bontsema J, Cartain RF, Schumacher JM (1988) Robust control of flexible systems: A case study, Automatica 24:177–186

Braun T, Barwich V, Ghatkesar MK, Bredekamp AH, Gerber C, Hegner M, Lang HP (2005) Micromechanical mass sensors for biomolecular detection in a physiological environment. Phys Rev 72:031907

Britton CL, Jones RL, Oden PI, Hu Z, Warmack RJ, Smith SF, Bryan WL, Rochelle JM (2000) Multiple-input microcantilever sensors. Ultramicroscopy 82:17–21

Brokate M, Sprekels J (1996) Hysteresis and phase transitions. Springer, New York

Bumbu GG, Kircher, Wolkenhauer M (2004) Synthesis and characterization of polymer brushes on micromechanical cantilevers. Macro Chem Phys 205:1713

Busch-Vishniac IJ (1999) Electromechanical sensors and actuators, Springer, New York

Cady WG (1964) Piezoelectricity, Dover, New York

Caliano G, Lamberti N, Iula A, Pappalardo M (1995) Piezoelectric bimorph static pressure sensor. Sens Actuators A: Phys 46:176–178

Canfield S, Frecker M (2000) Topology optimization of compliant mechanical amplifier for piezoelectric actuators. Struct Multidis Optim 20:269–279

Carlson JD (1994) The promise of controllable fluids. In: Borgmann H, Lenz K (eds) Actuator 94, fourth international conference on new actuators, Axon Technologies Consult GmbH, pp 266–270

Carlson JD, Sprecher AF, Conrad H (eds) (1989) Elecrorheological fluids. Technomic, Lancaster, PA

Chaghai R, Lining S, Weibin R, Liguo C (2004) Adaptive inverse control for piezoelectric actuator with dominant hysteresis. Proceedings of IEEE international conference on control applications, vol 2. Taipei, Taiwan, pp 973–976

Chaghai R, Lining S (2005) Improving positioning accuracy of piezoelectric actuators by feed-forward hysteresis compensation based on a new mathematical model. Rev Sci Instrum 76:095111-1:8

Chai WK, Tzou HS (2002) Constitutive modeling of controllable electrostrictive thin shell structures. ASME international mechanical engineering congress, Symposium on advances of solids and structures. New Orleans, LA, November 17–22

Chen BM, Lee TH, Hang CC, Guo Y, Weerasooriya S (1999) An H^{∞} almost disturbance decoupling robust controller design for a piezoelectric bimorph actuator with hysteresis. IEEE Trans Contr Syst Technol 7:160–174

Chen GY, Thundat T, Wachter EA, Warmack RJ (1995) Adsorption-induced surface stress and its effects on resonance frequency of microcantilevers. J Appl Phys 77(8):3618–3622

Chen W, Lupascu DC, Rodel J, Lynch CS (2001) Short crack R-curves in ferroelectric and electrostrictive PLZT. J Am Ceram Soc 84(3):593–597

Choi SB (1999) Vibration control of flexible structures using ER dampers. ASME J Dyn Syst Measur Control 121:134–138

Chopra NG, Zettl A (1998) Measurement of the elastic modulus of a multi-wall boron nitride nanotube. Solid State Commun 105(5):297–300

Chu C-H, Shih W-P, Chung S-Y, Tsai H-C, Shing T-K, Chang P-Z (2007) A low actuation voltage electrostatic actuator for RF MEMS switch applications. J Micromech Microeng 17:1649–1656

Clark WW (2000) Vibration control with state-switched piezoelectric materials. J Intell Mater Syst Struct 11(4):263–271

Clark, Saunders, Gibbs (1998) Adaptive structures: dynamics and control, Wiley, New York

Collins PG, Bradley K, Ishigami M, Zeatl A (2000) Extreme oxygen sensitivity of electronic properties of carbon nanotubes. Science 287:1801

Corbeil J, Lavrik N, Rajic S, Datskos PG (2002) Self-leveling uncooled microcantilever thermal detector. Appl Phys Lett 81:1306

Courty S, Mine J, Tajbakhsh AR, Terentjev EM (2003) Nematic elastomers with aligned carbon nanotubes: New electromechanical actuators Condens Matter 1:234–237

Crespo da Silva MRM (1988) Nonlinear flexural–flexural-torsional-extensional dynamics of beams – I formulation. Int J Solid Struct 24:1225–1234
Crespo da Silva MRM, Glynn CC (1978) Nonlinear flexural-flexural-torsional dynamics of inextensional beams: I. Equations of motion J Struct Mech 6(4):437–448
Crick FHC, Hughes AFW (1950) The physical properties of cytoplasm: A study by means of the magnetic particle method. Exp Cell Res 1:37–80
Culshaw (1996) Smart structures and materials, Artech House
Cummings J, Zettl A (2000) Mass-production of boron nitride double-wall nanotubes and nanococoons. Chem Phys Lett 316:211
Curie J, Curie P (1880) Développement, par pression, de l'électricité polaire dans les cristaux hémièdres à faces inclines. Comptes Rendus de l'Académie des Sciences, Paris 91:294–295
Curtis R, Mitsui T, Ganz E (1997) Ultrahigh vacuum high speed scanning tunneling microscope. Rev Sci Instrum 68:2790–2796
Dadfarnia M, Jalili N, Liu Z, Dawson DM (2004a) An observer-based piezoelectric control of flexible Cartesian robot arms: theory and experiment. Control Eng Pract 12:1041–1053
Dadfarnia M, Jalili N, Xian B, Dawson DM (2004b) A Lyapunov-based piezoelectric controller for flexible cartesian robot manipulators. ASME J Dyn Syst Measur Control 126 (2):347–358
Dadfarnia M, Jalili N, Xian B, Dawson DM (2004c) Lyapunov-based vibration control of translational Euler-Bernoulli beams using the stabilizing effect of beam damping mechanisms. J Vib Control 10:933–961
Dai H, Hafner JH, Rinzler AG, Ccbert DT, Smalley RE (1996) Nanotubes as nanoprobes in scanning probe microscopy. Nature 384:147
Damjanovic D (1998) Ferroelectric, dielectric and piezoelectric properties of ferroelectric thin films and ceramics. Rep Prog Phys 61:1267–1324
Dankert H, Dankert J (1995) Technische Mechanik, vol 2. Auflage B.G. Teubner, Stuttgart
Dareing DW, Thundat T (2005) Simulation of adsorption-induced stress of a microcantilever sensor. J Appl Phys 97:043526
Datskos PG, Sauers I (1999) Detection of 2-mercaptoethanol using gold-coated micromachined cantilevers. Sens Actuators B 61:75–82
Datskos PG, Oden PI, Thundat T, Wachter EA, Warmack RJ, Hunter SR (1996) Remote infrared radiation detection using piezoresistive microcantilevers. Appl Phys Lett 69(20):2986–2988
Dauber-Osguthorpe P et al (1988) Structure and energetics of ligand binding to proteins: Escherichia coli dihydrofolate reductase-trimethoprim, a drug-receptor system. Proteins Struct Funct Genet 4:31
de Querioz Querioz MS, Dawson DM, Agrawal M, Zhang F (1999) Adaptive nonlinear boundary control of a flexible link robot arm. IEEE Trans Rob Autom 15(4):779–787
de Querioz MS, Dawson DM, Nagarkatti SP, Zhang F (2000) Lyapunov-based control of mechanical systems, Birkhauser, Boston MA
DeSimone A, James RD (2002) A constrained theory of magnetoelasticity. J Mech Phys Solids 50:283–320
Dillon AC et al (1997) Storage of hydrogen in single-walled carbon nanotubes. Nature 386:377
Dimarogonas-Andrew D, Kollias A (1993) Smart electrorheological fluid dynamic vibration absorber. Intell Struct Mater Vib ASME Des Div 58:7–15
Duclos TG (1988) Design of devices using electrorheological fluids. Future Transp Techn Conf Exp SAE Paper 881134, San Francisco, CA, pp 8–11
Dyer PE, Srinivasan R (1989) Pyroelectric detection of ultraviolet laser ablation products from polymers. J Appl Phys 66:2608–2611
Elmali H, Olgac N (1992) Sliding mode control with perturbation estimation (SMCPE): A new approach. Int J Control 56:923–941
Elmali H, Olgac N (1996) Implementation of sliding mode control with perturbation estimation (SMCPE). IEEE Trans Control Syst Technol 4(1):79–85
Eringen AC (1952) Nonlinear theory of continuous media. McGraw-Hill Companies, New York, NY

Eslimy-Isfahany SHR, Banerjee JR (2000) Use of generalized mass in the interpretation of dynamic response of bending-torsion coupled beams. J Sound Vib 238(2):295–308
Esmaeili M, Jalili N, Durali M (2007) Dynamic modeling and performance evaluation of a vibrating microgyroscope under general support motion. J Sound Vib 301(1–2):146–164
Esmailzadeh E, Jalili N (1998a) Optimum design of vibration absorbers for structurally damped Timoshenko beams. ASME J Vib Acous 120(4):833–841
Esmailzadeh E, Jalili N (1998b) Parametric response of Cantilever Timoshenko beams with tip mass under harmonic support motion. Int J Nonlinear Mech 33:765–781
Fan S et al (1999) Self-oriented regular arrays of carbon nanotubes and their field emission properties. Science 283:512
Feldman Y, Wasserman E, Srolovitz DJ, Tenne R (1995) High-rate gas-phase growth of MoS_2 nested inorganic fullerenes and nanotubes. Science 267(5195):222–225
Filipovic and Schroder (1999) Vibration absorption with linear active resonators: continuous and discrete time design and analysis. J. of Vib. Control 5:685–708
Frecker MI, Ananthasuresh GK, Nishiwaki S, Kikuchi N, Kota S (1997) Topological synthesis of compliant mechanism using multi-criteria optimization. ASME Trans J Mech Design 119:238–245
Friedman A (1982) Foundation of modern analysis. Dover, New York
Fukada E (2000) History and recent progress in piezoelectric polymers. IEEE Trans Ultrason Ferroelectr Freq Control 47:1277
Fukuda T, Dong L (2003) Assembly of nanodevices with carbon nanotubes through nanorobotic manipulations. Proc IEEE 91:1803–1818
Furutani K, Urushibata M, Mohri N (1998) Displacement control of piezoelectric element by feedback of induced charge. Nanotechnology 9:93–98
Gabbert U, Tzou HS (eds) (2001) IUTAM symposium on smart structures and structonic systems, Kluwer Academic Publishers, Dordrecht
Gahlin R, Jacobson S (1998) Novel method to map and quantify wear on a micro-scale. Wear 222:93–102
Galinaitis WS (1999) Two methods for modeling scalar hysteresis and their use in controlling actuators with hysteresis. PhD Dissertation. Virginia Polytechnic Institute and State University, Blacksburg, VA
Galvagni J, Rawal B (1991) A comparison of piezoelectric and electrostrictive actuator stacks. SPIE Adapt Adapt Opt Comp 1543:296–300
Gandhi, Thompson (1992) Smart materials structure, Chapman and Hall
Garcia E, Dosch J, Inman DJ (1992) The application of smart structures to the vibration suppression problem. J Intell Mater Syst Struct 3:659–667
Gawronski WK (2004) Advanced structural dynamics and active control of structures, Springer, New York
Ge P, Jouaneh M (1995) Modeling hysteresis in piezoceramic actuators. Precision Eng 17:211–221
Ge P, Jouaneh M (1997) Generalized Preisach model for hysteresis nonlinearity of piezoceramic actuators. Precision Eng 20:99–111
Ge SS, Lee TH, Gong JQ (1999) A robust distributed controller of a single link SCARA/Cartesian smart materials robot Mechatronics 8:65–93
Ge SS, Lee, TH, Zhu G (1996) Energy-based Robust controller design for multi-link flexible robots. Mechatronics 6(7):779–798
Ge SS, Lee TH, Zhu G (1997) A nonlinear feedback controller for a single-link flexible manipulator based on a finite element method. J Robotic Syst 14(3):165–178
Ge SS, Lee TH, Zhu G (1998a) Asymptotically stable end-point regulation of a flexible SCARA/cartesian robot. IEEE/ASME Trans Mechatron 3(2):138–144
Ge SS, Lee TH, Gong JQ, Xu JX (1998b) Controller design for a single-link flexible smart materials robot with experimental tests. Proceedings of the 37th IEEE conference on decision and control, Tampa, FL, USA, December 1998
Gfeller KY, Nugaeva N, Hegner M (2005) Rapid biosensor for detection of antibiotic-selective growth of Escherichia coli. Appl Environ Microbiol 71(5):2626–2631

Giessibl FJ (2003) Advances in atomic force microscopy. Rev Modern Phys 75:949–983
Gimzewski JK, Gerber Ch, Meyer E, Schlittler RR (1994) Observation of a chemical reaction using a micromechanical sensor. Chem Phys Lett 217:589–594
Ginder JM, Ceccio SL (1995) The effect of electrical transients on the shear stresses in electrorheological fluids. J Rheol 39(1):211–234
Giurgiutiu V, Chaudhry Z, Rogers CA (1995) Stiffness issues in the design of ISA displacement amplification devices: Case study of a hydraulic displacement amplifier. Smart structures and materials. Paper # 2443-12, SPIE. 2443:105–119
Glazounov AE, Zhang QM, Kim C (1998) Piezoelectric actuators generating torsional displacement from the d15 shear strain. Appl Phys Lett 72:2526
Goldfarb M, Celanovic N (1997a) A lumped parameter electromechanical model for describing the nonlinear behavior of piezoelectric actuators. ASME J Dyn Syst Measur Control 119:478–485
Goldfarb M, Celanovic N (1997b) Modeling piezoelectric stack actuators for control of micromanipulation. IEEE Trans Control Syst Technol 17:69–79
Gonda S, Doi T, Kurosawa T, Tanimura Y, Hisata N, Yamagishi T, Fujimoto H, Yukawa H (1999) Accurate topographic images using a measuring atomic force microscope. Appl Surf Sci 144–145:505–509
Gorbet RB, Morris KA, Wang DW (2001) Passivity-based stability and control of hysteresis in smart actuators. IEEE Trans Control Syst Technol 9:5–16
Grigorov AV, Davis ZJ, Rasmussen PA, Boisen A (2004) A longitudinal thermal actuation principle for mass detection using a resonant microcantilever in a fluid medium. Microelectronic Eng 73–74:881–886
Grutter P, Godin M, Tabbard-Cosa V, Bourque H, Monga T, Nagai Y, Lennox RB (2006) Cantilever-based sensing: Origins of surface stress, International Workshop on Nanomechanical Sensors, Copenhagen, Denmark, pp 36–37, May 7–10
Gupta A, Akin D, Bashir A (2004a) Detection of bacterial cells and antibodies using surface micromachined thin silicon cantilever resonators. J Vac Sci Technol 32(4):2785–2791
Gupta A, Akin D, Bashir R (2004b) Single virus particle mass detection using microresonators with nanoscale thickness. Appl Phys Lett 84(11):1976–1978
Gurjar M, Jalili N (2007) Towards ultrasmall mass detection using adaptive self-sensing piezoelectrically-driven cantilevers. IEEE/ASME Trans Mechatronics 12(6):680–688
Gurjar M, Jalili N (2006) Closed-form expression for self-sensing microcantilever-based mass sensing. Proceedings of the 2006 SPIE smart structures and NDE conference, San Diego, CA, Paper no. 6173, pp 61730Q1-10, (February 26–March 02, 2006)
Hagan MF, Majumdar A, Chakraborty AK (2004) Nanomechanical forces generated by surface grafted DNA. J Phys Chem B 106:10163–10173
Hagood NW, Von Flotow A (1991) Damping of structural vibrations with piezoelectric materials and passive electrical networks. J Sound Vib 146(2):243–268
Haitjema H (1996) Dynamic probe calibration in the μm region with nanometer accuracy. Precision Eng 19:98–104
Han W, Bando Y, Kurashima K, Sato T (1998) Synthesis of boron nitride nanotubes from carbon nanotubes by a substitution reaction. Appl Phys Lett 73(21):3085
Hansen KM, Ji H-F, Wu G, Datar R, Cote R, Majumdar A, Thundat T (2001) Cantilever-based optical deflection assay for discrimination of DNA single-nucleotide mismatches. Anal Chem 73 (7):1567–1571
Hartmut J (ed) (1999) Adaptronics and smart structures, basics, materials, design and applications, Springer, Berlin, Heidelberg
Henke A, Kümmel MA, Wallaschek J (1999) A piezoelectrically driven wire feeding system for high performance wedge wedge-bonding machines. Mechatronics 9:757–767
Hesselbach J, Ritter R, Thoben R, Reich C, Pokar G (1998) Visual control and calibration of parallel robots for microassembly. Proceedings of SPIE, vol 3519. Boston, MA, pp 50–61
Hildebrand FB (1965) Methods of applied mathematics, 2nd edn. Prentice-Hall Inc., Englewood Cliffs NJ

Hiremath S, Jalili N (2006) Optimal control of electrospinning for fabrication of nonwoven textile-based sensors and actuators. Proceedings of 3rd international conference of textile research, Cairo, Egypt, Apr 2006

Hiremath S (2006) Development of an automated electrospinning process for nanofiber-based electronic-textile fabrication. MS Thesis, Department of Mechanical Engineering Clemson, Dec

Hofmann G, Walther L, Schieferdecker J, Neumann N, Norkus V, Krauss M, Budzier H (1991) Construction, properties and application of pyroelectric single-element detectors and 128-element CCD linear arrays. Sensor Actuator 25–27:413–416

Hsieh S, Shaw SW, Pierre C (1994) Normal modes for large amplitude vibration of a cantilever beam. Int J Solids Struct 31:1981–2014

http://www.physikinstrumente.com

http://www.piezoelectric.net

http://www.smart-material.com/

http://www.catalyticmaterials.com

http://www.ecpsystems.com

http://www.kynol.com

http://www.nanoamor.com

http://www.pcb.com

http://www.physics.nist.gov

http://www.polytec.com

Hu H, Ben-Mrad R (2003) On the classical Preisach model for hysteresis in piezoceramic actuators. Mechatronics 13:85–94

Hu H, Georgiou HMS, Ben-Mrad R (2005) Enhancement of tracking ability in piezoceramic actuators subject to dynamic excitation conditions. IEEE/ASME Trans Mechatr 10(2):230–239

Hu YT, Yang JS, Jiang Q (2000) Wave propagation in electrostrictive materials under biasing fields. IEEE Ultrason Symp 7803:6365

Hu YT, Yang JS, Jiang Q (2004) Wave propagation in electrostrictive materials under biased fields. Acta Mechancia Solida Sinica 17(3) ISSN 0894–9166

Huang YC, Cheng CH (2004) Robust tracking control of a novel piezodriven monolithic flexure-hinge stage. Proceedings of IEEE international conference on control applications, vol 2. Taipei, Taiwan, pp 977–982

Huber F, Hegner M, Gerber C, Guntherodt H-J, Lang HP (2006) Label free analysis of transcription factors using microcantilever arrays. Biosens Bioelectron 21:1599–1605

Hughes D, Wen JT (1997) Preisach modeling of piezoceramic and shape memory alloy hysteresis. Smart Mater Struct 6:287–300

Hussain T, Baig AM, Saadawi TN, Ahmed SA (1995) Infrared pyroelectric sensor for detection of vehicle traffic using digital signal processing techniques. IEEE Trans Veh TEchnol 44:683–688

Hwang CL, Chen YM, Jan C (2005) Trajectory tracking of large displacement piezoelectric actuators using a nonlinear observer-based variable structure control. IEEE Trans Control Syst Technol 13:56–66

Ibach H (1997) The role of surface stress in reconstruction, epitaxial growth and stabilization of mesoscopic structures. Surf Sci Rep 29:193–263

Iijima S (1991) Helical microtubules of graphitic carbon. Nature 354:56

Ikeda T (1996) Fundamentals of piezoelectricity, Oxford University Press, UK

Ilic B, Czaplewski D, Zalalutdinov M, Craighead HG, Neuzil P, Campagnolo C,Batt C (2001) Single cell detection with micromechanical oscillators. J Vac Sci Technol B 19(6):2825–2828

Ilic B, Czaplewsky D, Craighead HG, Neuzil P, Campagnolo C, Batt C (2000) Mechanical resonant immunospecific biological detector. Appl Phys Lett 77:450–452

Ilic B, Yang Y, Craighead HG (2004) Virus detection using nanoelectromechanical devices. Appl Phys Lett 85(13):2604

Inman DJ (2007) Engineering vibration, 3rd edn. Prentice Hall Inc

Itoh T (1993) Micro-machine technology tackles challenge of motor miniaturization. J Electron Eng 30(313):58–62

Itoh T, Lee C, Suga T (1996) Deflection detection and feedback actuation using a self-excited piezoelectric Pb(Zr,Ti)O_3 microcantilever for dynamic scanning force microscopy. Appl Phys Lett 69(14):2036–2038

Iyer PN (2001) An investigation of physical properties of fluoropolymer carbon nanotube composite matrix materials. Master's Thesis, Department of Material Science and Engineering, Clemson University

Jalili N (in press) Nanomechanical cantilever systems: from sensing to imaging and manipulation, in preparation, Springer, Norwell, MA (scheduled to appear in 2010)

Jalili N, Olgac N (1998) Time-optimal/sliding mode control implementation for robust tracking of uncertain flexible structures. Int J Mechatron 8(2):121–142

Jalili N, Olgac N (1998a) Time-optimal/sliding mode control implementation for robust tracking of uncertain flexible structures. Mechatronics 8(2):121–142

Jalili N, Olgac N (1998b) Optimum delayed feedback vibration absorber for MDOF mechanical structures. Proceedings of 37th IEEE conference on decision control (CDC'98), Tampa, Florida, Dec

Jalili N (2000) A new perspective for semi-automated structural vibration control. J Sound Vib 238(3):481–494

Jalili N, Olgac N (2000a) Identification and re-tuning of optimum delayed feedback vibration absorber. AIAA J Guid Control Dyn 23(6):961–970

Jalili N, Olgac N (2000b) A sensitivity study of optimum delayed feedback vibration absorber. ASME J Dyn Sys Measur Cont 122:314–321

Jalili N, Esmailzadeh E (2001) Optimum active vehicle suspensions with actuator time delay. ASME J Dyn Syst Measur Control 123:54–61

Jalili N (2001a) An infinite dimensional distributed base controller for regulation of flexible robot arms. ASME J Dyn Sys, Measur Cont 123(4):712–719

Jalili N (2001b) Semi-active suspension systems, chapter 12 of the mechanical systems handbook: Modeling, measurement and control, CRC Press LLC, ISBN/ISSN: 0-849385962, 12:197–220

Jalili N, Esmailzadeh E (2002) Adaptive-passive structural vibration attenuation using distributed absorbers. J Multi-body Dyn 216:223–235

Jalili N, Dawson DM, Carroll D (2002a) Next generation actuators utilizing functional nanotube composites. Proceedings of the 2002 international mechanical engineering congress and exposition (IMECE'02), Symposium on nanocomposite materials and structures, New Orleans, LA, Nov

Jalili N, Wagner J, Dadfarnia M (2002b) Piezoelectric driven ratchet actuator mechanism for automotive engine valve applications. Proceedings of 8th mechatronics forum international conference – mechatronics 2002, Enschede, Netherlands, June

Jalili N, Wagner J, Dadfarnia M (2003) A piezoelectric driven ratchet actuator mechanism with application to automotive engine valves. Int J Mechatron. 13:933–956.

Jalili N, Esmailzadeh E (2003) A nonlinear double-winged adaptive neutralizer for optimum structural vibration suppression. J Comm Nonlinear Sci Num Simul 8(2):113–134

Jalili N (2003) Nanotube-based actuator and sensor paradigm: conceptual design and challenges. Proceedings of 2003 ASME international mechanical engineering congress and exposition, Washington, DC

Jalili N, Knowles DW (2004) Structural vibration control using an active resonator absorber: modeling and control implementation. Smart Mater Struct 13(5):998–1005

Jalili N, Laxminarayana K (2004) A review of atomic force microscopy imaging systems: Application to molecular metrology and biological sciences. Mechatronics 14:907–945

Jalili N, Dadfarnia M, Dawson DM (2004) A fresh insight into the microcantilever-sample interaction problem in non-contact atomic force microscopy. ASME J Dyn Sys Measur Cont 126(2):327–335

Jalili N, Esmailzadeh E (2005) Vibration control, chapter 23 of the vibration and shock handbook, CRC Press LLC, ISBN/ISSN: 0-84931580, 23:1047–1092

Jalili N, Wagener EH, Ballato JM, Smith DW (2005) Electroactive polymeric composite materials incorporating nanostructures, US Provisional Application Serial No. 60/685,789 (filed May 31, 2005)

Jensenius H, Thaysen J, Rasmussen AA, Veje LH, Hansen O, Boisen A (2001) A microcantilever-based alcohol vapor sensor-application and response model. Appl Phys Lett 76(18):2615–2617

Ji H-F, Hansen KM, Hu Z, Thundat T (2001) Detection of pH variation using modified microcantilever sensors. Sens Actuators B-Chem 72(3):233–238

Jiang Q, Kuang ZB (2004) Stress analysis in two dimensional electrostrictive material with an elliptic rigid conductor. Eur J Mech A/Solids 23:945–956

Jin L, Bower C, Zhou O (1998) Alignment of carbon nanotubes in a polymer matrix by mechanical stretching. Appl Phys Lett 73(9):1197–1199

Jones L, Gracia E, Waites H (1994) Self-sensing control as applied to a PZT stack actuator used as a micropositioner. Smart Mater Struct 3:147–156

Jones RM (1965) Mechanics of composite materials. Scientific Publishers, Inc. Cambridge MA

Kajiwara K, Hayatu M, Imaoka S, Fujita T (1997) Application of large-scale active microvibration control system using piezoelectric actuators to semiconductor manufacturing equipment. Proceedings of SPIE, vol 3044. Bellingham, WA, pp 258–269

Kallio P, Koivo HN (1995) Microtelemanipulation: a survey of the application areas. Proceedings of the international conference on recent advances in mechatronics, ICRAM'95, Istanbul, Turkey, Aug, pp 365–372

Kaqawa Y, Wakatsuki N, Takao T, Yoichi T (2006) A tubular piezoelectric vibrator gyroscope. IEEE Sens J 6:325–330

Kellogg RA, Russell AM, Lograsso TA, Flatau AB, Clark AE, Wun-Fogle M (2004) Tensile properties of magnetostrictive iron-gallium alloys. Acta Materialia 52:5043–5050

Kim P, Lieber CM (1999) Nanotube nanotweezers. Science 286:2148

Kirk DE (1970) Optimal control theory. Prentice-Hall, Englewood Cliffs NJ

Kirstein K-U, Li Y, Zimmermann M, Vancura C, Volden T, Song WH, Lichtenberg J, Hierlemannn A (2005) Cantilever-based biosensors in CMOS technology. Proceedings of the design, automation and test in Europe conference and exhibition (DATE'05):1340–1341

Kleindiek S Nanorobots for material science, biology and micro mounting. Technical Report from Kleindiek Nanotechnik, http://www.nanotechnik.com/mm3a.html

Knowles D, Jalili N, Khan T (2001) On the nonlinear modeling and identification of piezoelectric inertial actuators. Proceedings of 2001 international mechanical engineering congress and exposition (IMECE'01), New York, NY, Nov

Ko F, Gogotsi Y, Ali A, Naguib N, Ye H, Yang G, Li C, Willis P (2003) Electrospinning of continuous nanotube-filled nanofiber yarns. Adv Mater 15(14):1161

Kong J et al (2000) Nanotube molecular wires as chemical sensors. Science 287:622

Korenev BG, Reznikov LM (1993) Dynamic vibration absorbers: theory and technical applications. Wiley, Chichester, England

Kota S, Hetrick J, Li Z, Saggere L (1999) Tailoring unconventional actuators using compliant transmissions: design methods and applications. IEEE/ASME Trans Mechatron 4(4)

Krasnosel'skii MA, Pokrovskii AV (1989) Systems with hysteresis. Springer, New York

Krejci P, Kuhnen K (2001) Inverse control of systems with hysteresis and creep. IEE Proc Control Theory Appl 148:185–192

Kuhnen K, Janocha H (2001) Inverse feedforward controller for complex hysteretic nonlinearities in smart-material systems. Control Intell Syst 29:74–83

Kunstler W, Wegener M, Seib M, Gerhard-Multhaupt R (2001) Preparation and assessment of piezo- and pyroelectric poly(vinylidene fluoride-hexafluoropropylene) copolymer films. Appl Cond Matter Phys A73:641–645

Lam DCC, Yang F, Chong ACM, Wang J, Tong P (2003), Experiments and theory in strain gradient elasticity. J Mech Phys Solids 51:1477–1508

Lang SB (1982) Sourcebook of pyroelectricity. Gordon and Breach, New York

Lang HP, Berger R, Battiston F, Ramseyer J-P, Meyer E, Andreoli C, Brugger J, Vettiger P, Despont M, Mezzacasa T, Scandella L, Güntherodt H-J, Gerber Ch, Gimzewski JK (1998) A chemical

sensor based on a micromechanical cantilever array for the identification of gases and vapors. Appl Phys A 66(7):S61–S64
Law WW, Liao W-H, Huang J (2003) Vibration control of structures with self-sensing piezoelectric actuators incorporating adaptive mechanism. Smart Mater Struct 12:720–730
Laxminarayana K, Jalili N (2005) Functional nanotube-based textiles: pathway to next generation fabrics with enhanced sensing capabilities. Textile Res J 75(9):670–680
Lee CJ et al (1999) Synthesis of uniformly distributed carbon nanotubes on a large area of Si substrates by thermal chemical vapor deposition. Appl Phys Lett 75:1721
Lee D, Ono T, Esashi M (2000) High-speed imaging by electro-magnetically actuated probe with dual spring. J Microelectromech Syst 9(4):419–424
Lee FS (1999) Modeling of actuator systems using multilayer electrostrictive materials. Proceedings of 1999 IEEE International Conference of Control Applications 0-7803-5446-X/99
Lee H-C, Park J-H, Park Y-H (2007) Development of shunt type ohmic RF MEMS switches actuated by piezoelectric cantilever. Sens Actuators A 136:282–290
Lee J, Hwang K, Park J (2005a) Immunoassay of prostate-specific antigen (PSA) using resonant frequency shift of piezoelectric nanomechanical microcantilever. Biosens Bioelectron 20:2157
Lee JH, Yoon KH, Hwang KS, Park J, Ahn S, Kim TS (2004) Label free novel electrical detection using micromachined PZT monolithic thin film cantilever for the detection of C-reactive protein. Biosens Bioelectron 20:269–275
Lee JH, Hwang KS, Park J, Yoon KH, Yoon DS, Kim TS (2005b) Immunoassay of prostate-specific antigen (PSA) using resonant frequency shift of piezoelectric nanomechanical microcantilever, Biosens Bioelectron 20:2157–2162
Lee TH, Ge SS, Wang ZP (2001) Adaptive robust controller design for multi-link flexible robots. Mechatronics 11(8):951–967
Lee-Glauser GJ, Ahmadi G, Horta LG (1997) Integrated passive/active vibration absorber for multistory buildings. ASCE J of Struc Eng 123(4):499–504
Leo DJ (2007) Smart material systems: analysis, design and control. Wiley, New York
Lining S, Changhai R, Weibin R, Liguo C, Kong M (2004) Tracking control of piezoelectric actuator based on a new mathematical model. J Micromech Microeng 14:1439–1444
Liu Z, Jalili N, Dadfarnia M, Dawson DM (2002) Reduced-order observer based piezoelectric control of flexible beams with translational base. Proceedings of the 2002 international mechanical engineering congress and exposition (IMECE'02), New Orleans, Louisiana, Nov
Liu W, Montana V, Chapman ER, Mohideen U, Parpura, V (2003) Botulinum toxin type B micromechanosensor. Proc Nat Acad Sci USA 100(23):13621–13625
Lockhart DJ, Winzeler EA (2000) Genomics, gene expression and DNA arrays. Nature 405: 827–836
Lopez SJ, Miribel CP, Montane E, Puig VM, Bota SA, Samitier J, Simu U, Johansson S (2001) High accuracy piezoelectric-based microrobot for biomedical applications. IEEE Symp Emer Technol Factory Autom ETFA 2:603–609
Lord Corporation, http://www.rheonetic.com
Lou ZH (1993) Direct strain feedback control of flexible robot arms: New theoretical and experimental results. IEEE Trans Automat Control 38(11):1610–1622
Lu KL, Lago RM, Chen YK, Green MLH, Harris PF, Tsang SC (1996) Mechanical damage of carbon nanotubes by ultrasound. Carbon, 34:814–816
Lu P, Shen F, O'Shea SJ, Lee KH, Ng TY (2001) Analysis of surface effects on mechanical properties of microcantilevers. Mater Phys Mech 4:51–55
Luo ZH, Kitamura N, Guo BZ (1995) Shear force feedback control of flexible robot arms. IEEE Trans Rob Autom 11(5):760–765
Mahmoodi SN, Khadem SE, Jalili N (2006) Theoretical development and closed-form solution of nonlinear vibrations of a directly excited nanotube-reinforced composite cantilever beam. Arch Appl Mech 75 153–163
Mahmoodi SN, Afshari M, Jalili N (2008a) Nonlinear vibrations of piezoelectric microcantilevers for biologically-induced surface stress sensing. J Commun Nonlinear Sci Numer Simul 13:1964–1977

Mahmoodi SN, Jalili N, Daqaq MF (2008b) Modeling, nonlinear dynamics and identification of a piezoelectrically-actuated microcantilever sensor. IEEE/ASME Trans Mechatron 13(1):1–8
Mahmoodi SN, Jalili N (2008) Coupled flexural-torsional nonlinear vibrations of piezoelectrically-actuated microcantilevers with application to friction force microscopy. ASME J Vib Acoust 130(6) 061003:1–10
Mahmoodi SN, Jalili N (2007) Nonlinear vibrations and frequency response analysis of piezoelectrically-driven microcantilevers. Int J Non-Linear Mech 42(4):577–587
Majumdar A, Lai J, Chandrachood M, Nakabeppu O, Wu Y, Shi Z (1995) Thermal imaging by atomic force microscopy using thermocouple cantilever probes. Rev Sci Instrum 66:3584–3592
Malatkar P, Nayfeh AH (2002) Calculation of the jump frequencies in the response of SDOF non-linear systems. J Sound Vib 254(5):1005–1011
Malvern LE (1969) Introduction to the mechanics of a continuous medium. Prentice-Hall, Englewood Cliffs, NJ
Margolis D (1998) Retrofitting active control into passive vibration isolation systems. ASME J Vib Acoust 120:104110
Marquez HJ (2003) Nonlinear control system: Analysis and design, Wiley, New York
Matsunaka T et al (1988) Porous piezoelectric ceramic transducer for medical ultrasonic applications. Ultras Symp Proc 2:681–684
Matyas J (1965) Random optimization. Autom Remote Control 22:246–253
Mayergoyz I (2003) Mathematical models of hysteresis and their applications. Elsevier, New York
McFarland AW, Poggi MA, Doyle MJ, Bottomley LA, Colton JS (2005) Influence of surface stress on the resonance behavior of microcantilevers. Appl Phys Lett 87:053505
McKendry R, Zhang J, Arntz Y, Strunz T, Hegner M, Lang HP, Baller MK, Certa U, Meyer E, Guntherodt H-J, Gerber C (2002) Multiple label-free biodetection and quantitative DNA-binding assays on a nanomechanical cantilever array. Proc Nat Acad Sci USA 99(15):9783–9788
Meirovitch L (1986) Elements of vibrations analysis, 2nd edn. McGraw-Hill, Inc
Meirovitch L (1997) Principles and techniques of vibrations. Prentice Hall, Inc
Meirovitch L (2001) Fundamentals of vibrations, McGraw Hill
Meldrum DR (1997) A biomechatronic fluid-sample-handling system for DNA processing. IEEE/ASME Trans Mechatron 2:99–109
Mele EJ, Kral P (2002) Electric polarization of heteropolar nanotubes as a geometric phase. Phys Rev Lett 88:568031–568034
Mele EJ, Kral P (2001) Quantum geometric phases in molecular nanotubes, abstracts of third international conference on nanotechnology in carbon and related materials, Sussex, UK, Aug
Micro System Analyzer Manual MSA-400, Polytec Inc., www.polytec.com.
Millar AJ, Howell LL, Leonard JN (1996) Design and evaluation of complaint constant-force mechanisms. Proceedings of the 1996 ASME design engineering technical conference, 96-DETC/MECH, pp 1209
Mindlin RD (1961) On the equations of motion of piezoelectric crystals. Problems of Continuum Mechanics, NI Muskhelishvili 70th Birthday Vol, SIAM Philadelphia, 70:282–290
Miyahara K, Nagashima N, Ohmura T, Matsuoka S (1999) Evaluation of mechanical properties in nanometer scale using AFM-based nanoindentation tester. Nanostruct Mater 12:1049–1052
Moheimani SOR, Fleming AJ (2006) Piezoelectric transducers for vibration control and damping, Springer, New York
Munch WV, Thiemann U (1991) Pyroelectric detector array with PVDF on silicon integrated circuit. Sensor Actuator 25–27:167–172
Nagakawa Y, Shafer R, Guntherodt H (1998) Picojoule and submillisecond calorimetry with micromechanical probes. Appl Phys Lett 73:2296
Nagashima N, Matsuoka S, Miyahara K (1996) Nanoscopic hardness measurement by atomic force microscope. JSME Int J Series A Mech Mater Eng 39:456–462
Nakamura K, Ogura H, Maeda S, Sangawa U, Aoki S, Sato T (1995) Evaluation of the microwobble motor fabricated by concentric build-up process. Proc MEMS:374–379
Nayfeh AH, Nayfeh JF, Mook DT (1992) On methods for continuous systems with quadratic and cubic nonlinearities. Nonlinear Dynam 3:145–162

Nayfeh AH, Mook DT (1979) Nonlinear Oscillations, Wiley, New Jersey
Nayfeh AH, Pai PF (2004) Linear and nonlinear structural mechanics. Wiley, Hoboken, New Jersey
Nayfeh AH (1973) Perturbation methods, Wiley, New Jersey
Newcomb C, Filnn I (1982) Improving linearity of piezoelectric ceramic actuators. Electron Lett 18:442–444
Oden PI, Chen GY, Steele RA, Warmack RJ, Thundat T (1999) Viscous drag measurements utilizing microfabricated cantilevers. Appl Phys Lett 68(26):3814–3816
Olgac N, Holm-Hansen B (1994) Novel active vibration absorption technique: delayed resonator. J Sound Vib 176:93–104
Olgac N, Jalili N (1998) Modal analysis of flexible beams with delayed-resonator vibration absorber: Theory and experiments. J Sound Vib 218(2):307–331
Olgac N (1995) Delayed resonators as active dynamic absorbers, United States Patent # 5431261
Olgac N, Elmali H, Vijayan S (1996) Introduction to dual frequency fixed delayed resonator (DFFDR). J Sound Vib 189:355–367
Olgac N, Elmali H, Hosek M, Renzulli M (1997) Active vibration control of distributed systems using delayed resonator with acceleration feedback. ASME J Dyn Syst Measur Control 119:380–389
Onran AG, Degertekin AG, Hadimioglu B, Sulchek T, Quate CF (2002) Actuation of atomic force microscope cantilevers in fluids using acoustic radiation pressure. Fifteenth IEEE international micro electro mechanical systems conference, Las Vegas, Nevada
Pancharal P, Wang ZL, Ugarte D, Heer WD (1999) Electrostatic deflections and electromechanical resonances of carbon nanotubes. Science 283:1513
Park KH, Lee JH, Kim SH, Kwak YK (1995) High speed micro positioning system based on coarse/fine pair control. Mechatronics 5(6):645–663
Pei J, Tian F, Thundat T (2004) Glucose biosensor based on the microcantilever. Anal Chem 76:3194
Perazzo T, Mao M, Kwon O, Majumdar A, Varesi JB, Norton P (1999) Infrared vision using uncooled micro-optomechanical camera. Appl Phys Lett 74 (23):3567–3569
Petek NK, Romstadt DL, Lizell MB, Weyenberg TR (1995) Demonstration of an automotive semi-active suspension using electro-rheological fluid. SAE Paper No. 950586
Piezo Film Sensors, Technical Manual (1999) Measurement Specialties Inc, www.msiusa.com
Ping G, Musa J (1997) Generalized Preisach model for hysteresis nonlinearity of piezoceramic actuators. Precision Eng 20:99–111
Piquette JC, Forsythe SE (1998) Generalized material model for lead magnesium niobate (PMN) and an associated electromechanical equivalent circuit. J Acoust Soc Am 104
Porter SG (1981) A brief guide to pyroelectricity. Gordon and Breach, New York
Preisach FZ (1935) Physics 94:277
Preumont A (2002) Vibration control of active structures: An introduction, 2nd edn. Kluwer Academic Publishers, Dordrecht
Puksand H (1975) Optimum conditions for dynamic vibration absorbers for variable speed systems with rotating and reciprocating unbalance. Int J Mech Eng Educ 3:145–152
Rabe U, Hirsekorn S, Reinstädtler M, Sulzbach T, Lehrer Ch, Arnold W (2007) Influence of the cantilever holder on the vibrations of AFM cantilevers. Nanotechnology 18:044008
Rajoria H, Jalili N (2005) Passive vibration damping enhancement using carbon nanotube-epoxy reinforced composites. Comp Sci Technol 65(14):2079–2093
Ramaratnam A (2004) Semi-active vibration control using piezoelectric-based switched stiffness. Master's Thesis, Department of Mechanical Engineering, Clemson University
Ramaratnam A, Jalili N (2006a) A switched stiffness approach for structural vibration control: Theory and real-time implementation. J Sound Vib 291(1–2):258–274
Ramaratnam A, Jalili N (2006b) Reinforcement of piezoelectric polymers with carbon nanotubes: pathway to development of next-generation sensors. J Intell Mater Syst Struct 17(3):199–208
Ramaratnam A, Jalili N (2004) Novel carbon nanotube reinforced electro-active polymer sensors and actuators for vibration control. Proceedings of the 2004 ASME international mechanical engineering congress and exposition, IMECE2004-60794, Anaheim, CA

Ramaratnam A, Jalili N, Rajoria H (2004a) Development of a novel strain sensor using nanotube-based materials with applications to structural vibration control. Proceedings of the international society for optical engineering, sixth international conference on vibration measurements by laser techniques: advances and applications, vol 5503. Ancona, Italy, pp 478–485

Ramaratnam A, Jalili N, Dawson DM (2004b) Semi-active vibration control using piezoelectric-based switched stiffness. Proceedings of American control conference, Boston, MA

Ramaratnam A, Jalili N, Grier M (2003) Piezoelectric vibration suppression of translational flexible beams using switched stiffness, Proceedings of 2003 international mechanical engineering congress and exposition (IMECE 2003-41217), Washington DC

Rangelow IW, Grabiec P, Gotszalk T, Edinger K (2002) Piezoresistive SXM Sensors, Surf Interface Anal 33:59–64

Rao SS (1995) Mechanical vibrations, 3rd edn. Addison-Wesley Publishing Company

Rao SS (2007) Vibration of continuous systems, Wiley, Hoboken NJ

Rappe AK, Casewit CJ, Colewell KS, Goddard III WA, Skiff WM (1992) UFF, a full periodic table force field for molecular mechanics and molecular dynamics simulations. J Am Chem Soc 114(25):10024–10035

Ren Q, Zhao Y-P (2004) Influence of surface stress on frequency of microcantilever-based biosensors. Microsyst Technol 10:307–314

Ren W, Masys AJ, Yang G, Mukherjee BK (2002) Nonlinear strain and DC bias induced piezoelectric behavior of electrostrictive lead magnesium niobate-lead titanate ceramics under high electric fields. J Phys D, Appl Phys 35:1550–1554

Renzulli M, Ghosh-Roy R, Olgac N (1999) Robust control of the delayed resonator vibration absorber. IEEE Trans Control Syst Technol 7(6):683–691

Richard D, Guyomar D, Audigier, Ching G (1999), Semi-passive damping using continuous switching of a piezoelectric device, smart structures and materials. Passive Damping Isolation 3672:104–111

Rogers L, Manning, Jones M, Sulchek T, Murray K, Beneshott N, Adams J (2003) Mercury vapor detection with self-sensing, resonating, piezoelectric cantilever. Rev Sci Instrum 74:4899

Saeidpourazar R, Jalili N (2008a) Towards fused vision and force robust feedback control of nanorobotic-based manipulation and grasping. mechatronics. Int J 18:566–577

Saeidpourazar R, Jalili N (2008b) Nano-robotic Manipulation using a RRP nanomanipulator: Part A – Mathematical modeling and development of a robust adaptive driving mechanism. J Appl Math Comput 206:618–627

Saeidpourazar R, Jalili N (2008c) Microcantilever-based force tracking with applications to high-resolution imaging and nanomanipulation IEEE Trans Ind Electron 55(11):3935–3943

Saeidpourazar R, Jalili N (2008d) Nano-robotic manipulation using a RRP nanomanipulator: Part B Robust Control of Manipulator's Tip using Fused Visual Servoing and Force Sensor Feedbacks. J Appl Math Comput 206:628–642

Saeidpourazar R, Jalili N (2009) Towards microcantilever-based force sensing and manipulation: modeling, control development and implementation. Int J Robotics Res 28(4):464–483

Salah M, McIntyre M, Dawson DM, Wagner JR (2007) Robust tracking control for a piezoelectric actuator. Proceedings of the American Control Conference, New York, NY

Salapaka S, Sebastian A, Cleveland JP, Salapaka MV (2002) High bandwidth nano-positioner: a robust control approach. Rev Sci Instrum 73:3232–3241

Salehi-Khojin A, Jalili N (2008a) A comprehensive model for load transfer in nanotube reinforced piezoelectric polymeric composites subjected to electro-thermo-mechanical loadings. J Composites Part B Eng 39(6):986–998

Salehi-Khojin A, Jalili N (2008b) Buckling of boron nitride nanotube reinforced piezoelectric polymeric composites subject to combined electro-thermo-mechanical loadings. Composites Sci Technol 68(6):1489–1501

Salehi-Khojin A, Zhong WH (2007a) Enthalpy relaxation of reactive graphitic nanofibers reinforced epoxy. J Mater Sci 42:6093

Salehi-Khojin A, Zhong WH (2007b) Thermal-mechanical properties of a graphitic-nanofibers reinforced epoxy. J Nanosci Nanotech 7:898

Salehi-Khojin A, Bashash S, Jalili N (2008) Modeling and experimental vibration analysis of nanomechanical cantilever active probes. J Micromech Microeng 18, 085008:1–11
Salehi-Khojin A, Hosseini MR and Jalili N (2009a) Underlying mechanics of active nanocomposites with tunable properties. Composites Sci Technol 69:545–552
Salehi-Khojin A, Bashash S, Jalili N, Müller M, Berger R (2009b) Nanomechanical cantilever active probesfor ultrasmall mass detection. J Appl Phys 105(1):1–8
Sastry S, Bodson M (1989) Adaptive control: stability, convergence, and robustness, Englewood Cliffs, NJ
Sato T (1994) Step from 2- to 3-D process break grounds for microfabricated wobble motors. J Electron Eng 31(332):67–70
Savran CA, Burg TP, Fritz J, Manalis SR (2003) Microfabricated mechanical biosensor with inherently differential readout. Appl Phys Lett 83(20):1659
Schell-Sorokin AJ, Tromp RM (1990) Mechanical stress in (Sub)monolayer epitaxial films. Phys Rev Lett 64(9):1039–1042
Schitter G, Stemmer A (2004) Identification and open-loop tracking control of a piezoelectric tube scanner for high-speed scanning probe microscopy. IEEE Trans Control Syst Technol 12:449–454
Schmoeckel F, Fahlbusch S, Seyfried J, Buerkle A, Fatikow S (2000) Development of a microrobot-based micromanipulation cell in scanning electron microscope (SEM). Proc SPIE 4194:13-20, Boston, MA
Sennett M, Welsh E, Wright JB, Li WZ, Wen JG, Ren ZF (2003) Dispersion and alignment of carbon nanotubes in polycarbonate. Appl Phys A76:111–113
Seoul C, Kim Y, Baek C (2003) Electrospinning of poly(vinylidene fluoride)/dimethylformamide solutions with carbon nanotubes. J Polymer Sci Part B: Polymer Phys 41:1572
Sepaniak M, Datskos P, Lavrik N, Tipple C (2002) Microcantilever transducers: A new approach in sensor technology. Anal Chem 74(21):568A
Shaoze Y, Fuxing Z, Zhen Q, Shizhu W (2006) A 3-DOFs mobile robot driven by a piezoelectric actuator. Smart Mater Struct 15:N7–N13
Shaw J (1998) Adaptive vibration control by using magnetostrictive actuators. J Intell Mater Syst Struct 9:87–94
Shen Z, Shih WY, Shih W-H (2006) Self-exciting, self-sensing PbZr0:53Ti0:47O3=SiO2 piezoelectric microcantilevers with Femtogram/Hertz sensitivity. Appl Phys Lett 89:023506
Shi L, Plyasunov S, Bachtold A, McEuen PL, Majumdar A (2000) Scanning thermal microscopy of carbon nanotubes using batch-fabricated probes. Appl Phys Lett 77:4295–4297
Shimizu Y, Moriyoshi Y, Tanaka H (1999) Boron nitride nanotubes, webs, and coexisting amorphous phase formed by plasma jet method. Appl Phys Lett 76:929
Shuttleworth R (1950) The surface tension of solids. Proc Phys Soc 63(5):444–457
Sinha A (1988) Optimum vibration control of flexible structures for specified modal decay rates. J Sound Vib 123(1):185–188
Slotine JJ, Sastry SS (1983) Tracking control of non-linear systems using sliding surface with application to robot manipulators. Int J Control 38:465–492
Slotine JJ (1984) Sliding controller design for nonlinear systems. Int J Control 40:421–434
Slotine JJE, Li W (1991) Applied nonlinear control, Prentice Hall
Smith RC (2005) Smart material systems: Model development, Society for Industrial and Applied Mathematics, Philadelphia
Sodano HA, Inman DJ, Park G (2005) Comparison of piezoelectric energy harvesting devices for recharging batteries. J Intell Mater Syst Struct 16:799–807
Sodano HA, Park G, Inman DJ (2004) An investigation into the performance of macro-fiber composites for sensing and structural vibration applications. Mech Syst Signal Process 18(3):683–697
Soong TT, Constantinou MC (1994) Passive and active structural control in civil engineering, Springer, Wien and New York NY

Spencer BF, Yang G, Carlson JD, Sain MK (1998) Smart dampers for seismic protection of structures: A full-scale study. Proceedings of 2nd world conference on structure control, Kyoto, Japan, June 28–July 1

Spinks GM, Wallace GG, Carter C, Zhou D, Fifield LS, Kincaid C, Baughman RH (2001) Conducting polymer, carbon nanotube and hybrid actuator materials. Proc SPIE 4329:199–208

Srinivasan, MacFarland (2001) Smart structures: analysis and design, University Press, Cambridge

Stachowiak JC, Yue M, Castelino K, Chakraborty A, Majumdar A (2006) Chemomechanics of surface stresses induced by DNA hybridization. Langmuir 22:263–268

Stepanenko Y, Su CY (1998) Intelligent control of piezoelectric actuators, Proceedings of 37th IEEE conference on decision and control, vol 4. pp 4234–4239

Stoney GG (1909) The tension of metallic films deposited by electrolysis. Proc R Soc Lond A 82:172–175

Stroscio JA, Kaiser WJ (1993) Scanning tunneling microscopy. Academic Press, pp 149–150

Su CY, Stepanenko Y, Svoboda J, Leung TP (2000) Robust adaptive control of a class of nonlinear systems with unknown backlash-like hysteresis. IEEE Trans Automatic Control 45:2427–2432

Su M, Li S, Dravid VP (2003) Microcantilever resonance-based DNA detection with nanoparticle probes. Appl Phys Lett 82(20):3562

Suleman (2001) Smart structures: Applications and related technologies, Edited, Springer, New York

Sun JQ, Jolly MR, Norris MA (1995) Passive, adaptive, and active tuned vibration absorbers – A survey. ASME Trans, Special 50th Anniversary, Design Issue. 117:234–242

Susuki Y (1996) Novel microcantilever for scanning thermal imaging microscopy. Jpn J Appl Phys 35:L352–L354

Takagi T (1996) Recent research on intelligent materials. J Intell Mater Syst Struct 7:346–357

Takaway T, Fukudaz T, Takadaz T (1997) Flexural – torsion coupling vibration control of fiber composite cantilevered beam by using piezoceramic actuators. Smart Mater Struct 6:477–484

Takayuki S, Kazuya U, Eiji M, Shiro S (2004) Fabrication and characterization of diamond AFM probe integrated with PZT thin film sensor and actuator. Sens Actuators A Phys 114:398–405

Tans SJ, Verschueren RM, Dekker C (1998) Room-temperature transistor based on a single carbon nanotube. Nature 393:40

Tao G, Kokotovic PV (1996) Adaptive control of systems with actuator and sensor nonlinearities, Wiley, New Jersey

Thomson WT, Dahleh M (1998) Theory of vibration with applications, 5th edn. Prentice Hall Inc

Thundat T, Warmack RJ, Chen GY, Allison DP (1994) Thermal and ambient-induced deflections of scanning force microscope cantilevers. Appl Phys Lett 64:2894–2898

Thundat T, Sharp S, Fisher W, Warmack R, Wachter E (1995) Micromechanical radiation dosimeter. Appl Phys Lett 66:1563

Tian F, Pei J, Hedden D, Brown G, Thundat T (2004) Observation of the surface stress induced in microcantilevers by electrochemical redox processes. Ultramicroscopy 100:217

Tomikawa Y, Okada S (2003) Piezoelectric angular acceleration sensor. Proc IEEE Ultras Symp 2:1346–1349

Townsend PH, Barnett DM, Brunner TA (1987) Elastic relationship in layered composite media with approximation for the case of thin films on a thick substrate. J Appl Phys 62(11): 4438–4444

Tse F, Morse IE, Hinkle RT (1978) Mechanical vibrations, theory and applications, 2nd edn. Allyn and Bacon Inc

Tutorial: Piezoelectrics in positioning contents, Physik Instrumente manual, www.pi.ws

Tzen JJ, Jeng SL, Chieng WH (2003) Modeling of piezoelectric actuator for compensation and controller design. Precis Eng 27:70–76

Tzou HS, Anderson GL (eds) (1992) Intelligent structural systems, Kluwer Academic Publishers

Tzou HS, Ye R (1996) Pyroelectric and thermal strain effects in piezoelectric (PVDF and PZT) devices. Mech Syst Signal Pr 10:459–479

Tzou HS, Chai WK, Arnold SM (2003) Micro-structronics and control of hybrid electrostrictive/piezoelectric thin shells. ASME International Mechanical Engineering Congress, Symposium on Adaptive Structures and Material Systems. Washington DC, November 16–21

Tzou HS, Lee HJ, Arnold SM (2004) Smart materials, precision sensors/actuators, smart structures, and structronic systems. Mech of Adv Mat Struc 11:367–393

Uhea S, Tomikawa Y (1993) Ultrasonic motors: Theory and application, Oxford University Press, UK

Utkin VI (1977) Variable structure systems with sliding modes. IEEE Trans Automat Control 22:212–222

Vaccarini L, Goze C, Henrard L, Hernandez E, Bernier P, Rubio A (2000) Mechanical and electronic properties of carbon and boron nitride nanotubes. Carbon 38:1681–1690

Vishnewsky W, Glob R (1996) Piezoelectric rotary motor. Proc Actuator 96:245–248, Berman, Germany

Visintin A (1994) Differential models of hysteresis, Springer, Berlin, Heidelberg

Volkert CA, Minor AM (2007) Focused ion beam microscopy and micromachining. MRS Bull 32:389

Vora K, Bashash S, Jalili N (2008) Modeling and forced vibration analysis of rod-like solid-state actuators. Proceedings of the 2008 ASME Dynamic Systems and Control Conference (DSCC'08), Ann Arbor, MI (Oct 20–22, 2008)

Wachter EA, Thundat T (1995) Micromechanical sensors for chemical and physical measurements. Rev Sci Instrum 66(6):3662–3667

Wallerstein DV (2002) A variational approach to structural analysis. Wiley, New York, NY

Wang KW, Kim YS, Shea DB (1994) Structural vibration control via electrorheological-fluid-based actuators with adaptive viscous and frictional damping. J Sound Vib 177(2):227–237

Wang QH et al (1998) A nanotube-based field-emission flat panel display. Appl Phys Lett 72:2912

Warburton GB, Ayorinde EO (1980) Optimum absorber parameters for simple systems. Earthquake Eng Struc Dyn 8:197–217

Washington G (2004) Class notes on introduction to smart materials and intelligent systems, Ohio State University, Columbus, OH

Weigert S, Dreier M, Hegner M (1996) Frequency shifts of cantilevers vibrating in various media. Appl Phys Lett 69(19):2834–2836

Weiss KD, Carlson JD, Nixon DA (1994) Viscoelastic properties of magneto- and electro-rheological fluids. J Intell Mater Syst Struct 5:772–775

Wilder JWG et al (1998) Electronic structure of atomically resolved carbon nanotubes. Nature 39:6662

Wilkie WK, Bryant RG, High JW, Fox RL, Hellbaum RF, Jalink A, Little BD, Mirick PH (2000) Low-cost piezocomposite actuator for structural control applications. Proceedings of 7th SPIE international symposium on smart structures and materials, Newport Beach, CA

Wu G, Ji H, Hansen K, Thundat T, Datar R, Cote R, Hagan MF, Chakraborty AK, Majumdar A (2001) Origin of nanomechanical cantilever motion generated from bimolecular interactions. Proc Natl Acad Sci 98:1560–1564

Wun-Fogle M, Restorff JB, Clark AE (2006) Magnetomechanical coupling in stress-annealed Fe–Ga (Galfenol) alloys. IEEE Trans Magn 42(10)

Wun-Fogle M, Restorff JB, Clark AE, Dreyer E, Summers E (2005) Stress annealing of Fe–Ga transduction alloys for operation under tension and compression. J Appl Phys 97:10M301

Xian B, de Queiroz MS, Dawson DM, McIntyre ML (2003) Output feedback variable structure control of nonlinear mechanical systems, Proceedings of IEEE conference on decision and control, Hawaii

Xie WC, Lee HP, Lim SP (2003) Nonlinear dynamic analysis of MEMS switches by nonlinear modal analysis. Nonlinear Dyn 31:243–256.

Xing S (2002) Novel piezoelectric and pyroelectric materials: PVDF copolymer-carbon nanotube composites, Master's Thesis, Department of Material Science and Engineering, Clemson University

Xu Y, Meckl PH (2004) Time-optimal motion control of piezoelectric actuator: STM application, Proceedings of the 2004 American control conference, vol 5. pp 4849–4854
Yang J (2005) An Introduction to the theory of piezoelectricity, Springer, Berlin, Heidelberg
Yang JS, Fang HY (2003) A piezoelectric gyroscope based on extensional vibrations of rods. Int J Appl Electromagn Mech 17:289–300
Yang M, Zhang X, Vafai K, Ozkan CS (2003) High sensitivity piezoresistive cantilever design and optimization for analyte-receptor binding. J Micromech Microeng 13:864–872
Yang Y, Ji HF, Thundat T (2003) Nerve agents detection using a Cu/lcysteine bilayercoated microcantilever. J Am Chem Soc 125(20):1124–1125
Yue M, Lin H, Dedrick DE, Satyanarayana S, Majumdar A, Bedekar AS, Jenkins JW, Sundaram S (2004) A 2-D microcantilever array for multiplexed biomolecular analysis. J Microelectromech Syst 13(2):290–299
Yuh J (1987) Application of discrete-time model reference adaptive control to a flexible single-link robot. J Robotic Sys 4:621–630
Zhang J, Feng H (2004) Antibody-immobilized microcantilever for the detection of Escherichia coli. Anal Sci 20:585
Zhang W, Meng G (2005) Nonlinear dynamical system of micro-cantilever under combined parametric and forcing excitations in MEMS. Sens Actuators A 119:291
Zhang Y, Ji H-F (2004) A pH sensor based on a microcantilever coated with intelligent hydrogel. Instrum Sci Technol 34:361
Zhi C et al (2005) Characteristics of boron nitride nanotube–polyaniline composites. Angew Chem Int Ed 44:7929
Zhou J, Li P, Zhang S, Huang Y, Yang P, Bao M, Ruan G (2003) Self-excited piezoelectric microcantilever for gas detection. Microelectronic Eng 69:37
Zhou J, Wen C, Zhang Y (2004) Adaptive backstepping control of a class of uncertain nonlinear systems with unknown backlash-like hysteresis. IEEE Trans Control Syst Technol 49:1751–1757
Zhu G, Ge SS, Lee TH (1997) Variable structure regulation of a flexible arm with translational base. Proceedings of 36th IEEE conference on decision and control, San Diego, CA, pp 1361–1366
Ziegler C (2004) Cantilever-based biosensors. Anal Bioanal Chem 379:946–959
Zurn S, Hsieh M, Smith G, Markus D, Zang M, Hughes G, Nam Y, Arik M, Polla D (2001) Fabrication and structural characterization of a resonant frequency PZT microcantilever. Smart Mater Struct 10:252–263

Index

Active materials, smart structure
  electrostrictive
    constitutive relationship, 125
    relaxor ferroelectrics, 126
  ER fluids, 120–121
  magnetostrictive
    converse effect, 127
    definition, 126
  MR fluids, 121–123
  piezoelectric
    applications, 118–119
    behavior and constitutive models, 116–118
    electricity, 116
  pyroelectric
    common materials, 120
    constitutive model, 119–120
  SMA
    applications, 124
    physical principles and properties, 123–124
Active resonator absorber (ARA)
  application, 238–239
  autotuning proposition
    real-time transfer function, 240
    retuned control parameters, 240–241
    time harmonic function, 241
  characteristic equation, 237
  compensator transfer function, 238
  numerical simulations
    autotuning iteration, 241, 243
    primary system and absorber displacements, 241–242
  stability analysis and parameters sensitivity, 239
Actuated microcantilevers
  DNA detection, 157
  species detection, 156–157
Actuators and sensors
  actuation and sensing mechanism
    macroscopic configurations, 424–425
    materials and methods, 425–426
    PVDF/SWNT thin film, 423–424
  classification, 421
  composites
    forced vibration, 441–446
    free vibration, 436–441
    vibration damping and control, fabrication, 434–436
  conductive plastic, 420–421
  configurations
    axial and laminar actuator, 152
    disadvantages, 153–154
    linear electromechanical constitutive relations, 153
    patch, 154
    stack, 151, 153
  electrical and mechanical properties, 420
  electronic textiles
    CNT-based fabric sensors, 459–461
    concept, 455
    nonwoven CNT fabrication, 455–458
  film sensors fabrication
    copper foils attachment, 427
    experimental setup, procedures, and results, 428–431
    mixture preparation, 426–427
    thin films preparation, 426
  n-layer solid-state, 185
  piezoelectricity
    CNTs property, 422–423
    PVDF copolymers, 421–422
  properties
    d_{31}, 432–433
    film capacitance, 433–434
    Young's Modulus, 432

PZT inertial actuators
displacement, 154–155
parameter identification problem, 156
resonance, 155–156
tunable properties
continuum level elasticity model, 451
interphase zone control, 446–448
molecular dynamic simulations, 448–450
numerical results and, 451–454
AFM. *See* Atomic force microscope
AMM. *See* Assumed mode method
ARA. *See* Active resonator absorber
Assumed mode method (AMM), 102–104
Atomic force microscope (AFM). *See also* Nano-positioning systems, multiple-axis PZT
NMC-based force sensing, 319, 320
non-contact, 318–319
operation and sub-components, 318
vs. STM, 315, 319
Axial configuration, actuator control
controller bandwidth assessment
approximations and tracking results, 258, 259
four-mode model, 257–258
steady-state tracking error comparison, 258, 260
observer design
closed- and open-loop system, 253–254
pole optimal location, 255
state errors, 255, 256
state-space controller/observer diagram, 256
robust state-space development
first- and second-order time derivatives, 259–260
hard switching signum function, 261–262
Lyapunov function, 261
modified state-space equation, 258
phase portrait comparison, 263
sliding mode, 262–263
steady-state error amplitude, 262
state-space controller design
first- and second-order control law, 252–253
simulation results, 253, 254
tracking error, 252
Axial piezoelectric actuators, vibration analysis
equivalent actuation force, 192
forced, 194–195
modal, 193–194
numerical simulations, 195–198

Bar longitudinal vibration
boundary conditions, 73–74
Lagrangian expression, 71
potential energy, 70
spatial integration, 72
Beam-absorber-exciter system
configuration, 245
numerical values, 248
Beam transverse vibration
Euler-beam theory, 74–75
Euler–Bernoulli beam assumptions, 75–76
geometrical/essential boundary conditions, 80–81
motion equations derivation, 77–79
normal stress distribution, 76–77
Bigham, 122
Biological species detection, NMCS
mathematical modeling
layer positions, 401–402
Lennard–Jones potential formulation, 403
monolayer arrangement, 403–404
potential energy, microcantilever beam, 404–405
total kinetic energy, 402
motion equation
Hamilton's principle, 405
time-dependent, 406
numerical simulation
error percentage comparison, 409
frequency response, plain silicon microcantilever, 407–408
Lennard-Jones constants, 407
linear and nonlinear frequency response, 408–409
Boron nitride nanotubes (BNNT)
vs. CNTs, 423
molecular structure, 422
shear stress, 453
synthesis, 420
theory, 423–424
Bounded-input-bounded-output (BIBO) stability, 469–470

Calculus of variations
concept
function and functional, 36, 38
and infinitesimal displacements, 36–37
variation, definition, 37–38

functional constrained minimization
Euler equation, 45
Lagrange multiplier, 44
stationary conditions, 43
fundamental theorem
boundary condition, 40–43
Euler equations, 39
Taylor's series, 39–40
mathematical tool, 35
operator δ properties, 38
Capacitance bridge network, 302–303
Capacitive readout method, NMCS, 365–366
Carbon nanotubes (CNTs). *See also* Electronic textiles, CNT composites
description, 420
electrical properties, 422
probe, TEM images, 421
shear stress, 453
Chemical vapor deposition (CVD), 411, 421
Compensation techniques
control schemes, actuators position, 180–181
feedforward and feedback controllers, 179
Constitutive-based hysteresis model
curve alignment, 175
memory-dominant
actuator response, triangular input signals, 173
ascending and descending curves, 172–173
exponential expression, 175
hysteresis path, 177
model response, memory units, 178
n internal loop response, 176–177
PI *vs.* memory-based model, 179, 180
properties, 172
vs. phenomenological approaches, 170
turning points recording, 174–175
wiping-out effect, 175, 176
Constitutive constants
coefficients
coupling, 146–147
crystallographic axes, 143
dielectric constants, 145
elastic stiffness, 147–148
physical origin, 142
piezoelectric shunting, 145–146
strain constants, 143–144
voltage constants, 144–145
relationships
electric field, 142
matrix forms, 140–141
transverse isotropic, 141
Constitutive models
electric displacement, 134
Maxwell equation, 135
nonlinear characteristics
creep, 139–140
hysteretic, 139
relations
linear constitutive equations, 137
material constants definition, 138
piezoelectricity and material constants, 139
potential energy, 135–136
total energy density, 136
Continuum level elasticity model, 451
Controller bandwidth assessment
approximations and tracking control results, 258, 259
four-mode actuator model, 257–258
steady-state tracking error comparison, 258, 260
Control observer design
closed- and open-loop system, 253–254
pole optimal location, 255
state observer errors, 255, 256
state-space controller/observer diagram, 256
tracking, steady-state response, 256–257
Coulomb electrostatic energy, 450
Coupled flexural-torsional vibration analysis, NMCS
assumed mode model expansion
comparison functions, 395–396
frequency equation, 396–397
Galerkin approximation, 395
dynamic system modeling
curvature and position vector, 389–390
Euler angle rotations, 388
gyroscopic effect, 388
Lagrangian expression, 391–392
motion equation, 390
strain tensor, 390
total potential energy, 391–392
fully symmetric uniform beam, 393–394
inextensible beam, 394–395
longitudinal vibration, 393
numerical simulations
natural frequency, 397–398
three nonlinear natural frequencies, 399, 400
1 V chirp excitation signal experimental result, 398–399

Curve alignment, 175

Degrees-of-freedom (DOFs), 11, 319
Delayed-resonator (DR) absorber
AMM, 246
beam-absorber-exciter system
configuration, 245
numerical values, 248
combined system stability, 247–248
control and variable parameters, 244–245
experimental setup, 248
feedback laws, 246–247
Laplace domain transformation, 243
motion governing equation, 242
root locus plot, 244
simulations and comparison, 248–250
Discrete systems vibration
damping ratio, modal, 27
3DOF system, 25
modal frequency response, 27–28
natural frequencies, 26
Distributed-parameter systems
eigenvalue problem, continuous systems
eigenfunctions expansion method, 100–105
equations and separable solution, 87–97
normal modes analysis, 97–100
equilibrium state and kinematics, deformable body
differential equations, 56–58
strain–displacement relationships, 58–62
stress–strain relationships, 62–64
examples, continuous systems
bar longitudinal vibration, 70–74
beam transverse vibration, 74–81
plate transverse vibration, 81–86
virtual work, deformable body
divergence theorem, 65
Hamilton's principle, 64
normal surface vector, 65–66
potential energy, 69
surface forces, 67
vibration-control systems, 68
Dynamic mode frequency response, 362
Dynamic system, coupled flexural-torsional vibration analysis
curvature and position vector, 389–390
Euler angle rotations, 388
gyroscopic effect, 388
Lagrangian expression, 391–392
motion equation, 390
strain tensor, 390
total potential energy, 391–392

Eigenfunction expansion method
AMM, 102–104
comparison/admissible functions, 100
convergence issues, 104–105
eigensolution and discretization, 101–102
expansion theorem, 100–101
Eigenvalue problem, continuous system
boundary conditions, 86–87
eigenfunctions expansion method
AMM, 102–104
comparison/admissible functions, 100
convergence issues, 104–105
eigensolution and discretization, 101–102
expansion theorem, 100–101
equations and separable solution
bar axial vibration, 88–89
beam transverse vibration, 91–93
1D vibration problems., 96–97
eigenfrequency equation, 90
plate transverse vibration, 93–96
spatial and temporal coordinates, 86–87
normal modes analysis
orthogonality conditions, 97–100
self-adjoint functions, 97
Electronic textiles, CNT composites
concept, 455
fabric sensors, electrospinning
characterization, nonwoven, 459–460
nonwoven processing, 459
and plain polymer sensors response, 460–461
nonwoven fabrics fabrication
electrospinning, polymer melt, 456–458
polymer/CNT melt preparation, 456
Electrorheological (ER) fluids
damper, 121
definition, 120
flow motion, 120–121
Energy-dispersive x-ray spectroscopy (EDX), 411
Engineering applications, piezoelectric material
electromechanical transducers, 148
miniature motors
mechanical displacement, 150
PZT-based, 151
motion magnification, piezoceramic actuation
displacement amplification, 149
sub-nanometer resolution, 150
piezoceramics, mechatronic systems, 149

Equilibrium points/states, 468–469
Equilibrium state and kinematics, deformable body
  differential equations
    arbitrary deformable continuum, 58
    normal/shear stress, 56
    stress field components, 56–57
  strain–displacement relationships
    components, 61–62
    Eulerian strain, 60
    rectangular parallelepiped continuum, 59
  stress–strain constitutive relationships
    components, 62
    compressed notation assignment, 63–64
    materials, 63
Equivalent bending moment actuation
  neutral axis calculation, 217–218
  resultant electrical virtual work, 218
  stress and strain expression, 215–217
Equivalent circuit models, sensor
  laminar
    charge and current amplifier, 231
    Poisson's effect, 232
  output voltage, 231–232
  voltage source, 230–231
ER fluids. *See* Electrorheological fluids
e-Spinning working principle, 457
Euler angle rotations, 388
Euler-beam theory, 74–75
Euler–Bernoulli beam theory, 369, 440
Euler–Bernoulli model, 216
Euler equation
  applications, 49–50
  definition, 39, 41
  optimization problem, 42

Fast Fourier transform, tip deflection, 375, 377
Focused ion beam (FIB) technique, 411
Frequency response function (FRF)
  description, 17–18
  plain epoxy and MWNT-epoxy beam, 444
  SWNT-epoxy and CF-epoxy beams, 445
Frequency transfer function (FTF), 17
FRF. *See* Frequency response function

Galerkin approximation, 102
Gibbs energy, 184
Green's theorem, 65

Hamilton principle, 51, 185, 187, 190, 202, 218, 223, 227, 372, 383
Hard switching signum function, 261–262
Heaviside function, 177, 371
Hook's law, 62, 64, 200
Hysteresis characteristics
  compensation techniques
    control schemes, actuators position, 180–181
    feedforward and feedback controllers, 179
  description, 161–162
  modeling framework
    classification, 164
    constitutive-based, 170–179
    phenomenological approach, 165–170
  nonlinearity, 163–164
  rate-independent
    local *vs.* nonlocal memories, 163
    and rate-dependent, 162–163

Indicial notation convention, 466–467
Invariant set theorems
  global, 475
  local, 474–475

Kronecker delta, 467–468

Lagrange's equations, 39, 49–51
Lagrangian system, 371–372
Laminar actuators
  active probe® vibration analysis, 205–213
  energy-based modeling
    coordinate system, 198–199
    integrant vanish, 203
    PDEs, input voltage, 203–204
    strain–displacement relationship, 199–201
    viscous and structural damping mechanism, 201–203
    voltage profile, 204–205
Laminar configuration, vibration control
  controller
    derivation, 267–268
    design, 276–278
    implementation, 268–269
  experiment
    arm base equation, 275
    beam field equations, 273
    high-level block diagram, 270, 274
    partial derivatives, 272
    results, with and without piezoelectric, 270, 274
    structure, 270, 273
  governing equation, 279–280

implementation issues, 281
mathematical modeling
base motion, 265
beam deflection, 266
kinetic energy, 265
piezoelectric actuator, 264
Matlab software programming, 280–281
numerical simulations, 269, 270–272
objectives
moving flexible beam structure, 263–264
reduced-order observer, 264
results
eight-mode model, piezoelectric actuator, 281, 283
system response, 281–282
tip displacement and controller comparison, 282, 284
stability analysis, 278–279
LaSalle's theorem, 474–475
Lead zirconate titanate (PZT)
ceramics, 118–119
material properties, 128
strains, 126
Lennard–Jones potential formulation, 403, 407
Linear and nonlinear vibration analysis, NMCS
detection methodologies, 368
experimental setup and methods
microcantilever beam properties, 375–376
velocity signal frequency response, 375, 376
geometry and inextensibility
inertial and principal axes, 369–370
Taylor's series expansion, 370
modal analysis
amplitude and natural frequency, 374–375
clamped-free beam shape, 374
Galerkin method, 373
Lagrangian approach, 373–374
motion equation
angular velocity, 370
electrical displacement vector, 371
Hamilton principle, 372
Lagrangian system, 371–372
piezoelectric layer, 373
nonlinearity addition, piezoelectric materials
constitutive equations, 380
Hamilton's principle, 383
kinetic energy, 382
total strain energy, 381–382
numerical and experimental results comparison
Fast Fourier Transform, tip deflection, 375, 377
nonlinear frequency response curves, 379–380
resonance frequency, 376
tip vibration amplitude, 377–378
reduced-order modeling
material nonlinearities effect, 385
modal time-independent coefficient, 383–384
nonlinear frequency-response equation, 384
and small-scale *vs.* large-scale, 363
validation
backbone curve, 386–387
frequency-response curves, piezoelectrically-actuated microsensor, 385–386
Linear discrete systems, 13–14
Lumped-parameters systems
discrete systems vibration
damping ratio, modal, 27
3DOF system, 25
modal frequency response, 27–28
natural frequencies, 26
linear discrete, vibration characteristics, 13–14
MDOF
classically damped, 21–22
eigenvalue problem and, 19–21
non-proportional damping, 23–25
SDOF
FRF, 17–18
time-domain response characteristics, 15–16
Lyapunov function, 261
Lyapunov stability theorems
direct method, 473
linear, 471–473
local and global, 473–474

Magnetorheological (MR) fluids
damper, 122
definition, 121–122
and ER fluids, 122–123
Mathematical model, dynamic systems
linear *vs.* nonlinear
small-amplitude vibrations, 9
structure, 10

lumped *vs.* distributed parameters
continuous system, 11
displacement variables, 12
methods, 9
Mathematical modeling
laminar configuration
base motion, 265
beam deflection, 266
kinetic energy, 265
piezoelectric actuator, 264
species detection
layer positions, 401–402
Lennard–Jones potential formulation, 403
monolayer arrangement, 403–404
potential energy, microcantilever beam, 404–405
total kinetic energy, 402
MDOF. *See* Multi-degree-of-freedom system
Memory-dominant hysteresis model
actuator response, triangular input signals, 173
ascending and descending curves, 172–173
paradigm
exponential expression, 175
hysteresis path, 177
model response, memory units, 178
n internal loops, response, 176–177
PI and memory-based model comparison, 179, 180
properties, 172
Micro and nano-positioning systems
actuators, STM systems
arrangement, 322, 323
modeling, 322, 324–329
benefit, 321–322
hysteresis, 322
multiple-axis control
piezo-flexural, coupled parallel, 336–351
three-dimension, 351–358
nanoscale control and manipulation
categories, 314–315
vs. macroscale, 313–314
nanofiber, 314
NRMs, 319–321
SPM. *See* Scanning probe microscopy
single-axis control
charge-driven circuits, 328–329
feedback, 329, 332–336
feedforward, 329–332
Micromanipulators, 156
Micro system analyzer (MSA), 363
MIMO. *See* Multiple-input-multiple-output
MM3A nanomanipulator, 320–321
Motion via analytical method, 51–52
MSA. *See* Micro system analyzer
Multi-degree-of-freedom system (MDOF)
classically damped, 21–22
eigenvalue problem and
definition, 19
modal coordinates, 21
orthogonality conditions, 20
matrix representation, 18–19
non-proportional damping
mass and stiffness matrices, 23
ODEs, 24–25
right and left eigenvalues, 23–24
Multiple-input-multiple-output (MIMO), 17

Nanoelectromechanical systems (NEMS), 74, 211, 313–314
Nanomechanical cantilever (NMC) probes. *See also* Vibration analysis
beam
cross-sectional discontinuity, 206
models, 213
uniform and discontinuous model comparison, 214
MSA-400, 211
Veeco DMASP *vs.* US penny, 212
Nanomechanical cantilever sensors (NMCS)
applications
clinical, 367
physical, 366–367
biological species detection
mathematical modeling, 401–405
motion equation, 405–406
numerical simulation, 406–410
coupled flexural-torsional vibration analysis
assumed mode model expansion, 395–397
description, 393
dynamic system modeling, 388–393
fully symmetric uniform beam, 393–394
inextensible beam, 394–395
numerical simulations and experimental results, 397–399
DNA hybridization, 360
linear and nonlinear vibration analysis
detection methodologies, 368
experimental setup and methods, 375
geometry and inextensibility, 369–370
modal analysis, 373–375

motion equation, 370–373
numerical and experimental results comparison, 375–379
piezoelectric materials nonlinearity addition, 379–383
reduced-order modeling, 383–385
and small-scale *vs.* large-scale, 363
operation
dynamic mode frequency response measurement, 362
microcantilever biosensor, functionalized surface, 361
static mode deflection detection method, 361–362
signal transduction methods
capacitive, 365–366
optical, 363–364
piezoelectric, 365
piezoresistive, 364–365
ultrasmall mass detection, active probes
experimental setup and procedure, 411–412
identification algorithm and sensitivity study, 412–417
Nanoobject manipulation, 314
Nano-positioning systems, multiple-axis PZT
piezo-flexural, parallel
closed-loop control, 348–351
configuration and observations, 339
controller design, 344–345
description, 336
nonlinear crosscoupling, 340–342
Physik Instrumente P-733.2CL, 339–340
proportional-integral (PI) control, 342–343
robust adaptive control, 343–344
soft switching mode control, 345–348
and STM operation, 339
three-dimension, model and control
high-speed laser-free AFM, 352, 354–358
surface topography tracking, 351–353
Nanorobotic manipulation (NRM)
3D space, 318–319
MM3A nanomanipulator, 320–321
Nanotubes-based composites
continuum level elasticity model, 447, 448, 451
fabrication, 434–436
forced vibration
impact test, 442
results, 443, 446
sinusoidal sweep test, 442–445
free vibration
beam length, damped natural frequency, 436–439
damping ratio, beam length, 438–440
experimental setup, 436
loss modulus, 441
storage modulus, 440–441
interphase zone control
arbitrary levels, 447
definition, 446
interatomic force, 447
representative volume element (RVE), 447–448
molecular dynamic simulations
nonbonded atoms interaction, 450
potential energy, 449–450
SWCNT-PVDF and BNNT-PVDF, 448–449
numerical results
axial normal stress, 452–454
BNNT-PVDF and CNTPVDF, 451–452
continuum level model, 452
shear stress, 453–454
vibration damping and control, fabrication
epoxy, 435–436
SEM images, 434–435
Newtonian approach, 9, 48
Newton's law, 45
NMCS. *See* Nanomechanical cantilever sensors

Ordinary differential equations (ODEs), 11, 12, 22, 24, 25

Parallel-kinematics, 339
Partial differential equations (PDEs), 12, 13
Phenomenological hysteresis models
modified PI
experimental and identified model response, 170, 171
modeling error comparisons, 170, 172
Physik Instrumente P-753.11c PZT-driven nano-positioner setup, 168–169
primary backlash operators, 168
threshold values, 170
PI
backlash operator, 166
drawback, 168
threshold and weight values, 167

Preisach model, 165–166
Physical principles, piezoelectric materials
actuated microcantilevers
DNA detection, 157
species detection, 156–157
actuators and sensors
configurations, 151–154
PZT inertial actuators, 154–156
constitutive constants
coefficients, 142–148
relationships, 140–142
constitutive relations
electrical potential energy, 136
linear constitutive equations, 137
material constants definition, 138
piezoelectric and material constants relationship, 139
potential energy, 135
definitions, 134–135
engineering applications
high precision miniature motors, 150–151
motion magnification strategies, 149–150
piezoceramics, mechatronic systems, 149
PZT materials, 148
micromanipulators, 156
nonlinear characteristics
creep, 139–140
hysteretic nonlinearity, 139
piezoelectricity
crystallographic structure, 132–133
polarization and piezoelectric effects, 130–131
translational nano-positioners, 158
Physik Instrumente P-753.11c PZT-driven nano-positioner setup, 168–169
Piezoelectric actuation, 2D
energy-based modeling
kinetic energy, 222–223
Kirchhoff plate, 219
plate transverse vibration, PDE, 223
stress–strain relationships, 220
uniform plate geometry, 220–222
equivalent bending moment
vs. 1D expression, 225–226
expression, plate, 224
stress–strain state, 224
Piezoelectric-based systems modeling
actuators, axial/stacked configuration
external forces virtual work, 186
external load, 189–192
no external load, 186–189
potential and kinetic energies, 185
vibration analysis, 192–198
2D piezoelectric actuation
energy-based, 219–223
equivalent bending moment generation, 224–226
preliminaries and assumptions, 183–184
sensors
equivalent circuit, 230–232
laminar, 229–230
stacked, 227–229
stress field, 226
transverse (bender) configuration
active probe®, vibration analysis, 205–213
bending moment actuation generation, 213–218
laminar, energy-based, 198–205
Piezoelectricity
applications
ceramic and polymeric forms, 118–119
natural and synthetic, 118
behavior and constitutive models
axial and laminar configurations, 116–117
coupling, 118
electrical and mechanical field interaction, 117–118
crystallographic structure, piezoelectric materials
piezoceramics, 132
Weiss domains, 133
definition, 116
piezoelectric effects
direct and converse, 130–131
electric polarization, 130
Piezoelectric laminar sensors, 229–230
Pin-force model, 216
Plate transverse vibration
biharmonicoperator, 84–85
flexural rigidity, 84
motion equation derivation, 82
piezoelectric sensors, 81–82
shear deformation, 86
stress–strain relationships, 83
uniform rectangular plate, 85
Poisson's ratio, 63
Polyvinylidene fluoride (PVDF) copolymers, 421–422
Prandtl–Ishlinskii (PI) hysteresis operator model
backlash operator, 166

modified
experimental and identified model response, 170, 171
modeling error comparisons, 170, 172
Physik Instrumente P-753.11c PZT-driven nano-positioner setup, 168–169
primary backlash operators, 168
threshold values, 170
weight values, 167
Preisach hysteresis model, 165–166
Preliminaries and definitions
autonomous and nonautonomous systems, 464
divergence theorem, 465
gradient operator, 464–465
invariant set and total differential, 464
linearization, 465–466
local and global positive definite function, 463–464
Lyapunov function and radially unbounded function, 464
2-norm and ∞–norm, 463
PZT. *See* Lead zirconate titanate

Rate-independent hysteresis
local *vs.* nonlocal memories, 163
and rate-dependent, 162–163
Reduced-order modeling, linear and nonlinear vibration analysis
material nonlinearities effect, 385
modal time-independent coefficient, 383–384
nonlinear frequency-response equation, 384
Representative volume element (RVE), 447–448
Resistive-inductive (R-L) circuit, 294
Resonance frequency, 362
Routh–Hurwitz method, 239

Scanning electron microscope (SEM), 321, 367, 435
Scanning probe microscopy (SPM)
AFM. *See* Atomic force microscope
applications, 315
STM
description, 315
electron density, 315–316
operation principle and image, 316
space imaging, 317
tracking controller, 317–318
Scanning tunneling microscope (STM). *See also* Scanning probe microscopy (SPM)
arrangement, piezoelectric actuators, 322, 323
piezoelectric actuators modeling
effective and tip mass, 324–325
error values, 329
hysteresis relation, 325–326
hysteretic and dynamic behaviors, 324–325
input/output hysteresis, 328
low-rate and high-rate response, 327
mathematical model, 325
stiffness and natural frequency, 326
working frequency, 322, 324
SDOF. *See* Single-degree-of-freedom systems
Self-sensing actuation, piezoelectric
actuator capacitance, 303
adaptation strategy
compensatory self-sensing mechanism, 304–305
constant forgetting factor, 305
modified mechanism, 305–306
capacitance bridge network, 303
implementation, 303
mass detection application
implementation, 307–308
result, 309
setup, 306–307
Shape memory alloys (SMA)
applications, 124
physical principles and properties
atomic rearrangement and crystallographic changes, 124
shape change and deformation, 123
Signal transduction methods, NMCS
capacitive readout, 365–366
optical
AFM, 363–364
MSA 400 setup, 364
piezoelectric, 365, 366
piezoresistive, 364–365
Single axis PZT, nano-positioning system
charge-driven circuits, 328–329
feedback control
frequencies high/low, 334
perturbation estimation, 335–336
real-time, 337
sliding mode, 334–335
trajectory tracking, 332, 334, 338

feedforward control
inverse modelbased, 329, 330
multiple-frequency trajectories, 330–332, 333
tracking error values, 331–332, 333
Single-degree-of-freedom systems (SDOF)
equilibrium state, 14
FRF
normalized frequency response, 18
transfer function, 17
mass-spring system, 288–289
time-domain response characteristics
damped natural frequency, 16
equation, 15
SMA. *See* Shape memory alloys
Smart structure, piezoelectric material
active, 4
definition and attributes, 3–4
potential applications, 4–5
SPM. *See* Scanning probe microscopy
Spring-damper compliant adaptor. *See* Stacked actuators
Stability, dynamic
concept
asymptotic and exponential, 470–471
definition, 470
internal and external behavior, 469
structural, 471
theorems
local and global invariant set, 474–475
Lyapunov local and global, 471–474
Stacked actuators
external load
input voltage, 190–191
potential and kinetic energies, 189–190
stiffness definition, 191
tip deflection *vs.* input voltage, 192
no external load
constants relationships, 188–189
mechanical virtual work, 186–187
PDEs, 188
Stacked sensors
force and acceleration, 228–229
modeling and preliminaries
axial configuration, 227
charge generation, 228
open circuit configuration, 228
State-space controller design
first- and second-order
control law, 252–253
time derivatives, 259–260
hard switching signum function, 261–262
Lyapunov function, 261
modified state-space equation, 258
phase portrait comparison, 263
simulation results, 253, 254
sliding mode, 262–263
steady-state error amplitude, 262
tracking error, 252
Static mode deflection detection method
Poisson's effect, 362
Stoney's formula, 361–362
STM. *See* Scanning tunneling microscope
Stoney's formula, 361–362
Switched-stiffness concept
control law, 290
experimentation
actual position, observed position and relay control, 301, 303
frequency domain response, 300–301
setup, 298–300
velocity obtainment, 301–301
high stiffness state, 286–287
limitations, 287–288
piezoelectric materials
a beam tip displacement response, 296
control law, 295
different circuit configurations, 294–295
elastic stiffness values, 293
magnitude tracking, 296–297
resistive (R)/resistive-inductive (R-L) circuit, 294
results, phase tracking observer, 298
simulated *vs.* observed velocities, 296, 297
real-time implementation
parameters, SDOF system, 292
performance, velocity observer, 292, 293
position and velocity observation error, 292, 294
velocity observer design, 290–292
SDOF mass-spring system, 288–289

Taylor's series, 39, 45
Theorem proofs, 477–485
Timoshenko theory, 74
Translational positioners, 158
Tunnel current, 315

Ultrasmall mass detection, active probes
experimental setup and procedure
EDX, 412
MSA-400 microsystem analyzer, 412
resonant frequencies, 412, 413

FIB technique, 411
identification algorithm and sensitivity study
forward and backward approaches, 413
mass measurement error *vs.* parametric uncertainty percentage, 416–417
modes, 414
resonant frequencies, before/after mass deposition, 414–415

van der Waals energy, 450
Variation mechnics
control
absorption *vs.* control, 7
classifications, 8
isolation *vs.* absorption, 6–7
modeling approaches, 5–6
equations deriving steps, 51–52
Euler equation application
Hamilton's principle, 50
Lagrange's equations, 49–50
work-energy theorem and
ariable resultant force, 45
extended Hamilton's principle, 47
Newtonian approach, 48
potential energy, 46
Vibration analysis
axial actuators. *See* Axial piezoelectric actuators, vibration analysis
NMC active probe®
applications, 205–206
beam, cross-sectional discontinuity, 206
modal frequency response comparisons, 215
model development, 207–211
theoretical *vs.* experimental, 211–214
Vibration control system, actuators and sensors
absorption concept
active, 237–242
delayed, 242–250
passive and active structure, 235
resonator design, 235–236
active
axial configuration, 252–263
laminar actuators, 263–284
notion, 233–234
self-sensing actuation
adaptation strategy, capacitance, 304–306
mass detection application, 306–309
preliminaries, 302–303
semiactive
real-time implementation, 290–293
switched-stiffness concept, 286–290

Wheatstone's bridge circuit, 364–365
Wiping-out effect, 175, 176
Work-energy theorem
ariable resultant force, 45
extended Hamilton's principle, 47
Newtonian approach, 48
potential energy, 46

Young's modulus, 222

About the Author

Nader Jalili, PhD, is currently an Associate Professor in the Department of Mechanical and Industrial Engineering at Northeastern University (Boston, MA). Before joining Northeastern in 2009, he was Associate Professor of Mechanical Engineering and Founding Director of Clemson University Smart Structures & NEMS Laboratory. His research interests and expertise include piezoelectric-based actuators and sensors, dynamic modeling and vibration control of distributed-parameters systems, dynamics and control of microelectromechanical and nanoelectromechanical actuators and sensors and control and manipulation at the nanoscale. Dr. Jalili is currently, Associate Editor of ASME *Journal of Dynamic Systems, Measurement and Control*, founding Chair of ASME Technical Committee on Vibration and Control of Smart Structures, and member of numerous ASME committees including Technical Committee on Vibration and Sound (TCVS). As the past the Technical Editor of IEEE/ASME *Transactions on Mechatronics* and Chair and Vice-Chair of the Vibration and Noise Control Panel of the ASME, he is the author/co-author of more than 270 technical publications including over 85 journal papers. He is the recipient of many national and international awards including, but not limited to, the 2003 CAREER Award from the National Science Foundation, the 2002 Ralph E. Powe Junior Faculty Enhancement Award from Department of Energy, Recipient of 2009 Clemson University College of Engineering and Science (CoES) McQueen Quattlebaum Faculty Achievement Award for exemplary leadership in the engineering profession, 2008 Clemson University CoES Murray Stokley Award for Excellence in Teaching (the highest distinctions awarded to engineering faculty) and 2007 Clemson University Outstanding Young Investigator of the Year. Dr. Jalili obtained his BS and MS degrees, both with first class honors, from Sharif University of Technology, Tehran, Iran in 1992 and 1995, respectively, and his Doctorate in Mechanical Engineering from University of Connecticut (Storrs CT, USA) in 1998.